

Handbook of textile fibre structure

The Textile Institute and Woodhead Publishing

The Textile Institute is a unique organisation in textiles, clothing and footwear. Incorporated in England by a Royal Charter granted in 1925, the Institute has individual and corporate members in over 90 countries. The aim of the Institute is to facilitate learning, recognise achievement, reward excellence and disseminate information within the global textiles, clothing and footwear industries.

Historically, The Textile Institute has published books of interest to its members and the textile industry. To maintain this policy, the Institute has entered into partnership with Woodhead Publishing Limited to ensure that Institute members and the textile industry continue to have access to high calibre titles on textile science and technology.

Most Woodhead titles on textiles are now published in collaboration with The Textile Institute. Through this arrangement, the Institute provides an Editorial Board which advises Woodhead on appropriate titles for future publication and suggests possible editors and authors for these books. Each book published under this arrangement carries the Institute's logo.

Woodhead books published in collaboration with The Textile Institute are offered to Textile Institute members at a substantial discount. These books, together with those published by The Textile Institute that are still in print, are offered on the Woodhead website at www.woodheadpublishing.com. Textile Institute books still in print are also available directly from the Institute's website at www.textileinstitutebooks.com.

A list of Woodhead books on textile science and technology, most of which have been published in collaboration with The Textile Institute, can be found on pages xv–xx.

Woodhead Publishing in Textiles: Number 88

Handbook of textile fibre structure

Volume 1: Fundamentals and
manufactured polymer fibres

Edited by
S. J. Eichhorn, J.W.S. Hearle, M. Jaffe and
T. Kikutani



The Textile Institute



CRC Press
Boca Raton Boston New York Washington, DC

WOODHEAD PUBLISHING LIMITED
Oxford Cambridge New Delhi

Published by Woodhead Publishing Limited in association with The Textile Institute
Woodhead Publishing Limited, Abington Hall, Granta Park, Great Abington,
Cambridge CB21 6AH, UK
www.woodheadpublishing.com

Woodhead Publishing India Private Limited, G-2, Vardaan House, 7/28 Ansari Road,
Daryaganj, New Delhi – 110002, India

Published in North America by CRC Press LLC, 6000 Broken Sound Parkway, NW,
Suite 300, Boca Raton, FL 33487, USA

First published 2009, Woodhead Publishing Limited and CRC Press LLC

© 2009, Woodhead Publishing Limited

The authors have asserted their moral rights.

This book contains information obtained from authentic and highly regarded sources. Reprinted material is quoted with permission, and sources are indicated. Reasonable efforts have been made to publish reliable data and information, but the authors and the publishers cannot assume responsibility for the validity of all materials. Neither the authors nor the publishers, nor anyone else associated with this publication, shall be liable for any loss, damage or liability directly or indirectly caused or alleged to be caused by this book.

Neither this book nor any part may be reproduced or transmitted in any form or by any means, electronic or mechanical, including photocopying, microfilming and recording, or by any information storage or retrieval system, without permission in writing from Woodhead Publishing Limited.

The consent of Woodhead Publishing Limited does not extend to copying for general distribution, for promotion, for creating new works, or for resale. Specific permission must be obtained in writing from Woodhead Publishing Limited for such copying.

Trademark notice: Product or corporate names may be trademarks or registered trademarks, and are used only for identification and explanation, without intent to infringe.

British Library Cataloguing in Publication Data

A catalogue record for this book is available from the British Library.

Library of Congress Cataloging in Publication Data

A catalog record for this book is available from the Library of Congress.

Woodhead Publishing ISBN 978-1-84569-380-0 (book)

Woodhead Publishing ISBN 978-1-84569-650-4 (e-book)

CRC Press ISBN 978-1-4398-0119-2

CRC Press order number N10017

The publishers' policy is to use permanent paper from mills that operate a sustainable forestry policy, and which has been manufactured from pulp which is processed using acid-free and elemental chlorine-free practices. Furthermore, the publishers ensure that the text paper and cover board used have met acceptable environmental accreditation standards.

Typeset by Replika Press Pvt Ltd

Printed by TJ International Limited, Padstow, Cornwall, UK

Contents

Contributor contact details *xi*

Part I Introduction

1	Fibre structure: its formation and relation to performance J W S HEARLE, University of Manchester, UK	3
1.1	Introduction	3
1.2	Formation of fibres	5
1.3	Development of ideas of fibre structure	10
1.4	Structure and performance	16
1.5	Conclusion: fibres as a special class of materials	18
1.6	Future trends	19
1.7	Sources of further information	20
1.8	References	20
2	Spectroscopic characterisation of polymer fibres S J EICHHORN, University of Manchester, UK	22
2.1	Introduction	22
2.2	Historical perspectives on spectroscopic characterisation of polymers	22
2.3	Infrared spectroscopy of polymers	23
2.4	Raman spectroscopy of polymers	28
2.5	Nuclear magnetic resonance spectroscopy of polymers	34
2.6	Discussion and conclusions	39
2.7	References	40
3	X-ray analysis of partial crystalline fibre structure P ZUGENMAIER, Clausthal University of Technology, Germany	46
3.1	Introduction	46
3.2	Diffraction	48

3.3	Theoretical considerations	54
3.4	Data reduction	64
3.5	Structure determination	70
3.6	Crystallinity and disorder	87
3.7	Reflection profile, crystallite size and disorder	98
3.8	Preferred orientation	106
3.9	Conclusions	114
3.10	References	116

4	Analysis of fibres using microscopy L A DONALDSON, Scion, New Zealand	121
---	--	-----

4.1	Introduction	121
4.2	Optical microscopy	121
4.3	Electron microscopy	130
4.4	Infrared techniques (FTIR and Raman)	135
4.5	Scanning probe microscopy	136
4.6	X-ray tomography and other techniques	137
4.7	Identification of natural and artificial fibres by microscopy	138
4.8	Future trends	140
4.9	Acknowledgements	140
4.10	References	140

Part II Manufactured polymer fibres

5	Structure development in synthetic fiber production T KIKUTANI, Tokyo Institute of Technology, Japan	157
5.1	Introduction	157
5.2	Basic concept of fiber structure and its formation in fiber processing	158
5.3	Fundamental mechanism of structure development	160
5.4	Analyses of structure development behavior in fiber processing	170
5.5	Conclusions and future trends	176
5.6	Sources of further information and advice	177
5.7	References	177

6	The structure of polyester fibers A J EAST, Medical Device Concept Center, USA	181
---	---	-----

6.1	Introduction	181
6.2	The main types of polyester	185
6.3	Chemistry of PET	189
6.4	Chemistry of PBT	198
6.5	Chemistry of PTT or PPT	200

6.6	Chemistry of PEN	206
6.7	Chemistry of aliphatic polyesters	209
6.8	Chemistry of disposable fibers	213
6.9	Melt-spinning polyester fibers and associated fiber processing	215
6.10	Effect of fibre structure on properties	222
6.11	Conclusions	223
6.12	Sources of further information	225
6.13	References	225
7	Polyamide fiber formation: structure, properties and characterization N VASANTHAN, Long Island University, USA	232
7.1	Introduction	232
7.2	Fiber formation	233
7.3	Characterization	240
7.4	Influence of microstructure on properties	248
7.5	Conclusions	251
7.6	Future trends	252
7.7	References	252
8	Synthesis, properties and structure of polylactic acid fibres M MOCHIZUKI, Kyoto Institute of Technology, Japan	257
8.1	Introduction	257
8.2	Synthesis and properties of polylactic acid	258
8.3	Properties and structure of polylactic acid fibres	263
8.4	Functional properties of polylactic acid fibres	266
8.5	Applications	272
8.6	Conclusions	274
8.7	References	274
9	The structure of polyolefin fibres R R MATHER, Heriot-Watt University, UK	276
9.1	Introduction	276
9.2	Structures and configurations of polyolefin chains	277
9.3	Arrangements of polyolefin chains	280
9.4	Crystalline structures	282
9.5	Crystal morphology	284
9.6	Fibre profile	285
9.7	Processing–structure relationships	294
9.8	Plasma treatments and auxetic fibres	299
9.9	Conclusion	300

viii	Contents	
9.10	Sources of further information	301
9.11	References	301
10	The structure of acrylic, polyvinylalcohol and polyvinylchloride fibers H C KIM, Chonbuk National University, South Korea	305
10.1	Acrylic and modacrylic fibers	305
10.2	Polyvinylalcohol fiber	312
10.3	Polyvinylchloride fiber	318
10.4	References	323
11	The processing, structure and properties of elastomeric fibers J U Otaigbe and S A Madbouly, The University of Southern Mississippi, USA	325
11.1	Introduction	325
11.2	Polyurethane fibers	327
11.3	Production of polyurethane fibers	329
11.4	Polyester copolymer fibers	336
11.5	Styrene copolymers elastomeric fibers	337
11.6	Polyolefin elastomeric fibers	340
11.7	Elastomeric polymer alloy fibers	342
11.8	Conclusions and future trends	349
11.9	Acknowledgements	349
11.10	References	349
12	Production and properties of high-modulus and high-strength polyethylene fibres I M WARD, University of Leeds, UK and P J LEMSTRA, Technical University Eindhoven, The Netherlands	352
12.1	Introduction	352
12.2	Melt spun high modulus-polyethylene fibres	353
12.3	Fibres based on ultra high-molecular weight polyethylene	372
12.4	References	388
13	Structure and properties of aramid fibres S VAN DER ZWAAG, Technical University Delft, The Netherlands	394
13.1	Introduction	394
13.2	Chemistry of aramid fibres	395
13.3	Relationship between spinning conditions and resulting microstructure	395
13.4	Relationship between microstructure and resulting properties	403

13.5	Future trends	409
13.6	Acknowledgements	409
13.7	References	410
14	The structure and properties of high-modulus, high-tenacity Vectran™ fibres Y YAMAMOTO and J NAKAGAWA, Kuraray Co. Limited, Japan	413
14.1	Introduction	413
14.2	Thermotropic liquid crystal and its fibre formation	414
14.3	Thermotropic liquid crystal fibre (polyarylate fibre)	417
14.4	High initial modulus type	423
14.5	Properties of polyarylate fibre	423
14.6	Examples using the characteristics of Vectran™	425
14.7	Conclusion	428
14.8	References	428
15	The structure of high-modulus, high-tenacity (poly- <i>p</i> -phenylenebenzobisoxazole) fibres T KITAGAWA, Toyobo Co., Ltd, Japan	429
15.1	Introduction	429
15.2	Synthesis and polymerization	430
15.3	Molecular design and theoretical modulus	430
15.4	Fibre structure	430
15.5	PBO fibre structure under deformation	439
15.6	Future trends	449
15.7	Conclusions and comments	450
15.8	References and further reading	451
16	The structure of high-modulus, high-tenacity PIPD 'M5' fibre J W S HEARLE, University of Manchester, UK	455
16.1	The problem of lateral weakness	455
16.2	Chemistry of PIPD	455
16.3	Crystal structure	456
16.4	Modulus calculations	458
16.5	Coarse structure and conclusion	459
16.6	References	459
17	Electrospinning and its influence on the structure of polymeric nanofibers K GARG, S A SELL and G L BOWLIN, Virginia Commonwealth University, USA	460
17.1	Introduction	460

x	Contents	
17.2	Types of fibers produced by electrospinning	469
17.3	Fiber structure	476
17.4	Influence of structure on properties	478
17.5	Future trends and conclusion	480
17.6	Sources of further information and advice	481
17.7	References	481
18	Melt spinning and other techniques for the production of nanofibers and microfibres Y OHKOSHI, Shinshu University, Japan	484
18.1	Introduction	484
18.2	Conjugated melt spinning	486
18.3	Melt spinning of polymer blends	486
18.4	Laser-heated flow drawing	486
18.5	Nanofibres made by conjugated melt spinning and laser-heated flow drawing	488
18.6	Conclusion	489
18.7	References	490
	<i>Index</i>	491

Contributor contact details

(* = main contact)

Editors

Dr Stephen J. Eichhorn
Materials Science Centre
School of Materials
Grosvenor Street
University of Manchester
Manchester M1 7HS
UK

E-mail: s.j.eichhorn@manchester.ac.uk

John W. S. Hearle
Emeritus Professor of Textile
Technology
University of Manchester
UK
and
The Old Vicarage
Mellor
Stockport SK6 5LX
UK

E-mail: johnhearle@hearle.eclipse.co.uk

Professor Mike Jaffe
Department of Biomedical
Engineering
New Jersey Institute of Technology
Medical Device Concept
Laboratory
111 Lock Street
Newark, NJ 07103
USA

Professor Takeshi Kikutani
Graduate School of Science and
Engineering
Department of Organic and
Polymeric Materials
Tokyo Institute of Technology
2-12-1-S8-32
O-okayama
Meguro-ku
Tokyo 152-8552
Japan

E-mail: kikutani.t.aa@m.titech.ac.jp

Chapters 1 and 16

John W. S. Hearle
Emeritus Professor of Textile
Technology
University of Manchester
UK
and
The Old Vicarage
Mellor
Stockport SK6 5LX
UK

E-mail: johnhearle@hearle.eclipse.co.uk

Chapter 2

Dr Stephen J. Eichhorn
Materials Science Centre
School of Materials
Grosvenor Street
University of Manchester
Manchester M1 7HS
UK

E-mail: s.j.eichhorn@manchester.ac.uk

Chapter 3

Dr Peter Zugenmaier
Clausthal University of Technology
D-38678 Clausthal-Zellerfeld
Germany

E-mail: zugenmaier@pc.tu-clausthal.de

Chapter 4

Dr Lloyd Donaldson
Scion
Private Bag 3020
Rotorua
New Zealand
E-mail lloyd.donaldson@scionresearch.com

Chapter 5

Professor Takeshi Kikutani
Graduate School of Science and
Engineering
Department of Organic and
Polymeric Materials
Tokyo Institute of Technology
2-12-1-S8-32
O-okayama
Meguro-ku
Tokyo 152-8552
Japan

E-mail: kikutani.t.aa@m.titech.ac.jp

Chapter 6

Professor Anthony J East
Department of Biomedical
Engineering
Medical Device Concept Center
111 Lock Street
Newark, NJ 07013
USA

E-mail: tony east@verizon.net

Chapter 7

Dr Nadarajah Vasanthan
Polymer and Physical Chemistry
Long Island University
Brooklyn, NY 11201
USA

E-mail: Nadarajah.Vasanthan@liu.edu

Chapter 8

Dr Masatsugu Mochizuki
Kyoto Institute of Technology
Japan

E-mail: mmochizuki@kit.ac.jp

Chapter 9

Dr Robert R. Mather
School of Engineering and Physical
Sciences
Heriot-Watt University
Edinburgh EH14 4AS
UK

E-mail: R.R.Mather@hw.ac.uk

Chapter 10

Professor Hwan Chul Kim
Department of Organic and Fiber
Materials
Chonbuk National University
Dukjin-Dong, Dukjin-Gu
Chonju, Chonbuk
561-756
South Korea

E-mail: hckim@chonbuk.ac.kr

Chapter 11

Professor Joshua U. Otaigbe* and
Dr Samy A. Madbouly
School of Polymers and High
Performance Materials
The University of Southern
Mississippi
118 College Drive #10076
Hattiesburg, MS 39406
USA

E-mail: Joshua.Otaigbe@usm.edu

Chapter 12

Professor Ian M Ward*
University of Leeds
School of Physics and Astronomy
Leeds LS2 9JT
UK

E-mail: i.m.ward@leeds.ac.uk

Professor Piet Lemstra
Technical University Eindhoven
Chemical Engineering and
Chemistry
PO Box 513
5600 MB Eindhoven
The Netherlands

E-mail: P.J.Lemstra@tue.nl

Chapter 13

Professor Sybrand van der Zwaag
Faculty of Aerospace Engineering
Technical University Delft
Kluyverweg 1, 2629 HS Delft
The Netherlands

E-mail: S.vanderZwaag@tudelft.nl

Chapter 14

Youichi Yamamoto and Junyo
Nakagawa
Fibre Materials Planning and
Development Department
Production Technology
Development Centre
Kuraray Co. Ltd
7471 Tamashimaotoshima
Kurashiki
Okayama
Japan

E-mail: YOUICHI_YAMAMOTO@
kuraray.co.jp;

Chapter 15

Dr Tooru Kitagawa
New Research & Project Planning
Group
Corporate Research Center
Toyobo Co., Ltd
Research Center
2-1-1, Katata
Otsu
Shiga 520-0292
Japan

E-mail: tooru_kitagawa@toyobo.jp

Chapter 17

Koyal Garg,* Scott A. Sell and
Gary L. Bowlin
Virginia Commonwealth University
P.O. Box 843067
Richmond
VA, 23284-3067
USA

E-mail: gargk@vcu.edu
glbowlin@vcu.edu

Chapter 18

Professor Yutaka Ohkoshi
Faculty of Textile Science and
Technology
Shinshu University
3-15-1 Tokida
Ueda
Nagano 386-8567
Japan

E-mail: yokoshi@shinshu-u.ac.jp

Woodhead Publishing in Textiles

- 1 **Watson's textile design and colour Seventh edition**
Edited by Z. Grosicki
- 2 **Watson's advanced textile design**
Edited by Z. Grosicki
- 3 **Weaving Second edition**
P. R. Lord and M. H. Mohamed
- 4 **Handbook of textile fibres Vol 1: Natural fibres**
J. Gordon Cook
- 5 **Handbook of textile fibres Vol 2: Man-made fibres**
J. Gordon Cook
- 6 **Recycling textile and plastic waste**
Edited by A. R. Horrocks
- 7 **New fibers Second edition**
T. Hongu and G. O. Phillips
- 8 **Atlas of fibre fracture and damage to textiles Second edition**
J. W. S. Hearle, B. Lomas and W. D. Cooke
- 9 **Ecotextile '98**
Edited by A. R. Horrocks
- 10 **Physical testing of textiles**
B. P. Saville
- 11 **Geometric symmetry in patterns and tilings**
C. E. Horne
- 12 **Handbook of technical textiles**
Edited by A. R. Horrocks and S. C. Anand
- 13 **Textiles in automotive engineering**
W. Fung and J. M. Hardcastle

- 14 **Handbook of textile design**
J. Wilson
- 15 **High-performance fibres**
Edited by J. W. S. Hearle
- 16 **Knitting technology Third edition**
D. J. Spencer
- 17 **Medical textiles**
Edited by S. C. Anand
- 18 **Regenerated cellulose fibres**
Edited by C. Woodings
- 19 **Silk, mohair, cashmere and other luxury fibres**
Edited by R. R. Franck
- 20 **Smart fibres, fabrics and clothing**
Edited by X. M. Tao
- 21 **Yarn texturing technology**
J. W. S. Hearle, L. Hollick and D. K. Wilson
- 22 **Encyclopedia of textile finishing**
H-K. Rouette
- 23 **Coated and laminated textiles**
W. Fung
- 24 **Fancy yarns**
R. H. Gong and R. M. Wright
- 25 **Wool: Science and technology**
Edited by W. S. Simpson and G. Crawshaw
- 26 **Dictionary of textile finishing**
H-K. Rouette
- 27 **Environmental impact of textiles**
K. Slater
- 28 **Handbook of yarn production**
P. R. Lord
- 29 **Textile processing with enzymes**
Edited by A. Cavaco-Paulo and G. Gübitz
- 30 **The China and Hong Kong denim industry**
Y. Li, L. Yao and K. W. Yeung
- 31 **The World Trade Organization and international denim trading**
Y. Li, Y. Shen, L. Yao and E. Newton

- 32 **Chemical finishing of textiles**
W. D. Schindler and P. J. Hauser
- 33 **Clothing appearance and fit**
J. Fan, W. Yu and L. Hunter
- 34 **Handbook of fibre rope technology**
H. A. McKenna, J. W. S. Hearle and N. O'Hear
- 35 **Structure and mechanics of woven fabrics**
J. Hu
- 36 **Synthetic fibres: nylon, polyester, acrylic, polyolefin**
Edited by J. E. McIntyre
- 37 **Woollen and worsted woven fabric design**
E. G. Gilligan
- 38 **Analytical electrochemistry in textiles**
P. Westbroek, G. Priniotakis and P. Kiekens
- 39 **Bast and other plant fibres**
R. R. Franck
- 40 **Chemical testing of textiles**
Edited by Q. Fan
- 41 **Design and manufacture of textile composites**
Edited by A. C. Long
- 42 **Effect of mechanical and physical properties on fabric hand**
Edited by Hassan M. Behery
- 43 **New millennium fibers**
T. Hongu, M. Takigami and G. O. Phillips
- 44 **Textiles for protection**
Edited by R. A. Scott
- 45 **Textiles in sport**
Edited by R. Shishoo
- 46 **Wearable electronics and photonics**
Edited by X. M. Tao
- 47 **Biodegradable and sustainable fibres**
Edited by R. S. Blackburn
- 48 **Medical textiles and biomaterials for healthcare**
Edited by S. C. Anand, M. Miraftab, S. Rajendran and J. F. Kennedy
- 49 **Total colour management in textiles**
Edited by J. Xin

- 50 **Recycling in textiles**
Edited by Y. Wang
- 51 **Clothing biosensory engineering**
Y. Li and A. S. W. Wong
- 52 **Biomechanical engineering of textiles and clothing**
Edited by Y. Li and D. X-Q. Dai
- 53 **Digital printing of textiles**
Edited by H. Ujiie
- 54 **Intelligent textiles and clothing**
Edited by H. Mattila
- 55 **Innovation and technology of women's intimate apparel**
W. Yu, J. Fan, S. C. Harlock and S. P. Ng
- 56 **Thermal and moisture transport in fibrous materials**
Edited by N. Pan and P. Gibson
- 57 **Geosynthetics in civil engineering**
Edited by R. W. Sarsby
- 58 **Handbook of nonwovens**
Edited by S. Russell
- 59 **Cotton: Science and technology**
Edited by S. Gordon and Y-L. Hsieh
- 60 **Ecotextiles**
Edited by M. MirafTAB and A. Horrocks
- 61 **Composite forming technologies**
Edited by A. C. Long
- 62 **Plasma technology for textiles**
Edited by R. Shishoo
- 63 **Smart textiles for medicine and healthcare**
Edited by L. Van Langenhove
- 64 **Sizing in clothing**
Edited by S. Ashdown
- 65 **Shape memory polymers and textiles**
J. Hu
- 66 **Environmental aspects of textile dyeing**
Edited by R. Christie
- 67 **Nanofibers and nanotechnology in textiles**
Edited by P. Brown and K. Stevens

- 68 **Physical properties of textile fibres Fourth edition**
W. E. Morton and J. W. S. Hearle
- 69 **Advances in apparel production**
Edited by C. Fairhurst
- 70 **Advances in fire retardant materials**
Edited by A. R. Horrocks and D. Price
- 71 **Polyesters and polyamides**
Edited by B. L. Deopura, R. Alagirusamy, M. Joshi and B. S. Gupta
- 72 **Advances in wool technology**
Edited by N. A. G. Johnson and I. Russell
- 73 **Military textiles**
Edited by E. Wilusz
- 74 **3-D fibrous assemblies: Properties, applications and modelling of three-dimensional textile structures**
J. Hu
- 75 **Medical textiles 2007**
Edited by J. Kennedy, A. Anand, M. Miraftab and S. Rajendran
- 76 **Fabric testing**
Edited by J. Hu
- 77 **Biologically inspired textiles**
Edited by A. Abbott and M. Ellison
- 78 **Friction in textiles**
Edited by B .S. Gupta
- 79 **Textile advances in the automotive industry**
Edited by R. Shishoo
- 80 **Structure and mechanics of textile fibre assemblies**
Edited by P. Schwartz
- 81 **Engineering textiles: Integrating the design and manufacture of textile products**
Edited by Y. E. El-Mogahzy
- 82 **Polyolefin fibres: Industrial and medical applications**
Edited by S. C. O. Ugbolue
- 83 **Smart clothes and wearable technology**
Edited by J. McCann and D. Bryson
- 84 **Identification of textile fibres**
Edited by M. Houck

- 85 **Advanced textiles for wound care**
Edited by S. Rajendran
- 86 **Fatigue failure of textile fibres**
Edited by M. MirafTAB
- 87 **Advances in carpet technology**
Edited by K. Goswami
- 88 **Handbook of textile fibre structure**
Edited by S. Eichhorn, J.W.S Hearle, M.Jaffe and T. Kikutani
- 89 **Advances in knitting technology**
Edited by T. Dias
- 90 **Smart textile coatings and laminates**
Edited by W.C. Smith
- 91 **Tensile failure of fibres handbook**
Edited by A. Bunsell
- 92 **Interior textiles: Design and developments**
Edited by T. Rowe
- 93 **Textiles for cold weather apparel**
Edited by J. Williams
- 94 **Modelling and predicting textile behaviour**
Edited by X. Chen
- 95 **Textiles for construction**
Edited by G. Pohl
- 96 **Engineering apparel fabrics and garments**
J. Fan and L. Hunter

Fibre structure: its formation and relation to performance

J W S HEARLE, University of Manchester, UK

Abstract: The chapter opens with a discussion of the definitions of *fibre* and the essential nature of fibres. The modes of formation of natural, regenerated, synthetic polymer, high-modulus/high-tenacity, inorganic, specialist and smart fibres are described. An account of the historical development of ideas of fibre structure starts with a consideration of the ways in which a partially ordered polymer assembly can be described. Means of investigating fibre structure are listed. The changes from earlier ideas due to acceptance of the macromolecular hypothesis around 1930 and studies of the fundamentals of polymer crystallisation in the 1950s are described. Finally, the relations between fibre structure and performance in use are outlined and the identification of fibres as a special class of material is emphasised.

Key words: fibre definitions, fibre formation, fibre types, characterisation of fibre structure, fibre performance.

1.1 Introduction

1.1.1 What are fibres?

Somewhat bizarrely to modern ears, the opening fourteenth century definition of fibre in the Oxford English Dictionary is *a lobe or portion of the liver*. The last is *dietary material that is resistant to the action of the digestive enzymes*. In between, there are definitions related to biological structures and to metaphorical usage. The first in the context of this book is Faraday's 1827 reference to *a silk fibre* and the most relevant is *a fibrous substance fit for use in textile fabrics*.

The Textile Institute (Denton and Daniels, 2002) is more specific: *textile raw material, generally characterised by flexibility, fineness and high ratio of length to thickness*. Until the second half of the twentieth century, textile fibres fell within the range of about 10 to 50 μm in diameter¹ and were longer than 1 cm. Coarser bristles and monofilaments, although woven and braided, were not regarded as fibres. Short wood fibres in paper-making pulp are too short and do not have the distinct identity to be included.

¹Although diameters are easily appreciated, a more useful measure of fineness is linear density. The standard unit is *tex* = g/km, but, due to its closeness to the older unit *denier* = g/9000 m, *dtex* = g/10000 m is widely used. The above range corresponds roughly to 1 to 25 dtex.

More recently, finer fibres of less than 1 dtex are included. Microfibres are made either by modifying the melt-spinning process or by the islands-in-a-sea method. Nanofibres are made by electro-spinning or by a large increase in the number of 'islands in the sea'. Carbon nanotubes are the most recent form of nanofibres.²

In order to be useful, textile fibres need adequate strength and stability. The major types can be classified in four groups: natural and regenerated fibres with moderate strength and breaking extension; synthetic polymer fibres with high toughness; organic and inorganic high-modulus, high-tenacity (HM-HT) fibres; and elastomeric fibres. Weak inorganic fibres, such as rock wool, are of limited use. More importantly, there are a large number of fibres with chemical, thermal, biological or other properties, which are used in protective, medical or other specialised applications. The more advanced of these are smart fibres, which have active rather than passive responses.

1.1.2 The nature of fibres

As described above, fibres are long, slender units of matter. Their component atoms are joined into molecules, which assemble in particular fine structures. The fibres for the traditional textile uses in clothing, household goods and some technical applications are all *partially crystalline, partially oriented, linear polymers*. Remarkably, they are of only six chemical types: cellulosic, protein, polyamide, polyester, polyvinyl (acrylic), and polyolefin (polypropylene). The HM-HT polymer fibres are more highly crystalline and oriented and more variable in chemistry. The inorganic fibres, glass and ceramic, may be amorphous or micro-crystalline. Carbon fibres are oriented forms of imperfect graphitic crystals.

In addition to the differences in chemistry, fibre structures depend on how they are formed. The slow growth of natural fibres under genetic control gives different structures from the fast routes of industrial production. Differences within each group, for example between cotton, wool and silk or between melt and solution spinning, lead to a variety of structures. Within each basic form, there are quantitative differences that depend on the production parameters. In addition to the major textile fibres that are discussed below and covered in this book, there are many others that have been or are still produced in smaller quantities.

²The terminology is questionable. Carbon nanotubes can be described as stiff molecules. However, they are long fine units of matter that can be assembled into yarns. In that sense, they are nanofibres.

1.2 Formation of fibres

1.2.1 Natural fibres

Cotton, which is second only to polyester in world fibre usage, forms in the seeds of cotton plants. Although perennial, cotton is grown commercially as an annual plant. Historically, cotton ranged from coarse Asiatic cottons (3 dtex, 1.5 cm) to fine Sea Island cottons (1 dtex, 5 cm), but most of the world's crop now consists of American varieties in the middle of the range.

After flowering, seeds with attached cotton fibres form within the cotton boll. At maturity the boll opens and the fibres dry. In the living seed cells, cellulose molecules grow by the addition of glucose molecules at enzyme complexes. From a structural viewpoint, the important feature is that this is virgin polymerisation, with the molecules being laid down as they are formed. Thirty molecules form at each enzyme complex and assemble into fibrils, which are the building blocks of the structure. First, a primary wall forms with the ultimate dimensions of the fibre. The bulk of the material is laid down in helical layers as a secondary wall. At maturity, there is still an open lumen at the centre of the fibre, which collapses to give a kidney-shaped fibre cross-section. Reversals in the sense of the helices cause the cotton to form a twisted ribbon on drying. The genetic evolution, which was presumably driven by the need to disperse seeds, turns out, when enhanced by cotton breeding, to give a structure from molecules to whole fibres that is ideal for many textile uses. Other vegetable fibres, such as flax, jute, hemp and sisal, which are used in textiles are reinforcements in the stems or leaves of plants. They are multicellular and have smaller helix angles than cotton.

The genetic control of wool and hair leads to even more complicated structures. The fibres grow from follicles in the skin. They are composed of many elongated cells linked by a cell membrane complex, which contains peptides. Different proteins are laid down in sequence as the cell grows. First come keratin molecules, which in their central rods have a characteristic 1A–L1–1B–L12–2A–L2–2B sequence of amino-acid residues. Keratin crystallises in an α -helical lattice, which under tension opens to extended β -sheets. The molecules assemble in a sequence of twisted pairs to form fibrils³ containing 32 molecules of two types. Terminal domains emerge into the matrix space between the fibrils, which in the next stage of growth is filled with keratin-associated proteins (KAPs). Finally, proteins form in the outer cells to give a multi-layer cuticle. There are other larger-scale features. The core of the fibre is divided into an ortho- and para-cortex, with differences in the composition of the KAPs. The two halves contract differently on drying, causing wool to develop crimp. The cuticle has a structure of scales, which

³*Intermediate filaments* in the biological literature.

are like an escarpment with steep faces towards the tip and gentle slopes to the root. Consequently, wool has differential friction, which tends to prevent dirt penetrating into the fleece. Since wool and hair provide warm, protective coats for animals, it is not surprising that they have good textile properties. Indeed skins were the first form of clothing and are replicated in modern fleece garments.

Although not a subject for this book, it is worth noting, as an example of the subtlety of genetic control of protein structures, the structure of hagfish slime threads,⁴ which form in surface gland cells and are ejected as a protective mechanism. There is the same 1A–L1–1B–L12–2A–L2–2B sequence plus terminal domains, but the amino-acids are completely different and there are no KAPs to form a matrix. The threads extend plastically to over 200%, in contrast to wool's 50% elastic extension.

Silks are different again. They are simpler protein block copolymers, which form within gland cells and are then extruded through cell walls, which act as spinnerets. The process is similar to solution spinning of manufactured fibres, but with an important difference. Virgin polymerisation leads to a molecular assembly of extended chains that are not allowed to fold back into a disordered state. Control of the protein composition and the extrusion process leads to the diversity of silks from silkworms and spiders, which have mechanical properties matched to purpose.

In general we can say that slow growth, from cm/minute for silks or cm/month for cotton and wool compared with km/minute in industrial production, and genetic control lead to complex specificity in fibre structures that cannot be matched in commercial manufacturing. Useful textile fibres, with different structures, can be made by regenerating cellulose from solution, but attempts to dissolve proteins have led to poorly organised fine structures which lacked the virtues of wool or silk and were too weak to survive commercially as textile fibres (Hearle, 2007).

1.2.2 Regenerated fibres

In the seventeenth century, Robert Hooke wrote: *I have often thought that probably there might be a way of making an artificial glutinous substance much resembling, if not fully as good, nay better than, the excrement or whatever substance it may be, out of which the silk-worm wire-draws his clew.* It was to be 300 years before spider silk was matched industrially.

In the nineteenth century, efforts were made to regenerate fibres from waste cotton or wood pulp (Woodings, 2001). A variety of routes involving chemical modification of cellulose were tried. Cellulose nitrate (nitrocellulose) forms a solution in alcohol and ether, which can be extruded through fine holes

⁴See Hearle (2007) for more information and references.

(spinnerets). In the Chardonnet process, the solvent evaporates in air (*dry spinning*). The resulting fibres are inflammable and need to be reconverted to cellulose. By forming a complex, cellulose will dissolve in a solution of copper sulphate and ammonia. Extruded filaments solidify in a coagulating bath (*wet spinning*) in the cuprammonium process. By far the most successful was the viscose process. Cellulose is reacted with caustic soda and then carbon bisulphide to form a solution of sodium cellulose xanthate. The extruded filaments are coagulated in an acid bath to give viscose rayon.

From a structural viewpoint, the interesting feature of the viscose process is its versatility in allowing fibres with different structures to be formed. The influence of degree of orientation, brought about by stretching filaments, is common to all polymer fibres, as is the option to cut fibres into short staple as an alternative to continuous filament yarns. The involvement of chemistry, rather than simple solidification, gives other possibilities. It was found early on that the addition of zinc ions to the coagulating bath, which leads to intermediate formation of the zinc salt, gave stronger fibres, probably because the bivalency brings the cellulose molecules together to give a finer structure. These 'standard' rayon fibres have a serrated skin–core structure, because hydrogen ions move faster than zinc ions and give a weaker structure in the centre of the fibre. Subsequent research led to the development of stronger 'all-skin' tyre-cord yarn. Another variant had an asymmetric skin that gave crimped rayon. In all these processes, regeneration and crystallisation precede orientation by stretching. A more fibrillar structure is formed when a solid fibre of the cellulose derivative is first oriented and then regenerated to crystallise as cellulose. These are the *polynosic*, *high-wet-modulus* or *modal* rayons.

Cellulose is also soluble in organic amine-oxides, and this led in the later twentieth century to the production of *Lyocell* fibres by spinning through an air gap into a water bath. On an experimental basis, high-performance cellulose fibres have been spun from solution in phosphoric acid.

In the 1920s secondary cellulose acetate (five-sixths conversion of –OH groups to acetate) dissolved in acetone, which had been used in dope to coat aircraft fabrics, was dry-spun into fibres. This also led to another route to a cellulose fibre, *Fortisan*, which was used as a strong fibre in the 1940–50s: a highly stretched acetate fibre was converted back to cellulose. Later, fully converted triacetate fibres were produced, and showed some similarity to the new synthetic fibres.

1.2.3 Synthetic polymer fibres

In the 1920s, chemists took up polymer synthesis, with new fibres as one of the commercial goals. Attention first settled on several polyvinyl and polyvinylidene fibres. Polyacrylonitrile (acrylic) fibres are the main survivor

of this fibre chemistry. They are notable in being able to be spun either from the melt or from solution by dry or wet spinning. Mostly, they contain up to 15% of a copolymer in order to make dyeing possible. They have a quasi-crystalline structure with molecules packed side-by-side but not in transverse register. Solvent-rich zones lead to a porous structure after drying.

The major breakthrough in synthetic polymer fibres was the synthesis of polyhexamethylene adipamide, nylon 66, by Carothers in the 1930s, followed by its cousin, nylon 6. Possibly more important from a structural viewpoint was the development of melt spinning, as distinct from the earlier solution spinning. Subsequently, polyethylene terephthalate was synthesised and melt spun. Commonly known as *polyester*, though some other polyesters are now produced as fibres, it is now the most produced textile fibre, used in a wide variety of applications.

Nylon and polyester fibres were first produced in a series of stages: first by polymerisation and collection of polymer chip, then by melt extrusion to produce unoriented fibre, followed by drawing to orient the structure. The main variable was the degree of orientation, though subtler changes could be achieved by heat treatments. Advances in engineering led to a progressive integration of the steps. Polymer was fed directly to extrusion and drawing occurred before wind-up. A more significant change was the use of high wind-up speeds, which led to crystallisation by tilting the competition between molecular alignment due to attenuation of the molten threadline and randomisation by relaxation. Partially oriented polyester yarn, wound up at about 3000 m/min, has incipient crystallinity and is particularly suitable as a feedstock for false-twist texturing. Draw is completed in the texturing, or in other processes such as draw-warping. Higher speeds, around 6000 m/min, give a more crystalline yarn with lower molecular orientation than conventional polyester yarns, but which is suitable for direct use in some applications.

1.2.4 High-modulus, high-tenacity (HM-HT) fibres

The family of manufactured fibres that had become available to the textile industry by 1960 were, except for glass, all linear polymers with a degree of crystallinity no more than 50% and with mean orientation angles no more than about 20°. Then the technology moved beyond mimicking the natural fibres in structure and uses. The discovery of liquid-crystals in solutions of linear polymers with stiff molecules enabled fibres to be produced with almost perfect crystallinity (albeit with some lack of register of neighbouring regions within a fibrillar structure), almost perfect orientation, and, most importantly, fully extended chain molecules. The para-aramid *Kevlar*, which is an aromatic polyamide of benzene rings joined by $-\text{CO.NH}-$ groups, was the first. US Air Force research led to other materials, such as PBO, with

five- and six-membered rings. Apart from their molecular rigidity, the key features were their use of strong acids, sulphuric or phosphoric, as solvents and dry-jet wet spinning, with an air gap between spinneret and coagulating bath. In another route, fully aromatic co-polyesters are melt spun and drawn and then heat-treated to increase molecular weight (chain length).

Instead of using rigid, interactive polymers, which form liquid crystals, similar structures can be made from polyethylene, which is a flexible and inert molecule at the other end of the spectrum. These molecular features allow super-drawing to produce high orientation, fully extended molecules, and strong crystallisation. Melt-spinning and drawing are possible, but gel-spinning from a solution of ultra-high molecular weight polyethylene gives the highest strength. Unfortunately, no way has been found to produce similar structures in nylon or polyester fibres.

1.2.5 Inorganics

Glass is the one inorganic fibre that has a long history as a decorative material. In the early twentieth century, both centrifugal spinning and sending streams of glass into air or steam blowers produced glass fibres for insulation. Continuous filament yarns, which are extensively used in fibre-reinforced composites, are made by melt extrusion, cooling and wind-up. Drawing is not necessary, except for attenuation in the threadline to produce fine fibres, because the resulting structure is always an unoriented, amorphous network.

Carbon fibres are part of the late twentieth-century development of high-performance fibres for composites. The starting material is a polymer fibre that can be heat treated without melting. Cellulosic fibres can be used, but acrylic fibres are the standard precursor. The first stage of heating drives off some nitrogen and hydrogen and gives a partially carbonised fibre with good thermal resistance. Further heating completes the carbonisation and final heating under tension gives an oriented structure of imperfect graphitic crystals.

The demand for high-temperature composites has led to the production of ceramic fibres, mostly based on silicon carbide or alumina. Production routes involve precursor fibres produced by melt-spinning of organo-silicon polymers or solution-spinning from a viscous liquid containing aluminium salts. Heat treatments then produce micro-crystalline ceramic fibres. Although inherently rigid materials, the fibre fineness gives the necessary flexibility for textile processing.

1.2.6 Specialist and smart fibres

Selection of suitable polymers gives fibres with high chemical or thermal resistance for particular applications or with properties good for medical uses,

such as wound-healing or tissue engineering. Other fibres have particular electrical or magnetic properties. Hollow fibres are used for gas or liquid separation. These fibres are made by methods similar to those used for mainstream manufactured fibres and have similar structures.

Smart fibres have active constituents. They can change colour, act mechanically or electromechanically, generate latent heat, perform as sensors, or have other actions. Wearable electronics is an example of their utility.

Nanofibres give other possibilities for textile miniaturisation. Electrospinning by extrusion in a high electric field leads to a whirling action that produces a high attenuation of the fibres. Melts or solutions can be electrospun, so that the underlying structure can be expected to be similar to that of large fibres of the same material, but with a greater importance of surface and near-surface forms.

Carbon nanotubes are the ultimate in fibre fineness: the molecule as fibre. What distinguishes them from other molecules, except for giant molecules like diamond, is that they can be observed and manipulated as individual entities. An earlier Textile Institute definition of *fibre* started as *a unit of matter*. Nanotubes would fit that definition as well as the characteristics of flexibility, fineness and high aspect ratio. Structurally, they are single- or multi-walled cylinders of hexagonally bonded carbon atoms. They can be assembled together and twisted or otherwise converted into yarns of indefinite length.⁵

1.3 Development of ideas of fibre structure

1.3.1 Characterisation and methods of investigation

Although many techniques are more widely applicable, the details in this and the following section relate primarily to linear polymer fibres.

The macroscopic form of fibres was studied from the first days of optical microscopy. The constituent compounds in natural fibres were separated and identified towards the end of the nineteenth century, but it was not till the polymer hypothesis, the existence of linear macromolecules of indefinite length, was accepted in the 1920s that their chemical constitution was accepted. Before that these natural materials were regarded as some colloidal form of small molecules of defined size. Now the full tool kit of chemical analysis is used to determine the total chemical constitution of fibres. This includes complexities such as the sequence of amino-acid residues in fibrous proteins and the collection of proteins in the matrix of wool, copolymer content in synthetic fibres, molecular weight distributions, chain length and

⁵The above terminology seems best from a textile viewpoint. Some of the nanotube literature refers to nanotubes being twisted together to form fibres, which can be assembled into coarser yarns.

branching, tacticity and so on. Whenever needed, the chemistry of fibres can be determined by well-known procedures.

Optical microscopy, later supported by transmission and scanning electron microscopy, enables coarse structural features to be identified. These include skin–core differences in viscose rayon, the lumen at the centre of cotton, the cells in wool, bicomponent forms of synthetic fibres and so on.

The fine structure, the way in which the molecules pack together, is more difficult to decipher. More is known about the well-defined forms in natural fibres and about the highly oriented HM-HT fibres, but understanding of the fine structure of the common manufactured fibres – rayon, nylon, polyester, polypropylene – is still uncertain, particularly in quantitative detail of the three-dimensional fibre paths through crystalline and amorphous regions. The definitive geometry of a crystal is defined by a few bond lengths and a fully amorphous material by a few statistical parameters. Partially ordered structures would require details of the paths and interactions of many molecules for a comprehensive description. The selection of descriptors for important characteristic features is not easy.

Hearle and Greer (1970) list six general features, which they regard as of most importance, though each may require several parameters for a quantitative description:

- *Degree of order*, which is frequently referred to as crystallinity
- *Degree of localisation of order*, which differentiates between structures with a well-defined separation into crystalline and amorphous regions and more uniform structures described as paracrystalline, as amorphous with correlation, or as containing distributed crystal defects
- *Length/width ratio of localised units*, which distinguishes between lamellar, micellar and fibrillar forms
- *Degree of orientation*, which may be separated into crystalline and amorphous orientation and may include transverse as well as axial orientation
- *Size of localised units*, which may include cross-sectional shape
- *Molecular extent*, which is an inverse measure of the degree to which molecules are folded to-and-fro, either at the ends of crystallites or in amorphous regions, or alternatively are more or less fully extended along the fibre.

No single technique gives unambiguous information about the fine structure of fibres, so that it is necessary to develop ideas from the indications of many techniques developed over the last 100 years, including advances that are still continuing. Digital processing and increasing computer power greatly increase the useful information that can be extracted from the physical instrumentation. Details of methods of investigation are covered in the next few chapters, but the following is a list of those that are most useful.

- Microscopy:
 - optical microscopy, which includes measurement of birefringence for orientation and newer developments such as confocal microscopy
 - scanning electron microscopy, mainly for fibre surfaces
 - analytical electron microscopy for atomic identification
 - transmission electron microscopy, including high voltage examination of thick specimens with tomography to give 3-D images
 - atomic force microscopy
- Spectroscopy to identify chemical bond vibrations and changes with the local atomic environment:
 - absorption of infrared radiation
 - Raman scattering of light
- Diffraction:
 - optical diffraction for coarse features
 - X-ray and electron diffraction, wide-angle for crystal lattices and more diffuse data for amorphous structures, small-angle for larger organisation, real time possible with synchrotron radiation
- Nuclear magnetic resonance
- Thermal analysis, which picks up crystallisation and melting and second-order glass transitions
- Density and moisture absorption, which are related to crystallinity.

The information from the techniques that can be directly related to structural features must be combined with inferences from the chemistry of the fibre material, the mode of fibre formation and the general physical properties in order to build up a picture of the likely fine structure.

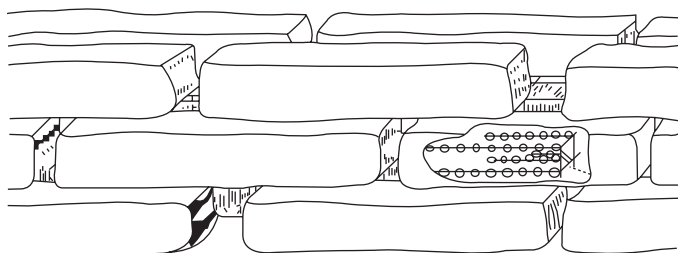
1.3.2 Interpreting the information for linear polymer fibres

A hundred years ago, there was controversy about the basic nature of fibre structures.⁶ The first lead into understanding the structure of plant fibres was Nageli's suggestion in the middle of the nineteenth century that cell membranes were composed of sub-microscopic crystallites, *micelles*, embedded in a matrix of some indeterminate *inter-micellar* substance. Organic chemistry developed in a mind-set that each molecule contained fixed numbers of various atoms, the molecular formula which determined the molecular weight. It was not until the 1920s that it was accepted that atoms or groups of atoms could add on indefinitely to form macromolecules, polymers composed of many monomers, with a range of molecular weights. By then X-ray diffraction had confirmed that the fibres contained both crystalline and amorphous material.

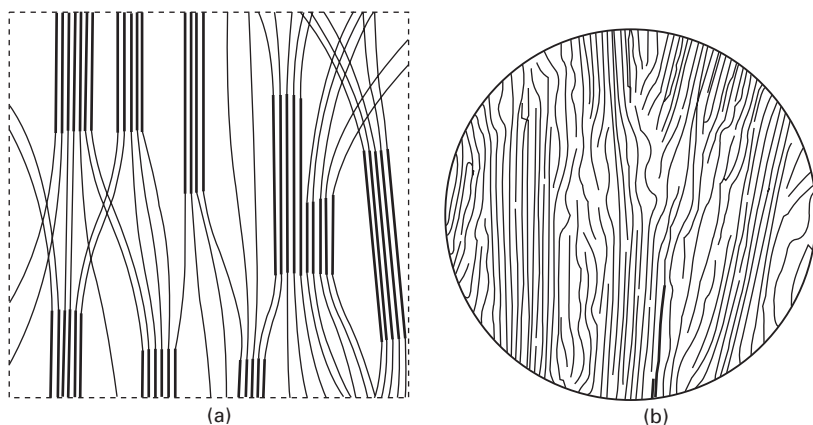
⁶The early history of the subject is based on a longer account by Hearle (1963).

Seifriz (1929) and Meyer (1930) modified Nageli's hypothesis by showing the micelles as composed of polymers, but still separated by an indeterminate matrix, Fig. 1.1. Speakman suggested similar ideas for wool.

Molecular weight determinations then showed that the polymer molecules were about ten times longer than the length of crystallites estimated from the width of X-ray diffraction spots from fibres such as viscose rayon, as well as natural cellulose fibres. This led Gerngross and Herrmann to propose a *fringed micelle structure*, in which polymer molecules passed in and out of crystallites through an amorphous matrix. For 25 years, this was the conventional view. Although a verbal statement was easy, the detailed views varied greatly, often reflecting the personality or artistic skill of the author as much as the scientific evidence, as shown by the two examples in Fig. 1.2. One feature that is common to all the drawings from this period is that the molecules run continuously along the oriented fibre structures with no folding back.



1.1 Micellar model as drawn by Seifriz (1929) and Meyer (1930).



1.2 Fringed micelle structure as drawn by (a) Frey-Wyssling (1938, 1953) and (b) Mark (1940).

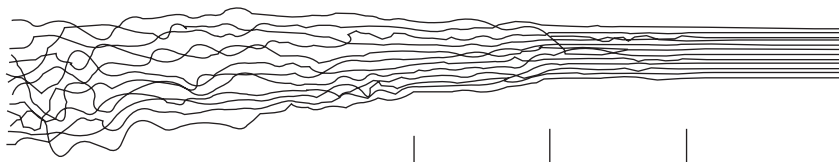
Staudinger took a different view. He suggested that the structure was a continuous imperfect crystal in which the ends of the molecules acted as local defects, Fig. 1.3.

Views changed in the 1950s for several reasons. Howsmon and Sisson (1954) pointed out that there could be a whole spectrum of increasing order from a fully random arrangement to perfect crystals, Fig. 1.4. In natural fibres, electron microscopy showed that the structure was fibrillar and not micellar. In cotton, the structure was in one sense wholly crystalline: crystalline fibrils laid down in a helical array in the cell walls. The apparent evidence from density, moisture absorption, X-ray diffraction and other sources that cotton was two-thirds crystalline and one-third amorphous resulted from a lack of register between fibrils with a diameter of about 3 nm. In wool, keratin fibrils of 7 nm diameter were spaced 10 nm apart in a matrix of KAPs.

For manufactured fibres, two results of laboratory studies of polymer crystallisation led to a change of view of fibre structure, particularly for melt-spun nylon and polyester fibres. Slow crystallisation of polymer melts or solutions starts from small nuclei, but as crystallisation proceeds there is repeated branching until crystal growth is equal in all directions. This continues until the spherulites run into each other. At the centre of spherulites, the nuclei are present as sheaf-like assemblies of parallel molecular segments fringing off into the first branches. Some conditions of melt-spinning, which have been used to delustre nylon, can lead to occluded spherulites within the fibres. However, normal spinning and drawing conditions lead to a high density of nuclei, which gives a degenerate form of spherulitic crystallisation, just the central sheaves, that is a fringed micelle structure.



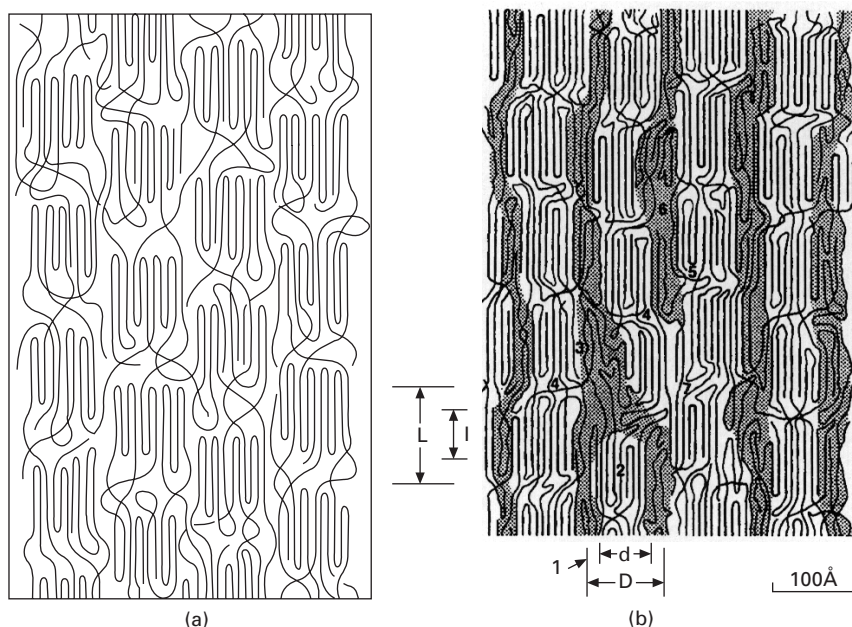
1.3 Staudinger's continuous structure (Staudinger, 1932).



1.4 Range of molecular order as drawn by Howsmon and Sisson (1954).

More surprising was Keller's discovery of single crystals of polyethylene in which the molecules folded back and forth at the ends of the crystal. Chain folding in single crystals was confirmed for many flexible polymer molecules (see Geil, 1963). This led to a modified fringed micelle model. At the ends of the crystallites, there was a mixture of chain folding and fringing into tie-molecules, which led to other crystallites. This became a common working model for fibres such as nylon and polyester. A typical illustration, Fig. 1.5(a), is taken from the cover of a book on macromolecules in condensed systems (Nagasawa, 1988). However, although the basic idea is accepted, there are limitations in the two-dimensional representations and a lack of quantitative data, which would show differences depending on the polymer and the conditions of fibre formation. One example, which takes experimental data to attempt a more quantitative picture, is shown in Fig. 1.5(b). It is worth noting that a typical crystallinity of 50% would mean that in a 3-D structure the separation between crystallites must on average be 0.5 cubed (or one-eighth) of the linear dimensions of the crystallites. Hence the crystallites must be packed in a fairly regular quasi-fibrillar structure.

Alternative, more uniform structures, such as paracrystalline, crystals with distributed defects, or amorphous with correlation, were also proposed. It has been suggested (Hearle, 1977) that this is related to multiple melting found in thermo-analytical studies of nylon and polyester. Form I, which is formed



1.5 Modified fringed micelle structure: (a) from Nagasawa (1988); (b) a quantitative model for nylon 6 by Murthy *et al.* (1990).

by rapid quenching, is a more uniform structure, illustrated in Fig. 1.6, and form II after annealing is a micellar structure. With a stiffer molecule, such as cellulose, chain folding is unlikely. The old fringed micelle structure of Fig. 1.2 may be a reasonable model for regular viscose rayon, but the high wet modulus types may have a fringed fibrillar structure. For the highly crystalline, highly oriented HM-HT fibres, Staudinger's suggestion in Fig. 1.3 is a first approximation to the structure, with actual forms having some additional fibrillar disorder.

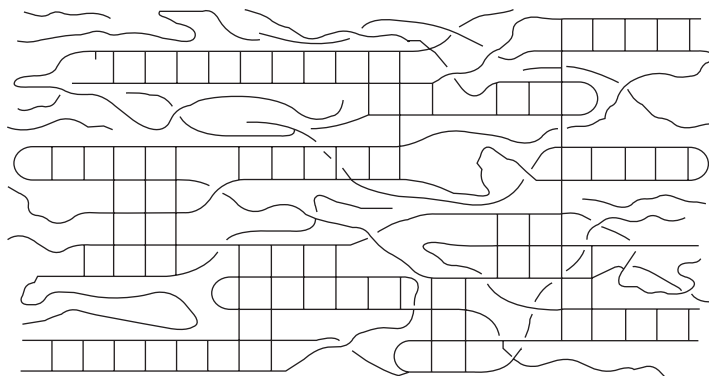
1.3.3 Inorganic fibres

The inorganic fibres, glass and ceramic, have a variety of amorphous or micro-crystalline structures. Their description follows work on bulk forms of these materials. The starting point for carbon fibres is the known structure of graphite, but the introduction of some disorder leads to many speculative forms drawn by different authors in a way that is similar to the variety of forms drawn for the structures of linear polymer fibres.

1.4 Structure and performance

1.4.1 Performance requirements for traditional uses

The first requirements for a textile fibre are fineness and length. The second is adequate mechanical, chemical and thermal stability. Then requirements divide according to the use of the fibre. For the traditional uses, the mechanical properties should be intermediate between those of brittle crystals or glasses or rigid elastic-plastic metals, with high moduli, and those of elastomeric rubbers, with low moduli. There should be at least partial elastic recovery up to extensions between 5% and 50%. This is achieved by the special chemical



1.6 A more uniform structure from Hearle (1977).

or structural forms of natural fibres and the partially crystalline, partially oriented forms of manufactured fibres. Stiffer fibres, such as cotton, provide crisp fabrics, whereas lower modulus fibres, such as cellulose acetate, give limp drapable fabrics. Fashion dictates which is preferred. For manufactured fibres, control of orientation leads to a range of fibres of increasing stiffness and strength and reducing break extensions. For clothing, the more extensible forms are preferred, but for industrial uses, such as tyre cords, the less extensible forms are used.

Moisture absorption is useful for comfort, though the open assembly of fine fibres, even if non-absorbing, in a textile is more important. Absorbed moisture also provides electrical conductivity and disperses static electricity, which otherwise requires the use of anti-static finishes. Dyeability is another requirement for clothing and furnishings. For natural or regenerated fibres that swell in water and have interactive groups, dyeing is easy. Natural dyestuffs have been known for thousands of years and synthetic dyestuffs since the end of the nineteenth century. For synthetic polymer fibres, more research was needed to achieve good dyeability and for acrylic fibres it necessitated copolymerisation.

1.4.2 Performance requirements for new uses

In the second half of the twentieth century, advances in materials science and new uses for fibre-based materials opened up a market for fibres with properties that differed from those of the traditional uses. Although other applications have been found, composites were the major driving force for HM-HT fibres. Glass came first with GFRP (glass fibre reinforced plastics). Its tightly bonded amorphous structure gives the necessary stiffness. The regular 2-D covalent bonding in carbon fibres gave greater strength and stiffness. The stiff and interactive linear polymer materials give high axial stiffness and strength due to their high orientation and fully extended molecules. Ceramic fibres have a structure that combines stiffness and sufficient strength with a resistance to high temperatures that makes them suitable for use in composites for engines. The major advantage of these materials, particularly for use in aircraft, is their low weight, which gives them an advantage over the metals previously used.

The weak transverse interaction of oriented linear polymer fibres gives poor resistance to shear and to axial compression, which is a disadvantage in composites. The transverse hydrogen bonding in M5 fibres improves these properties, but the commercial future of this fibre is uncertain. However, for some purposes, axial yielding, which allows for large extensions at low stress, is an advantage. In bending, the neutral plane moves towards the outside of the bend, so that the fibres can withstand high curvatures and be bent back on themselves without breaking. In contrast to this, the three-dimensionally

bonded forms give brittle fibres that break at low curvature when the outer surface reaches the low tensile breaking extension. For ballistic impact resistance, there is severe bending at the edges of the impact, so that brittle fibres, however strong, would be useless. The other requirements for ballistic protection are the conflicting features of high work of rupture, which depends on the product of break load and break extension, and high modulus, which gives high wave velocity and spreads the effect of the impact over a larger area of material. Although nylon was successful, because of its high work of rupture, the high modulus fibres are better even though the energy to break is less.

Other technical uses of fibres, such as for ropes and cables, which are liable to have fibre bending in production or use are another market for the linear polymer HM-HT fibres. However, it should be noted that this applies to stress-driven applications. For strain-driven applications, for example oil-rigs moored in deep water with displacements due to wave motion, lower modulus materials such as for polyester ropes are needed.

For chemical resistance, a range of polymers with suitable molecular constitutions combined with the structures that have been found to give good textile fibre properties are used. For thermal resistance, materials with high melting points, or high temperatures for chemical decomposition, if that happens first, are needed. Linear polymers with mainly aromatic or other ring groups can be used to 200°C or higher. Partial carbonisation of acrylic fibres leads to a ladder structure in fibres with good thermal resistance. A completely different structure is found in thermoset polymer fibres, such as melamine–formaldehyde or phenolic resins, which are composed of a highly crosslinked 3-D network. Inorganic fibres, with asbestos being used until its health hazard was recognised, give the highest thermal resistance.

Smart fibres and other fibres designed for specific applications have particular structures to fit purpose. These are too various to discuss in this general chapter, but are covered later in the book.

1.5 Conclusion: fibres as a special class of materials

Ever since fibres were collected from plants and animals and used for clothing over 10 000 years ago, fibres have been recognised as a special type of material. They are defined by their macroscopic structure: length and fineness. The inventions of spinning, weaving and knitting showed how these *microgram* particles of matter could be assembled into strong, self-locking sheets of material, which could weigh *kilograms* per square metre. Despite their solidity, woven and knitted fabrics retained a freedom of movement between the constituent fibres that gave them a special flexibility. Other sheet materials, such as paper or film, can bend easily in one direction but cannot

accommodate double curvature, which is needed for the graceful drape of textiles. The other special use of fibres as reinforcement also has a long history, for example as horse hair in plaster, but only became a major technology in the twentieth century. Fibre aspect ratio is a controlling parameter.

As chemistry advanced in the nineteenth and twentieth centuries, it became clear that the natural fibres were special in terms of their internal structure. They were partially oriented, partially crystalline, linear polymer structures. This led on to an early example of biomimetics in the practical realisation of Hooke's idea with the production of manufactured fibres from synthetic polymers.

1.6 Future trends

The range of properties found in current commercial fibres meets the needs of general textile uses. This results from the structures that have evolved naturally or have come from mid-twentieth century technology. It is unlikely that any major new structural forms will be found to provide better textile fibres, but environmental and economic factors may change the choice of polymers or the way of making those used today. The introduction of polylactic acid fibres derived from corn may be a precursor for greater change, but this depends on how fibre production competes with food and biofuel. When oil runs out, coal could come back as a source for the organic chemicals needed to synthesise polymers. In the longer term, new ways of generating energy would make it worthwhile to find novel ways of synthesis from the atmospheric availability of carbon, hydrogen, oxygen and nitrogen, the four elements that are dominant in textile fibres. This would be biomimetics at a molecular level.

More change may come in high-performance fibres for technical uses, particularly in reducing costs. There is a short-term challenge, which has defeated researchers for decades, in the possibility of making stronger fibres from the widely available polyamides and polyesters. Present commercial production hits a barrier at a strength of around 1 N/tex and a break extension of around 10%. Beyond this, there is a missing region, before the HM-HT fibres are reached at around 2 N/tex strength and 4% break extension. This intermediate region, say 1.5 N/tex strength and 7% break extension, would be useful industrially. Theoretically, we know what structural changes are needed and what are the limiting factors. We need greater orientation and greater molecular extent. In a melt, the chain molecules are in random coils in continually reversing directions. In spinning and drawing, their orientation increases and many folds are pulled out. Eventually entanglements lock the structure. On a larger scale this is what happens when one tries to straighten out a tangled hose pipe or electric cable. Pulling gets part way, but then the entanglements must be separated by hand. Unfortunately, there is no Maxwell

demon to do this with polymer molecules and no satisfactory way of doing this has been found.

The structure of the HM-HT fibres from linear polymers is well known and the properties of those made from rigid polymer molecules, which inhibit folding, are excellent. However, both the polymers and the processes are inherently expensive. HMPE from a flexible polymer with weak interactions, which can be superdrawn to remove folds, suffers from a low melting point and a tendency to creep. If nylon or polyester could be formed into a highly oriented, highly crystalline, chain-extended structure, this would offer economic and technical advantages.

Carbon fibre composites are becoming dominant in aircraft production. Big increases in volume production will be needed. This will not only improve the economics but also stimulate research to optimise structures. For engines, there is an incentive to optimise ceramic fibre structures.

Finally, there are the emerging fields of nanofibres, fibres with properties needed in medical and other specialised applications, and smart fibres. Increasing research into structure can lead to optimum forms with new and enhanced performance.

1.7 Sources of further information

The main source of new information on fibre structure is the scientific literature from the textile, polymer, materials and biological journals and in conferences such as the biennial Polymer Fibres Conference in Manchester. The digital archive makes old and new papers more accessible through the World Wide Web, which also provides access to news of commercial advances.

Starting with *Regenerated Cellulosic Fibres* in 2001 and finishing with *Cotton: Science and Technology* in 2007, the Woodhead Series on fibres, published in association with The Textile Institute, provides comprehensive accounts of the whole range of textile fibres, including information on structure. Another recent book covers structure formation in manufactured fibres (Salem, 2001). However, there is much detailed information in older books from the golden age of fibre research (Matthews, 1954; Hearle and Peters, 1963; Hearle and Greer, 1970; Cook, 1984). The relations between fibre structure, fibre formation and mechanical properties have been reviewed by Hearle (1967, 1977, 1991).

1.8 References

- Cook J G (1984), *Handbook of Textile Fibres: I Natural Fibres; II Man-made Fibres*, 5th edition, Merrow, Shildon, UK.
- Denton M J and Daniels P N (2002), editors, *Textile Terms and Definitions*, 11th edition, The Textile Institute, Manchester, UK.

- Frey-Wyssling A (1938), *Submikroskopische Morphologie des Protoplasmas und seiner Derivate*, Gebrüder Borntraeger, Berlin; (1953), 2nd English edition, *Submicroscopic Morphology of Protoplasm*, Elsevier, Amsterdam.
- Geil P H (1963), *Polymer Single Crystals*, Interscience, New York.
- Hearle J W S (1963), in *Fibre Structure*, editors Hearle J W S and Peters R H, The Textile Institute, Manchester, UK, p 209.
- Hearle J W S (1967), *J Polym Sci C*, No. 20, 215.
- Hearle J W S (1977), *J Appl Polym Sci, Appl Polym Symp*, **31**, 137–161.
- Hearle J W S (1991), *J Appl Polym Sci, Appl Polym Symp*, **47**, 1.
- Hearle J W S (2007), *J Mater Sci*, **42**, 2010–2019.
- Hearle J W S and Greer R (1970), Fibre structure, *Text Prog*, **2**, No. 4.
- Hearle J W S and Peters R H (1963), editors, *Fibre Structure*, The Textile Institute, Manchester, UK.
- Howsmon J A and Sisson W A (1954), in *Cellulose and Cellulose Derivatives, Part I*, 2nd edition, editors Ott E, Spurlin H M and Grafen M W Interscience, New York, p. 251.
- Mark H (1940), *J Phys Chem*, **44**, 764.
- Matthews J (1954), *Matthews' Textile Fibers: their physical, microscopic and chemical properties*, 6th edition, editor Mauersberger H R, Wiley, New York.
- Meyer K H (1930), *Kolloid-Z*, **53**, 8.
- Murthy N S, Reimschuessel A C and Kramer V J (1990), *J Appl Polym Sci*, **40**, 249.
- Nagasawa M (1988), editor, *Molecular Conformation and Dynamics of Macromolecules in Condensed Systems*, Elsevier, Amsterdam.
- Salem D R editor (2001), *Structure formation in polymer fibres*, Hanser Publishers, Munich, Germany.
- Seifriz W (1929), *Amer Nat*, **63**, 110.
- Staudinger H (1932), *Die Hochmolekularen Organischen Verbindungen*, Springer-Verlag, Berlin.
- Woodings C (2001), editor, *Regenerated Cellulose Fibres*, Woodhead, Cambridge, UK.

Spectroscopic characterisation of polymer fibres

SJ EICHHORN, University of Manchester, UK

Abstract: This chapter discusses the use of infrared, Raman and NMR spectroscopies for studying the structure and properties of polymeric fibres. General introductions to the techniques are given, with specific methodologies employed for polymer fibres. Examples of a few main applications of these techniques to polymer fibres are also described, namely stress measurement, orientation determination and dynamic measurements. The theory behind the use of these spectroscopic methods is also given. New directions and modern developments in technology are also presented.

Key words: spectroscopy, fibre, Raman, infrared, NMR.

2.1 Introduction

This chapter will focus on the use of infrared, Raman and NMR spectroscopy for the characterisation of polymeric fibres. In order to do this it is necessary to introduce these techniques for the general characterisation of polymers in non-fibrous forms. Where this is presented, the theoretical principles behind the techniques are also covered. Attention is paid to only a small number of applications (e.g., stress measurement, orientation determination and dynamic measurements) and so is by no means exhaustive. These forms of spectroscopy are used widely in the polymeric field, but applications have been restricted to fibres only. Where relevant, non-polymeric fibres are also briefly discussed.

2.2 Historical perspectives on spectroscopic characterisation of polymers

The discovery of infrared radiation is attributed to Sir William Herschel, the then Astronomer Royal, when he measured the temperature of invisible radiation beyond the red part of the spectrum when white light is split by a prism (Herschel 1800). He found that the temperature for this radiation was higher than the visible forms (Herschel 1800). Despite this discovery it wasn't until the late 1880s that Abney and Festing grouped various inorganic materials according to their ability to absorb infrared radiation (Abney and Festing 1881). Pioneering work was then done by Coblentz on infrared absorption spectra, initially on gases (Coblentz 1905) and subsequently

on solid materials (Stair and Coblenz 1935). Some preliminary work was reported on rubber (Sheppard and Sutherland 1945) and subsequently on polymeric materials. Pioneering work by Jack Koenig then commenced, including advanced studies on stereoregularity in polymers (Koenig 1966; Koenig *et al.* 1966) where it was shown that changes in the infrared spectra for isotactic, atactic and syndiotactic polymers could be identified both theoretically and experimentally. Other initial studies looked at chain folding in polyethylene (Koenig and Witenhafer 1966).

Raman spectroscopy was fully developed much later than infrared, probably due to the fact that the optical effect itself was only discovered in 1928 by Raman and Krishnan (1928) and independently by Landsberg and Mandelstam (1928). Raman scattering is small compared to the dominant elastic or Rayleigh scattering effect from materials, hence it took several developments in technology before the technique became a credible alternative to infrared spectroscopy. These developments included lasers, and more importantly Rayleigh rejection filters (Flaugh *et al.* 1984) and the microscope Raman systems that allow greater spatial resolution (Delhaye and Dhamelincourt 1975). Despite this, it was possible to follow the polymerisation process using this technique as early as the 1930s (Monnier *et al.* 1938). Later studies included a characterisation of polystyrene (Palm 1951) and subsequent studies were able to obtain spectra from weakly scattering materials like cellulose (Blackwell *et al.* 1970; Atalla and Dimick 1975).

Nuclear magnetic resonance (NMR) spectroscopy began with the discovery of the effect in bulk matter by two independent groups in 1946 (Bloch *et al.* 1946; Purcell *et al.* 1946). Since then a large amount of research and development has been published on the use of this technique for a wide variety of materials and applications.

In terms of specific applications of these spectroscopic techniques to polymeric fibres, examples will now be given. Before that, some theoretical background to the techniques will be presented.

2.3 Infrared spectroscopy of polymers

2.3.1 Infrared absorption in polymeric materials

Infrared absorptions occur in vibrating molecules where there is a changing dipole moment between the atoms (Bower and Maddams 1992). In this sense, infrared spectroscopy is not sensitive to symmetric vibrations such as $-C-C-$. Therefore, for polymeric materials, the main-chain or backbone structure is often not detected using this technique, and it is usually the side-chain motions of atoms that give rise to absorptions. Infrared spectroscopy often also relies on the preparation of a thin sample of material, since it typically works in transmission, apart from when used in an ATR (Attenuated Reflectance)

mode. The technique can be used to glean a large amount of information on the structure, morphology and mechanical properties of polymeric fibres, and some specific examples of these will now be reviewed.

2.3.2 Polarisation and orientation analysis of polymeric fibres

Electromagnetic radiation comprises electric and magnetic fields which are oscillating sinusoidally at right angles to each other (Steinfeld 1979). It is the interaction of the electric vector of this radiation and the electric field vector of the electrons within the outer orbit of the atoms in the molecular structure of the polymer that cause the vibrations seen in infrared and Raman spectroscopy. In infrared spectroscopy the oscillating dipole and the electric field vector created by this oscillation will be directional. In a typical polymer, which is allowed to solidify from the melt or a solution, the chains are randomly oriented, and hence the coincidence of the electric field vector of the incoming radiation and that of the molecule will be coincident for a number of chains, i.e. for those molecular electric vectors that are parallel to the electric vector of the incoming field. As the sample is rotated there will be no dependence on the angle of the specimen of the intensity of the infrared absorptions recorded. If the polymer chains are preferentially oriented, however, as say in a fibre along the draw direction, then the intensity of infrared absorptions will vary as a function of the angle of the specimen to the polarisation axis or the direction of the electric field vector of the incoming radiation. Only the component of this vector which is parallel to the electric field vector of the oscillating dipole is effective in producing an infrared absorption and hence this will be maximum when they are parallel, and zero when at 90° to each other (Bower and Maddams 1992). The ratio of the absorption intensity parallel (A_{\parallel}) and perpendicular (A_{\perp}) to the axis of the sample, or fibre in this case, is called the *dichroic ratio*, and this can be used to determine the orientation functions for polymeric materials. This technique, in the early stages of its development, was mostly applied to the study of oriented polymeric films (Gailey 1961; Read and Stein 1968; Cunningham *et al.* 1974a, 1974b). A full description of the theoretical treatment for the orientation analysis for fibres and films is beyond the scope of this chapter, and the reader is referred to the paper by Cunningham *et al.* (1974a) where the effects of reflectivity and the electric field correction are accounted for. This analysis led to a relationship of the form

$$\frac{\phi_z - \phi_x}{\phi_z + 2\phi_x} = \frac{\phi_z - \phi_x}{3\phi_x} = P_2(\theta_m) P_2(\theta) \quad 2.1$$

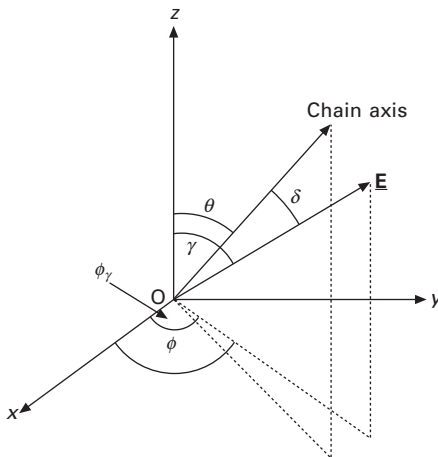
for a sample with fibre symmetry, where ϕ_z and ϕ_x are the angles that the electric vector makes with the draw direction of the film or fibre specimen

(Oz) and the perpendicular axis to this (Ox) (see Fig. 2.1), ϕ_0 is a convenient constant (which is found to be proportional to the concentration of the absorbing species, e.g. C–O etc.), and $P_2(\theta_m)$ is a constant quantity, which depends only on the molecular structure and is related to $P_2(\theta)$, a function for which was originally derived by Hermans (1949) as

$$P_2(\theta) = \frac{1}{2} (3 \cos^2 \theta - 1) \quad 2.2$$

$P_2(\theta_m)$ is also related to the distribution of the chain axis orientations $\langle P_2(\theta) \rangle$ using equation 2.1. The terms in equation 2.1 can be determined experimentally by polarising the infrared laser in different configurations and determining the angle at which maximum intensity of a particular band occurs, relative to the draw axis of the fibre; hence the orientation function can be determined. This complex analysis has not really been applied in full to fibrous materials, but a short discussion of the application of polarised infrared to the analysis of specifically polymer fibre orientation will now be given.

One of the first studies of infrared spectroscopy applied to polymer fibres was on protein fibres in 1950 (Ambrose and Elliott 1951). Other studies around the same time investigated the effect of drawing nylon-66 fibres on their orientation, as determined by the dichroic ratio (Caroti and Dusenbury 1956a, 1956b). Similar studies on the same material made clearer the problems associated with the simultaneous orientation of the ordered and disordered fractions within the fibres, something which had hitherto been ignored (Urbanczyk 1977). Attenuated total reflectance (ATR)



2.1 Orientation of the electric field E vector and the chain axis with respect to Cartesian coordinate axes (Ox , Oy , Oz). The plane of the specimen is conveniently in Oxz and the draw direction of the film is parallel to Oz .

spectroscopy of PET films and fibres was later reported by Xue (1985). The same approach was applied to polyester fibres (Xue *et al.* 1986) and to nylon and needle-like organic crystals using diffuse reflectance spectroscopy, which overcame difficulties of contacting a fibre with an ATR crystal (Gi 1986). Later studies, again on nylon-66 fibre yarns using infrared dichroism, corroborated X-ray data on the crystalline orientation (Samanta, *et al.* 1990). A study on polypropylene and polyamide fibres showed that the orientation of the former depended on the blend, and when stretched the fibres behaved differently from each other in terms of changes in orientation (Durcova *et al.* 1992). The orientation of polyurethane urea fibres was studied as a function of spinning parameters, where orientation factors derived from a number of infrared bands were found to plateau at a certain stress at the take-up point of the fibre (Kotani *et al.* 1992). Longitudinal acoustic mode (LAM) Raman spectroscopy of polyethylene fibres has been reported and compared to ATR infrared spectroscopy values of the skin orientation of the material (Tshmel, *et al.* 1993). It was found that the skin had a lower orientation than the core of the fibres (Tshmel *et al.* 1993). Many more studies have been reported on a wide range of polymeric fibres, a discussion of which is beyond the scope of this chapter. It is worth noting, however, that this technique can be applied to natural polymers, such as poly(β -L-aspartate) (Lopezcarrasquero *et al.* 1995).

2.3.3 Local stress measurements in polymeric fibres

During the 1970s it became clear that it was possible not only to characterise the orientation of polymer materials using infrared spectroscopy, but also to follow deformation (Cunningham *et al.* 1974b). Wool also showed that it was possible to directly follow, and theoretically model, the molecular deformation of polymers by recording a shift in the intensity maximum of an infrared band (Wool 1975, 1980), a phenomenon which had been observed by a number of independent researchers (Reynolds and Sternstein 1964; Zhurkov, *et al.* 1967; Roylance and Devries 1971; Wool and Statton 1974). This shift is characterised by two features: the peak shifts to longer wavelengths and the shifted band has a large tail on it. The shift itself is thought to be due to a direct molecular stressing of the molecular backbone of the material, and the shifting of the tail region of the band to a non-uniform stress distribution of the molecules (Wool and Statton 1974). The molecular shifts ($\Delta\nu$) in these bands were shown to follow a relationship of the type

$$\Delta\nu = \alpha\sigma \quad 2.3$$

where α is a constant of proportionality and σ is the stress (Roylance and

Devries 1971). The molecular stress distribution which is contained within the shape of the deformed band $D(\nu)$ is expressed by the convolution integral

$$D(\nu) = \int_{-\infty}^{\infty} F(\zeta)U(\nu - \zeta) d\zeta \quad 2.4$$

where $F(\zeta)$ is the stress-dependent frequency shift distribution and $U(\nu - \zeta)$ is the shape of the absorption band, which is assumed to be stress independent. $F(\zeta)$ is typically obtained using numerical deconvolution methods (Ergun 1968).

In terms of the application of the above experimental approach to determining molecular stress in polymer fibres, very little compared to Raman spectroscopic studies (Section 2.4.3) has been reported. This is probably due to the fact that the infrared spectroscopic approach is less sensitive to changes in stress. Raman spectroscopy is also more sensitive to symmetric vibrations, which are typical of the backbone moieties, the main structural load-bearing constituent of polymers. Nevertheless, shifts in infrared bands for oriented tapes of polyethylene have been reported (Sheiko *et al.* 1992). The molecular deformation of cellulose fibres has also been reported (Dadashian and Wilding 2003; Sturcova *et al.* 2006).

2.3.4 Dynamic FTIR spectroscopic characterisation of polymer fibres

The first report of a dynamic infrared measurement for a polymeric material was made by Noda *et al.* in the 1980s (Noda *et al.* 1983, 1988). The principle relies on making the dichroic measurements discussed in Section 2.3.2, whilst applying a modulated frequency vibration to the sample under investigation. It is particularly effective for investigating intra- and intermolecular bonding within polymeric materials as the dynamic signals recorded depend on the molecular environment of the particular bonded group under investigation. Little has been reported on single fibres, as it is difficult to prepare a sample for transmission (required for this technique). A large amount of work has, however, been done on sheets of oriented cellulose fibres, where subtleties in the hydrogen bonds within this structure have been elucidated (Hinterstoisser and Salmen 1999, 2000). By plotting a synchronous 2-D plot of the cross-correlation of the in-phase and out-of-phase spectra obtained from polarised infrared signals, specific highly localised contours can indicate specific interactions within the hydrogen bond networks of the materials.

2.4 Raman spectroscopy of polymers

2.4.1 Raman scattering from polymeric materials

The Raman effect is the inelastic scattering of light from a material due to the vibration of bonds within that material. In contrast to infrared, a small dipole is induced in a symmetric bond (e.g. C–C), and this oscillates at a frequency, radiating the inelastic component of the scattered radiation.

An electromagnetic wave can be transmitted, absorbed or scattered by a molecule. If an electromagnetic field, from a light source, interacts with the molecule then there is always some transfer of energy from the incoming radiation to the molecule, which is governed by the equation

$$\Delta E = h\nu_0 \quad 2.5$$

where ΔE is the gain in energy of the molecule, ν_0 is the frequency of the incident radiation and h is Planck's constant. In the case of the Raman effect, it is found that some of the scattered light has a component different from that of the excitation frequency. Three types of scattering of the light may occur as follows:

1. Rayleigh scattering – this is the most intense component, and has the same frequency as that of the incoming radiation. In this case the molecular energy neither increases nor decreases.
2. Stokes–Raman scattering – the incident photon excites a molecule to a higher vibration level, where the loss of energy of the photon is equal to the gain in energy of the molecule; the scattered photon has a frequency of $\nu_0 - \nu_m$.
3. Anti-Stokes–Raman scattering – this is the opposite to the Stokes–Raman effect where the molecules lose energy and the scattered photon has a higher frequency $\nu_0 + \nu_m$ than the incident photon.

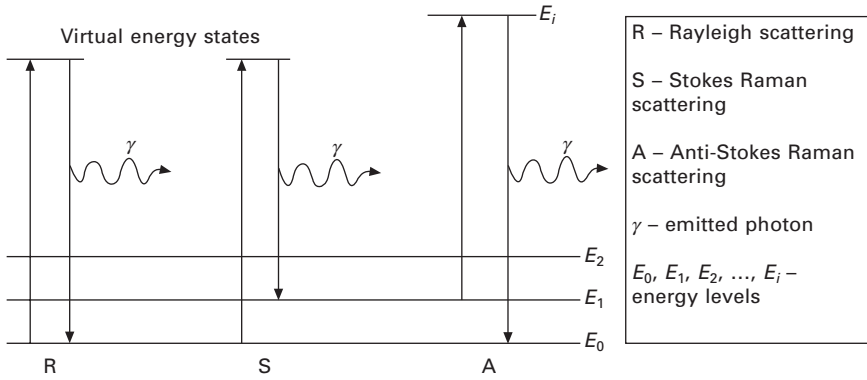
A schematic of these processes, showing the electronic transitions, is shown in Fig. 2.2. According to classical theory, Raman scattering can be explained as follows. An electromagnetic wave with an electric field strength E_s fluctuating with time t with a frequency ν_0 can be described by the equation

$$E_s = E_{s0} \cos(2\pi\nu_0 t) \quad 2.6$$

where E_{s0} is the vibration amplitude. When this wave interacts with a molecule an electric dipole moment P is induced, given by the equation

$$P = \alpha(q)E \quad 2.7$$

where $\alpha(q)$ is the polarisability, and is a function of the nuclear displacement q . If the molecule is vibrating, due to the electromagnetic wave, with a frequency ν_m , the nuclear displacement q is then given by the equation



2.2 Schematic of Rayleigh, Stokes-Raman and anti-Stokes-Raman scattering (reproduced from Ferraro and Nakamoto (1994)).

$$q = q_0 \cos(2\pi \nu_m t) \quad 2.8$$

where q_0 is the amplitude of the vibration. For small amplitudes $\alpha(q)$ can be approximated to a linear function, with only the first two terms of the power series, as

$$\alpha(q) = \alpha_0 + \left(\frac{\partial\alpha}{\partial q}\right)_0 q_0 + \dots \quad 2.9$$

where α_0 is the polarisability at the equilibrium position. By combining equations 2.6–2.9 the expression

$$P = \alpha_0 E_0 \cos(2\pi \nu_0 t) + \left(\frac{\partial\alpha}{\partial q}\right)_0 q_0 E_0 \cos(2\pi \nu_0 t) \cos(2\pi \nu_m t) \quad 2.10$$

is obtained, which can be expanded and alternatively written as

$$P = \alpha_0 E_0 \cos(2\pi \nu_0 t) + \frac{1}{2} \left(\frac{\partial\alpha}{\partial q}\right)_0 q_0 E_0 [\cos(2\pi(\nu_0 + \nu_m)t) + \cos(2\pi(\nu_0 - \nu_m)t)] \quad 2.11$$

The first term in equation 2.11 represents Rayleigh scattering and the second Raman scattering, which has two frequencies: $\nu_0 + \nu_m$ (anti-Stokes) and $\nu_0 - \nu_m$ (Stokes). For a particular bond type to be Raman active it must have a non-zero rate of change of polarisability with respect to nuclear displacement (i.e. $\partial\alpha/\partial q > 0$). The intensity of a Raman band is proportional to the rate of change of polarisability.

Raman spectroscopy is particularly suited to the study of polymeric materials since the backbone of these materials often comprises symmetrical or near-symmetrical vibrations (e.g. C–C, C=C, C≡C, C–O, C=O, etc.) that are highly polarisable.

2.4.2 Polarisation and orientation analysis of polymeric fibres

Most of the information for this section can be found in Bower and Maddams (1992). Some of the detail has been omitted for brevity and so the reader is referred to that text for more information. The use of Raman spectroscopy to follow the orientation of polymers is more complicated than for infrared spectroscopy, and as a consequence more powerful, because the polarisation of both the incident and scattered components of the radiation must be considered (Bower and Maddams 1992).

Depolarisation ratios can be determined for Raman active modes, in a similar manner to the analysis using infrared spectroscopy described in Section 2.3.2. The differential polarisability of a molecular bond $(\partial\alpha/\partial q)_0$ is a second-rank tensor, called the 'Raman tensor'. Consider a polarised light source which is incident on a single molecule with the electric field of the electromagnetic wave parallel to the axis Ox_j of a set of axes $Ox_1x_2x_3$ fixed in space. These axes are such that the only non-zero component of the electric field is E_j . If the scattered radiation passes through an analyser, which only allows light whose electric vector is parallel to Ox_i to pass, then the amplitude of the light transmitted will be proportional to μ_i , the amplitude of the induced dipole. Hence, the observed intensity of the Raman scattering is proportional to α_{ij}^2 . The constant of this proportionality depends on the incident light intensity E_{j0} and on the efficiency with which the Raman scattering is collected. If a correction is made for any polarisation sensitivity within the spectrometer, it is possible to say that

$$I_{ij} = I_0\alpha_{ij}^2 \quad 2.12$$

where I_{ij} is the observed intensity for the incident and scattered light polarisation vectors \mathbf{E} parallel to the axes Ox_j and Ox_i and I_0 is a constant independent of both i and j . With this relationship established it is now possible to calculate the linear depolarisation ratio ρ_l where

$$\rho_i = \frac{I_{\text{perp}}}{I_{\text{para}}} = \frac{\sum \alpha_{ij}^2}{\sum \alpha_{ii}^2} = \frac{\langle \alpha_{ij}^2 \rangle}{\langle \alpha_{ii}^2 \rangle} \quad 2.13$$

where summations \sum are over all molecules which contribute to the scattered light and the brackets $\langle \rangle$ denote average values of a parameter over all the random distribution of the molecules. In order to perform these averages, the principal components of the polarisability tensor $[\alpha]$, namely α_1, α_2 and α_3 , are introduced, and the expression

$$\alpha_{ij} \sum_k a_{ik} a_{jk} \alpha_k \quad 2.14$$

is used, where a_{ij} are the elements of the direction cosine matrix which

relate the principal axes of $[\alpha]$ to the fixed axes $Ox_1x_2x_3$. With some work the expression

$$\rho_l = \frac{3\beta^2}{45\alpha^{-2} + 4\beta^2} \quad 2.15$$

is obtained, where

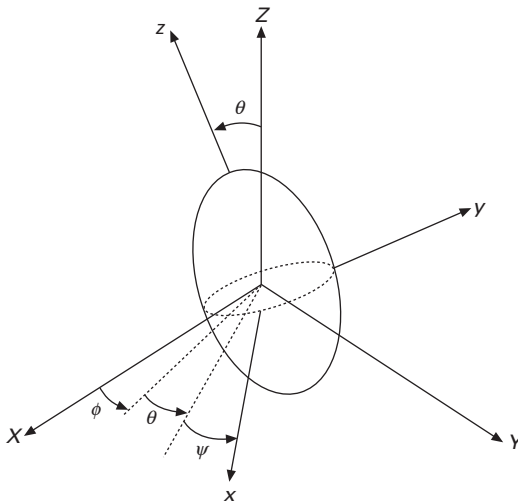
$$\bar{\alpha} = \frac{1}{3} (\alpha_1 + \alpha_a + \alpha_3) \quad 2.16$$

and

$$2\beta^2 = (\alpha_1 - \beta_2)^2 + (\alpha_2 - \alpha_3)^2 + (\alpha_3 - \alpha_1)^2 \quad 2.17$$

$\bar{\alpha}$ is the mean value of the three principal components $[\alpha]$ and is called the 'spherical part' of the tensor. β represents the anisotropy of the tensor since it is zero only when all principal components are zero, i.e. when $[\alpha]$ has spherical symmetry. This analysis is for an isotropic system of scattering molecules. The result is different when the scattering geometry is not symmetrical, i.e. where there is uniaxial orientation, such as for a fibre.

To understand this type of symmetry and the effect on the orientation it is necessary to introduce the concept of the orientation distribution function where $N(\phi, \theta, \psi) \sin \theta \, d\theta \, d\psi \, d\phi$ is the fraction of scattering units having orientation within the general solid angle $\sin \theta \, d\theta \, d\psi \, d\phi$ using the angles as defined in Fig. 2.3. This function is found to be, as a function of $\cos \theta$ (Roe 1965),



2.3 Definitions of the Euler angles (θ, ϕ, ψ) the molecular and Raman tensor axes (x, y, z) and the specimen axes (X, Y, Z) .

$$\begin{aligned}
 N(\phi, \xi, \psi) &= \sum_{l=0}^{\infty} \sum_{m=-l}^l \sum_{n=-l}^l v_{lmn} Z_{lmn}(\xi) e^{-im\psi} e^{-in\phi} \\
 &= \sum_{lmn} v_{lmn} Z_{lmn}(\xi) e^{-im\psi} e^{-in\phi}
 \end{aligned}
 \tag{2.18}$$

where $\xi = \cos\theta$ and v_{lmn} and $Z_{lmn}(\xi)$ are the expansion coefficients and the general Legendre polynomials of the lmn orders respectively. In a uniaxially oriented sample, such as for a fibre, the molecular orientation distribution coefficients, typically denoted P_{lmn} , are only non-zero when $m = n = 0$ and l is even (0, 2, 4, ...). These coefficients are correlated with the function $N(\theta)$ in equation 2.18 by the expression

$$P_{200} = \frac{\int_0^\pi N(\theta) P_{100} \cos \theta \sin \theta \, d\theta}{\int_0^\pi N(\theta) \sin \theta \, d\theta}
 \tag{2.19}$$

where the fraction of polymer chains at an angle θ is $N(\theta)d\theta$ and the functions $P_{100}(\cos \theta)$ are Legendre polynomials. It is found that $P_{100}(\cos \theta) = \frac{1}{2}$ and for $l = 2, 4$ then

$$P_{200}(\cos \theta) = \frac{1}{2} (3 \cos^2 \theta - 1)
 \tag{2.20}$$

$$P_{400}(\cos \theta) = \frac{35 \cos^4 \theta - 30 \cos^2 \theta + 3}{8}
 \tag{2.21}$$

It must be noted that equation 2.20 is equivalent to Herman's orientation function (see equation 2.2). More detailed information on this approach can be found in a review by Tanaka and Young (2006) where there is also a case study on PET fibres. Tanaka and Young (2006) found that the observed modulus of fibres correlated well with values calculated using a Reuss estimate and orientation functions derived from spectroscopy. Recently $P_{200}(\cos \theta)$ and $P_{400}(\cos \theta)$ have been derived for electrospun nylon fibres (Bellan and Craighead 2008). Spider silk has also been analysed using the same approach (Lefevre *et al.* 2007) from the orientation function (combining P_{200} and P_{400}) of the spectral peaks for carbonyl groups (Rousseau *et al.* 2004).

The first study of this kind on polymeric fibres was on PET filaments by Bower and Ward (1982). Although no formal analysis of $P_{200}(\cos \theta)$ and $P_{400}(\cos \theta)$ was reported in early studies of natural materials, a key investigation of the orientation of proteins in muscle fibres from barnacles was published by Caillé *et al.* (1987). Similar studies were carried out on synthetic fibres such as PEEK (Everall *et al.* 1991). A comprehensive study

of the polarisation ratios and orientation coefficients has been carried out for DNA fibres (Thomas *et al.* 1995). Readers are referred to the general treatment by Tsuboi for anisotropic and oriented biopolymers using this technique (Tsuboi *et al.* 1995) if they want to read more about these particular classes of materials. Not so many papers use the full analysis of molecular orientation in fibres, and so it is thought that further work is required in this direction.

2.4.3 Local stress measurements in polymeric fibres

The detection of local stress in polymeric fibres using Raman spectroscopy is now at a mature stage in terms of research effort. The technique requires the measurement of shifts in the position of characteristic Raman bands as a function of the macroscopic deformation of the fibre. The first report of a Raman band shift was for a polydiacetylene single crystal by Mitra *et al.* in 1977. The shift was thought at that time to be due to a direct straining of the molecular backbone of the polydiacetylene crystal. This chain stretching leads to an alteration of the force constant dictating the vibrational frequency ν_i of the particular Raman mode via the equation (Mitra *et al.* 1977)

$$\nu_i = (4\pi^2 c^2 \mu)^{-1/2} (F_2')_i^{1/2} \quad 2.22$$

where c is the speed of light, μ is the reduced mass of the oscillator, $(F_2')_i$ is the anharmonic force constant that is a function of the separation of the atoms within the molecule; so as the atoms are pulled apart the force constant changes accordingly. This explanation was subsequently confirmed both theoretically and experimentally (Batchelder and Bloor 1979).

Despite these initial advances, the detection of Raman band shifts in polymer fibres was fraught with difficulty. Initial studies on Kevlar fibres reported no shift (Penn and Milanovich 1979) from which it was mistakenly concluded that 'no major bond stretching or bending occurs during elongation'. Similar results were reported by Edwards and Hakiki (1989). It was, however, pointed out at a later stage that both the work of Penn and Milanovich (1979) and that of Edwards and Hakiki (1989) were flawed in that they used a high power laser which probably damaged the fibre samples during deformation, hence the reason for observing no band shifts. Shortly after the paper by Penn and Milanovich, Galiotis *et al.* (1985) showed that it was possible to follow the molecular deformation in a Kevlar fibre using this technique, but with a much lower power laser. Subsequently many other polymeric and non-polymeric fibres have been studied using this technique. Notable examples include polyethylene (Prasad and Grubb 1989) where evidence for taut-tie molecules was gleaned from the non-symmetrical broadening of Raman peaks during deformation. The molecular deformation of rigid rod fibres, such as PBT (poly(*para*-phenylene benzobisthiazole)) (Day *et al.*

al. 1987) and PBO (poly(*para*-phenylene benzobisoxazole)) (Young *et al.* 1990) fibres, has also been reported. Non-polymeric fibres such as carbon (Robinson *et al.* 1987) and silicon carbide fibres (Day *et al.* 1989) have also been studied. The molecular deformation of natural fibres such as cellulose (Hamad and Eichhorn 1997; Eichhorn *et al.* 2000, 2001a, 2001b; Gierlinger *et al.* 2006; Peetla *et al.* 2006), silk (Shao, *et al.* 1999a, 1999b; Sirichaisit *et al.* 2000, 2003) and collagen (Wang *et al.* 2000) has been reported. The technique has been particularly useful for following the interfacial properties of composites where a fibre embedded in a resin material is used as a local deformation sensor. The reader is referred to a number of review articles which discuss this in detail (Schadler and Galiotis 1995; Young 1996; Young and Eichhorn 2007).

2.4.4 Surface enhanced Raman scattering from polymeric fibres

If the frequency of incident radiation used to excite Raman scattering from a material approaches an electronic transition in the molecule (or material) being examined then a resonant effect occurs; an enhancement of the Raman scattering occurs, sometimes by as much as a factor of 10^4 or greater (Bower and Maddams 1992). The effect can be induced in low scattering materials by coating the sample with gold or silver particles, as was first observed for pyridine (Fleischmann *et al.* 1974). Little has been published, however, on the detection of surface enhanced Raman scattering (SERS) of fibres. One study on carbon fibres has shown modest enhancement of the Raman scattering using silver particles coated on the surface of filaments (Tadayoni and Dando 1991). Claims of enhancement of the scattering from lipids in wool fibres have also been reported (Carter and Fredericks 1997). In recent times electrospun polyacrylonitrile fibres have been coated with gold particles, and although Raman spectra of these samples have not been reported, they are discussed in light of their potential as a SERS substrate (Zhao *et al.* 2008).

2.5 Nuclear magnetic resonance spectroscopy of polymers

In order for the reader to grasp the importance of nuclear magnetic resonance (NMR) for studying polymeric materials, a basic understanding of the origins of the effect are required. These origins will be now summarised, but for more detailed explanations the reader is referred to other texts. Most of the information for this section, unless otherwise stated, comes from Steinfeld (1979) and Paudler (1987). The part of this section that specifically discusses polymeric materials comes from Young and Lovell (1991).

The principle of the technique of NMR spectroscopy is based on the quantum mechanical magnetic properties of an atom's nucleus. All nuclei that contain an odd number of neutrons and protons have an inherent magnetic moment associated with them, which can interact with and undergo motion within an applied magnetic field. Magnetic moments μ within nuclei are quantised, governed by what is called their spin quantum number I . This spin quantum number can take either an integral or a half integral value, depending on the mass number of the nucleus, or the charge of the atom. There are some basic selection rules which govern this, namely:

- If the mass number is odd, the nuclear spin is given a half value (e.g., H^1 , C^{13} and N^{15} have $I = \frac{1}{2}$ and for O^{17} , $I = \frac{5}{2}$).
- If the mass number and charge are both even then the nucleus has $I = 0$ (e.g., C^{12} , O^{16} and S^{32}).
- If the mass number is even and the charge is odd then $I = 1, 2, 3 \dots, n$, i.e. an integral value (e.g., H^2 , N^{14}).

Since the magnetic moment and the angular momentum are parallel vectors, the equation

$$\gamma = \frac{\mu}{I\hbar} \quad 2.23$$

can be used to describe the magnetic properties of the particular nucleus, where γ is defined as the gyromagnetic (sometimes magnetogyric) ratio and \hbar is equal to $h/2\pi$ where h is Planck's constant.

A nucleus with spin quantum number $\frac{1}{2}$ can align itself in two states, either with ($I = +\frac{1}{2}$) or against ($I = -\frac{1}{2}$) it. Since the energy difference between these two states is small the number of nuclei in each is almost the same, and only a small excess will be in alignment ($I = +\frac{1}{2}$); this very small excess gives rise to the NMR signal.

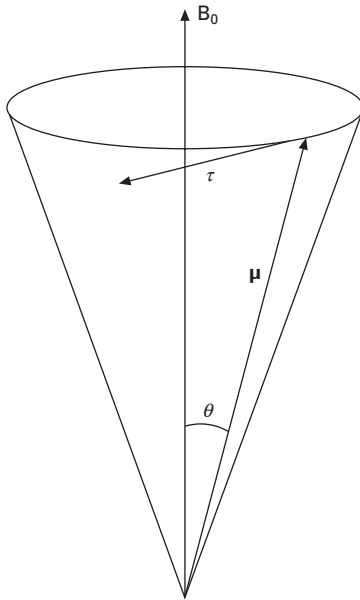
If we consider a classical magnetic moment in a static magnetic field, as depicted in Fig. 2.4, at any moment in time there will be a torque on the moment which is exerted by the magnetic field, described by the equation

$$\boldsymbol{\tau} = \boldsymbol{\mu} \times \mathbf{B} \quad 2.24$$

where $\boldsymbol{\tau}$ is the torque, $\boldsymbol{\mu}$ is the magnetic moment and \mathbf{B} is the magnetic field strength. As torque is the rate of change of the angular momentum \mathbf{J} which is related to the magnetic moment $\boldsymbol{\mu}$ by the gyromagnetic ratio, this leads to the equation

$$\frac{d\boldsymbol{\mu}}{dt} = \gamma (\boldsymbol{\mu} \times \mathbf{B}) \quad 2.25$$

the solution of which is the precession of $\boldsymbol{\mu}$, as shown in Fig. 2.5. The greater the applied magnetic field (\mathbf{B}_0) the more aligned the nuclei and the smaller the alignment angle θ . The solution of equation 2.25 leads to the concept

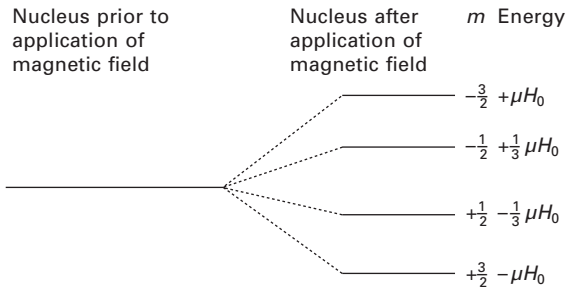


2.4 Schematic of the magnetic moment μ in a constant magnetic field \mathbf{B}_0 indicating the torque exerted which results in a precession around the field direction; θ is the alignment angle.

of a precessional frequency ω_0 which will also increase with an increase in the magnetic field. These factors are not, however, governed simply by Newtonian mechanics but also by quantum mechanical considerations. These latter considerations limit the number of alignments of the nuclei in the applied magnetic field to a selected number, and the angular momentum can only have whole multiples of \hbar . The precessional frequency, called the Larmor frequency, is found to be related to the magnetic field strength and the gyromagnetic ratio via the equation

$$\omega_0 = -\gamma H_0 \quad 2.26$$

using the scalar H_0 . A magnetically active nucleus will have $2I + 1$ possible alignments when placed in a magnetic field. This means that a nucleus say with a spin quantum number of $I = \frac{1}{2}$ will be aligned either with ($I = +\frac{1}{2}$) or against ($I = -\frac{1}{2}$) i.e. $2I + 1 = 2$. The aligned state ($I = +\frac{1}{2}$) is of course a lower and more favourable state. So the nucleus enters a split energy state with different probabilities of each state occurring, and therefore different energies. This type of splitting is known as Zeeman splitting, and the energies E of the subsequent magnetic states (pictorially represented in Fig. 2.5) are governed by the equation



2.5 Zeeman splitting of nuclear energy levels for a nucleus with spin $I = \frac{3}{2}$.

$$E = -\frac{\mu}{IH_0 m_I} \quad 2.27$$

where m_I is the magnetic quantum number and can have values of $I, I - 1, I - 2, \dots, -I$.

In order to observe nuclear magnetic resonance in a material the induction of transitions between different Zeeman levels must be achieved. This is done by applying a variable radio frequency (RF) to the nuclei in the magnetic field. It is applied perpendicularly to the applied magnetic field, and when the frequency of this RF matches the precessional frequency then a transition will occur between nuclear spin states. When a transition occurs a state of resonance is said to exist, and the Larmor frequency will be the same as the applied frequency; hence the term nuclear magnetic resonance. The resonant frequency required to 'flip' between states is given by the equation

$$\nu = \frac{B_0 \gamma}{2\pi} \quad 2.28$$

This quantity can be derived quite easily and gives the resonances seen in a nuclear magnetic resonance spectrum characteristic of the particular nuclei present in the material.

In terms of polymeric materials, ^1H and ^{13}C are by far the most utilised methods for identification purposes. Since linear polymers of low molecular weight often show unique absorptions due to the end-groups, it is possible to derive the number average molar mass by comparison with the monomer resonances. It is also possible to investigate branching in polymers and to also gain insight into chain dynamics by following the relaxation behaviour of the excited nuclei. Early NMR spectrometers used a permanent magnet or electromagnet and were of a continuous-wave type, in which a single radiowave frequency was applied continuously whilst a small sweep coil

would apply the magnetic field over an appropriate range of \mathbf{B}_0 . Modern spectrometers are now of a pulsed Fourier transform type, in which \mathbf{B}_0 is fixed and a short pulse of radiowaves, over the whole range of frequencies of interest, is applied in order to promote the nuclei to the higher energy states.

2.5.1 NMR studies of polymeric fibres

A study of nuclear magnetic resonance in polyethylene and polypropylene fibres was one of the first to be published (Hyndman and Origlio 1959) showing that it was possible to find peaks within the proton derivative line shapes corresponding to orientation, thus confirming other studies using complementary techniques such as infrared and Raman spectroscopy. A later study by the same group reporting work done on Dacron (PET) fibres (Hyndman and Origlio 1960) confirmed the findings of Ward (1960) on unoriented samples that even below the glass transition temperature, considerable motion of the methylene groups occurs.

Before going into specific detail about how NMR can be and has been used to obtain information on polymer chain orientation in fibres, it is necessary to define a few terms. One will recall that all nuclei have their own localised magnetic field as each nucleus 'feels' the field of its neighbours (McBrierty and Douglass 1981). In a liquid this local field is averaged to zero, as the atoms are moving around randomly due to Brownian motion and the angular dependence of the dipolar interaction (McBrierty and Douglass 1981). Therefore the behaviour of a polymer is somewhere between a solid and a liquid, where some averaging, as in liquids, takes place due to side group motions. It is the detection, particularly the shape and size, of this average field that is most important in the use of NMR for solid polymers. Fluctuations in the local field give rise to spin transitions, in the same manner as the applied field, and so a flow of energy occurs between the spin system and the lattice of atoms. If one measures this flow rate, termed $1/T_1$, then one can obtain information on the rate of molecular motion responsible for driving the fluctuation (McBrierty and Douglass 1981). The term T_2 is the time constant which describes the loss of phase coherence when nuclei are subjected to a short burst of resonant radiation; this is typically short in polymers (McBrierty and Douglass 1981). When a solid state NMR experiment is carried out where the radio frequencies are swept through resonance there is an absorption envelope, which is a reflection of the distribution of the local field. This absorption spectrum has two parameters that describe it, namely the line width between points of inflexion and the mean square deviation, or second moment, M_2 . Fourth-order moments (M_4) are also derivable from this absorption spectrum (McBrierty and Douglass 1981).

In order to investigate the orientation of polymeric fibres using NMR it

is necessary to vary the angle of the sample within the magnetic field H_0 . Comparative techniques, such as linear dichroism, are limited to second-order moments, but as already described, NMR can achieve fourth-order moments. Perhaps the most well-known work on the orientation of polymer fibres using NMR techniques is that of Smith, Manuel and Ward (Smith *et al.* 1975) on highly drawn polyethylene fibres. It was shown by Capaccio and Ward (1974) that highly oriented polyethylene fibres could be obtained, where the resulting material is highly anisotropic. Derivative NMR spectra were collected from these materials and it was shown that three components were present. These were an isotropic and narrow component, which was assigned to low molecular weight molecules which do not form ordered or crystalline regions, a broad component assigned to oriented ordered crystalline regions, and an intermediate component that relates to constrained interconnecting chains (between regions of order) which are allowed to freely rotate (Smith *et al.* 1975). Since this groundbreaking research many other researchers have reported the use of NMR spectroscopy to analyse polymer fibres. Notable examples of these include chain flipping and rotation of crystallites in polyethylene fibres (Hu *et al.* 1999), the monitoring of structural changes in silk during the spinning process (Ohgo *et al.* 2003) and ultra-highly drawn polyethylene fibres (Hu and Schmidt-Rohr 2000).

2.6 Discussion and conclusions

Spectroscopy has been shown to be a highly powerful tool for relating structural morphology of polymeric fibres to mechanical properties and other macroscale features of these industrially useful materials. The techniques covered, namely infrared, Raman and NMR spectroscopies, have also been shown to be complementary to each other. The development of highly specialised equipment for each of these techniques has allowed detailed analysis of polymer structure. Indeed it is these developments that have allowed the elucidation of crystal-amorphous interactions, chain dynamics and orientation to be understood. Specifically, it has been shown that both Raman and infrared spectroscopy are useful tools for determining the complex orientation distributions in polymeric fibres of a number of different types. Both techniques, particularly the former, have been useful tools for the following of molecular stress in fibres, and this continues to be the case as new highly oriented fibres are developed. NMR spectroscopy has developed considerably over the last 30–40 years, and now with these developments ever more sensitive measurements of discrete relaxations are possible.

It is true to say that the scattering and relaxations found in biopolymeric fibres have been much less amenable to the applications of all three techniques covered in this chapter. With the development of advanced technology in recent times, it is likely that the use of infrared, Raman and NMR spectroscopy

will increase, as the polymer community endeavours to better understand the biological world. It is thought therefore that this area will see considerable growth in research in the years to come.

2.7 References

- Abney, W. and Festing E. R. (1881). 'On the influence of the atomic grouping in the molecules of organic bodies on their absorption in the infra-red region of the spectrum'. *Philosophical Transactions of the Royal Society of London (1776–1886)* 172: 887–918.
- Ambrose, E. J. and Elliott A. (1951). 'Infra-red spectra and structure of fibrous proteins'. *Proceedings of the Royal Society of London, Series A – Mathematical and Physical Sciences* 206(1085): 206–219.
- Atalla, R. H. and Dimick B. E. (1975). 'Raman-spectral evidence for differences between conformations of cellulose-I and cellulose-II'. *Carbohydrate Research* 39(1): C1–C3.
- Batchelder, D. N. and Bloor D. (1979). 'Strain dependence of the vibrational modes of a diacetylene crystal'. *Journal of Polymer Science, Part B – Polymer Physics* 17(4): 569–581.
- Bellan, L. M. and Craighead H. G. (2008). 'Molecular orientation in individual electrospun nanofibers measured via polarized Raman spectroscopy'. *Polymer* 49(13–14): 3125–3129.
- Blackwell, J., Vasko P. D. *et al.* (1970). 'Infrared and Raman spectra of cellulose from cell wall of *Valonia ventricosa*'. *Journal of Applied Physics* 41(11): 4375–4379.
- Bloch, F. Hansen W. W. *et al.* (1946). 'The nuclear induction experiment'. *Physical Review* 70(7–8): 474–485.
- Bower, D. I. and Maddams W. F. (1992). *The Vibrational Spectroscopy of Polymers*. Cambridge, Cambridge University Press.
- Bower, D. I. and I. M. Ward (1982). 'Quantitative characterization of orientation in PET fibers by Raman-spectroscopy'. *Polymer* 23(5): 645–649.
- Caillé, J. P., Pigeongosselin M. *et al.* (1987). 'Orientation of the contractile proteins of muscle-fibers by Raman and infrared-spectroscopy'. *Biophysical Journal* 51(2): A279.
- Capaccio, G. and Ward I. M. (1974). 'Preparation of ultrahigh modulus linear polyethylenes – effect of molecular-weight and molecular-weight distribution on drawing behavior and mechanical properties'. *Polymer* 15(4): 233–238.
- Caroti, G. and Dusenbury J. H. (1956a). 'Effect of drawing on the infra-red dichroism of nylon-66 filaments'. *Nature* 178(4525): 162–163.
- Caroti, G. and Dusenbury J. H. (1956b). 'Effect of drawing on the infrared dichroism of nylon-66 filaments'. *Journal of Polymer Science* 22(102): 399–407.
- Carter, E. A. and Fredericks P. M. (1997). 'FT-Raman spectroscopy of silvered wool fibres: a SERS effect?' *Mikrochimica Acta* 14: 741–743.
- Coblentz, W. W. (1905). 'Infra-red absorption spectra: I. Gases'. *Physical Review (Series I)* 20(5): 273.
- Cunningham, A. Davies G. R. *et al.* (1974a). 'Determination of molecular orientation by polarized infra-red radiation in an oriented polymer of high polarizability'. *Polymer* 15(11): 743–748.
- Cunningham, A. Ward I. M. *et al.* (1974b). 'An infra-red spectroscopic study of molecular

- orientation and conformational changes in poly(ethylene terephthalate)'. *Polymer* 15(11): 749–756.
- Dadashian, F. and Wilding M. A. (2003). 'Deformation micromechanics of lyocell fibres subjected to tensile strain'. *Indian Journal of Fibre and Textile Research* 28(4): 385–392.
- Day, R. J. Robinson I. M. *et al.* (1987). 'Raman-spectroscopy of stressed high modulus poly(*para*-phenylene benzobisthiazole) fibers'. *Polymer* 28(11): 1833–1840.
- Day, R. J. Piddock V. *et al.* (1989). 'The distribution of graphitic microcrystals and the sensitivity of their Raman bands to strain in SiC fibers'. *Journal of Materials Science* 24(8): 2898–2902.
- Delhaye, M. and Dhmelincourt P. (1975). 'Raman microprobe and microscope with laser excitation'. *Journal of Raman Spectroscopy* 3(1): 33–43.
- Durcova, O. Grof I. *et al.* (1992). 'Fibers from polypropylene polyamide 6-blends – application of FT-IR dichroism for study of fiber molecular orientation'. *Polymer Testing* 11(3): 193–203.
- Edwards, H. G. M. and Hakiki S. (1989). 'Raman-spectroscopic studies of Nomex and Kevlar fibers under stress'. *British Polymer Journal* 21(6): 505–512.
- Eichhorn, S. J. Hughes M. *et al.* (2000). 'Strain induced shifts in the Raman spectra of natural cellulose fibers'. *Journal of Materials Science Letters* 19(8): 721–723.
- Eichhorn, S. J. Sirichaisit J. *et al.* (2001a). 'Deformation mechanisms in cellulose fibres, paper and wood'. *Journal of Materials Science* 36(13): 3129–3135.
- Eichhorn, S. J. Young R. J. *et al.* (2001b). 'Deformation processes in regenerated cellulose fibers'. *Textile Research Journal* 71(2): 121–129.
- Ergun, S. (1968). 'Direct method for unfolding convolution products – its application to X-ray scattering intensities'. *Journal of Applied Crystallography* 1: 19–23.
- Everall, N. J. Lumsdon J. *et al.* (1991). 'The use of polarized Fourier transform Raman spectroscopy in morphological studies of uniaxially oriented peek fibers – some preliminary results'. *Spectrochimica Acta, Part A – Molecular and Biomolecular Spectroscopy* 47(9–10): 1305–1311.
- Ferraro, J. R. and Nakamoto K. (1994). *Introductory Raman Spectroscopy*. London, Academic Press.
- Flaugh, P. L. O'Donnell S. E. *et al.* (1984). 'Development of a new optical wavelength rejection filter – demonstration of its utility in Raman spectroscopy'. *Applied Spectroscopy* 38(6): 847–850.
- Fleischmann, M. Hendra P. J. *et al.* (1974). 'Raman spectra of pyridine adsorbed at a silver electrode'. *Chemical Physics Letters* 26(2): 163–166.
- Gailey, J. A. (1961). 'Determination of molecular orientation in polymer films by infrared spectrophotometry'. *Analytical Chemistry* 33(13): 1831–1834.
- Galiotis, C., Robinson I. M. *et al.* (1985). 'Strain dependence of the Raman frequencies of a Kevlar-49 fiber'. *Polymer Communications* 26(12): 354–355.
- Gi, X. (1986). 'Orientation studies of fiber surfaces using Fourier transform infrared diffuse reflectance attachment'. *Journal of Physics and Chemistry of Solids* 47(6): 609–611.
- Gierlinger, N. Schwanninger M. *et al.* (2006). 'Molecular changes during tensile deformation of single wood fibers followed by Raman microscopy'. *Biomacromolecules* 7(7): 2077–2081.
- Hamad, W. Y. and Eichhorn S. (1997). 'Deformation micromechanics of regenerated cellulose fibers using Raman spectroscopy'. *Journal of Engineering Materials and Technology – Transactions of the ASME* 119(3): 309–313.

- Hermans, P. H. (1949). *Physics and Chemistry of Cellulose Fibres*. London, Elsevier.
- Herschel, W. (1800). 'Investigation of the powers of the prismatic colours to heat and illuminate objects; with remarks, that prove the different refrangibility of radiant heat. to which is added, an inquiry into the method of viewing the sun advantageously, with telescopes of large apertures and high magnifying powers. By William Herschel, LL. D. F. R. S'. *Philosophical Transactions of the Royal Society of London (1776–1886)* 90: 255–283.
- Hinterstoisser, B. and Salmen L. (1999). 'Two-dimensional step-scan FTIR: a tool to unravel the OH-valency range of the spectrum of cellulose I'. *Cellulose* 6(3): 251–263.
- Hinterstoisser, B. and Salmen L. (2000). 'Application of dynamic 2D FTIR to cellulose'. *Vibrational Spectroscopy* 22(1–2): 111–118.
- Hu, W. G. and Schmidt-Rohr, K. (2000). 'Characterization of ultradrawn polyethylene fibers by NMR: crystallinity, domain sizes and a highly mobile second amorphous phase'. *Polymer* 41(8): 2979–2987.
- Hu, W. G. Boeffel C. *et al.* (1999). 'Chain flips in polyethylene crystallites and fibers characterized by dipolar C-13 NMR'. *Macromolecules* 32(5): 1611–1619.
- Hyndman, D. and Origlio G. F. (1959). 'Nuclear magnetic resonance in polyethylene and polypropylene fibers'. *Journal of Polymer Science* 39(135): 556–558.
- Hyndman, D. and Origlio G. F. (1960). 'NMR study of oriented dacron fibers'. *Journal of Polymer Science* 46(147): 259–261.
- Koenig, J. L. (1966). 'Infrared measurement of configuration and stereoregularity in polymers-I. Theory'. *Spectrochimica Acta* 22(7): 1223–1232.
- Koenig, J. L. and Witenhafer, D. E. (1966). 'Infrared studies of polymer chain folding-I. Linear polyethylene'. *Makromolekulare Chemie* 99(Dec.): 193–204.
- Koenig, J. L. Wolfram L. E. *et al.* (1966). 'Infrared measurement of configuration and stereoregularity in polymers—II. Application to syndiotactic polypropylene'. *Spectrochimica Acta* 22(7): 1233–1242.
- Kotani, T. Hayashi S. *et al.* (1992). 'Structure and properties of dry-spun segmented polyurethane urea elastic fibers'. *Journal of Macromolecular Science – Physics* B31(1): 65–86.
- Landsberg, G. and Mandelstam L. (1928). 'Eine neue Erscheinung bei der Lichtzerstreuung in Krystallen'. *Die Naturwissenschaften* 16: 557–578.
- Lefevre, T. Rousseau M. E. *et al.* (2007). 'Protein secondary structure and orientation in silk as revealed by Raman spectromicroscopy'. *Biophysical Journal* 92(8): 2885–2895.
- Lopezcarrasquero, F. Aleman C. *et al.* (1995). 'Conformational analysis of helical poly(beta-L-aspartate)s by IR dichroism'. *Biopolymers* 36(3): 263–271.
- McBrierty, V. J. and Douglass D. C. (1981). 'Recent advances in the NMR of solid polymers'. *Macromolecular Reviews, Part D – Journal of Polymer Science* 16: 295–366.
- Mitra, V. K. Risen W. M. *et al.* (1977). 'Laser Raman study of stress dependence of vibrational frequencies of a monocrystalline polydiacetylene'. *Journal of Chemical Physics* 66(6): 2731–2736.
- Monnier, D. Susz B. *et al.* (1938). 'Spectres Raman de l'acide acrylique et des méthacrylates de méthyle et d'éthyle à divers degrés de polymérisation'. *Helvetica Chimica Acta* 21(1): 1349–1355.
- Noda, I. Dowrey A. E. *et al.* (1983). 'Dynamic infrared linear dichroism of polymer films under oscillatory deformation'. *Journal of Polymer Science, Part C – Polymer Letters* 21(2): 99–103.
- Noda, I. Dowrey A. E. *et al.* (1988). 'A spectrometer for measuring time-resolved

- infrared linear dichroism induced by a small-amplitude oscillatory strain'. *Applied Spectroscopy* 42(2): 203–216.
- Ohgo, K. Zhao C. H. *et al.* (2003). 'Preparation of non-woven nanofibers of *Bombyx mori* silk, *Samia cynthia ricini* silk and recombinant hybrid silk with electrospinning method'. *Polymer* 44(3): 841–846.
- Palm, A. (1951). 'Raman spectrum of polystyrene'. *Journal of Physical and Colloid Chemistry* 55(8): 1320–1324.
- Paudler, W. W. (1987). *Nuclear Magnetic Resonance: General Concepts and Applications*, New York, Wiley Interscience.
- Peetla, P. Schenzel K. C. *et al.* (2006). 'Determination of mechanical strength properties of hemp fibers using near-infrared Fourier transform Raman microspectroscopy'. *Applied Spectroscopy* 60(6): 682–691.
- Penn, L. and Milanovich F. (1979). 'Raman spectroscopy of kevlar-49 fiber'. *Polymer* 20(1): 31–36.
- Prasad, K. and Grubb D. T. (1989). 'Direct observation of taut tie molecules in high-strength polyethylene fibers by Raman spectroscopy'. *Journal of Polymer Science, Part B – Polymer Physics* 27(2): 381–403.
- Purcell, E. M. Torrey H. C. *et al.* (1946). 'Resonance absorption by nuclear magnetic moments in a solid'. *Physical Review* 69(1-2): 37–38.
- Raman, C. V. and Krishnan K. S. (1928). 'A new type of secondary radiation'. *Nature* 120: 726–727.
- Read, B. E. and Stein R. S. (1968). 'Polarized infrared studies of amorphous orientation in polyethylene and some ethylene copolymers'. *Macromolecules* 1(2): 116–126.
- Reynolds, J. and Sternstein S. S. (1964). 'Effect of pressure on the infrared spectra of some hydrogen bonded solids'. *Journal of Chemical Physics* 41(1): 47–50.
- Robinson, I. M. Zakikhani M. *et al.* (1987). 'Strain dependence of the Raman frequencies for different types of carbon fibers'. *Journal of Materials Science Letters* 6(10): 1212–1214.
- Roe, R.-J. (1965). 'Description of crystallite orientation in polycrystalline materials. III. General solution to pole figure inversion'. *Journal of Applied Physics* 36(6): 2024–2031.
- Rousseau, M. E. Lefevre T. *et al.* (2004). 'Study of protein conformation and orientation in silkworm and spider silk fibers using Raman microspectroscopy'. *Biomacromolecules* 5(6): 2247–2257.
- Royle, D. K. and Devries K. L. (1971). 'Determination of atomic stress distribution in oriented polypropylene by infrared spectroscopy'. *Journal of Polymer Science, Part B – Polymer Letters* 9(6): 443–447.
- Samanta, S. R. Lanier W. W. *et al.* (1990). 'Fiber structure study by polarized infrared attenuated total reflection spectroscopy – orientation development of nylon-66 at various spinning speeds'. *Applied Spectroscopy* 44(7): 1137–1142.
- Schadler, L. S. and Galiotis C. (1995). 'Fundamentals and applications of micro-Raman spectroscopy to strain measurements in fiber-reinforced composites'. *International Materials Reviews* 40(3): 116–134.
- Shao, Z. Vollrath F. *et al.* (1999a). 'Analysis of spider silk in native and supercontracted states using Raman spectroscopy'. *Polymer* 40(10): 2493–2500.
- Shao, Z. Z. Young R. J. *et al.* (1999b). 'The effect of solvents on spider silk studied by mechanical testing and single-fibre Raman spectroscopy'. *International Journal of Biological Macromolecules* 24(2–3): 295–300.

- Sheiko, S. Frey H. *et al.* (1992). 'FT-IR studies on the mechanical response of the crystalline fraction in ultrastrong polyethylene tapes'. *Colloid and Polymer Science* 270(5): 440–445.
- Sheppard, N. and Sutherland G. (1945). 'Some infra-red studies on the vulcanisation of rubber'. *Transactions of the Faraday Society* 41(4–5): 261–271.
- Sirichaisit, J. Young R. J. *et al.* (2000). 'Molecular deformation in spider dragline silk subjected to stress'. *Polymer* 41(3): 1223–1227.
- Sirichaisit, J. Brookes V. L. *et al.* (2003). 'Analysis of structure/property relationships in silkworm (*Bombyx mori*) and spider dragline (*Nephila edulis*) silks using Raman spectroscopy'. *Biomacromolecules* 4(2): 387–394.
- Smith, J. B. Manuel A. J. *et al.* (1975). 'Broadline NMR-studies of ultrahigh modulus polyethylenes'. *Polymer* 16(1): 57–65.
- Stair, R. and Coblenz W. W. (1935). 'Infrared absorption spectra of plant and animal tissue and of various other substances'. *Journal of the Research of the National Bureau of Standards* 15: 295–316.
- Steinfeld, J. I. (1979). *Molecules and Radiation*. Cambridge, MA, MIT Press.
- Sturcova, A. Eichhorn S. J. *et al.* (2006). 'Vibrational spectroscopy of biopolymers under mechanical stress: processing cellulose spectra using bandshift difference integrals'. *Biomacromolecules* 7(9): 2688–2691.
- Tadayyon, M. A. and Dando N. R. (1991). 'Normal and surface-enhanced Raman investigations of carbon materials'. *Applied Spectroscopy* 45(10): 1613–1616.
- Tanaka, M. and Young R. J. (2006). 'Polarised Raman spectroscopy for the study of molecular orientation distributions in polymers'. *Journal of Materials Science* 41(3): 963–991.
- Thomas, G. J. Benevides J. M. *et al.* (1995). 'Polarized Raman spectra of oriented fibers of A DNA and B DNA: anisotropic and isotropic local Raman tensors of base and backbone vibrations'. *Biophysical Journal* 68(3): 1073–1088.
- Tshmel, A. Gorshkova I. A. *et al.* (1993). 'Contribution of the surface layer to the straight-chain-segment length distribution in oriented polyethylene fibers'. *Journal of Macromolecular Science – Physics* B32(1): 1–13.
- Tsuboi, M. Ueda T. *et al.* (1995). 'Localized Raman tensors in some biopolymers'. *Journal of Molecular Structure* 352: 509–517.
- Urbanczyk, G. W. (1977). 'Orientation changes caused by stretching of PTE and PA-6 fibers evaluated on basis of IR spectroscopy'. *Journal of Polymer Science, Part C – Polymer Symposium* (58): 311–321.
- Wang, Y. N. Galiotis C. *et al.* (2000). 'Determination of molecular changes in soft tissues under strain using laser Raman microscopy'. *Journal of Biomechanics* 33(4): 483–486.
- Ward, I. M. (1960). 'Nuclear magnetic resonance studies of polyethylene terephthalate and related polyesters'. *Transactions of the Faraday Society* 56(5): 648–659.
- Wool, R. P. (1975). 'Mechanisms of frequency shifting in infrared spectrum of stressed polymer'. *Journal of Polymer Science, Part B – Polymer Physics* 13(9): 1795–1808.
- Wool, R. P. (1980). 'Infrared studies of deformation in semi-crystalline polymers'. *Polymer Engineering and Science* 20(12): 805–815.
- Wool, R. P. and Statton W. O. (1974). 'Dynamic polarized infrared studies of stress relaxation and creep in polypropylene'. *Journal of Polymer Science, Part B – Polymer Physics* 12(8): 1575–1586.
- Xue, G. (1985). 'Orientation studies of poly(ethylene-terephthalate) film and fiber

- surfaces using FT-IR diffuse reflectance optics'. *Makromolekulare Chemie – Rapid Communications* 6(12): 811–814.
- Xue, G., Jiang S. G. *et al.* (1986). 'Characterization of orientation at polyester fiber surface by modified infrared reflection technique'. *Polymer Bulletin* 15(4): 363–368.
- Young, R. J. (1996). Evaluation of composite interfaces using Raman spectroscopy. In *Interfacial Effects in Particulate, Fibrous and Layered Composite Materials*, edited by T. W. Clyne. Key Engineering Materials 116–117, Trans-Tech Publications, Zürich, pp. 173–192.
- Young, R. J. and Eichhorn S. J. (2007). 'Deformation mechanisms in polymer fibres and nanocomposites'. *Polymer* 48(1): 2–18.
- Young, R. J. and Lovell P. A. (1991). *Introduction to Polymers*. Boca Raton, FL, CRC Press.
- Young, R. J. Day R. J. *et al.* (1990). 'The structure and deformation behavior of poly(p-phenylene benzobisoxazole) fibers'. *Journal of Materials Science* 25(1A): 127–136.
- Zhao, S. Z. Guo B. *et al.* (2008). 'Metallization of electrospun polyacrylonitrile fibers by gold'. *Materials Letters* 62(21–22): 3751–3753.
- Zhurkov, S. N. Vettegren V. I. *et al.* (1967). 'Polymer bonds under mechanical stress investigated by infrared spectroscopy'. *Doklady Akademii Nauk SSSR* 176(3): 623.

X-ray analysis of partial crystalline fibre structure

P ZUGENMAIER, Clausthal University of Technology,
Germany

Abstract: Fibre diffraction by X-rays on partial crystalline synthetic and natural polymeric fibres combined with computer-aided modelling are presented and their potentials and results in structure determination are discussed. X-ray methods are described for the characterization of polymeric fibres with regard to crystallinity and disorder, crystallite sizes and the orientation distribution of crystallized chain molecules in fibres. These diversified investigations provide insight into the interaction of molecules and atoms and chain arrangements in partially crystalline polymers, establish correlations with desired properties and point towards improving and tailoring materials.

Key words: fibre diffraction of X-rays, molecular and crystal structure determination, crystallinity and disorder, crystallite size and disorder, preferred orientation.

3.1 Introduction

Structural investigations of materials belong to the prime interests of basic and applied research, since they provide insights into the interactions of molecules and atoms, establish correlations with desired properties and point towards improving and tailoring materials. Tools and techniques for such investigations include microscopy, spectroscopy and diffraction. Diffraction represents the technique of choice for crystalline materials if the crystal and molecular structure is needed, but spectroscopy may provide useful additional information concerning the preferred orientation of domains, the proportion of crystalline materials in polymers and characterization of the various polymorphs of biopolymers.

Here we will restrict ourselves to structural investigations of partially crystalline fibres, which normally exhibit axial symmetry along the fibre axis, and will introduce X-ray fibre diffraction as the main tool for a detailed structure evaluation. The main feature of such a study is based on the determination of the structure amplitude, which is the interference function relying on the position of every atom in a crystalline domain causing interference of waves and resulting in interference maxima, also called diffraction spots. The interaction of the electromagnetic field of the X-rays with the electrons of the atoms represents the essential feature of

the X-ray method. The diffraction of neutrons with matter also depends on the structure amplitude of the crystalline domains but here the interaction of the particle wave takes place with the nucleus of the atoms. In contrast to the interaction of X-rays the scattering power, that is, the strength of the interaction, does not depend on the scattering angle but rather represents a constant for a certain element due to the specific interaction and the small size of the nucleus and exhibits different relative strength as compared to X-ray diffractions. For example, the ratio of the scattering power of carbon to that of hydrogen is much in favour for hydrogen in neutron scattering, and neutron scattering is preferred for the determination of the position of hydrogen. A still better contrast can be obtained by replacing the hydrogen atoms in a molecule by deuterium. However, neutron scattering has the disadvantage that a nuclear reactor is needed for generation of a sufficient neutron flux. The collimation and monochromatization of a neutron beam requires large-scale equipment and also large samples are needed.

Electron diffraction is another possibility for the determination of the structure amplitude required for a crystalline structure evaluation (Dorset, 1995). Such an experiment can be performed in an electron microscope. The interaction of the particle waves with matter rests here on the electric field between the electrons and the nuclei of the atoms, and several difficulties have to be solved in collecting and reducing the intensities as well as the strong absorbance of electrons by matter and the decay of the crystals. Nevertheless, electron diffraction represents an excellent tool for the determination of interference maxima of polymeric single crystals of small thickness or of tiny fibrils of naturally occurring fibres. The position of the diffraction spots is less affected by the disadvantages caused by the scattering power of bound atoms.

In recent years synchrotron radiation has developed into a powerful and indispensable X-ray tool in a wide range of research fields. Electrons orbiting in a storage ring emit the electromagnetic waves of synchrotron radiation. This radiation source has high intensity (many orders of magnitude more than that of X-rays produced in conventional X-ray tubes), shows high collimation, i.e. small angular divergence of the beam, is widely tunable in energy/wavelength by monochromatization and has a high level of polarization (linear or elliptical). The high brightness is ideally suited to microbeam and imaging applications, including X-ray microscopy (Zafeiropoulos *et al.*, 2005). It is technically possible to record spatially resolved wide-angle X-ray patterns from single polymeric fibres down to $\sim 10 \mu\text{m}$ thickness (Riekkel *et al.*, 1997) with a beam of few microns in diameter in a few seconds per pattern. This opens new possibilities for in-situ experiments but also for the study of smaller samples, e.g. the skin core effect of fibrils (Müller *et al.*, 2000) or the preferred orientation of molecules in tiny starch granules

as first observed by Kreger with conventional X-rays (1951) and later with synchrotron radiation by Buléon *et al.* (1997) and Waigh *et al.* (1997). The detection system by synchrotron experiments is well developed, which means the data collected can be easily processed.

Besides the determination of the crystal and molecular structure, careful evaluation of the wide-angle X-ray diffraction diagrams of polymeric materials leads to further significant structural features. An overall consideration of the scattering of radiation into diffraction spots versus the scattering into the background leads to an estimation of the crystalline portion of the materials, that is, the ratio of the amount of crystalline to amorphous (non-crystalline materials) present in the materials, an important quantity needed to describe the performance of polymers. But such an evaluation also provides insights into the defects and disorder within the crystalline domains. Further, the orientation of the domains along the fibre axis can be determined by the evaluation of the extension or arcs of the X-ray diffraction spots. This structural feature represents a major and significant property for describing the performance of fibres. The determination of preferred orientation is very much simplified by the axial symmetry of the fibres, and the quite general and lengthy treatment for preferred orientation by the investigation of pole figures can be avoided (Alexander, 1969).

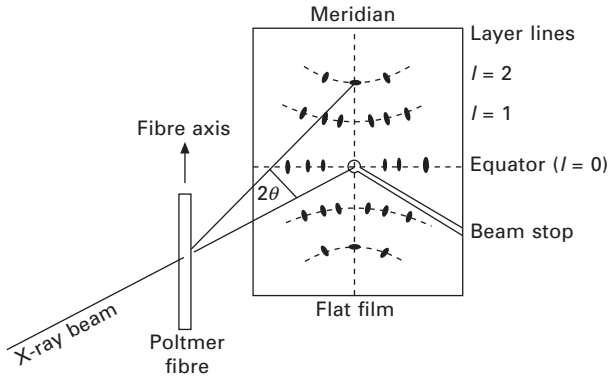
3.2 Diffraction

3.2.1 Basics

Structural details of natural and synthetic polymers can be obtained by scattering experiments using electromagnetic or particle waves of various origins. In most cases X-ray diffraction studies are preferred in the evaluation of fibres. Figure 3.1 represents the experimental setup for a fibre diffraction experiment for a partially crystalline fibre with uniaxially oriented crystalline domains along the fibre axis.

The diffraction pattern on the detection device (flat film) consists of spots lying on layer lines, termed $l = 0, 1, 2$, etc. The vertical line on the equator ($l = 0$) through the origin is denoted the meridian. The regular appearance of spots on the meridian plays a significant role in the interpretation of the shape of chain molecules. The primary beam is absorbed by a beam stop to avoid overexposure of the film. The scattering angle 2θ describes the deviation of the scattered beam from the primary one.

Crystalline materials are a necessity to evaluate detailed structural properties by scattering experiments. Such investigations can provide accurate conformation and packing arrangements of the atoms or molecules, if sufficient diffraction spots are available. Single crystals with almost perfect alignment of the crystalline domains provide the necessary amount of reflections. However,



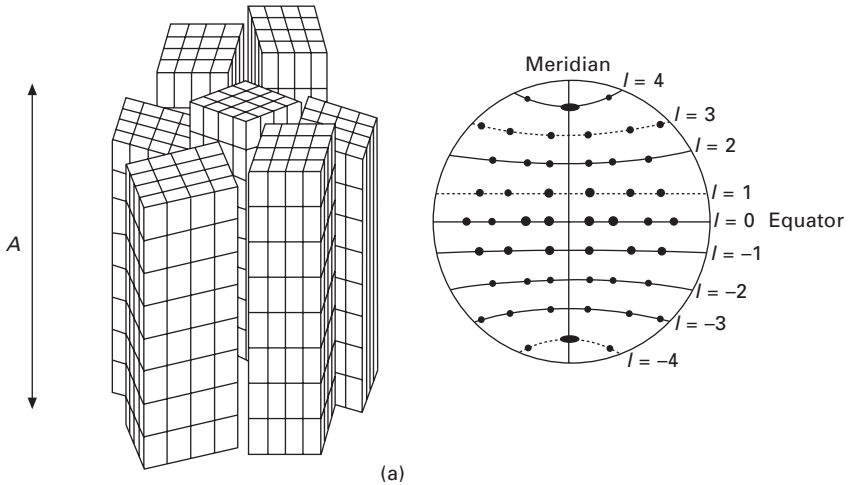
3.1 Experimental setup for fibre diffraction of a partial crystalline polymeric specimen. The detection device may be a film, an imaging plate or other electronic device. Fibre axis vertically oriented.

polymers usually do not crystallize in such a perfect form. Normally, solid-state materials of polymers are only available in which the crystallites are distributed either randomly or in a uniaxial or partly biaxial distribution in disordered crystalline domains and these materials exhibit few reflections only. Idealized packing arrangements of the crystalline domains and the corresponding diffraction patterns are shown in Fig. 3.2.

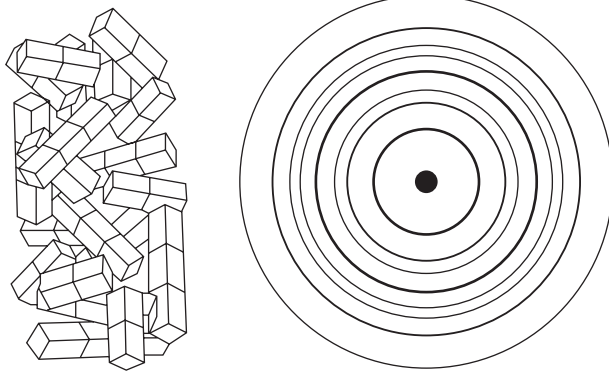
A uniaxial distribution of crystalline domains in polymeric materials occurs mostly in fibres and the resulting diffraction pattern is called a fibre pattern in contrast to the random or isotropic distribution of crystalline domains, which resembles a crystalline powder. The diffraction pattern of such a sample consists of concentric rings and is called a powder pattern or Debye–Scherrer pattern. The fibre pattern is a better choice in evaluating the X-ray data, since it shows fewer overlapping reflections and usually exhibits better resolution.

A diffraction pattern contains manifold structural information. The integral intensity of the reflection spots is needed for an evaluation of the position of every atom in the crystalline domains. The width of a reflection is influenced by the size of the crystalline domains but also by disorder of various kinds. The size of the arcing of a reflection, e.g. an equatorial reflection on $l = 0$ in the meridional direction, represents the deviation from perfect orientation. The amount of crystalline material, that is, the ratio of ordered material contained in the crystalline domains versus the amorphous or imperfectly ordered material, can be determined by an evaluation of the overall intensity of the reflection spots versus the corrected background intensity. A disorder factor can be introduced describing the deviations from perfectly ordered domains.

Some of the addressed information can be demonstrated by the application



(a)



(b)

3.2 Common packing arrangements of crystalline domains and their expected X-ray diffraction pattern of polymeric materials: (a) uniaxial packing arrangement as in a crystalline fibre; (b) random packing arrangement as in a crystalline powder. (Adapted from Chandrasekaran, 1997.)

of analogous two-dimensional optical transforms, that is, by light scattering experiments on ordered motifs.

3.2.2 Optical transforms of lattices

The application of optical transforms represents an excellent tool for simulating X-ray patterns of realistic two-dimensional models of finite size and for demonstrating certain structural features and disorder influencing

the diffraction patterns. Structural models can be easily introduced and the diffraction pattern visualized of special ordered and disordered arrays of motifs. The diffraction masks are drawn by computers, reproduced on optical film and placed in a beam of a coherent laser light source. The electromagnetic waves of the light interact with the density of blackening on the optical film. An idealized setup for a device to obtain optical transforms is shown in Fig. 3.3.

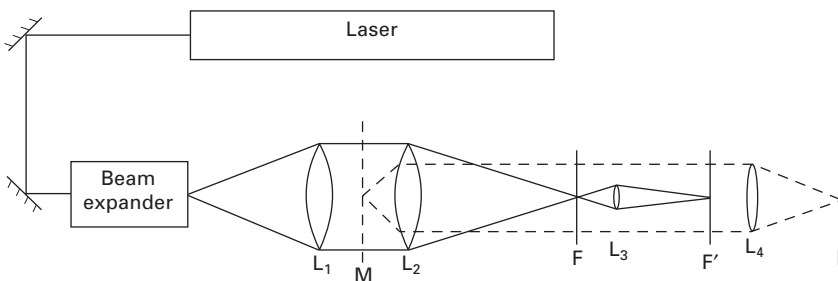
A mask M (optical film) with motifs is placed between two lenses L_1, L_2 and the optical transform can be collected in the focal plane F or in reduced form in F' . The image of the mask is observed in the plane I .

In Fig. 3.4 a series of masks are shown on the top and the corresponding diffraction patterns on the bottom. A circle as a motif results in concentric circles as a diffraction pattern (*cf.* also Fig. 3.5 below). A one-dimensional lattice as a scattering object results in an interference pattern with extinctions in one direction of the original diffraction pattern of the circle. The larger the original lattice, that is, the more scattering points available, the narrower the diffraction lines (first line or first row in Fig. 3.4). If a two-dimensional lattice is considered, the interferences in the two directions overlap and a two-dimensional lattice of diffraction spots results within the contours of the original diffraction pattern of the circle. A strong correlation between the size of the lattice and the width of the diffractions spots can be concluded.

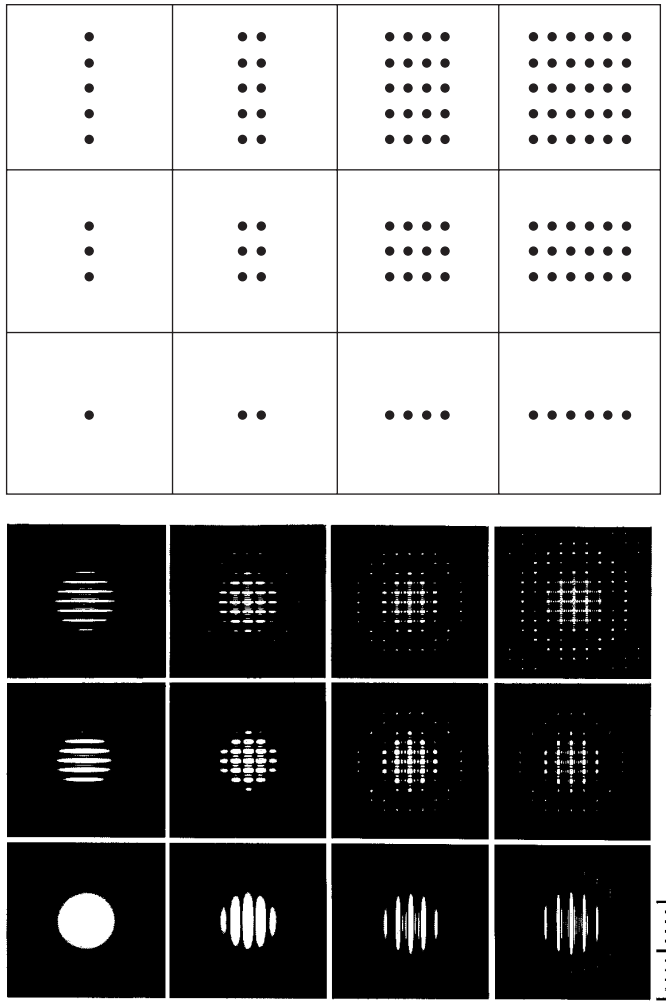
The effect of circles of different sizes on the diffraction patterns as well as the variation of the distance between the circles on the diffraction pattern is demonstrated in Fig. 3.5. These general features also hold for scattering in three dimensions of various waves as X-rays, electrons or neutrons and can be verified by theoretical considerations.

3.2.3 Optical transforms of chain molecules

Significant features of diffraction patterns produced by helical structures of chain molecules can be deduced by optical transforms. The diffraction pattern



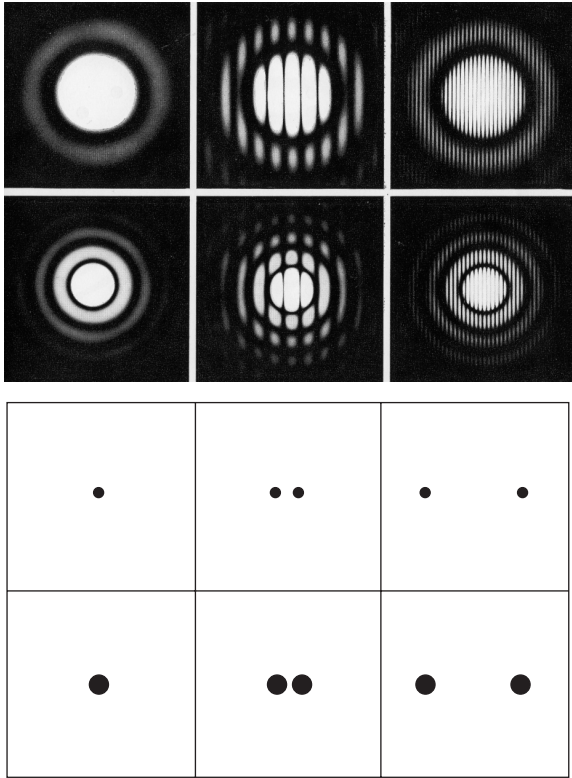
3.3 Setup for obtaining optical transforms. (Adapted from Harburn *et al.*, 1975.)



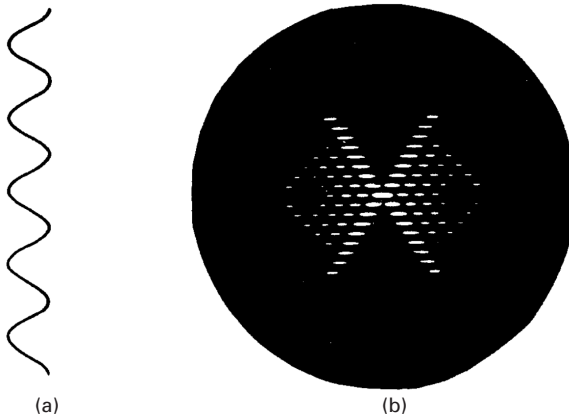
3.4 A sequence of masks (top) and their corresponding optical transforms (bottom). (Adapted from Harburn *et al.*, 1975.)

of a projected single continuous helix on a plane used as a diffraction mask is shown in Fig. 3.6. Two features are remarkable: an X-shaped diffraction pattern is observed with no reflections inside the cross, and no diffraction spots occur on the meridian.

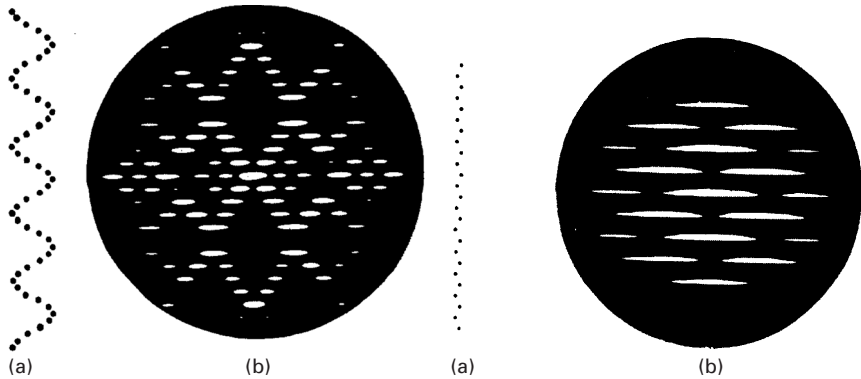
In Fig. 3.7 two discontinuous single helices are compared. On the left, the mask of a helix (a) with ten motifs (points) per repeat is shown with the corresponding diffraction pattern in (b), and on the right picture the mask of a helix (a) with two motifs per repeat and the corresponding diffraction pattern are shown in (b). The tenfold helix exhibits a diffraction spot on the



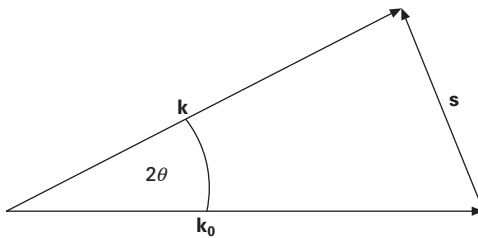
3.5 Optical transforms of circles of different sizes and different distances. (Adapted from Harburn *et al.*, 1975.)



3.6 (a) Projection of a single continuous helix on a plane serving as a mask for optical transforms; (b) optical transform for the helix of (a). (Reproduced by permission of John Wiley & Sons, Inc., from Holmes and Blow, 1966.)



3.7 Masks (a) and corresponding optical transforms (b) for two different single helices. Left: discontinuous helix with 10 motifs (points) per repeat and the diffraction pattern with a diffraction spot on the median of the tenth layer line (note the fifth layer line is missing). Right: discontinuous helix with two motifs (points) per repeat and the diffraction pattern with diffraction spots on the meridian of every second layer line. (Left: reproduced by permission of John Wiley & Sons, Inc., from Holmes and Blow, 1966. Right: reproduced by permission of *Pure and Applied Chemistry*, from Taylor, 1969.)



3.8 Representation of the scattering geometry.

meridian of the tenth layer line; the twofold helix shows a spot on every second layer line on the meridian. These observations can be generalized: if meridional diffraction spots are found on every n th layer line, an n -fold helix may be concluded as causing these reflections.

3.3 Theoretical considerations

The geometry of the scattering of a beam by a monochromatic electromagnetic wave as represented in Fig. 3.8 can be described by two wave vectors: the wave vector \mathbf{k}_0 of the primary beam and that of the scattered beam \mathbf{k} . The deviation from the primary beam \mathbf{k}_0 is represented by the scattering vector \mathbf{s} or scattering angle 2θ as shown in Fig. 3.8. The two wave vectors, \mathbf{k}_0 for the primary beam and \mathbf{k} for the scattered beam, depend on the wavelength λ

of the electromagnetic wave (eq. 3.1) and have the same length in the case of elastic scattering considered here:

$$|\mathbf{k}| = |\mathbf{k}_0| = 2\pi/\lambda \quad 3.1$$

A scattering vector \mathbf{S} can be introduced by

$$\mathbf{S} = s/2\pi = (\mathbf{k} - \mathbf{k}_0)/2\pi \quad 3.2$$

which leads to (*cf.* Fig. 3.1)

$$(|s|/2)/|\mathbf{k}| = \sin\theta; \quad s = 4\pi \sin\theta/\lambda; \quad S = 2\sin\theta/\lambda \quad 3.3$$

The intensity of the diffraction spots is caused by the interference of waves from different motifs (atoms, electron distribution, etc.; *cf.* Fig. 3.4) distributed in space. The electric or magnetic field of the electromagnetic wave cannot be measured but only the intensity of the wave, that is, the squared amplitude of the wave.

The function $F(\mathbf{S})$ that represents the interference of the waves from various scattering centres or generally from a continuous distribution $\rho(\mathbf{r})$, e.g. electron distribution, is given by

$$F(\mathbf{S}) = \int \rho(\mathbf{r})e^{2\pi i(\mathbf{S}\mathbf{r})}dV_{\mathbf{r}} \quad 3.4$$

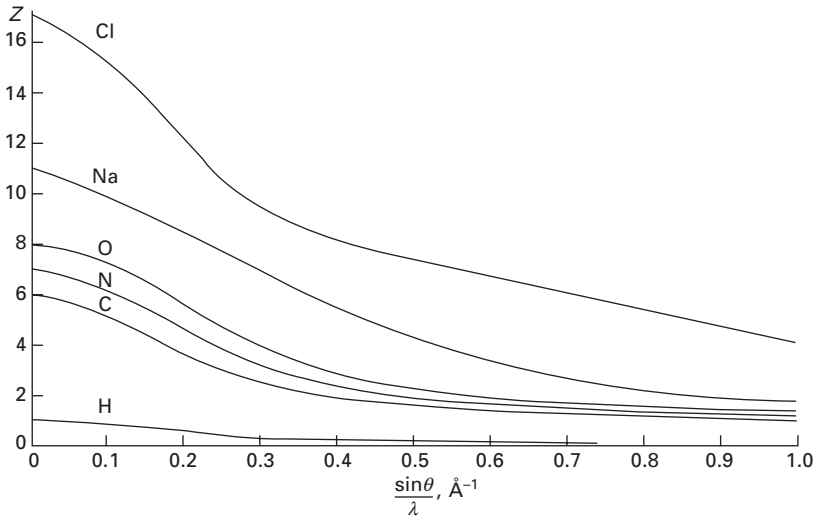
with \mathbf{r} the vector from the origin of space to $v_{\mathbf{r}}$, the scattering motif (*cf.* Vainshtein, 1966). The intensity is proportional to $|F(\mathbf{S})|^2$. In Cartesian coordinates:

$$F(XYZ) = \iiint_{x,y,z} \rho(x, y, z)e^{2\pi i(xX+yY+zZ)}dx dy dz \quad 3.5$$

with x, y, z being the coordinates representing the space in the sample ranging from $-\infty$ to $+\infty$ (mask, *cf.* Fig. 3.4) and X, Y, Z the coordinates on the film.

Two reductions will be introduced, which simplify the structure determination considerably: first, the X-ray scattering amplitude of a single atom, and second, the reduction of the structure amplitude of the crystalline materials in a sample to the content of a unit cell.

For an atom the electron density distribution can be assumed to be centrosymmetric, $\rho(\mathbf{r}) = \rho(\mathbf{r})$, and to be calculated by quantum mechanics. The resulting centrosymmetric atomic scattering function $f(S)$ (*cf.* eq. 3.4), $S/2 = \sin\theta/\lambda$, is plotted in Fig. 3.9 for various kinds of single atoms. The scattering amplitude $f(0)$ amounts to Z , that is, the number of electrons in an atom. The scattering of an assembly of atoms can be regarded as a scattering of point-like centres with a scattering power depending on the kind of atoms and on S that means on half the scattering angle θ with the wavelength λ fixed.



3.9 Atomic scattering amplitudes $f(S)$ as a function of $S/2 = \sin \theta / \lambda$ for various elements. (Adapted from Vainshtein, 1966.)

If a group of n atoms is considered, the electron density at points $\mathbf{r}_1, \mathbf{r}_2, \dots, \mathbf{r}_n$ is

$$\sum_{j=1}^n \rho_j(\mathbf{r} - \mathbf{r}_j) \tag{3.6}$$

Substituting into eq. 3.4 and introducing the structure amplitude of atoms (*cf.* Fig. 3.9), that is, scattering of a point with the respective atomic scattering amplitudes $f_j(s)$, the scattering amplitude for a set of atoms $F(\mathbf{S})$ is obtained:

$$F(\mathbf{S}) = \sum_{j=1}^n f_j(s) e^{2\pi i(\mathbf{S} \cdot \mathbf{r}_j)} \tag{3.7}$$

If the crystal lattice of the sample is now considered to obey translational symmetry in three dimensions of a so-called unit cell with edges a, b, c , the evaluation of the scattering amplitude can be reduced to the content of the unit cell. Repetition of the unit cell generates the entire crystal lattice and the scattering amplitude (eqs 3.4, 3.5) can be replaced by a Fourier integral of a periodic function:

$$\begin{aligned} F_{hkl} &= \frac{1}{abc} \int_0^a \int_0^b \int_0^c \rho(xyz) e^{2\pi i(hx/a + ky/b + lz/c)} dx \, dy \, dz \\ &= \int_{\mathcal{V}} \rho(\mathbf{r}) e^{2\pi i(\mathbf{r} \cdot \mathbf{H})} d\mathbf{r} \end{aligned} \tag{3.8}$$

The density ρ is a periodic function in a , b and c . The exponential function in eqs 3.4 and 3.5 has the same periodicity if $X = h/a$, $Y = k/b$ and $Z = l/c$ with h , k , l integers, which are termed Miller indices; Ω represents the volume of the unit cell and $\mathbf{H} = \{h/a, k/b, l/c\}$. The scattering amplitude F_{hkl} is then also periodic and differs only from zero for integer values (hkl) in detector space or reciprocal space as demonstrated in Fig. 3.4. Each point in reciprocal space for a non-zero value of F_{hkl} can be described by

$$\mathbf{H} = h\mathbf{a}^* + k\mathbf{b}^* + l\mathbf{c}^* \quad 3.9$$

with \mathbf{a}^* , \mathbf{b}^* , \mathbf{c}^* the basic vectors of the lattice in reciprocal space.

Introducing $\mathbf{S} = \mathbf{H}$ and the fractional coordinates $\{x_j, y_j, z_j\}$, eq. 3.7 leads to a structure amplitude F_{hkl} , which depends on the various kinds of atoms placed within the unit cell (eq. 3.10).

$$F(hkl) = \sum_j f_j e^{2\pi i(\mathbf{r}_j \cdot \mathbf{H})} \sum_j f_j e^{2\pi i(hx_j + ky_j + lz_j)} \quad 3.10$$

The equality $\mathbf{S} = \mathbf{H}$ or $|\mathbf{S}| = |\mathbf{H}|$ leads with $S = 2\sin\theta/\lambda$ according to eq. 3.3 and \mathbf{H} according to eq. 3.9 to

$$S = 2\sin\theta/\lambda = (h^2\mathbf{a}^{*2} + k^2\mathbf{b}^{*2} + l^2\mathbf{c}^{*2})^{1/2} = d_{hkl}^* \quad 3.11$$

with d_{hkl}^* the spacing of the layers in three-dimensional reciprocal space represented by the Miller indices hkl . Since \mathbf{H} can also be represented by $\{h/a, k/b, l/c\}$ it follows that

$$2\sin\theta/\lambda = (h^2/a^2 + k^2/b^2 + l^2/c^2)^{1/2} = 1/d_{hkl} \quad 3.12$$

where d_{hkl} is the layer spacing in direct space. Comparing eq. 3.11 with eq. 3.12 the relationship 3.13 is obtained

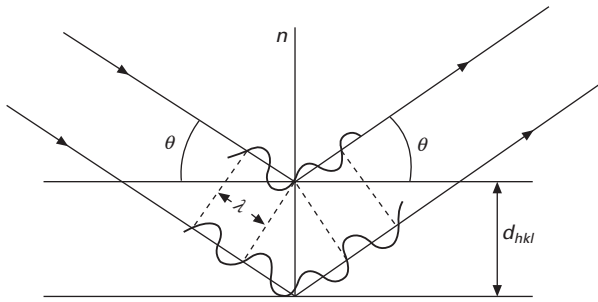
$$d_{hkl}^* = 1/d_{hkl} \quad 3.13$$

Equation 3.12 can be written as

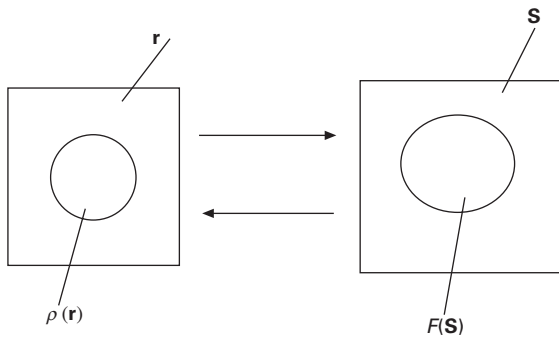
$$\lambda = 2 d_{hkl} \sin\theta \quad 3.13a$$

a geometric relationship introduced by Bragg to explain the appearance of X-ray diffraction spots by a reflection at atomic layers with the so-called Bragg reflection angle θ defined by the incident beam towards the layers (hkl) in space (Fig. 3.10).

The relationship provided in eqs 3.4 and 3.10 establishes a geometric relationship between the direct \mathbf{r} -space and the reciprocal \mathbf{S} -space (Fig. 3.11). The limited \mathbf{r} -space is transformed by the Fourier integral (eq. 3.4) to the limited \mathbf{S} -space and the \mathbf{S} -space can be transformed by the reverse Fourier integral to the \mathbf{r} -space (eq. 3.14):



3.10 Representation of Bragg's law as reflection of the X-ray beam on atomic layer planes of distance d_{hkl} , n normal to layer planes. (Adapted from Vainshtein, 1966.)



3.11 Schematic representation of direct space \mathbf{r} and reciprocal space \mathbf{S} , which are related by Fourier transforms.

$$\rho(xyz) = \int_{-\infty}^{+\infty} \int \int F(XYZ) e^{-2\pi i(xX+yY+zZ)} dXdYdZ$$

$$\rho(\mathbf{r}) = \int F(\mathbf{S}) e^{-2\pi i(\mathbf{S}\cdot\mathbf{r})} dV_{\mathbf{S}} \quad 3.14$$

$\rho(xyz)$ represents the desired quantity of a diffraction experiment, that is, the position of the atoms in the sample. For the determination of $\rho(xyz)$ the structure amplitude $F(\mathbf{S})$ has to be known. However, only $|F(\mathbf{S})|$ can be determined by an evaluation of the X-ray intensities, which means with $F(\mathbf{S}) = |F(\mathbf{S})| \exp(i\alpha)$ that besides the amplitude $|F(\mathbf{S})|$, the phase α in the complex (Gaussian) plane has also to be known. In single-crystal crystallography with many reflections, computer methods have been developed to overcome this phase problem. In fibre and powder diffraction, molecular modelling leads to a starting solution, which can then be refined as discussed later.

The limitation of the \mathbf{r} -space is given by the size of the sample bathed in the primary X-ray beam and the limitation of the \mathbf{S} -space is given by the

wavelength of the radiation. With $S = 2\sin\theta/\lambda$ (eq. 3.3 or 3.11) the maximum size of \mathbf{S} is given as a circle with 0 as the centre and a radius of $2/\lambda$, since $\sin\theta$ cannot exceed 1.

If we consider a fibre with perfectly aligned mosaic crystallites and an incident beam perpendicular to the fibre axis, it may occur that certain layer planes of the crystal cannot be positioned according to the Bragg reflection condition. This can occur especially for the meridional reflection spots. The layer planes lie perpendicular to the fibre axis and parallel to the incident beam. In this case no meridional reflections appear on the fibre diagram. However, they show up if the fibre axis is tilted by the Bragg angle of the specific meridional diffraction spot.

The complex function F_{hkl} can be split into a real and an imaginary part:

$$F_{hkl} = \sum_j f_j [\cos(hx_j + ky_j + lz_j) + i \sin(hx_j + ky_j + lz_j)] = A + iB \quad 3.15$$

$$|F_{hkl}| = (A^2 + B^2)^{1/2} \quad 3.16$$

3.3.1 Temperature and disorder factor

The decrease of the scattering power of an atom with scattering angle relies on the finite size of the electron cloud. If this electron cloud is enlarged, the scattering power drops much faster. Higher temperatures cause a wider spread of the electron cloud due to motion and a faster decrease of the scattering power f . A Gaussian type of function can express the decrease:

$$f = f_0 \exp\{-\{B\sin^2\theta\}/\lambda^2\} \quad 3.17$$

$$B = 8\pi^2 \overline{u^2} \quad 3.18$$

with f_0 the original atomic scattering amplitude and $\overline{u^2}$ the mean-squared amplitude of the atomic vibration. Distortions also cause a spread of the electron cloud, which can be incorporated into the factor B . Instead of B a factor k is introduced, which contains the thermal motion and disorder, and f is then expressed by

$$f = f_0 \exp(-ks^2) \quad 3.19$$

In fibre diffraction with few observed reflections, it is common to introduce the same overall temperature and disorder factor for all atoms contributing to the scattering amplitude as an approximation, which reduces the number of variables. Equation 3.15 leads to

$$F_{hkl} = \exp(-ks^2) \sum_j f_j [\cos(hx_j + ky_j + lz_j) + i \sin(hx_j + ky_j + lz_j)] \quad 3.20$$

3.3.2 Space groups

A further reduction of the number of scattering units (e.g. atoms) in the unit cell is possible if the content of the unit cell can be obtained by symmetry operations on a so-called asymmetric unit as part of the unit cell. A classification of the three-dimensional lattices can be carried out according to the symmetry elements present and specific space groups introduced. These space groups are tabulated in the *International Tables* (1969) and the symmetry elements are listed, which have to be applied on the asymmetric unit to obtain the content of the unit cell. The symmetry elements of a space group lead to relationships between the atoms or molecules and cause specific extinction of diffraction spots. These extinctions are helpful in identifying the space group and are also listed in the *International Tables* (1969); however, a choice of several possibilities may still exist.

A considerable reduction of the number of possible space groups exists for biological materials, which are devoid of inversion symmetry in their packing arrangement due to the chirality of the molecules as, for example, in polysaccharides. These possible space groups for biological materials are listed in Table 3.1.

Table 3.1 List of biological space groups (cubic space groups excluded)

Space group	Minimum symmetry
Triclinic P1	None
Monoclinic P2, P2 ₁ C2	Twofold axis parallel to <i>b</i>
Orthorhombic P222, P2 ₁ 2 ₁ 2 ₁ , P222 ₁ , P2 ₁ 2 ₁ 2 C222, C222 ₁ I222, I2 ₁ 2 ₁ 2 ₁ F222	Three mutually perpendicular twofold axes
Tetragonal P4, P4 ₁ , P4 ₃ , P4 ₂ I4, I4 ₁ P422, P4 ₁ 22, P4 ₃ 22, P4 ₂ 22 P4 ₂ 12, P4 ₁ 2 ₁ 2, P4 ₃ 2 ₁ 2, P4 ₂ 2 ₁ 2 I422, I4 ₁ 22	Fourfold axis parallel to <i>c</i>
Trigonal R3 P3, P3 ₁ , P3 ₂ R32 P321, P312 P3 ₁ 21, P3 ₂ 21, P3 ₁ 12, P3 ₂ 12	Threefold axis parallel to <i>c</i>
Hexagonal P6, P6 ₁ , P6 ₅ P6 ₃ , P6 ₂ , P6 ₄ P622, P6 ₁ 22, P6 ₅ 22 P6 ₃ 22, P6 ₂ 22, P6 ₄ 22	Sixfold axis parallel to <i>c</i>

3.3.3 Orientation

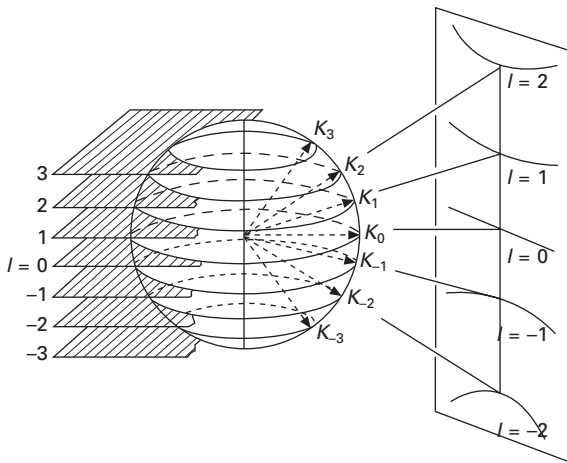
Oriented chain molecules will now be considered with a repeat distance c along z in a Cartesian coordinate system and atoms irregularly arranged in the plane perpendicular to z . The structure amplitude $F(X, Y, l/c)$ is then represented by eq. 3.7 and an idealized diffraction pattern is shown in Fig. 3.12, with the intensity proportional to the square of the structure amplitude. Figure 3.12 shows that the diffraction intensity is concentrated on continuous layer lines and also suggests that it should be possible to obtain the repeat c along z from the spacing of the layer lines:

$$F(\mathbf{S}) = F(X, Y, l/c) = \sum f_j e^{2\pi i(x_j X + y_j Y + l z_j / c)} \tag{3.21}$$

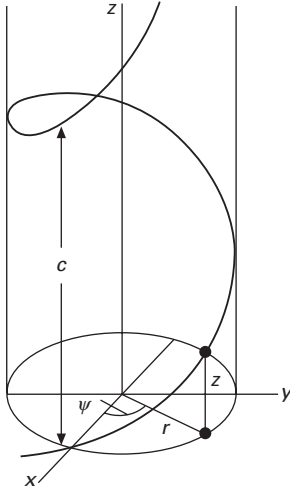
A description of chain molecules in cylindrical coordinates is often advantageous, especially if these molecules form regular helices. The following transformations lead from the Cartesian to the cylindrical coordinate system (cf. Fig. 3.13):

$$\begin{aligned} x &= r \cos \psi & X &= R \cos \Psi \\ y &= r \sin \psi & Y &= R \sin \Psi \\ z &= z & Z &= Z \end{aligned} \tag{3.22}$$

The structure amplitude for a system with a repeat distance c in z is obtained with eq. 3.5 in cylindrical atomic coordinates $\{r, \psi, z\}$ (Vainshtein, 1966) and $Z = lc^*$; c^* is the repeat distance in Z and ρ_M is the density along the helix:



3.12 Diffraction pattern of a chain molecule with a repeat distance c and irregularly arranged atoms in the plane perpendicular to z leading to continuous layer lines. (Adapted from Vainshtein, 1966.)



3.13 Description of a helix with cylindrical coordinates. (Adapted from Vainshtein, 1966.)

$$F_l(R, \Psi, lc^*) = \int_0^\infty \int_0^{2\pi} \int_0^c \rho_M(r, \psi, z) \exp\{2\pi i [Rr \cos(\psi - \Psi) + lz c^*]\} r dr d\psi dz \quad 3.23$$

and diffraction intensities occur on layer lines l only.

If we consider a continuous helix of radius r_0 and repeat c :

$$r = r_0, \psi = 2\pi z/c \quad 3.24$$

then a unit density along the helix can be represented by two Dirac δ -functions:

$$\rho(r, \psi, z) = \delta(r - r_0) \delta(\psi - 2\pi z/c) \quad 3.25$$

Integration over z in eq. 3.23 gives:

$$\int_0^c \delta(\psi - 2\pi z/c) \exp(i l (2\pi z/c)) dz = \exp(i l \psi) \quad 3.26$$

and integration over r leads to:

$$F(R, \Psi, lc^*) = \int_0^{2\pi} r_0 \exp(2\pi i R r_0 \cos(\psi - \Psi) + i l \psi) d\psi \quad 3.27$$

Introducing the definition of the Bessel function J_n of order n ,

$$\int_0^{2\pi} \exp(i u \cos \varphi + i n \varphi) d\varphi = 2\pi i^n J_n(u) \quad 3.28$$

and substitution of $2\pi R r_0 = u$ and $\psi - \Psi = \varphi$ ($r_0 =$ radius of the helix), the scattering amplitude

$$|F_l| = |2\pi r_0 J_l(2\pi r_0 R)| \quad 3.29$$

is obtained. The intensity $I_l \propto |F_l|^2$ on every single layer line lc^* is axial symmetric and proportional to J_l . Since the first maximum of the Bessel function $J_l(u)$ lies approximately at $u = l$, a diffraction pattern as shown in Fig. 3.6 for the optical transform of a continuous helix is obtained.

For a discontinuous helix (Vainshtein, 1966) with two Dirac δ -functions and unit density

$$\rho(r, \psi, z) = \sum_n \delta(r_n - r_0) \delta(\psi - 2\pi z_n/c) \quad 3.30$$

the structure amplitude

$$F_l(R, \Psi, lc) = \sum_n \sum_j f_j J_n(2\pi r_j R) \exp \left\{ i \left[n \left(\Psi - \psi_j + \frac{\pi}{2} \right) + 2\pi l z_j/c \right] \right\} \quad 3.31$$

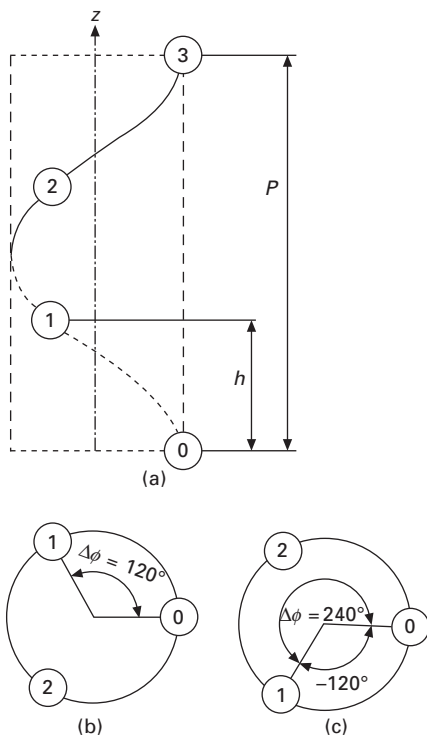
is obtained. A summation over n Bessel functions on each layer line l has to be carried out.

The two periodicities, one for the continuous helix c and the other for the periodicity c' for the regular motifs on the helix, have to be considered and result in the presence of combined layer lines l fulfilling both conditions with non-zero diffraction spots. These layer lines can be described by the so-called selection rule (Vainshtein, 1966):

$$l = nt + mu \quad 3.32$$

with n and m integers, u the number of points or motifs on the helix in the actual period c , t the number of turns of the helix in c , c the crystallographic identity in z , and P the pitch of the helix. P represents the distance equivalent to one turn in z (Fig. 3.14). The ratio u/t has to be expressed by whole numbers and can be used to characterize or describe a discontinuous helix.

If we consider the diffraction spots on the meridian ($R = 0$) on layer line l , only the Bessel function J_0 of order 0 has a maximum on the meridian, which means that $n = 0$ in eq. 3.32 and the selection rule reduces to $l = mu$. This equality can be deduced directly with $n = 0$ from eq. 3.31. A periodicity in F_l is obtained by $c'/lc = m$ (m integer) or $l = mu$ ($u = c/c'$, where c' is the periodicity in z). With $m = \pm 1, \pm 2, \text{etc.}$, that is, $l = \pm u, \pm 2u, \text{etc.}$, meridional reflections are expected on the u th, $2u$ th, etc. layer line as shown in Fig. 3.7 by optical transforms. For $m = 0$ the zero point on the equator ($l = 0$) is obtained, that is, the point where the primary beam hits the detector. An observation of the meridional reflections results in a determination of the number of motifs u . The number of turns t and the direction in which the helix proceeds, left- or right-handed, is left to a conformational analysis to be addressed later.



3.14 Schematic representation of a threefold helix (a) by u/t , $u = 3$, $t = 1$ and $\Delta\Phi = 2\pi t/u$; (b) $\Delta\Phi > 0$ right-handed helix ($u = 3$, $t = 1$); (c) $\Delta\Phi < 0$ left-handed helix ($u = 3$, $t = -1$ or $t = 2$). P is the pitch of the helix (repeat of one turn in z); the distance between two adjacent motifs in z is $h = c' = c/u$.

3.4 Data reduction

If the structure of a crystalline sample is known, the calculation of the structure amplitudes as well as the intensity of the diffraction spots is straightforward. For a comparison between structure calculation and diffraction data, the structure amplitudes are preferred and the measured intensities data have to be converted into structure amplitudes. It should be stressed that the intensity $I(\mathbf{S})$ observed is proportional to $|F(\mathbf{S})|^2$ and therefore only $|F(\mathbf{S})|$ is available from the experimental data for comparison and not $F(\mathbf{S})$, which represents a complex quantity. The proportionality factor between $|F(\mathbf{S})|^2$ and $I(\mathbf{S})$, that is, K' in eq. 3.33, depends on the scattering angle 2θ and further quantities and will now be discussed.

$$I(\mathbf{S}) = K' |F(\mathbf{S})|^2 \quad 3.33$$

Equation 3.33 also represents a useful relationship for testing the correct

alignment of an experimental diffraction pattern. Replacing the scattering vector \mathbf{S} by the centrosymmetric one $-\mathbf{S}$ leads to the same intensity:

$$\begin{aligned} |F(\mathbf{S})|^2 &= F(\mathbf{S}) F^*(\mathbf{S}) = F(\mathbf{S}) F(-\mathbf{S}) = F(-\mathbf{S}) F(\mathbf{S}) \\ &= F^*(\mathbf{S}) F(\mathbf{S}) = |F(\mathbf{S})|^2 = A^2 + B^2 \end{aligned} \quad 3.34$$

A correct alignment implies that $|F(\mathbf{S})|^2$ or the diffraction spots of two centrosymmetric related reflections on the detector device should exhibit the same intensity.

The general geometric site for all possible reflections described by the wave vector \mathbf{k} (cf. eq. 3.1) represents a sphere of radius k with the centre in the origin of the scattered waves. These sites on the sphere can also be described by the scattering vectors \mathbf{s} representing diffraction spots. However, if the scattering vector $\mathbf{H} = \mathbf{S} = \mathbf{s}/2\pi$ representing a reciprocal lattice point \mathbf{H} is introduced, the radius of the sphere has to be reduced to $k/2\pi$ as condition for a reflection spot of a net point \mathbf{H} to be placed on the surface of the sphere. Normally, a net point of the reciprocal lattice for a single crystal does not fall on the surface of the sphere described, but this kind of placement can be realized by a rotation of the crystal. Only those points lying on the sphere give rise to real reflections on the detector. A random distribution of crystals in a powder will always exhibit a rotational position to fulfil the required condition and will even show a continuous line on the surface of the sphere for an individual reflection plane (hkl). A uniaxial distribution of the crystallites within the sample leads to single diffraction spots of some size on the surface of the sphere due to a rotation about a single axis of the aligned crystallites. However, some of the reciprocal lattice points lie beyond the range of reflecting positions.

The corrections to be applied for obtaining the structure amplitude from the intensities are mostly of a geometric nature and are related to the devices used for measurements. This includes the polarization p of the radiation, the absorption A occurring within the specimen, the amount or time for layers placed in the reflection position described by the Lorentz factor L and the multiplicity j of the layers contributing to a reflection. All these factors have to be applied to the intensities measured by the detection device to reduce the intensity data to the $|F_{hkl}|$ (eq. 3.33). It is common that the measured intensities are corrected and the structure amplitudes are used for comparison of observed and calculated values (eq. 3.35). A further advantage of preferring the structure amplitudes lies in the fact that they are needed for the calculation of electron density maps from which the position of atoms can be determined.

$$|F_{hkl}| = (KI_{hkl}/jLpA)^{1/2} \quad 3.35$$

K depends on the crystal size, primary beam intensity and a number of fundamental constants. It represents a constant for any set of measurements

with the same primary beam intensity. The exact value of K is not of importance for the structure determination considered here. Therefore, this term is omitted from the data reduction calculation and the values obtained are called relative structure amplitudes.

$$|F_{\text{rel}}| = (I_{hkl}/jLpA)^{1/2} \quad 3.36$$

The polarization factor p for unpolarized radiation without crystal-monochromatized radiation is given by (Klug and Alexander, 1954):

$$p = (1 + \cos^2 2\theta)/2 \quad 3.37$$

The multiplicity factor j represents the number of different sets of layer planes (hkl) that contribute to a single reflection.

The absorption factor A for X-rays of a particular specimen depends not only on its elemental composition and the radiation wavelength but also on the shape and size of the specimen. For small samples, A can be omitted, but if necessary the adsorption factor A for fibres of cylindrical form is available as well as for sheets (Klug and Alexander, 1954; Alexander, 1969).

The Lorentz factor L accounts for the fact that only crystal planes diffract the incident beam, which are in a reflecting position (*cf.* Fig. 3.10), i.e. the Bragg angle θ of the incoming beam equals the scattering angle θ of the diffracted beam, both measured towards the crystal planes (Bragg's law). The reflecting position can be obtained by kinematics of the diffraction system but it may already be present by the distribution of crystallites in the sample. For the single crystal rotation technique this geometric factor represents a measure of the relative amount of time by which sets of layer planes are located in the diffraction position. For the powder method with a random distribution of crystallites it is the fractional number of reciprocal lattice points in the diffraction position. For the fibre diffraction technique, it was recognized that the standard single crystal rotation correction factor is inadequate when applied to diffractions of partially crystalline and oriented fibres (Schiebold, 1944; De Wolff, 1962; Franklin and Gosling, 1953; Arnott, 1965). Cella *et al.* (1970) provided a formalism for deriving the Lorentz factor for any geometric distribution of crystallites in a polycrystalline sample including the uniaxial orientation of crystalline polymers in a fibre.

The Lorentz factor L can be formulated in terms of a generalized distribution function of a number of well-ordered crystallites with weighted ($\Psi(\rho, \theta)$) orientations given by $\Omega(\rho, \theta)$ where the limits of the integration depend on the diffraction geometry. Here ρ represents the angle between the fibre axis and the unit normal \hat{n} to the plane (hkl) in a given crystallite, and θ is the scattering angle (Bragg reflection angle; 2θ is the angle between the incident and diffracted beams). If the fibre is tilted by an angle μ with respect to a plane normal to the primary beam, then the Lorentz factor can be described by:

$$L = \frac{1}{\sin \theta} \int_{f_1(\mu, \theta)}^{f_2(\mu, \theta)} \Omega(\rho, \theta) \Psi(\rho, \theta) \sin \rho d\rho \quad 3.38$$

where

$$\Psi(\rho, \theta) = [\cos^2 \theta \cos^2 \mu - (\cos \rho + \sin \theta \sin \mu)^2]^{-1/2} \quad 3.39$$

3.4.1 Random distribution

The unit normals are uniformly distributed for randomly oriented crystallites as occurring in a powder pattern. The distribution function $\Omega(\rho, \theta)$ is independent of ρ and θ and equal to $1/4\pi$, that is, the fractional number of unit normals per unit solid angle. With μ equal to 0 and with $\Psi(\rho, \theta)$ (eq. 3.39) performing the integration from $f_1(\theta, \mu) = \theta + \mu$ and $f_2(\theta, \mu) = \pi - \theta + \mu$, the well-established Lorentz factor for powder samples is obtained:

$$L_{\text{ran}} = (4\sin\theta)^{-1} \quad 3.40$$

3.4.2 Single crystal rotation

The Lorentz factor L for rotation measurement of single crystals in the normal beam technique ($\mu = 0$, fibre axis perpendicular to the direction of the primary beam) is given by (Alexander, 1969; Stout and Jensen, 1968; *International Tables for X-ray Crystallography*, vol II, 1972):

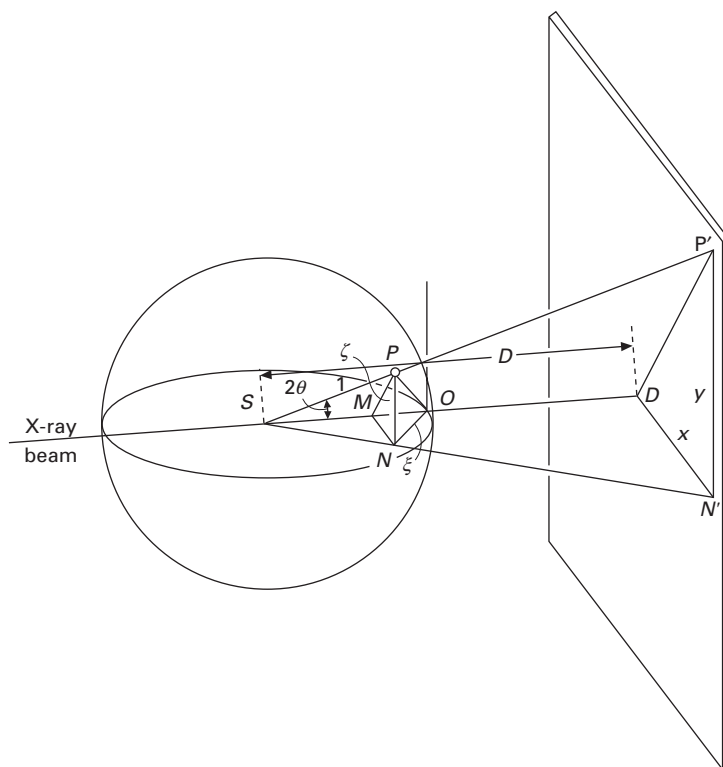
$$L_{\text{rot}} = \cos \theta (\sin 2\theta)^{-1} (\cos^2 \Phi_{hkl,z} - \sin^2 \theta)^{-1/2} \quad 3.41$$

where $\Phi_{hkl,z}$ is the angle between the normal to the reflection plane and the fibre axis. The established Lorentz factor for the general inclination method is provided by Cella *et al.* (1970).

3.4.3 Uniaxial fibre orientation in the normal beam technique

The geometry of an experiment using a flat film as detector is shown in Fig. 3.15. The fibre is placed in S, its axis perpendicular on the plane SON. $P(\xi, \zeta)$ is a reciprocal lattice point whose diffraction spot appears on the flat film in $P'(x, y)$ with the sample to film distance D . ζ is the axial coordinate of the reciprocal lattice point P_{hkl} . Lines of constant ζ on the diffraction pattern represent layer lines. ξ is the radial coordinate of P_{hkl} . Lines of constant ξ are called row lines. An approximated arc-orientation correction factor Γ has to be introduced for variable arc-sizes and the Lorentz factor is then given by

$$L = L_{\text{rot}}/\Gamma \quad 3.42$$



3.15 Geometry of a diffraction experiment using a flat film as detector. (Adapted from Alexander, 1969.)

where

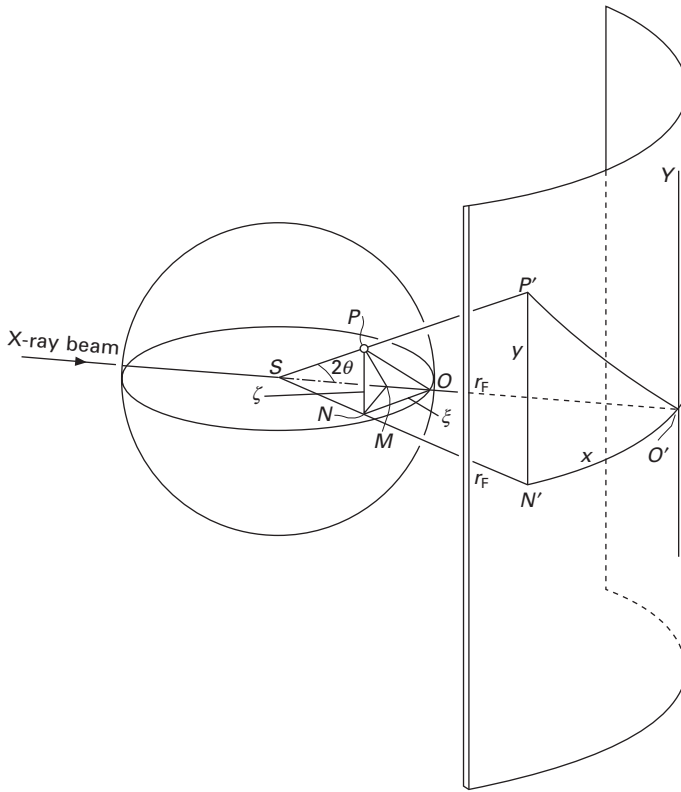
$$\Gamma = \frac{\xi}{2 - \sigma^2} \left[1 - \frac{4\xi^2}{4\sigma^2 - \sigma^4} \right]^{-m/2} \quad 3.43$$

$$\sigma = 2\sin\theta$$

for a flat film (Fig. 3.15) and

$$\Gamma = \frac{\xi}{(1 - \zeta^2)^{3/2}} \left[1 + \frac{\zeta^2}{\frac{4}{(2 - \sigma^2)^2} - \frac{1}{1 - \zeta^2}} \right]^{m/2} \quad 3.44$$

for a cylindrical film with coinciding fibre axis and cylindrical film axis (Fig. 3.16). $m = 0$ if the peak intensity is integrated along a path which is



3.16 Geometry of a diffraction experiment using a cylindrical-shaped film as detector. (Adapted from Alexander, 1969.)

perpendicular to the fibre axis and $m = 1$ for a radial tracing on a flat film.

The coordinate transformation for the flat film detector from x, y to ξ, ζ is provided in this representation by eqs. 3.45 and 3.46 with D the distance from the fibre to the film (*International Tables*, 1972):

$$\zeta = \frac{y}{\sqrt{(D^2 + x^2 + y^2)}} \quad 3.45$$

$$\xi = \sqrt{1 + \frac{D^2 + x^2 - 2D\sqrt{(D^2 + x^2 + y^2)}}{D^2 + x^2 + y^2}} \quad 3.46$$

$$\xi^2 + \zeta^2 = d_{hkl}^{*2} = 4\sin^2\theta \quad 3.46$$

and for a cylindrical film from y, r to ξ, ζ , with r the radius of the cylinder, by eq. 3.47:

$$\zeta = \frac{y}{\sqrt{(r^2 + y^2)}} \quad 3.47$$

$$\xi = \sqrt{\left\{ 1 + \frac{r^2}{r^2 + y^2} - \frac{2r}{\sqrt{(r^2 + y^2)}} \cos\left(\frac{360x}{2\pi r}\right) \right\}}$$

The proposed Lorentz factor is only applicable to the normal beam technique ($\mu = 0$). The correction factor for additional data obtained by tilting the fibre becomes exceedingly complex and Cella *et al.* (1970) advised the use of these data cautiously, if at all, in the data refinement.

De Wolff (1962) came to the following expressions for the Lorentz factor of a uniaxial fibre:

$$L(hk0) = (\sin^2\theta \cos \theta)^{-1} \quad 3.48$$

$$L(hkl) = (\sin^2\theta \cos \theta \sin \Phi_{hkl,z})^{-1} \quad 3.49$$

except $L(00l)$; $\Phi_{hkl,z}$ is the angle between the normal to the reflection plane and the fibre axis. Kreuzer and Ruland (1985) further developed the Lorentz factor of De Wolff for diatropic (meridional) reflections for a fibre diagram.

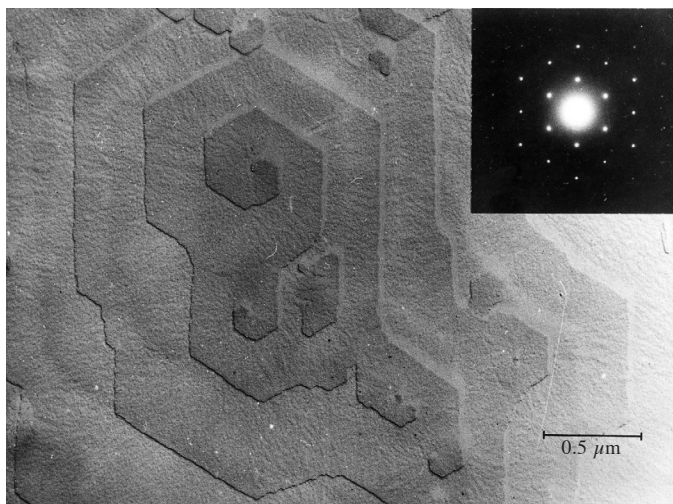
3.5 Structure determination

The goal of structure determination consists of deriving the density function $\rho(\mathbf{r})$, that is, for example, the position of all the atoms within the sample. $F(\mathbf{S})$ or $F(XYZ)$ in eqs 3.4 and 3.5 represents Fourier integrals with the property of reciprocity by a reverse transform, that is $\rho(\mathbf{r})$ or $\rho(xyz)$ can be determined if the structure factor F is known (*cf.* eq. 3.14). However, only $|F(\mathbf{S})|$ can be extracted and not $F(\mathbf{S})$ from a fibre diffraction experiment. Therefore, eq. 3.14 cannot be applied and the structure determination follows a different path, which will now be addressed.

For an evaluation of the information contained in a diffraction pattern, it is necessary first to determine the lattice parameters \mathbf{a} , \mathbf{b} , \mathbf{c} , which are related to the position of the spots on the diffractogram (*cf.* optical transforms), and to identify each spot by the Miller indices (hkl) , i.e. to identify the reflection planes from which the reflections originate. Evaluation of this information may also lead to identifying the crystal system (triclinic, monoclinic, etc.) and proposing a space group. Procedures were developed for using eqs 3.11 and 3.12 with the lattice parameters as fixed quantities and the Miller indices as variables (e.g. De Wolff, 1957) or the lattice parameters can be determined by trial and error with a certain number of reflections. This step is difficult to achieve for randomly arranged crystallites in polymers, which contain two sets of unknowns in eqs 3.11 and 3.12, the lattice parameters and the Miller indices.

In a fibre X-ray diagram the distance of the first layer line on the meridian ($h = k = 0$) provides c^* , the second layer line $2c^*$, etc., and c^* can be determined. The remaining unknowns h , k and a^* , b^* in eq. 3.11 for a given layer line have to be determined in a consistent way by trial and error. The wavelength of the radiation λ is known and θ is experimentally determined. Here additional electron diffractograms of polymeric single crystals are very helpful, since generally the chain axes c of the polymer are placed perpendicular on the support (*cf.* Fig. 3.17). The axes a^* and b^* are positioned in the plane of the support and show in different space directions; h and k can be easily assigned and a^* and b^* determined (*cf.* Fig. 3.4). The conversion from reciprocal unit cell parameters to direct ones is provided in textbooks of crystallography (e.g. Stout and Jensen, 1968). These are simple expressions for orthorhombic systems with $a^* = 1/a$, $b^* = 1/b$, $c^* = 1/c$ and $\alpha = \beta = \gamma = \alpha^* = \beta^* = \gamma^* = 90^\circ$.

Evaluating the observed intensities and indexing the diffraction spots and further correcting the intensities according to the appropriate correction factors leads to the observed structure amplitudes $|F_o|$, which are needed for comparison with the calculated ones. It may be possible to determine the phases of the observed structure amplitudes for single crystal measurements using procedures involving large numbers of diffraction spots involved. However, this is not possible for fibre diffraction studies of chain molecules and a procedure has been developed to solve the structure in the following manner.



3.17 Polymeric single crystals of triethylcellulose and the corresponding electron diffractogram (insert). These crystals are too tiny to be used in single-crystal procedures of mosaic crystals.

First a conformation analysis is performed, followed by a packing analysis. The fibre repeat c and symmetry elements along the chain lead to the introduction of constraints for the conformation of a single chain as the type of helix (*cf.* Section 3.3.3), rise per residue, etc. The conformation can be calculated by a so-called conformational analysis with known standards of bond lengths, bond angles and torsion angles of a monomeric unit of the chain molecule. These standard geometric values and their limits are accessible from similar low molecular weight compounds by single crystal structure determination. This conformational analysis rests on energy minimization for pair potentials for non-bonded contacts and on simple potentials for bond lengths, angles and torsion angles. Nevertheless, several conformations especially for pendant groups are probable. These possible conformations will then be packed within the determined unit cell and a refinement with packing pair potentials of non-bonded contacts leads to a low-energy packing structure. The conformation and packing analysis may also be performed simultaneously. Certain conformation and packing analysis procedures such as molecular dynamics simulation also allow the determination of the lattice parameters of the unit cell (Allinger and Yuh, 1980).

The procedure of conformation and packing analysis can be supported and placed on a more secure basis if additional information is introduced. Hydrogen bonds of specific oxygen involved, e.g. in cellulose structures, may be detected by IR spectroscopic studies. If polarized radiation is used, the directions of the bonds can be determined and NMR solid state studies may provide specific torsion angles.

In contrast to diffraction studies, spectroscopic investigations on crystalline materials rely on energy transfer to certain atoms and groups of a molecule, which are bound and influenced by force fields of the materials. The transfer of energy by electromagnetic waves of a certain frequency may then serve for an evaluation of the interactions between atoms or groups in a molecule and for structural insights of conformation and packing arrangements of a molecule. Frequency-related quantities instead of the frequency itself are generally used for a description of the measurements as wavelength or wavenumber for IR and Raman or the relative quantity of chemical shift for NMR investigations. For solid-state cellulose vibrational IR and Raman or high-resolution solid-state ^{13}C -CP/MAS-NMR (cross-polarization/magic angle spinning nuclear magnetic resonance) experiments are appropriate methods for gathering spectroscopic data, which can be utilized for a characterization or to supplement X-ray data in a determination of polymeric structures. The chemical shift of NMR experiments describes the shielding of a nucleus by its environment and represents a structure-sensitive quantity. The vibrational frequencies of IR and Raman investigations lie in the infrared wavelength region and powerful spectrometer with Fourier-transform techniques are available. Raman spectroscopy can be performed in the visible wavelength

region, since the difference in energy transfer from the applied wavelength as a standard is the needed quantity and can be detected with application of modern lasers and high resolution apparatus. A change of the polarization of the material, i.e. electric dipoles, during energy transfer is requested for the use of IR spectroscopy and a change of polarizability, i.e. induced dipoles from an electric field, for Raman studies. Therefore, these two spectroscopy techniques are complementary, which means that IR absorbance bands are particularly sensitive to vibrations of polar groups as OH and Raman bands to the non-polar skeletal bonds as C–C and C–O and both types of information can be processed to gain structural information. Bonds that are highly polar and possess relatively high dipole moments result in intense bands in the infrared and are relatively weak in Raman spectra, and bonds that are primarily covalent with a high polarizability generally result in intense bands in the Raman and in weak bands in the infrared spectrum. Structural information can be evaluated if the modes in the vibrational spectra or the chemical shift in the NMR spectra have been assigned to certain groups, which is a prerequisite for the quantitative use of these data.

Solid state NMR measurements provide useful additional structural data which can be incorporated into the conformation and packing analysis. Horii *et al.* (1983) investigated the relationship between the ^{13}C chemical shift obtained by CP/MAS ^{13}C -NMR spectra and the torsion angle χ about the exo-cyclic C–C bond for different monosaccharides, oligosaccharides and cellulose (*cf.* Fig. 3.21 below). They found a simple linear relationship between the chemical shift of the CH_2OH carbon and the torsion angle χ about the exo-cyclic C–C bond determined by single crystal X-ray experiments. The chemical shifts fell into three groups of 60–62.6 ppm, 62.5–64.5 ppm and 65.5–66.5 ppm, which are related to *gauche–gauche*, *gauche–trans* and *trans–gauche* conformations of the exo-cyclic C–C bond, respectively. The terminology *gauche–trans* means the bond C6–O6 lies *gauche* to C5–O5 and *trans* to C5–C4, and similarly for *trans–gauche* and *gauche–gauche*. On the basis of these results Horii *et al.* predicted the rotational position of the torsion angle χ of regenerated cellulose II along the two chains of the unit cell as gt, which turned out to be correct as was later confirmed by Langan *et al.* (2001) with X-ray evaluation. At the time of the prediction one chain was thought to expose O6tg, the other chain O6gt. For native cellulose I the NMR and X-ray data were in agreement from the beginning concerning the O6 position.

A similar linear correlation between the chemical shift of ^{13}C carbon atoms and torsion angles was also observed for the ring carbons C1 and C4 as function of the bridge torsion angles Φ and Ψ , respectively (see Fig. 3.21, Horii *et al.*, 1987). High-resolution ^{13}C -CP/MAS-NMR spectra provide valuable data needed in many ways to complement diffraction experiments of solid state materials. Especially valuable are predictions of symmetry

elements along the chain and packing arrangements in the unit cell. The experimental data from solid state NMR studies may be incorporated into a conformation and packing analysis in which the X-ray data should still play a dominant role.

With the knowledge of the content of the unit cell derived from conformation and packing analysis, the structure amplitude can be calculated directly according to eqs 3.16 and 3.20 and compared with the observed values $|F_0|$. At this stage the simple temperature or disorder factor D can be adjusted and refined. A structure amplitude refinement of the geometry of the chain molecule against minimal deviation between observed and calculated structure amplitude then results in the crystal and molecular structure of the crystallites in a fibre. Because of the low data to parameter ratio during this refinement, it is advisable to constrain the geometry of the molecule within the known geometry of monomers and oligomers and to perform a simultaneous conformation, packing and structure amplitude refinement (*cf.* Fig. 3.18).

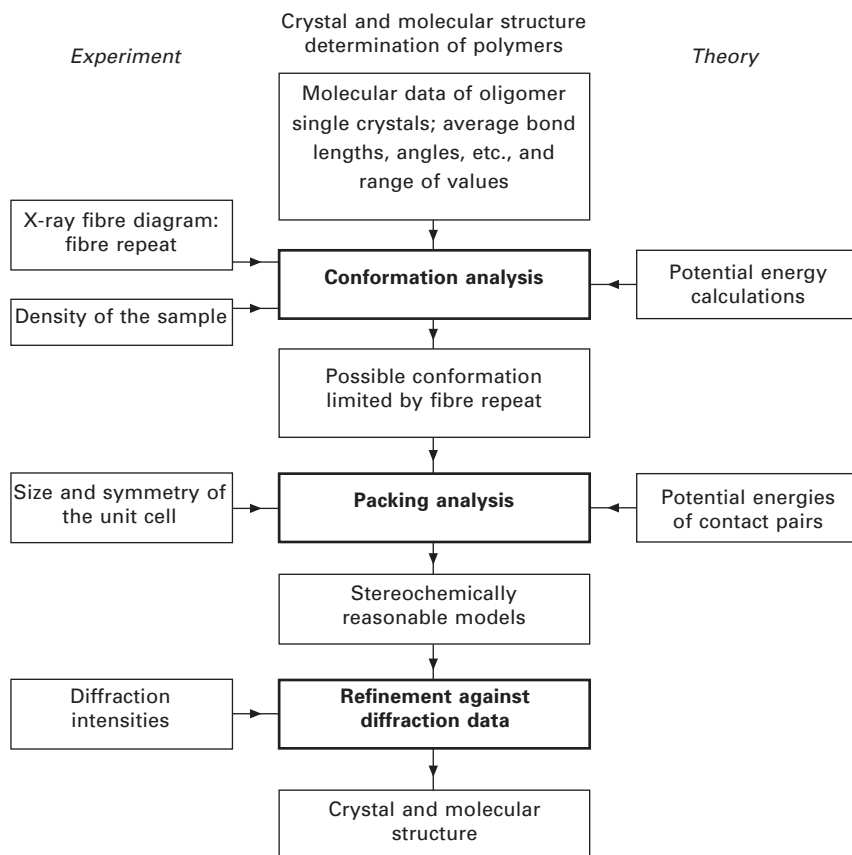
This procedure strongly depends on a correct unit cell as well as the proposed symmetry elements of the space group. Including the symmetry elements of the space group, applied on the asymmetric unit of the unit cell from the beginning of the investigation a faster calculation with better resolution of the structure is obtained. In contrast the refinement against the whole content of the unit cell also gives some advantages, since in this case the symmetry elements of the space group may be derived and the space group confirmed. Further, a refinement in a larger, multiple unit cell of the smallest and correct one should exhibit the translational symmetry elements as well as the space group symmetry. A first hint of a correctly established unit cell is provided by agreement between the observed and calculated density for the content of the unit cell.

A possible procedure for a conformation and packing analysis leading to the determination of the molecular and crystal structure of molecules is shown in the graph in Fig. 3.18. Different structural refinement evaluations have been developed: a linked atom least-squares procedure (Smith and Arnott, 1978), a simplex procedure (Zugenmaier and Sarko, 1980) based on a mathematical routine proposed by Box (1965), molecular mechanics calculation (Allinger and Yuh, 1980) and recently a constrained single crystal determination procedure developed by Sheldrick (1997) (Nishiyama *et al.*, 2002). All these procedures have been successfully applied to the structure determination of cellulose.

The commonly accepted residual index may serve for judging the goodness of fit:

$$R = (|\sum |F_0| - |F_{\text{cal}}||) / (\sum |F_0|) \quad 3.50$$

Two polymeric structures are chosen to demonstrate the described procedures: the first is of biological origin, a derivatized amylose, trimethylamylose

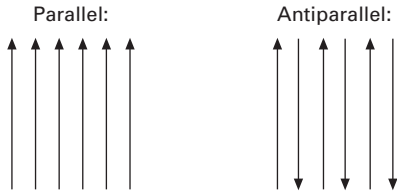


3.18 Flow diagram of a computer-aided procedure for the determination of fibrous polymeric crystal structures.

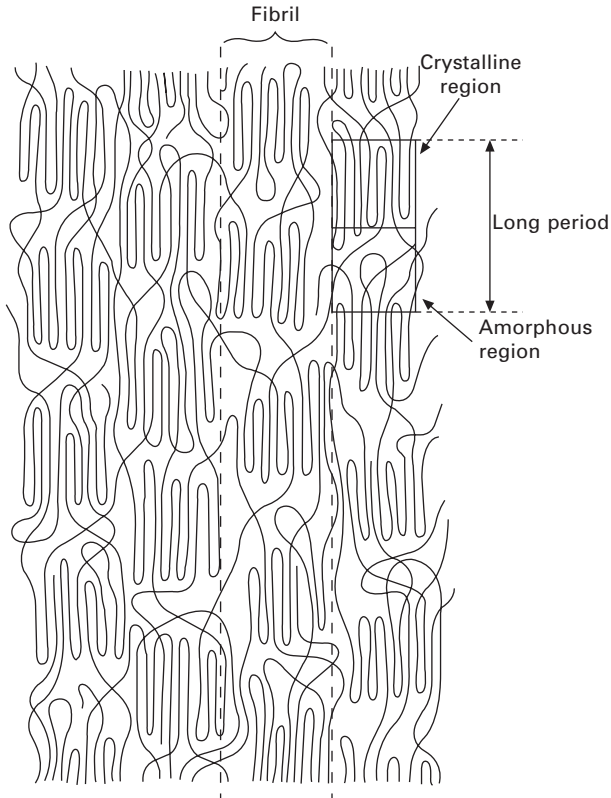
(TMA), and the second is a synthetic polymer, polyethylene (PE). In enzymatic polymerized chiral materials in which a molecular chain direction is established, the molecular chains can pack in either a parallel or an antiparallel arrangement (*cf.* Fig. 3.19). In most synthetic polymers, which exhibit folded fibrils or lamellae, antiparallel arrangements of chains can be expected (Fig. 3.20). Polyethylene seems to be an excellent example for which to discuss the influence of long-chain molecules on the geometry of the structures, that is, on the arrangement of the chains, the influence of internal and external parameters and the disorder in the crystalline domains.

3.5.1 Trimethylamylose, TMA

Polysaccharides such as cellulose may be produced in fibrous form by nature and have been used by people for centuries. In contrast, amylose as

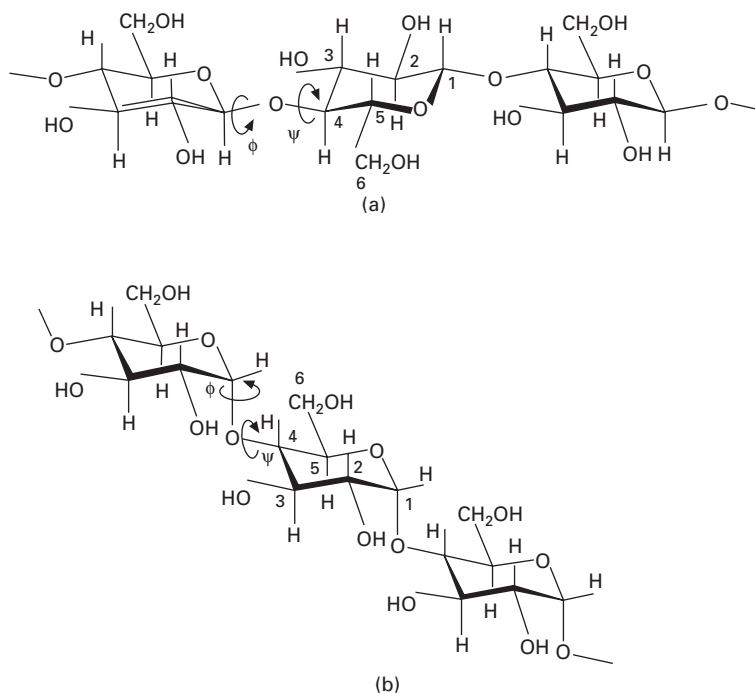


3.19 Schematic representation of parallel and antiparallel arranged chains.



3.20 Schematic representation of folded chain arrangements in a fibre. (Reproduced by permission of John Wiley & Sons, Inc., from Heuvel *et al.*, 1976.)

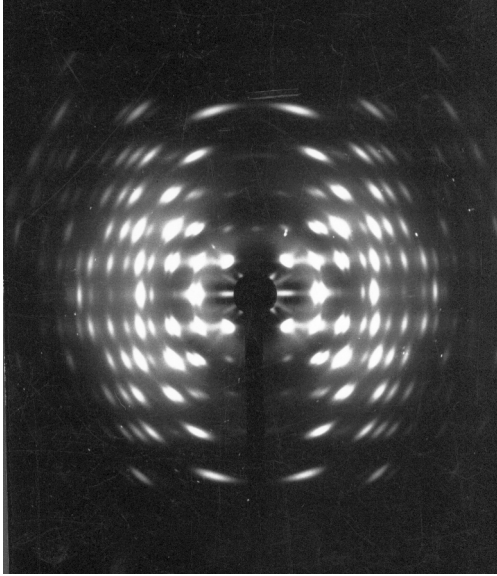
a reserve polysaccharide and used as a food supply has a granular shape in nature. The shape of the amylose molecules is more versatile than that of cellulose and their crystal and molecular structure have been at the centre of investigations for a long time (Fig. 3.21). Here we will discuss the structure of trimethylamylose (TMA), which was prepared by a homogeneous



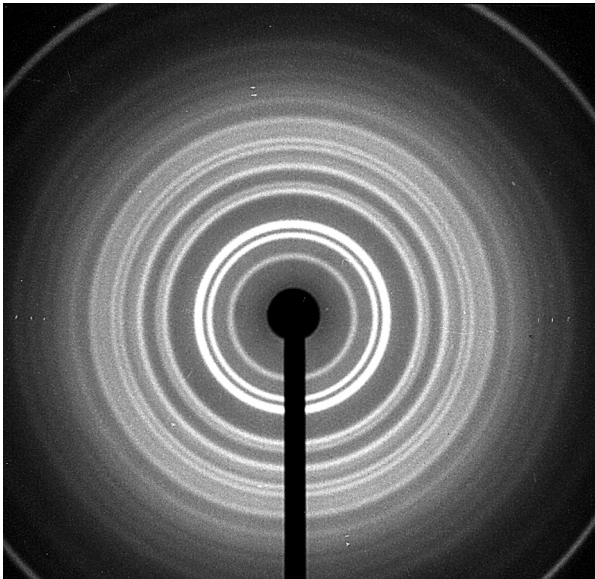
3.21 Schematic representation of (a) cellulose and (b) amylose with labelling of the carbon atoms. Rotation around Ψ , Φ leads to different helices.

methylation of commercially available AVEBE amylose (Zugenmaier *et al.*, 1977). Suitable fibres for X-ray measurements were obtained by stretching TMA films, cast from methylene chloride, by about 300% in a stream of hot air at 60 °C. Such fibres showed perfect orientation but low crystallinity. Annealing at 220 °C for about 10 minutes improved crystallinity dramatically but did not affect the orientation of the crystallites. A typical fibre X-ray diagram is shown in Fig. 3.22 and compared with a diagram of an annealed cast film, which gave a Debye–Scherrer diagram (Fig. 3.23). Due to an almost perfect orientation the meridional reflections are missing (Fig. 3.22), but every second meridional reflection is observed by tilting the fibre axis to the appropriate Bragg angle.

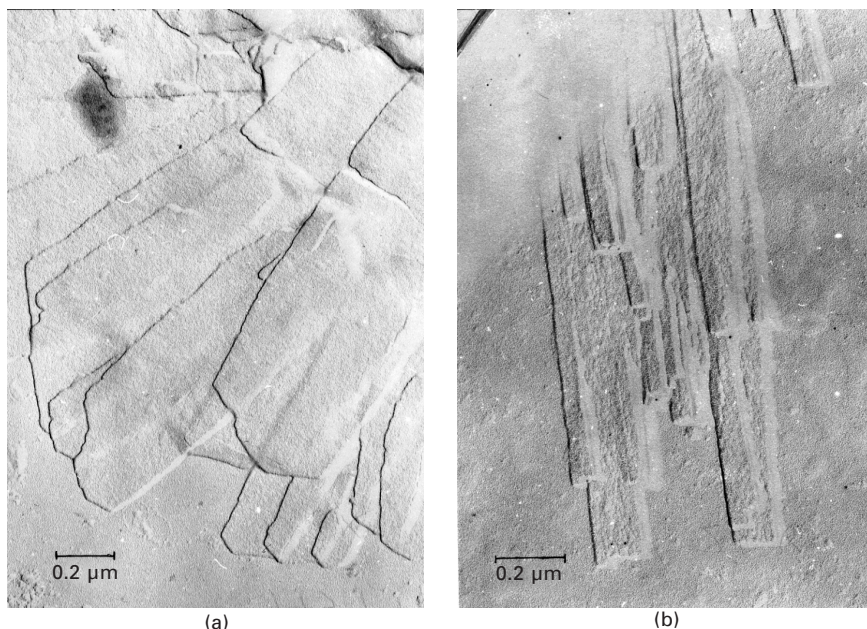
Polymeric single crystals were grown in diethyleneglycol at elevated temperature between 180–150 °C (Fig. 3.24(a)) and showed a Debye–Scherrer X-ray diagram with d -spacing in agreement with those of the diagrams in Figs 3.22 and 3.23. A schematic electron diffraction diagram obtained in the diffraction mode of an electron microscope is represented in Fig. 3.25 of which the size of unit cell parameters \mathbf{a} , \mathbf{b} , $\gamma = 90^\circ$ can be obtained with an internal standard. The electron diffractogram also suggests that twofold



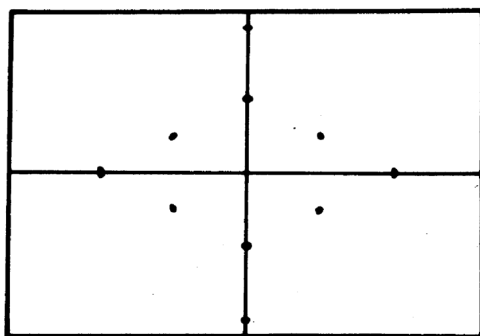
3.22 Fibre diffraction diagram of TMA, the second meridional reflection faintly visible. The second, fourth, sixth, eighth, tenth and twelfth meridional reflections are obtained by tilting the fibre to the appropriate Bragg angle.



3.23 Debye-Scherrer diagram of TMA. The outer ring, only partly visible, originates from the calibration compound NaF_2 .



3.24 Electron micrograph of single crystals of TMA grown (a) at $180^{\circ} - 150^{\circ}\text{C}$ in diethyleneglycol and (b) at room temperature in a solvent-non-solvent mixture of dioxane and 60% octane.



3.25 Schematic drawing of the electron diffraction pattern of single crystals of TMA represented in Fig. 3.24(a).

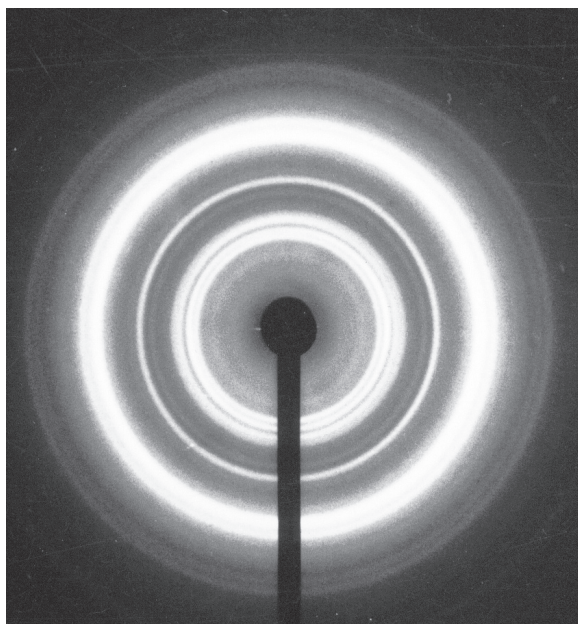
axes are present along the a and b axes due to the missing (100) - and (010) -reflection and with the missing reflections $(00l)$, l odd, a twofold axis can also be assumed in the c direction. With these data the X-ray fibre diagram can be indexed with an orthorhombic unit cell and the parameters refined to $a = 17.24 \pm 0.01 \text{ \AA}$, $b = 8.704 \pm 0.009 \text{ \AA}$ and c (fibre repeat) = $15.637 \pm 0.008 \text{ \AA}$.

No further systematic absences are detected. A comparison of orthorhombic space groups in Table 3.1 of biological materials suggests $P2_12_12_1$ as the most probable space group. Taking into account the measured density of 1.20 g cm^{-3} the unit cell contains eight monomeric units along two chains on 2_1 screw axes of the unit cell, that is, two chains with four monomeric units each. A dimer represents the asymmetric unit, since the fibre repeat c of 15.64 \AA can only be obtained with two dimers in one chain. A monomeric unit has a virtual bond between O4 and the adjacent O4' of $4\text{--}4.6 \text{ \AA}$, and therefore two monomeric units cannot account for the fibre repeat c with a 2_1 screw along the chain axis.

Single crystals were also grown at room temperature as shown in Fig. 3.24(b) but exhibit a different crystal structure, since the X-ray Debye–Scherrer pattern in Fig. 3.26 differs from that of Fig. 3.23.

The intensities of the X-ray spots of Fig. 3.22 were reduced to the observed structure amplitudes. A conformation and packing analysis was performed and the strategy applied as described. The structure amplitudes of overlapping reflections were calculated by

$$|F_{\text{cal}}| = \left(\sum_i^n j_i F_{ci}^2 \right)^{1/2} \quad 3.51$$



3.26 Debye–Scherrer pattern of the single crystal modification shown in Fig. 3.24(b).

where j_i are the multiplicity of the overlapping reflections i .

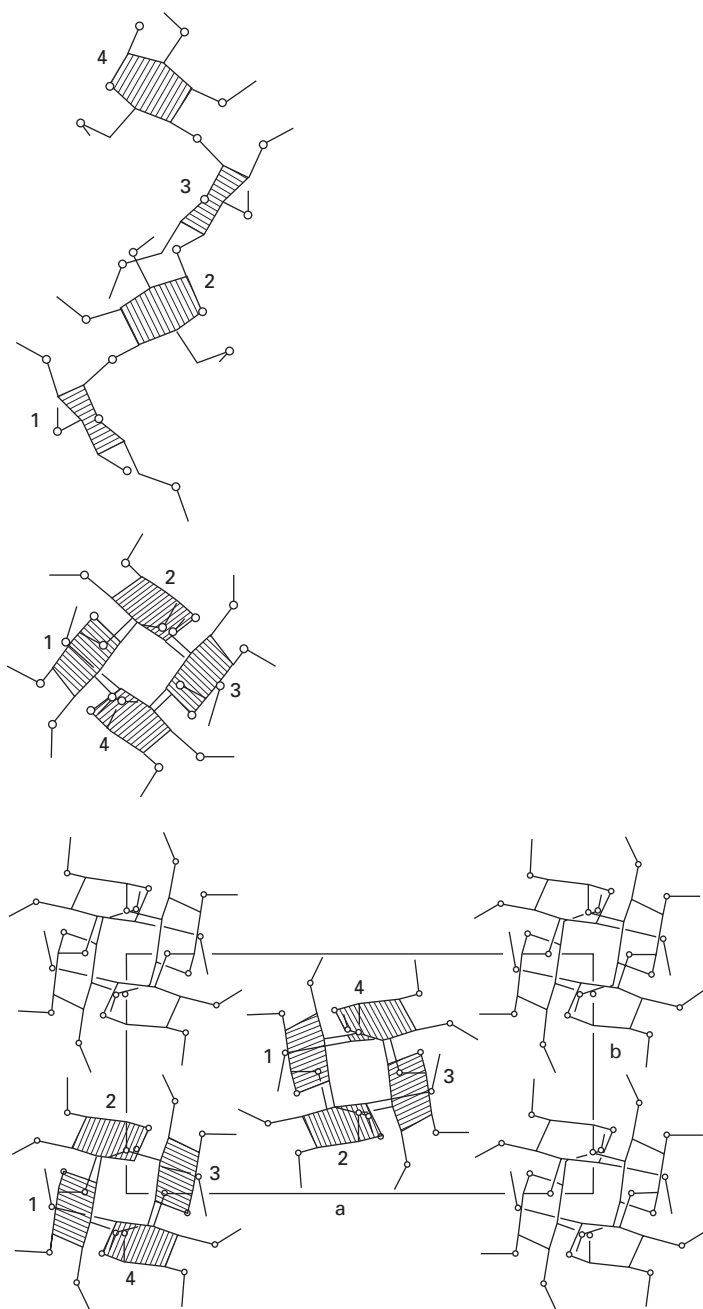
Since the fibre repeat consists of four monomeric units, the starting model for the conformation analysis of the skeleton of amylose was chosen as a left-handed fourfold 4_3 helix. A right-handed one exhibits higher energy. A symmetrical structure of a contact free conformation with neighbouring chains should provide the lowest potential energy, which may be disturbed by packing contacts, especially by the pendant groups at O6 next to C6 in Fig. 3.21. Packing analysis reduces the fourfold helix to a twofold one. Two succeeding monomeric units of the asymmetric dimer show O6 in tg (residues 1 and 3; tg means O6-C6 *trans* to C5-O5 and *gauche* to C5-C4) and in the adjacent residue in the gt position (residues 2 and 4) as shown in Fig. 3.27. As represented in the single chain conformation and the packing arrangement of Fig. 3.27, the methyl groups C2M and C3M attached to C2-O2- and C3-O3- are in equivalent rotational position along the helix concerning the pendant methyl carbon atoms but the rotational positions of the attached hydrogen show small differences. These deviations from a fourfold helix cause a reduction of the helix symmetry to a twofold screw axis only. The possibility of changes in the amylose backbone of the two monomers in the asymmetric unit was not tested due to limitations in computer power in 1977 when the structure refinement was performed.

The coordinates of the crystal and molecular structure are provided in Zugenmaier *et al.* (1977). The conformation and packing within a unit cell are shown in Fig. 3.27. The chains are packed in antiparallel fashion as expected for polymers crystallized from solution in contrast to the parallel packed chains in native amylose.

3.5.2 Polyethylene, PE

Structural investigation on polyethylene (PE) as a flexible chain molecule introduces features that are not observed in single crystal structure determination of small molecules and that will now be discussed. In contrast to native cellulose and some other polysaccharides, polyethylene crystallizes in folded lamellae, folded fibrils (Fig. 3.20) or folded polymer single crystals. Crystallization conditions change the morphology, the back-fold length and the length of the straight chain molecules in the lamellae or fibrils until they are folded back, and these conditions influence the crystal structure. Polyethylene represents a simple molecule and its structure can be described with few adjustable quantities. Therefore, the changes caused by external settings can be easily investigated and have to be considered in discussing further properties, e.g. crystallinity.

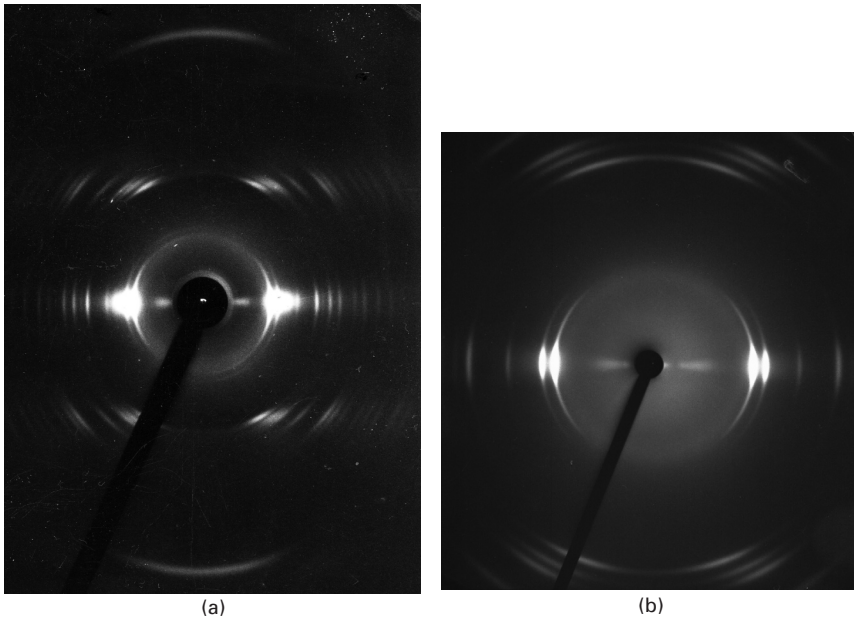
In 1939 Bunn studied polyethylene (PE), indexed the reflection spots and published a crystal structure relying on the atomic scattering factors of carbon only. It can be assumed that the PE investigated was branched and



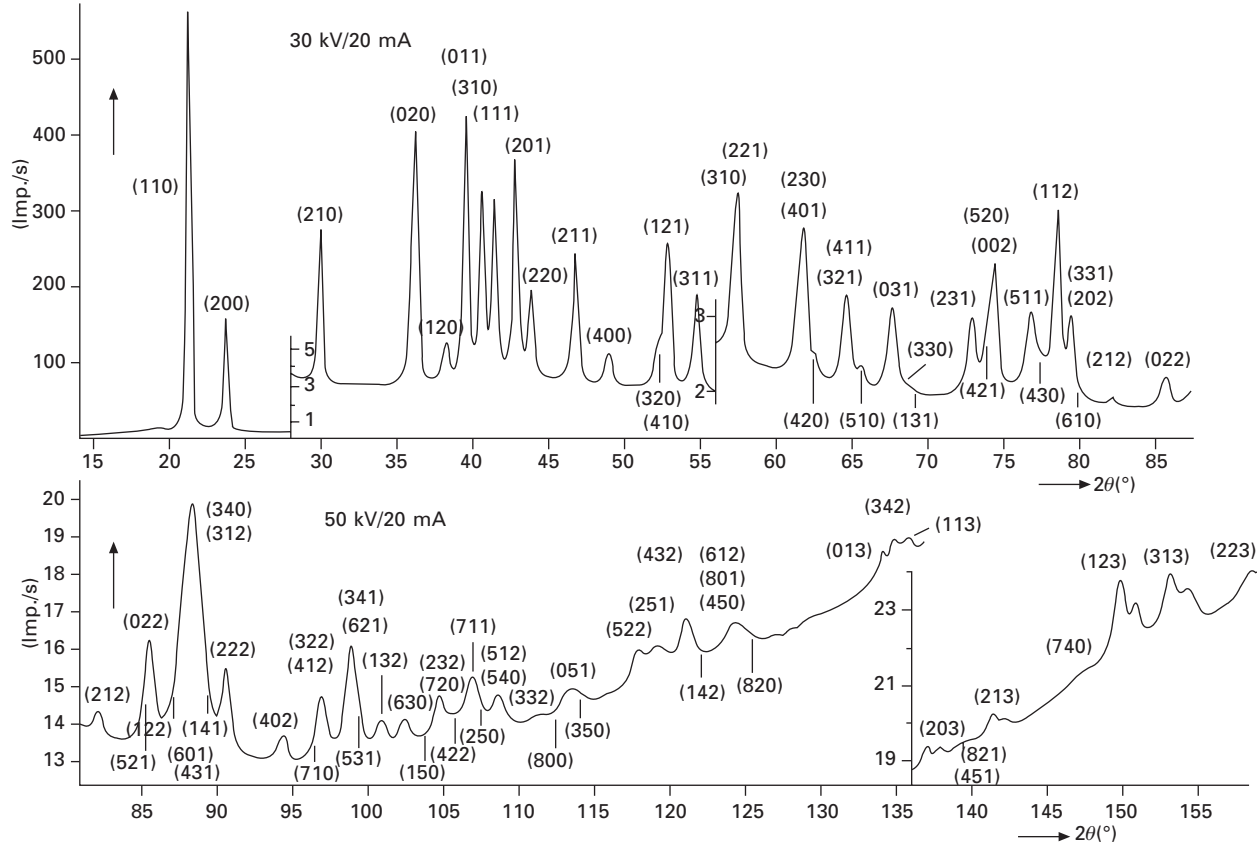
3.27 Representation of the conformation in two projections (top) and packing within the unit cell (bottom) of TMA. The TMA molecule in the centre of the unit cell is packed in antiparallel arrangement with respect to the corner chains.

an equilibrium structure of a linear chain was not obtained. Wide-ranging X-ray investigations on linear PE and ethylene–propylene copolymers were carried out by Zugenmaier (1969) and by Kavesh and Schultz (1970). Melt crystallized samples, differently treated, as well as mats of single PE crystals were investigated using the Debye–Scherrer goniometer technique. The different crystallization conditions led to various morphologies, which influence the crystal structure. Especially, changes in lamellae thickness (crystallite height) and crystallization conditions lead to loose and tight back-folds on the surface of the lamellae.

A fibre X-ray diagram taken with $\text{MoK}\alpha$ is shown in Fig. 3.28(a), and in Fig. 3.28(b) one with $\text{CuK}\alpha$ to provide a better resolution of the innermost reflections. The goniometer diagram of a linear PE kept in the melt at $200\text{ }^\circ\text{C}$ for 2 hours to destroy any texture and then annealed for 20 hours at $130\text{ }^\circ\text{C}$ is shown in Fig. 3.29. It should be noticed that the reflections at the highest scattering angle 2θ are split according to the non-separated radiation from $\text{CuK}\alpha_1$ and $\text{CuK}\alpha_2$. The diffractogram also suggests an anisotropic disorder factor, since the reflections with $(hk2)$ and $(hk3)$ dominate the diagram at high angles and are less reduced than those with $(hk0)$. The lattice parameters of the orthorhombic unit cell have been determined to be $a = 7.418_4 \pm 0.001\text{ \AA}$,



3.28 X-ray fibre diagrams of cold-drawn PE taken (a) with $\text{MoK}\alpha$ radiation and (b) with $\text{CuK}\alpha$ at various sample to film distances. Note the small reflection spacing on the equator as compared to the large layer line spacing in the meridional direction.



3.29 Goniometer X-ray diagram of highly annealed and randomly oriented crystallites of linear PE taken with $\text{CuK}\alpha$ radiation. Note the different scaling of various parts of the diagram. (Reproduced by permission of Springer, Heidelberg, from Zugenmaier and Cantow 1969a.)

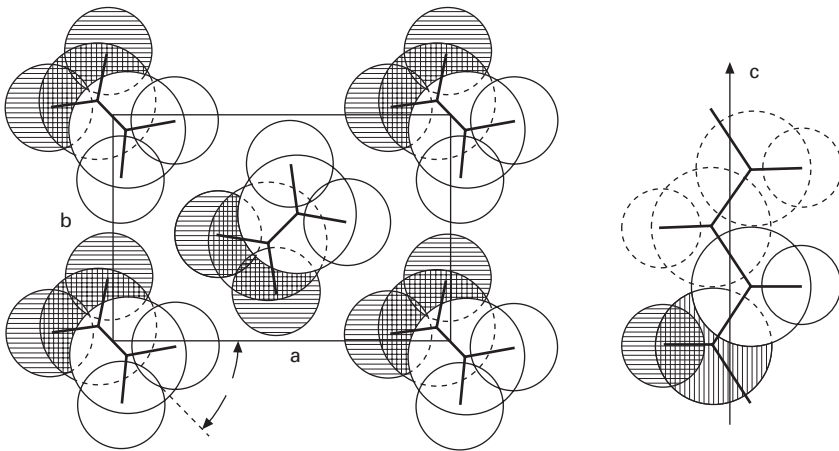
$b = 4.945_6 \pm 0.001 \text{ \AA}$, c (chain axis) $= 2.545_5 \pm 0.001 \text{ \AA}$ at $25 \text{ }^\circ\text{C}$, proposed space group P_{nam} . These values agree well with those determined by Swan (1962a, 1962b) and Schauer and Wilke (1995).

A structure determination was performed with Lorentz-polarization and absorption corrections applied for a random crystallite distribution. Only one geometric variable remained for the description of the structure, the setting angle δ , the angle of the molecular plane of the C-C chain towards the lattice parameter \mathbf{a} (Fig. 3.30). As indicated above, an anisotropic disorder factor $D = \exp(-s\mathbf{k}\mathbf{s})$ ($s = 2\sin\theta/\lambda$) with two parameters was introduced, where

$$\underline{k} = \begin{pmatrix} k_1, 0, 0 \\ 0, k_1, 0 \\ 0, 0, k_3 \end{pmatrix} \quad 3.52$$

The z position of the chain is fixed by the special setting of the space group, and the C-C (1.543 \AA) and C-H (1.09 \AA) bond lengths and H-C-H (109.5°) bond angle are provided by values from paraffin structures (Cole and Holmes, 1960). A special procedure was developed for the independent determination of the three variables δ , k_1 , k_3 , and their values were later confirmed by a computer-aided procedure.

The setting angle δ was determined for highly annealed PE to be $\delta = 45 \pm 1^\circ$ and an anisotropic disorder factor D was established (Zugenmaier and Cantow, 1969b). Normal crystallized, not annealed polyethylene showed changes only in k_3 (Table 3.2).



3.30 Representation of the conformation and packing of polyethylene (PE) in space group P_{nam} . The only geometrical parameter to be refined is the setting angle δ .

Table 3.2 Structural parameters of differently treated linear and branched polyethylene at 25 °C (Zugenmaier 1969)

Polyethylene	$\delta(^{\circ})$	$k_1/(\text{\AA}^2)$	$k_3/(\text{\AA}^2)$
Annealed	45	2.2	0.65
Normal crystallized	45	2.2	1.4
Single crystals (lamella thickness 80 \AA)	42	2.7	–
As polymerized	40	2.8	–
Copolymers [ethylene (82 mol%), propylene (18 mol%)]			
As polymerized	35	8.5	–
Treated with HNO ₃	45	5.3	–

The investigation of solution-grown single crystal mats with differences in the lamellae thickness (80 \AA, electron microscope measurement) versus the melt grown crystals (*ca.* 400–600 \AA), which also differ in the kind of loops within the folds, resulted in $\delta = 42^{\circ}$, $k_1 = 2.7 \text{\AA}^2$ and k_3 estimated to 1\AA^2 . The smallest setting angle δ was found for PE as polymerized with $\delta = 40^{\circ}$ (*cf.* Table 3.2).

In addition, polyethylene with CH₃ side groups was investigated and their influence on the crystalline structure evaluated. An ethylene–propylene copolymer with 82 mol% ethylene and 18 mol% propylene was used in powder form as polymerized which led to unit cell parameters $a = 7.615 \text{\AA}$, $b = 4.986 \text{\AA}$ and c (fibre axis) = 2.550\AA . A setting angle δ of 35° and $k_1 = 8.5 \text{\AA}^2$ was determined; k_3 is difficult to estimate but exceeds 1\AA^2 considerably as compared with linear polyethylene.

All these differences in the setting angle seem to be correlated with constraints due to the folds at the lamellae surfaces. The corner chains exit with a setting angle of δ and the centre chains, which are connected by the fold, enter with $-\delta$. Therefore, removing the amorphous folds by oxidation with fuming concentrated HNO₃, the setting angle δ should no longer be constrained and should move back to the equilibrium value of 45° . A six-hour treatment of the copolymer with HNO₃ at 60 °C led to a setting angle of $\delta \approx 45^{\circ}$ and $k_1 = 5.3 \text{\AA}^2$. After this treatment a shortening of chains was detected by gel permeation chromatography.

It can be concluded that the equilibrium setting angle δ is 45° , which is obtained with high lamellae thickness by high annealing. In this case the border regions close to the surface of the lamellae can be neglected. However, if the interior of the lamellae (length of the chains in the crystallite) is short, a mean value over the lamellae thickness will be detected averaged over the border region and the inner region.

The disorder factor is to a large extent determined by the deviation of the atoms from the ideal positions and is strongly influenced by constraints. The disorder caused by paracrystalline (second kind) defects is of minor

importance and amounts to $k_{p1} \approx 0.2 \text{ \AA}^2$. These conclusions are supported by the k values obtained for PE at an elevated temperature of 80°C . The value of k_3 increases by $\approx 0.1 \text{ \AA}^2$ and the change in k_1 as compared to 25°C lies within the accuracy of the measurement.

Changes in the crystal structure of polymers as well as in the anisotropy of the disorder factor influence their properties and will be discussed in the next section.

3.6 Crystallinity and disorder

The wide angle X-ray diffraction of partial crystalline materials provides, besides the crystal and molecular structure, detailed information about its microstructure and morphology that is about the crystallinity, the crystallite size and lattice distortion of the crystallites and also about the orientation distribution of oriented samples. These structural features determine to a large extent the thermal and mechanical properties of the materials. As represented in an idealized molecular model in Fig. 3.20 for a drawn polymer, the proposed two-phase model is composed of alternately crystalline and amorphous regions. The molecules run through successive crystalline and amorphous regions and may also fold back in the boundary layers. Generally folding does not occur for some native biopolymers such as cellulose. The structural units or microfibrils formed are made up of linked crystalline and amorphous regions. The various structures in a fibre can be characterized by the following typical dimensions. Adjacent molecules are about $4\text{--}5 \text{ \AA}$ apart. The long period of parallel chains is about 100 \AA but may reach 500 \AA , which is small with respect to the length of a molecule of about 2000 \AA . The diameter of a microfibril may amount to about 80 \AA and tens of millions of microfibrils run through the cross-section of a filament.

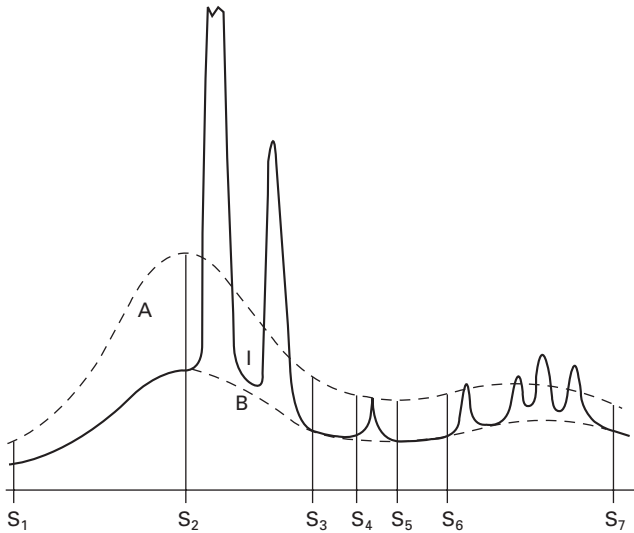
X-ray investigations of polymers in the solid state have shown that polymers consist of partially crystalline materials, i.e. crystalline and amorphous (non-crystalline) materials are present. The ratio of crystalline to non-crystalline portions determines the physical and mechanical properties. Therefore, correlations of the crystalline fraction with physical properties are desirable for a characterization of the materials to be used in application. It is possible to determine the mass fraction of crystalline and non-crystalline parts with physical methods but one should keep in mind that the results are approximations, since polymeric materials represent a large variety of states in their composition. It should also be noted that the separation in crystalline and amorphous parts represents a two-phase model and neglects continuous transitions from the amorphous to the crystalline state. The amorphous state may consist of different arrangements of chains as well as the crystalline state, of which a slightly different packing arrangement of chains occurs, as observed for polyethylene depending on the crystallization conditions

(Section 3.5.2). The folding of the chains causes stress and leads to non-equilibrium arrangement of the chains at the border zones of the crystallites.

The imperfect structure of polymers with crystalline and amorphous regions and defective crystallites leads to a diffraction pattern with few broadened peaks and a high background. Imperfect crystallites are caused by various lattice defects, which can be classified as first- and second-order lattice distortion. Both types of distortion are characterized by local displacement of atoms from their ideal position. In the state of disorder of the first kind the magnitude of displacement is independent of location in the crystal and long-range order is preserved. In contrast, the displacement is increasing for any given origin for disorder of the second kind and the long-range order is diminished or destroyed. Thermal motion, point defects, chain ends, etc., produce disorder of the first kind. Packing disorder of chain molecules by microstrain and paracrystallinity generates disorder of the second kind. Both types of distortions reduce the intensities of the reflection spots and redistribute scattered radiation to the background. Such effects can be described by a disorder factor D , which includes a term for thermal motions, disorders of the first and second kinds. The determination of D will be discussed later.

The fraction of crystalline material in comparison with the amorphous parts can be described by the degree of crystallinity x_c of the polymeric specimen or fibres, represents an important parameter for characterizing the fibre texture and determines to a large extent the properties of the materials. The degree of crystallinity x_c can be evaluated by several physical methods and the different methods may provide differences in the values obtained for x_c , since the various methods detect different properties, such as the force field by IR, the extension of crystallites and amorphous domains in density measurements and order by X-ray diffraction. The actually present intermediate states between crystal and non-crystal and their disorder may also contribute differently to x_c when various methods are applied. Therefore, x_c is sometimes referred to as the index of crystallinity. Here, we will concentrate on the X-ray diffraction method and discuss procedures to determine the degree of crystallinity by this method.

A prerequisite for its determination is the isotropy of the sample, which for fibres requires that they are placed in a sample holder with complete arbitrariness of the single fibres and X-ray diffraction with a monochromatic X-ray beam. A cooled polymeric sample from the melt normally fulfils this requirement as shown for polyethylene in Fig. 3.29. The X-ray diagram then represents a powder pattern as schematically represented in Fig. 3.2 and the intensity distribution can be depicted by a one-dimensional plot of the intensity I versus the scattering angle 2θ or the related scattering variable $s = 2\sin\theta/\lambda$ (Fig. 3.31). The peaks of the diagram represent the scattering from the crystallites. The underlying background, curve B, is a contribution of several parts, the scattering from the amorphous regions but also from



3.31 Illustration of a powder X-ray diagram with crystalline peaks and background B. The intensity of a pure amorphous sample is indicated by the broken line of curve A. (Adapted from Vonk 1973.)

incoherent scattering (Compton scattering), scattering from disordered crystallites and from the white radiation, if the primary beam is not fully monochromatized. Curve A illustrates the scattering from totally amorphous materials. In Fig. 3.31 curve A was multiplied by a factor in appropriate intervals to fit the background curve of B. In some cases, if intervals cannot be uniquely established, one constant factor will be applied.

3.6.1 Method of Hermans and Weidinger

Hermans and Weidinger (1948, 1949) proposed a procedure, first for cellulose and later also for polyethylene and isotactic polypropylene, to derive the degree of crystallinity from powder patterns under certain strict experimental conditions.

The monochromatic radiation passes through a uniformly thick layer of the specimen of constant dimension and constant weight and is corrected with regard to absorption and scattering from the air. The primary beam intensity should be kept constant and controlled for the measurements to be compared. Two or more samples of the same polymer are selected with unknown crystalline fractions x_c and y_c . From the diffraction pattern a suitable quantity proportional to x_c and y_c is chosen and another quantity proportional to the amorphous fractions $1 - x_c$ and $1 - y_c$. With these two ratios, two equations are established:

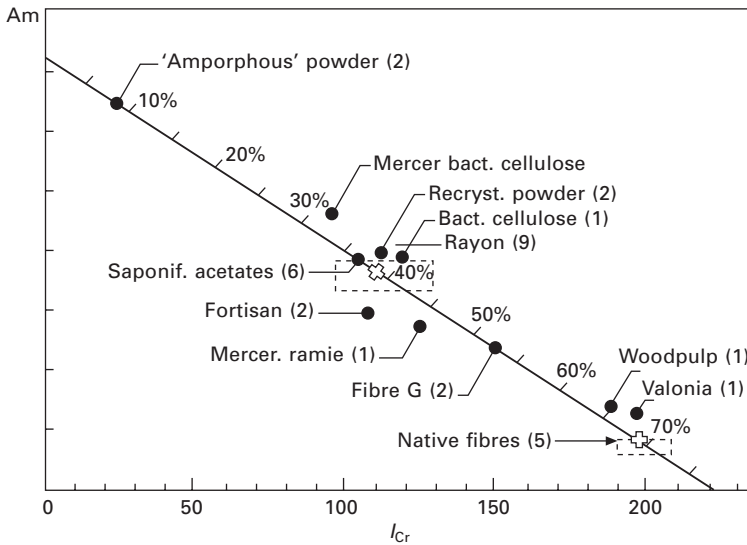
$$x_c/y_c = A, (1 - x_c)/(1 - y_c) = B \tag{3.53}$$

with experimentally known A and B . From these two equations x_c and y_c can be determined. If more samples are investigated, a regression line can be plotted, which may serve for the determination of the degree of crystallinity of further samples.

For polyethylene (*cf.* Fig. 3.29), Hermans and Weidinger (1961) chose the two strongest reflections and integrated the intensity between $2\theta = 15^\circ$ and 26° for the representation of the crystalline fraction but also extended the interval to $2\theta = 50^\circ$, i.e. including further peaks. As a quantity proportional to the amorphous fraction they took either the height of the background near its maximum or a suitable selected part of the integrated background intensity. All these investigations with variation of the intervals led to very close results.

A regression line in a crystallinity nomogram for various native and regenerated celluloses is shown in Fig. 3.32. A crystallinity nomogram was also published for polyethylene as well as for polypropylene (Hermans and Weidinger, 1961, Weidinger and Hermans, 1961). The results obtained by this method compare well with other sources.

Weidinger and Hermans (1961) critically judged the validity of their procedure for the determination of the degree of crystallinity: the integrated peaks in an interval are proportional to the crystalline fraction and possess



3.32 Regression line in a plot of amorphous scattering A_m versus integrated crystalline intensity I_{cr} for various types of native and treated cellulose. (Reproduced by permission of John Wiley & Sons, Inc., from Hermans and Weidinger, 1949.)

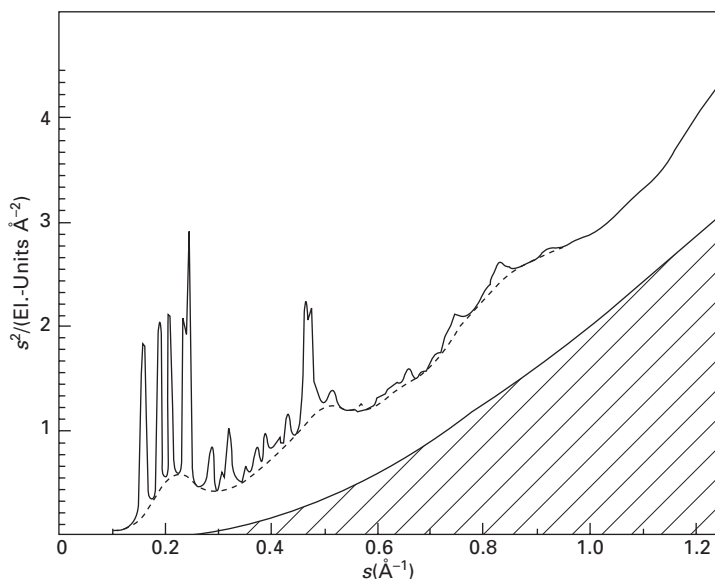
the same constant only if the lattice structure and the disorder remain the same in all specimens concerned. The disorder factor does not affect the peak intensities very much at low scattering angles. Comparing the ratios of x_c/y_c , only very large deviations in the two disorder factors of the two specimens play a role but actually may not affect the result, even at higher scattering angles. Small deviations in the lattice structures as occurring in polyethylene also may not influence the scattering amplitudes extensively, if appropriate reflections are selected. The assumption that the integrated background is proportional to $(1 - x_c)$ neglects a possible change of structure of the non-crystalline region of the sample, depending on the crystallinity, and neglects the incoherent scattering and a possible modulation of the background scattering due to thermal motion and disorder as well. Incoherent scattering is small for low scattering angles and may not have to be considered.

3.6.2 Methods of Ruland and Vonk

Ruland (1961) developed an X-ray method for the evaluation of crystallinity that considers explicitly the diffuse scattering due to disorder, i.e. lattice imperfections and thermal motion in the crystalline part of materials by a disorder function D , and is considered the method with the best theoretical foundation. The disorder D represents the overall disorder in the crystalline part of the material and takes into account all kinds of disorder averaged over all directions in space. The prerequisites for the application of this X-ray method are the same as for the Hermans and Weidinger method but the scattering curve has to be measured over a wide range of s , the magnitude of the radial vector in reciprocal space ($s = 2\sin\theta/\lambda$, where 2θ is the diffraction angle and λ is the wavelength of the monochromatic radiation), and corrected with respect to absorption, Lorentz and polarization effects and incoherent scattering (Compton effect). The quantitative corrections to be applied are outlined in Ruland (1961, 1964a, 1964b) and Vonk (1973), as is the experimental setup, and will not be discussed here. The degree of crystallinity is then given by

$$x_c = \frac{\int_0^\infty s^2 I_c ds}{\int_0^\infty s^2 I ds} \frac{\int_0^\infty s^2 \overline{f^2} ds}{\int_0^\infty s^2 \overline{f^2} D ds} \quad 3.54$$

where I is the total coherent scattering of an isotropic distributed substance, and I_c the part of the coherent scattering that is concentrated in the diffraction peaks; both parts can be obtained by the Debye–Scherrer diffraction technique (Fig. 3.33). Integration over the whole reciprocal space s ($s = 2\sin\theta/\lambda$) leads to eq. 3.54 representing the ratio of the crystalline portion versus the total amount of the sample. According to eq. 3.54 the s interval is extended from



3.33 Separation of crystalline peaks from background and incoherent scattering for isotactic polypropylene. Note that s^2/I is plotted versus s . (Reproduced by permission of the International Union of Crystallography, from Ruland, 1961.)

the lower limit $s_0 = 0$ to the upper limit $s_p = \infty$. The disorder function D can be approximated by a Gaussian-type function representing the thermal motion, imperfection of the first and second kind given by a value k (Ruland, 1961):

$$D(s) = \exp(-ks^2) \quad 3.55$$

If the scattering factors of N_i atoms of type i are denoted by f_i then the average $\overline{f^2}$ is given by $\sum N_i f_i^2 / \sum N_i$.

The s space is limited by the wavelength and cannot extend to infinity. It was found that it is possible to choose a number of limited integration intervals between the lower limit s_0 and the higher limit s_p over larger regions of s so that

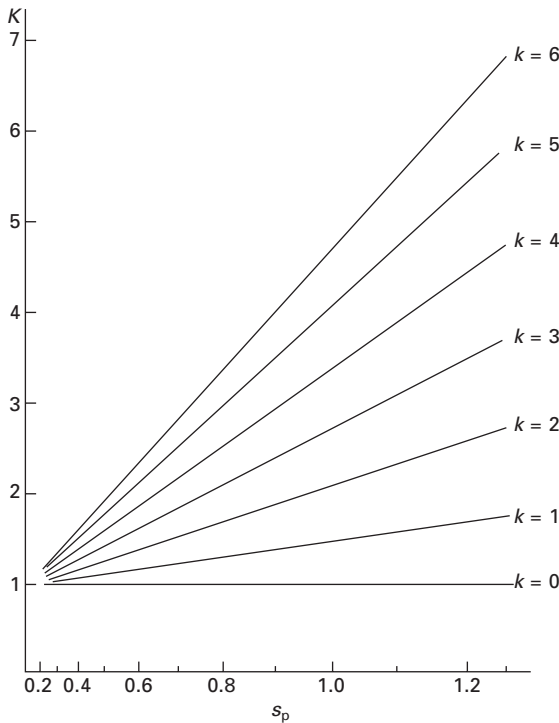
$$\int_{s_0}^{s_p} s^2 I(s) ds = \int_{s_0}^{s_p} s^2 \overline{f^2} ds \quad 3.56$$

is independent of the crystallinity of the material. These regions can be established experimentally by studying samples with different crystallinity. It should be remarked that eq. 3.56 is correct for the integration limits $s_0 = 0$ and $s_p \rightarrow \infty$ (Ruland, 1961). Eq. 3.54 for x_c can then be written:

$$x_c = \left\{ \frac{\int_{s_0}^{s_p} s^2 I_c(s) ds}{\int_{s_0}^{s_p} s^2 I(s) ds} \right\} K(s_0, s_p, D, \overline{f^2}) = \text{const} \tag{3.57}$$

$$K = \int_{s_0}^{s_p} s^2 \overline{f^2} ds / \int_{s_0}^{s_p} s^2 \overline{f^2} D ds$$

Ruland proceeds with the normalization of the scattering power and a separation of the crystalline peaks from the background on one side and the incoherent calculated Compton scattering on the other as shown in Fig. 3.33 (first part of eq. 3.57). K defined by eq. 3.57 was calculated and plotted in a nomogram as shown in Fig. 3.34 as a function of s_p with a fixed lower limit of $s_0 = 0.1$ and the parameter k as introduced by eq. 3.55. The two parameters k and s_p were varied until the crystallinity x_c remained constant over the $s_0 \rightarrow s_p$ interval. This constant x_c is the requested crystallinity. The crystallinity x_c varied between 0.31 and 0.65 with $k = 4 \text{ \AA}^2$ for differently



3.34 Nomogram of K values for polypropylene as a function of s_p ($s_0 = 0.1$) and parameter k . (Reproduced by permission of the International Union of Crystallography, from Ruland, 1961.)

thermally treated isotactic polypropylene, and for low-pressure polyethylene $x_c = 0.55$ and $k = 2 \text{ \AA}^2$ were obtained.

This method of Ruland requires laborious calculations and a large amount of experimental data. Therefore, Vonk (1973) introduced two major modifications that make the evaluation easier and enable an adaptation to computer techniques.

A quantity $R(s_p)$ is introduced, which represents part of eq. 3.57 with I and I_c the coherently scattered intensities, which have to be determined in a second step:

$$R(s_p) = \int_0^{s_p} I s^2 ds / \int_0^{s_p} I_c s^2 ds \quad 3.58$$

The full eq. 3.57 for x_c can be expressed as

$$R(s_p) \approx K/x_c \quad 3.59$$

Ruland (1961) found that K can be approximated by

$$K = 1 + b s_p^2 \quad 3.60$$

with b a constant, which is set for practical reasons to $k/2$ (*cf.* eq. 3.55). Replacing K in eq. 3.59 and plotting $R(s_p)$ versus s_p^2 should then lead to an approximation by a straight line $y(s_p^2)$:

$$y(s_p^2) = 1/x_c + (k/2x_c) s_p^2 \quad 3.61$$

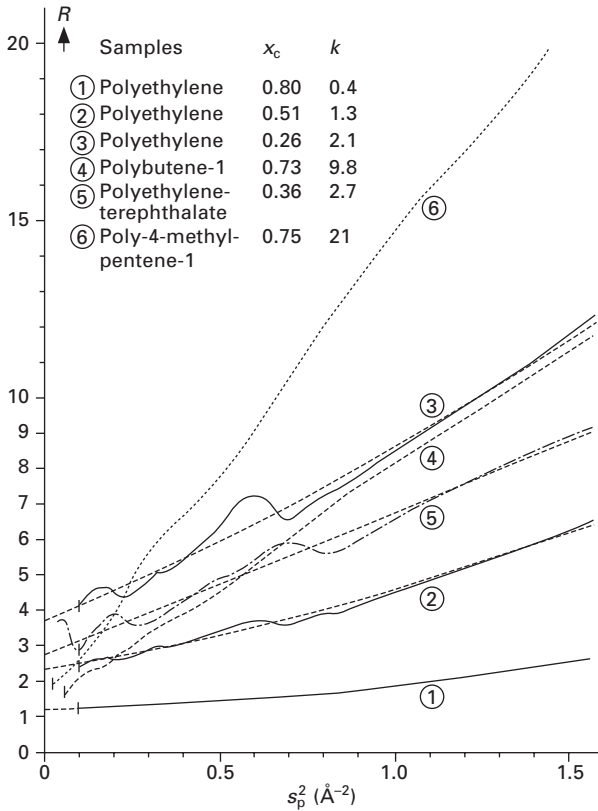
The representation of $R(s_p)$ versus s_p^2 is shown for various polymers in Fig. 3.35. In a number of cases the curves show an upward curvature, which can be accounted for by fitting a second-degree curve. The crystallinity x_c is found by extrapolating the curve to $y(0)$, i.e. $x_c = 1/y(0)$, and k from $k = 2x_c y'(0)$ or the slope which is extended over a wider function range, which means $k' = 2x_c [y(1) - y(0)]$, e.g. y taken at $s_p^2 = 1$ and $s_p^2 = 0$, if the derivative $y'(0)$ is too sensitive at zero. Choosing various limits for s_p the accuracy of the method can be tested. $R(s_p)$ was introduced by Vonk (1973) and enabled the determination procedure for x_c to be run on a computer with data obtained from an X-ray powder diffractometer.

A second modification is concerned with the correction of the total observed intensity I_{tot} for incoherent scattering I_{inc} . From eq. 3.56 with the proportional constant α one obtains

$$\alpha \int_0^{s_p} I s^2 ds \approx \int_0^{s_p} \overline{f^2} s^2 ds \quad 3.62a$$

and similarly

$$\alpha \int_0^{s_p} I_c s^2 ds \approx x_c \int_0^{s_p} \overline{f^2} s^2 D(s) ds \quad 3.62b$$



3.35 Plot of R versus s_p^2 for various polymers. The corresponding y curve is shown as a broken line for some samples. (Reproduced by permission of the International Union of Crystallography, from Vonk, 1973.)

Introducing

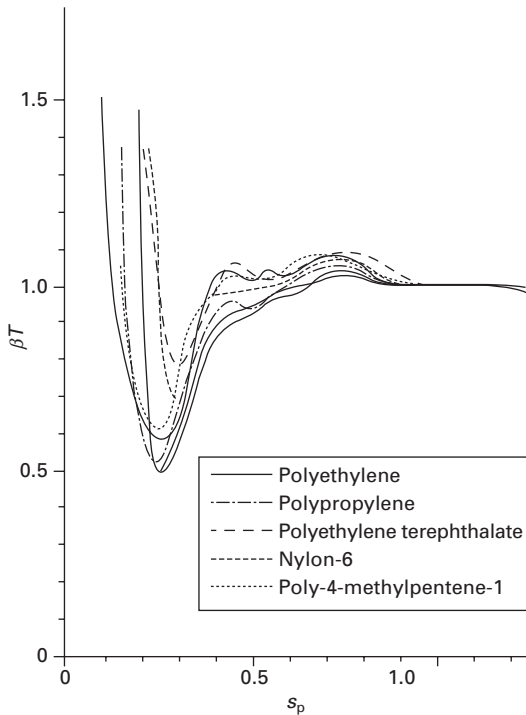
$$T(s_p) \approx \alpha \tag{3.63}$$

with

$$T(s_p) = \int_0^{s_p} (\overline{f^2} + \overline{J}) s^2 ds / \int_0^{s_p} I_{\text{tot}} s^2 ds \tag{3.64}$$

$I_{\text{tot}} = I + I_{\text{inc}}$ and \overline{J} is the average of the incoherent intensities in electron units for the atoms present in the structure. Equation 3.64 is equivalent to eq. 3.62a when adding \overline{J} to the right and I_{inc} to the left side of eq. 3.62a.

The value of $T(s_p)$ should approach α at increasing s_p . The value of α for various polymers can be normalized by introducing a variable β and setting $\beta T = 1$ at $s_p = 1$. Figure 3.36 illustrates this procedure. In practice α can be



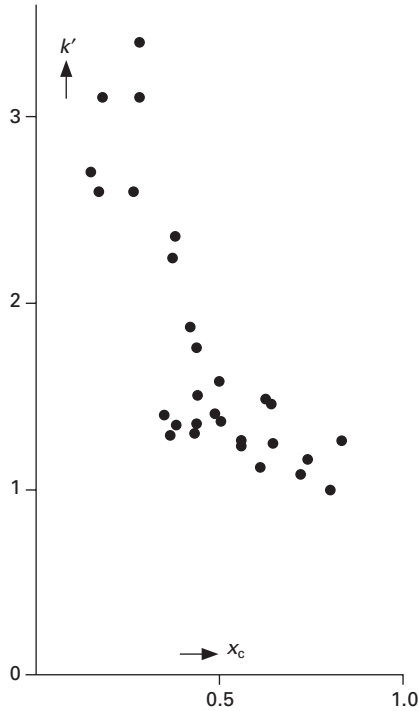
3.36 Plot of βT versus s_p for various polymers. (Reproduced by permission of the International Union of Crystallography, from Vonk, 1973.)

determined from T at a lower s_p , e.g. at 0.6, and the intensities are brought to an absolute scale by multiplication by α and reduced to coherent intensities by subtraction of \bar{J} . The crystallinity x_c differs by less than 0.03 from the values found by the normal procedure (Vonk, 1973).

Care has to be taken in the determination of the coherent intensity from the total intensity, since the white radiation causes some problems and is not totally extinct by most monochromators. Therefore, Vonk (1973) recommended the use of a crystal monochromator in the primary beam as a good solution.

3.6.3 Results for crystallinity x_c and disorder factor D

Vonk (1973) investigated 29 differently treated polyethylene samples and found x_c ranging from 0.14 to 0.83 and k' from 1.1 to 3.4. The k values are very similar to those determined from the crystal structure evaluation but the actual anisotropy of the disorder factor was not included in these investigations. The correlation of k' as a function of x_c is shown in Fig. 3.37



3.37 Disorder parameter k' represented as a function of crystallinity x_c for differently treated polyethylene samples. (Reproduced by permission of the International Union of Crystallography, from Vonk, 1973.)

and demonstrates that the higher the degree of crystallinity the lower the disorder. Crystallinity values x_c as well as k values for cellulose are provided by Fink *et al.* (1985).

Ruland (1967) has studied two limiting cases of an anisotropic disorder factor $D = \exp(-\mathbf{sks})$ with

$$\underline{k} = \begin{pmatrix} k_1, 0, 0 \\ 0, k_2, 0 \\ 0, 0, k_3 \end{pmatrix} \tag{3.65}$$

$k_1 = k_2 = k_3$ (isotropic) and $k_1 = k_2, k_3 = 0$ and found an increase of the degree of crystallinity of less than 0.07 (absolute scale) applying the anisotropic disorder factor for linear polyethylene. A more realistic estimation of the disorder parameter \underline{k} is not possible by the investigation of D determined by an evaluation of the degree of crystallinity. Actually, the values for normal crystallized polyethylene have been obtained as $k_1 = k_2 = 2.0 \text{ \AA}^2$ and $k_3 = 1.0 \text{ \AA}^2$ using the structure refinement procedure (see Section 3.5.2).

A separation in the individual terms of the disorder factor is rather difficult (Ruland 1967). The disorder factor can be expressed to a good approximation by a Gaussian function $D = \exp(-ks^2)$ with

$$k = k_T + k^{(1)} + k^{(2)} \quad 3.66$$

k_T represents the thermal vibrations ($B = 4k_T$), $k^{(1)}$ the lattice distortion of the first kind and $k^{(2)}$ that of the second kind. Since the lattice distortions of the second kind influence the line profile, they can be determined by line width analysis. According to eq. 3.66, $\Delta k = k - k_T = k^{(1)} + k^{(2)}$ and with $k = 2.0\text{\AA}^2$, $\Delta k = 0.2\text{\AA}^2$, $k^{(2)} = 0.1\text{\AA}^2$ at $x_c = 0.55$ for PE (Ruland 1964b, 1967), Δk , $k^{(2)}$ both independent on temperature, the thermal factor k_T and distortion of first kind $k^{(1)}$ can be determined. The significance of the lattice distortions of the second kind on the total distortions k is relatively small.

A method of mixing two samples, one with known crystallinity and both with known structure amplitudes, has been proposed by Corradini *et al.* (1967) to determine crystallinity by a single reflection method. Further X-ray methods of crystallinity evaluation have been published by Thygesen *et al.* (2005).

3.7 Reflection profile, crystallite size and disorder

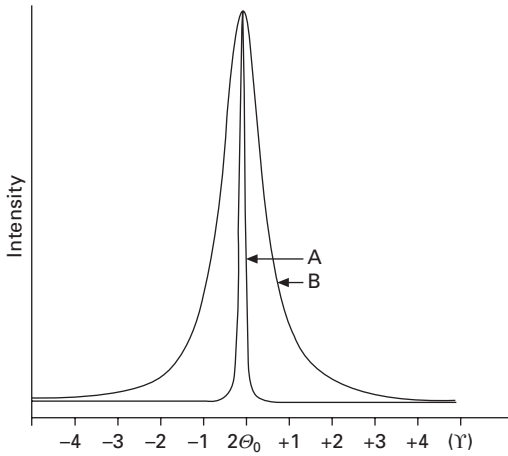
X-ray diffraction represents a powerful tool to determine crystallite sizes of microfibrils or lamellae, if the reflection peaks are separated. Small crystallites lead to a broadening of the reflections as shown by optical transforms in Fig. 3.4 and eventually an overlap occurs in Debye–Scherrer patterns. Powder diffraction patterns as well as the fibre diagrams often show overlapping reflections. A separation of peaks by mathematical means is frequently necessary but is sometimes difficult to achieve.

A mean crystallite size \bar{D} can be obtained with the Scherrer equation 3.67 if the half-width β at half the maximum is known of a separated peak from a layer plane (hkl):

$$\bar{D} = 0.89\lambda/(\beta \cos\theta_{\max}) \quad 3.67$$

where \bar{D} is perpendicular to the lattice planes (hkl), and θ_{\max} is the diffraction angle of the maximum at the peak height. A maximal deviation from \bar{D} of + 10% is reported applying the simple eq. 3.67 versus a more elaborate evaluation, if the line broadening by the apparatus and the lattice distortions of the second kind have been taken care of in a correction procedure. As an example a comparison between line broadening of gold with crystallites of considerable sizes, which may be representative of the instrumental broadening, and nylon-6 is shown in Fig. 3.38. Therefore, the instrumental broadening can be neglected for many applications in the field of polymers.

The diffraction curve $I(\theta)$ after subtraction of the total background under



3.38 Comparison of the X-ray diffraction profiles of (A) gold and (B) nylon-6. (Adapted from Heuvel *et al.*, 1976.)

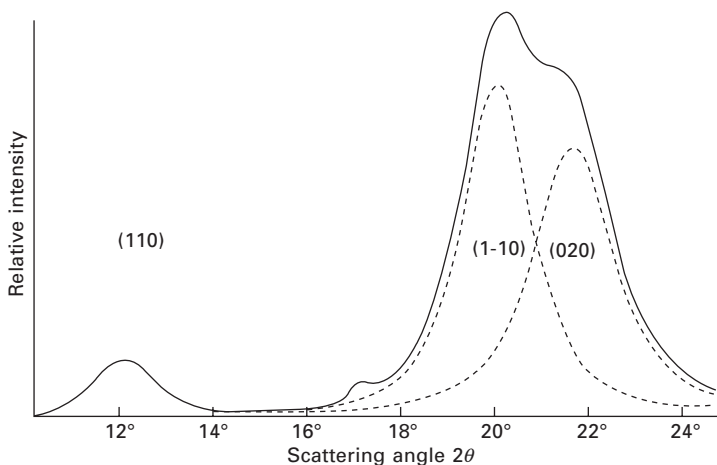
the bell-shaped curves serves for the evaluation of the half-width β to be used in eq. 3.67. The overlapping peaks have to be separated by mathematical means, i.e. computer programs are available to fit the total overlapped diffraction curve by a number of single bell-shaped curves. It was found that the intensity distribution of a single peak as a function of θ_n can be well described by a Pearson VII function $P(\theta_n)$:

$$P(\theta_n) = I_{\max} [1 + 4\beta^{-2} (2\theta_n - 2\theta_{\max})^2 (2^{1/m} - 1)]^{-m} \quad 3.68$$

The shape of the curve can be varied over a wide range by varying the shape parameter m : $m = 1$ for a Lorentz (Cauchy) curve, $m \rightarrow \infty$ for a Gauss curve; either is theoretically expected or a form between the two can be achieved. Using the Pearson VII function P_i for the i th reflection, the intensity distribution I_c summed up for l reflections can be described in the respective interval by

$$I_c(\theta_n) = \sum_{i=1}^l P_i(\theta_n) \quad 3.69$$

I_c is fitted to the experimental curve by a least-squares procedure with independent variation of the parameters for every reflection: I_{\max} the maximal intensity at θ_{\max} , β the half-width and m the shape parameter. The goodness of fit between the calculated and measured intensities of the distribution can be provided by an R_f parameter (eq. 3.70) similar to that used in the structure refinement procedure for crystal structures (Fink *et al.*, 1985, 1995). Such a fit is shown in Fig. 3.39 for regenerated cellulose II.



3.39 Separation of equatorial peaks of regenerated cellulose II with Pearson VII functions. (Reproduced by permission of Springer, Heidelberg, from Fink *et al.*, 1995.)

$$R_f = \frac{\left\{ \sum_{n=1}^m [I_c^{obs}(\theta_n) - I_c^{calc}(\theta_n)]^2 \right\}^{1/2}}{\sum_{n=1}^m I_c^{obs}(\theta_n)} \quad 3.70$$

Reflection line broadening is caused by the crystallite size but also by crystallite distortion. If information on the crystallite distortion is needed, the procedure that determines the line broadening by the crystallite size has to be refined and line broadening by the distortion introduced. Two methods have been proposed to separate the broadening caused by crystallite size on one side and distortion on the other: the line width method and the Fourier transform method.

3.7.1 Line width method

The line profile of a reflection of the wide-angle diagram of an isotropic, polycrystalline sample is determined by a lattice and a shape factor (Martis and Wilke, 1977). The lattice factor Z describes the line broadening by lattice distortions and the shape factor S^2 the influence of the crystallite size distribution perpendicular to the reflecting plane; Z and S^2 are introduced to characterize the two line broadening effects. For an evaluation of the two factors, the two contribution have to be separated, which is possible if certain prerequisites are fulfilled, e.g. independent contributions and additivity.

The integral width of a reflection $\delta\beta$ of a peak at θ_{max} is defined by

$$\delta\beta = \left(\int I(b') db' \right) / I(0) \quad 3.71$$

$$b' = (2\sin\theta/\lambda) - (2\sin\theta_{\max}/\lambda) \quad 3.72$$

The contribution from distortions is dependent on the order of the reflection p . In the case of crystals with quasi-long-range order, $\delta\beta_h(Z)$ can be calculated with the model of an ideal paracrystal (Wilke *et al.*, 1970) to be

$$\delta\beta_h^p(Z) = \frac{\pi^2 g_s^2}{d_h^2} p^2 \quad 3.73$$

for powder diagrams where g_s is a measure of the lattice distortion (relative distance fluctuation of the net planes: $g_s = \Delta d_{\hat{h}}/d_{\hat{h}}$), \hat{h} are the Miller indices without common measure and p is the order of a reflection $h = \{h_1, h_2, h_3\}$.

In case the line width is influenced by a Gaussian strain distribution, Wilke and Martis (1974) proposed for the line width

$$\delta\beta_h^s(Z) = \frac{\sqrt{2\pi}}{d_h} \sqrt{\langle \varepsilon_h^2 \rangle} p \quad 3.74$$

$\langle \varepsilon_h^2 \rangle$ is the mean strain fluctuation of the net planes d_h : $\langle \varepsilon_h^2 \rangle = (\Delta d/d)^2$. The measured set of $\delta\beta_h^2(Z)$ for various reflections gives a set of $\langle \varepsilon_h^2 \rangle$ and a transformation leads to the strain fluctuation tensor $\langle \varepsilon_{ij} \rangle$. The contribution to the line broadening caused by the crystallite size is (Guinier, 1963)

$$\delta\beta_h(S^2) = \frac{1}{\overline{D_h}} \quad 3.75$$

where $\overline{D_h}$ is the mean crystallite size in the direction of the normal of the lattice planes $h = \{h_1, h_2, h_3\}$. If the two measured line widths caused by paracrystalline or strain distortions can be described by Lorentz functions independent of the order of the reflections, then

$$\delta\beta_h = \delta\beta_h(S^2) + \delta\beta_h(Z) \quad 3.76$$

This formula represents a good approximation for Lorentz or Lorentz² profiles.

Assuming paracrystalline disorder, the integral width $\delta\beta_h$ of succeeding reflections of order p , e.g. (110), (220), (330), is given by:

$$\delta\beta_h = \delta\beta_h(S^2) + \delta\beta_{h,p=1}(Z) p^2 \quad 3.77$$

Then a plot of $\delta\beta_h$ versus p^2 provides a straight line with slope $\delta\beta(Z)$ and consequently a distortion of the second kind can be assumed. At least three reflections are necessary to prove this relationship, i.e. paracrystalline disorder. The intersection with the coordinate axis at $p = 0$ gives $\delta\beta(S^2)$ and

with eq. 3.75 the crystallite size. A distinction between paracrystalline and microstrain distortions is possible, since the integral line width influenced by microstrains with a Gaussian distribution shows a p -dependency only (*cf.* eq. 3.74).

The determination of the paracrystalline disorder with the line width method was falsely applied to polyethylene in several investigations, since the peak of the third-order reflection (330) of the above introduced series of reflections is too small to be included in the proposed procedure (*cf.* Fig. 3.29) and erroneously the (031) reflection was used in the paracrystalline evaluation (Wilke *et al.*, 1970).

The existence of paracrystalline disorder was proven by Schönfeld *et al.* (1972) for polyethylene and therefore a two-reflection procedure can be applied for the determination of the paracrystalline g factor according to eq. 3.77. However, generally this procedure is not applicable for many polymers due to too few reflections observed. It should be remarked that Windle (1975) found no indication of any paracrystalline disorder of the (002) peak profile in the [001] direction of polyethylene.

3.7.2 Fourier method

Many diffraction patterns of polymers show few reflections and a single reflection profile method seems to present a solution of the problem separating the crystallite size and lattice distortion effects. A single X-ray profile method was proposed by Hofmann and Walenta (1987) and applies Fourier transforms to the profile of reflections of the first order. Assuming the profile broadening of a single reflection (hkl) is caused by the finite coherent length of the crystallite size and another independent broadening by the disorder in the crystallites, then a Fourier analysis of the profiles leads to the product of the real normalized Fourier cosine coefficients, provided a conversion to the s -scale ($s = 2\sin\theta/\lambda$) has been carried out and the profiles considered are nearly symmetrical:

$$A_n = A_n^s A_n^d \quad 3.78$$

The Fourier cosine coefficients are A_n for the whole profile, A_n^s for the size-broadened profile and A_n^d for the distortion-broadened profile (Hofmann and Walenta, 1987). Assuming a Gaussian profile, which was suggested by a peak separation of superimposed peaks by a Pearson VII function (Fink *et al.*, 1995), the actual integral line width β can be expressed by:

$$\beta^2 = \beta_s^2 + \beta_i^2 + \beta_d^2 \quad 3.79$$

with β_d for distortion, β_i for instrumental and β_s for crystallite line width. Correction concerning parasitic scattering, absorption and polarization should be performed prior to the procedure of peak separation and crystallite size

determination, and monochromatic radiation with correction for $K\alpha_1\alpha_2$ broadening should be used.

The Fourier coefficient A_n is experimentally determined from the peak intensity curve corrected for instrumental influence and data reduction. Single-line analysis requires special assumptions and the following expressions are obtained for first-order reflections ($p = 1$) with a size parameter N_3 representing the number of cells in a special model (*cf.* eq. 3.84 below) (Fink *et al.*, 1990, 1995):

$$A_n^s = 1 - n/N_3 \quad 3.80$$

$$A_n^d = 1 - 2\pi^2 n^2 \langle e^2 \rangle - 2\pi^2 n^3 \langle ee' \rangle \quad 3.81$$

where $\langle e^2 \rangle$ and $\langle ee' \rangle$ are distortion parameters. The normalized experimental A_n can then be expressed by a third-order polynomial in n :

$$A_n = 1 - n/N_3 - 2\pi^2 \langle e^2 \rangle n^2 + (2\pi^2 \langle e^2 \rangle / N_3 - 2\pi^2 \langle ee' \rangle) n^3 \quad 3.82$$

A mean-squared microstrain variable of nearest neighbours $\langle e_1^2 \rangle$ is introduced by the microstrain model and can be expanded as a Taylor series.

$$\langle e_1^2 \rangle = \langle e^2 \rangle + \langle ee' \rangle + \dots \approx \langle e_0^2 \rangle \quad 3.83$$

$e = e_0$ is a somewhat vaguely defined upper limit of the lattice distortion, and e' is the second derivative of the displacement variable.

A fit of the third-order polynomial of eq. 3.82 to the experimental data leads to the requested data (N_3 , $\langle e^2 \rangle$, $\langle ee' \rangle$) and the separation of the two broadening effects (eqs 3.80 and 3.81). According to the model applied, each crystallite consists of an assemblage of columns parallel to the normal of the reflection plane and each column is composed of a stack of unit cells with an average height d . The number average of the crystallite size L can then be expressed by

$$L = N_3 d \quad 3.84$$

with N_3 the mean number of cells parallel to the reflection plane averaged over all columns and all crystallites.

The single-line method was effectively applied to diffractograms with only a few reflections as in native and regenerated cellulose in an appropriate angular range. The following results were obtained for mercerized and regenerated cellulose II for the equatorial (110)-reflection (Fink *et al.*, 1995). The shape parameter m of the Pearson VII function varied between 6 and 12 and suggests an approximated Gaussian shape. Lateral crystallite sizes varied between 3 and 6 nm and are confirmed from other sources, e.g. regenerated cellulose II (rayon) exhibits 3 to 5 nm, mercerized linters show an almost constant value of 6 nm. The lattice distortion $\langle e_1^2 \rangle$ values did not differ much for all samples and were about 3%.

Hosemann *et al.* (1985) introduced an empirical inverse relationship between lattice distortion and crystallite dimensions, the so-called α^* law, on the basis of the paracrystal model, which expresses a crystal growth limitation by lattice distortion. In case of the microstrain model, α^* is defined by

$$\alpha^* = (\langle e_1 \rangle L/d)^{1/2} \quad 3.85$$

The value of α^* should be constant for a certain class of materials. An almost constant value of 0.075 was obtained for cellulose II, which agrees well with the results by Haase *et al.* (1975) using the paracrystalline model for similar materials. It seems that both models, microstrain and paracrystal, are adequate and suitable for analysing lateral reflection profiles, at least for some specific materials.

Another procedure applying Fourier transforms was introduced by Vogel *et al.* (1974) who considered besides the microstrain influence on the structure also paracrystalline distortions by analysing wide-angle X-ray powder reflection profiles. They came up with a method that is not disturbed by crystallite size effects. In contrast to the single-line method by Hofmann and Walenta (1987), reflections of succeeding orders are needed and the line profile is extended to Lorentz profiles for paracrystalline distortions. Paracrystalline distortions cause a broadening of the wide-angle X-ray reflections proportional to the square of the order p of the reflections; the microstrain distortions cause a proportionality in p derived from Gaussian or Lorentz² reflection profiles. A Lorentz function can be excluded for microstrain distortions. The Fourier transformation of a reflection of order p results in the product of two functions $A^S(x)A^Z(p,x)$, A^S representing the crystallite size and A^Z the distortions. Dividing two transforms, one resulting from a reflection of order p , the other from order $p + 1$, the function representing the crystallite size cancels and the remaining part contains information about distortions only. Now evaluating the ratio of two Fourier coefficients of the Fourier transforms for two reflections of different order, eq. 3.86 is obtained for paracrystalline distortions:

$$\ln (A_n(p)/A_n(p + 1)) = 2\pi^2(2p + 1)g^2 n \quad 3.86$$

A quantity $x = n\bar{d}$ is preferred, x independent of $\delta\beta_1$, \bar{d} the mean distance between lattice planes, p is the order of reflection and $\delta\beta_1$ is the width of the reflection of first order. Equation 3.86 results in a straight line when the ratio is plotted against n . From the slope, the paracrystalline g value (*cf.* eq. 3.73) can be derived representing the relative distance fluctuation of the lattice vector perpendicular to the planes considered.

In the case of microstrain distortions with Gaussian reflection profile this relationship is changed for small n to:

$$\ln (A_n(p)/A_n(p + 1)) = 2\pi^2(2p + 1) \langle \varepsilon^2 \rangle n^2 \quad 3.87$$

where $\langle \varepsilon^2 \rangle = (\Delta d/d)^2$ is the mean squared lattice expansion.

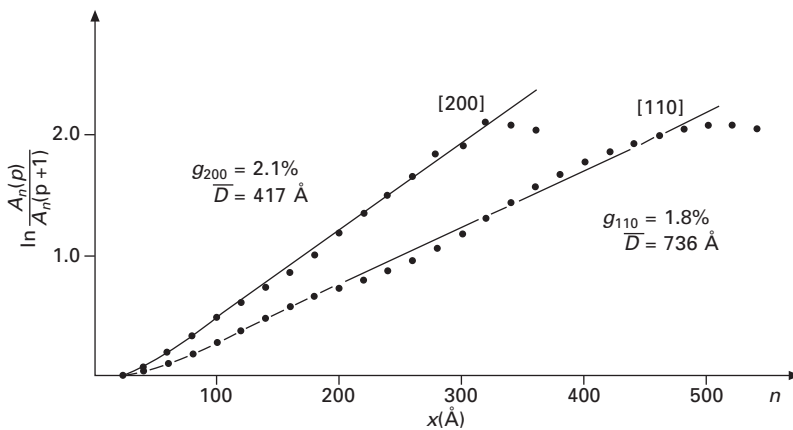
Simultaneous microstrain (Gaussian profile) and paracrystalline distortions lead to the following expression:

$$\ln (A_n(p)/A_n(p+1)) = 2\pi^2(2p+1)(g^2n + \langle \varepsilon^2 \rangle n^2) \quad 3.88$$

The best results concerning the evaluation of distortions are expected by application of the Fourier transform method with truncated Lorentz functions (Vogel *et al.*, 1974). The Lorentz function exhibits a long tail until reaching the background. Therefore, the integration should be carried out with a truncated function. However, truncation has the disadvantage that the integral width $\delta\beta'$ of this function is smaller than $\delta\beta$ and a correction has to be applied, which is outlined by Vogel *et al.* (1974). A correction has also to be considered for the g value: $\delta\beta'/\delta\beta = (g'/g)^2$. The results for melt crystallized and annealed polyethylene are represented in Fig. 3.40.

Since the existence of paracrystalline disorder was proven by Schönfeld *et al.* (1972) for polyethylene, a two-reflection procedure is justified for the determination of the paracrystalline g factor according to eq. 3.77 and the two pairs of reflections (110), (220) and (200), (400) were chosen.

The results of the crystallite sizes extracted from wide-angle diffraction (WAXS) are supported by small-angle X-ray scattering (SAXS), since the crystallites represent particles of their own surrounded by some non-crystalline materials. If these particles are somewhat regular in size and arrangement, they give rise to diffraction spots, which appear in the small-angle range due to the size of the crystallites. The crystallite length and width have



3.40 Differently treated melt crystallized linear polyethylene. The full lines are calculated with a truncated Lorentz function (width 4 or $5\delta\beta$). (Reproduced by permission of Zeitschrift für Naturforschung, from Vogel *et al.*, 1974.)

been compared determined by both methods and additional information was obtained.

The length of the crystallites along the fibre of regenerated cellulose II (viscose) has been determined to be 11.2 nm by the WAXS line width method (Haase and Renwanz, 1972). But 5.6 nm have to be added for the non-crystalline disordered region to result in somewhat regular ordered and repeated particle sizes of 16.8 nm as detected by SAXS measurements. The average fibre diameter (WAXS) amounts to 4.1 nm for this regenerated cellulose II sample (Haase *et al.*, 1973). The lateral crystallite or microfibril sizes for cellulose II vary between 3.3 and 5.8 nm for samples of different origin (Hofmann *et al.*, 1989). Actually some larger fibrillar diameters have been found by a careful SAXS analysis. These larger diameters relate to the small ones by a ratio of 1:2:4:8 for native cellulose I (Ramie) and for rayon (viscose cellulose II) but by a ratio of 1:2:3 for native bacterial cellulose I and Fortisan (deacetylated cellulose II of different origin) (Haase *et al.*, 1974). These larger particles for Ramie and rayon do not coherently scatter X-rays and therefore cannot be detected by wide-angle experiments, in contrast to some synthetic polymers for which these larger particles scatter coherently. For algal and bacterial cellulose a recrystallization of the small particles takes place to form larger, coherently scattering particles.

Neutron small-angle scattering of selectively deuterated cellulose (Fischer *et al.*, 1978), which provides a higher contrast by diffusion of deuterium into the non-crystalline regions of cellulose II, exhibits a long-period Bragg reflection of 16.5 nm for Fortisan and 19.3 nm for rayon fibres, values quite similar to the 16.8 nm found as the length of the particles by Haase *et al.* (1973).

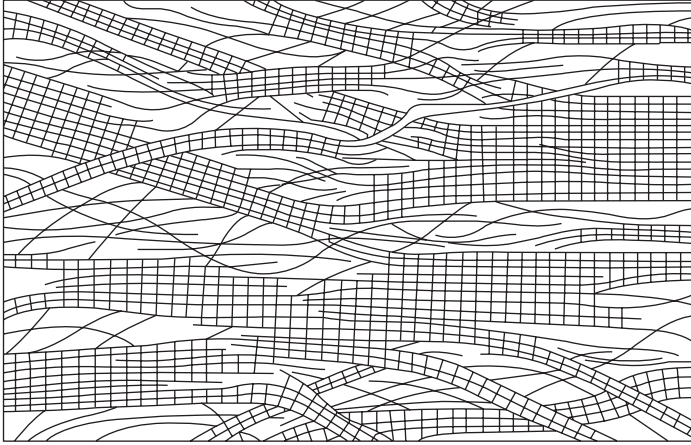
The different cross-sections of native cellulose I can be traced back to differences in imperfections of chain packing by disorder and defects as proposed by Hosemann and coworkers (1967). Differences in chain packing will also weakly influence the size of the unit cells and have actually been found in native cellulose I from different sources (Wellard, 1954).

The microfibrillar model of Hearle (1958) with elongated crystallites represents these findings. Microfibrils join in some sections to form wider microfibrils or bundles of microfibrils as shown schematically in Fig. 3.41. At a larger scale many of these microfibrils are hooked together and form fibrils and fibres. The interconnections of the microfibrils then give rise to the high tenacity observed in cellulose fibres.

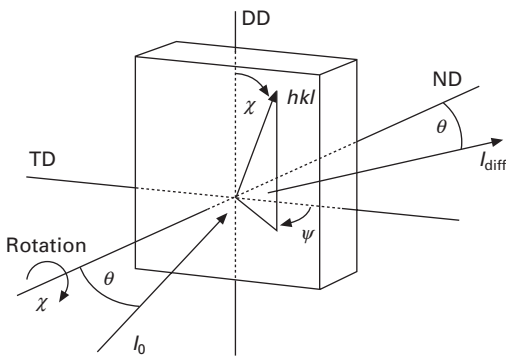
3.8 Preferred orientation

3.8.1 Basics

An important structural description of partially crystalline polymeric fibres relies on the determination of the orientation of the crystallites, which



3.41 Model of non-uniform Fransen micelles as expected for extended native cellulose. Representation according to Hearle (1958). (Reproduced by permission of Zellcheming, Darmstadt, from Fink and Walenta, 1994.)



3.42 Schematic representation of the geometry for a fibre X-ray diffraction. Angles χ and ψ define the position of the normal to an (hkl) crystal plane in the sample reference system. Fibre axis or drawing direction: DD; normal direction: ND; transverse direction: TD; Bragg angle: θ . (Adapted from Lafrance *et al.*, 1991.)

strongly correlate with mechanical properties. Wide-angle X-ray diffraction is commonly used for investigating the distribution of orientation for the molecular axes in polymeric materials but also in liquid crystals. Normally fibres exhibit axial symmetry around the so-called fibre axis or deformation direction and also the molecular X-ray scattering exhibits this symmetry. These symmetry elements simplify the evaluation of the orientation distribution considerably. In this case the molecular orientation distribution N can be solely described by the polar angle χ , defined by the inclination between

the plane or molecule normal and the reference direction (Fig. 3.42), and can generally be expanded by a suitable series of even-ordered Legendre polynomials $P_n(\cos \chi)$ (Lafrance *et al.*, 1991):

$$N(\chi) = \sum_{n=0}^{\infty} (n + \frac{1}{2}) \langle P_n(\cos \chi) \rangle P_n(\cos \chi) \quad 3.89$$

The odd terms vanish for reasons of symmetry. The Legendre polynomials considered have their maximum values at $\chi = 0^\circ$ and possess either a maximum or a minimum at $\chi = 90^\circ$. $\langle P_n(\cos \chi) \rangle$ is defined by

$$\langle P_n(\cos \chi) \rangle = \int_0^{90^\circ} N(\chi) P_n(\cos \chi) d\chi \quad 3.90$$

The same expansion as in eq. 3.89 can be applied to the X-ray intensity distribution of a fibre. The distribution of orientation for the molecular axes can be determined if a quantitative correlation with the X-ray intensity distribution can be established, i.e. if a relationship between the coefficients $\langle P_n \rangle$ exists.

The normalized background corrected diffracted X-ray intensity distribution $N(\chi)$ of a single reflection in a polar scan $I^*(\chi)$ is given by:

$$N(\chi) = \frac{I^*(\chi)}{\int_0^{90^\circ} I^*(\chi) \sin \chi d\chi} \quad 3.91$$

With eq. 3.90 the coefficients $\langle P_n \rangle_{hkl}$ are obtained for the intensity distribution:

$$\langle P_n(\cos \chi) \rangle = \frac{\int_0^{90^\circ} I^*(\chi) P_n(\cos \chi) \sin \chi d\chi}{\int_0^{90^\circ} I^*(\chi) \sin \chi d\chi} \quad 3.92$$

They are available by a numerical integration using Simpson's rule.

Lovell and Mitchell (1981) have shown that the required coefficient in eq. 3.89 can be determined by the $\langle P_n \rangle_{hkl}$ coefficients of eq. 3.92. If the orientation distribution of (hkl) crystal planes exhibits cylindrical symmetry with respect to the reference direction and provides a sharp reflection at angle χ , the Legendre polynomial coefficients $\langle P_n \rangle_c$ characterizing the molecular chain orientation are expressed by

$$\langle P_n \rangle_c = \frac{\langle P_n \rangle_{hkl}}{P_n(\cos \Phi_{hkl})} \quad 3.93$$

with Φ_{hkl} the angle between the normal to the (hkl) planes and the chain axis.

The extent of orientation is often described with the so-called 'orientation function' or order parameter introduced by Hermans involving the second-order Legendre polynomial (Hermans and Platzek, 1939):

$$f = \langle P_2(\cos \chi) \rangle = (3 \langle \cos^2 \chi \rangle - 1)/2 \quad 3.94$$

$f = 1.0$ for a perfect parallel orientation $\chi = 0^\circ$, $f = -0.5$ for a perfect perpendicular orientation $\chi = 90^\circ$ and $f = 0$ for unoriented material. However, $\langle P_2 \rangle$ for a highly oriented polymer with a reflection oriented around $\chi = 54.7^\circ$ has a value close to zero as obtained for unoriented material and is not suited for a determination of the orientation (Lafrance *et al.*, 1996).

The use of the order parameter has some advantages. The order parameter can be determined by many experimental characterization methods such as birefringence, infrared dichroism, polarized Raman measurements and X-ray diffraction. In addition $\langle P_4 \rangle$ can also be obtained by polarized Raman. Wide-angle diffraction is the only technique from which all coefficients $\langle P_n \rangle$ are available. Further, the calculation of $\langle P_2 \rangle$ for axes that cannot be observed directly is possible from values from other crystal planes (Wilchinsky, 1963).

If polyethylene with an orthorhombic unit cell is considered where the c -axis lies parallel to the molecular axis, the (002) plane characterizes the molecular chain orientation distribution. Equation 3.93 can be used to calculate the $\langle P_2 \rangle_c$ coefficient from ($hk0$) reflections:

$$\langle P_2 \rangle_c = \frac{\langle P_2 \rangle_{hk0}}{P_2(\cos \pi/2)} = -2 \langle P_2 \rangle_{hk0} \quad 3.95$$

In general, as shown by Lovell and Mitchell (1981) one obtains from eq. 3.93:

$$\text{Meridional reflections } (\Phi_{00l} = 0): \quad \langle P_{2n} \rangle_c = \langle P_{2n} \rangle$$

$$\text{Equatorial reflections } (\Phi_{hk0} = \pi/2): \quad \langle P_{2n} \rangle_c = (-1)^n \frac{1 \cdot 3 \cdot 5 \dots \cdot (2n-1)}{2 \cdot 4 \cdot 6 \dots \cdot 2n} \langle P_{2n} \rangle$$

For a specimen with uniaxial symmetry, the higher moments of the orientation distribution can be obtained from the azimuthal profile of an arbitrary reflection, which means that the full orientation distribution can be calculated without recourse to solving integral equations (Lovell and Mitchell, 1981). The molecular orientation distribution N can then be expressed with eq. 3.89 by:

$$N(\chi) = \sum_{n=0}^{\infty} \left(n + \frac{1}{2} \right) \langle P_n(\cos \chi) \rangle P_n(\cos \chi) / P_n(\cos \Phi_{hkl}) \quad 3.96$$

For an isotopic sample all of the $\langle P_n \rangle$ coefficients are equal to zero, except

$\langle P_0 \rangle = 1$. For perfect orientation parallel to the reference direction, all $\langle P_n \rangle = 1$.

For special cases, e.g. for meridional and equatorial reflections, one obtains (c.f. eq. 3.89, only even-ordered Legendre polynomials):

Meridional reflections:

$$N(\chi) = \sum_{n=0}^{\infty} (n + \frac{1}{2}) \langle P_n(\cos \chi) \rangle P_n(\cos \chi) / P_n(\cos \Phi_{hkl})$$

$$= \frac{I^*(\chi)}{\int_0^{90^\circ} I^*(\chi) \sin(\chi) d\chi} \quad 3.97$$

Equatorial reflections:

$$N(\chi) = \sum_{n=0}^{\infty} (n + \frac{1}{2}) (-1)^n \frac{1 \cdot 3 \cdot 5 \dots \cdot (2n-1)}{2 \cdot 4 \cdot 6 \dots \cdot 2n} \langle P_n \rangle P_n(\cos \chi) \quad 3.98$$

For the axial distribution $N(\chi)$ Lovell and Mitchell estimate that it is unlikely that usually more than seven terms are needed in the series, depending on the sharpness of the reflections. Some attempts have been made to derive an equatorial distribution function $N(\chi)$ directly from the experimentally determined X-ray intensity. For an equatorial reflection Hermans *et al.* (1946) have shown that Kratky's (1933) expression

$$I^*_{\text{eq}}(\chi) = \int_{\frac{\pi}{2} - \chi}^{\frac{\pi}{2} + \chi} \frac{N(\chi') \sin \chi' d\chi'}{(\sin^2 \chi - \cos^2 \chi')^{1/2}} \quad 3.99$$

can be converted with the substitution $y = \cos \chi'$ and $z = \sin \chi$ to obtain the distribution function:

$$N(z) = \frac{1}{2\pi} \frac{d}{dz} \int_0^z \frac{y I^*_{\text{eq}}(y) dy}{(z^2 - y^2)^{1/2}} \quad 3.100$$

Biangardi (1980) inverted eq. 3.99 with the use of Fourier series and determined the distribution function N for drawn amorphous polyethylene terephthalate.

Burger and Ruland (2006) have re-evaluated the equatorial orientation distribution of Kratky (eq. 3.99) and that of Leadbetter and Norris (1979), both in use, the latter preferred by the liquid crystal community. The two orientation distributions led to non-comparable results. Burger and Ruland came to the conclusion that the integral transformation by Leadbetter and Norris is incorrect due to a mix-up of the polar angles of the orientable unit and of the oriented ensemble, and their orientation distribution formula should no longer be used.

3.8.2 Experimental determination

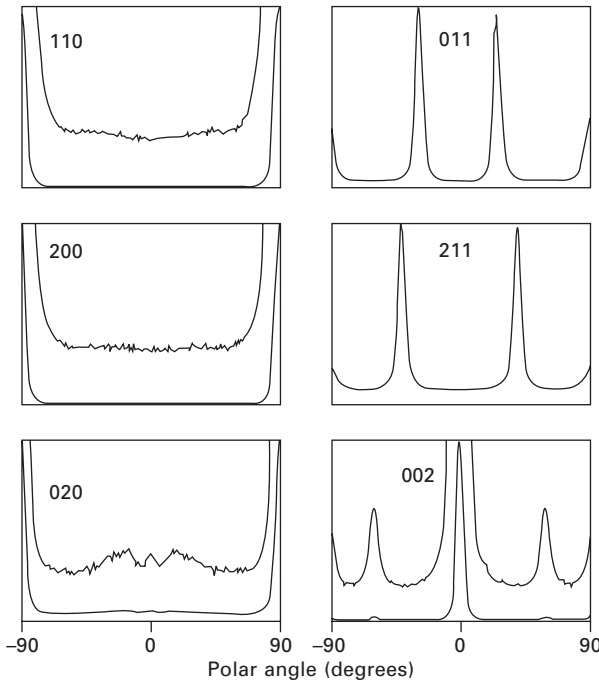
The $\langle P_n \rangle$ intensity coefficients (Lafrance *et al.*, 1991, 1993, 1996) were calculated using eq. 3.92 from $n = 2$ to an upper limit of n_{\max} either with the expressions tabulated for the Legendre polynomials or with the recurrence formula

$$(n + 1) P_{n+1}(\cos \chi) = (2n + 1)\cos \chi P_n(\cos \chi) - nP_{n-1}(\cos \chi) \quad 3.101$$

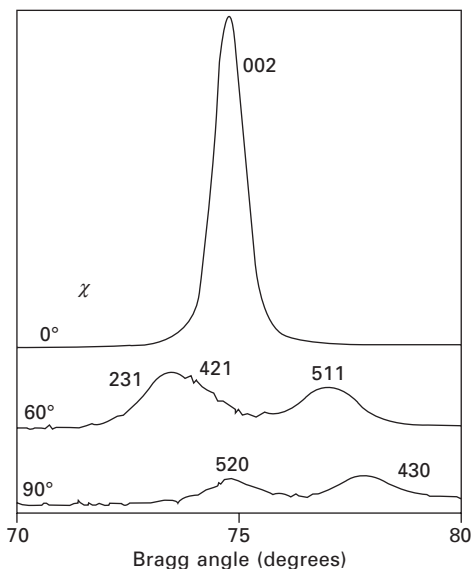
The X-ray intensity $I^*(\chi)$ is recorded as a function of the polar angle χ in Fig. 3.43. For comparison the X-ray intensity as a function of the Bragg angle θ for various χ is shown in Fig. 3.44. The numerical integration of $I^*(\chi)$ was performed by Simpson's rule or by using the Pearson VII function $\rho(\chi)$ for the normalized experimental distribution: $q(\chi) = I^*(\chi) / \int_0^{90^\circ} I^*(\chi) \sin \chi d\chi$:

$$\rho(\chi) = I_0 / \{1 + 4[(\chi - \chi_0)/a]^2 (2^{1/m} - 1)\}^m \quad 3.102$$

where I_0 is the maximum intensity, χ_0 is the peak position, a is related to the width of the distribution and m is a shape factor. The fit between the



3.43 X-ray intensity measured as a function of the polar angle χ for polyethylene (draw ratio $\lambda = 12$) for six crystal planes. (Reproduced by permission of The American Chemical Society, from Lafrance *et al.*, 1991.)



3.44 X-ray intensity as a function of the Bragg angle θ for polyethylene (draw ratio $\lambda = 12$) at different polar angles χ . The curve for $\chi = 0$ is reduced by a factor of 15. (Adapted from Lafrance *et al.*, 1991.)

experimental distribution $q(\chi)$ and the analytical curve $\rho(\chi)$ can be optimized by minimization of the error function σ in a certain angular range enclosing the peak maximum:

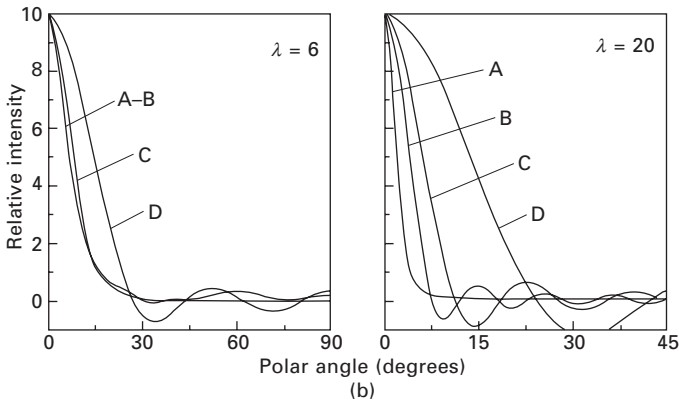
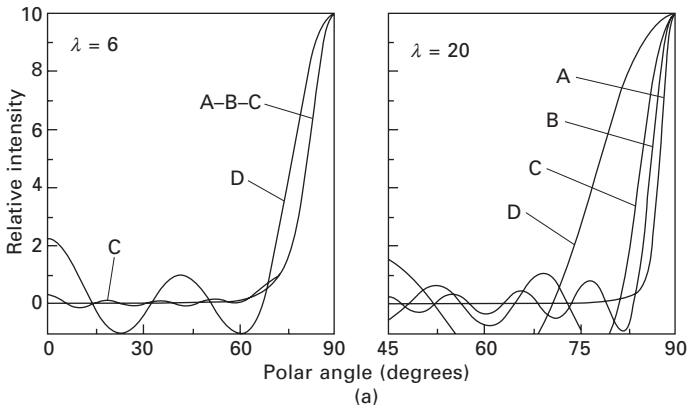
$$\sigma = \frac{\sum [q(\chi) - \rho(\chi)]^2}{\sum q(\chi)^2} \tag{3.103}$$

The order parameters $\langle P_2 \rangle$ for $(hk0)$ reflections for three draw ratios are collected for polyethylene in Table 3.3. The values for the various reflections are close and near the value of perfect orientation of -0.5 . However, the $\langle P_n \rangle$ coefficients for higher n ($n = 4, 6, 8$) differ for $\lambda = 6$ from $\lambda = 12$ and 20 considerably, which can be concluded by comparing the plots of the normalized X-ray intensity distributions $q(\chi)$ and the distribution function calculated with the coefficients $\langle P_n \rangle$ up to $n_{\max} = 32$ for the (200)- and (002)-reflections shown in Fig. 3.45.

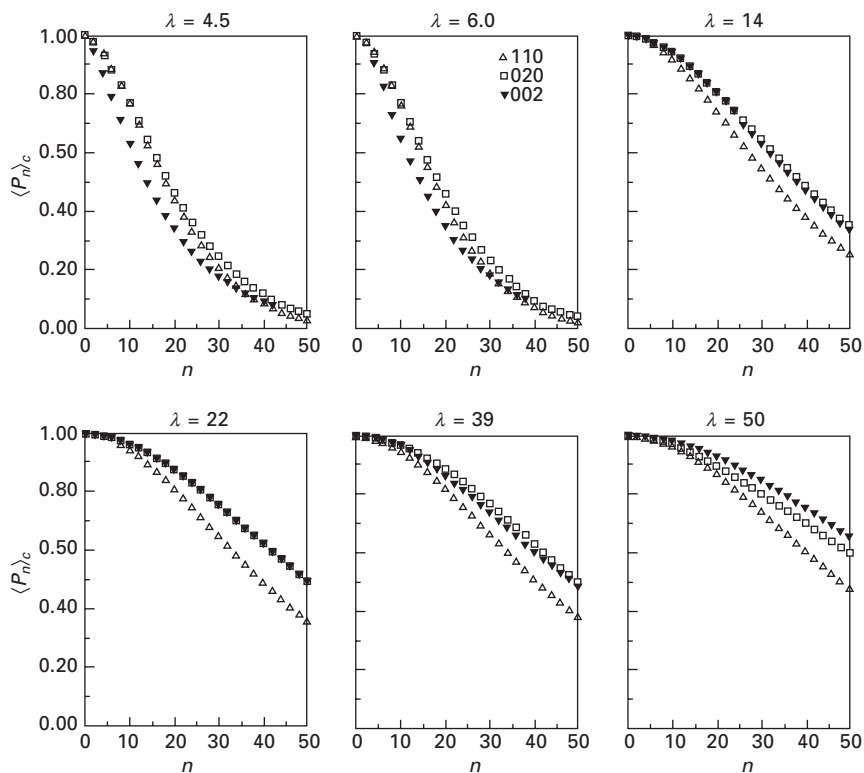
The chain orientation coefficients $\langle P_n \rangle_c$ calculated from fitting Pearson VII curves to the X-ray intensity distribution of the (110)-, (020)- and (002)-reflections for ultrahigh molecular weight polyethylene are shown in Fig. 3.46. The draw ratios are extended to very large values up to $\lambda = 50$ as are the order of the Legendre polynomials to $n_{\max} = 50$. The shapes of the curves for $\langle P_n \rangle_c$ as a function of n are similar for the three considered reflections for a specific draw ratio. The curves drop fast for low draw ratios and the curves for the (110)- and (200)-reflections overlap. For higher draw ratios the curves drop slowly and an overlap occurs for the (020)- and (002)-reflections.

Table 3.3 Order parameter $\langle P_2 \rangle$ for $(hk0)$ planes for drawn polyethylene to different draw ratios λ (Lafrance *et al.*, 1991). Perfect orientation $\langle P_2 \rangle = -0.50$

Draw ratio	$(hk0)$ Reflections		
	(110)	(200)	(020)
$\lambda = 6$	-0.44	-0.46	-0.45
$\lambda = 12$	-0.49	-0.49	-0.49
$\lambda = 20$	-0.49	-0.49	-0.49



3.45 Normalized X-ray intensity distribution $q(\chi)$ (A), and distribution function calculated with $\langle P_n \rangle$ up to $n_{\max} = 32$ (B), to $n_{\max} = 20$ (C), to $n_{\max} = 8$ (D): (a) for the (200) reflection of polyethylene for draw ratios $\lambda = 6$ and 20; (b) for the (002) reflection of polyethylene for draw ratios $\lambda = 6$ and 20. (Reproduced by permission of The American Chemical Society, from Lafrance *et al.*, 1991.)

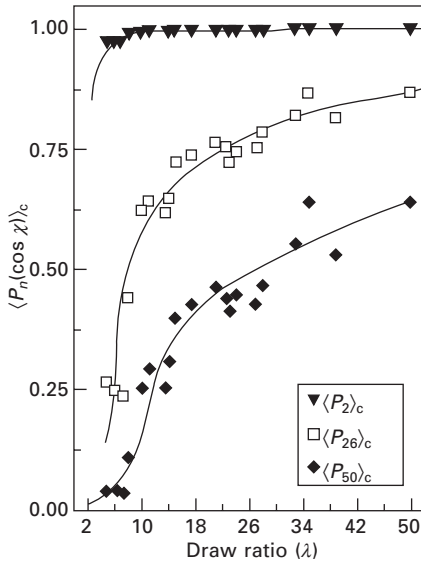


3.46 $\langle P_n \rangle_c$ coefficients calculated from fitting Pearson VII curves to the intensity distribution for (110), (020) and (002) reflections of ultra-high molecular weight polyethylene films drawn to extremely high draw ratios λ . (Reproduced by permission of John Wiley & Sons, Inc., from Lafrance *et al.*, 1993.)

If specific values of $\langle P_n \rangle_c$ coefficients are considered as a function of the draw ratio for the two reflections (020) and (002) as in Fig. 3.47, it can be concluded that the order parameter $\langle P_2 \rangle_c$ already increases at very low draw ratio to its maximum value of 1.0 and remains constant by increasing the draw ratio. This means that the order parameter, which represents a weighted average of the orientation distribution function, cannot describe the orientation at high draw ratios. Higher-order polynomials $\langle P_n \rangle_c$ have to be included, which slowly increase from low draw ratios to high ones and therefore are necessary for characterization of the orientation distribution.

3.9 Conclusions

Fibre diffraction in conjunction with conformation and packing analysis represents a powerful tool for the determination of molecular and crystal



3.47 Values of some selected $\langle P_n \rangle_c$ coefficients as a function of λ for the 020 and 002 planes. (Reproduced by permission of John Wiley & Sons, Inc., from Lafrance *et al.*, 1993.)

structures of polymers. X-ray equipment (X-ray tube in the laboratory or synchrotron radiation from storage rings at many research centres) with powerful detector devices for data collection is now easily available and the data can be electronically processed. Computer-aided simulations for the conformation and packing analysis and a simultaneous refinement with X-ray data lead to the required structure of chain molecules as the basis for structure–property relationships of polymers with few experimental data.

Selected reflections deserve special attention and should be differently weighted as they may provide strong individual structural details. For example, the ratio of the intensities of the first two reflections for polyethylene (PE), (110) and (200), are sensitive with regards to the setting angle δ , which can be estimated by this ratio since the disorder factor can be omitted due to the close vicinity of these two reflections at low angles. Some reflections of PE are strongly influenced by the scattering of the hydrogen, e.g. (210), (120), (111) and (212), and the influence of the hydrogen atoms can be evaluated. Furthermore, the ratio of intensities of certain reflections provides the anisotropic disorder factor (Zugenmaier, 1969; Kavesh and Schultz, 1970).

X-ray analysis provides further structural information needed for improving and tailoring solid polymer materials to applications such as crystallinity, preferred orientation of the macromolecular chains or disorder in the crystalline regions. These diversified investigations provide insight into the interaction

of molecules and atoms and the chain arrangements of polymers, establish correlations with desired properties and point towards improving fibres. They provide basic ideas about the origin of disorder and the size of the crystallites introduced by special treatment of specimens or by annealing.

Surveys of specific fields in structural research and analysis are provided in textbooks and many structural details on specific materials are collected, which can be used for further studies. They may be found in Alexander (1969), Bunn (1961), Dorset (1995), Fraser and MacRae (1973), Guinier (1963), Klug and Alexander (1954), Stout and Jensen (1968), Tadokoro (1979), Vainshtein (1966) and Walton and Blackwell (1973).

3.10 References

- Alexander L E (1969), *X-ray Diffraction Methods in Polymer Science*, New York, Wiley-Interscience.
- Allinger N L, Yuh Y H (1980), *Quantum Chemistry Program Exchange No 423*, Chemistry Department, Indiana University, Bloomington, IN, USA.
- Arnott S (1965), 'The geometry of diffraction of crystalline fibres', *Polymer*, 6, 478–482.
- Biangardi H J (1980), 'Calculation of the intrinsic birefringence of amorphous polyethylene terephthalate from the wide-angle X-ray scattering', *J Polym Sci, Polym Phys Ed*, 18, 903–905.
- Box M J (1965), 'A new method of constrained optimization and a comparison with other methods', *Comp J*, 8, 42–52.
- Buléon A, Pontoire B, Riekel C, Chanzy H, Helbert W, Vuong R (1997), 'Crystalline ultrastructure of starch granules revealed by synchrotron radiation microdiffraction mapping', *Macromolecules*, 30, 3952–3954.
- Bunn C W (1939), 'The crystal structure of long-chain normal paraffin hydrocarbons. The "shape" of the CH_2 group', *Trans Farad Soc*, 35, 482–491.
- Bunn C W (1961), *Chemical Crystallography*, London, Oxford University Press
- Burger C, Ruland W (2006), 'Evaluation of equatorial orientation distributions', *J Appl Cryst*, 39, 889–891.
- Cella R J, Byungkook L, Hughes R E (1970), 'Lorentz and orientation factors in fiber X-ray diffraction analysis', *Acta Cryst*, A26, 118–124.
- Chandrasekaran R (1997), 'Molecular architecture of polysaccharide helices in oriented fibers', in Horton B, *Advances in Carbohydrate Chemistry and Biochemistry*, San Diego, CA, Academic Press, pp 311–439.
- Cole E A, Holmes D R (1960), 'Crystal lattice parameters and the thermal expansion of linear paraffin hydrocarbons, including polyethylenes', *J Polym Sci*, 46, 245–256.
- Corradini P, Martuscelli E, Martynov M A (1967), 'An absolute method for the determination of crystallinity in polymers', *Makromol Chem*, 108, 285–287.
- De Wolff P M (1957), 'On the determination of unit-cell dimensions from powder diffraction patterns', *Acta Cryst*, 10, 590–595.
- De Wolff P M (1962), 'On the Lorentz factor for integrated intensities from azimuthal and radial diffractometer records of fiber patterns', *J Polym Sci*, 60, S34–S36.
- Dorset D L (1995), *Structural Electron Crystallography*, New York, Plenum Press.
- Fink H-P, Walenta E (1994), 'Röntgenbeugungsuntersuchungen zur übermolekularen Struktur von Cellulose im Verarbeitungsprozeß', *Papier*, 48, 739–748.

- Fink H-P, Fanter D, Philipp B (1985), 'Röntgen-Weitwinkeluntersuchungen zur übermolekularen Struktur beim Cellulose-I-II-Phasenübergang', *Acta Polymerica*, 36, 1-8.
- Fink H-P, Hofmann D, Purz H J (1990), 'Zur Fibrillarstruktur nativer Cellulose', *Acta Polymerica*, 41, 131-137.
- Fink H-P, Hofmann D, Philipp B (1995), 'Some aspects of lateral chain order in cellulose from X-ray scattering', *Cellulose*, 2, 51-70.
- Fischer E W, Herchenröder P, Manley R St J, Stamm M (1978), 'Small-angle neutron scattering of selectively deuterated cellulose', *Macromolecules*, 11, 213-217.
- Franklin R E, Gosling R G (1953), 'The structure of sodium thymonucleate fibres. 2. The cylindrically symmetrical Patterson function', *Acta Cryst*, 6, 678-685.
- Fraser R D B, MacRae T P (1973), *Conformation in Fibrous Proteins*, New York, Academic Press.
- Guinier A (1963), *X-ray Diffraction in Crystals, Imperfect Crystals and Amorphous Bodies*, San Francisco, London, Freeman.
- Haase J, Renwanz B (1972), 'Profilanalyse der Röntgenweitwinkelreflexe in Kettenrichtung von Cellulose II', *Kolloid-Z u Z Polymere*, 250, 503-505.
- Haase J, Hosemann R, Renwanz B (1973), 'Parakristalline Gitterstörungen in Kettenrichtung von Cellulose I und II', *Kolloid-Z u Z Polymere*, 251, 871-875.
- Haase J, Hosemann R, Renwanz B (1974), 'Röntgenweit- und Röntgenkleinwinkeluntersuchungen an Zellulose', *Colloid & Polymer Sci*, 252, 712-717.
- Haase J, Hosemann R, Renwanz B (1975), 'Axiale und laterale Ordnung in regenerierten Zellulosefasern', *Cellulose Chem Technol*, 9, 513-527.
- Harburn G, Taylor C A, Welberry T R (1975), *Atlas of Optical Transforms*, London, G. Bell & Sons.
- Hearle J W S (1958), 'A fringed fibril theory of structure of crystalline polymers', *J Polym Sci*, 28, 432-435.
- Hermans J J, Hermans P H, Vermaas D, Weidinger A (1946), *Recl Trav Chim Pays-Bas*, 65, 427-447.
- Hermans P H, Platzeck P (1939), 'Beiträge zur Kenntnis des Deformationsmechanismus und der Feinstruktur der Hydratzellulose', *Kolloid-Z*, 88, 68-72.
- Hermans P H, Weidinger A (1948), 'Quantitative X-ray investigations on the crystallinity of cellulose fibers. A background analysis', *J Appl Phys*, 19, 491-506.
- Hermans P H, Weidinger A (1949), 'X-ray studies on the crystallinity of cellulose'. *J Polym Sci*, 4, 135-144.
- Hermans P H, Weidinger A (1961), 'On the determination of the crystalline fraction of polyethylene from X-ray diffraction', *Makromol Chem*, 44-46, 24-36.
- Heuvel H M, Huisman R, Lind K C J B (1976), 'Quantitative information from X-ray diffraction of nylon-6 yarns. I. Development of a model for the analytical description of equatorial X-ray profiles', *J Polym Sci, Polym Phys Ed*, 14, 921-940.
- Hofmann D, Walenta E (1987), 'An improved single-line method for the wide-angle X-ray scattering profile analysis of polymers', *Polymer*, 28, 1271-1276.
- Hofmann D, Fink H-P, Philipp B (1989), 'Lateral crystallite size and lattice distortions in cellulose II samples of different origin', *Polymer*, 30, 237-241.
- Holmes K C, Blow D M (1966), *The Use of X-ray Diffraction Study of Protein and Nucleic Acid Structures*, New York, Wiley-Interscience.
- Horii F, Hirai A, Kitamaru R (1983), 'Solid-state ¹³C-NMR study of conformations of oligosaccharides and cellulose. Conformation of CH₂OH group about the exo-cyclic C-C bond', *Polym Bull*, 10, 357-361.

- Horii F, Hirai A, Kitamaru R (1987), 'Cross-polarization-magic angle spinning carbon-13 NMR approach to the structural analysis of cellulose', in Atalla R H, *The Structures of Cellulose – Characterization of the Solid States*, ACS Symposium Series No 340, Washington, DC, American Chemical Society, pp 119–134.
- Hosemann R, Lemm K, Schönfeld A, Wilke W (1967), 'Teilchengrößen und parakristalline Gitterstörungen', *Kolloid-Z u Z Polymere*, 216, 103–110.
- Hosemann R W, Henschel M, Balta-Calleja F J, Lopez Carbarcos E, Hindeleh A (1985), 'Bestimmung des α^* -Wertes von Polymeren, Biopolymeren und Katalysatoren', *Experimentelle Technik der Physik*, 33, 135–143.
- International Tables for X-ray Crystallography vol I* (1969), Birmingham, The Kynoch Press.
- International Tables for X-ray Crystallography vol II* (1972), Birmingham, The Kynoch Press.
- Kavesh S, Schultz J M (1970), 'Lamellar and interlamellar structure in melt-crystallized polyethylene. 1. Degree of crystallinity, atomic positions, particle size, and lattice disorder of the first and second kinds', *J Polym Sci, Part A-2*, 8, 243–276.
- Klug H P, Alexander L E (1954), *X-ray Diffraction Procedures*, New York, Wiley.
- Kratky O (1933), 'Zum Deformationsmechanismus der Faserstoffe, I', *Kolloid-Z*, 64, 213–222.
- Kreger D R (1951), 'The configuration and packing of the chain molecules of native starch as derived from X-ray diffraction of part of a single starch grain', *Biochimica et Biophysica Acta*, 6, 406–425.
- Kreuzer E, Ruland W (1985), 'Lattice defects in poly(*p*-phenylene-terephthalamide) fibers', *Colloid & Polymer Sci*, 263, 554–562.
- Lafrance C-P, Pézolet M, Prud'homme R E (1991), 'Study of the distribution of molecular orientation in highly oriented polyethylene by X-ray diffraction', *Macromolecules*, 24, 4948–4956.
- Lafrance C-P, Debigaré J, Prud'homme R E (1993), 'Study of crystalline orientation in drawn ultra-high-molecular weight polyethylene films', *J Polym Sci, Part B: Polym Phys*, 31, 255–264.
- Lafrance C-P, Prud'homme R E, Brisson J (1996), 'On the calculation of $\langle P_n(\cos \chi) \rangle$ coefficients from X-ray diffraction measurements made on *hkl* reflections', *Polymer*, 37, 1509–1512.
- Langan P, Nishiyama Y, Chanzy H (2001), 'X-ray structure of mercerized cellulose II at 1 Å resolution', *Biomacromolecules*, 2, 410–416.
- Leadbetter A J, Norris E K (1979), 'Distribution functions in three liquid crystals from X-ray diffraction measurements', *Mol Phys*, 38, 669–686.
- Lovell R, Mitchell G R (1981), 'Molecular orientation distribution derived from an arbitrary reflection', *Acta Cryst*, A37, 135–137.
- Martis K W, Wilke W (1977), 'Orientierungsabhängige Änderungen der Kristallitgröße beim Verstrecken von Polyäthylen', *Progr Colloid & Polymer Sci*, 62, 44–58.
- Müller M, Riekkel C, Vuong R, Chanzy H (2000), 'Skin/core micro-structure in viscose rayon fibres analysed by X-ray microbeam and electron diffraction mapping', *Polymer*, 41, 2627–2632.
- Nishiyama Y, Langan P, Chanzy H (2002), 'Crystal structure and hydrogen-bonding system in cellulose I β from synchrotron X-ray and neutron fiber diffraction', *J Am Chem Soc*, 124, 9074–9082.
- Riekkel C, Cedola A, Heidelbach F, Wagner K (1997), 'Microdiffraction experiments on single polymeric fibers by synchrotron radiation', *Macromolecules*, 30, 1033–1037.

- Ruland W (1961), 'X-ray determination of crystallinity and diffuse disorder scattering', *Acta Cryst*, 14, 1180–1185.
- Ruland W (1964a), 'Crystallinity and disorder parameters in Nylon 6 and Nylon 7', *Polymer*, 5, 89–102.
- Ruland W (1964b), 'Röntgenographische Bestimmung des Ordnungszustandes von Hochpolymeren' *Faserforschung und Textiltechnik*, 15, 533–537.
- Ruland W (1967), 'Röntgenographische Bestimmung der Temperaturabhängigkeit des Ordnungszustandes von Polyäthylen' *Faserforschung und Textiltechnik*, 18, 59–63.
- Schauer K, Wilke W (1995), 'Wide-angle X-ray scattering studies on polyethylene at low temperatures', *Polym Bull*, 34, 477–483.
- Schiebold E (1944), 'Beitrag zur Struktur der Zellulose. 1', *Kolloid-Z*, 108, 248–265.
- Schönfeld A, Wilke W, Höhne G, Hosemann R (1972), 'Kristallitgröße und Gitterstörungen in Polyäthylen und deren Änderung beim Nitrieren', *Kolloid-Z u Z Polymere*, 250, 102–110.
- Sheldrick G M (1997), SHELX-97 'Program for the refinement of crystal structures', University of Göttingen, Germany.
- Smith P J C, Arnott S (1978), 'LALS: a linked-atom least squares reciprocal-space refinement system incorporating stereochemical restraints to supplement sparse diffraction data', *Acta Cryst*, A34, 3–11.
- Stout G H, Jensen L H (1968), *X-ray Structure Determination*, London, Macmillan.
- Swan P R (1962a), 'Polyethylene unit cell variations with temperature', *J Polym Sci*, 56, 403–407.
- Swan P R (1962b), 'Polyethylene unit cell variation with branching', *J Polym Sci*, 56, 409–416.
- Tadokoro H (1979), *Structure of Crystalline Polymers*, New York, Wiley-Interscience.
- Taylor C A (1969), 'Optical methods as an aid in structure determination', *Pure Appl Chem*, 18, 533–550.
- Thygesen A, Oddershede J, Lilholt H, Thomsen A B, Ståhl K (2005), 'On the determination of crystallinity and cellulose content in plant fibres', *Cellulose*, 12, 563–576.
- Vainshtein B K (1966), *Diffraction of X-rays by Chain Molecules*, Amsterdam, London, New York, Elsevier.
- Vogel W, Haase J, Hosemann R (1974), 'Linienprofilanalyse von Röntgen-Weitwinkelreflexen mittels Fourier-Transformation zur Bestimmung von Mikrospannungen und parakristallinen Störungen', *Z Naturforsch*, 29a, 1152–1158.
- Vonk C G (1973), 'Computerization of Ruland's X-ray method for determination of the crystallinity in polymers', *J Appl Cryst*, 6, 148–152.
- Waigh T A, Hopkinson I, Donald A M, Butler M F, Heidelberg F, Riekel C (1997), 'Analysis of the native structure of starch granules with X-ray microfocus diffraction', *Macromolecules*, 30, 3813–3820.
- Walton A G, Blackwell J (1973), *Biopolymers*, New York, Academic Press.
- Weidinger A, Hermans P H (1961), 'On the determination of the crystalline fraction of isotactic polypropylene from X-ray diffraction', *Makromol Chem*, 50, 98–115.
- Wellard H J (1954), 'Variation in the lattice spacing of cellulose', *J Polym Sci*, 13, 471–476.
- Wilchinsky Z W (1963), 'Recent developments in measurement of orientation in polymers by x-ray diffraction', *Adv X-Ray Analysis*, 6, New York, Plenum, 231–241.
- Wilke W, Martis K W (1974), 'Kristallitgröße und Gitterstörungen in verrecktem Polyäthylen', *Colloid & Polymer Sci*, 252, 718–733.
- Wilke W, Vogel W, Hosemann R (1970), 'Die Bestimmung des Gestalt- und

- Fluktuationstensors aus den Linienbreiten im Röntgenweitwinkeldiagramm des Polyäthylens', *Kolloid-Z u Z Polymere*, 237, 317–325.
- Windle A H (1975), 'Wide angle X-ray diffraction study of the microstructure of chain-folded polyethylene crystals', *J Mater Sci*, 10, 252–268.
- Zafeiropoulos N E, Davies R J, Roth S V, Burghammer M, Schneider K, Riekel C, Stamm M (2005), 'Microfocus X-ray scattering scanning microscopy for polymer applications', *Macromol Rapid Commun*, 26, 1547–1551.
- Zugenmaier P (1969), 'Strukturuntersuchungen an partiell-kristallinem Polyäthylen und Äthylen-Propylen-Copolymeren', Dissertation, Universität Freiburg.
- Zugenmaier P, Cantow H-J (1969a), 'Ein einfaches Verfahren zur Indizierung von Röntgenweitwinkel-Reflexen von Substanzen mit orthorhombischer Elementarzelle. Messungen an Polyäthylen und Äthylen-Propylen-Copolymeren', *Kolloid-Z u Z Polymere*, 230, 229–236.
- Zugenmaier P, Cantow H-J (1969b), 'Strukturuntersuchungen an partiell-kristallinem Polyäthylen und Äthylen-Propylen-Copolymeren', *Angew Chemie*, 81, 340.
- Zugenmaier P, Sarko A (1980), 'The variable virtual bond. Modeling technique for solving polymer crystal structures', in French A D and Gardner K H, *Fiber Diffraction Methods*, ACS Symposium Series No 141, Washington, DC, American Chemical Society, pp 225–237.
- Zugenmaier P, Kuppel A, Husemann E (1977), 'Conformation and packing analysis of polysaccharides and derivatives. Detailed refinement of trimethylamylose', in Arthur J C, Jr, *Cellulose Chemistry and Technology*, ACS Symposium Series No 48, Washington, DC, American Chemical Society, pp 115–132.

Analysis of fibres using microscopy

L A DONALDSON, Scion, New Zealand

Abstract: Modern microscopes are of three basic types: those that use electromagnetic radiation (light microscopes); those that use electrons (electron microscopes); and those that work by scanning a microscopically sharp probe across surfaces (scanning probe microscopes). Microscopes can be used not only for imaging in two or three dimensions, but for measurement of physical and chemical properties by diffraction, spectroscopy and other specialised methods. This chapter briefly describes some of the microscope techniques used to investigate fibre structure and properties, including an overview of fibre identification.

Key words: microscopy of fibres, scanning electron microscopy, polarisation microscopy, confocal microscopy, scanning probe microscopy, X-ray tomography.

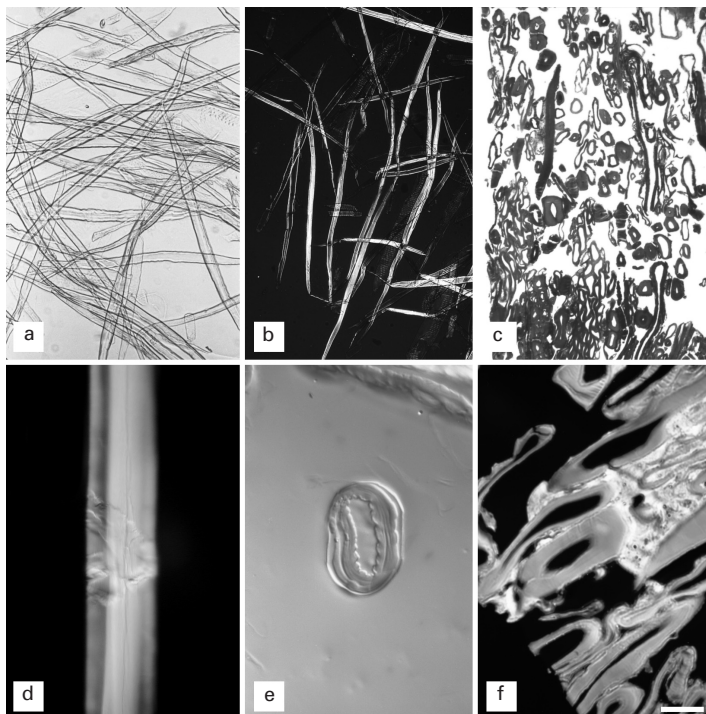
4.1 Introduction

Modern microscopes are of three basic types: those that use electromagnetic radiation and optical lenses to magnify the object (light microscopes); those that use electrons and electromagnetic lenses to magnify the object (electron microscopes); and those that work by scanning a microscopically sharp probe across surfaces, that produce images by measuring the interaction of the probe with the surface (scanning probe microscopes). Microscopes can be used not only for imaging, but for measurement of physical and chemical properties by diffraction, spectroscopy and other specialised methods. All of these instruments have been used to investigate fibre structure and properties, and some of the techniques and applications are briefly described. For further reading on the topic of fibre microscopy the following texts may be useful: Côté (1965, 1980), Sawyer and Grubb (1996), Hearle and Lomas (1998), Summerscales (1998), and Cruthers *et al.* (2005).

4.2 Optical microscopy

4.2.1 Optical techniques for unstained fibres

Unstained fibres can be examined easily with no preparation provided the fibres are mounted in a medium of lower refractive index (Fig. 4.1). Plant fibres typically have a refractive index of 1.53–1.55 (Donaldson 1985; Donaldson *et al.* 2001) so a medium such as glycerol, which has a refractive index of 1.47, is typically used. Most of the contrast will come from refraction at the



4.1 Light microscopy of plant fibres. (a) Brightfield image of unstained hardwood fibres. Scalebar = 60 μm . (b) Polarised light image of unstained hardwood fibres. Scalebar = 120 μm . (c) Brightfield image of medium density fibre board embedded in acrylic resin, sectioned with a glass knife at 3 μm thickness, and stained with toluidine blue. Scalebar = 50 μm . (d) Polarised light image of a softwood fibre showing compression failures in the cell wall. Scalebar = 20 μm . (e) Cross-sectional image of a thermomechanical pulp fibre embedded in epoxy resin and imaged using differential interference contrast (DIC). Scalebar = 12 μm . (f) Interference contrast (Jamin–Lebedeff interference) image of embedded medium density fibre board showing fibre in light grey ($N_o = 1.54$) and urea formaldehyde resin in white ($N_o = 1.44$). Scalebar = 12 μm .

boundary of the fibre and the mounting medium. The contrast can be further enhanced by lowering the condenser, or on some microscopes by removing the lens on the front of the sub-stage condenser, which also improves the depth of field. It is also possible to enhance depth of field using digital image processing, a procedure known as extended depth of field. A series of digital images at different focal planes can be combined using software to select the in-focus areas and produce a high depth of field image, thus allowing all of the fibres in the field of view to be in focus (Forster *et al.* 2004). Modern

microscope cameras and software make this otherwise complex procedure as simple as pushing a button.

Techniques such as phase contrast and differential interference contrast (DIC) can be used to provide optical contrast for either stained or unstained fibres (Fig. 4.1). Phase contrast provides edge contrast and works best with very thin samples such as fines on paper fibres, or thin cross-sections of fibres. DIC provides shadow contrast and is suitable for imaging both fines and fine surface details on fibres (Heath 2005; Cox 2006).

4.2.2 Brightfield imaging of stained fibres

While it is possible to examine fibres without staining, the use of coloured stains has the advantage of providing improved contrast, and can be used to differentiate different fibre types in a mixture (Fig. 4.1). Plant fibres contain cellulose, hemicellulose and often lignin, all of which can be readily stained with general-purpose dyes such as toluidine blue, safranine, astra blue and others (Stockert *et al.* 1984; Ruzin 1999; Haseloff 2003). Lignified plant fibres can also be stained with reagents that provide information on the type of lignin, and hence help to identify the origin of the fibre. Some types of manufactured or natural fibre, as in textiles, may already contain coloured dye added during manufacturing, and hence can be examined directly.

Staining of plant fibre is best carried out on wet fibre. If the sample is dry it can be re-saturated by soaking in water, or more quickly by soaking in 50% ethanol under mild vacuum followed by further soaking in water. Keep in mind that fibre that has not been previously dried may have different properties from fibre that has been dried and then re-wetted, particularly in relation to cell wall porosity and surface fibrillation. Staining is a simple procedure involving treatment with the stain typically for 5–10 minutes followed by washing. In the case of bulk fibre, a filter paper funnel can facilitate washing. For sections of embedded fibre, the sections will normally adhere to the glass microscope slide and can easily be washed under a gentle stream of distilled water. Both toluidine blue and safranine should work well at a concentration of 0.01–0.1% for both embedded and bulk fibre (Ruzin 1999).

4.2.3 Histochemical staining of fibres

The Weisner reagent produces a red colouration in the presence of guaiacyl lignin, while the Maule reagent can distinguish guaiacyl lignin from syringyl lignin, and can hence be used to distinguish hardwood or bast fibres, which contain syringyl lignin, from softwood fibres, which contain only guaiacyl lignin.

The Weisner reagent consists of 1% phloroglucinol in 95% ethanol (Johansen

1940; Nakano and Meshitsuka 1992; Ruzin 1999). This reagent characterises aldehyde groups of the cinnamic type which are characteristic of guaiacyl lignin (Clifford 1974). Fibres are treated for 2–5 minutes followed by addition of a few drops of concentrated HCl, resulting in a bright red colouration for lignified fibres. The two reagents can be mixed together and used as a single treatment if required. The colour will fade within half an hour, so the fibres should be mounted in glycerol and photographed as soon as possible. Care should be taken to ensure HCl fumes do not cause damage to microscope equipment by blotting the fibres prior to mounting and/or sealing the coverslip. The Weisner reagent will not work on embedded sections of fibres. It may be possible to extend the life of the coloured reaction product by mounting in glycerol/lactic acid together with small amounts of the original reagents and sealing the coverslip to make a semi-permanent mount (Speer 1987). Calcium chloride has also been recommended for the same purpose (Herr 1992).

For Maule staining, fibres are immersed in 1% (w/v) potassium permanganate solution for 5 min at room temperature, and then washed twice with 3% hydrochloric acid until the colour turns from black or dark brown to light brown. Samples are then treated with 0.1 M ammonia solution to yield a yellow-brown colour for softwoods (guaiacyl lignin) and a red-purple colour for hardwoods (syringyl lignin). Fibres can be mounted in glycerol for imaging. The Maule reagent is used to detect syringyl lignins and can thus be used to differentiate softwood and hardwood fibres (Nakano and Meshitsuka 1992).

The Cross and Bevan reagent also distinguishes fibres containing guaiacyl lignin from those containing syringyl lignin. Treatment with chlorine solution for 10 minutes followed by 4% sodium sulphite solution produces a brown colouration with guaiacyl lignin and a red colouration with syringyl lignin, essentially the same as the Maule reagent but less stable (Nakano and Meshitsuka 1992).

Mirande's reagent can be used to distinguish between lignified and unligified fibres (Mondolot *et al.* 2001). The reagent consists of iodine green and alum carmine stains. Fibres are immersed in sodium hypochlorite for 10 minutes, rinsed in acidified distilled water (acetic acid) and stained in the Mirande's reagent for 15 minutes. Fibres are examined using a fluorescence microscope with UV excitation. Softwood fibres fluoresce green while hardwood fibres fluoresce pink and blue-green.

Although not technically a histochemical stain, Simons stain has been used to detect changes in fibre wall structure resulting from beating during the papermaking process (Simons 1950; Blanchette *et al.* 1992; Yu *et al.* 1995). This stain consists of two components, one of which stains unbeaten fibres blue, while the other component stains orange the regions of damaged wall resulting from beating. This differential staining occurs as a result of

differences in molecular weight and substrate affinity between the two dye components, which allows the detection of more porous damaged regions of the fibre wall (Yu *et al.* 1995).

4.2.4 Polarised light microscopy of plant fibre

Plant fibres with secondary cell walls contain partially crystalline cellulose in the form of highly oriented microfibrils (Abe and Funada 2005). Such fibres are thus birefringent and can rotate the plane of polarised light (Preston 1934; Cousin 1972; Page and El-Hosseiny 1974; Leney 1981; Donaldson 1991). Using a microscope equipped with two polarising filters in the crossed position, birefringent fibres placed between the filters become visible as bright objects on a black background (Fig. 4.1). This method can be used to confirm the presence of crystalline cellulose, to measure the microfibril angle (Cousin 1972; Page and El-Hosseiny 1974; Leney 1981; Donaldson 1991) and to study compression failures in the fibre wall, which are highlighted by this technique (Nyholm *et al.* 2001; Terziev *et al.* 2005; Thygesen and Ander 2005; Thygesen *et al.* 2006).

4.2.5 Interference microscopy

A modification of polarised light microscopy that produces interference contrast between light that passes through the sample and light from a reference beam can be used to measure the refractive index of the fibre in a thin cross-section (Fig. 4.1) (Baas 1975; Barakat and Hamza 1990; Donaldson 1992). Refractive index measurement has been used for polymer identification in artificial fibres such as nylon, to study core/coating layers (Barakat and Hamza 1990; Fouda *et al.* 1997; El-Bakary 2007) and to measure the cross-sectional shape of nylon fibres (Hamza *et al.* 2002).

Interference microscopy has also been used to determine the chemical composition and porosity of plant fibres (Boutelje 1972; Donaldson 1985, 1992; Donaldson *et al.* 2001), and the interaction of polymers with wood fibres (Baas 1975). A number of procedures, including variation of wavelength, temperature or mounting medium, can be used to determine the refractive index, depending on the type of equipment available (Barakat and Hamza 1990; Donaldson 1992; Sokkar and El-Bakary 2001).

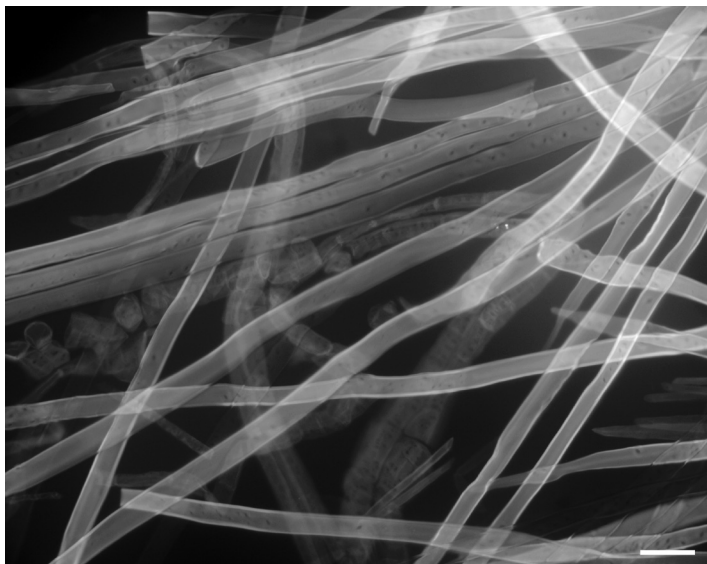
4.2.6 Widefield fluorescence microscopy

Lignified plant fibres will autofluoresce with UV or blue light excitation but this tends to be quite dim, and thus difficult to photograph. A variety of fluorescent dyes is available for both lignified and delignified/unlignified plant fibres, and hence fluorescence microscopy can be used to distinguish between

these types of fibres (Kutscha and McOrmond 1972; Mori and Bellani 1996; Olmstead and Gray 1997; Donaldson and Bond 2005). Common fluorescent stains for plant fibres include calcofluor (Fig. 4.2), which stains cellulose, as well as acriflavin and berberine sulphate, which are general fibre stains (Brundrett *et al.* 1988; Donaldson and Bond 2005). Calcofluor is excited by UV light and emits in the blue and green range, while acriflavin and berberine sulphate are excited by blue light and emit at green, yellow and red wavelengths. Immunocytochemistry using fluorescently labelled antibodies or enzyme binding modules is increasingly being used to localise specific components of the fibre wall, in relation to fibre properties (Filonova *et al.* 2007a, b; Kukkola *et al.* 2008).

There is little information on staining artificial fibres with fluorescent dyes. The fibres themselves can be considered non-fluorescent. However, some artificial fibres may show fluorescence from optical brightening agents used in textile manufacture. Presumably some textile dyes are also fluorescent and may therefore impart fluorescence to the fibres thus treated.

Fluorescence and UV-Vis microspectrophotometry have been used to examine dyed fibres such as wood pulp, cotton, polyester, acrylics and nylon. In the case of pulp fibres, microspectroscopic analysis allows the determination of lignin content or kappa number (Liu *et al.* 1997, 1999; Li and Reeve 2004). Multivariate analysis of spectra allows discrimination of different fibre types (Morgan *et al.* 2004). Fluorescence microscopy has



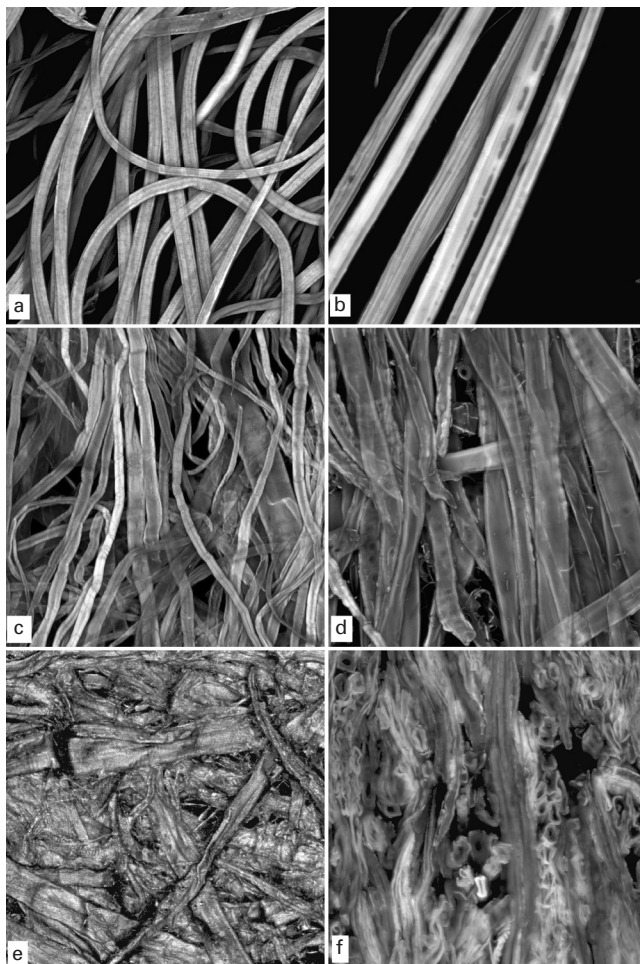
4.2 Widefield fluorescence image of softwood pulp fibres stained with calcofluor. Excitation 360 nm, emission 400+ nm. Scalebar = 60 μm .

also been used to discriminate among types of cotton fibres from textiles for forensic examination (Cantrell *et al.* 2001).

4.2.7 Confocal fluorescence microscopy

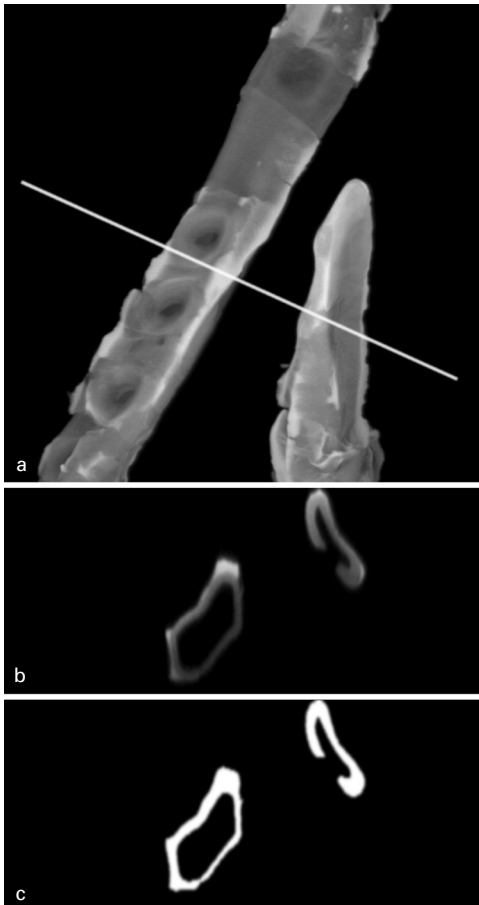
Wide-field fluorescence microscopy suffers from out-of-focus haze. Confocal fluorescence microscopy overcomes this problem by using a pinhole to reject out-of-focus light, producing high-resolution optical slices, or projections with extended depth of focus (Fig. 4.3). This makes it an ideal imaging method for fibre-based materials including paper and textiles. Confocal microscopy produces a series of optical slices from 0.5 to 5 μm thick depending on the numerical aperture (NA) of the objective lens (high NA gives a thinner slice and hence greater z -axis resolution) (Knebel and Schnepf 1991; Haseloff 2003; Hibbs 2004; Donaldson and Bond 2005). These slices can be combined to represent a volume, which when rendered on a computer can be used to view the fibres from any perspective, even allowing computer-generated cross-sections without the need for physical cutting of the material (Fig. 4.4). In general, the same dyes that are used for widefield fluorescence can also be used for confocal fluorescence imaging. However, some dyes such as calcofluor, for example, are bifluorescent, producing polarised fluorescence images because of the natural polarisation of the dye molecules, and this can be a disadvantage because only parts of the fibre will appear fluorescent, depending on orientation (Verbelen and Stickens 1995; Jang 1998). This phenomenon can, however, be used to advantage for measuring microfibril angle (Batchelor *et al.* 1997; Jang 1998; Bergander *et al.* 2002; Sedighi-Gilani *et al.* 2005).

Confocal fluorescence microscopy has been used for a wide range of studies on mainly wood and paper fibres, and also bast fibres, including measurement of fibre dimensions (Jang *et al.* 1991, 1992, 1995a, b; Carstensen and Schultz 1993; Weise 1993; Weise and Paulapuro 1995; Seth *et al.* 1997; Xu *et al.* 1997a; Chan *et al.* 1998; Jang and Seth 1998; Dickson 1999, 2000; Xu and Parker 1999; Jang 2005; Newman *et al.* 2007), microfibril angle (Verbelen and Stickens 1995; Batchelor *et al.* 1997; Jang 1998; Bergander *et al.* 2002), fibre composition (Taylor *et al.* 1996; Donaldson *et al.* 2001), localisation of additives such as adhesives (Shaler *et al.* 1996; Grigsby and Thumm 2002; Loxton *et al.* 2003; Grigsby *et al.* 2004; Xing *et al.* 2005; Cyr *et al.* 2007; Pakdel *et al.* 2007), and three-dimensional structure (Nanko and Ohsawa 1990; Jang *et al.* 1991, 1995a, b; Robertson *et al.* 1991; Moss *et al.* 1993; Béland and Mangin 1995; Shaler *et al.* 1996; McDonald *et al.* 1997; Xu *et al.* 1997b; Jang and Seth 1998; He *et al.* 2004) including fibre–fibre bonding (Thomson *et al.* 2007). Confocal microscopy has been used to measure individual fibre cross-sectional dimensions in studies of fibre mechanical properties (Groom *et al.* 2002; Mott *et al.* 2002).



4.3 Confocal fluorescence and reflection microscopy of plant fibres. These images are projections made from a series of optical slice images. (a) Cotton stained with berberine sulphate. (b) Jute stained with berberine sulphate. (c) Tissue paper (mostly hardwood fibres) stained with berberine sulphate. (d) Paper towel (softwood fibres) stained with berberine sulphate. (e) Reflection image of paper towel. (f) Medium density fibre board stained with acriflavin, embedded in wax and surfaced with a microtome. All images are 0.5×0.5 mm field of view. For the fluorescence images, excitation was 488 and 568 nm, while emission was 530 and 600 nm. For the reflection image a wavelength of 488 nm was used.

Confocal fluorescence microscopy has also been used for imaging artificial fibres in order to understand dye penetration (Kelch *et al.* 2000; Song *et al.* 2000; De Clerck *et al.* 2004, 2005), to localise additives on the surface of



4.4 Confocal fluorescence image of thermomechanical pulp fibre stained with berberine sulphate. (a) A maximum intensity projection of 112 optical slices over a z-distance of $58.5\ \mu\text{m}$. Field of view is $159 \times 159\ \mu\text{m}$. (b) An xz slice at the position of the white line in (a) above showing the transverse view of the two fibres. Field of view is $170 \times 58.5\ \mu\text{m}$. (c) The same view as in (b) after segmentation using a variable threshold that overcomes the progressive darkening of the image with distance from the top of the sample. This image allows measurement of wall thickness and lumen diameter. Field of view is $170 \times 58.5\ \mu\text{m}$.

fibres (Cortez *et al.* 2004, 2007; Rous *et al.* 2004), and to determine three-dimensional structure (Kumar *et al.* 2002).

4.2.8 Confocal reflection microscopy

In the same way that confocal microscopy can visualise fluorescence to produce three-dimensional images, a reflection signal can also be used to

image fibre surfaces (Fig. 4.3). The light incident on the fibre will tend to be reflected by large refractive index boundaries, such as those at the surface of the fibre. This signal can produce high-resolution images of the fibre surface similar to those produced by scanning electron microscopy. This method has been used to study the surface texture of wood fibres in order to determine the microfibril angle (Donaldson and Frankland 2004).

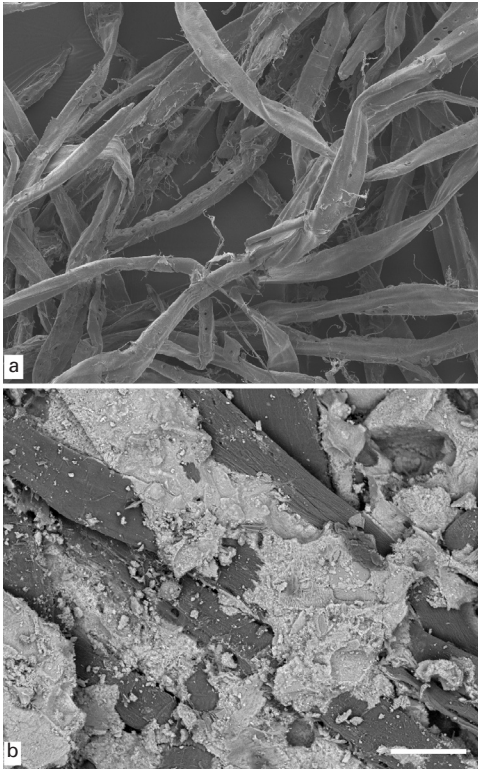
4.3 Electron microscopy

4.3.1 Scanning electron microscopy

Scanning electron microscopy (SEM) is used to produce high-resolution surface images of fibres with high depth of field (Duchesne and Daniel 1999; Williams and Drummond 2000; Goldstein *et al.* 2003; Tomes *et al.* 2007). It is the most commonly used form of microscopy for fibres, especially when high resolution is required. In some studies SEM has been directly compared to other techniques such as polarised light microscopy, using the same individual fibre for both techniques. This has been especially useful for studying compression failures or kinks in fibres (Thygesen *et al.* 2006).

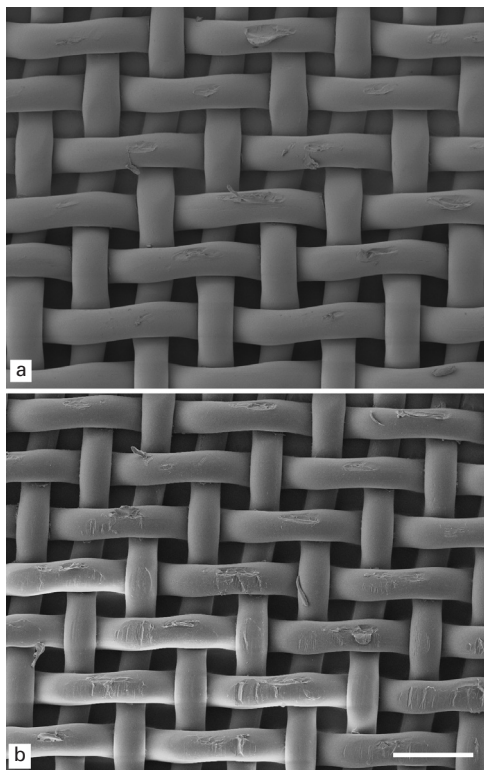
SEM and more particularly field emission SEM (FESEM) has the advantage of high resolution and large depth of field, producing images of rough surfaces over a wide range of magnifications from images of fibre networks to high-resolution images of fibre surfaces at the near-molecular level (Fig. 4.5). For imaging fibre composites, SEM can also identify inorganic phases in the composite by using atomic number contrast, a characteristic of backscattered electrons (Fig. 4.5) (Rothbard 2002; Roux *et al.* 2008). X-ray analysis by energy dispersive spectroscopy (EDS) can also determine the elemental composition of fibres and composites (Roux *et al.* 2008; Goldstein *et al.* 2003).

Despite its advantages in fibre imaging, fibre samples can be problematic for SEM because of their poor conductivity, particularly when they are formed into products such as paper or textiles (Fig. 4.6). Additionally, samples must be dried to make them compatible with the high vacuum of the microscope. Techniques include air drying from solvents such as ethanol or *t*-butyl alcohol, or more sophisticated methods such as freeze-drying using liquid nitrogen, or critical point drying using liquid CO₂ (Duchesne and Daniel 1999). In some cases it may be advantageous to freeze the sample in liquid nitrogen and observe it in the frozen state using a cryo-stage in the SEM (Howard 1987; Moss *et al.* 1989a, b; Duchesne and Daniel 1999; Goldstein *et al.* 2003). The dry or frozen sample is typically sputter-coated with gold or other metals to improve conduction. Unfortunately, the porous network formed by most fibre-based products is not well infiltrated by sputter coating, and charging problems resulting from the poorly grounded fibre network can



4.5 Scanning electron microscopy of wood fibre. (a) Thermomechanical (TMP) pulp fibres from a typical softwood showing a surface decorated with fines or cell wall fragments. Accelerating voltage 3 kV. Scalebar = 117 μm . (b) Fibre-cement board using backscattered electrons to produce atomic number contrast between fibre (dark) and cement (bright). Accelerating voltage 15 kV. Scalebar = 38 μm .

lead to poor-quality images, particularly on older SEM instruments that use higher kV electron beams. In extreme cases, an electrostatic mirror may be formed in which case the sample itself becomes invisible. Newer low kV instruments operating at 1–3 kV, compared to 10–20 kV on older instruments, can eliminate charging problems and provide much greater resolution on fibre surfaces because of reduced beam penetration effects. Further improvement can be achieved by ensuring fibres are in a thin monolayer with little overlap or contact with adjacent fibres, thus ensuring that the fibres are well grounded. For fibre-based materials like paper or textiles, the sample should be small and securely attached to the sample holder with conducting adhesives such as colloidal silver. Charging artefacts can be recognised as bright or dark areas, by apparent image drift, and by distortion of the image in the direction of beam scan (Fig. 4.6).



4.6 Fibres can be problematic because of their poor conductivity, especially when in a fibre network. This nylon mesh demonstrates the importance of selecting an optimum accelerating voltage to reduce or eliminate undesirable charging contrast. (a) Nylon mesh at 1 kV accelerating voltage. This image shows topography without any significant charging contrast. (b) Nylon mesh at 5 kV accelerating voltage. This image shows both topography and mild charging contrast. Scalebar = 100 μm .

An alternative to conventional SEM for difficult-to-image materials is environmental SEM (ESEM) (Kifetew and Sandberg 2000; Donald 2003; Goldstein *et al.* 2003; Turkulin *et al.* 2005a, b). In this technique, the high vacuum of a conventional SEM is replaced by a low pressure water vapour atmosphere, which provides charge neutralising capability in addition to allowing examination of wet fibres, with the ability to vary pressure and temperature to maintain water saturation, or to allow controlled drying. For this method, fibres do not require coating with metal and can thus be re-examined after successive treatments. This method has the disadvantage that water is opaque to electrons and hence structures that are covered in a water film cannot be seen clearly. Hence most applications have examined

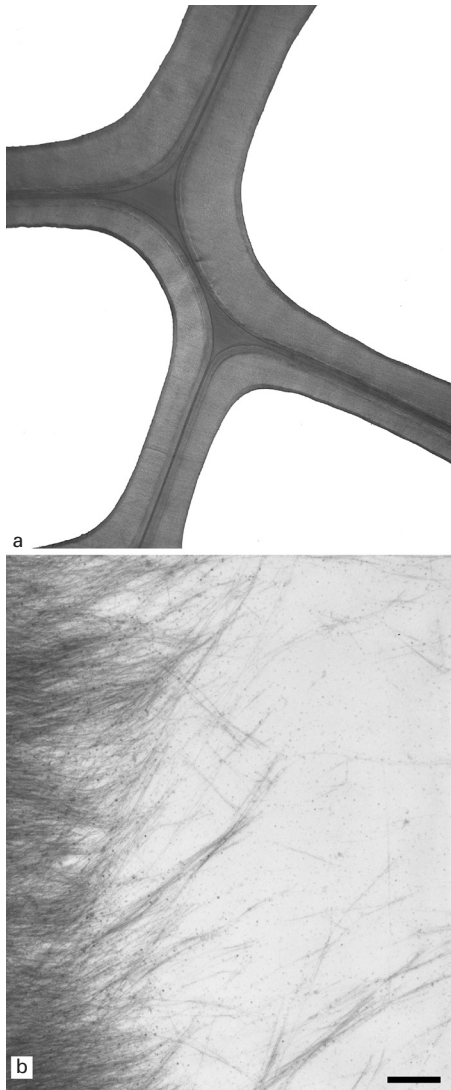
partially or fully dried fibres, the primary advantage being elimination of the need for metal coating to allow *in-situ* deformation experiments on single fibres inside the microscope (Mott *et al.* 1995, 1996; Shaler *et al.* 1996; Bos and Donald 1999; Donald 2003; Orso *et al.* 2006; Thygesen *et al.* 2007). ESEM has also been used to study the wetting properties of paper fibres (Liukkonen 1997).

4.3.2 Transmission electron microscopy

Transmission electron microscopy (TEM) is a rarely used method to study fibres because of the often complicated specimen preparation. Prior to the development of SEM, TEM of surface replicas was often used to characterise fibre surfaces (Côté 1965), but this method is complex, allows only limited areas of the fibre to be imaged, and is now largely superseded by high resolution FESEM (Duchesne and Daniel 1999). A modern version of the replica method involves freeze/fixation in liquid nitrogen and deep etching of surfaces, followed by replication. This method, known as rapid freeze deep etching, allows high-resolution imaging of fibre surfaces in the frozen hydrated state (Bardage *et al.* 2004).

Several key points must be kept in mind when using TEM to study fibres. Conventional TEM requires ultra-thin (60–120 nm) sections of embedded fibres produced using a diamond knife. In order to infiltrate plant fibres with resin it is necessary to work with fibres that have not been previously dried, to avoid the loss of porosity and hornification that occurs as a result of drying (Rajinder 2001). Fibres are thus dried by solvent exchange followed by gradual infiltration in resin/solvent mixtures. Orientation of fibres to achieve a cross-sectional view can be problematic unless the fibres are examined *in situ* before extraction from the plant stem, but methods have been developed to deal with separated fibres (Nelson and Woods 1996; Trancik *et al.* 2001). Very thick-walled bast fibres will be demanding in terms of quality of preparation because of difficulty with infiltration and because of the hardness of the sample (because of the large wall thickness), which makes sectioning difficult. Provided that sections 60–120 nm can be achieved, then staining and imaging are quite straightforward (Fig. 4.7). Staining is typically achieved using heavy metal salts such as uranyl acetate, lead citrate or, potassium permanganate, or organic silver salts such as in the PATAg procedure (Bland *et al.* 1971; Brändström *et al.* 2005; Donaldson 2006; Billosta *et al.* 2007). Immunocytochemistry using antibodies or enzyme binding modules tagged with colloidal gold can be used to localise specific components of the fibre wall (Ruel and Joseleau 1984; Ruel *et al.* 1994; Duchesne *et al.* 2003; Brändström *et al.* 2005).

One special type of fibre has been the subject of a number of recent investigations. Cellulose nanofibrils, also known as cellulose whiskers, are



4.7 Transmission electron microscopy can range from near light microscopy resolution to macromolecular resolution. (a) Wood fibres showing cell wall layers, including the middle lamella which binds adjacent fibres together. (b) Individual cellulose microfibrils in a delignified wood fibre. Scalebar 2 μm for (a) and 100 nm for (b).

members of a special class of fibre known as nanofibres because of their very small size. Nanofibres are typically less than 100 nm in diameter and are thus small enough to be examined directly by drying a suspension onto a support film and imaging with TEM (Favier *et al.* 1995; Kvien *et al.* 2005; Stenstad

et al. 2008). TEM is typically used to measure the size of the nanofibres, and to study their interaction with other polymers in nanocomposite materials (Favier *et al.* 1995; Goussé *et al.* 2002; Kvien *et al.* 2005; Oksman *et al.* 2006; van den Berg *et al.* 2007; Park *et al.* 2007; Wang and Sain 2007).

TEM can be used to perform electron diffraction, where a diffraction pattern is produced by interaction of the incident electrons and the specimen (Heath 2005). Like X-ray diffraction, the analysis of the electron diffraction pattern gives information on crystallinity. Electron diffraction is used where changes in crystallinity are investigated at high spatial resolution, compared to X-ray diffraction which is generally a bulk technique. Arguably, the main application of electron diffraction to fibres is in the identification of asbestos, where Chrysotile has a unique diffraction pattern that distinguishes it from Amphibole (Langer *et al.* 1974; Veblen 1980). Electron diffraction has been used to measure small-scale variations in crystallinity in polymer fibres (Scott 1962; Oudet *et al.* 1984; Müller *et al.* 2000). The use of electron diffraction on plant fibres is limited by damage caused by the electron beam, which results in loss of crystallinity within short periods of exposure unless low dosage conditions are applied (Chanzy *et al.* 1978; Sugiyama *et al.* 1986; Müller *et al.* 2002).

4.4 Infrared techniques (FTIR and Raman)

A Fourier transform infrared microscope uses infrared illumination (as an interferogram) to illuminate the sample and collect an infrared absorption interferogram from a point on the sample. This is subsequently converted back to a spectrum by Fourier transform (FTIR). By building up an array of spectra across the sample a chemical map can be created (Naumann and Polle 2006). This method allows simultaneous collection of all infrared absorption wavelengths, either by transmission or by reflection (Heath 2005).

A Raman microscope uses Raman scattering to map chemical composition across the sample (Lewis and Edwards 2001; Ferraro and Nakamoto 2003). Raman scattering of infrared light includes inelastic and superelastic scattering due to the polarisation of molecules containing covalent bonds. The sample is illuminated with a laser using monochromatic light, and filters are used to remove Rayleigh scattering (non-characteristic elastic scattering). A spectrometer is then used to produce a Raman spectrum which provides information on the types of chemical bonds present in the sample (Lewis and Edwards 2001; Ferraro and Nakamoto 2003; Heath 2005).

Resolution of FTIR microscopy is typically limited by signal to noise ratio, to a spot size of about 10 μm , which makes single spot analysis more useful than mapping an array of spots (Naumann and Polle 2006), but some types of Raman spectrometer allow much greater spatial resolution. Therefore, Raman microscopy is more commonly used for mapping applications (Gierlinger

and Schwanninger 2006, 2007). FTIR can be combined with SEM imaging by placing the spectrometer inside the SEM chamber (Beltran *et al.* 2002; Mwaikambo and Ansell 2002), while Raman spectroscopy is often coupled with confocal microscopy and scanning probe microscopy to yield greatly improved spatial resolution.

Both FTIR and Raman microscopy can be used to measure the chemical composition of natural and artificial fibres, which can be applied to fibre identification for forensic investigations (Bard *et al.* 1997, 2004; Wiggins 2001; Causin *et al.* 2004; Robertson and Roux 2004; Causin *et al.* 2005a, b; Rinaudo *et al.* 2004) and to localise different fibre components and additives (Signori and Lewis 1996; Bogoeva-Gaceva *et al.* 1997; Beltran *et al.* 2002; Mwaikambo and Ansell 2002; Gañán and Mondragon 2002; Röder and Sixta 2004; Röder *et al.* 2004; Burgert *et al.* 2005; Causin *et al.* 2005b; Fleming *et al.* 2005; Gierlinger *et al.* 2005; Baley *et al.* 2006; Gierlinger and Schwanninger 2006, 2007; Morán *et al.* 2008).

4.5 Scanning probe microscopy

Scanning probe microscopy is a general term for a family of imaging techniques that involve scanning a very sharp probe in close proximity to the surface of the specimen to acquire topographic, chemical or physical data at very high spatial resolution (Meyer *et al.* 2004; Foster and Hofer 2006). Such instruments consist of a sharp tip usually positioned on a cantilever, a scanning system, usually using piezoelectric devices to move the probe with nanometre resolution, a motion sensor to detect the position of the probe using a laser beam reflected from the cantilever, an electronic control system for regulating/measuring interactions between the probe and specimen, a computer to receive and process signals, and a light microscope for positioning the specimen. A vibration isolation system is also required.

There are many types of scanning probe microscopy that can be used for imaging or for measurement of physical properties. The three basic types are scanning tunnelling microscopy (STM) atomic force microscopy (AFM), and scanning near-field optical microscopy (SNOM) (Heath 2005; Cox 2006). In the case of plant fibres, AFM (phase imaging mode and tapping mode) has been used to study cellulose microfibril clustering in plant fibres (Hanley and Gray 1994, 1999; Maxwell *et al.* 2003; Fahlén and Salmén 2002, 2003; Kangas and Kleen 2004; Salmén 2004; Gañán *et al.* 2008) and to study the structure of native or modified plant fibre surfaces (Börås and Gatenholm 1999; Wong *et al.* 2000; Maximova *et al.* 2001; Gustafsson *et al.* 2003; Gradwell *et al.* 2004; Koljonen *et al.* 2004; Yan *et al.* 2004; Chhabra *et al.* 2005; Fahlén and Salmén 2005; Poggi *et al.* 2005; Demir *et al.* 2006; Westbye *et al.* 2006; Guan *et al.* 2007). AFM has been used to measure the surface roughness of thermomechanical pulp fibres in relation to refiner pressure

(Snell *et al.* 2001). AFM has also been used to study the characteristics of cellulose whiskers and their nanocomposites (Edgar and Gray 2003; Kvien *et al.* 2005; Park *et al.* 2007; Wang and Sain 2007; Henriksson *et al.* 2007; Morán *et al.* 2008).

Both plant fibres and hair or wool fibres have been examined for surface hardness/stiffness using nano-indentation with a stiff cantilever to measure force \times penetration relationships (Furuta and Gray 1998; Parbhu *et al.* 1999; Gindl and Gupta 2002; Gindl *et al.* 2004; Maxwell and Huson 2005; Sasaki *et al.* 2006). AFM in combination with other techniques has been used to study fibre–fibre bonding, showing the relation between surface roughness and bonding (Kang *et al.* 2004). Measurement of adhesion force between the AFM tip and the fibre surface can be used as a measure of wet ability of natural fibres such as hemp (Pietak *et al.* 2007).

AFM has been used to characterise artificial fibre surface properties (Maxwell and Huson 2005; Pietak *et al.* 2007), to study the effect of surface treatments (Periyasamy *et al.* 2007; Pietak *et al.* 2007; Wei *et al.* 2007, 2008) and to localise surface-bound reagents such as sizing (Mäder *et al.* 2007).

AFM can potentially yield better resolution than FESEM, for example, because no metal coating is required and damage from the electron beam is avoided. However, AFM requires a very smooth surface to yield good results, and can only be used on relatively small areas, so has not been used to the same extent as SEM. One advantage is the ability to image at high resolution in water so that cellulose fibres can be examined in the swollen state (Furuta and Gray 1998; Hanley and Gray 1999; Sasaki *et al.* 2006). Softening of fibre surfaces may, however, cause imaging problems for wet samples (Sasaki *et al.* 2006).

4.6 X-ray tomography and other techniques

X-ray tomography, using both conventional and synchrotron sources, has been used to study fibre networks by computing three-dimensional reconstructions of millimetre-scale volumes for paper (Samuelsen *et al.* 2001; Thibault and Bloch 2002; Hansson and Rasmuson 2004; Rolland du Roscoat *et al.* 2005), fibreboard (Faessel *et al.* 2005), composite materials (Kastner *et al.* 2004; Schell *et al.* 2006; Tan *et al.* 2006) and textiles (Eberhardt and Clarke 2002; Pandita *et al.* 2002; Pandita and Verpoest 2003; Parnas *et al.* 2003; Desplentere *et al.* 2005). In comparison, electron tomography has much greater resolution (~ 1 nm) but is not well suited to investigations of whole fibres because it requires thin sections. Caldwell *et al.* (2005) have used electron tomography to study intermediate filaments in wool fibres, while Xu *et al.* (2007) have studied the structure and organisation of cellulose microfibrils in thin sections of delignified wood fibres.

Serial sectioning has also been used to create three-dimensional

reconstructions of fibres and fibre networks such as paper, with the advantage of greater spatial resolution compared to X-ray techniques, but this approach is obviously very tedious (Aronsson 2002; Chinga *et al.* 2004). Recent advances in robotic sectioning combined with sequential SEM imaging of the prepared surface provide an opportunity for fine-scale three-dimensional reconstruction of fibre networks in the future (www.gatan.com).

Optical coherence tomography is a technique based on a Michelson interferometer that allows optical sectioning over much longer distances than confocal microscopy but with poorer spatial resolution. This technique has been applied to the study of fibre networks of various types, including paper and composite materials, in a small number of reports (Alarousu *et al.* 2005; Fabritius *et al.* 2006; Peiponen *et al.* 2006; Wiesauer *et al.* 2007). UV absorbance microscopy has been used to measure lignin distribution in wood fibres and tracheids by measuring the absorbance at 280 nm, the absorbance maximum of lignin (Wood and Goring 1971; Fukazawa and Imagawa 1981; Koch and Kleist 2001). Finally, secondary ion mass spectroscopy (SIMS) has been used for such applications as mapping inorganic components (surfactants) on the surface of paper fibres (Brinen and Proverb 1991).

4.7 Identification of natural and artificial fibres by microscopy

Microscopic examination can readily be used to distinguish plant, animal, mineral and artificial fibres from one another. Natural plant fibres are always hollow, even though the lumen may be very small in some types of xylem or phloem fibres, while artificial fibres are usually solid. Plant fibres are also relatively short, typically 1–10 mm, whereas artificial fibres maybe much longer. Bast fibres, which are often utilised as intact bundles of individual fibres, can be metres in length. Animal fibres are proteinaceous, have no lumen, are multicellular and often have scales or other decorations on the surface. They can also be much larger in diameter (20–180 μm) and are much longer than plant fibres. Identification of plant and animal fibres is mainly carried out by microscopy while there are a range of testing procedures used to further identify artificial fibres, including burning tests, staining, solubility, melting point and spectroscopy (Causin *et al.* 2004; Morgan *et al.* 2004; Robertson and Roux 2004).

Plant fibres can be divided into four groups based on origin of the fibre, bast fibres (phloem fibres or other non-xylem fibres including jute, hemp, flax, ramie, kenaf, rattan, bagasse and others), softwood fibres, hardwood fibres, and monocotyledon fibres including palms and grasses. The term fibre here is used in an industrial sense as any long narrow cell with a secondary cell wall. However, technically softwood ‘fibres’ are known as tracheids because of their water-conducting function, as opposed to true fibres which

do not conduct water and only have a role in support of stems or leaves. The anatomical feature which distinguishes tracheids from fibres is the presence of bordered pits. Tracheids occur in all softwoods, and in some hardwoods in addition to fibres.

Individual bast fibres typically have very thick cell walls that exhibit multiple wall layers in cross-section. Softwood fibres (tracheids) are relatively long (2–5 mm) and wider in diameter (25–50 μm) than hardwood fibres (1–2 mm long and 10–25 μm wide), and can be distinguished using the Maule test for syringyl lignin in hardwood fibres. Hardwood fibres may include non-fibre cell types such as vessel elements, when examining paper or pulp for example. Anatomical features such as pitting may be used to further identify fibres but identification to species is rarely possible without knowledge of the country of origin of the fibre (Côté 1980).

Asbestos and glass fibres are inorganic and thus easy to distinguish from organic fibres. Identification can involve polarised light microscopy, energy dispersive X-ray analysis (EDS), electron diffraction, or Raman spectroscopy. Glass fibres are not birefringent (they remain dark at all orientations under polarised light) and are single long tubular fibres with a more or less smooth surface. EDS analysis indicates SiO_2 in addition to Al, B, Ca, Mg and other trace elements, depending on the type of glass used.

Asbestos fibres are small (< 2 μm) birefringent crystal fibres that occur in finely divided fibrous clusters that are often splayed at the ends (Langer *et al.* 1974). The fibres are hollow with a small internal capillary. Chrysotile fibres (white asbestos) are composed of bundles of fibrils that are often curved and have splayed ends, and also have a unique electron diffraction pattern that distinguishes these fibres from other types of asbestos (Langer *et al.* 1974). Amphibole fibres tend to be straight and fragment easily, and curved fibres may occasionally be present. Crocidolite (blue asbestos) has the shortest fibres, with longer fibres found in Amosite (brown asbestos) and Anthophyllite. Asbestos fibres are small enough to be directly mounted on grids for TEM imaging and electron diffraction analysis. Fibres are sensitive to the electron beam and may change with time of exposure, particularly in relation to the size of the capillary (Langer *et al.* 1974). Refractive index varies among the asbestos types and can be used for identification. Chrysotile has a refractive index of 1.55, Amosite 1.67 and Crocidolite 1.70.

Raman spectroscopy is also used for identification of asbestos type (Bard *et al.* 1997, 2004; Rinaudo *et al.* 2004). EDS using TEM indicates the presence of Si, Al, Fe, Mg, Ca and Na with Crocidolite rich in Fe (32% FeO) compared to Chrysotile (1.3% FeO) which is enriched with Mg (48% MgO, *cf.* 1.8% in Crocidolite) (Malami and Grasserbauer 1982; Rinaudo *et al.* 2004).

4.8 Future trends

Increasingly, new developments in the field of microscopy combine spectroscopic information and three-dimensional imaging to characterise the substrate both chemically and structurally. Such developments are often led by improved computer processing power and include Raman confocal microscopy, transmission electron tomography and fluorescence lifetime imaging, among others. Another trend is for resolution beyond the diffraction limit using so-called super-resolution confocal microscopes which use various physical methods (STED, 4Pi, PALM) to constrain the point spread function, achieving sub-100 nm resolution with a light microscope. This is a rapidly developing but highly specialised field.

4.9 Acknowledgements

The following people provided some of the samples or images used in this chapter: Armin Thumm, Dianne Brookes, and Dr Paul Kibblewhite (Scion). The author is grateful to Dr Tim Strabala, Armin Thumm, and Dr Alan Dickson (Scion) for their helpful comments on the manuscript.

4.10 References

- Abe H and Funada R (2005), 'Review – The orientation of cellulose microfibrils in the cell walls of tracheids in conifers', *IAWA J*, 26, 161–174.
- Alarousu E, Krehut L, Prykäri T and Myllylä R (2005), 'Study on the use of optical coherence tomography in measurements of paper properties', *Meas Sci Technol*, 16, 1131–1137.
- Aronsson M (2002), 'Slice-based digital volume assembly of a small paper sample', *Nordic Pulp Paper Res J*, 17, 29–33.
- Baas P (1975), 'Interference microscopic studies on wood plastic and cell wall–liquid interactions in beech', *J Microscopy*, 104, 83–90.
- Baley C, Busnel F, Grohens Y and Sire O (2006), 'Influence of chemical treatments on surface properties and adhesion of flax fibre-polyester resin', *Composites Part A*, 37, 1626–1637. doi:10.1016/j.compositesa.2005.10.014
- Barakat N and Hamza AA (1990), *Interferometry of Fibrous Materials*, CRC Press, Boca Raton, FL.
- Bard D, Yarwood J and Tylee B (1997), 'Asbestos identification by Raman microspectroscopy', *J Raman Spectroscopy*, 28, 803–809.
- Bard D, Tylee B, Williams K and Yarwood J (2004), 'Use of a fibre optic probe for the identification of asbestos fibres in bulk materials by Raman spectroscopy', *J Raman Spectroscopy*, 35, 541–548. doi:10.1002/jrs.1167
- Bardage S, Donaldson L, Tokoh C and Daniel G (2004), 'Ultrastructure of the cell wall of unbeaten Norway spruce pulp fibre surfaces', *Nordic Pulp Paper Res J*, 19, 448–452.
- Batchelor WJ, Conn AB and Parker IH (1997), 'Measuring the fibril angle of fibres using confocal microscopy', *Appita J*, 50, 377–380.

- Béland M-C and Mangin PJ (1995), 'Three-dimensional evaluation of paper surfaces using confocal microscopy', in Conners TE and Banerjee S, *Surface Analysis of Paper*, CRC Press, Boca Raton, FL, 1–40.
- Beltran R, Hurren CJ, Kaynak A and Wang X (2002), 'Correlating the fineness and residual gum content of degummed hemp fibres', *Fibres and Polymers*, 3, 129–133.
- Bergander A, Brändström J, Daniel G and Salmén L (2002), 'Fibril angle variability in earlywood of Norway spruce using soft rot cavities and polarisation confocal microscopy', *J Wood Sci*, 48, 255–263. doi:10.1007/BF00831344
- Billosta VC, Joseleau J-P, Cochaux A and Ruel K (2007), 'Tying together the ultrastructural modifications of wood fibre induced by pulping processes with the mechanical properties of paper', *Cellulose*, 14, 141–152.
- Blanchette RA, Akhtar M and Attridge M C (1992), 'Using Simons stain to evaluate fibre characteristics of biomechanical pulps', *Tappi J*, 75, 121–124.
- Bland DE, Foster RC and Logan AF (1971), 'The mechanism of permanganate and osmium tetroxide fixation and distribution of lignin in the cell wall of *Pinus radiata*', *Holzforschung*, 25, 137–143.
- Bogoeva-Gaceva G, Mäder E, Häussler L and Dekanski A (1997), 'Characterisation of the surface and interphase of plasma-treated HM carbon fibres', *Composites Part A*, 28A, 445–452.
- Börås L and Gatenholm P (1999), 'Surface composition and morphology of CTMP fibres', *Holzforschung*, 53, 188–194. doi:10.1515/HF.1999.031
- Bos HL and Donald AM (1999), 'In situ ESEM study of the deformation of elementary flax fibres', *J Mater Sci*, 34, 3029–3034. doi:10.1023/A:1004650126890
- Boutelje JB (1972), 'Calculation of lignin concentration and porosity of cell wall regions by interference microscopy', *Svensk Papperstidning*, 75, 683–686.
- Brändström J, Joseleau J-P, Cochaux A, Giraud-Telme N and Ruel K (2005), 'Ultrastructure of commercial recycled pulp fibres for the production of packaging paper', *Holzforschung*, 59, 675–680. doi:10.1515/HF.2005.108
- Brinen JS and Proverb RJ (1991), 'SIMS imaging of paper surfaces. Part 2. Distribution of organic surfactants', *Nordic Pulp Paper Res J*, 4, 177–183.
- Brundrett MC, Enstone DE and Peterson CA (1988), 'A berberine–aniline blue fluorescent staining procedure for suberine, lignin and callose in plant tissue', *Protoplasma*, 146, 133–142.
- Burgert I, Gierlinger N and Zimmermann T (2005), 'Properties of chemically and mechanically isolated fibres of spruce (*Picea abies* [L.] Karst.). Part 1: Structural and chemical characterization', *Holzforschung*, 59, 240–246. doi:10.1515/HF.2005.038
- Caldwell JP, Mastrorarde DN, Woods JL and Bryson WG (2005), 'The three-dimensional arrangement of intermediate filaments in Romney wool cortical cells', *J Struct Biol*, 151, 298–305. doi:10.1016/j.jsb.2005.07.002
- Cantrell S, Roux C, Maynard P and Robertson J (2001), 'A textile fibre survey as an aid to the interpretation of fibre evidence in the Sydney region', *Forensic Sci Int*, 123, 48–53. doi:10.1016/S0379-0738(01)00520-5
- Carstensen JM and Schultz N (1993), 'Analyzing confocal laser scanning micrographs of pulp fibres', *2nd European Research Symposium on Image Analysis for Pulp and Paper Research and Production*, Darmstadt, Germany, 2–3 September, 63–67.
- Causin V, Schiavone S, Marigo A and Carresi P (2004), 'Bayesian framework for the evaluation of fibre evidence in a double murder – a case report', *Forensic Sci Int*, 141, 159–170. doi:10.1016/j.forsciint.2004.01.009
- Causin V, Marega C, Guzzini G and Marigo A (2005a), 'The effect of exposure to the

- elements to the forensic characterisation by infrared spectroscopy of polyethylene terephthalate fibres', *J Forensic Sci*, 50, 1–7.
- Causin V, Marega C, Schiavone S and Marigo A (2005b), 'A quantitative differentiation method for acrylic fibres by infrared spectroscopy', *Forensic Sci Int*, 151, 125–131. doi:10.1016/j.forsciint.2005.02.004
- Chan BK, Jang HF and Seth RS (1998), 'Measurement of fibre wall thickness by confocal microscopy and image analysis', *Appita J*, 51, 229.
- Chanzy H, Imada K and Vuong R (1978), 'Electron diffraction from the primary wall of cotton fibres', *Protoplasma*, 94, 299–306.
- Chhabra N, Spelt JK, Yip CM and Kortschot MT (2005), 'An investigation of pulp fibre surfaces by atomic force microscopy', *J Pulp Paper Sci*, 31, 52–56.
- Chinga G, Johnsen PO and Diserud O (2004), 'Controlled serial grinding for high-resolution three-dimensional reconstruction', *J Microscopy*, 214, 13–21. doi:10.1111/j.0022-2720.2004.01288.x
- Clifford MN (1974), 'Specificity of acidic phloroglucinol reagents', *J Chromatography*, 94, 321–324.
- Cortez J, Bonner PLR and Griffin M (2004), 'Application of transglutaminases in the modification of wool textiles', *Enz Microbial Technol*, 34, 64–72.
- Cortez J, Anghieri A, Bonner PLR, Griffin M and Freddi G (2007), 'Transglutaminase mediated grafting of silk proteins onto wool fabrics leading to improved physical and mechanical properties', *Enz Microbial Technol*, 40, 1698–1704.
- Côté WA (1965), *Cellular Ultrastructure of Woody Plants*, Syracuse University Press, Syracuse, NY.
- Côté WA (1980), *Papermaking Fibres – A Photomicrographic Atlas*, Syracuse University Press, Syracuse, NY.
- Cousin WJ (1972), 'Measurement of mean microfibril angles of wood tracheids', *Wood Sci Technol*, 6, 58.
- Cox G (2006), *Optical Imaging Techniques in Cell Biology*, CRC Press/Taylor & Francis, Boca Raton, FL.
- Cruthers N, Carr D, Niven B, Girvan E and Laing R (2005), 'Methods for characterizing plant fibres', *Microscopy Res Tech*, 67, 260–264. doi:10.1002/jemt.20206
- Cyr P-L, Riedl B and Wang X-M (2007), 'Investigation of urea-melamine-formaldehyde (UMF) resin penetration in medium-density fibreboard (MDF) by high resolution confocal laser scanning microscopy', *Holz Roh Werkstoff*, 66, 129–134. doi 10.1007/s00107-007-0216-2.
- De Clerck K, Van Oostveldt P, Rahier H, Van Mele B, Westbroek P and Kiekens P (2004), 'Dye diffusion studies in PET fibres by confocal laser scanning microscopy and the interrelation with the glass transition', *Polymer*, 45, 4105–4112. doi:10.1016/j.polymer.2004.03.103
- De Clerck K, Van Oostveldt P, Rahier H, Van Mele B, Westbroek P and Kiekens P (2005), 'Variations in diffusion coefficient of disperse dyes in single PET fibres: monitored and interpreted by confocal laser scanning microscopy', *Polymer*, 46, 101–108. doi:10.1016/j.polymer.2004.10.074
- Demir H, Atikler U, Balköse D and Tihminlioğlu F (2006), 'The effect of fibre surface treatments on the tensile and water sorption properties of polypropylene–luffa fibre composites', *Composites Part A*, 37, 447–456. doi:10.1016/j.compositesa.2005.05.036
- Desplentere F, Lomov SV, Woerdeman DL, Verpoest I, Wevers M and Bogdanovich A (2005), 'Micro-CT characterisation of variability in 3D textile architecture',

- Composites Sci Technol*, 65, 1920–1930. doi:10.1016/j.compscitech.2005.04.008
- Dickson AR (1999), 'Quantitative analysis of paper cross-sections', *53rd Appita Annual Conference*, Rotorua, New Zealand, 2, 735–739.
- Dickson AR (2000), 'The quantitative microscopic analysis of paper cross-sections: sample preparation effects', *Appita J*, 53, 362–366.
- Donald AM (2003), 'The use of environmental scanning electron microscopy for imaging wet and insulating materials', *Nature Materials*, 2, 511–516. doi:10.1038/nmat898
- Donaldson LA (1985), 'Critical assessment of interference microscopy as a technique for measuring lignin distribution in cell walls', *NZ J For Sci*, 15, 349–60.
- Donaldson LA (1991), 'The use of pit apertures as windows to measure microfibril angle in chemical pulp fibres', *Wood Fibre Sci*, 23, 290–295.
- Donaldson LA (1992), 'Interference microscopy', in Lin SY and Dence CW, *Methods in Lignin Chemistry*, Springer Verlag, Berlin, 122–132.
- Donaldson LA (2006), 'Determining xylem cell wall properties using model plant species', in Stokke D and Groom LH, *Characterisation of the Cellulosic Cell Wall*, Blackwell Publishing, Ames, IA, 67–86.
- Donaldson LA and Bond J (2005), *Fluorescence Microscopy of Wood*, Scion, Rotorua, New Zealand (CD-ROM).
- Donaldson LA and Frankland A (2004), 'Ultrastructure of iodine treated wood', *Holzforschung*, 58, 219–225. doi:10.1515/HF.2004.034
- Donaldson LA, Hague JRB and Snell R (2001), 'Lignin distribution in coppice poplar, linseed and wheat straw', *Holzforschung*, 55, 379–385. doi:10.1515/HF.2001.063
- Duchesne I and Daniel G (1999), 'The ultrastructure of wood fibre surfaces as shown by a variety of microscopical methods', *Nordic Pulp Paper Res J*, 14, 129–139.
- Duchesne I, Takabe K and Daniel G (2003), 'Ultrastructural localization of glucomannan in Kraft fibres', *Holzforschung*, 57, 62–68. doi:10.1515/HF.2003.010
- Eberhardt CN and Clarke AR (2002), 'Automated reconstruction of curvilinear fibres from 3D datasets acquired by X-ray microtomography', *J Microscopy*, 206, 41–53. doi:10.1046/j.1365-2818.2002.01009.x
- Edgar CD and Gray DG (2003), 'Smooth model cellulose I surfaces from nanocrystal suspensions', *Cellulose*, 10, 299–306. doi:10.1023/A:1027333928715
- El-Bakary MA (2007), 'The effect of mechanical drawing on optical and structural properties of nylon 6 fibres', *Optics and Laser Technol*, 39, 1273–1280. doi:10.1016/j.optlastec.2006.07.014
- Fabritius T, Alarousu E, Prykäri T, Hast J and Myllylä R (2006), 'Characterisation of optically cleared paper by optical coherence tomography', *J Quant Electron*, 36, 181–187.
- Faessel M, Delisée C, Bos F and Castéra P (2005), '3D modeling of random cellulosic fibrous networks based on X-ray tomography and image analysis', *Composites Sci Technol*, 65, 1931–1940. doi:10.1016/j.compscitech.2004.12.038
- Fahlén J and Salmén L (2002), 'On the lamellar structure of the tracheid cell wall', *Plant Biology*, 4, 339–345. doi:10.1055/s-2002-32341
- Fahlén J and Salmén L (2003), 'Cross-sectional structure of the secondary cell wall of wood fibres as affected by processing', *J Mater Sci*, 38, 119–126.
- Fahlén J and Salmén L (2005), 'Ultrastructural changes in a holocellulose pulp revealed by enzymes, thermoporosimetry and atomic force microscopy', *Holzforschung*, 59, 589–597. doi:10.1515/HF.2005.096
- Favier V, Chanzy H and Cavaille JY (1995), 'Polymer nanocomposites reinforced by cellulose whiskers', *Macromolecules*, 28, 6365–6367.

- Ferraro JR and Nakamoto K (2003), *Introductory Raman Spectroscopy*, 2nd edn, Academic Press, San Diego, CA.
- Filonova L, Gunnarsson LC, Daniel G and Ohlin M (2007a), 'Synthetic xylan-binding modules for mapping of pulp fibres and wood sections', *BMC Plant Biology*, 7, 54. doi:10.1186/1471-2229-7-54.
- Filonova L, Kallas AM, Greffe L, Johansson G, Teeri TT and Daniel G (2007b), 'Analysis of the surfaces of wood tissues and pulp fibres using carbohydrate-binding modules specific for crystalline cellulose and mannan', *Biomacromolecules*, 8, 91–97.
- Fleming OS, Kazarian SG, Bach E and Schollmeyer E (2005), 'Confocal Raman study of polyethylene terephthalate fibres dyed in supercritical carbon dioxide: dye diffusion and polymer morphology', *Polymer*, 46, 2943–2949.
- Forster B, Van de Ville D, Berent J, Sage D and Unser M (2004), 'Complex wavelets for extended depth-of-field: a new method for the fusion of multichannel microscopy images', *Microscopy Res Tech*, 65, 33–42. doi:10.1002/jemt.20092
- Foster A, Hofer W (2006), *Scanning Probe Microscopy – Atomic Scale Engineering by Forces and Currents*, Springer, New York.
- Fouda IM, El-Tonsy MM, Metawe FM, Hosny HM and Easawi KH (1997), 'Optothermal properties of fibres. VII. Optical investigation of annealed nylon-6 fibres', *J Appl Polym Sci*, 65, 1293–1306.
- Fukazawa K and Imagawa H (1981), 'Quantitative analysis of lignin using an UV microscopic image analyzer. Variation within one growth increment', *Wood Sci Technol*, 15, 45–55.
- Furuta T and Gray DG (1998), 'Direct force–distance measurements on wood-pulp fibres in aqueous media', *J Pulp Paper Sci*, 24, 320–324.
- Gañán P and Mondragon I (2002), 'Surface modification of fique fibres. Effects on their physico-mechanical properties', *Polym Comp*, 23, 383–394.
- Gañán P, Zuluaga R, Cruz J, Vélez JM, Retegi A and Mondragon I (2008), 'Elucidation of the fibrous structure of *Musaceae* matured rachis', *Cellulose*, 15, 131–139. doi:10.1007/s10570-007-9150-z
- Gierlinger N and Schwanninger M (2006), 'Chemical imaging of poplar wood cell walls by confocal Raman microscopy', *Plant Physiol*, 140, 1246–1254. doi:10.1104/pp.105.066993.
- Gierlinger N and Schwanninger M (2007), 'The potential of Raman microscopy and Raman imaging in plant research', *Spectroscopy*, 21, 69–89.
- Gierlinger N, Hansmann C, Roder T, Sixta H, Gindl W and Wimmer R (2005), 'Comparison of UV and confocal Raman microscopy to measure the melamine-formaldehyde resin content within cell walls of impregnated spruce wood', *Holzforschung*, 59, 210–213. doi:10.1515/HF.2005.033
- Gindl W and Gupta HS (2002), 'Cell-wall hardness and Young's modulus of melamine-modified spruce wood by nano-indentation', *Composites Part A*, 33, 1141–1145.
- Gindl W, Gupta HS, Schöberl T, Lichtenegger HC and Fratzl P (2004), 'Mechanical properties of spruce wood cell walls by nanoindentation', *Appl Phys A*, 79, 2069–2073. doi:10.1007/s00339-004-2864-y
- Goldstein J, Newbury DE, Joy DC, Lyman CE, Echlin P, Lifshin E, Sawyer LC and Michael JR (2003), *Scanning Electron Microscopy and X-ray Microanalysis*, Springer, New York.
- Goussé C, Chanzy H, Excoffier G, Soubeyrand L and Fleury E (2002), 'Stable suspensions of partially silylated cellulose whiskers dispersed in organic solvents', *Polymer*, 43, 2645–2651. doi:10.1016/S0032-3861(02)00051-4

- Gradwell SE, Renneckar S, Esker AR, Heinze T, Gatenholm P, Vaca-Garcia C and Glasser W (2004), 'Surface modification of cellulose fibres: towards wood composites by biomimetics', *CR Biologies*, 327, 945–953. doi:10.1016/j.crv.2004.07.015
- Grigsby WJ and Thumm A (2002), 'Qualitative analysis of the relationship between wax and resin on MDF fibre', *Proceedings of the Sixth European Panel Products Symposium*, Llandudno, Wales, 9–11 October.
- Grigsby WJ, Thumm A and Gaugler M (2004), 'Visualisation of interfacial behaviors of natural fibre–plastic composites', *Proceedings of the Eighth European Panel Products Symposium*, Llandudno, Wales, 13–15 October.
- Groom L, Mott L and Shaler S (2002), 'Mechanical properties of individual southern pine fibres. Part I. Determination and variability of stress–strain curves with respect to tree height and juvenility', *Wood Fibre Sci*, 34, 14–27.
- Guan Y, Xiao H, Sullivan H and Zheng A (2007), 'Antimicrobial-modified sulfite pulps prepared by in-situ copolymerization', *Carbohydrate Polymers*, 69, 688–696. doi:10.1016/j.carbpol.2007.02.013
- Gustafsson J, Lehto JH, Tienvieri T, Ciofica L and Peltonen J (2003), 'Surface characteristics of thermomechanical pulps: the influence of defibration temperature and refining', *Colloids and Surfaces A: Physicochem Eng Aspects*, 225, 95–104.
- Hamza AA, Sokkar TZN, El-Bakary MA and Ali AM (2002), 'Interferometric determination of regular and/or irregular transverse sectional shape of homogeneous fibres', *Meas Sci Technol*, 13, 1931–1936. doi:10.1088/0957-0233/13/12/317
- Hanley SJ and Gray DG (1994), 'Atomic force microscope images of black spruce wood sections and pulp fibres', *Holzforschung*, 48, 29–34.
- Hanley SJ and Gray DG (1999), 'AFM images in air and water of Kraft pulp fibres', *J Pulp Paper Sci*, 25, 196–200.
- Hansson MT and Rasmuson A (2004), 'Characterization of freeze-dried pulp fibre suspensions using X-ray computed tomography and image analysis', *J Pulp Paper Sci*, 30, 177–182.
- Haseloff J (2003), 'Old botanical techniques for new microscopes', *BioTechniques*, 34, 1174–1182.
- He J, Batchelor WJ and Johnston RE (2004), 'A microscopic study of fibre–fibre contacts in paper', *Appita J*, 57, 292–298.
- Hearle JWS and Lomas B (1998), *Atlas of Fibre Fracture and Damage to Textiles*, CRC Press, Boca Raton, FL.
- Heath JP (2005), *Dictionary of Microscopy*, Wiley, Chichester.
- Henriksson M, Henriksson G, Berglund LA and Lindstrom T (2007), 'An environmentally friendly method for enzyme-assisted preparation of microfibrillated cellulose (MFC) nanofibres', *Eur Polym J*, 43, 3434–3441.
- Herr JM (1992), 'New uses for calcium chloride solution as mounting medium', *Biotechnic Histochem*, 67, 9–13.
- Hibbs AR (2004), *Confocal Microscopy for Biologists*, Kluwer Academic/Plenum Publishers, New York.
- Howard RC (1987), 'The wet structure of pulp and paper examined by Cryo-SEM', *Paper Technology and Industry*, March, 425–427.
- Jang HF (1998), 'Measurement of fibril angle in wood fibres with polarisation confocal microscopy', *J Pulp Paper Sci*, 24, 224–230.
- Jang HF (2005), 'Determining the transverse dimensions of fibres in wood using confocal microscopy', *Wood Fibre Sci*, 37, 615–628.

- Jang HF and Seth RS (1998), 'Using confocal microscopy to characterize the collapse behavior of fibres', *Tappi J*, 81, 167–174.
- Jang HF, Robertson AG and Seth RS (1991), 'Optical sectioning of pulp fibres using confocal scanning laser microscopy', *Tappi J*, 74, 217–219.
- Jang HF, Robertson AG and Seth RS (1992), 'Transverse dimensions of wood pulp fibres by confocal scanning laser microscopy and image analysis', *J Mater Sci*, 27, 6391–6400.
- Jang HF, Amiri R, Seth RS and Karnis A (1995a), 'Fibre characterization using confocal microscopy – Collapse behavior of mechanical pulp fibres', *Tappi J*, 79, 203–221.
- Jang HF, Howard RC and Seth RS (1995b), 'Fibre characterization using confocal microscopy – Effects of recycling', *Tappi J*, 78, 131–137.
- Johansen DA (1940), *Plant Microtechnique*, McGraw-Hill, New York.
- Kang T, Paulapuro H and Hiltunen E (2004), 'Fracture mechanism in interfibre bond failure: microscopic observations', *Appita J*, 57, 199–203.
- Kangas H and Kleen M (2004), 'Surface chemical and morphological properties of mechanical pulp fines', *Nordic Pulp Paper Res J*, 19, 191–199.
- Kastner J, Schlotthauer E, Burgholzer P and Stifter D (2004), 'Comparison of X-ray computed tomography and optical coherence tomography for characterization of glass-fibre polymer matrix composites', *16th World Conference on Non-destructive Testing*, 30 August to 3 September, 2004, Montreal, Canada.
- Kelch A, Wessel S, Will T, Hintze U, Wepf R and Wiesendanger R (2000), 'Penetration pathways of fluorescent dyes in human hair fibres investigated by scanning near-field optical microscopy', *J Microscopy*, 200, 179–186. doi:10.1046/j.1365-2818.2000.00756.x
- Kifetew G and Sandberg D (2000), 'Material damage due to electron beam during testing in the environmental scanning electron microscope (ESEM)', *Wood Fibre Sci*, 32, 44–51.
- Knebel W and Schnepf E (1991), 'Confocal laser scanning microscopy of fluorescently stained wood cells: a new method for three-dimensional imaging of xylem elements', *Trees*, 5, 1–4.
- Koch G and Kleist G (2001), 'Application of scanning UV microspectrophotometry to localize lignins and phenolic extractives in plant cell walls', *Holzforschung*, 55, 563–567. doi:10.1515/HF.2001.091
- Koljonen K, Österberg M, Kleen M, Fuhrmann A and Stenius P (2004), 'Precipitation of lignin and extractives on kraft pulp: effect on surface chemistry, surface morphology and paper strength', *Cellulose*, 11, 209–224. doi:10.1023/B:CELL.0000025424.90845.c3
- Kukkola E, Saranpää P and Fagerstedt K (2008), 'Juvenile and compression wood cell wall layers differ in lignin structure in Norway spruce and Scots pine', *IAWA J*, 29, 47–54.
- Kumar S, Doshi H, Srinivasarao M, Park JO and Schiraldi DA (2002), 'Fibres from polypropylene/nano carbon fibre composites', *Polymer*, 43, 1701–1703. doi:10.1016/S0032-3861(01)00744-3
- Kutscha NP and McOrmond RR (1972), 'The suitability of using fluorescence microscopy for studying lignification in balsam fir', *Univ Maine Tech Bull*, 62, 1–15.
- Kvien I, Tanem BS and Oksman K (2005), 'Characterisation of cellulose whiskers and their nanocomposites by atomic force and electron microscopy', *Biomacromolecules*, 6, 3160–3165.
- Langer AM, Mackler AD and Pooley FD (1974), 'Electron microscopical investigation of asbestos fibres', *Environmental Health Perspectives*, 9, 63–80.

- Leney L (1981), 'A technique for measuring fibril angle using polarised light', *Wood Fibre*, 13, 13–16.
- Lewis IR and Edwards HGM (2001), *Handbook of Raman Spectroscopy*, CRC Press, Boca Raton, FL.
- Li K and Reeve DW (2004), 'Fluorescent labeling of lignin in the wood pulp fibre wall', *J Wood Chem Technol*, 24, 169–181.
- Liu Y, Gustafson R, Callis J and McKean B (1997), 'Fluorescence microphotometry in determining the lignin content of single pulp fibres', *9th International Symposium on Wood and Pulping Chemistry*, 9–12 June, Montreal, Canada.
- Liu Y, Gustafson R, Callis J and McKean B (1999), 'Microspectroscopic analysis and kappa determination of single pulp fibres stained with acridine orange', *J Pulp Paper Res*, 25, 351–355.
- Liukkonen A (1997), 'Contact angle of water on paper components: sessile drops versus environmental scanning electron microscope measurements', *Scanning*, 19, 411–415.
- Loxton C, Thumm A, Grigsby WJ, Adams TA and Ede RM (2003), 'Resin distribution in medium density fibre board. Quantification of UF resin distribution on blowline and dry-blended MDF fibre and panels', *Wood Fibre Sci*, 35, 370–380.
- Mäder E, Rothe C and Gao S-L (2007), 'Commingled yarns of surface nanostructured glass and polypropylene filaments for effective composite properties', *J Mater Sci*, 42, 8062–8070. doi:10.1007/s10853-006-1481-x
- Malami C and Grasserbauer M (1982), 'Identification of respirable asbestos fibres by quantitative X-ray microanalysis with a scanning transmission electron microscope (STEM)', *Fresenius J Anal Chem*, 311, 1–6.
- Maximova N, Osterberg M, Koljonen K and Stenius P (2001), 'Lignin adsorption on cellulose fibre surfaces: effect on surface chemistry, surface morphology and paper strength', *Cellulose*, 8, 113–125. doi:10.1023/A:1016721822763.
- Maxwell JM and Huson MG (2005), 'Scanning probe microscopy examination of the surface properties of keratin fibres', *Micron*, 36, 127–136. doi:10.1016/j.micron.2004.10.001
- Maxwell JM, Gordon SG and Huson MG (2003), 'Internal structure of mature and immature cotton fibres revealed by scanning probe microscopy', *Textile Res J*, 73, 1005–1012.
- McDonald AG, Donaldson LA, Singh AP, Alexander J and Murton KD (1997), 'Characterisation of radiata pine HTMP fibres by electron, UV, and confocal laser scanning microscopy', *Proceedings of the First European Panel Products Symposium*, Llandudno, Wales, 9–10 October.
- Meyer E, Hug HJ and Bennewitz R (2004), *Scanning Probe Microscopy*, Springer, Berlin, Heidelberg, New York.
- Mondolot, L, Roussel J-L and Andary C (2001), 'New applications for an old lignified element staining reagent', *Histochemical J*, 33, 379–385. doi:10.1023/A:1013798426161
- Morán JI, Alvarez VA, Cyras VP and Vázquez A (2008), 'Extraction of cellulose and preparation of nanocellulose from sisal fibres', *Cellulose*, 15, 149–159. doi:10.1007/s10570-007-9145-9
- Morgan SL, Nieuwland AA, Mubarak CR, Hendrix JE, Enlow EM and Vasser BJ (2004), 'Forensic discrimination of dyed textile fibres using UV-VIS and fluorescence microspectrophotometry', *Proceedings of the European Fibres Group, Prague*, 25 May, 1–11.
- Mori B and Bellani LM (1996), 'Differential staining for cellulosic and modified plant cell walls', *Biotechnic Histochem*, 71, 71–72.

- Moss P, Retulainen E, Paulapuro H and Aaltonen P (1993), 'Taking a new look at pulp and paper: applications of confocal laser scanning microscopy (CLSM) to pulp and paper research', *Paperi ja Puu*, 75, 74–79.
- Moss PA, Howard RC and Sheffield E (1989a), 'Artefacts arising during preparation of hydrated paper pulp samples for low-temperature SEM', *J Microscopy*, 156, 343–351.
- Moss PA, Kropholler HW and Sheffield E (1989b), 'LTSEM – great potential for pulp evaluation', *Paper Technology*, 30, 12–14.
- Mott L, Shaler SM, Groom LH and Liang BH (1995), 'The tensile testing of individual wood fibres using environmental scanning electron microscopy and video image analysis', *Tappi J*, 78, 143–148.
- Mott L, Shaler SM and Groom LH (1996), 'A technique to measure strain distributions in single wood pulp fibres', *Wood Fibre Sci*, 28, 429–437.
- Mott L, Groom LH and Shaler S (2002), 'Mechanical properties of individual southern pine fibres. Part II. Comparison of earlywood and latewood fibres with respect to tree height and juvenility', *Wood Fibre Sci*, 34, 221–237.
- Müller M, Riekel C, Vuong R and Chanzy H (2000), 'Skin/core micro-structure in viscose rayon fibres analysed by X-ray microbeam and electron diffraction mapping', *Polymer*, 41, 2627–2632. doi:10.1016/S0032-3861(99)00433-4
- Müller M, Hori R, Itoh T and Sugiyama J (2002), 'X-ray microbeam and electron diffraction experiments on developing xylem cell walls', *Biomacromolecules*, 3, 182–186. doi:10.1021/bm015605h
- Mwaikambo LY and Ansell MP (2002), 'Chemical modification of hemp, sisal, jute and kapok fibres by alkalization', *J Appl Polym Sci*, 84, 2222–2234. doi:10.1002/app.10460
- Nakano J and Meshitsuka G (1992), 'The detection of lignin', in Lin SY and Dence CW, *Methods in Lignin Chemistry*, Springer-Verlag, New York, 23–61.
- Nanko H and Ohsawa J (1990), 'Scanning laser microscopy of the drying process of wet webs', *J Pulp Paper Sci*, 16, J6–J12.
- Naumann A and Polle A (2006), 'FTIR imaging as a new tool for cell wall analysis of wood', *NZ J For Sci*, 36, 54–59.
- Nelson WG and Woods JL (1996), 'An effective method for mounting fibres to allow simple processing, embedding and alignment for sectioning', *J Microscopy*, 181, 88–90.
- Newman RH, Clauss EC, Carpenter JEP and Thumm A (2007), 'Epoxy composites reinforced with deacetylated *Phormium tenax* leaf fibres', *Composites Part A: Applied Science and Manufacturing*, 38, 2164–2170. doi:10.1016/j.compositesa.2007.06.007
- Nyholm K, Ander A, Bardage S and Daniel G (2001), 'Dislocations in pulp fibres – their origin, characteristics and importance – a review', *Nordic Pulp Paper Res J*, 16, 376–384.
- Oksman K, Mathew AP, Bondeson D and Kvien I (2006), 'Manufacturing process of cellulose whiskers/poly(lactic acid) nanocomposites', *Composites Sci Technol*, 66, 2776–2784. doi:10.1016/j.compscitech.2006.03.002
- Olmstead JA and Gray DG (1997), 'Fluorescence spectroscopy of cellulose, lignin and mechanical pulps: a review', *J Pulp Paper Sci*, 23, 571–581.
- Orso S, Wegst UGK and Arzt E (2006), 'The elastic modulus of spruce wood cell wall material measured by an in situ bending technique', *J Mater Sci*, 41, 5122–5126. doi:10.1007/s10853-006-0072-1
- Oudet C, Bunsell AR, Hagege R and Sotton M (1984), 'Structural changes in polyester fibres during fatigue', *J Appl Polym Sci*, 29, 4363–4376.

- Page DH and El-Hosseiny F (1974), 'The birefringence of wood pulp fibres and the thickness of S1 and S3 layers', *Wood Fibre*, 6, 186–192.
- Pakdel H, Cyr P-L and Riedl B (2007), 'Quantification of urea formaldehyde resin in wood fibres using X-ray photoelectron spectroscopy and confocal laser scanning microscopy', *Wood Sci Technol*, 42, 133–148. doi:10.1007/s00226-007-0155-4.
- Pandita SD and Verpoest I (2003), 'Prediction of the tensile stiffness of weft knitted fabric composites based on X-ray tomography images', *Composites Sci Technol*, 63, 311–325.
- Pandita SD, Falconet D and Verpoest I (2002), 'Impact properties of weft knitted fabric reinforced composites', *Composites Sci Technol*, 62, 1113–1123.
- Parbhu AN, Bryson WG and Lal R (1999), 'Disulfide bonds in the outer layer of keratin fibres confer higher mechanical rigidity: correlative nano-indentation and elasticity measurement with an AFM', *Biochemistry*, 38, 11755–11761.
- Park W-I, Kang M, Kim H-S and Jin H-J (2007), 'Electrospinning of poly(ethylene oxide) with bacterial cellulose whiskers', *Macromol Symp*, 249–250, 289–294. doi:10.1002/masy.200750347
- Parnas RS, Wevers M and Verpoest I (2003), 'Using textile topography to analyze X-ray CT data of composite microstructure', *Polymer Composites*, 24, 212–220.
- Peiponen K-E, Alarousu E, Juuti M, Silvennoinen R, Oksman A, Myllylä R and Prykäri T (2006), 'Diffractive optical element based glossmeter and interferometer in assessment of local surface quality of paper', *Optical Engineering*, 45, 043601 doi:10.1117/1.2188963
- Periyasamy S, Gupta D and Gulrajani ML (2007), 'Modification of one side of mulberry silk fabric by monochromatic VUV excimer lamp', *Eur Polym J*, 43, 4573–4581. doi:10.1016/j.eurpolymj.2007.07.014
- Pietak A, Korte S, Tan E, Downard A and Staiger MP (2007), 'Atomic force microscopy characterization of the surface wet ability of natural fibres', *Appl Surface Sci*, 253, 3627–3635. doi:10.1016/j.apsusc.2006.07.082
- Poggi MA, Mancosky DG, Bottomley LA and Lucia LA (2005), 'Atomic force microscopic analysis of hydrogen peroxide bleached kraft northern black spruce fibres', *J Microscopy*, 220, 77–83. doi:10.1111/j.1365-2818.2005.01518.x
- Preston RD (1934), 'Organisation of the cell wall of the conifer tracheid', *Roy Soc Phil Trans B*, 224, 131–173.
- Rajinder SS (2001), 'The differences between never-dried and dried chemical pulps', *Tappi J*, 1, 1–23.
- Rinaudo C, Belluso E and Gastaldi D (2004), 'Assessment of the use of Raman spectroscopy for the determination of amphibole asbestos', *Mineralogical Magazine*, 68, 455–465. doi:10.1180/0026461046830197
- Robertson AG, Jang HF and Seth RS (1991), 'Three-dimensional visualization of confocal images of wood pulp fibres', *J Mat Sci Lett*, 11, 1416–1418.
- Robertson J and Roux C (2004), 'Forensic examination of fibres – a review: 2001–2004', *14th International Forensic Science Symposium, Lyon, France*, 19–22 October, 70–84.
- Röder T and Sixta H (2004), 'Confocal Raman spectroscopy – Applications on wood samples', *Lenzinger Berichte*, 83, 13–16.
- Röder T, Koch G and Sixta H (2004), 'Application of confocal Raman spectroscopy for the topochemical distribution of lignin and cellulose in plant cell walls of beech wood (*Fagus sylvatica* L.) compared to UV microspectrophotometry', *Holzforschung*, 58, 480–482. doi:10.1515/HF.2004.072
- Rolland du Roscoat S, Bloch J-F and Thibault X (2005), 'Characterisation of the 3D

- paper structure with X-ray synchrotron radiation microtomography', *13th Fundamental Research Symposium*, Cambridge, 11–16 September, 901–920.
- Rothbard DR (2002), 'Applied microscopy for the paper industry', *Microscopy and Microanalysis*, 8, 178–179. doi:10.1017.s1431927602101693
- Rous MA, Manian AP, Röder T, Lichtscheidl I and Schuster KC (2004), 'Fluorescent molecular probes for the characterization of fibre structure and distribution of textile resin finishing on lyocell', *Lenzinger Berichte*, 83, 92–98.
- Roux S, Feugeas F, Bach M, Fagon M, Bettinger C, Mourad S and Cornet A (2008), 'Determination of paper filler z -distribution by low-vacuum SEM and EDX', *J Microscopy*, 229, 44–59. doi:10.1111/j.1365-2818.2007.01864.x
- Ruel K and Joseleau J-P (1984), 'Use of enzyme-gold complexes for the ultrastructural localization of hemicelluloses in the plant cell wall', *Histochem*, 81, 573–580.
- Ruel K, Faix O and Joseleau J-P (1994), 'New immunogold probes for studying the distribution of the different lignin types during plant cell wall biogenesis', *J Trace Microprobe Tech*, 12, 247–265.
- Ruzin SE (1999), *Plant Microtechnique and Microscopy*, Oxford University Press, Oxford.
- Salmén L (2004), 'Micromechanical understanding of the cell-wall structure', *CR Biologies*, 327, 873–880. doi:10.1016/j.crvi.2004.03.010
- Samuelsen EJ, Gregersen OW, Houen PJ, Helle T, Raven C and Snigirev A (2001), 'Three-dimensional imaging of paper by use of synchrotron X-ray microtomography', *J Pulp Paper Sci*, 27, 50–53.
- Sasaki T, Okamoto T and Meshitsuka G (2006), 'Influence of deformability of kraft pulp fibre surface estimated by force curve measurements on atomic force microscope (AFM) contact mode imaging', *J Wood Sci*, 52, 377–382. doi:10.1007/s10086-005-0786-8
- Sawyer LC and Grubb DT (1996), *Polymer Microscopy*, Springer.
- Schell JSU, Renggli M, van Lenth GH, Muller R and Ermanni P (2006), 'Micro-computed tomography determination of glass fibre reinforced polymer meso-structure', *Composites Sci Technol*, 66, 2016–2022.
- Sedighi-Gilani M, Sunderland H and Navi P (2005), 'Microfibril angle non-uniformities within normal and compression Wood tracheids', *Wood Sci. Technol*, 39: 419–430. doi: 10.1007/s00226-005-0022-0.
- Scott RG (1962), 'A study of the crystalline structure of synthetic fibres by dark field electron microscopy', *J Polym Sci*, 57, 405–414.
- Seth RS, Jang HF, Chan BK and Wu CB (1997), 'Transverse dimensions of wood pulp fibres and their implications for end use', *Transactions of the 11th Fundamental Research Symposium*, Cambridge, 21–27 September, 1, 473–503.
- Shaler SM, Groom L and Mott L (1996), 'Microscopic analysis of wood fibres using ESEM and confocal microscopy', *Wood Fiber-Plastic Composites Proceedings 7291*, Forest Products Society, Madison, WI, 25–32.
- Signori V and Lewis DM (1996), 'FTIR analysis of cysteic and cysteine-s-thiosulphate on untreated and bleached human hair', *12th European Symposium on Polymer Spectroscopy*, Lyon, France, 8–10 July, 119, 235–240.
- Simons FL (1950), 'A stain for use in the microscopy of beaten fibres', *Tappi J*, 33, 312–314.
- Snell R, Groom LH and Rials TG (2001), 'Characterizing the surface roughness of thermomechanical pulp fibers with atomic force microscopy', *Holzforschung*, 55, 511–520. doi:10.1515/HF.2001.083
- Sokkar TZN and El-Bakary MA (2001), 'The refractive index profile of highly-oriented fibres', *J Phys D: Appl Phys*, 34, 373–378. doi:10.1088/0022-3727/34/3/321

- Song Y, Srinivasarao M, Tonelli A, Balik CM and McGregor R (2000), 'Laser scanning confocal microscopy study of dye diffusion in fibres', *Macromolecules*, 33, 4478–4485. doi:10.1021/ma991584w
- Speer EO (1987), 'A method of retaining phloroglucinol proof of lignin', *Stain Technol*, 62, 279–280.
- Stenstad P, Andresen M, Tanem BS and Stenius P (2008), 'Chemical surface modifications of microfibrillated cellulose', *Cellulose*, 15, 35–45. doi:10.1007/s10570-007-9143-y
- Stockert JC, Canete M and Colman OD (1984), 'Histochemical mechanism for the orthochromatic staining and fluorescence reaction of lignified tissues', *Cell Mol Biol*, 30(6), 503.
- Sugiyama J, Otsuka Y, Murase H and Harada H (1986), 'Toward direct imaging of cellulose microfibrils in wood', *Holzforschung*, 40, 31–36.
- Summerscales J (1998), *Microstructural Characterisation of Fibre-reinforced Composites*, Woodhead Publishing, Cambridge.
- Tan JC, Elliott JA and Clyne TW (2006), 'Analysis of tomography images of bonded fibre networks to measure distributions of fibre segment length and fibre orientation', *Adv Eng Mat*, 8, 495–500.
- Taylor JG, Haigler CH, Kilburn DG and Blanton RL (1996), 'Detection of cellulose with improved specificity using laser-based instruments', *Biotechnic Histochem*, 71, 215–223.
- Terziev N, Daniel G and Marklund A (2005), 'Dislocations in Norway spruce fibres and their effect on properties of pulp and paper', *Holzforschung*, 59, 163–169. doi:10.1515/HF.2005.025
- Thibault X and Bloch JF (2002), 'Structural analysis by X-ray microtomography of a strained nonwoven papermaker felt', *Textile Res J*, 72, 480–485.
- Thomson CI, Lowe RM and Ragaukas AJ (2007), 'Imaging cellulose fibre interfaces with fluorescence microscopy and resonance energy transfer', *Carbohydrate Polymers*, 69, 799–804.
- Thygesen LG and Ander P (2005), 'Quantification of dislocations in spruce pulp and hemp fibres using polarised light microscopy and image analysis', *Nordic Pulp Paper Res J*, 20, 64–71. doi:10.1016/j.indcrop.2006.03.009
- Thygesen LG, Bilde-Sorensen JB and Hoffmeyer P (2006), 'Visualisation of dislocations in hemp fibres: a comparison between scanning electron microscopy (SEM) and polarised light microscopy (PLM)', *Industrial Crops and Products*, 24, 181–185.
- Thygesen LG, Eder M and Burgert I (2007), 'Dislocation in single hemp fibres – investigations into the relationship of structural distortions and tensile properties at the cell wall level', *J Mater Sci*, 45, 558–564. doi:10.1007/s10853-006-1113-5
- Tomes C, Jones T, Carr CM and Jones D (2007), 'Three-dimensional imaging and analysis of the surface of hair fibres using scanning electron microscopy', *Int J Cosmetic Sci*, 29, 293–299.
- Trancik JE, Czernuszka JT, Merriman C and Viney C (2001), 'A simple method for orienting silk and other flexible fibres in transmission electron microscopy specimens', *J Microscopy*, 203, 235–238. doi:10.1046/j.1365-2818.2001.00947.x
- Turkulin H, Holzer L, Richter K and Sell J (2005a), 'Application of the ESEM technique in wood research: Part I. Optimisation of imaging parameters and working conditions', *Wood Fibre Sci*, 37, 552–564.
- Turkulin H, Holzer L, Richter K and Sell J (2005b), 'Application of the ESEM technique in wood research: Part II. Comparison of operational modes', *Wood Fibre Sci*, 37, 565–573.

- Van den Berg O, Schroeter M, Capadona JR and Weder C (2007), 'Nanocomposites based on cellulose whiskers and (semi)conducting conjugated polymers', *J Mater Chem*, 17, 2746–2753. doi:10.1039/b700878c
- Veblen DR (1980), 'Anthophyllite asbestos: microstructures, intergrown sheet silicates, and mechanisms of fibre formation', *American Mineralogist*, 65, 1075–1086.
- Verbelen JP and Stickens D (1995), 'In vivo determination of fibril orientation in plant cell walls with polarisation CSLM', *J Microscopy*, 177, 1–6.
- Wang B and Sain M (2007), 'Isolation of nanofibres from soybean source and their reinforcing capability on synthetic polymers', *Composites Sci Technol*, 67, 2521–2527. doi:10.1016/j.compscitech.2006.12.015
- Wei Q, Wang Y, Yang Q and Yu L (2007), 'Functionalisation of textile materials by plasma enhanced modification', *J Industrial Textiles*, 36, 301–309.
- Wei Q, Yu L, Hou D and Huang F (2008), 'Surface characterization and properties of functionalized nonwoven', *J Appl Polym Sci*, 107, 132–137. doi:10.1002/app.26940
- Weise UWH (1993), 'Image analysis applied to images gained by confocal laser scanning microscopy: fibre cross-sectional measurements', *2nd European Research Symposium on Image Analysis for Pulp and Paper Research and Production*, Darmstadt, Germany, 2–3 September, 51–62.
- Weise U and Paulapuro H (1995), 'Changes of pulp fibre dimensions during drying', *International Paper Physics Conference*, Niagara-on-the, Ontario, Canada, 11–14 September, 121–124.
- Westbye P, Svanberg C and Gatenholm P (2006), 'The effect of molecular composition of xylan extracted from birch on its assembly onto bleached softwood kraft pulp', *Holzforschung*, 60, 143–148. doi:10.1515/HF.2006.023
- Wiesauer K, Pircher M, Götzinger E, Hitzemberger CK, Oster R and Stifter D (2007), 'Investigation of glass-fibre reinforced polymers by polarisation-sensitive, ultra-high resolution optical coherence tomography: internal structures, defects and stress', *Composites Sci Technol*, 67, 3051–3058.
- Wiggins K (2001), 'Forensic textile fiber examination across the USA and Europe', *J Forensic Sci*, 46, 1–6.
- Williams GJ and Drummond JG (2000), 'Preparation of large sections for the microscopical study of paper structure', *J Pulp Paper Sci*, 26, 188–193.
- Wong KK, Tao XM, Yuen CWM and Yeung KW (2000), 'Topographical study of low temperature plasma treated flax fibres', *Textile Res J*, 70, 886–893.
- Wood JR and Goring DAI (1971), 'The distribution of lignin in stem and branch wood of Douglas fir', *Pulp Pap Mag Can*, 72, T95–T102.
- Xing C, Riedl B, Cloutier A and Shaler SM (2005), 'Characterisation of urea-formaldehyde resin penetration into medium density fibreboard fibres', *Wood Sci Technol*, 39, 374–384. doi:10.1007/s00226-005-0294-4
- Xu L and Parker I (1999), 'Correction of fluorescence attenuation with depth in fibre and paper images collected by confocal laser scanning microscopy', *Appita J*, 52, 41–44.
- Xu L, Filonenko Y, Li M and Parker I (1997a), 'Measurement of wall thickness of fully collapsed fibres by confocal microscopy and image analysis', *Appita J*, 50, 501–504.
- Xu L, Parker I and Osborne C (1997b), 'Technique for determining the fibre distribution in the z -direction using confocal microscopy and image analysis', *Appita J*, 50, 325–328.
- Xu P, Donaldson LA, Gergely ZR and Staehelin LA (2007), 'Dual-axis electron tomography:

- a new approach for investigating the spatial organization of wood cellulose microfibrils', *Wood Sci Technol*, 41, 101–116. doi:10.1007/s00226-006-0088-3
- Yan L, Li W, Yang J and Zhu Q (2004), 'Direct visualisation of straw cell walls by AFM', *Macromol Biosci*, 4, 112–118. doi:10.1002/mabi.200300032
- Yu X, Minor JL and Atalla RH (1995), 'Mechanism of action of Simons' stain', *Tappi J*, 78, 175–180.

Structure development in synthetic fiber production

T KIKUTANI, Tokyo Institute of Technology, Japan

Abstract: This chapter discusses the fundamental mechanism of fiber structure development in melt spinning and drawing processes. The chapter first reviews the general concept of fiber structure and the mechanism of its formation in the processes of synthetic fiber production. The chapter then focuses on the development of molecular orientation and crystallization, and explains the mechanisms of their development categorizing crystalline polymers into two groups depending on their glass transition temperatures. The chapter also describes the history and recent advancement in the macroscopic and microscopic analyses of fiber formation behavior through modeling and on-line measurements.

Key words: molecular orientation, non-isothermal crystallization, fiber structure, on-line measurement of fiber production processes, modeling of process dynamics and structure development for fiber production processes.

5.1 Introduction

High-strength poly(ethylene terephthalate) (PET) fibers for tire-cords have a tensile strength of around 1.0 GPa (0.72 N/tex) and elongation at break of around 10%, while undrawn PET fibers prepared at a spinning speed of 500 m/min have those values of around 100–200 MPa and 300–500%, respectively. Such significant differences in mechanical properties of fibers of the same material are due to the difference in higher-order structure, i.e. the spatial arrangement of molecular chains in the fiber. Even comparing the fibers of final products, ordinary polyethylene (PE) fibers have a strength of around 200–300 MPa while high-strength PE fibers produced through the gel spinning and super-drawing processes of ultra-high-molecular weight polymer reach 3 GPa. These facts demonstrate the importance of the control of structure development in the production of fibers.

Fiber structure is usually characterized by high molecular orientation and high crystallinity with uniaxial structural symmetry with respect to the fiber axis. For the control of the structure development in fiber processing, mechanism of fiber structure development in both the melt and solid states needs to be clarified. The former mainly corresponds to the spinning process, and the latter to the drawing process. To simplify the discussion, fiber production through the melt spinning process will be mainly dealt with in this chapter.

It is well known that the synthetic polymers can be classified into crystalline and amorphous polymers. Most synthetic fibers are produced from crystalline polymers. On the other hand, from the viewpoint of the processing of polymer melt, crystalline polymers can be classified into two groups depending on their glass transition temperatures being higher or lower than the room temperature. This classification is useful for distinguishing the difference in the fundamental mechanisms of fiber structure formation through the melt spinning and drawing processes.

In comparison with other polymer processing technologies involving shaping of polymer melt such as injection molding, blow molding, etc., processes for fiber production appear to be rather simple since in most cases they can be defined as the process of steady-state uniaxial stretching. However, the processes are still complicated if one tries to predict the effects of the changes of some parameters on the process behaviors and the properties of resultant products. For such problems, fundamental analyses of the processes through on-line (in-situ) measurement and modeling are necessary. In those analyses, not only the variations of macroscopic parameters such as filament diameter, velocity, temperature, etc., but also those of structural parameters such as birefringence, crystallinity, etc., along the spinning line and drawing line need to be considered.

In this chapter, fundamental mechanisms of fiber structure development in the processes of fiber production will be discussed, paying particular attention to both the effects of processing on structure formation and conversely the effects of structure formation on the processing behavior.

5.2 Basic concept of fiber structure and its formation in fiber processing

5.2.1 Structural model and related characteristics of fibers

Although the structure of manufactured fibers appears to be much simpler than that of natural fibers, it still consists of a hierarchical structure, and control of the structure at each level of the hierarchy may be necessary to obtain fibers of good properties. The hierarchical structure arises because of the nature of polymeric materials, i.e. the structure in the polymer products is always in a thermodynamically unstable state because of the presence of long relaxation time components such as molecular entanglement. Accordingly, a crystalline phase with limited crystallite size and an amorphous phase of various states always coexist in crystalline polymeric materials.

Various levels of hierarchical structure can be classified as follows. The first-order structure of the polymer is defined as the structure that can be altered only through chemical reaction. The chemical structure of the repeating

unit, including various types of copolymers, is categorized in the first-order structure. In addition, molecular weight, molecular weight distribution, branching, stereo-regularity, etc., are also included in this category.

On the other hand, there are many more possibilities for structural differences in polymeric materials, such as the variations of molecular conformation, orientation, crystallinity, crystallite size, long period, liquid crystalline state, mesomorphic state, etc. Such structural variations arise only through the difference in the spatial arrangement of molecules without any effect of chemical modification. Those kinds of structure are usually defined as the higher-order structure.

In some cases, the higher-order structure is divided into the second-, third- and higher-order structures. The second-order structure is defined as the variation of the posture of individual molecules arising from the difference in conformation such as planar zig-zag conformation, helical conformation, etc. The third-order structure is defined as the state of the inter-chain ordering such as crystalline, amorphous, liquid crystalline and mesomorphic phases.

The structure on the larger scale such as the shape and size of crystallites, the long period of the alternative structure of crystalline and amorphous phases, and the fibrillar structure can be defined as the higher-order structure. The orientations of the molecular chain and crystalline unit cell, which need to be characterized with respect to a reference-axis fixed to polymer products, are also defined as the higher-order structure.

Structural modeling of fibers has a long history. It started from the proposal of the fringed micelle model (Herrmann *et al.*, 1930), followed by the fringed micellar micro-fibril model (Hess and Kiessig, 1944), and the layered paracrystalline model (Bonart and Hosemann, 1962) which incorporated the concept of folded chain lamellae crystals (Keller, 1957; Till, 1957; Fischer, 1957). The introduction of the concept of taut-tie molecules (Peterlin, 1969), the finding of the shish-kebab structure (Pennings and Kiel, 1965) and the proposal of the interlocked shish-kebab structure (Bashir *et al.*, 1986) are closely related to the high mechanical properties of fibers.

In fiber processing, the first-order structure is assumed to be intact (except for a certain degree of thermal degradation, trans-esterification, etc.), and therefore the structure control can be regarded as the process for the control of the higher-order structures. The distinctive characteristics of the mechanical properties of fibers are the co-possession of strength and flexibility, i.e. fibers are stiff and strong against tensile stress along the fiber axis, but at the same time fibers are flexible and soft for bending and twisting deformations. The thin and long shape of the fiber itself brings about such unique characteristics, and the property can be enhanced by the alignment of molecular chains along the fiber axis to utilize the strength of their covalent bonds. The alignment of molecular chains (or a certain axis or a certain plane in a crystalline unit

cell) along a certain direction in the material is called the 'orientation'. In the case of fibers, the orientation factor usually denotes the degree of alignment of the molecular chain along the fiber axis under the assumption of uniaxial symmetry.

Dimensional stability at elevated temperatures is another important feature of fibers. The thermal stability of polymeric materials can be greatly improved through the formation of a well-developed crystalline structure. Therefore, control of 'crystallization' is another crucial subject in fiber processing. Mechanical properties and some other properties may also be improved by crystallization.

5.2.2 Formation of the shape and structure of fibers through fiber processing

As described in the previous section, the higher-order structure has significant effects on the characteristics of resultant fibers. Accordingly, the formation of the thin and long shape as well as the development of higher-order structure needs to be carefully controlled in fiber production. Development of the higher-order structure is mainly represented by the molecular orientation and crystallization.

The conventional process for the production of synthetic fibers consists mainly of the spinning process and the drawing process. To a first approximation, it can be said that the shape of fibers is formed mainly in the spinning process, whereas the structure of fibers is formed mainly in the drawing process. Naturally, there can be a certain degree of structure formation in the spinning process, which may affect the properties of fibers after drawing, and also there is a certain degree of thinning of fibers during the drawing process.

Extreme exceptions in terms of the separated roles of the spinning and drawing processes are the high-speed melt spinning process and the spinning of liquid crystalline polymers. In both cases, the formation of fiber shape as well as the development of fiber structure can be completed in the spinning process.

5.3 Fundamental mechanism of structure development

5.3.1 Two types of crystalline polymers from the viewpoint of fiber processing

Processing conditions for the melt spinning and drawing processes and the corresponding structure development will be outlined in this section. It is well known that polymers can be classified into crystalline polymers and amorphous polymers. Most synthetic fibers in the market are produced from

crystalline polymers, mainly because of the necessity for high heat resistance. Spinning of fibers can be accomplished by either melt spinning or solution spinning. The latter can be classified into wet spinning, dry spinning and dry-jet-wet spinning (air-gap wet spinning). It is always desirable to produce fibers through the melt spinning process from the viewpoints of the simplicity of the process, low production cost, environmental friendliness, etc. Solution spinning may be adopted when the fibers produced through such processes have distinguishable properties.

To discuss the mechanism of structure development in the production of fibers, it is convenient to classify crystalline polymers into two groups: those with their glass transition temperature (T_g) higher than the room temperature (T_a) such as poly(ethylene terephthalate) (PET), polyamide 66 (PA66), polyamide 6 (PA6), poly(phenylene sulfide) (PPS), etc., and those with their T_g lower than T_a such as polyethylene (PE), polypropylene (PP), polyoxymethylene (POM), etc.

The polymers with $T_g > T_a$ usually have a relatively low crystallization rate. In the melt spinning process, molten polymer extruded from the spinneret cools down and solidifies to form fibers. In this group of polymers, solidification usually occurs because of the glass transition. Accordingly, amorphous fibers with low molecular orientation are formed in the melt spinning process. In the drawing process, such fibers are heated to a temperature slightly higher than T_g to enhance the molecular mobility, and stretched. The fibers gain high molecular orientation after the stretching while crystallinity is still low. Subsequently, the fibers pass through an annealing zone to gain higher crystallinity. During the annealing, fiber length is basically kept constant (a small amount of additional stretching or relaxation may be given to control the stress-strain behavior and dimensional stability). The annealing temperature is assumed to be between T_g and T_m . A higher annealing temperature may result in higher crystallinity and larger crystallite size. Multiple-step drawing and annealing with increasing temperature may be necessary to apply high drawing tension and a high annealing temperature.

In the case of polymers with $T_g < T_a$, molten polymer needs to be crystallized in the spinning process to obtain solidified fibers. Usually, this group of polymers have high crystallization rate, and crystallized fibers with low molecular orientation may be obtained in the melt spinning process. Theoretically, drawing of the crystallized fibers should be performed at a temperature higher than its crystalline dispersion temperature where molecules in the crystals gain enough mobility. In many cases, molecular mobility of the polymers in this category is fairly high and the drawing of those fibers can be carried out even at room temperature. In this stage, destruction and reorganization of crystallites may proceed to form a highly oriented crystalline structure. An additional annealing process may be necessary as in the case of polymers with $T_g > T_a$ to obtain a well-ordered and stabilized structure.

Differences in the structure development behavior in the spinning and drawing processes of the two types of polymers are schematically summarized in Fig. 5.1.

It is interesting to note that there is a demand for producing fibers from polymers which have the characteristics of the combination of $T_g < T_a$ and low crystallization rate. Typical examples are aliphatic polyesters and their copolymers, including aliphatic–aromatic copolyesters (Shi *et al.*, 2005; Shi *et al.*, 2006), which are known to be biodegradable, and the elastomeric PPs with extremely low tacticity prepared using metallocene catalysts. In these cases, special care needs to be given to the melt spinning process, since the fibers tend to be wound up on the bobbin in a rubbery state (without crystallization) and may stick together in the worst cases. In addition, structural changes such as crystallization and molecular orientation continue to occur for a long time after the melt spinning. In contrast to most aliphatic polyesters, poly(lactic acid) (PLA) has its T_g higher than room temperature. From this viewpoint, PLA has better processability in comparison with other aliphatic polyesters (Takasaki *et al.*, 2003).

5.3.2 Fundamental mechanism of molecular orientation

Molecular orientation in the molten polymer generally follows the stress-optical rule (SOR). The SOR for fiber spinning can be described by the following formula:

$$\Delta n = C\sigma \quad 5.1$$

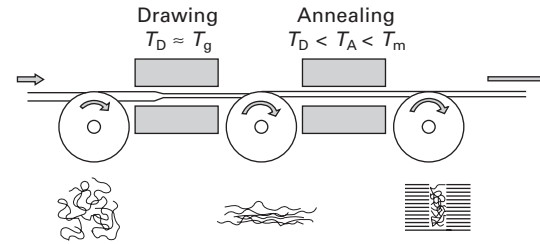
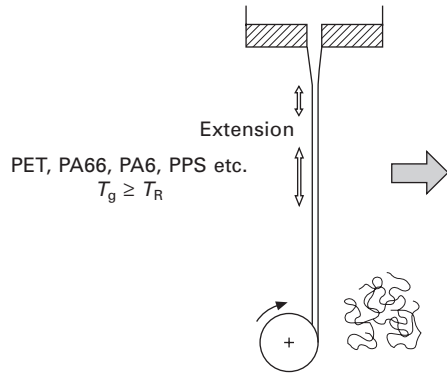
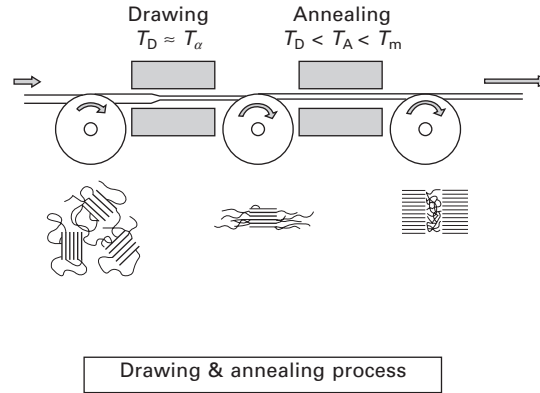
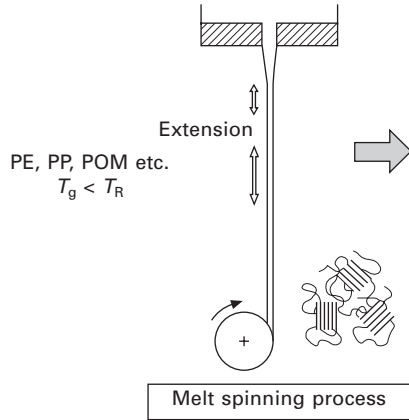
where Δn is the birefringence and σ is the tensile stress. The stress-optical coefficient C can be described as follows:

$$C = \frac{2\pi}{45 kT} \frac{(n^2 + 2)^2}{n} (\alpha_1 - \alpha_2) \quad 5.2$$

where k is the Boltzmann constant, n the mean refractive index and α_1 and α_2 are the polarizability of the segment in the parallel and perpendicular directions to the molecular chain axis respectively. If the intrinsic birefringence of the polymer melt can be defined as Δn_c^* , the orientation factor f can be described as follows:

$$f = \frac{\Delta n}{\Delta n_c^*} = C^* \sigma \quad 5.3$$

where $C^* = \frac{C}{\Delta n_c^*} \quad 5.4$



5.1 Schematic of structure formation behavior in spinning and drawing processes for the polymers with their T_g higher or lower than T_R . T_g , glass transition temperature; T_R , melting temperature; T_R , room temperature; T_D , drawing temperature; T_A , annealing temperature; T_{α} , crystalline dispersion temperature.

The parameter C^* , which can be called the stress-orientation coefficient, represents the orientability of polymers in the flow. The stress-orientation coefficient should have close correlation with the rigidity of the molecular chain.

In principle, the stress-optical rule is based on the correlation between the developments of entropic stress and optical anisotropy of elongated chains. Accordingly, this rule can be applied to a wide variety of polymer melts regardless of their characteristics being either viscous or viscoelastic.

From the viewpoint of fiber processing, lower temperature and higher strain rate lead to a higher degree of molecular orientation because of the development of higher tensile stress. It should be noted that the amount of deformation, such as the draw-down ratio in the spinning process, does not have a direct influence on the orientation development. In principle, polymers with higher rigidity of the molecular chain and with higher anisotropy of polarizability between the directions parallel and perpendicular to the molecular chain axis have a high stress-optical coefficient. The influence of the difference in polarizability–anisotropy on the stress-optical coefficient can be eliminated and the rigidity of the polymer chain can be directly compared if the parameter C^* given in eq. 10.4 is introduced. Unfortunately, the definition of Δn_c^* is not clear; however, if the intrinsic birefringence of the crystalline unit cell is used instead of Δn_c^* , stress-optical coefficients and stress-orientation coefficients of some polymers can be compared as listed in Table 5.1.

In general, it can be said that the rigid molecules such as those of liquid crystalline polymers can be aligned easily in a molten state utilizing the extensional flow in the spinning process, whereas it would be more reasonable to align flexible molecules such as those of PE and PP in a solid state using the drawing process (Ziabicki, 1993). This principle is applicable as far as the molecular orientation in the polymer melt is considered. It should be noted, however, that the mechanism of orientation development of PE and

Table 5.1 Stress-optical coefficient and stress-orientation coefficient of various polymers

Polymer	Stress-optical coefficient (GPa ⁻¹)	Intrinsic birefringence	Stress-orientation coefficient (GPa ⁻¹)
Polyethylene (PE)	1.2	0.12	10
Polypropylene (PP)	0.83	0.060	13
Polyamide 6 (PA6)	1.8	0.094	19
Poly(ethylene terephthalate) (PET)	4.9	0.22	22
Poly(ethylene naphthalate) (PEN)	13	0.49	27

PP fibers after melt processing follows a different principle, which will be discussed later (Section 5.4.3).

On the other hand, orientation development in the solid state is basically governed by the degree of deformation, i.e. the draw ratio in uniaxial stretching. Two extreme cases can be considered. One is the stretching of a rubber-like solid with a limited number of physical crosslinks. In this case, under the condition of the affine deformation of the crosslinked network structure, the relation between the stretch ratio λ and the orientation factor f can be described as follows:

$$f = KN_c \left(\lambda^2 - \frac{1}{\lambda} \right) \quad 5.5$$

where N_c is the number of molecular chains between entangled points, and K is a constant. This formula is based on the same concept as that for eqs 5.1 and 5.2 in that the length of the molecule between the two adjacent physically crosslinked points is considered to be much greater than the distance between those crosslinked points. The other extreme case assumes the affine deformation of every segment in the system, where the orientation factor can be described as follows:

$$f = \frac{3 \langle \cos^2 \theta \rangle - 1}{2} \quad 5.6$$

where

$$\langle \cos^2 \theta \rangle = \frac{(1 + r^2)(r - \tan^{-1} r)}{r^3} \quad 5.7$$

and

$$r = \sqrt{\lambda^3 - 1} \quad 5.8$$

This corresponds to the highly cooperative mutual displacement of molecules in the system. Equations 5.5 and 5.6 predict the minimum and maximum values of the orientation factor, respectively.

5.3.3 Fundamental mechanism of crystallization under non-isothermal conditions

Fundamental researches on polymer crystallization have been carried out mostly under quiescent and isothermal conditions, whereas crystallization in the fiber processing occurs under anisotropic and non-isothermal conditions.

The time-course increase of crystallinity is usually described using the Avrami equation:

$$\frac{X(t)}{X_\infty} = 1 - \exp [-(Kt)^{n^*}] \quad 5.9$$

where $X(t)$ is the crystallinity at time t and X_∞ is the infinite crystallinity. K is the crystallization rate constant and n^* is the Avrami exponent.

Under the assumption of the isokinetic condition, where the crystallization behavior can be described based on the instantaneous crystallinity and temperature and is independent of the crystallization history, the Avrami equation can be extended to the equation for the non-isothermal crystallization as follows (Nakamura *et al.*, 1972).

$$\frac{X(t)}{X_\infty} = 1 - \exp \left\{ - \left[\int_0^t K(\tau) d\tau \right]^{n^*} \right\} \quad 5.10$$

In this equation the term in the exponential function corresponds to the imaginary non-dimensional volume of the crystal without the effects of overlapping and impingement during the crystal growth.

For the prediction of crystallization behavior using eq. 5.10, information on the temperature-dependent crystallization rate is necessary. In general, crystallization does not proceed at temperatures below the glass transition temperature T_g and above the melting temperature T_m , and accordingly the temperature dependence of the crystallization rate has a bell-shaped curve with a maximum around the midpoint of T_g and T_m .

Crystallization in the melt spinning process occurs under the cooling condition. If the latent heat of crystallization is considered, the relation between the variations of temperature T and crystallinity X can be described as follows (Nakamura *et al.*, 1972):

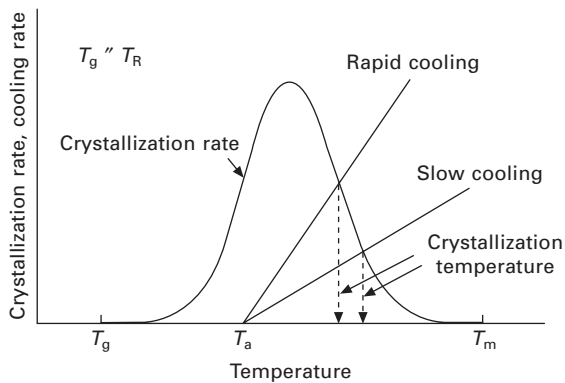
$$\frac{dT}{dt} = - \frac{R}{C_p} (T - T_a) + \frac{\Delta H}{C_p} \frac{dX}{dt} \quad 5.11$$

where R is a parameter representing the cooling rate, C_p the specific heat, T_a the ambient temperature and ΔH the latent heat for 100% crystallization.

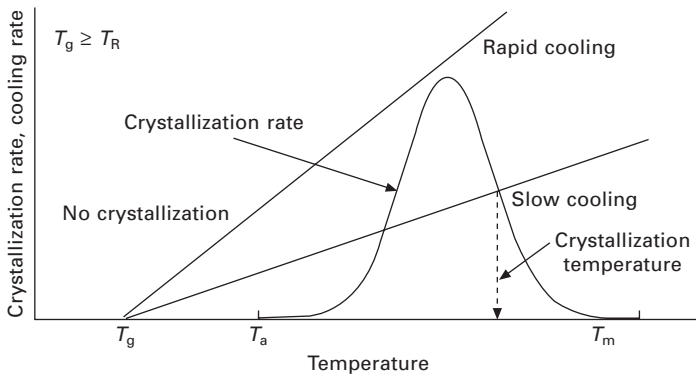
The most probable condition for crystallization under cooling is considered to be the crystallization at a constant temperature where the heat removed by the cooling and the heat generated by the crystallization are balanced. Such condition can be determined as the intersection point of the crystallization rate curve and the cooling rate line as shown schematically in Fig. 5.2(a). In this figure, the straight line representing the cooling rate corresponds to the first term on the right-hand side of eq. 5.11, which indicates that the rate of heat removal from the system decreases linearly with the cooling, i.e. in proportion with the decrease of temperature difference between the polymer and the ambient air. It may be easily understood from this diagram that

the crystallization temperature becomes lower with the increase of cooling rate.

It should be noted that Fig. 5.2(a) represents the behavior of polymers with their T_g lower than room temperature, such as PE, PP, POM, etc. On the other hand, Fig. 5.2(b) corresponds to polymers with T_g higher than room temperature, such as PET, PA66, PA6, PPS, etc. In the slow cooling of such polymers, the behavior is similar to that observed in Fig. 5.2(a); however, in the rapid cooling, there can be a condition where there is no intersection point between the crystallization rate and cooling rate lines. In such condition, fibers in an amorphous state may be obtained.



(a) PE, PP, POM, etc.



(b) PET, PA66, PA6, etc.

5.2 Schematic of the relation between temperature-dependent crystallization rate curve and cooling rate line of different cooling rates: (a) polymers with $T_g < T_a$, (b) polymers with $T_g > T_a$.

5.3.4 Effect of flow on crystallization

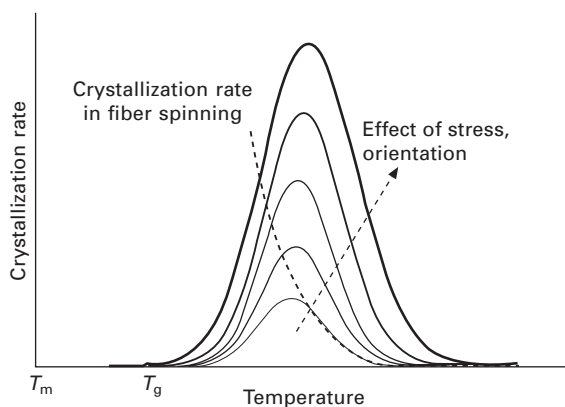
It is well known that the crystallization rate increases in the flow field where development of molecular orientation proceeds. The following explanation is generally given for the mechanism of the enhancement of crystallization in the flow. Because of the molecular orientation, entropy of the melt decreases, and the entropy difference between the crystalline state and the molten state decreases. This leads to the increase of the equilibrium melting temperature, and therefore the increase of crystallization rate at a given temperature.

The effect of the orientation on the crystallization kinetics can be incorporated by adding a term of orientation or stress to the equation for the crystallization rate. For example, the following formula for describing the effect of birefringence development on the crystallization rate was proposed (Alfonso *et al.*, 1978):

$$K(T, \Delta n) = K(T, 0) \exp(A \Delta n^2) \quad 5.12$$

The effect of stress or orientation on the crystallization rate can be schematically expressed as shown in Fig. 5.3. In fiber processing, development of molecular orientation near the extrusion temperature is negligible. Orientation increases gradually with the thinning and cooling of the spinning line. Therefore the crystallization rate in fiber processing may vary in a way represented by the broken line in Fig. 5.3.

It is interesting to note here that there is a possibility of the occurrence of crystallization at a temperature below that of the maximum crystallization rate. In this case, evolution of the heat of crystallization leads to an increase in temperature and to a further increase of the crystallization rate. In other words, once crystallization starts to occur, the heat of crystallization enhances

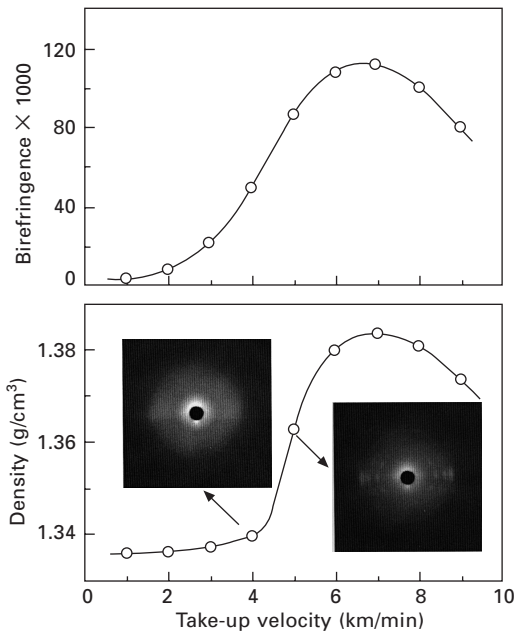


5.3 Schematic of the effect of applied stress or orientation on crystallization rate. The broken line indicates the change of crystallization rate in the melt spinning process.

the crystallization, and the crystallization proceeds up to the maximum value of crystallinity because the ‘snowball effect’ governs the progress of crystallization.

The sudden increase of crystallinity with a slight change of processing condition can be found in typical birefringence and density vs. take-up velocity plots for high-speed spinning of PET as shown in Fig. 5.4. This figure shows that molecular orientation (birefringence) increases gradually with the take-up velocity while crystallinity (density) shows a sudden increase at the take-up velocity of around 4 km/min (Shimizu *et al.*, 1981). On-line temperature measurement of the high-speed spinning line of PET and PA66 also showed a temperature increase, not a plateau, because of crystallization at a position immediately below the neck-like deformation (Kikutani *et al.*, 1989; Haberkorn *et al.*, 1993).

Molecular orientation has a significant influence on crystallization rate. For example, the crystallization rate analyzed through on-line temperature measurement in the high-speed melt spinning process of PET is 10^4 to 10^5 times higher than that in the quiescent state. More specifically, it takes about 10 seconds for the PET sitting still to crystallize at 160°C, the temperature close to that of the maximum crystallization rate, whereas the crystallization



5.4 Birefringence and density plotted against take-up velocity for poly(ethylene terephthalate) fibers obtained in the high-speed melt spinning process. Wide angle X-ray diffraction patterns of fibers obtained at 4 and 5 km/min are inserted in the figure.

of PET in the high-speed melt spinning process at the take-up velocity of 6 km/min proceeds within 1 ms. It should be noted here that the filament runs 10 cm in 1 ms at the speed of 6 km/min, and analysis of crystallization rate within the time-resolution of 1 ms is possible through the detection of the heat of crystallization in temperature measurement of the steady-state melt spinning line (Kikutani *et al.*, 1989).

5.3.5 Limitation of the theory based on the assumption of isokinetic crystallization

Up to this point, crystallization kinetics have been discussed based on the assumption of isokinetic conditions. There is a certain limitation to the validity of this assumption. For example, it was pointed out that crystallization with the growth of spherulites simply does not follow this assumption. This fact can be explained as follows. At a certain degree of crystallinity, the system can contain either a small number of large spherulites or a large number of small spherulites, depending on the temperature history the materials experienced up to that moment. If the linear growth rate of each spherulite is independent of spherulite size, the latter (large number of small spherulites) has a higher crystallization rate because of the larger total surface area of the spherulites. This contradicts the assumption of isokinetic conditions in that the crystallization rate at a certain temperature is only a function of instantaneous crystallinity.

To overcome such a contradiction, a theory on the crystallization kinetics under the effect of flow based on the formation of a shish-kebab structure was proposed (Eder and Janeschitz-Kriegl, 1997). In this theory, the nucleation and unidirectional growth of shish and also the epitaxial growth of disk-like kebab around the shish were assumed as in the case of the nucleation and growth theory for the spherulites under the quiescent state. It is interesting to note that the spontaneous increase of molecular orientation accompanied by crystallization also can be predicted based on this theory.

5.4 Analyses of structure development behavior in fiber processing

5.4.1 Incorporation of crystallization kinetics into the numerical analysis of the melt spinning process

Modeling of the melt spinning process was accomplished by Kase and Matsuo (1965) by numerically solving the fundamental equations, i.e. mass balance equation, momentum balance equation, energy balance equation and the constitutive equation, which describe the flow behavior of the polymer melt. In the numerical simulation, variations of macroscopic parameters

such as diameter, velocity, temperature and tensile force along the spinning line can be predicted.

On the other hand, for the prediction and control of the properties of melt-spun fibers, theoretical analysis of the structure formation behavior in the fiber processing is highly desirable. An equation describing the crystallization kinetics needs to be incorporated in order to predict the crystallization behavior in the spinning process. In the analysis, the crystallization rate may be expressed as a function of crystallinity, temperature and either molecular orientation or tensile stress as discussed in the previous section. In addition, the effect of the evolution of latent heat needs to be incorporated into the energy balance equation. Another important feature which needs to be considered is the effect of crystallization on the flowability of the polymer melt.

There have been various attempts to predict structure development behavior in the melt spinning process. Attempts to incorporate crystallization behavior into the numerical simulation of the melt spinning process appeared in the book on high-speed fiber spinning (Katayama and Yoon, 1985; Shimizu *et al.*, 1985a). In these reports, crystallization was predicted based on the assumption of isokinetic conditions. Subsequently, many researchers proposed the improvement of models for prediction of structure development (Zieminski and Spruiell, 1988; Bhuvanesh and Gupta, 1995; Ziabicki *et al.*, 1998; Forest and Ueda, 1999).

More recently, the effect of crystallization on the flow behavior was incorporated into the numerical model of the melt spinning process, assuming that the polymer flow consists of a stretchable amorphous phase simulated as a viscoelastic fluid and a non-stretchable but orientable crystalline phase approximated to a rigid rod (Doufas *et al.*, 2000). In this model, the amorphous phase and the crystalline phase which grows and orients in the flow are coupled through the stress and momentum balance, while the crystallization behavior is still predicted based on the isokinetic condition.

On the other hand, a model for the description of crystallization behavior in both low- and high-speed spinning has recently been proposed (Meerveld *et al.*, 2008). The effects of quiescent nucleation and growth of spherulites and flow-induced nucleation and longitudinal growth of fibrils were incorporated in this model, and accordingly the appearance of a minimum in the relationship between take-up velocity and crystallinity of as-spun fibers was predicted. This prediction qualitatively agrees well with the experimental observation for the melt spinning of polypropylene in that crystallinity decreases with increasing take-up velocity in the low-speed region because of the increase of cooling rate, while crystallinity increases with the take-up velocity in the high-speed region because of the enhanced effect of flow-induced crystallization (Cao *et al.*, 1989).

Researches on the modeling of structure development in the drawing

process are limited because of the difficulty of obtaining an appropriate constitutive model for deformation. The profiles of the fiber velocity, stress, strain rate, temperature and crystallinity between the take-up roll and the draw roll were simulated (Makradi *et al.*, 2006) using a cooperative elastic–viscoplastic model for the constitutive equation and the isokinetic model for crystallization following Doufas’ model (Doufas *et al.*, 2000). In the energy balance equation, heat generation by viscous dissipation and the latent heat of crystallization were incorporated.

5.4.2 On-line measurement of crystallization

On-line monitoring in the spinning and drawing processes provides valuable information for better understanding of the mechanism of fiber formation including structure development. Velocity, diameter, tensile force and temperature of the spinning line and drawing line are the macroscopic parameters which represent the fiber formation behavior from the viewpoint of the transfer phenomena. On the other hand, from the viewpoint of structure development, on-line measurements of structural parameters such as molecular orientation and crystallinity are indispensable.

Since the 1960s, there have been various attempts at on-line measurement of the wide-angle X-ray diffraction (WAXD) and small-angle X-ray scattering (SAXS) patterns of the spinning line to capture the information on crystallization, crystalline orientation, development of the crystals of multiple orientation modes, etc. (Katayama *et al.*, 1968; Ishizuka and Koyama, 1976; Haberkorn *et al.*, 1993). The availability of synchrotron radiation facilities provided significant progress in this field (Cakmak *et al.*, 1993; Samon *et al.*, 1999). The simultaneous appearance of *c*-axis and *a**-axis oriented crystals was confirmed in the low-speed melt spinning of polypropylene (Kolb *et al.*, 2000a). On-line measurement of the crystallization behavior for polymers with high crystallizability such as PE and PP is relatively easy because crystallization proceeds under mild spinning conditions. On-line measurement in the melt spinning process of PET is much more difficult because a high spinning speed is required for the occurrence of crystallization. Capturing the crystalline reflections of PET in WAXD patterns was accomplished by adopting special measurement techniques such as the use of helium gas for the reduction of air-scattering (Hirahata *et al.*, 1996; Kolb *et al.*, 2000b).

On-line X-ray measurement during the continuous drawing process was attempted for the drawing line of polyamide 66 using a low-power X-ray generator (Hsiao *et al.*, 1996). Recently, combination of the applications of a synchrotron radiation source and the irradiation of a carbon dioxide laser for the heating of running fiber made it possible to capture the crystallization behavior in the continuous drawing process of PET with an extremely high time-resolution of less than 600 μs . In this analysis the formation of a

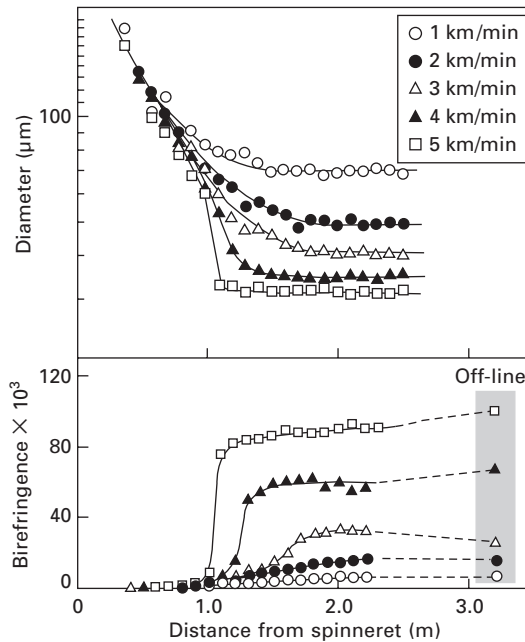
mesomorphic structure prior to the development of a highly oriented triclinic structure was clearly detected (Yamaguchi *et al.*, 2008).

On-line temperature measurement is also a useful method for the analysis of crystallization behavior if the heat of crystallization can be detected as described previously (Kikutani *et al.*, 1989). The heat of crystallization was also detected in the continuous drawing process of PET with carbon dioxide laser irradiation (Yamaguchi *et al.*, 2005).

5.4.3 On-line measurement of orientation development

Development of molecular orientation can be detected through the on-line measurement of birefringence. In this section, analysis of the structure development behavior through on-line birefringence measurement will be discussed, comparing the results for the melt spinning of two typical crystalline polymers, PET and PP.

Variations of diameter and birefringence along the spin-line for high-speed melt spinning of high molecular weight PET with intrinsic viscosity of 1.0 dl/g at various take-up velocities are shown in Fig. 5.5 (Kikutani *et al.*, 1999). The final diameter decreased with the take-up velocity because

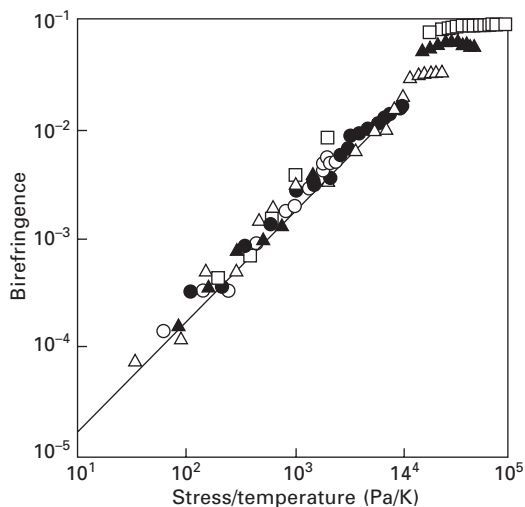


5.5 Changes of diameter and birefringence along the spinning line for high-speed melt spinning of high molecular weight PET.

the throughput rate was kept constant. Diameter reduction along the spinning line tended to concentrate near the solidification point with an increase in the take-up velocity, and showed a so-called neck-like deformation at 4 and 5 km/min. The birefringence increased steeply at the neck-like deformation. The solidification point also shifted upstream with the take-up velocity, which indicated the increase of crystallization temperature. It can be noticed that even at 3 km/min, there was a concentration of birefringence development around 160–180 cm where a relatively steep diameter reduction occurred.

In order to confirm the applicability of the stress-optical rule, variations of temperature and tensile stress along the spinning line were analyzed based on the tensile force measurement near the take-up position and the numerical analysis of the spinning line dynamics. Considering the temperature dependence of the stress-optical coefficient shown in eq. 5.2, a log–log plot of the relation between birefringence and a parameter calculated by dividing the tensile stress by the absolute spinning line temperature was prepared as shown in Fig. 5.6.

It can be seen from this figure that the birefringence and the stress/temperature showed a linear relation with a slope of unity up to a birefringence of about 0.020. From the intercept of the straight line at birefringence of 10^0 , a $C \times T$ value of 1.66 K/MPa, which corresponds to a stress-optical coefficient of 4.8 GPa^{-1} at 70°C , was obtained. Above this region there was a steep increase of birefringence followed by a tendency of saturation

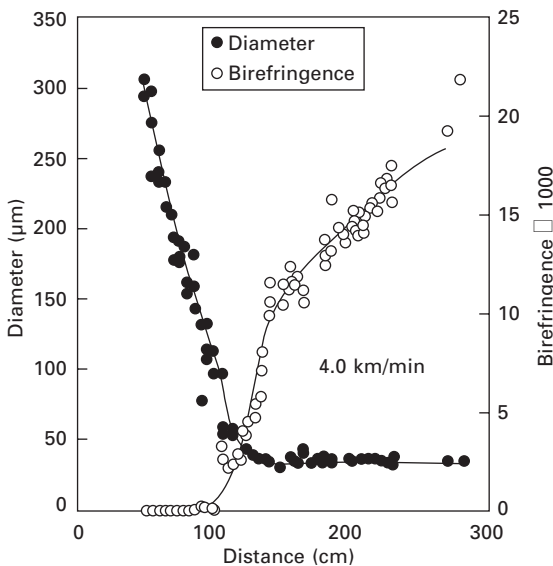


5.6 Log–log plot of the relation between birefringence and stress/temperature obtained through on-line measurement in the melt spinning of PET.

at different levels depending on the take-up velocity. The steep increase of birefringence indicated the starting of the spontaneous birefringence increase. This region corresponds to the formation of partially oriented yarn (POY), and the spontaneous birefringence increase is the origin for the applicability of the draw-texturing process to POY.

A similar experiment was carried out for PP with MFR 35 at an extrusion temperature of 200°C and a throughput rate of 3.0 g/min (Urabe *et al.*, 2000). As shown in Fig. 5.7a, steep diameter reduction along with the steep birefringence increase was observed at around 140 cm from the spinneret at the take-up velocity of 4 km/min. It is interesting to note that birefringence increased continuously even after the completion of thinning. It was also confirmed that there was a continuation of gradual birefringence increase even after the spinning process.

It has been known that the birefringence of PP fibers estimated from applied tensile stress in the spinning process is far below the birefringence of as-spun fibers if the stress-optical coefficient obtained through the fundamental analysis of polymer melt of PP is adopted (Shimizu *et al.*, 1985b). Continuation of the increase of birefringence after the solidification of the spinline observed in Fig. 5.7 should be the origin of such a discrepancy. Analyses of tensile stress in this spinning condition suggested that the stress-optical rule is applicable only up to the end part of steep thinning. After that, spontaneous increase of birefringence, which is probably accompanied



5.7 Changes of diameter and birefringence along the spinning line for high-speed melt spinning of PP at take-up velocity 4 km/min.

by the crystallization, started. The starting point of the spontaneous increase of birefringence corresponded to the spinline stress of about 1 MPa. The discrepancy between the birefringence of as-spun fibers and that estimated from the spinline stress was prominent even at low take-up velocities such as 0.5 km/min.

As shown in Table 5.1 in Section 5.3.2, the stress-optical coefficient of PET is about six times higher than that of PP. If the intrinsic birefringence of crystals is used instead of the birefringence of fully oriented polymer melt, the stress-orientation coefficient of PET is 1.6 times higher than that of PP. In addition, the results of on-line birefringence measurement suggested that the critical level of orientation from which spontaneous orientation development starts is 0.085 for PET and only 0.013 for PP.

The extremely low level of critical orientation for the start of spontaneous orientation development, which may be accompanied by flow-induced crystallization, results partly from the use of the intrinsic birefringence of crystals instead of the intrinsic birefringence of polymer melt; however, it would be more appropriate to consider that not only the instantaneous orientation (or stress) level but also the flow history plays an important role in the occurrence of flow-induced crystallization. The importance of flow history may depend strongly on the type of polymers and processing conditions.

Recently, various researchers have conducted analyses on the effect of flow on the crystallization behavior of PP using synchrotron radiation facilities. Even though flow was applied to the polymer melt for a certain period, and the crystallization behavior was analyzed after the cessation of flow, enhancement of the crystallization behavior was clearly observed (Kornfield *et al.*, 1999; Swartjes *et al.*, 2003).

5.5 Conclusions and future trends

In the production of fibers, understanding of the relation between processing, structure and properties is the most important concept for the development of fibers with distinguishable properties.

There can be two types of research on fiber structure development. One is the analysis of structure development behavior of polymers under well-defined conditions, and the other is research on the dynamic behavior of the fiber processing and structure development in which mutual effects of the processing and structure development need to be considered.

In the former case, although the degrees of orientation and crystallinity are considered to be the dominant factors for determining the properties of fibers, mechanisms of the formation of more complicated hierarchical structures should be investigated. A typical example proving the importance of this subject is the control of the amount of 'shish' (or tie-molecules), which is

considered to be closely related to the ultimate mechanical properties of fibers. Recent researches suggest the importance of molecular entanglement for the formation of ‘shish-kebab’ structure, and there has been intense discussion on the mechanism of shish-kebab structure formation such as whether the shish consists selectively of high molecular weight components (Ogino *et al.*, 2006; Kimata *et al.*, 2007). Another important subject is the detailed analysis of structure development behavior at temperatures near T_g , where the material behaves like solid or molten polymer depending on the processing conditions.

In the latter case, researches on the effect of structure development on the flowability and deformability of a polymer are an important subject. The effect of flow history on the viscoelastic properties of polymer melt has been widely studied; however, researches on the effect of crystallization on the variation of flowability of polymer melt are limited (Lamberti *et al.*, 2007).

5.6 Sources of further information and advice

- Ziabicki A (1976), *Fundamentals of Fibre Formation – The Science of Fibre Spinning and Drawing*, John Wiley & Sons
- Ziabicki A and Kawai H, eds (1985) *High-speed Fiber Spinning – Science and Engineering Aspects*, John Wiley & Sons
- Nakajima T, ed. (1994), *Advanced Fiber Spinning Technology*, Woodhead Publishing
- Larson R G (1988), *Constitutive Equations for Polymer Melts and Solutions*, Butterworths Publishers
- Salem D R, ed. (2001), *Structure Formation in Polymeric Fibers*, Hanser

5.7 References

- Alfonso G C, Verdone M P, Wasiak A (1978), ‘Crystallization kinetics of oriented poly(ethylene terephthalate) from the glassy state’, *Polymer*, 19 (6), 711–716
- Bashir Z, Hill M J, Keller A (1986), ‘Comparative study of etching techniques for electron microscopy using melt processed polyethylene’, *J Mater Sci, Lett*, 5, 876–878
- Bhuvanesh Y C, Gupta V B (1995), ‘Computer simulation of melt spinning of polypropylene fibers using a steady-state model’, *J Appl Polym Sci*, 58, 663–674
- Bonart R, Hosemann R (1962), ‘Fibrillar structure in cold-stretched linear polyethylene’, *Kolloid-Z*, 186 (1), 16–29
- Cakmak M, Teitge A, Zahmann H G, White J L (1993), ‘On-line small-angle and wide-angle X-ray scattering studies on melt-spinning poly(vinylidene fluoride) tape using synchrotron radiation source’, *J Polym Sci, Part B: Polym Phys*, 31 (3), 371–381
- Cao J, Kikutani T, Takaku A, Shimizu J (1989), ‘Nonisothermal orientation-induced crystallization in melt spinning of polypropylene’, *J Appl Polym Sci*, 37, 2683–2697

- Doufas, A K, McHugh A J, Miller C (2000), 'Simulation of melt spinning including flow-induced crystallization. Part I. Model development and predictions', *J Non-Newtonian Fluid Mech*, 92, 27–66
- Eder G, Janeschitz-Kriegl H (1997), 'Crystallization', in Meijer H E H, *Materials Science and Technology, Volume 18, Processing of Polymers*, VCH Verlagsgesellschaft mbH, 270–342
- Fischer E W (1957), 'Stufen- und spiralförmiges Kristallwachstum bei Hochpolymeren', *Naturforschung*, 120, 753–754
- Forest M G, Ueda T (1999), 'An isothermal model for high-speed spinning of liquid crystalline polymer fibers – coupling of flow, orientation, and crystallization', *J Non-Newtonian Fluid Mech*, 84, 109–121
- Haberkorn H, Hahn K, Breuer H, Dorrer H-D, Matthies P (1993), 'On the neck-like deformation in high-speed spun polyamides', *J Appl Polym Sci*, 47 (9), 1551–1579
- Herrmann K, Gerngross O, Abitz W (1930), 'Zur röntgenographischen Strukturermittlung des Gelatinemicells', *Z Phys Chem*, B10, 371–374
- Hess K, Kiessig H (1944), 'Long-period interferences and micellar fiber-fine structure of synthetic polymers (polyamides and polyesters)', *Z Phys Chem*, A193, 196–217
- Hirahata H, Seifert S, Zachmann H G, Yabuki K (1996), 'On-line measurements of orientation induced crystallization of PET during high speed spinning', *Polymer*, 37 (23), 5131–5137
- Hsiao B S, Barton R, Quintana J (1996), 'Simple on-line X-ray setup to monitor structural changes during fiber processing', *J Appl Polym Sci*, 62, 2061–2068
- Ishizuka O, Koyama K (1976), 'Crystal growth in a running filament in melt spinning', *Sen-i Gakkaishi*, 32, T-43–T-48
- Kase S, Matsuo T (1965), 'Studies on melt spinning. I. Fundamental equations on the dynamics of melt spinning', *J Polym Sci*, 3, 2541–2554
- Katayama K, Yoon M G (1985), 'Polymer crystallization in melt spinning: mathematical simulation', in Ziabicki A and Kawai H, *High-Speed Fiber Spinning*, John Wiley & Sons, 207–223
- Katayama K, Amano T, Nakamura K (1968), 'Structural formation during melt spinning process', *Kolloid Z and Z für Polymere*, 226 (2), 125–134
- Keller A (1957), 'Single crystals in polymers: evidence of a folded-chain configuration', *Phil Mag*, 2, 1171–1175
- Kikutani T, Kawahara Y, Matsui T, Takaku A, Shimizu J (1989), 'Measurement of filament temperature and analysis of orientation-induced crystallization behavior in high-speed melt spinning process', *Seikei-Kakou*, 1 (3), 333–339
- Kikutani T, Nakao K, Takarada W, Ito H (1999), 'On-line measurement of orientation development in the high-speed melt spinning process', *Polym Eng Sci*, 39 (12), 2349–2357
- Kimata S, Sakurai T, Nozue Y, Kasahara T, Yamaguchi N, Karino T, Shibayama M, Kornfield J A (2007), 'Molecular basis of the shish-kebab morphology in polymer crystallization', *Science*, 316, 1014–1017
- Kolb R, Seifert S, Stribeck N, achmann H G (2000a), 'Simultaneous measurements of small- and wide-angle X-ray scattering during low speed spinning of poly(propylene) using synchrotron radiation source', *Polymer*, 41 (4), 1497–1505
- Kolb R, Seifert S, Stribeck N, Zachmann H G (2000b), 'Investigation of the high speed spinning process of poly(ethylene terephthalate) by means of synchrotron X-ray diffraction source', *Polymer*, 41 (8), 2931–2935

- Kornfield J A, Kumaraswamy G, Wang P, Verma R K, Yeh F, Hsiao B S (1999), 'Effect of shear history on crystallization of isotactic polypropylene', *Polym Mater Sci Eng*, 81, 326–327
- Lamberti G, Peters G W M, Titomanlio G (2007), 'Crystallinity and linear rheological properties of polymers', *Intern Polym Process*, 22 (3), 303–310
- Makradi A, Cox C L, Anzi S, Belouettar S (2006), 'Postspinning draw of polymeric fibers: multiscale micromechanical model for a solid polymer under finite deformation and strain-induced crystallization', *J Appl Polym Sci*, 100, 2259–2266
- Meerveld J, Hutter M, Peters G W M (2008), 'Continuum model for the simulation of fiber spinning, with quiescent and flow-induced crystallization', *J Non-Newtonian Fluid Mech*, 150, 177–195
- Nakamura K, Watanabe T, Katayama K, Amano T (1972), 'Some aspects of nonisothermal crystallization of polymers. I. Relationship between crystallization temperature, crystallinity and cooling conditions', *J Appl Polym Sci*, 16 (5), 1077–1091
- Ogino Y, Fukushima H, Matsuba G, Takahashi N, Nishida K, Kanaya T (2006), 'Effects of high molecular weight component on crystallization of polyethylene under shear flow', *Polymer*, 47, 5669–5677
- Pennings A J, Kiel A M (1965), 'Fractionation of polymers by crystallization from solution. III. The morphology of fibrillar polyethylene crystals grown in solution', *Kolloid-Zund Für Polymere*, 205 (2), 160–162
- Peterlin A (1969), 'Bond rupture in highly oriented crystalline polymers', *J Polym Sci*, A-2 (7), 1151–1163
- Samon J M, Schultz J M, Hsiao B S, Seifert S, Stribeck N, Gurke I, Collins G, Saw C (1999), 'Structure development during the melt spinning of polyethylene and poly(vinylidene fluoride) fibers by in situ synchrotron small- and wide-angle X-ray scattering techniques', *Macromolecules*, 32 (24), 8121–8132
- Shix X Q, Almi K, Ito H, Ando S, Kikutani T (2005), 'Characterization on mixed-crystal structure of poly(butylene terephthalate succinate/adipate) biodegradable copolymer fibers', *Polymer*, 46, 751–760.
- Shi X Q, Takasaki M, Ito H, Kikutani T (2006), 'Structure development and properties of melt spun poly(butylene succinate) and poly(butylene terephthalate-co-succinate-co-adipate) biodegradable fibers', *Intern Polym Process*, 21, 64–69
- Shimizu J, Okui N, Kikutani T (1981), 'High-speed melt spinning of poly(ethylene terephthalate)-radial variation across fibers-', *Sen-i Gakkaishi*, 37 (4), T-135–T-142
- Shimizu J, Okui N, Kikutani T (1985a), 'Simulation of dynamics and structure formation in high-speed melt spinning', in Ziabicki A and Kawai H, *High-Speed Fiber Spinning*, John Wiley & Sons, 173–201
- Shimizu J, Okui N, Kikutani T (1985b), 'Fine structure and physical properties of fibers melt-spun at high speeds from various polymers', in Ziabicki A and Kawai H, *High-Speed Fiber Spinning*, John Wiley & Sons, 483
- Swartjes F H M, Peters G W M, Rastogi S, Meijer H E H (2003), 'Stress induced crystallization in elongational flow', *Intern Polym Process*, 18 (1), 53–66
- Takasaki M, Ito H, Kikutani T (2003), 'Structure development of polylactides with various D-lactide contents in the high-speed melt spinning process', *J Macromol Sci, Part B Phys*, B42 (1), 57–73
- Till P H Jr (1957), 'The growth of single crystals of linear polyethylene', *J Polym Sci*, 24 (106), 301–306
- Urabe H, Ito H, Kikutani T, Okui N (2000), 'On-line measurement of orientation development in the high-speed melt spinning process of polypropylene', *Seikei-Kakou*, 12 (11), 729–735

- Yamaguchi T, Ohkoshi Y, Gotoh Y, Nagura M (2005), 'Energy balance in the laser drawing process of poly(ethylene terephthalate) fiber', *Seikei-Kakou*, 17 (9), 649–653
- Yamaguchi T, Kim K-H, Murata T, Koide M, Hitoosa S, Urakawa H, Ohkoshi Y, Gotoh Y, Nagura M, Kotera M, Kajiwara K (2008), 'Initial stage of fiber structure development in the continuous drawing of poly(ethylene terephthalate)', *J Polym Sci: Part B: Polym Phys*, 46, 2126–2142
- Ziabicki A (1993), 'Orientation mechanisms in the development of high-performance fibers', *Progr Colloid Polym Sci*, 92, 1–7
- Ziabicki A, Jarecki L, Wasiak A (1998), 'Dynamic modelling of melt spinning', *Comp Theor Polym Sci*, 8 (1/2), 143–157
- Zieminski K F, Spruiell J (1988), 'On-line studies and computer simulation of the melt spinning of nylon-66 filaments', *J Appl Polym Sci*, 35, 2223–2245

Abstract: The chemistry of condensation polymers and ring-opening polymerization is described. The polyesters discussed include both aromatic and aliphatic polyesters and their chemical and thermal stability. Polymer morphology, amorphous and semi-crystalline polymers and the concept of T_g are discussed and how chemical structure governs fiber properties. Processes like melt-spinning and drawing, and texturizing are summarized.

Key words: polyesters, polycondensation, ring opening polymerization, PET, PEN PBT, PTT, polylactide, biodegradable polyesters.

6.1 Introduction

Polyesters comprise the largest amount of totally synthetic polymer produced in the world. A press report (1) in March 2007 estimated the total global production to be 25 million tonnes, growing at a rate of 5% p.a. Polyester accounts for 75% of all man-made fibers in the world. The vast majority is polyethylene terephthalate (PET) and while most of this goes into fibers, a substantial portion (between 10 and 20%) now goes into PET beverage bottles. Other polyesters such as poly(butylene terephthalate) (PBT), poly(trimethylene terephthalate) (PTT) and polyethylene naphthalate (PEN) are miniscule in volume compared with PET, but have their particular markets, as we shall see (2, 3).

Polyesters are *condensation polymers* or step-growth polymers and as such are quite different in polymerization chemistry, molecular structure and polymer architecture from *addition polymers* such as polyethylene, polypropylene and polyvinyl chloride (PVC). *Polymers*, from the Greek for ‘many parts’, are long-chain molecules built up systematically from smaller molecules called *monomers* (Greek ‘one part’). Condensation polymers are usually made by a *polycondensation* reaction. Taking PET as typical, two *monomers*, which are both *bifunctional* (i.e. *two* reactive groups) react together to split out a third component, usually a small molecule, such as water. It was this elimination of water that originally gave rise to the name *polycondensation*. The reaction used to form PET uses so-called AA, BB monomers. The reactive groups are of two types, A and B, which in this case are $[-COOH]$ and $[-OH]$, and each monomer molecule contains two identical groups, either A or B. Other monomers are of the AB type, where each monomer has one each of group A and B at opposite ends. It will be appreciated that to obtain a *long* molecular

chain, and hence a high molecular weight (mass), exactly the same number of A and B groups must be present. Polymer chemists call this *stoichiometric balance*. If there is any imbalance, eventually an extra A or B group will 'play gooseberry at the dance' and have no partner with which to link up, hence the growing polymer chain will come to a dead end. AB monomers have the advantage that correct stoichiometry is automatic, unless one of the reactive ends decomposes before it can fully react. However, often the molecular architecture for the desired fiber end-use requires a polymer of the AA, BB type.

There is another type of polyester-forming monomer, related to the AB type, which uses a different polymerization reaction. This is the *ring-opening polymerization (ROP)* reaction. The monomer is a cyclic ester called a *lactone* (the name is derived from lactic acid) with the reactive groups A and B already combined to make a preformed ester link as part of a ring. In the presence of certain catalysts, the rings split open at the ester group and the nascent A, B groups rejoin to form a long polymer chain joined by new ester linkages. Nothing is split out and no substances are evolved. The polymer is identical in structure to the linear polyester made by from an AB monomer but ROP polymerizations have different kinetics and molecular weight distributions. It is possible to make extremely high MW polymers in this way, and in some ways the ROP reaction is more akin to a double bond *addition* polymerization. If you think of a double bond as a two-atom ring, the parallel is clearer. Typical polyester monomers that polymerize by ROP reactions are glycolide, lactide and ϵ -caprolactone. The polymers are aliphatic polyesters and these are used in biodegradable or bio-erodable polymers, either for biomedical applications (like soluble sutures) or in environmentally friendly, disposable items which will degrade into harmless products on exposure to the weather.

Polyesters, as their name indicates, are made by forming ester units as the link-forming reaction, so the ester units ($-\text{CO}-\text{O}-$) form an integral part of the polymer chain. PET is made up from terephthalic acid, which is benzene 1,4-dicarboxylic acid, and ethane-1,2-diol, usually called ethylene glycol. This was once familiar as automotive antifreeze, but is now being replaced by less toxic materials. In formal terms, the two monomers split out a molecule of water and form a link in the polyester chain, but this is an oversimplification. In practice, the chemical process is more complex, as we shall see.

There are many other kinds of condensation polymers besides polyesters. Depending on the linking group, these include polyamides ($-\text{CONH}-$), polyurethanes ($-\text{NH}-\text{CO}-\text{O}-$), polycarbonates ($-\text{O}-\text{CO}-\text{O}-$), polythioesters ($-\text{CO}-\text{S}-$), polyureas ($-\text{NH}-\text{CO}-\text{NH}-$), polyhydrazides ($-\text{NH}-\text{NH}-\text{CO}-$), polyazomethines ($-\text{CH}=\text{N}-$); in fact *any* molecular grouping that is readily formed by a condensation reaction can be adapted to make a polymer. Some

linkages are too costly or too thermally unstable to be satisfactory and the main commercial condensation polymers are chiefly polyesters, polyamides, polycarbonates and polyurethanes.

One important consideration is the *type of chemistry* involved in making the polymer links. The overriding consideration is that the reaction must go in 100% yield; if it does not, we shall not obtain high molecular weights. Thus for polyesters, we must examine all the ways to make ester links in high yield. These include direct esterification of an acid with an alcohol, ester exchange, and more exotic methods such as reaction of an acid chloride with a hydroxyl group, often in the presence of a base to remove the hydrogen chloride by-product. The most convenient reactions are those which do not evolve corrosive by-products and can be carried out in the *liquid phase*, preferably in the melt. There are cases where an inert solvent is needed, as in the case of certain polycarbonates. Here one of the reactants is phosgene, a gas, which dissolves in the solvent. There is also *solid-phase polymerization* which is widely used to increase the molecular weight of polyesters and we shall meet it later on.

Condensation polymer chemistry started around the early 1930s. Its 'father' was Dr Wallace H. Carothers of the DuPont Company (4). He began a serious study of melt-phase polymerization of various small molecules with the aim of making large polymeric molecules. This was only 15 years after the ideas of Hermann Staudinger (5) were published, implying that polymers were simply very large molecules linked by normal chemical bonds. This idea may seem obvious now, but was quite revolutionary at the time and in eventually in 1953, Staudinger was awarded the Nobel Prize for Chemistry. Carothers used various monomers, including hydroxy-acids (AB type), diacids and diols (AA, BB type) and in some of his earliest work he even made polymeric acid anhydrides, such as polysebacic anhydride.

He recognized that his monomers must contain a certain minimum length of carbon chain or else they would simply react with themselves to form cyclic esters or lactones. Knowing that five-, six- and seven-membered rings are the most easily formed, he used omega-hydroxy-acids with 8–10 carbon atoms. He found that to remove the last traces of volatile by-products like water or methanol from the polymer melt was difficult and needed elaborate high vacuum equipment with mercury diffusion pumps. During this work he established a fundamental rule for condensation polymers, often called *Carothers' Law*, which states that if the extent of a chemical reaction is p (where $1 > p > 0$) then the molecular weight of the polymer varies as $1/(1 - p)$. In other words, as the extent of reaction approaches 100%, the MW of the polymer approaches infinity. This means that removing those last few traces of by-product drive the molecular weight up on a logarithmic scale. By the same token, extremely pure monomers must be used, for any non-functional impurity would lower the ultimate molecular

weight. The importance of his pioneering studies cannot be minimized: he laid logical foundations for all the studies of polymer chemistry that have since followed.

Carothers was able to make aliphatic polyesters with a molecular weight high enough ($MW > 9000$) and melts that were viscous enough for fibers to be drawn from the melt. Such fibers could be stretched (cold-drawn) to become surprisingly strong. But they were very low-melting (around $55\text{--}70^\circ\text{C}$) and easily soluble in chloroform and various dry-cleaning solvents, thus rendering them useless for textile fibers. He theorized that *polyamides* would be higher-melting and also insoluble in such solvents and went on to discover *nylon*, the first entirely synthetic fiber to be a commercial success. Nylon needs no description, but many people may not know that its first commercial use in the late 1930s was not in hosiery at all, but as an improved toothbrush bristle!

6.1.1 Polymer viscosity and molecular weight

In discussing *polymers*, we must know how to characterize them. One of the major parameters of any polymer is its molecular weight (MW), which is related to the length of the polymer chain. Generally, the longer the chain, the stronger and tougher the fiber made from the polymer. MW is a statistical property because any polymer sample contains many polymer chains of different individual MWs. One way to get an approximate MW is to measure the *solution viscosity* of the polymer. As the MW of the polymer rises, the more viscous a standard solution of the polymer in a solvent becomes. This measurement is usually measured in a Ubbelohde viscometer, where a set volume of polymer solution flows through a capillary tube and the flow time between two marks is measured. The viscometer is sensitive to changes in temperature, so it is held at $25^\circ\text{C} (\pm 0.5^\circ)$ in a constant temperature bath. The flow time of a standard solution is compared with the blank flow time of pure solvent. The polymer concentration c is measured in g/deciliter. This simple measurement gives the *relative viscosity* or *viscosity ratio* (RV or η_{rel}). Another parameter is *reduced viscosity* which is $(RV - 1)$. The quantity $(RV - 1)/c$ is called the *specific viscosity* (η_{sp}). Finally, *inherent viscosity*, (η_{inh}) is $(\log_e RV)/c$. If we plot the values of η_{sp} and η_{inh} against c at increasing dilution, we obtain two converging linear plots which tend to the same value as c tends to zero. This asymptotic value is the *intrinsic viscosity* (IV), $[\eta]$, and its units are deciliters/g. IV is important because we can calculate the molecular weight from the IV by the Mark–Houwink Equation. This says that:

$$[\eta] = KM_v^\alpha$$

where M_v is the viscosity average MW and K and α are constants which

depend on the solvent. This is an empirical relation but useful nonetheless. For absolute values of MW, other methods such as osmometry or light scattering must be used, which can be time-consuming. By comparing results, the constants M and α have been calculated for many polymer/solvent combinations.

Semi-crystalline polymers like PET will only dissolve in aggressive solvents like *o*-chlorophenol or a mixture of phenol and tetrachloroethane. Acidic solvents like hexafluoroisopropanol (HFIP) and mixtures of HFIP with pentafluorophenol (PFP) have been introduced in recent years. They will dissolve *at room temperature* highly crystalline polymers, like PBT or PET that has been subjected to solid-phase polymerization. In earlier days, drastic conditions such as dichloroacetic acid at 100°C were necessary to dissolve SPP PET and later work showed that these severe conditions degraded the polymer. In fact, the IV achieved by the SPP process was significantly higher than at first thought.

6.2 The main types of polyester

Polyethylene terephthalate (PET) was invented in 1941 by J. Rex Whinfield and J. T. Dickson in England at the Calico Printers Association Laboratories (6). In addition to PET (2GT), Whinfield and his colleagues also invented PBT (4GT) and PTT (3GT) and not only made the polymers, but melt-spun them into fibers and measured their fiber properties. It was a remarkable piece of work, considering the difficult times during the early days of World War II. Because of this, there was no possibility at all that these materials could be developed commercially until the war was over. Around 1946–48, ICI in England and DuPont in the USA began to develop PET as a commercial product, called *Terylene*TM in the Britain and *Dacron*TM in the USA. With the benefit of hindsight, it may seem surprising that Carothers did not investigate PET, but we must remember that terephthalic acid in the 1930s was a laboratory curiosity of no commercial interest. There is circumstantial evidence that one of Carothers' colleagues *did* try to make PET but the results were disappointing and the idea was never pursued. Happenstance often affects innovation in this way. In fact, once the route to making consistently high MW was developed, PET turned out to have very desirable properties as a textile fiber. It was strong, flexible and readily melt-spun into very fine fibers. It had a tensile modulus much higher than nylon, and fabrics made from PET, once heat-set, were remarkably resistant to creasing. Pleats set in by steaming maintained their crease, even after washing with hot water. Fortunately at this time (early 1950s) accordion-pleated ladies' skirts were fashionable and PET/wool blend fabrics were very suitable. Likewise wool/PET men's suiting fabrics maintained their style without constant pressing. Pants stayed in crease, jackets kept their drape without wrinkling and PET/

cotton shirts remained crisp: the phrase 'wash-and-wear' began to enter the common parlance! These fortunate conjunctions in popular taste and fashion (for both genders) ensured that polyester fiber got off to a good commercial start.

PBT (4GT) was made using butane-1,4-diol as the glycol in place of ethylene glycol. In pre-WWII Germany, Dr P. Schlack had developed a melt-spinnable polyurethane fiber (*Perlon-U*) based on butanediol. W. J. Reppe at the I. G. Farbenindustrie had developed a route to butanediol from acetylene and formaldehyde and this technology became available in the aftermath of war. It was found that PBT had a lower melting point than PET and as a result it was easier to melt-spin. The fibers were elastic and much more resilient than PET, and the fiber was very white and stayed white even after prolonged weathering. Unlike nylon, it did not yellow with age.

At one time, high hopes were entertained for PBT as a textile fiber but the only *fiber* market in which it has ever achieved success is bulked continuous filament (BCF) polyester carpet yarns, where its resilience and resistance to staining are superior to those of nylon (7). Butanediol has always been much more expensive than ethylene glycol and PBT is more expensive than nylon, let alone PET.

The last polyester that the Whinfield team worked on was polytrimethylene terephthalate, PTT or 3GT, made from propane-1,3-diol, variously called PDO or trimethylene glycol (8). This polymer has a remarkable history. It was recognized, even in Whinfield's day, that it has superb resilience and excels in fiber recovery properties. But for 60 years there was no economically viable route for making PDO, so the polymer languished. In 1962–63, as a young polymer chemist at ICI Fibers Division, the author was repeatedly told about the marvelous fiber properties of 3GT!

Recently this picture has dramatically altered. Several chemical routes to PDO have emerged, one being the Shell Chemicals process by hydroformylation of ethylene oxide. Shell has done a great amount of work and developed 3GT as a commercial polyester fiber, particularly for the non-stain polyester carpet market. More recently still, PDO has been made by a DuPont fermentation process and the work won a USA Presidential Green Chemistry Award (9). Several full-size fermentation plants are now in being, utilizing genetically engineered bacteria to make PDO by fermentation of various grains. The idea dates back to WWI, where glycerol, an essential material for making military explosives and propellants, was made extensively by fermentation, via the biochemical reduction of the intermediate 1,3-dihydroxyacetone. The new strains of bacteria are able to further reduce the central carbonyl group to a $-\text{CH}_2-$ group and thus give PDO. Firms like Invista are making 3GT on a large scale and it is said that the 'green-process' PDO gives a very high quality product.

PTT (3GT) has been thoroughly investigated as a fiber (see ref. 8). It

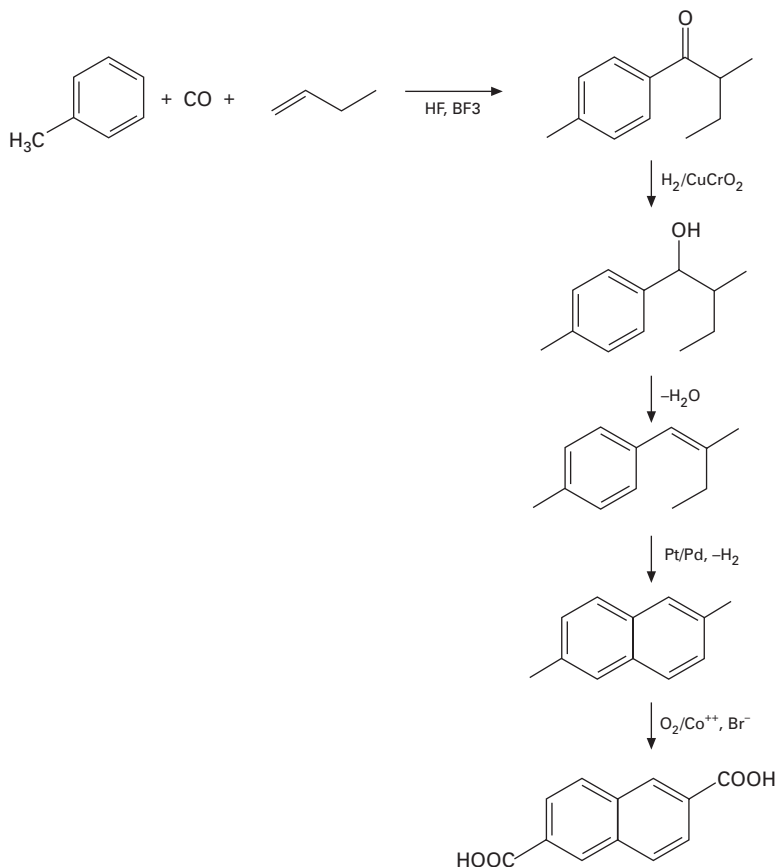
has excellent tread resilience in carpets and gives bulked yarns which make attractive knitwear fabrics. It dyes at the boil to clear bright colors with disperse dyes without the need for pressure dyeing, unlike PET. Nylon, being a polyamide and therefore similar to a protein, has always dyed readily with acid dyes (so does wool) but because of this very affinity, it stains easily with tea or coffee and other household spills. By contrast, PTT carpets resists these staining agents and this is being touted as a major product advantage.

Both PBT and PTT crystallize quickly and readily from the melt, unlike PET, which crystallizes only reluctantly without a nucleating agent. PBT has been used since 1970 as an injection molding engineering plastic resin, especially for automobile and electronic components. PTT is poised to encroach on this market, as PDO is said to be considerably cheaper than butanediol, although still more expensive than ethylene glycol. Thus, from being alone on the shelf for so many years, 3GT has now blossomed with a vengeance in the commercial world.

The last of the polyester family is polyethylene naphthalate (PEN) which was discovered at ICI in 1948 (10) and is made from ethylene glycol and naphthalene-2,6-dicarboxylic acid (NDA). The polymer is sometimes denoted 2GN. This polyester was found to have very desirable physical properties for industrial fibers. It has a higher melting point than PET, but not so high that melt-spinning is a problem. Above all, it has a much higher tensile modulus than PET and is thus very suitable for low-stretch, high-tensile industrial yarns and tire cords. A bonus is that the fiber has outstanding resistance to degradation by UV light because the naphthalene rings act as a built-in UV absorber.

Once again this polymer had to wait until there was an economic source of the naphthalene diacid. The acid can be made by oxidation of 2,6-dimethyl naphthalene (11) but this intermediate was not available in a pure form until the late 1990s when companies in Japan such as Mitsubishi Gas Chemical developed synthetic routes (12–14). The Mitsubishi route starts with an oxo reaction between carbon monoxide, 1-butene and toluene to make tolyl-4-isobutyl ketone, which is reduced to the alcohol and dehydrated to the olefine, which is finally catalytically cyclized and dehydrogenated to 2,6-dimethylnaphthalene. Air-oxidation (as for TA) produces NDA see Structure 6.1.

Early in the new millennium, firms like Amoco began to advertise commercial supplies of the dimethyl ester of NDA and in 2002 Honeywell Performance Fibers (15) commercialized PEN fibers under the trade name *Pentex*TM. The markets are in high-tensile, low-stretch industrial yarns. PEN films and bottle resins are characterized by low permeability to gases like CO₂ and oxygen, and PEN bottles have been used to protect products sensitive to UV light. PEN has textile opportunities in fabrics for sailcloths and tentage fabrics where the high modulus and resistance to UV can be exploited.



Structure 6.1 Production of 2,6-NDA by the Mitsubishi Gas Chemical/Amoco process.

Aliphatic polyesters are, so far, a specialized market, largely in biomedical and drug-release polymers, but there is much effort to develop cheap disposable and environmentally friendly polymers and fabrics. Polylactic acid is the polymer of choice, since dilactide, the cyclic dilactone from lactic acid, can readily be made by a fermentation reaction from corn syrup. In October 2007 a new company called Natureworks was formed by Teijin in Japan and Cargill in the USA (16) specially to bring to market bio-derived polymers such as polylactide. Polylactide is made by an ROP reaction from lactide, together with other monomers such as glycolide, to form copolymers to modify the properties. Since lactic acid is chiral, there are several stereoisomerides of dilactide. The stereo-pure homopolymer is highly crystalline and has a melting point about 178°C, but by using other lactide stereoisomers it is possible to make less crystalline stereo-copolyesters which are both tougher

and less brittle. Work is in progress on polylactide fibers as disposable fabrics which will rapidly degrade to harmless breakdown products. Biodegradable fibers used in sutures are made by ROP on various cyclic monomers such as glycolide, lactide, α -caprolactone, the cyclic esters trimethylene carbonate and 1,4-dioxanone.

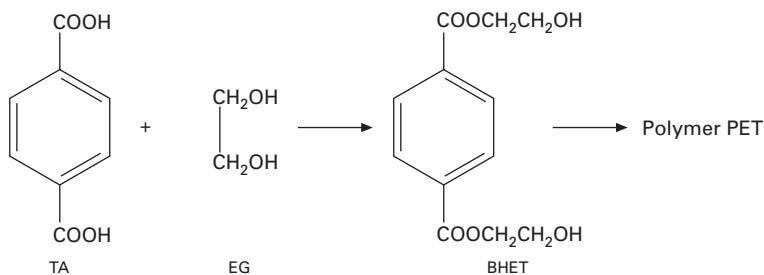
The chemical structures and processes involved in the manufacture of various polyesters will now be covered in a general way. If the reader needs more detailed descriptions, there are several publications that deal with the topics in an admirable fashion (see Sources of further information).

6.3 Chemistry of PET

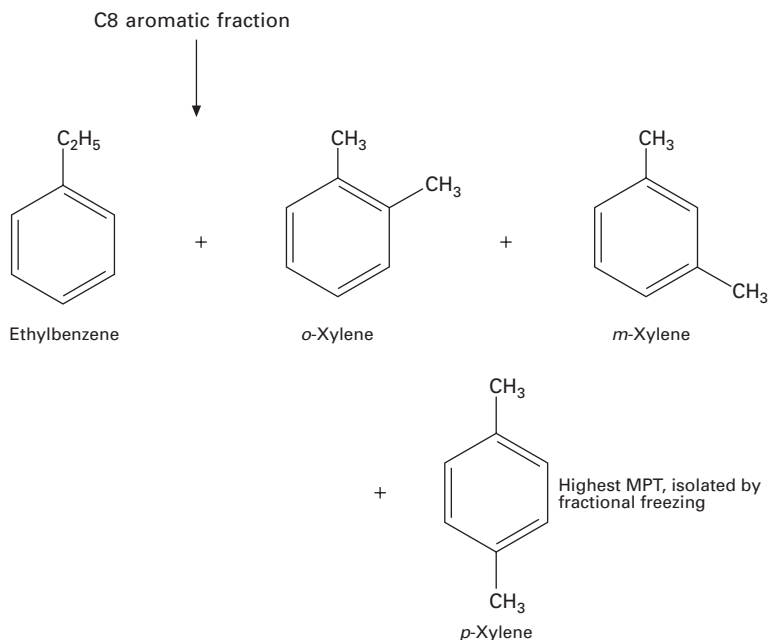
PET is made, as we have seen, from terephthalic acid (TA) and ethylene glycol (EG) and the formal process is shown in Structure 6.2.

Terephthalic acid is made by the air-oxidation of *p*-xylene (1,4-dimethylbenzene) which is a petrochemical product (17). It is derived from the C₈ aromatic distillate fraction, which includes all three xylenes and ethylbenzene. Since *p*-xylene is the most symmetrical molecule in the mixture, it has the highest melting point and is isolated by fractional crystallization. The residues can be isomerized into more *p*-xylene by cationic rearrangements using Freidel–Crafts type catalysts (18). See Structure 6.3.

The oxidation step uses air under pressure, often in a titanium vessel, in superheated acetic acid at around 140°C. The catalysts are cobalt and manganese salts, with a trace of bromide anion (19), and the very insoluble TA crystallizes out from the hot reaction medium. The crude TA needs to be purified. Two major impurities are *p*-toluic acid and 4-carboxybenzaldehyde (4-CBA). A leading process, developed originally by Amoco, recrystallizes TA from superheated water under pressure with concomitant catalytic hydrogenation to remove traces of 4-CBA. The latter is particularly undesirable in polymer-grade TA. The 4-CBA is reduced to *p*-toluic acid, which is already present and easily soluble in superheated water (20). Releasing the pressure



Structure 6.2 Production of the PET monomer *bit*-(2-hydroxyethyl) terephthalate (BHET) from terephthalic acid (TA) ethylene glycol (EG).



Structure 6.3 Production of ethylbenzene and xylenes from the C₈ aromatic fraction.

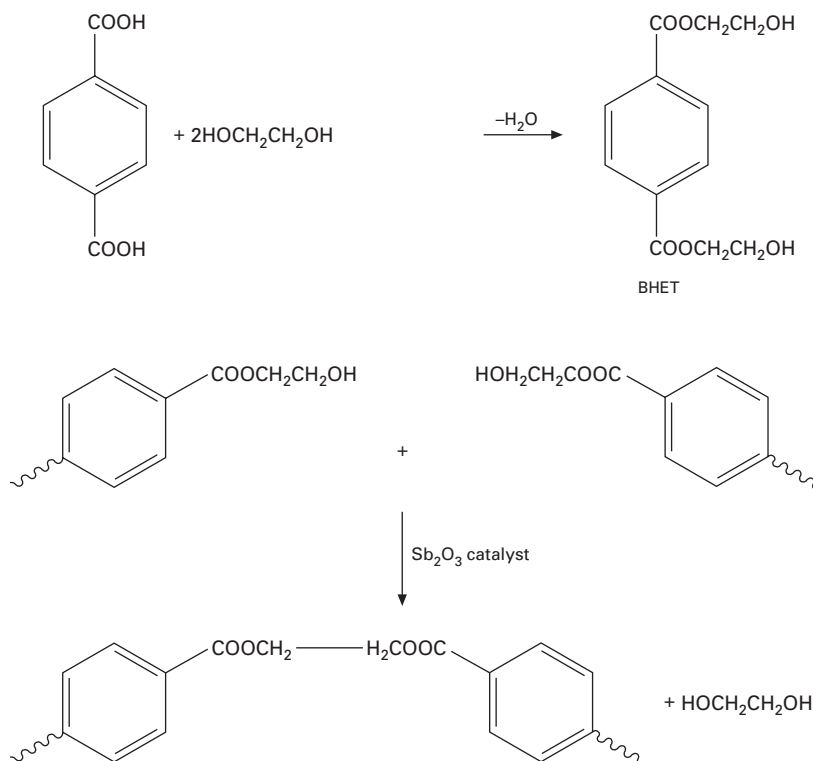
precipitates TA that is pure enough to allow direct esterification with ethylene glycol. This process forms *bis*-(2-hydroxyethyl) terephthalate (BHET), which is the essential PET monomer.

Older TA processes used aqueous nitric acid to oxidize *p*-xylene and the crude product contained various nitrogenous impurities which gave badly discolored polymer and were difficult to remove. Hence crude TA was esterified with methanol to make dimethyl terephthalate (DMT) and the ester was purified by high vacuum distillation and recrystallization to give polymer-grade DMT. Reaction with glycol under ester-interchange conditions likewise formed BHET, with evolution of methanol, which was redistilled and returned to the process stream. The ethylene glycol used in both processes was made by hydration of ethylene oxide, in turn made by catalytic air-oxidation of ethylene in the vapor phase. For many years the DMT process (called the EI process, for 'ester interchange') was normal but by the 1980s most plants had gone over to the direct esterification (DE) method which saves a whole process step. Interestingly, with the upsurge in recycled polyester (mainly from beverage bottles) there has been a small revival of the EI process since glycolysis/methanolysis of recycled bottles produces DMT as an end-product (21, 22).

The true polymerization of PET is actually a series of ester interchange reactions involving BHET: two BHET molecules extrude one mole of

glycol between them and form a PET dimer, and the growing chains add on monomer units and extrude more glycol. Ideally n moles of BHET give an n -mer polymer evolving $(n - 1)$ moles of glycol. The polymerization catalyst is often antimony trioxide, but some countries object to the use of heavy toxic metals like antimony, and less harmful (but more expensive) catalysts like germanium dioxide have been used. Titanium alkoxides and organo-tin compounds are excellent polymerization catalysts, but cause serious yellowing problems with PET and all polyesters based on ethylene glycol. They are satisfactory for PTT and PBT. Recently AKZO has introduced a polysilicon–oxygen–titanium network polymerization catalyst which works well without yellowing (23–25). The process is shown in Structure 6.4.

The ester interchange process needs two catalysts, one for the EI step and one for the polymerization. Antimony trioxide does not become active until the batch temperature exceeds 200°C, so it can be added at the start of the reaction with impunity. The EI catalysts are usually weak Lewis bases like calcium, zinc or manganese acetates (26–28). These are good EI catalysts but they promote ester group thermal cracking at high temperatures (29),



Structure 6.4 Polymerization of PET from BHET monomer.

so it is necessary to sequester them as insoluble phosphate salts by adding phosphoric or polyphosphoric acids, or aryl phosphates after the EI is complete, but before the polymerization stage begins (30).

Polymerizations can be run on a batch process or in a continuous polymerization process (CP). On a batch process, the reaction is usually run in two vessels, an esterifier or EI vessel, and a polymerization vessel. The latter can be large and hold several tonnes of polymer melt; all the vessels and piping are usually made of 316 stainless steel. The EI or esterifier vessel is charged with DMT or TA and excess glycol and heated slowly up to 230–240°C under a distillation column with a condenser. Water or methanol distils up the column and eventually the still-head temperature rises to about 220–230°C to indicate that pure glycol is distilling and the first stage is complete. The contents of the first vessel are then pumped under nitrogen pressure into the polymerizer. Sometimes, to save space, one polymerizer vessel is fed by two smaller esterifier vessels.

The polymerizer can be exhausted to high vacuum and has a large sealed anchor paddle stirrer, driven by a powerful hydraulic motor whose torque is monitored. By measuring the rise in torque (Δt) between the start and the end of polymerization and comparing it with a calibration database, it is possible to judge the desired melt viscosity fairly accurately and time the end-point so that each batch has a similar molecular weight. The polymerization stage operates under high vacuum and the distilled glycol is collected for purification and reuse. When not under vacuum, the autoclave is sparged with nitrogen to prevent the molten polymer oxidizing by contact with air. At the end of the polymerization run, a bottom valve is opened and the viscous molten polymer forced out under nitrogen gas pressure, often through a die plate that extrudes it as strands about a quarter-inch (6 mm) in diameter. The polymer goes through a water quench bath and the solidified strands are air-dried, chopped in a continuous strand cutter and stored in a drum ready for polymer drying. The polymerization is usually run at a constant temperature of 280–285°C. Between successive batches, the polymerization vessel is usually cleaned out with a mixture of dilute alkali and boiling glycol to remove the polymer residues from the previous batch.

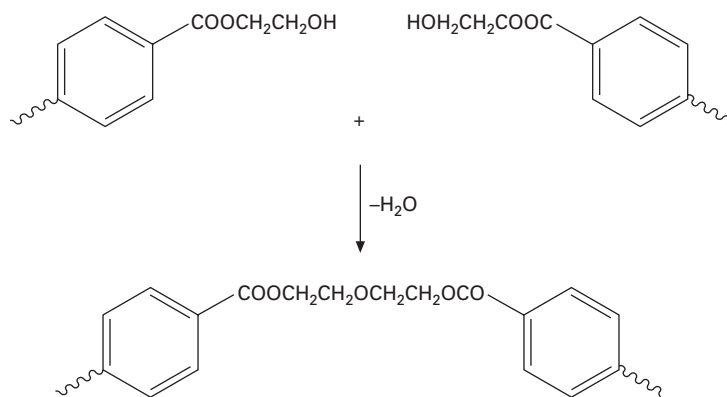
Aromatic ester groups begin to crack thermally at about 250–260°C, so the melt polymerization stage is a race between polymer chains growing and other chains degrading. A complication is the fact that, since the melt viscosity of PET is *ca.* 3000 poise at 285°C (at a shear rate of 1000 s⁻¹), there is significant viscous heating by the agitator paddle and temperatures can locally rise to 10–15°C above the nominal batch temperature. The thermal scission of glycol ester groups produces a vinyl ester end, via a McClafferty reaction (31), which then undergoes ester exchange, releasing vinyl alcohol, which instantly tautomerizes to acetaldehyde (32). This is very volatile (B.P. 23°C) and escapes from the melt. Other vinyl ester ends

thermally polymerize and the products undergo further pyrolysis, producing yellow-brown polyenes. The intensely yellow complexes that titanium and tin catalysts form with vinyl esters render such catalysts unsuitable. There is another degradation problem, which does not cause discoloration but adversely affects the polymer. This is the formation of diethylene glycol (DEG) links in the chain by dehydration and ether formation from two BHET ends (Structure 6.5). All PET contains a small amount of DEG for this reason and it depresses the polymer's melting point (33).

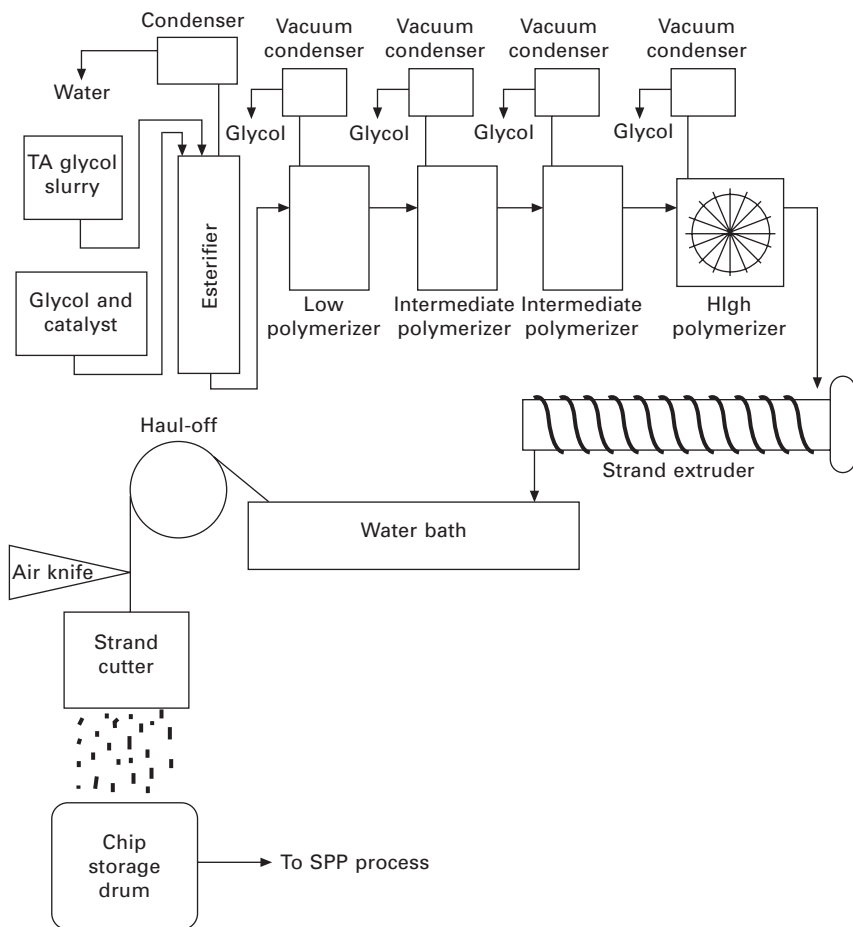
6.3.1 CP

The outline process described above is a batch process and, for large amounts of PET polymer, it would be uneconomic to make polymer in the volumes needed in this way. Starting around 40 years ago, continuous polymerization (CP) processes have been developed for PET and have now been brought to a high level of sophistication. Some of the latest CP lines can make as much as 20 tonnes of polymer per hour. The actual details of the process are quite complex and also contain highly proprietary information on such things as the agitator design, so it is only possible to give a broad overall description. Several schematic CP process descriptions and diagrams have been published (34). A schematic diagram of a typical CP unit is shown in Fig. 6.1.

A typical CP train consists of a series of units, each designed to complete one part of the polymerization process. The first stage is the *esterifier*, where glycol and PTA are reacted in a typical DE process to make BHET mixed with low oligomers. The output is still fluid and is pumped to the *pre-polymerizer* or low polymerizer. In a large unit, the next stage, the



Structure 6.5 Formation of diethylene glycol (DEG) links by dehydration of BHET ends.



6.1 Schematic of a typical PET continuous polymerization unit.

intermediate polymerizer, may be itself divided into two stages. Vacuum is applied and the increasingly viscous melt is pumped to the finishing-stage or *high polymerizer*. The melt is agitated, for example, in a wiped-wall reactor (as shown in Fig. 6.1) so that a continually regenerated, very thin film of polymer is constantly re-exposed to the high vacuum, to enable rapid disengagement of volatiles such as excess glycol and traces of water.

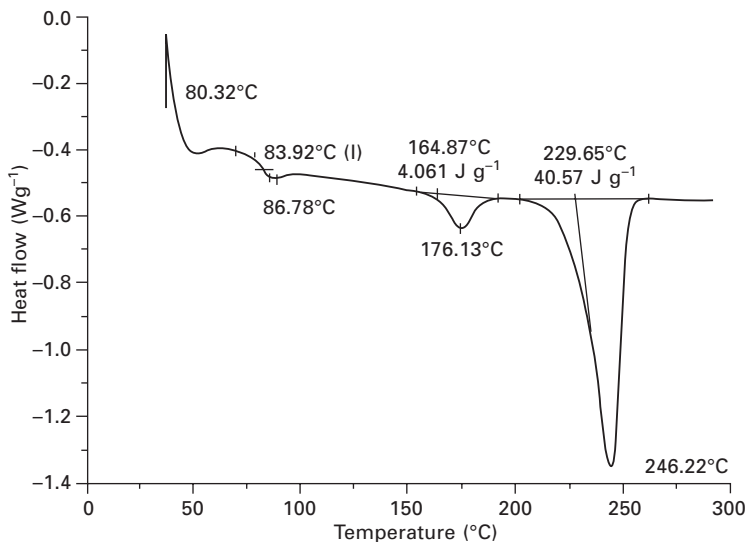
One of the key design features of any CP plant is to ensure scrupulously that there are no 'dead spaces' where stagnant polymer can accumulate and become overheated. This causes it to degrade thermally to a carbonaceous material which eventually breaks off and contaminates the polymer stream as 'black specks'. The polymer emerging from the finishing stage has by now reached the target molecular weight, which is usually of the order of

$IV = 0.65$. Molten polymer may be pumped directly to a melt-spinning unit in a so-called CP-spin-draw unit, which is thus completely integrated. Raw materials go in at one end; and drawn, finished polyester fiber comes out at the other. However, to take account of variations in demand and permit some process flexibility, it is more usual to pass the molten polymer through a large extruder and strand-cast the molten polymer into a water bath, then chip and dry it for further processing (e.g. solid phase polymerization, SPP) or store until needed. Figure 6.1 shows a strand extruder, with an integrated cutter; the air knife blows off excess water from the wet strands emerging from the water quench bath.

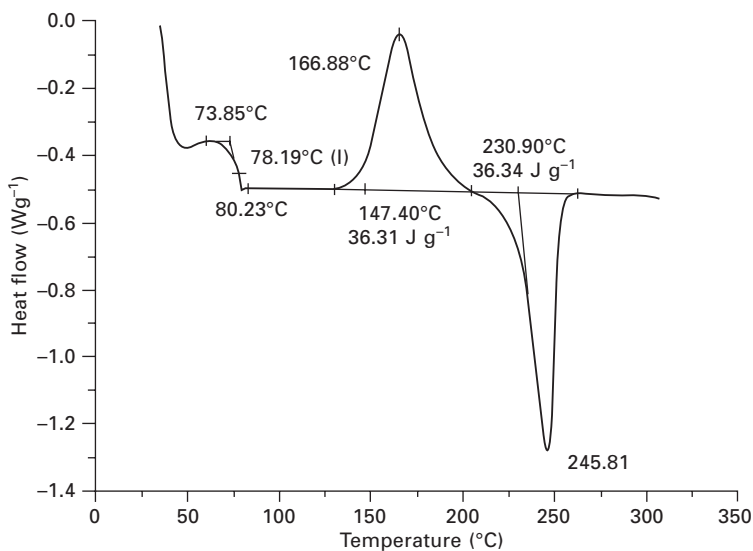
6.3.2 SPP

SPP is used when a higher molecular weight is needed than is practicable by melt polymerization. The polymer chips are firstly intensely dried and annealed at a gradually increasing temperature up to the point of maximum crystallization rate (160–170°C for PET) to encourage a high level of polymer chip crystallinity. This process has to be done with care as the water-quenched polymer chips are almost wholly amorphous and it is most important not to allow them to fuse or sinter together during the annealing step. Once the crystallization process starts, it is exothermic and the chips may fuse locally as a result. The author knows of one instance where several tonnes of polyester chip in a double-cone SPP unit sintered together so firmly that men with jack-hammers were needed to break up the mass in order to remove it! The process of SPP is well explained in textbooks (35). The differential scanning calorimetry (DSC) diagram shown in Fig. 6.2(a) shows a typical DSC trace for commercial PET polymer flake. The T_g inflexion is at 83.9°C and there is a weak endotherm due to a phase transition at 176°C and a T_m at 246°C. Figure 6.2(b) shows the DSC diagram for the same polymer after it has been quenched (or rapidly chilled) from the melt. Note that now there is a lower T_g transition at 78.2°C, a strong crystallization exotherm peaking at 167°C and a T_m endotherm at 245.8°C. Note that the enthalpy of melting has fallen from 40.57 J/g in Fig. 6.2(a) to 36.34 J/g in Fig. 6.2(b), as a result of the lower order of crystallinity.

Annealing raises the effective softening point by many degrees. The annealed chips are heated in a stream of hot inert gas or else agitated in a vacuum drier to remove small traces of glycol and other volatiles. Two main types of SPP apparatus are used: either a fluidized bed reactor where the polymer chips are agitated using a brisk flow of nitrogen or another inert gas, or a twin-cone rotary vacuum drier. A system for an integrated annealing and SPP process has been described (36). One commercial process uses a steady downward plug flow of polymer chips through a tall tower, up which a blast of hot inert gas flows in a countercurrent mode (37).



(a)



(b)

6.2 (a) A typical DSC trace for commercial PET polymer flake; (b) DSC of the same material after quenching from the melt. From W.R. Sorenson *et al.*, *Preparative Methods of Polymer Chemistry*, © 2001 John Wiley & Sons, reprinted by permission of John Wiley & Sons, Inc.

In the solid phase, volatile polymerization by-products have to diffuse only a short way (typically about 1–2 mm) to the surface of each polymer chip. When they reach the surface, they are instantly carried away, either by the gas flow or by high vacuum. The volatiles do not have to form bubbles

in a deep, viscous melt pool and rise to its surface before they can escape. Although solid state diffusion is much slower than diffusion through a liquid, the distances involved are very much shorter; paradoxically, the overall effect is to rapidly increase molecular weight. Since the reaction temperature is below the crystallized polymer softening point, the chips do not sinter together and the lower reaction temperature reduces degradation reactions. As we have said, melt polymerizations reach an equilibrium state where the chain-forming and chain-breaking reactions balance each other and no net chain growth occurs. Solid-state polymerization works so well because it allows chain growth to proceed while minimizing chain-breaking, owing to the difference in kinetics and activation energies of two different sets of reactions. Usually, melt-polymerized PET has an IV (intrinsic viscosity) of about 0.67 (for the significance of this, see above). It is quite possible by using the SPP process to raise the IV to 0.80–1.10. High IV polymer is needed for high tenacity PET fibers for slings and tire cords, and very much so for PET bottle resin. Bottles are made by a high-speed, stretch blow-molding process that is mechanically very severe. PET bottle resin polymer has IV \sim 0.92. Recycled PET bottles are ground up, dried and remelt-spun into polyester yarn for fiber-fill or for PET carpet yarns. One manufacturer (38) says that the so-called 'food grade' PET, made from recycled bottles, gives a more hard-wearing polyester carpet yarn. The higher yarn MW, which increases fiber toughness and work-to-break parameters, is the reason. Normal IV PET fibers are usually regarded as inferior to nylon for both durability and fiber resilience in carpets.

6.3.3 Oligomers

All polyesters based *upon diacids and diols* form cyclic oligomers in small amounts and 2GT, 3GT and 4GT are no exceptions. PET forms a stable, high-melting cyclic trimer which exists in an equilibrium concentration of about 1.8% w/w of polymer (39, 40). It can be extracted from (crystallized) PET chip with a solvent and isolated as a crystalline solid, but on remelting the chip, the oligomer simply reforms. The presence of this cyclic trimer causes awkward problems with fiber and film processing, since it exudes to the polymer surface, coats spinnerets and godet rolls and can be a nuisance during the dyeing of polyester yarns, since it floats around in the dyebath and coats the dyeing equipment. There is little that can be done to remove the oligomer, so processes must be adapted to cope with it. The author recalls a process he once worked on many years ago at Harrogate using a novel non-fuming spin finish which tended to soften the yarn surface. At the hot drawing stage, there was so much deposition of oligomer on the hot rolls that the process became inoperable and the new spin finish was eventually abandoned.

6.3.4 Morphology of PET

PET is a typical semi-crystalline polymer. The crystal habit is triclinic and the crystal parameters shown in Table 14.1 are recent and widely accepted values (41–44). Table 14.2 shows the Mark–Houwink constants for PET in four solvent systems.

6.4 Chemistry of PBT

A more accurate name for this polymer would be poly (tetramethylene terephthalate), but ‘PBT’ is a well-established acronym in the engineering resins business. It is a polyester that dates back to Whinfield and Dickson’s time in 1941 and its history has been complex. Originally developed as a textile fiber, it later became much more important as a thermoplastic *injection molding resin*. Nevertheless, it maintains a fiber presence in the market, chiefly as bulked continuous filament (BCF) carpet fiber, where resilience is important (46).

The essential raw material for PBT is butane-1,4-diol. It is still made commercially by the Reppe process dating back to pre-World War II Germany. One mole of acetylene reacts with two moles of formaldehyde to give

Table 6.1 Physical parameters for PET

Crystal habit	Triclinic, one chain per unit cell
α	100°
β	117°
γ	112°
a	0.444 nm
b	0.591 nm
c	1.067 nm
Cell density, calculated	1.52 g/cm ³
T_m (DSC)	260–265°C
ΔH_f	140 J/g; 33.5 cal/g
T_g (DSC) solid chip	78°C
T_g drawn fiber	120°C

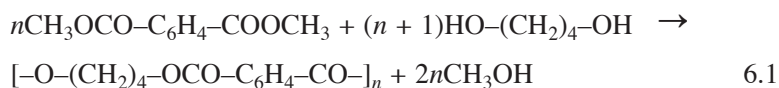
Table 6.2 Mark–Houwink coefficients for PET in various solvents (45)

Solvent	$K(10^{-4} \text{ dL/g})$	α
OCP	6.32	0.658
P/TCE	7.44	0.648
HFIP	5.20	0.723
PPF/HFIP	4.50	0.705

2-butyne-1,4-diol ($\text{HOCH}_2\text{-C}\equiv\text{C-CH}_2\text{-OH}$). This is then hydrogenated to butane-1,4-diol. While the chemistry is simple, a successful process depends on the details. The catalyst for the formaldehyde reaction is a bismuth/cuprous acetylide mixture (47) and the reduction step is better done in two stages with two different catalysts, via the intermediate 2-butene-1,4-diol ($\text{HOCH}_2\text{-CH=CH-CH}_2\text{OH}$) rather than proceeding directly to the end-product (48). Another route has been introduced by ARCO (49) based on the hydroformylation of allyl alcohol over a rhodium catalyst to give 4-hydroxybutyraldehyde, $\text{HOCH}_2\text{CH}_2\text{CH}_2\text{CHO}$. This is reduced to butanediol, but the process needs precise control to prevent side-reactions (50). Allyl alcohol can be made by rearrangement of propylene oxide, made by air oxidation of propylene. A third butanediol route has been piloted by Mitsubishi Chemical Industries (51). They react butadiene with acetic acid and oxygen over a palladium catalyst to form 1,4-diacetoxy-but-2-ene. This diester is hydrogenated (52) to 1,4-diacetoxy-butane and subsequently saponified to butanediol. Whereas ethylene glycol was once used as an antifreeze, butanediol crystallizes at 20°C , so precautions must be taken to heat trace and insulate bulk storage and shipping facilities outdoors to prevent it freezing solid in cold weather.

6.4.1 Manufacture of PBT

PBT is nearly always made using an ester interchange (EI) route from DMT, because heating TA directly with butanediol causes dehydration to the volatile cyclic ether, tetrahydrofuran (THF). Both batch and continuous polymerization processes (53–55) are used. Because vinyl ester ends are not formed by thermal degradation, titanium catalysts can be used without the yellowing problem. The final reaction temperature is around 250°C , so thermal degradation of PBT is reduced compared with PET and higher molecular weight polymers can be obtained by melt polymerization. PBT polymerizations are ‘cleaner’ than PET ones because the major thermal degradation product is THF, which simply boils off. No colorforming reactions are present, although excessive loss of THF can upset the reaction stoichiometry. PBT gives a very white polymer. As with PET, cyclic oligomers are formed in PBT polymer to about the same level, 1.4–1.8% w/w. In this case, the oligomers are an equal mixture of dimer and trimer (56) together with traces of higher cyclic oligomers.



Even though an EI route is used, there is still some loss of butanediol, because the ester chain ends undergo a ‘backbiting’ reaction and eliminate volatile

THF, which flashes off in the melt. Thus the MW can fall even though no color-forming reactions occur.

6.4.2 Properties of PBT

PBT exists in two polymorphs, an α -form and a β -form, and mechanical stress causes them to interchange (57, 58). Both systems are triclinic and the cell parameters are shown in Table 14.3, with the Mark–Houwink parameters shown in Table 6.4. The melting point of PBT is 222–224°C with a heat of fusion (H_f) of 140 J g⁻¹ (59). Its T_g is quoted (60) as 45°C. The annealed (highly crystalline) polymer density is about 1.33 g cm⁻³, while the amorphous polymer has a density (61) of 1.26 g cm⁻³. The relaxed α -form of the polymer is believed to have the three C–C bonds in the C₄ glycol unit arranged in a *trans-gauche-trans* conformation, while the stretched β -form has an all-*trans* arrangement of the same bonds (62).

6.5 Chemistry of PTT or PPT

A comprehensive review of poly(trimethylene terephthalate) and its chemistry and fiber processing has been published (63) by Chuah. Historically, Whinfield and Dickson in 1941 discovered poly(trimethylene terephthalate) along with PET and PBT and it is disclosed in their original patent (6). The material was recognized for many years by textile chemists as a fiber-forming polymer of outstanding resilience. The lack of an economic source of pure 1,3-propanediol (PDO) was an insuperable obstacle for many years, but now the situation has changed dramatically and 3GT fibers are a commercial fact.

Table 6.3 Crystal parameters for PBT

Cell parameter	Alpha-form (stretched)	Beta-form (stretched)
a (nm)	0.482	0.469
b (nm)	0.593	0.580
c (nm)	1.174 (1.165)*	1.3000
α (degrees)	100 (98.8)*	102
β (degrees)	115.5 (116.6)*	120.5
γ (degrees)	111	105
Cell density, g/cm ³	1.41	1.37

*These alternative values are from I M Ward and co-workers (58).

Table 6.4 Mark–Houwink parameters for PBT

Parameter	K (dL/g)	α
OCP solvent	6.62×10^{-6}	0.915
Phenol/TCE	1.17×10^{-4}	0.870

There is some confusion on an acronym for this polyester. Shell prefers to use the term PTT (polytrimethylene terephthalate) but DuPont and some earlier trade literature sources call it PPT [poly(propylene terephthalate)]. The latter is, strictly speaking, inaccurate, since the term 'propylene glycol' is conventionally applied to 1,2-propanediol. The Shell nomenclature is used here to avoid ambiguity, because this acronym emphasizes the *three-carbon* glycol unit.

6.5.1 The synthesis of PDO

Since PDO is the vital intermediate for PTT, it is worth outlining the various routes to its production. There are three main ones: two synthetic and one based on a biochemical (fermentation) route. A detailed report on the economic prospects for both PDO and PTT polymer was completed in 1999 (64). Degussa and Shell first developed the synthetic methods, which have now become commercial processes. In the Degussa process, water is added under pressure to acrolein, using an acidic ion exchange resin to give 3-hydroxypropionaldehyde (65):



The hydroxy-aldehyde is not isolated but is hydrogenated in aqueous solution over a Raney nickel catalyst (66). Acrolein has been manufactured by Degussa since the late 1930s, originally by condensation of acetaldehyde with formaldehyde, but later by a 1959 process using the air-oxidation of propylene (67). One problem with the Degussa reaction is the presence of acrolein dimer (2-formyl-2,3-dihydropyran) which reacts with PDO to form adducts and hemiacetals that are immiscible with the diol and cause turbidity. One method of removing these impurities is solvent extraction with cyclohexane (68).

The more recent Shell process uses hydroformylation (carbon monoxide plus hydrogen) of ethylene oxide to give 3-hydroxypropionaldehyde using synthesis gas and a transition metal catalyst. The aldehyde is then reduced to PDO. One of the first processes was by Beavers (Eastman Kodak) who used a rhodium or ruthenium catalyst (69). Shell improved upon this with a cobalt catalyst and there has been much patent activity on improved catalysts and conditions (70–73). The hydrogenation of 3-hydroxypropanal to PDO has been improved with better catalysts. Haas (74) uses a platinum or ruthenium catalyst, while Shell workers disclose nickel–molybdenum (75). The first commercial PDO plant using the Shell technology was actually opened in 2000 in Geismar, Louisiana. In 2003 it was announced (76) that it would be uprated to supply PDO to a new 50/50 venture formed between Shell and the Société Générale de Financement du Québec called PTT Poly Canada who are building a 95 000 tonne/year PTT polymer plant in Montreal (77).

A somewhat different process has been described in a 2001 Shell patent (78) where the starting material is methyl 3-hydroxypropionate rather than 3-hydroxy-propanal. The ester is made by reacting ethylene oxide with carbon monoxide and methanol using cobalt octacarbonyl as the catalyst. The hydroxy-ester is hydrogenated, without isolation, using a copper–zinc oxide catalyst. Greater efficiency is claimed, because esters do not form acetals and hemiacetals which contaminate the final product.

DuPont has taken a bold step for its source of PDO. The DuPont process is a modified enzymatic fermentation route using corn sugars (largely glucose) as feedstock to give PDO directly (79, 80), an ambitious application of ‘green chemistry’. Yeast converts sugars into the phosphate ester of dihydroxyacetone and thence to glycerol. It has long been known that certain bacteria can reduce glycerol to PDO (81) under anaerobic conditions. The difficulty lies in running a *high-yield* fermentation process without poisoning the bacteria with high levels of PDO. There is much patent activity in this area (82–85).

In collaboration with Genencor International, DuPont used genetic engineering to produce novel strains of the common bacterium *Escherichia coli*, genetically modified with genes from baker’s yeast (*Saccharomyces cerevisiae*) and the bacterium *Klebsiella pneumoniae*, to give improved conversions. A recent patent (86) claims a microorganism that will operate at PDO levels of 105 g/liter.

Isolation of PDO from the fermentation broth involves either solvent extraction or distillation. Several routes have been patented. One method, due to Archer Daniels Midland Co., uses ion exclusion resins (87) while a recent DuPont patent claims the use of molecular sieves (88). In June 2003, DuPont was awarded a Presidential Green Chemistry Challenge Award (89) for the PDO biosynthetic process. In May 2004 a new joint US venture called DuPont Tate & Lyle Bio-Products LLC was announced to manufacture industrial intermediates from renewable resources (e.g. corn, wheat) rather than petroleum. The product is named Bio-PDO™ and the \$100 million plant at Loudon, Tennessee, opened in mid-2006. According to a DuPont press release, the first saleable batch of Bio-PDO™ was shipped on 27 November 2006 (90). As well as using PDO for polymers like 3GT, it is also marketed as a high grade, low toxicity, biodegradable diol for personal care products called Zemea™ and other grades are being used industrially under the trade name Susterra™. The manufacturers claim that their bio-process plant uses 40% less energy and emits 20% less greenhouse gases than an equivalent operation using petroleum-based chemistry. It is also said to be free from any toxins and carcinogens that could be present in synthetic PDO.

6.5.2 PTT polymerization

PTT is polymerized in a significantly different way from PET (63). Either TA or DMT can be used, but Shell prefers the direct esterification route based upon TA. So far the process is like that for PET. However, unlike for PET, active metals such as titanium or tin can be used as polymerization catalysts (91–93) since yellowing is not a problem, because there are no vinyl ester ends. Unusually, the reaction is carried out *semi-batchwise* using a molten ‘heel’ of low MW polymer, left behind from the previous batch, as a reaction medium for the next batch. Whereas in the cases of PET, TA is soluble in hot ethylene glycol, it is not soluble in hot PDO, which boils at 214°C, so the uncatalyzed DE step must be run at 250–270°C under pressure. When esterification is complete, the mixture of oligomers is partially transferred to a polymerization vessel, leaving the ‘heel’ behind for the next esterification. The tin or titanium catalyst is then added and the final polymerization step is run under vacuum at 260–270°C. The polymer IV is 0.70–1.00. For IVs exceeding 1.0, polymer chips can be annealed and crystallized at 180–210°C and solid phase polymerized at 180–210°C in a current of inert gas. DuPont used a continuous polymerization process (94) in their plant at Kingston, NC.

As usual, there are side reactions. Two harmful degradation products result from the McLafferty rearrangement and pyrolysis of the PTT ester links, analogous to the degradation of PET (95). The products are allyl alcohol and its oxidation product, acrolein. Both are toxic and irritant, acrolein being particularly unpleasant. Addition of triaryl phosphites and hindered phenol antioxidants is claimed (96) to minimize acrolein formation. Special precautions must be taken to dispose of the vapors of such by-products during polymer processing. PTT also forms cyclic oligomers: in this case the dimer, which can be isolated as a crystalline solid, melting point 254°C. As with DEG formation in PET, ether-link formation takes place by dehydration of 3-hydroxypropyl ester ends, and this leads to *bis*(3-oxypropyl) ether links in the main chain, which lower the polymer melting point, just like DEG links in PET.

6.5.3 PTT morphology

PTT has a particularly interesting crystal structure. Once again the crystal system is triclinic, but along the *c* axis, two polymer chains lie with the glycol units twisted into *gauche-gauche* conformations so that the chains form tight zigzags as seen in the *ac* and *bc* planes. Crystal parameters (97–99) are given in Table 6.5. PTT has $T_m = 228^\circ\text{C}$; $\Delta H_f = 30$ kJ/mol repeat unit (146 J/g); $T_g = 45^\circ\text{C}$; cold crystallization temperature = 68°C (100–103).

Table 6.5 Crystal parameters for PTT

Parameter	Value
<i>a</i> (nm)	0.459
<i>b</i> (nm)	0.621
<i>c</i> (nm)	1.831
α (degrees)	98
β (degrees)	90
γ (degrees)	112
Crystal density	1.441 g/cm ³

Table 6.6 Mark-Houwink constants for PTT

Solvent	Temperature (°C)	<i>K</i> (10 ⁻⁴ dL/g)	α
HFIP	35	5.51	0.71
50/50 phenol/TCE	30	8.20	0.63
60/40 phenol/TCE	20	5.36	0.69

6.5.4 Polymer molecular weight

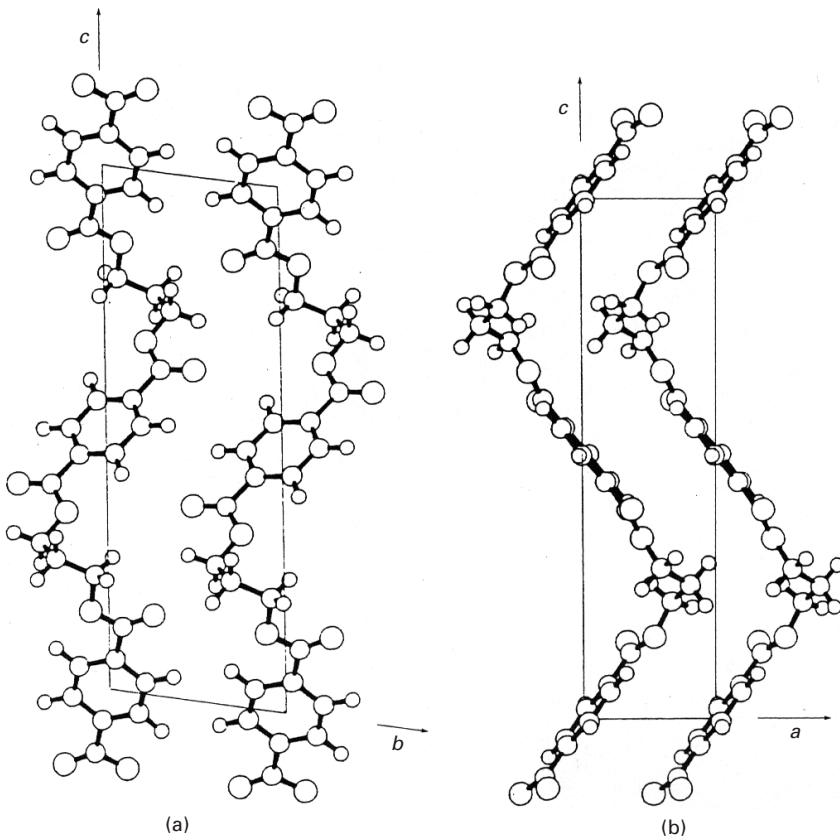
PTT crystallizes much faster than PET, although not quite as fast as PBT. This means that the quenched polymer chips are highly crystalline and do not dissolve at all easily in the usual polyester solvents. As a result, Shell uses hexafluoroisopropanol (HFIP) at room temperature as a viscometry solvent. A phenol-tetrachlorethane mixture can be used, but the temperature has to be carefully raised to 110°C to ensure complete dissolution. Mark-Houwink constants (104, 105) are shown in Table 6.6 for three solvent systems.

6.5.5 PTT resilience

Of the three major polyester fibers, PTT has by far the best resilience, that is, the best elastic recovery from deformations (106). According to DuPont information (107) on their PTT fiber *Sorona*[®], PTT flat yarn recovers 100% from elongations as high as 120%. It is vastly superior to PET and 2–3 times better than nylon-6,6 in this respect. PBT fiber, by comparison, recovers 100% from elongations of about 112%. Resilience is a valuable property in both textiles and carpet fibers. It was found the hard way, in the very early days of PET fiber development, that fine denier polyester filament yarns made into ladies' hose were a disaster because they quickly went 'baggy' around the knees! PTT would be expected to perform much better. DuPont information says that PTT gives extremely high fiber bulk in conventional draw texturing processes and thus yields superior covering power for the same weight of fiber.

The reason for the excellent recovery properties of PTT is due to its

crystal structure. It has a very low crystal modulus (108) (2.59 GPa, 550 psi) and the zig-zag structures (see Fig. 6.3) give a tightly wound helical structure to the polymer chains so that they can be imagined as behaving like coil springs on elongation. This is a naive explanation, but it is roughly true and easily understood. It is the double-*gauche* conformation of the two C–C bonds in the trimethylene chain that allows this structure to form. By contrast, PET is more fully extended and its crystal modulus (109) is much higher (107 GPa, 1.55×10^5 psi). PBT is an intermediate case: it is more elastic than PET because the four-carbon chains are not fully extended and likewise contain *gauche* conformations.



6.3 (a, b) X-ray study of PPT polymer crystal structure. Reprinted from I.J. Desborough, I.H. Hall and J.Z. Neisser, 'The structure of poly(trimethylene terephthalate)', *Polymer*, 1979, 20, 545, with permission from Elsevier.

6.6 Chemistry of PEN

A comprehensive review of PEN polymer chemistry and its use in film, fibers and molded articles was published in 2004 by Sakellarides (110). As already described, the diacid NDA is made by oxidation of 2,6-dimethylnaphthalene, but the majority of PEN polymer is made via the dimethyl ester of NDA (called NDC) because, like TA in the early days, it is not yet possible to make NDA of sufficient purity for direct esterification economically. The oxidation of dimethylnaphthalene is not as simple as that of *p*-xylene, because of extra side-reactions that do not occur with one benzene ring. Naphthalene molecules necessarily have one benzene ring and a quinonoid ring, which is more vulnerable to nuclear oxidation. Hence it is not surprising that trimellitic acid (benzene 1,2,4-tricarboxylic acid) is produced, as well as trimellitic anhydride (111). Another problem is that the bromide anion, a co-catalyst in the oxidation, brominates the naphthalene ring and one of the NDA impurities is a monobromo-NDA. In the early 1990s, Amoco built a plant to make NDC at Decatur, Illinois, and production of PEN began on a sizeable scale. Most of the output goes into high performance films, but blow-molded bottles and high modulus, low stretch fibers like Pentex™ are also made.

PEN has a higher T_m and T_g than PET. Table 6.7 compares directly PET, PBT and PEN, while PBN, the fast-crystallizing polymer from NDA and 4G, is included for comparison purposes.

6.6.1 Melt polymerization process

PEN can be made either by a batch or a continuous melt-phase polymerization (CP) process using NDC ester and ethylene glycol, very much like PET. The reactivities of DMT and NDC are similar and the same catalysts for both EI and polymerization are used; in fact PEN can be made on PET equipment with minor alterations in process temperature. Both batch and continuous polymerization processes have been used (112). Typically for PEN, the final

Table 6.7 Comparison of T_m and T_g for various polymers

Homopolymer	T_m (°C)	T_g (°C)
PET	250	80
PEN	268	125
PBT	223	46
PBN	242	82

Source: data supplied by BP Amoco Chemical Co. (110).

melt stage would be at 295°C. The melt viscosity of PEN is significantly higher than that of PET, even at lower IV values, and melt polymers usually have an IV in the range 0.4–0.6 dL/g. For many PEN end-uses, particularly bottle resin, SPP is necessary to raise the IV. The crystallization temperature is higher, around 180–220°C, as the T_g is higher and the SPP process is run at 240–260°C rather than at 210–240°C as for PET. Typical PEN polymers after SPP have IV values in the range 0.55–0.70 dL/g (113).

6.6.2 Properties and morphology of PEN

PEN is a semi-crystalline polyester, but it resembles PET in that quenching from the melt gives an amorphous phase with a density of 1.325 g/cm³, slightly lower than that of amorphous PET, which is 1.333 g/cm³. Like PBT and unlike PET, PEN forms two distinct polymorphic forms, called the α -form and the β -form. Both are triclinic (like PET) but the cell coefficients are different. Table 6.8 gives a direct comparison between the three unit cells.

PEN is used increasingly in high-performance polyester films and for high softening-point blow-molded bottles and containers. It was commercialized in 2002 by Honeywell Performance Fibers (formerly Allied Signal) as a high-performance fiber under the name Pentex[®] for industrial uses such as tire cord, belting, cordage and high-performance sailcloth, all markets where its high modulus, low stretch and good UV resistance have obvious advantages. The fiber is presently marketed in several gages from 560 dtex/70 fils to 1670 dtex/210 fils. The quoted tensile values for tenacity, modulus and elongation are 8.0 cN dtex⁻¹ (9.1 g/den), 220 cN dtex⁻¹ (250 g/den) and 6% respectively (116). The UV resistance is due to the naphthalene ring, which absorbs radiation about 18–20 times more strongly and over a wider range of wavelengths (300–390 nm) compared with PET.

Table 6.8 Comparison of three unit cells

Parameter	PET	α -PEN*	β -PEN [†]
Form	Triclinic	Triclinic	Triclinic
<i>a</i> (nm)	0.456	0.651	1.314
<i>b</i> (nm)	0.594	0.575	0.904
<i>c</i> (nm)	1.075	1.320	1.219
α (°)	98.5	81.2	129.31
β (°)	118	144	88.62
γ (°)	112	100	90.77
Calculated density (g/cm ³)	1.455	1.407	1.436

Sources: *Ref. 114, † Ref 115.

6.6.3 Melt-processing PEN

The main uses (70%) of PEN polymer are in high-performance, low-shrink polyester films with a smaller market, particularly in Japan, for blow-molded bottles for hot-fill end uses and as a UV-protective container for drugs and vitamins such as Vitamin C. Cosmetics are also packaged in clear PEN molded containers. However, although the scale is only about 15% of total PEN production, PEN fibers are produced. As well as Pentex™, Teijin in Japan, Kosa in Europe and Hyosung in Korea make PEN fiber. One market for PEN fibers is tire cord, where its high modulus, tenacity, low heat shrinkage and good heat-resisting properties are eminently suitable. The starting polymer is usually made to high IV, about 0.90, made by an SPP process. Physical properties of various competing high-strength polymers are compared in Table 6.9.

In 1999 Pirelli, the well-known Italian tire manufacturer, began to market tires made with PEN cords for both high-performance automobiles and motorcycles. The properties of PEN fiber are well suited to high-stress applications like these. Bridgestone Tires also make tires with PEN fiber. Reduction in tire weight becomes possible and the stiffness and rigidity of PEN cord reduces rolling resistance and improves gas mileage. It also reduces road noise, so that such tires are specified for up-market, high-end vehicles like the Lexus. There is also a drive to replace steel radial tire belts with a high-performance synthetic polymer to reduce weight, an elusive target pursued for 30 years or more. Aramid fibers have been used on racing cars, but they are too expensive for general use except for the most luxurious automobiles. PEN offers advantages, notably that it has good fatigue properties at low twist levels and a better compressive modulus than aramid fibers.

Another in-rubber market for high performance PEN fibers is belt and hose reinforcement fibers in automobile engines. As internal combustion engines grow more efficient and produce more power for their size, working

Table 6.9 Physical properties of various high-strength polymers (references in brackets)

Parameter	PEN	PET (117)	Nylon 66 (116)	Rayon (118)	Aramid (119)
Density	1.36	1.39	1.14	1.52	1.44
Tenacity (N/tex)	0.9 (120, 121)	0.8	0.8	0.44	2.0
Modulus (N/tex)	32 (120)	9.7	4.4	11	49
Elongation (%)	8 (121)	14	15	12	4
BWS*	1 (120)	5	8	Decomp.	<0.1
DHS†	4 (120)	8	10	6	<0.1

* Boiling water shrinkage.

† Dry heat shrinkage.

temperatures rise appreciably. The physical and chemical properties of PEN fiber resist mechanical and chemical stress in hot, wet environments and the fibers adhere well to rubber. Their modulus and fatigue resistance is outstanding and on a price/performance basis they outperform both aramids and PET cords.

Marine cordage and sailcloth are related areas where PEN fibers ought to excel, with a combination of high modulus, low stretch and a built-in resistance to UV radiation from sunlight. Pentex™ high tenacity PEN fiber was introduced into sailcloth in 1997 (122). Aramids have poor UV resistance: in fact, in extreme cases where sailboats race in major competition, sails may be replaced after each run (123).

6.7 Chemistry of aliphatic polyesters

Polyesters from hydroxyacetic acid (glycolic acid) were investigated early in the twentieth century since hydroxyacetic acid is potentially cheap, but their easy hydrolysis made them unsuitable for use as textiles and industrial yarns. Very much later, in the 1960s, it was realized that this apparent weakness could be exploited in the rapidly growing specialized area of biomedical polymers. A good review of synthetic biodegradable polymers has been published by Middleton and Tipton (124). Other reviews of environmentally friendly degradable polymers and specific biomedical polymers are available (125, 126).

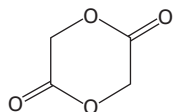
The first market opportunity was dissolvable sutures, which need no surgical removal. Suture materials have strict requirements if they are to be 'safe and effective' in FDA terms. These are listed below:

1. The suture must maintain integrity until the tissues heal.
2. The suture must not be so strong that it tears the tissue: its strength must be compatible with its end-use.
3. The material must not cause inflammatory or toxic reactions.
4. The suture must dissolve without trace, and not produce harmful metabolites.
5. The material should be readily processable into high-grade sutures.
6. It should have a long shelf-life.
7. Sutures must withstand sterilization regimes without degradation.

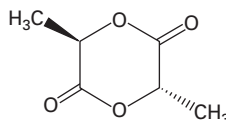
The earliest biomaterials were all polyesters but other polymers (notably polyurethanes and polyanhydrides) have since been developed, particularly in the area of controlled drug release, though these do not concern us here. A summary of the main monomers and the properties of their homopolymers is set out in Table 6.10. Degradation times are usually measured under so-called 'physiological conditions', i.e. pH 7.4 with a phosphate buffer at 37°C.

Table 6.10 Biodegradable polyester properties (homopolymers)

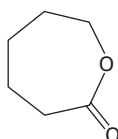
Polymer	$T_m(^{\circ}\text{C})$	$T_g(^{\circ}\text{C})$	Modulus (GPa)	Degradation time (months)
Polyglycolide	225–230	35–40	7.0	6–12
Poly-L-lactide	173–178	60–65	2.7	> 24
Poly-DL-lactide	Amorphous	55–60	1.9	12–16
Polycaprolactone	58–63	–65	0.4	> 24
Polydioxanone	Depolymerizes	–10	1.5	6–12



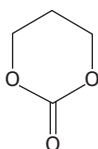
Glycolide



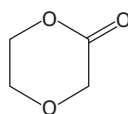
Lactide



Caprolactone



Trimethylene carbonate



Dioxanone

Structure 6.6 Monomers for biodegradable polyesters.

6.7.1 Monomers

Structure 6.6 shows the five monomers most often used in degradable polyesters. All are polymerized by ring-opening mechanisms, often with a tin catalyst such as stannous octoate or dibutyltin dilaurate. We will go through the properties of polymers derived from each of these monomers in turn.

6.7.2 Polyglycolide (PGA)

The polyester from self-condensation of hydroxyacetic acid is usually called polyglycolide after its dimeric lactone, glycolide. Polymerization is done by ring-opening (127), often with a Sn(II) salt such as stannous octoate. PGA is a highly crystalline polymer that melts at 225–230°C and has a T_g

of 35–40°C. It is a strong, stiff polymer with a modulus of about 7.0 GPa. PGA was first commercialized as a suture material under the name Dexon[®] in the late 1960s by Davis & Geck (now Sherwood-Davis & Geck). Because of its high crystallinity, it is insoluble in common polyester solvents, except very acidic ones such as hexafluoroisopropanol. It loses about 50% of its initial strength in 2 weeks and 100% in 4 weeks but takes 4–6 months to vanish completely. PGA is simply too stiff to make single filament (monofil) sutures; braided sutures of finer multifilaments are more flexible. A bioerodible ABA tri-block copolyesterether with a polyethylene glycol (PEG) block capped at both ends by PGA segments gives a satisfactory flexible monofil suture (128). This is made by a double-ended ROP reaction using a di-anion of the PEG segment.

6.7.3 Polylactide (PLA)

Polylactide is derived from the dimeric lactone of lactic acid (lactide), which can exist in D, L, racemic (DL) and meso forms. The naturally occurring variety is the L-form. The racemic form is a synthetic mixture of D- and L-lactides, while the meso form is made up of one molecule of D and one of L in a cyclic dimer. Only the stereochemically pure forms give highly crystalline polyesters. They have structures analogous to isotactic polypropylene. Poly (DL)-lactide is amorphous and is more easily degraded, which makes it more attractive in drug-delivery systems. Pure poly-L-lactide is about 37% crystalline and melts at 175–178°C. It degrades much more slowly than the amorphous form and can take up to 2 years to disappear completely. Copolymers of L-lactide and DL-lactide are used to graduate the biodegradation rate. The relationship between biodegradation rate and polymer composition is nonlinear. For example, a copolymer of 50% glycolide and 50% DL-lactide degrades faster than either homopolymer. Copolymers of glycolide with L-lactide containing 25–70% glycolide are amorphous owing to the disruption of chain regularity because of the copolymer effect. Ethicon markets a suture material made from 90% glycolide and 10% L-lactide under the trade name Vicryl[®]. This is absorbed completely in 3–4 months, but its strength retention is longer than that of pure glycolide (129, 130). A typical synthesis of polylactide or lactide–glycolide copolymers is given in a US Patent by Okuzumi and co-workers (131).

6.7.4 Polycaprolactone (PCL)

Caprolactone is the seven-membered ring lactone of epsilon-hydroxycaproic acid, made by a Baeyer–Villiger oxidation of cyclohexanone. In the presence of a stannous octoate catalyst it undergoes ROP to the homopolymer polycaprolactone. This melts at 59–64°C and has a very low T_g (–60°C). It

has a low modulus but forms strong, elastic, biocompatible fibers. Because it is more hydrophobic than either lactide or glycolide polymers, it has a long degradation time, of the order of 2–3 years. It is often combined with other monomers to reduce the degradation time. A block copolymer of caprolactone and glycolide is marketed by Ethicon (132, 133) under the brand name Monacryl[®].

6.7.5 Polydioxanone

Another monomer that undergoes ROP is 2-dioxanone, originally made by the reaction of disodium glycoloxide with chloroacetic acid. This monomer is polymerized with organometallic catalysts such as diethylzinc or zirconium acetylacetonate. It gives an alternating polyester–ether structure and forms a highly crystalline (55%) polymer with a low T_g (-10°C). It makes soft and flexible fibers well suited for sutures, but it has the disadvantage of depolymerizing readily on heating and thus it has to be melt-spun at as low a temperature as possible. It is a very biocompatible material which loses about 50% of its strength in 3 weeks; it is fully absorbed in 6 months. It is marketed by Ethicon as ‘PDS filament for sutures’. (134)

6.7.6 Polytrimethylene carbonate (TMC)

The cyclic carbonate of trimethylene glycol is readily synthesized by reacting trimethylene glycol with phosgene, an alkyl chloroformate or dimethyl carbonate (135–137). It easily undergoes ROP reaction and forms useful copolymers with glycolide and lactide. Typically these are made as ABA tri-block copolymers with terminal PGA segments. Davis & Geck market a glycolide–TMC copolymer suture under the name Maxon[®]. These copolymers are more flexible than pure PGA and lose 80% of their strength in 2 weeks but then decline more slowly, maintaining 25% of their strength after 7 weeks. They are fully absorbed within about 12 months.

6.7.7 Sterilization and packaging

All suture materials must be rendered sterile (124) before packaging ready for implantation and this is done either by chemical treatment (ethylene oxide gas) or by irradiation (gamma rays or electron beam, called E-beam). Ethylene oxide is effective but highly toxic, and all traces must be removed from the suture package before it is sealed.

Irradiation with ionizing radiation causes damage to all α -hydroxyacid polymers, and the level must be held to no more than about 2 Mrad. Since the degradation of these materials is primarily due to hydrolysis, they must be kept scrupulously dry. Packaged sterilized sutures are thoroughly vacuum-

dried and maintained in an anhydrous state by internal desiccants. They are usually stored in a freezer at around -20°C to ensure adequate shelf-life.

6.7.8 Mechanism of degradation

The actual breakdown of the polyesters *in vivo* is quite complex, although it is simpler for sutures than it is for drug release polymers because fibers have a much higher surface/volume ratio. Basically there are two mechanisms operating: bulk erosion and surface erosion, and these have different kinetic effects on strength loss. The process is described in a comprehensive article (138) by von Burkersroda *et al.* There are always two separate processes operating. One is the rate of diffusion of water into the material *in vivo*, and the other is the rate of chain-breaking reactions (hydrolysis). If the rate of hydrolysis is faster than the rate of water ingress, the polymer will surface-erode, a desirable state of affairs for a drug-release polymer. If the rate of chain breaking is slower than the rate of water diffusing into the material, then the latter becomes the rate-determining step and bulk erosion takes place. All commercial sutures degrade by bulk erosion, but the exact route of strength loss is a complicated process. All sutures are semicrystalline materials, so hydrolytic attack occurs first in the amorphous regions since these are more easily penetrated. The fiber is held together by those crystalline domains which remain unattacked, even though the overall molecular weight may have fallen appreciably. Eventually, after a catastrophic loss of strength, the structure falls apart. The fragments of monomer and oligomers are slowly broken down and metabolized in the body into harmless by-products, eventually to carbon dioxide and water. This is why the final disappearance can take many months, even though the zero-strength time may be only a few weeks.

6.8 Chemistry of disposable fibers

A new area for biodegradable polymeric materials based upon non-petroleum source biomass-derived raw materials has started to develop. The topic has been comprehensively reviewed by Stevens (125). There are two distinct areas here – polymeric materials that are compostable and environmentally friendly and minimize environmental damage, and those derived from natural renewable resources (biomass). These areas often overlap. A significant market for biodegradable fiber-forming polyesters has opened up with the emergence of Cargill Dow Polymers as a large-scale manufacturer of cheap L-lactide, derived from fermentation of cornstarch (139). Poly(L-lactide) is highly crystalline, and a less brittle fiber and film result if a little imperfection is introduced into the polymer chain to break up the regularity (140). The lactide was originally intended for biodegradable and compostable polylactide packaging film materials under the name Natureworks[®], but one

fiber manufacturer at least (FIT, Inc.) is interested in the implications for disposable fabrics (such as towels, diapers, wipes, etc.), where nonwovens predominate. J. Dugan, of that company, says that polylactide fiber has many good textile properties and could have a significant market in the disposable fabrics area. He has also used lactide polymer as a matrix for an 'islands in a sea' type of bicomponent fiber with PET to make PET microfibers by hydrolysis of the lactide. (141)

Another naturally derived polymer is Biopol[®], a copolymer made up of various poly- β -hydroxyacid ester units, notably the copolyester from 3-hydroxybutyric acid (PHB) and 3-hydroxyvaleric acid (PHV). These polymers belong to a class of polyesters called poly(3-hydroxyalkanoates) and the area has been recently reviewed by Ramsay and Ramsay (142). It has been known since the 1920s that certain bacteria, when starved of nitrogen, will make poly(hydroxybutyric acid) and store it as an energy source in the form of solid granules in the cells, much as higher organisms store fat globules. An early patent reference (143) to PHB is one by Baptist of W R Grace in 1962. Biopol[®] was originally made from bacterial sources by ICI on Teesside, UK, in the early 1970s, when ICI was developing large-scale fermentation reactors to produce single-cell bacterial protein for cattle feed. This project was not a commercial success, so the protein fermentation pilot plant was adapted to produce bacterial polyester on a comparatively large production scale (144). The chief microorganism used was *Alcaligenes eutrophus*, and the food source was usually glucose (145–148). As much as 80% dry weight of cells was polyester under optimal fermentation conditions. In 1990 ICI underwent a corporate reorganization and Biopol was eventually acquired by Monsanto, who continued the work and made important changes. Most notably, they found that PHB could be made from genetically modified higher plants such as *Arabidopsis thaliana* (leaves) and *Brassica napus* (seeds) and harvested by simple solvent extraction or expression, as used for rapeseed oil. But eventually Monsanto divested itself of the product in 1998, and it has now been taken up by Metabolix Inc. in Cambridge, MA, who obtained a US Department of Energy grant in 2001 to continue the studies (149).

Biopol is a crystalline thermoplastic with a melting point in the range 170–190°C. Its structure is much like isotactic polypropylene, since all the side groups project on the same side of every chain. Like a peptide, the chain has a helical conformation, but unlike peptides, this is due to non-bonded interactions between the carbonyls and the methyl groups. There are no hydrogen bonds, and this helix formation is unique. Biopol has a problem in that it tends to embrittle by secondary interlamellar crystallization. Biopol to date can hardly be called a commercial success, but it has been thoroughly investigated. A review of PHB polymer and copolymer production by Poirier *et al.* (150) was published in 1995. PHB has not been widely investigated as a fiber-forming polymer, although one idea is monofilaments for biodegradable

fishing nets. It is not suitable for sutures, since it does not break down by simple hydrolysis *in vivo*. It degrades both aerobically and anaerobically when exposed to certain lipases, as when composted or exposed to marine environments. It is likely to be of greater use as a disposable, environmentally friendly, thermoplastic polymer. A recent patent (151) describes the use of copolymers of 3-hydroxy and 4-hydroxalkanoates in medical devices such as bone screws, etc. These materials have been described by Hori *et al.* (152) and can be produced by a biosynthetic route (153) using recombinant bacteria such as *Escherichia coli*.

6.9 Melt-spinning polyester fibers and associated fiber processing

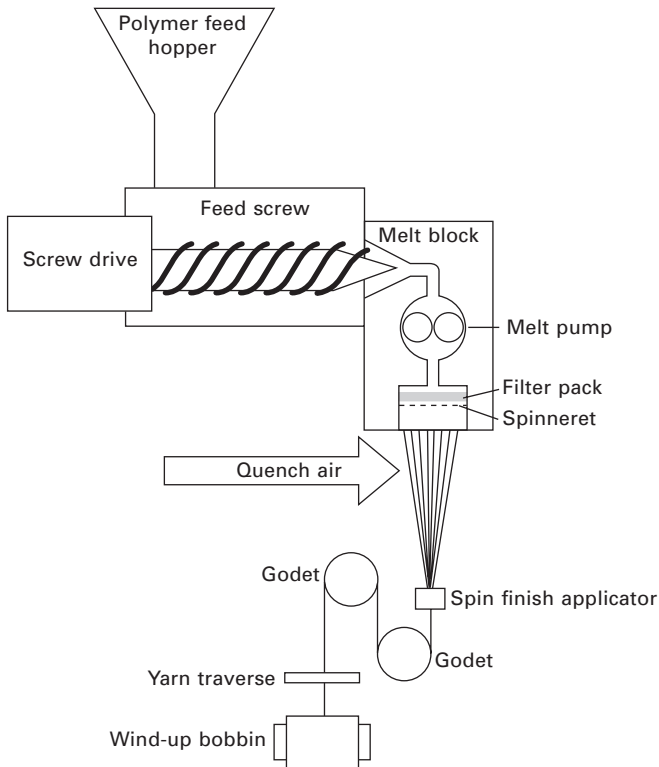
6.9.1 Introduction

This is a large topic and, for detailed descriptions, the reader is referred to specialized publications dealing with the subject. Good accounts will be found in Davis and Hill's article (154) on fiber spinning. The present chapter will give only a broad outline, and will deal only with PET melt spinning, by virtue of its huge volume. All synthetic fibers fall into two main categories: continuous filament yarn (F/Y) and *staple fiber*, which is discontinuous and cut to short lengths for blending with natural fibers like wool and cotton. This blending is done just prior to carding, and the blended and carded (combed) fibers are then twisted together ('spun') in modern versions of a process that dates back several millennia.

6.9.2 Filament yarn melt-spinning

Filament and staple polyester are melt-spun under different conditions, and their subsequent fiber processing is quite different. The melt-spinning process is simple in theory, yet complex in practice if optimum fiber properties are to be achieved. A diagram of a schematic F/Y melt spinner is shown in Fig. 6.4.

Rigorously dried polymer (moisture content < 30 ppm), stored in a sealed feed hopper and sparged with dry nitrogen, is melted at a temperature some 15–25°C above its crystalline T_m in a device such as a screw-extruder. The melt passes from the extruder under a positive back-pressure into the melt block. A coarse screen filter is interposed between the end of the screw extruder and the block. The heated block has a number (usually 2–8) of spinning packs within it, although only one is shown in the diagram. Each spinning pack has its own pump, auxiliary filter and spinneret assembly. The polymer melt is precisely metered by a positive displacement gear pump which delivers a fixed amount of polymer per revolution. The melt is



6.4 Schematic diagram of a typical F/Y melt spinner.

filtered just prior to the spinneret (to remove foreign bodies that might plug spinneret holes) by forcing it through either a filter bed made of particles of silica or aluminum oxide, or a shattered metal filter. Finally the melt is forced through tiny holes, typically 0.007–0.015 inch (0.180–0.400 mm) in diameter in a spinneret plate. The whole pack assembly is heated to the spinning temperature (usually 280–300°C) so the pack seals and gaskets are designed to function at this high temperature and prevent polymer leaks under pressures that can approach 5000 psi. Ideally, the thermal history of the whole polymer melt is uniform, with no dead spots, stagnant zones or circuitous melt pathways. Differing thermal histories lead to different thermal degradations along the yarn. This leads to unacceptable non-uniformity in the final dyed fabric.

The molten threadlines emerge from the spinneret and solidify as they fall. The cooling process is accelerated by a controlled flow of non-turbulent quenching air. Passing next around a take-off roll or ‘godet’, the bundle of filaments are wound up on a yarn package or sent directly to other processing steps. One very important parameter is the thickness of the as-spun filament,

and this is measured by the *denier count*, which is the weight in grams of 9 km of yarn. The official metric system uses the *decitex count*, which is the weight of 10 km of yarn (hence decitex is $1.11 \times$ denier); but it seems that the textile industry in much of the world (including the USA) resolutely retains the denier count, an archaic measurement dating back to the Lyon silk industry in eighteenth-century France!

Denier is decided by a combination of polymer density, polymer throughput in grams per hole per minute (fixed by the number of holes and the metering pump calibration and speed) and the wind-up speed in meters per minute at the godet surface. The polymer throughput per hole is usually in the range 1.0–5.0 g/hole/min. The linear speed (jetting velocity) of the polymer emerging from the spinneret is appreciably less than the haul-off speed at the godet: the ratio is called the *draw-down factor*. This stretching as the polymer cools induces molecular order and orientation in the fiber and develops tensile properties. The degree of orientation is measured on the spun filament by determining the optical birefringence. This is often done manually on a small sample of fiber with a polarizing microscope and a device called a Berek Compensator. As the wind-up speed increases, so does the birefringence in an exponential curve: at a wind-up speed of 3500 m min^{-1} , a typical PET spun yarn has a birefringence of about 50×10^3 units (154).

There are three regimes of F/Y spinning speed: slow speed is below 1000 m/min; medium-speed is run at 1000–4000 m/min, while high-speed spinning is run at over 4000 m/min. Very high spinning speeds introduce so much molecular orientation that the yarn needs little further drawing (155). This process is called ‘POY’, from the acronym for ‘partially oriented yarn’. One of the major technical breakthroughs in the 1970s was the introduction of high-speed yarn winders that made large yarn packages or ‘cheeses’ (typically 7 kg of yarn) and would run at over 4000 m/min (150 mph). The yarn traverse device was the stumbling block, for without a high-speed traverse to keep pace with the wind-up speeds, the process could not run. The problem was to reverse the traverse *instantaneously* at the end of each cross-stroke with no trace of ‘dwell’, or else the package would build up at the edges and the yarn simply slough off the package. Engineering solutions were found; nowadays, take-up speeds are even higher, as much as 8000 m/min (300 mph) (156–158).

Filament yarn drawing

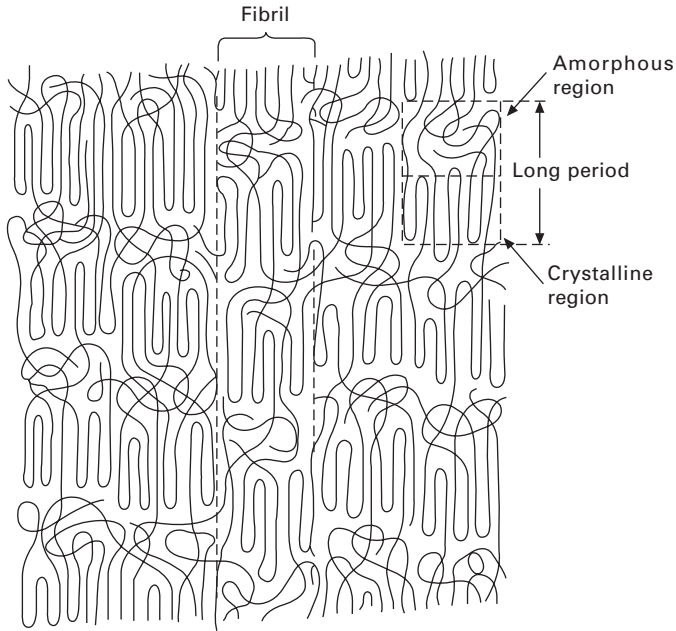
Although molecular orientation is partly introduced by the drawdown, the main increase in order is brought about by a separate drawing process (159). All fiber-forming polymers of adequate molecular weight show the phenomenon of cold drawing on stretching. The undrawn fiber (or a strip of film) necks down and elongates, and crystallization often occurs, evident

from a change in luster in the drawn filament, due to its optical anisotropy. PET fibers in the as-spun state are generally amorphous. They have molecular orientation but only become crystalline with oriented crystallites when fully drawn. Polymers such as PBT and nylon 6,6 form crystalline spun fibers, but they still need a drawing stage to develop full molecular orientation. It is the combination of molecular orientation and the presence of polymer chain crystallites to 'lock' this orientation into place, which governs such important parameters as tenacity, elongation at break and heat-shrinkage. In order for drawing to be effective, the fiber has to be elongated considerably, the ratio of yarn feed to draw-roll haul-off speed being the draw ratio. It can be anything from 1.5 up to 6.0 times. At higher draw ratios the yarn shrinkage falls and so does the elongation to break. The draw point where fiber necking takes place must be stabilized at a fixed point. In the early days this was done by a stationary heated metal pin, around which the yarn passed. The pin drawing temperature is set at about 10°C above T_g (i.e. about 85–90°C for PET) since at this temperature the polymer is in a rubbery state. The polymer chains are thus free to move and can reorganize and reorient themselves under the mechanical stress of the drawing process. Drawing is notably exothermic, as can easily be demonstrated by cold-drawing a narrow strip of undrawn PET film and carefully touching the film to the lower lip. Cold-drawing is somewhat thermodynamically analogous to the adiabatic compression of a gas. Once the drawing process starts, little heat is needed to keep it going. To stop the drawn yarn from having an unacceptable degree of heat shrinkage, the yarn has to be heat-set by passing it over a long hotplate at about 130–140°C, which is well above the effective T_g (125°C) of the drawn, oriented and crystallized yarn. The heat-setting stage encourages the final development of maximum molecular order and crystallinity; it may be considered as a continuous annealing process.

A diagram of the morphology of an oriented, partly crystalline PET fiber is shown in Fig. 6.5. This simple system was adequate when draw speeds were low (500 m/min) but as speeds rose, separately heated feed rolls and draw rolls were needed to achieve the same effect. The heated rolls allowed longer contact times for thermal transfer, the yarn being usually wrapped four or five times around each roll and a small idler roll. The draw ratio has a major effect on yarn elongation and tenacity. As one might expect, high draw ratios give high-tenacity yarns with higher yarn moduli and lower extensions; low draw ratios give lower tenacities with much more extension. A semi-empirical rule connecting elongation to break (e_b) and engineering tenacity (t) has been established (160) which says:

$$t = K/e_b^\alpha$$

where K and α are constants. Experimentally, $\alpha \sim 0.3$. K is a measure of



6.5 Morphology of PET fiber showing various features. Reprinted from H.F. Mark, 'Polyester fibers', in *Encyclopedia of Polymer Science and Technology*, © 2003 John Wiley & Sons, reprinted by permission of John Wiley & Sons, Inc.

the inherent fiber strength and is related to the molecular weight, hence polymer IV.

Heavy-duty industrial yarns for tire cords and for uses such as car safety belts are drawn under conditions favoring maximum yarn modulus and tenacity and minimum stretch.

Filament yarn texturizing

Drawn filament yarn can be treated in any number of ways. It may simply be wound onto a yarn package, or twisted on a ring frame as 'flat yarn' or sent for a yarn texturizing process. Many apparel yarns must be texturized or 'bulked' to give desirable aesthetics and textile properties, particularly for women's wear markets. This may be done in a separate operation or combined with the drawing process ('draw-bulking'). Draw-bulking or 'draw textured-yarn' (DTY) often uses POY yarns as a feedstock, since the required draw ratio is low, only about 1.6-fold. The topic of yarn bulking is highly specialized and related to textile yarn processing. Readers wanting detailed process descriptions are advised to consult reputable specialist sources. Several excellent books (161) and various websites (162, 163) are available.

Industrial filament yarn

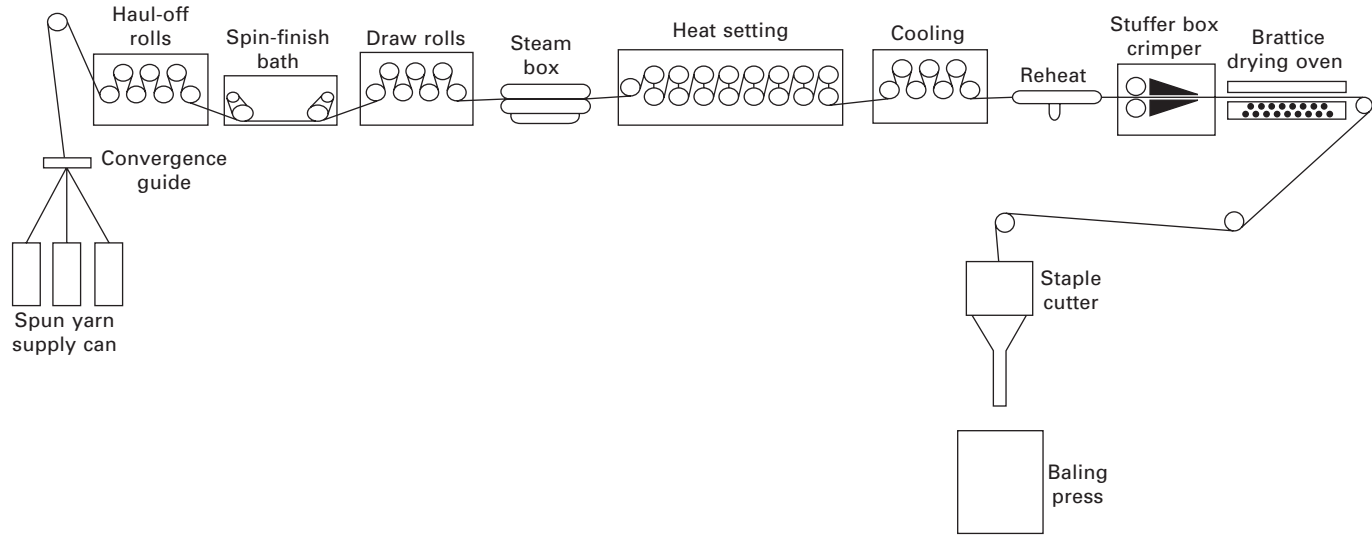
High-tenacity filament yarns for industrial use, such as tire cord, have to be melt-spun and drawn to give a high-modulus, low-heat-shrinkage, low-extension, high-tenacity product (usually called HMLS yarns) and special spinning and drawing conditions are needed. Some industrial yarns are made by a continuous polymerization spin-draw route (CP-spin-draw). Since industrial yarns are made to higher IV than apparel yarns, higher spinning temperatures are needed. To develop the high tensile properties, the yarn drawing may need to be done in a two-stage process to develop the exact characteristics required (164, 165).

Very low work loss (hysteresis) is important in car tires running at high speeds, because the constant flexing of the cord could build up serious tire heating if cord internal work loss were excessive. Tire cord is a highly specialized product. Other uses for high-strength polyester industrial yarns are reinforcing fibers for V-belts, hoses, and crane slings and automobile seat belts.

6.9.3 Staple fiber

The demands of staple fiber production are very different from those of filament yarns. The fibers are melt-spun using a large diameter, high-throughput extruder as the polymer melter. The melt is then metered via a high-capacity metering pump through a filtered staple spinning pack with a spinneret plate containing a large number of holes, many hundreds at a time. The bundle of fibers is hauled off via a bank of multiple godets (to prevent slippage) but it is not wound up; instead, the yarn is deposited loosely via an air-ejector into a large yarn drum or 'can'. When the yarn can is full, the fiber bundles from many cans are combined into a thick 'tow' which may have a yarn count of 1–5 million decitex.

This thick bundle of fibers is then drawn on a massively constructed drawframe (because the mechanical forces involved in drawing such a thick bundle of fibers are very considerable) using multiple feed rolls and draw rolls. It is heat-set in a steam-heated hot-box. The drawing is often done in two or even three stages. The drawn tow then passes to a crimper, often of the stuffer-box type. Here the tow is over-fed into a heated wedge-shaped compartment which compresses it into a concertina crimp. The stuffer box has a weighted or sprung trap door so that excess amounts of yarn are released mechanically and in this way the degree of crimp is controlled (166). The bulked tow is finally cut to the desired staple length by one of several proprietary designs of continuous staple cutter (167). The loose cut fiber is then compressed with a hydraulic press into bales. A schematic diagram of a staple line is shown in Fig. 6.6. A large staple unit can produce 200–300



6.6 Diagram of staple draw frame, showing only a single-stage drawing. Two or even three drawing stages are frequently used.

tonnes of staple fiber per day, which is later blended with cotton, wool or other natural fibers.

6.9.4 Spin finishes

All fibers need to be treated with a surface finish that alters the frictional characteristics of the yarn surface. Without it, the various processing steps such as drawing, texturizing and textile processing would be impossible, because so many of the processes rely on specific frictional properties of the fiber (for example, friction disk texturizing). Spin finishes are often water emulsions of various surfactants, either nonionic or anionic, with various lubricant mineral oils. Finish formulation is complex and something of an art as well as a science (168). Application of the finish is made early in the process, before the cooling threadline from the melt spinner hits the first godet. In early days, the finish was usually applied as a water emulsion from a smooth lick roll rotating slowly in a bath of spin finish. As spinning speeds increased, the finish was applied directly via a hollow ceramic guide as a neat oil formulation and metered at precise levels from a positive-feed metering pump. High-speed yarn texturizing processes have particularly difficult finish requirements: they cannot fume nor pyrolyze in the heater tubes of the texturizing machine. Polysiloxane oils are often used in these special formulations (169). Staple fiber is usually sprayed with emulsified finishes or else the whole tow is immersed in a bath of finish, and this may need to be repeated at intervals along the process chain. Some staple processes locate the drawing stage with the tow immersed in a hot bath of emulsified spin finish.

6.10 Effect of fiber structure on properties

The relationship between the polymer chemical structure and the physical properties of the resulting fiber is an area of continuing fascination for fiber scientists. Even after many decades, we have only sketchy ideas about the exact relationships. That said, some principles are well understood. The best fiber-forming polymers are linear, crystalline polymers with some mechanism to stiffen the chains and hold them together. Polyamides like nylon rely on inter-chain hydrogen bonds, while polyesters like PET rely on stiff rings in the chain. Polyesters like polycaprolactone are very 'floppy', although they are crystalline. The long aliphatic methylene chain has weak chain-to-chain forces, thus giving a low T_m (63°C) and a very low T_g (-60°C). On the other hand, polycaprolactam (nylon-6), which differs only by having a -CONH- group in place of -COO-, melts at 215°C. This illustrates the effectiveness of inter-chain hydrogen bonding. Nylon-6,6 melts at 260°C, very close to PET. Again hydrogen bonds are the reason. If the hydrogen

bonds are reduced by making a partially *N*-alkylated nylon, there is a serious fall in polymer softening point and the polymer becomes partly amorphous and becomes more soluble in solvents (170). PET has no hydrogen bonds but it does have many stiff 1,4-disubstituted benzene rings and these make the chains much more rigid, hence the high polymer melting point and T_g . PBT and PTT melt at lower temperatures than PET and have a lower T_g because they have longer and more flexible alkylene chains. If we combine terephthalic acid with ethylene diamine, we get nylon-2T which has both stiff rings and hydrogen bonds. Not surprisingly, this nylon melts at well over 400°C (171).

The effectiveness of stiff in-chain rings is well demonstrated by DuPont's Qiana™ fiber, a somewhat exotic nylon introduced in the 1970s made from diaminodicyclohexylmethane (PACM) and dodecane-1,12-dioic acid. The alicyclic diamine group has *trans-trans*, *cis-trans* and *cis-cis* rings in the polymer. It melted at 290°C (172). By the same token the rigid naphthalic acid group in PEN causes a significant rise in T_m and T_g over PET. PEN also shows the effect of structural anisotropy in the chain: the 2,6-naphthalenedicarboxylic acid increases substantially the aspect ratio of the acid group over terephthalic acid, which causes a significant rise in fiber modulus. A copolymer of 50/50 PEN and PEBB (from 4,4'-bibenzoic acid) gave a polyester with a tensile modulus of over 300 g/denier (173). This copolymer enters the region of thermotropic liquid crystal aromatic polyesters which form nematic melts and can give extremely high tensile properties (174).

While some empirical rules for high fiber modulus have been established, it is not so easy to predict good fiber resilience. As we have seen already, the particularly good recovery properties of PTT (which are better than nylon) seem to be due to the unique crystalline structure of PTT.

6.11 Conclusions

6.11.1 World markets, future trends and thoughts for the future

The total world market for polyester is about 25 million tonnes. Consumption is still growing, although at the time of writing (2008) the rate of increase is smaller than the 5–8% per year that was common hitherto. Over the past 20 years, there have been cataclysmic changes in the polyester producing fiber business. There has been a gradual eclipse of the textile industry in the USA and Western Europe, and it has shifted to Asia and other places, such as Central America and parts of Eastern Europe. The old-established, integrated synthetic fiber firms which were offshoots of chemical companies, such as DuPont, ICI, Hoechst and Monsanto, have vanished. In 2002 DuPont hived off its fiber interests as Invista, which was merged with KoSa in April

2004. KoSa and Invista are part of Koch Industries, and Invista, which is independently managed, is one of the world's largest integrated fiber and polymer producers. Along with the old companies, Eastman maintains a US presence, although most of its fiber output is cellulose acetate.

The new fiber producers buy polyester polymer on the open market as a commodity item and convert it into fiber and yarn. They have revolutionized the polyester market and superseded the old order. Invista, for example, buys 3GT polymer from Shell and spins Corterra[®] fibers and markets them, although Shell retains the trademark. KoSa announced in late 2002 a plan to expand the former Hoechst facility in Mexico (175) to make tire cord. Giant firms such as Wellman Industries and Invista in the USA and others in the Far East now dominate the picture. The emergence of China as a major consumer and as a growing producer of polyester fiber will have a further large effect on world markets.

The market for polyester fiber will certainly continue to grow overall, although as a major commodity item it is likely to be affected very much more than in the past by global economics and trade cycles. Certainly, the steep price increase of raw materials such as crude oil and natural gas will have a serious effect on process costs and markets. Nevertheless, there is still a trend to replace other fibers, both natural and synthetic, with polyester. Nylon is still losing overall markets to polyester. At present, nylon dominates polyester in domestic carpet yarns, but PET has a growing share of the contract carpet trade because it is cheaper. The new polyester microfibers and easy-to-dye polyesters with excellent resilience are expected to make big inroads into floor coverings and the apparel markets over the next few years.

A major change will surely be the drive to replace petrochemical sources with renewable bio-derived materials. DuPont's decision to invest in a large-scale plant for a fermentation route to PDO now looks like highly prescient foresight! Looking ahead, there are new non-oil-based biomass-derived processes in commercial production for making not just the intermediates for polyesters, but even the polymers themselves. The effect of a resurgence of recycling such valuable materials as polyester bottles into fiberfill and carpet yarns may also have unpredictable consequences.

There are likely to be surprising innovations in both fibers and fabrics. Thermochromic dyes, perhaps based on cholesteric liquid crystals (developed for LCD TV screens) which could change a fabric's color with ambient temperature, are one idea, as well as luminous fabrics (using OLED technology) and ones that change their luster and iridescence. Fibers that change their bulk inversely with temperature could lead to high comfort insulation when conditions are cold, changing to a less bulky, cooler material when it becomes warm again. Polyesters are likely to play a significant part in such innovative materials because of their price/performance ratio.

There has been a popular sentiment for many years that polyesters are an inferior substitute for the supposedly superior 'natural' fibers. This is a fallacy, since natural fibers have many deficiencies: cotton shrinks, linen wrinkles, wool shrinks, creases and is susceptible to moths! Polyester has boosted the overall performance of natural fibers in the form of blended yarns and fabrics ever since it was commercially available in the late 1940s! The latest generation of polyester fibers now emerging, such as polyester microfibers and the highly resilient and stain-resistant PTT fibers, and others that will follow, will meet, in their own right, the market demands of a new generation of fiber consumers in a constantly changing world.

6.12 Sources of further information

There are a number of good books that contain instructive reading on the subject of synthetic fibers in general and polyester fibers in particular. Two recent ones are *Synthetic Fibers, Nylon, Polyester, Acrylic, Polyolefin*, edited by J. E. MacIntyre (Woodhead Publishing, 2005) and *Handbook of Fiber Chemistry*, third edition, edited by M. Lewin (Taylor & Francis 2007). Much valuable and specific information can be found in reference books, notably the *Encyclopedia of Polymer Science and Technology*, third edition (John Wiley & Sons) and the *Kirk-Othmer Encyclopedia of Science and Technology*, fourth edition (John Wiley & Sons). For those who want to learn about yarn texturizing, there is *Yarn Texturing Technology* by Hearle, Hollick and Wilson (Woodhead, 2001); and for others interested in fiber and fabric dyeing, a very comprehensive work is *The Chemistry and Application of Dyes* by Waring and Hallas (Plenum Publishing, 1994).

6.13 References

1. Bharat Book Bureau, Mumbai, India, 1 March 2007.
2. Reese G., 'Polyester fibers', in *Encyclopedia of Polymer Science and Technology*, 3rd ed, Vol. 3, Wiley, New York, 2003, pp. 652–678.
3. Brown A.E. and Reinhart K.A., 'Polyester fiber: from its invention to its present position', *Science*, 1971, 16 July, pp. 287–293.
4. Mark H. and Whitby G.F., editors, *The Collected Papers of W.H. Carothers*, Interscience, New York, 1940.
5. Staudinger H., 'Über Polymerization', *Ber Deut Chem Ges*, 1920, 53, 1073.
6. Whinfield J.R. and Dickson J.T. (Imperial Chemical Industries Ltd), GB Patent 578 079, June 1946; also Whinfield J.R. and Dickson J.T. (E I duPont de Nemours & Co., Inc.), US Patent, 2 465 319, March 1949.
7. Clarke P. and Plage A., 'The development of a modern BCF carpet yarn from polybutylene terephthalate', *Chemiefasern Textilindustrie*, January 1990.
8. Chuah H.H., 'Polytrimethylene terephthalate', in *Encyclopedia of Polymer Science and Technology*, 3rd ed, Vol. 3, Wiley, New York, 2003, pp. 544–557.
9. *Chem Eng News*, 2003, 81(26), 33–34.

10. Cook J.G., Hugill H.P.W. and Low A.R. (Imperial Chemical Industries Ltd), GB Patent 604 073, 1948.
11. Harper J.J., Kuhlmann G.E., McMahon R.F., Sanchez P.A. and Larson K.D. (Amoco Corporation), US Patent 5 181 533, February 1993.
12. Abe T., Seiji U., Ojima T. and Kida K. (Mitsubishi Gas Chemical Company Inc.), US Patent 5 008 479, April 1991.
13. Inamasa K., Fushimi N. and Takagawa M. (Mitsubishi Gas Chemical Company Inc.), US Patent 5 276 230, January 1994.
14. Inamasa K., Fushimi N. and Takagawa M. (Mitsubishi Gas Chemical Company Inc.), US Patent 5 321 178, June 1994.
15. Pentex announcement.
16. myPlasticsindustry.com: Announcement, 1 October 2007.
17. Laurich S.A. (Chevron Research), US Patent 3 467 724, September 1969.
18. Broughton D.B. (Universal Oil Products Co.), US Patent 3 636 180, January 1972.
19. Witts W.S., *Chem Proc Eng*, 1970, 51, 55.
20. Meyer D.H. (Standard Oil Co.), US Patent 3 584 039, June 1971.
21. Milgrom J., *Outlook for Plastics Recycling in the USA*, Decision Resources Inc., 1993, pp. 25–27.
22. Domeshek K.A., in *Tomorrow's Ideas and Profits: Polyester: Fifty Years of Achievement*, editors Brunnschweiler D. and Hearle J., The Textile Institute, Manchester, 1993, pp. 288–290.
23. Barringer E.A. and Bowen H.K., *J Amer Ceram Soc*, 1982, 65C, 199.
24. Martl M. *et al.* (Akzo-Nobel NV), US Patent 5 684 116, November 1997.
25. Martl M. *et al.* (Akzo-Nobel NV), US Patent 5 789 528, August 1998.
26. Wilfong R.E., *J Polym Sci*, 1961, 54, 388.
27. ICI Ltd, French Patent 1 169 659, 1959.
28. Easley W.K. *et al.* (Chemstrand Corporation), Canadian Patent 573 301, 1959.
29. Zimmerman H. and Kim N.T., *Polym Sci Eng*, 1980, 20, 680–683.
30. Adams L.J. (Eastman Kodak Co.), US Patent 4 501 878, February 1985.
31. Loudon G.M., *Organic Chemistry*, 3rd ed, Benjamin/Cummings, Menlo Park, CA, 1995, p. 897.
32. Zimmerman H. and Kim N.T., *Polym Sci Eng*, 1980, 20, 680–683.
33. Mark H. and Whitby G.F., editors, *The Collected Papers of W.H. Carothers*, Interscience, New York, 1940, p. 22.
34. Davis G.W. and Hill E., *Kirk-Othmer Encyclopedia of Chemical Technology*, 3rd ed, Vol. 18, Wiley, New York, 1982, p. 535.
35. Sorensen W., Sweeney F. and Campbell T.W., editors, *Preparative Methods of Polymer Chemistry*, 3rd ed, Wiley, New York, 2001, pp. 181–185.
36. Herron D.J. (Bepex Corporation), US Patent 4 161 578, July 1979.
37. Callender D.G., *Polym Sci Eng*, 1985, 25, 453–457.
38. Mohawk Carpet Co., see <http://www.mohawkcarpets.com/fiber.html>.
39. Goodman I. and Nesbitt B., *J Polym Sci*, 1960, 48, 423–433.
40. Shiono S., *J Polym Sci, Polym Chem Ed*, 1979, 17, 4123.
41. Daubeny R. de P. and Bunn C.W., *Proc R Soc London, Ser A*, 1954, 226, 531.
42. Fakirov S., Fischer E.W. and Schmidt G.F., *Makromol Chem*, 1975, 176, 2459.
43. Bornscheegl E. and Bonart R., *Colloid Polym Sci*, 1980, 258, 319.
44. Kitano Y., Kinoshita Y. and Ashida T., *Polymer*, 1995, 36, 10.
45. Berkowitz S., *J Appl Polym Sci*, 1984, 29, 4353–4361.

46. Clarke P.G. and co-workers (Davy McKee AG), US Patent 4 877 572, October 1989.
47. Hort E.V. (G.A.F. Corp.), US Patent 3 920 759, November 1975.
48. Rudolf S. and DeThomas W. (G.A.F. Corp.), US Patent 3 950 441, April 1976.
49. Taylor P.D. (Celanese Corp.), US Patent 4 064 145, December 1977.
50. de Munck N.A. and Scholten J.F. (Stamicarbon BV), US Patent 4356125, October 1982.
51. Onoda T. and co-workers (Mitsubishi Chemical Industries Ltd), US Patent 3 922 300, November 1975.
52. Toriya M.J. and Shiraga K. (Mitsubishi Chemical Industries Ltd), US Patent 4 010 197, March 1977.
53. Heinze H. and co-workers (Davy McKee AG), US Patent 4 499 262, February 1985.
54. Pipper G. and co-workers (BASF AG), US Patent 4 973 655, November 1990.
55. Jackson R. and co-workers (E I du Pont de Nemours & Co., Inc.), US Patent 5 064 935, November 1991.
56. East G.C. and Girshab M., *Polymer*, 1982, 23, 323–324.
57. Hall I.H. and Pass M.G., *Polymer*, 1976, 17, 12.
58. Jakeways R., Ward I.M. and Wilding M.A., *J Polym Sci, Polym Phys Ed*, 1973, 13, 807–809.
59. Illers K.H., *Colloid Polym Sci*, 1980, 258(2), 117.
60. Cheng S.Z.D., Pan R. and Wunderlich B., *Makromol Chem*, 1988, 189, 2443.
61. Tashiro K. and co-workers, *Macromolecules*, 1980, 13, 137.
62. Jaquiss D.B., Borman W.F.H. and Campbell R.W., *Kirk-Othmer Encyclopedia of Chemical Technology*, 3rd ed, Vol. 18, Wiley, New York, 1982, p. 552.
63. Chuah H.H., 'Polytrimethylene terephthalate', in *Encyclopedia of Polymer Science and Technology*, 3rd ed, Vol. 3, Wiley, New York, 2003, pp. 544–557.
64. Process Economics Report No. 227: 1,3-Propane Diol and Polytrimethylene Terephthalate, SRI International, 1999.
65. Arntz D. and co-workers (Degussa AG), US Patent 5 015 789, May 1991.
66. Haas T. and co-workers (Degussa AG), US Patent 5 334 778, August 1994.
67. *Kirk-Othmer Encyclopedia of Chemical Technology*, 3rd ed, Vol 1, Wiley, New York, 1978, p. 286.
68. Breitkopf N. and co-workers (Ruhchemie AG), US Patent 5 008 473, April 1991.
69. Beavers W.A. (Eastman Kodak Co.), US Patent 4 973 741, November 1990.
70. Weider P.R. and co-workers (Shell Oil Co.), US Patent 5 689 016, November 1997.
71. Shaugh L.H. and co-workers (Shell Oil Co.), US Patent 5 723 389, March 1998.
72. Shaugh L.H. and co-workers (Shell Oil Co.), US Patent 5 731 478, March 1998.
73. Shaugh L.H. and co-workers (Shell Oil Co.), US Patent 5 841 003, November 1998.
74. Haas T. and co-workers (E I du Pont de Nemours & Co., Inc.), US Patent 6 297 408, October 2001.
75. Arhancet J.P. and co-workers (Shell Oil Co.), US Patent 6 342 464, January 2002.
76. See www.shellchemicals.com/1_3_propanediol.
77. *Chem Eng News*, 28 June 2004, 15.

78. Forschner T.C. and co-workers (Shell Oil Co.), US Patent 6 191 321, February 2001.
79. Tran-Dinh K. and Hill F.F. (Hüls AG), DE Patent 3 734 764 A1, May 1989.
80. Nair R.V. and co-workers (E I du Pont de Nemours & Co.; Genencor International, Inc.), WO Patent 9928480, June 1999.
81. Gottschalk G. and Averhoff B. (Unilever Patent Holdings BV), US Patent 5 164 309, November 1992.
82. Kretschmann J. and co-workers (Henkel Kommanditgesellschaft auf Aktien), US Patent 5 254 467, October 1993.
83. Nagarajan V. and Nakamura C.E. (E I du Pont de Nemours & Co., Inc.), US Patent 5 633 362, May 1997.
84. Nagarajan V. and Nakamura C.E. (E I du Pont de Nemours & Co., Inc.), US Patent 5 821 092, October 1998.
85. Emptage M. and co-workers (E I du Pont de Nemours & Co., Inc.), US Patent 6 514 733, February 2003.
86. Donald T.E. and co-workers (Genencore International Inc.), US Patent 6 558 933, May 2003.
87. Hilaly A.K. and Binder T.P. (Archer-Daniels-Midland Co.), US Patent 6 479 716, November 2002.
88. Corbin D.R. and Norton T. (E I du Pont de Nemours & Co., Inc.), US Patent 6 603 048, August 2003.
89. *Chem Eng News*, 2003, 81(26), 33–34.
90. DuPont Press Release: see www.newswire.com/mnr/dupont/26198.
91. Kuratsuji T. and Miki T. (Teijin Ltd), US Patent 4 611 049, September 1986.
92. Doerr M.L., Hammer J.J. and Dees J.R. (Hoechst Celanese Corporation), US Patent 5 340 909, August 1994.
93. Kurian J.V. and Liang Y. (E I du Pont de Nemours & Co., Inc.), US Patent 6 281 325, August 2001.
94. Giardino C.J. and co-workers (E I du Pont de Nemours & Co., Inc.), US Patent 6 353 062, March 2002.
95. Schauhoff S., *Chem Fibres Int*, 1996, 46, 263.
96. Kelsey D.R. (Shell Oil Co.), US Patent 6 093 786, July 2000.
97. Desborough I.J., Hall I.H. and Neisser J.Z., *Polymer*, 1979, 20, 545.
98. Poulin-Dandurand S. *et al.*, *Polymer*, 1979, 20, 419.
99. Moss B. and Dorset D.L., *J Polym Sci, Polym Phys Ed*, 1982, 20, 1789.
100. Lee K.M., Kim K.J. and Kim Y.H., *Polymer (Korea)*, 1999, 23, 56.
101. Huang J.M. and Chang F.C., *J Polym Sci, Polym Phys Ed*, 2000, 38, 939.
102. Pyda M. *et al.*, *J Polym Sci, Polym Phys Ed*, 1998, 36, 2499.
103. Chuah H.H., *Polym Eng Sci*, 2001, 41, 308.
104. Chuah H.H., Lin-Vien D. and Soni U., *Polymer*, 2001, 42, 7137.
105. Traub H.L. *et al.*, *Angew Makromol Chemie*, 1995, 230, 179.
106. Ward I.M., Wilding M.A. and Brody H., *J Polym Sci, Polym Phys Ed*, 1976, 14, 263.
107. Sorona® Technical Information Bulletin, ‘The Start of a High-performance Fiber’, DuPont, 2001 (obtainable from the Sorona® website).
108. Nakamae K. *et al.*, *Zairyo*, 1986, 35, 1066.
119. Sakurada I. and Kaji K., *J Polym Sci Part C*, 1970, 31, 57.
110. Sakellarides, S.L., *Encyclopedia of Polymer Science and Technology*, 3rd ed, Vol. 11, Wiley New York, 2004, pp. 88–113.

111. Machida, H. and co-workers (Mitsubishi Gas Chemical Co. Inc.), US Patent 6013831, January 2000.
112. Research Disclosure 29, 487, 1988.
113. Sakellarides; *loc cit*, ref. 111, p. 99.
114. Mencik Z., *Chem Prim*, 1978, **17**(2), 78.
115. Liu J., Myers J., Geil P., Kim J C and Cakmak M., *ANTEC 97 Technical Papers*, Volume XLIII, Society of Plastics Engineers, 1997, p. 740.
116. DuPont Technical Bulletin, X-272, Type 717.
117. Allied Technical Bulletin P-1, 1300–1392.
118. Avtex Fibers Inc., Brochure, Type 120 Yarn.
119. Dupont Technical Bulletin X-272, Kevlar 29 Type 964.
120. Teijin Ltd, GB Patent 1445464, October 1973.
121. Allied Signal, World Patent WO 93/14252, 1993.
122. Amoco NDC, 'Elements', News Update, Spring 1997.
123. Geoff Thomas, yachtsman, private communication.
124. Middleton J.C. and Tipton A.J., 'Synthetic biodegradable polymers as medical devices', *Medical Plastics Biomater*, March 1998.
125. Stevens E.S., 'Environmentally degradable plastics', in *Encyclopedia of Polymer Science and Technology*, 3rd ed, Vol. 6, Wiley, New York, 2003, pp. 135–162.
126. Kumar N., Krasko M., Ezro A., Ehrenfroind T and Domb A.J., 'Biodegradable polymers – medicinal uses', in *Encyclopedia of Polymer Science and Technology*, 3rd ed, Vol. 5, Wiley, New York, 2003, pp. 263–285.
127. Schmitt E.E. and Pollistina R.A. (American Cyanamid Company), US Patent 3297033, January 1967.
128. Casey D.J. and Roby M.S. (American Cyanamid Company), US Patent 4452973, June 1984.
129. Perrin D.E. and English J.P., 'Polylactide and polyglycolide', in *Handbook of Biodegradable Polymers*, editors Domb A.J., Kost J. and Wiseman D.M., Harwood Academic Publishers, New York, 1997.
130. Cam D., Hyon S. and Ikada Y., *Biomaterials*, 1995, **16**, 833–843.
131. Okuzumi Y., Mellon A.D. and Wasserman D. (Ethicon, Inc.), US Patent 4157437, June 1979.
132. Perrin D.E. and English J.P., 'Polycaprolactone', in *Handbook of Biodegradable Polymers*, editors Domb A.J., Kost J. and Wiseman D.M., Harwood Academic Publishers, New York, 1997.
133. Hiljanen-Vainio M., Karjalainen T. and Seppala J., *J Appl Polym Sci*, 1996, **59**, 1281–1288.
134. Doddi N., Versfelt C.C. and Wasserman D. (Ethicon, Inc.), US Patent 4052988, October 1997.
135. Boon W.H. and co-workers (Shell Oil Co.), US Patent 6451949, September 2002.
136. Bowman M.P. and Kreutzberger C.B. (PPG Industries Ohio, Inc.), US Patent 6506909, January 2003.
137. Bowman M.P. and Kreutzberger C.B. (PPG Industries Ohio, Inc.), US Patent 6580001, June 2003.
138. von Burkensroda F., Schedl L. and Göpferich A., *Biomaterials*, 2002, **24**, 4221–4231.
139. See <http://www.cargilldow.com>.
140. Drumright R.E., Gruber P.R. and Henton D.E., *Adv Mater*, 2000, **12**, 1841.

141. Dugan J.S., *Novel Properties of PLA Fibers*, Fiber Innovation Technology, Inc., Johnson City, TN, 2000.
142. Ramsay B.A. and Ramsay J.A., 'Poly 3-hydroxyalkanoates', in *Encyclopedia of Polymer Science and Technology*, 3rd ed, Vol. 5, Wiley, New York, 2002, pp. 263–285.
143. Baptist J.N. (W.R. Grace & Co.), US Patent 3044 942, July 1962.
144. Holmes P. *et al.*, 'Biologically produced R-3-hydroxyalkanoate polymers and copolymers', in *Developments in Crystalline Polymers*, Elsevier, London, 1988, pp. 1–65.
145. Barham P.J. and Holmes P.A. (Imperial Chemical Industries PLC), US Patent 4427 614, January 1984.
146. Holmes P.A. and co-workers (Imperial Chemical Industries PLC), US Patent 4477 654, October 1984.
147. Barham P.J. and Selwood A. (Imperial Chemical Industries PLC), US Patent 4391 766, July 1983.
148. Organ S.J. and co-workers (Imperial Chemical Industries PLC), US Patent 5 281 649, January 1994.
149. Metabolix Inc., Cambridge, MA, press release, October 2001.
150. Poirier Y., Nawrath C. and Somerville C., 'Production of polyhydroxyalkanoates, a family of biodegradable plastics and elastomers, in bacteria and plants', *Bio/Technology*, 1995, 13, 142–149.
151. Williams S.F. and co-workers (Metabolix, Inc.), US Patent 6 548 569, April 2003.
152. Hori Y. *et al.*, *Polymer*, 1995, 36, 4703–4705.
153. Valentin H., 'Production of poly (3-hydroxybutyrate-co-4-hydroxybutyrate) in recombinant *E. coli* grown on glucose', *J Biotechnol*, 1997, 58, 33–38.
154. Davis G.W. and Hill E.S., 'Polyester fibers', in *Kirk-Othmer Encyclopedia of Chemical Technology*, 3rd ed, Vol. 18, Wiley, New York, 1982, pp. 531–539.
155. Clayton G. and co-workers, *Text Prog*, 1976, 8(1), 31.
156. Schubert G., *International Textile Bulletin* (World Edition Spinning 3), 1980, 229.
157. Koschinek G. and co-workers (Davy McKee AG), US Patent 4 436 688, March 1984.
158. Richardson J. (Imperial Chemical Industries PLC), US Patent 5 182 068, January 1993.
159. Davis G.W. and Hill E.S., 'Polyester fibers', in *Kirk-Othmer Encyclopedia of Chemical Technology*, 3rd ed, Vol. 18, Wiley, New York, 1982, p. 539.
160. Reese G., 'Drawing of spun filaments', in *Encyclopedia of Polymer Science and Technology*, 3rd ed, Vol. 3, Wiley, New York, 2003, Section 6.
161. Hearle J.W.S., Hollick L. and Wilson D.K., *Yarn Texturing Technology*, Woodhead Publishing, Cambridge, 2001.
162. See <http://www.drawtexturing.org>.
163. Udo Schweizer, see <http://www.polyspintex.com> (February 2002).
164. Davis H.L., Jaffe M.L., LaNieve H.L. III and Powers E.J. (Celanese Corporation), US Patent 4 195 052, March 1980.
165. Davis H.L. and co-workers (Celanese Corporation), US Patent 4 101 525, July 1978.
166. Floyd T.S. and Williams J.A. (Celanese Corporation), US Patent 4 503 539, March 1985.

167. Waite R. and Stikeleather W.J. (Celanese Corporation), US Patent 4 483 228, November 1984.
168. Lees G. and Griffith R.L. (Celanese Corporation), US Patent 4 725 371, February 1988.
169. Yamamoto H. and co-workers (Takemoto Yushi Kabuishiki Kaisha), US Patent 4 561 987, December 1985.
170. Sorensen W.R., Sweeney F. and Campbell T.W., *Preparative Methods in Polymer Chemistry*, 3rd ed, Wiley-Interscience, New York, 2001, p. 67.
171. *ibid.*, p. 81.
172. Rumsey J.S., *Modern Textiles*, 1970, 51(2), 48.
173. Choe E.W. and Flint J.A., Hoechst Celanese Corporation, US Patent 5 453 321, September 1995.
174. Calundann G.W. and Jaffe M., *Proceedings of the Robert A Welch Conference on Chemical Research*, Vol XXVI, 1982, p. 247.
175. KoSa press release 4 January, 2000; see <http://www.kosa.com/news31.htm>.

Polyamide fiber formation: structure, properties and characterization

N VASANTHAN, Long Island University, USA

Abstract: The production of polyamide fibers by various spinning techniques yields fibers with a variety of microstructures. The chemical, physical and mechanical properties of these fibers depend on microstructure properties. This chapter reviews polyamide fiber formation and how various spinning methods affect the fiber microstructure, heat setting and mechanical properties. The chapter first discusses the various spinning techniques to form fibers and then discusses various characterization techniques to measure microstructure properties such as crystallinity, crystalline and amorphous orientation. Finally, the chapter reviews how microstructure properties would influence heat setting, dye diffusion and mechanical properties of polyamide fibers.

Key words: polyamides, fiber spinning, FTIR spectroscopy, molecular orientation, heat setting and dye diffusion.

7.1 Introduction

Polyamides (PAs) or nylons were among the first synthetic polymers used for fiber applications. Polyamide fibers are used for a variety of different applications ranging from textiles and carpets to reinforcement of tires.^{1,2} PAs are polymers where the repeat units are held together by an amide linkage. PAs can be classified into aromatic polyamides and aliphatic polyamides. Aliphatic PAs consist of only aliphatic chains whilst aromatic PAs consist of aromatic rings in the main chain.³ Most of the aliphatic PAs are synthesized by either condensation polymerization or ring opening polymerization. Aromatic PAs are difficult to synthesize using diacids and diamines due to the lower reactivity of aromatic amines compared to aliphatic amines, and therefore aromatic PAs are usually made from diamine and diacid chloride.⁴

Aliphatic polyamides can be further classified into several groups based on the length of the diamine and diacid monomer. They can be designated as either PA- x or PA- xy where x and y represent the number of carbon atoms between nitrogen atoms.⁵ PA66 is produced from hexamethylene diamine and adipic acid while PA6 is synthesized by ring-opening polymerization of ϵ -caprolactam. PA66 and PA6 fibers are moderately crystalline (35%) and crystallinity of these fibers can be increased by either heat setting, spinning at higher speed or drawing. More than 3.25 billion pounds of PAs are produced annually and 90% of them are either PA66 or PA6. Mostly PA66 or PA6 are

used for fiber application due to their good combination of tensile strength, flexibility and abrasion resistance.³ Therefore we limit our discussion to PA66 and PA6 fibers in this chapter.

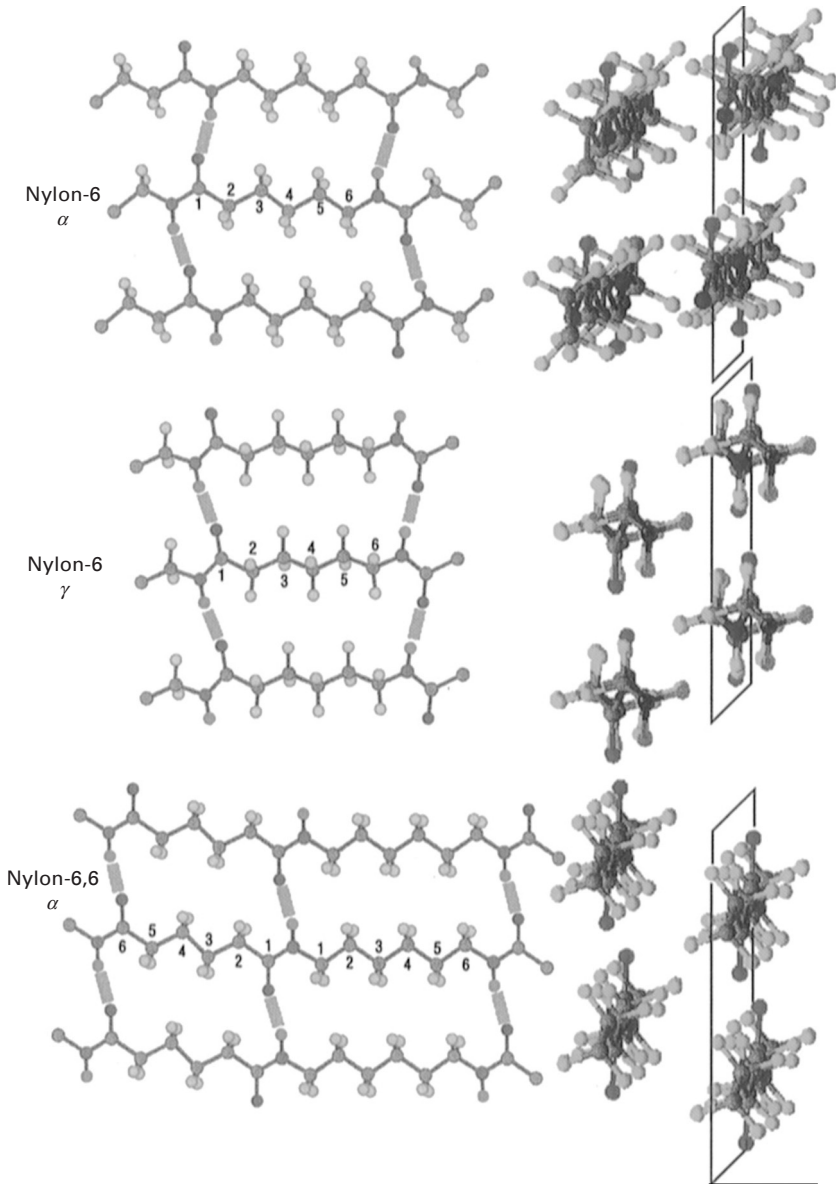
The covalent bonds in the polymer are responsible for the high strength. However, man-made polymers generally do not exhibit the corresponding potential high modulus.⁶ High modulus and strength may result from structural perfection, crystallinity, crystalline and amorphous orientation.^{5,6} It is well known that the highest elastic moduli reported for linear polymers are generally much smaller than their theoretical values. Moduli of ultra-drawn high molecular weight polyethylene (UHMW PE), isotactic polypropylene and Kevlar were reported as close to the theoretical values. Only one twentieth of their theoretical modulus value was obtained for PA fibers.⁶

PAs have hydrogen bonds between amide groups of neighboring polymer chains as well as dipole–dipole interactions. These hydrogen bonds play an important role in drawing of PAs.⁶ Hydrogen bonding prohibits high draw ratios in the PAs, which have a maximum draw ratio of only ~5.^{7,8} A number of research groups investigated the role of hydrogen bonding in controlling the tensile deformation behavior of PA66 and PA6 fibers.^{9–13} It was demonstrated that a high draw ratio can only possibly be made through tensile drawing by either suppression of crystallinity or modification of the number and strength of the hydrogen bonds within the polymer crystals. Many researchers attempted to overcome low extensibility by adding various plasticizers.^{9–13}

7.2 Fiber formation

Unlike polyethylene, polyamides have a high melting temperature, molecular rigidity and intermolecular hydrogen bonding. Hydrogen bonds play an important role in PA fiber formation. A number of attempts to produce high modulus fibers from PAs have been made either by various spinning methods or by solid state co-extrusion with various plasticizers. These methods transform conventional semicrystalline polymers that usually have relatively low modulus and strength into highly oriented fibers with relatively high modulus. Spinning and drawing is the main technique for developing oriented and extended polymer structures.^{14–16} Aliphatic polyamides are usually melt spun while aromatic polyamides are not melt spun. Aromatic polyamides are therefore outside the scope of this discussion. Melt spinning is one of the easiest spinning methods to make PA fibers. But it is not good for spinning of high molecular weight polymers, and therefore other spinning methods such as solution spinning, dry spinning, wet spinning, gel spinning and zone drawing and annealing have also been used to produce high modulus fibers.^{17–19} PA6 fibers have received much more attention compared to PA66 due to PA6's slow crystallization rate.²⁰

Both PA66 and PA6 are semicrystalline polymers that are able to crystallize well due to strong intermolecular forces (hydrogen bonding) and that are held together by van der Waals interactions in a three-dimensional lattice. PA6 crystallizes into two well-known crystal forms α and γ , while PA66 only crystallizes into an α crystal form (Fig. 7.1). It is generally recognized

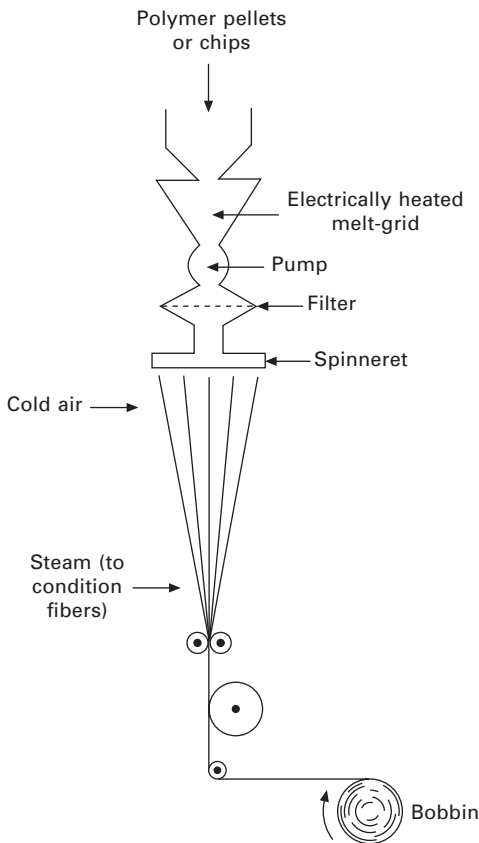


7.1 Crystal structures of PA66 and PA6, reprinted from ref. 21.

that the α crystal form is composed of extended chains and the γ form consists of pleated chains. Hydrogen bonding is parallel in the α form but perpendicular in the γ form. In PA6, spinning conditions affect the formation of α or γ or both crystal forms. Drawing of as-spun fiber leads to molecular orientation along the fiber axis and leads to higher crystallinity. Various spinning methods used to enhance crystallinity and molecular orientation of PA fibers are discussed below.

7.2.1 Melt spinning

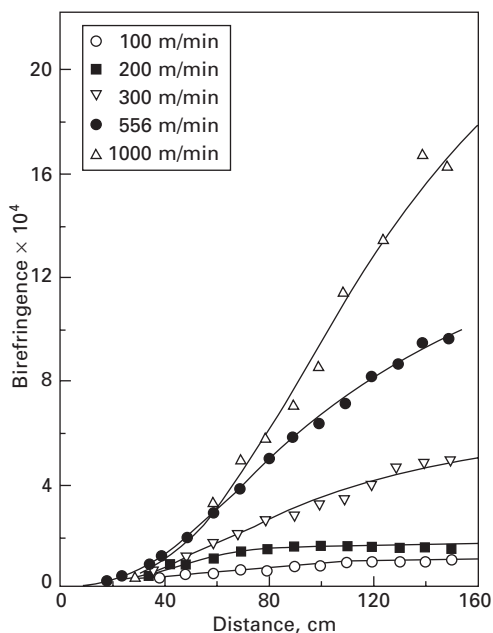
The melt spinning process is an important method based on continuous steady-state elongational flow of processing. Typical industrial melt spinning apparatus is shown in Fig. 7.2.⁴ In this method, molten polymer is extruded through spinnerets followed by rapid quenching, causing solidification. Fibers can then be stretched and annealed to obtain high mechanical properties.^{4,5}



7.2 Industrial-scale melt spinning apparatus, adapted from ref. 4.

It is usually carried out by melt spinning either into air or through an air gap into a cold water bath. PA66 and PA6 fibers are generally obtained by melt spinning.³ Ziabicki and Kedzierska studied melt spinning of PA6 fibers at spinning speeds of about 3500 to 4000 m/min using WAXD and birefringence.^{22,23} It was shown that PA6 fibers are initially amorphous and crystallize in the environment in a pseudo-hexagonal form. An increase in birefringence was observed with an increasing take-up stress, further confirming the formation of a poorly developed pseudo-hexagonal form. Online measurement of birefringence was measured as a function of spinline position as shown in Fig. 7.3.²⁴ An increase in the birefringence due to increase in the temperature of the melt around the spinline has been shown to occur for PA6.

On-line measurement of birefringence and X-ray pattern of PA66 fibers were measured at lower spinning speeds.²⁵ Online X-ray diffraction showed the formation of the α triclinic structure at a lower speed, which was different from the melt spinning of PA6, due to a higher crystallization rate. On the other hand, at higher spinning speeds, paracrystalline structures similar to the high-temperature γ form of PA66 were formed. Subsequent annealing under humid conditions converted the paracrystalline structure into an α



7.3 On-line birefringence vs distance of spinneret, reprinted from ref. 25.

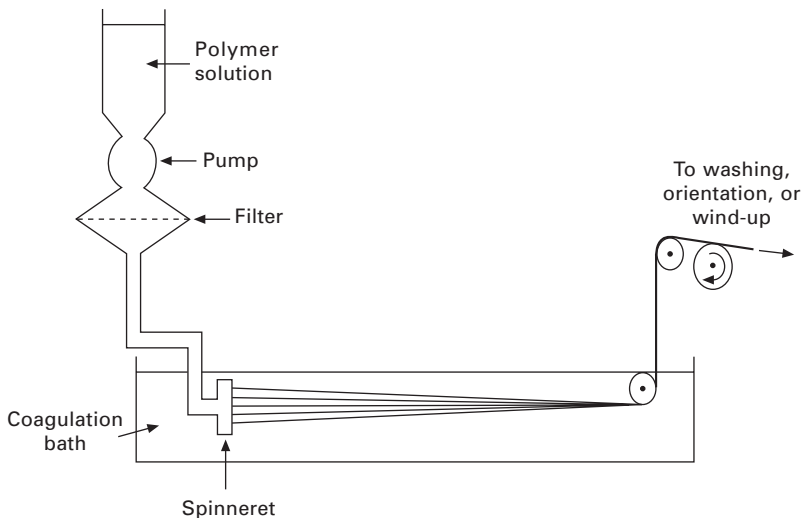
form and increased crystallinity. The density of as-spun filaments showed an increase with increasing spinning speeds.

7.2.2 Dry spinning

Dry spinning involves the extrusion of polymer solutions through a spinneret into a hot air stream that evaporates the solvent and leaves the polymer fiber.⁵ High modulus PA6 fibers were prepared by dry spinning of PA6 solution in cosolvent mixtures of formic acid and chloroform followed by hot drawing. Tensile strength at break and initial moduli of PA6 fibers prepared by this method were reported as 1 GPa and 16–19 GPa, respectively, compared to 0.5 GPa and 5 GPa for PA6 fibers prepared by melt spinning. It was also shown that mechanical properties of PA6 fibers strongly depend on draw ratio, molecular weight, concentration of polymer and solvent ratio.²⁶ Smook *et al.* described dry spinning of PA6 using solvent mixtures of formic acid and dichloromethane and failed to achieve draw ratios above 5 and better mechanical properties than PA6 fibers obtained by melt spinning.²⁷

7.2.3 Wet spinning

Solution spinning is the oldest method used to prepare synthetic fibers. This method has been successfully used to manufacture fibers from polar polymers such as polyacrylonitrile and polyvinyl alcohol on an industrial scale.^{28,29} Industrial scale wet spinning apparatus is shown in Fig. 7.4. In this method,



7.4 Equipment for the wet spinning of fibers, adapted from ref. 4.

a viscous solution of a polymer is extruded into a continuous filament and coagulation of the filament is usually carried out using a nonsolvent for the polymer. Hancock *et al.* studied the wet spinning of PAs in the 1970s.³⁰ Tensile properties obtained for the wet spun PA fibers were much lower than those obtained from dry and gel spinning, which was attributed to the lower molecular weight of the polymer (30 000 g/mole) used for wet spinning. The advantage of solution spinning is the ability to use high molecular weight polymer, as molecular weight plays an important role in the tensile strength of fibers. The disadvantages of this process are that it is difficult to obtain fibers with uniform diameter and it is not possible to spin fibers at higher spinning speed.

7.2.4 Gel spinning

Pennings *et al.* described the formation of ultra-high modulus polyethylene fibers by using gel spinning.³¹ A similar method was used to prepare PA fibers. Cho *et al.* studied the preparation and drawing mechanism for high strength PA6 fibers by the gel spinning/drawing technique using benzyl alcohol as a solvent. When gel spun fibers were drawn to draw ratio of 5.3 it was found that they had an initial modulus of 6.2 GPa.³² Matsuo *et al.* studied the deformation mechanism of PA6 films prepared by gelation/crystallization from solutions with three different solvent types – cosolvent mixtures of formic acid–chloroform, trifluoroethanol, and benzyl alcohol – and deformation of these films were compared with a melt pressed film.³³ Cosolvent mixtures of formic acid–chloroform yielded the best mechanical properties, but a relatively low modulus of 4 GPa and poor drawability with a maximum draw ratio of 4 was obtained.

7.2.5 Zone drawing and zone annealing

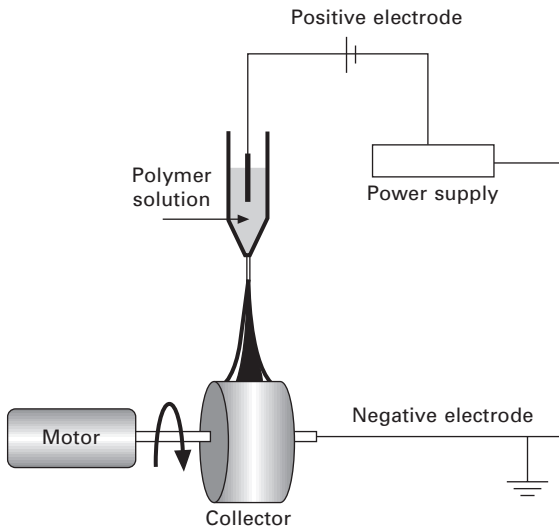
The zone drawing–annealing process is composed of two steps: zone drawing and zone annealing. In the zone drawing stage, the fiber has a high orientation and as low a crystallinity as possible. This spinning process is usually performed by taking a standard tensile tester and attaching a 2 mm wide band heater to the crosshead. The temperature and speed of the band heater are controlled and tension is applied to the lower fiber end by using a suitable weight. Drawing is accomplished below the crystallization temperature and above the glass transition temperature of the polymer. Kunugi *et al.* investigated the production of high modulus PA6 fibers obtained by the zone-annealing method. Tensile strengths up to 1 GPa and moduli up to 10 GPa were obtained for PA6 fibers prepared by this method. PA66 fibers with improved mechanical properties were also prepared by this method and tensile strengths up to 1.2 GPa and moduli up to 8 GPa were obtained.^{34–37}

7.2.6 Spinning with plasticizers

Zachariades and Porter investigated solid-state coextrusion of PA6 plasticized with ammonia and obtained fibers with enhanced moduli, up to 13 GPa. The plasticizer, ammonia, changed only the amorphous regions of PA6, whilst iodine can change both crystalline and amorphous regions of PA6.³⁸ Melt spinning of PA6 fibers from PA6/lithium bromide or PA6/lithium chloride mixtures yielded fibers with moduli in the range 9–13 GPa.³⁹ More recently, PA66 fibers were obtained from melt spinning of a PA66/GaCl₃ complex. Draw ratios of 7–13 were achieved for complexed fibers, under low strain rate stretching. PA66 fibers made from the GaCl₃ complexed state, using a high molecular weight polymer, provided initial moduli up to 13 GPa, compared to initial moduli of 6 GPa reported for commercial PA66 fibers.⁴⁰

7.2.7 Electrospinning

Electrospinning can produce PA6 and PA66 nanofibers in the submicron or nanometer scale.^{41–43} In this method, a solution or melt is placed in a syringe and an electrical force at the surface of polymer solution or polymer melt overcomes the surface tension, and a charged jet is ejected from the droplet. The jet travels a set distance and is collected on a counter electrode in the form of a membrane, as shown in Fig. 7.5.⁴³ The tensile deformation of PA66 nanofibers has been studied and compared with melt extruded microfibers.⁴² PA6 nanofibers ranging from 10 to a 100 nm have been successfully electrospun



7.5 Schematic representation of electrospinning set-up, adapted from ref. 43.

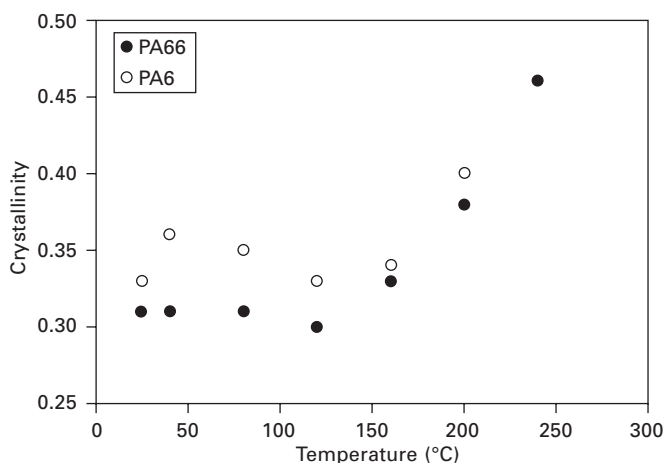
from hexafluoroisopropanol solution. Electrospinning of PA6 yielded a γ form of PA6 nanofibers, similar to high speed spinning. An orientation parallel to the fiber axis was confirmed using WAXD. Annealing PA6 nanofibers above 170°C transformed the γ crystalline phase into an α crystalline phase.⁴³

7.3 Characterization

7.3.1 Density and birefringence

Density increase is associated with crystallization of semicrystalline polymers where interchain distances become smaller. Crystallinity of semicrystalline polymers can be obtained using the crystalline and the amorphous densities. For most polymers the amorphous densities can be obtained by rapid quenching from the melt. The crystalline density can be calculated using unit cell parameters obtained from the WAXD pattern. Crystallinity obtained by density measurements is often used to study thermally induced crystallization and stress-induced crystallization of PA fibers. Density has also been used to study fiber formation on the spinline.

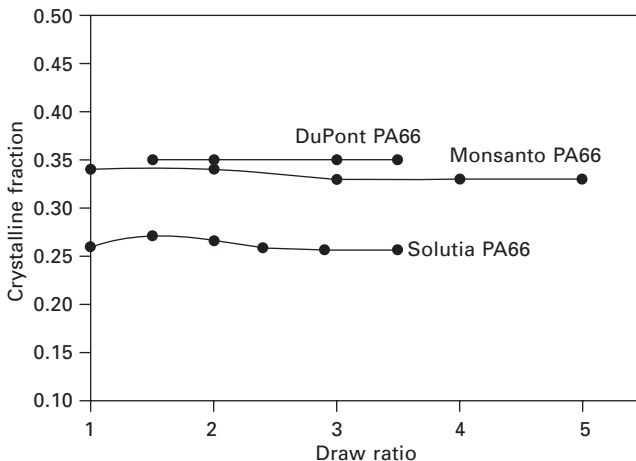
The density of PA66 fibers spun at different speeds increased with increasing spinning speed and always above the amorphous density of PA66, suggested that PA66 crystallizes at a lower spinning speed.²⁵ Vasanthan and Salem recently studied thermally induced crystallization of PA66 and PA6 fibers.^{44,45} Crystalline fractions obtained by density measurements of PA66 fibers heat treated for two minutes at temperatures of 40, 80, 120, 160, 200 and 240°C are reported in Fig. 7.6. Similar studies have been conducted for PA6 fibers. It is not easy to correlate directly the density with the crystallinity



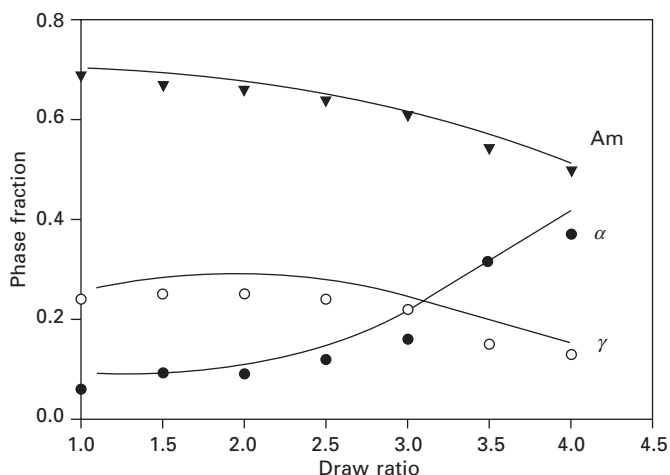
7.6 Volume fraction crystallinity as a function of heat-setting temperature for PA66 (●) and PA6 (○) fibers, adapted from ref. 74.

for PA6 due to the presence of two different crystal modifications, which have different density values. Density increases could occur either by additional crystallization or by transformation from one crystal form to the other (γ to α). Crystalline fractions of PA6, determined by IR and density, versus heat setting temperatures are also shown in Fig. 7.6. Crystalline fraction values were almost constant up to a temperature of 150°C and then increased once the heat treatment temperature exceeded this value. It was demonstrated that thermally induced crystallization of PA fibers was quite strongly time-dependent.⁴⁴

Crystallinity of three sets of PA66 fibers drawn to different draw ratios below T_g are shown in Fig. 7.7. No change in crystallinity with increasing draw ratio was observed. Below T_g , the efficiency of chain orientation was high, but crystallinity stayed almost the same or even decreased due to disruption of crystallites. Drawing above T_g does not produce significant orientation, but crystallinity increased significantly due to thermally induced crystallization.⁴⁶ Fractions of the α , γ and amorphous phases of PA6 fibers drawn to different draw ratios (1 to 4) at room temperature were measured by density and IR spectroscopy by Vasanthan and Salem, and α , γ and amorphous phase fractions versus draw ratio are depicted in Fig. 7.8. Crystallinity increases were attributed to changes in crystal form from γ to α as well as stress-induced crystallization of additional amorphous phases.⁴⁷ Density and birefringence of PA6 fibers spun at different speeds showed an increase up to a spinning speed of 5000 m/min and then leveled off, suggested that orientation-induced crystallization occurs at lower spinning speeds.⁴⁸



7.7 Volume fraction crystallinity as a function of draw ratio for PA66 fibers, adapted from ref. 46.



7.8 Volume fraction α , γ and amorphous fraction as a function of draw ratio for PA6 fibers, reprinted from ref. 47.

7.3.2 IR spectroscopy

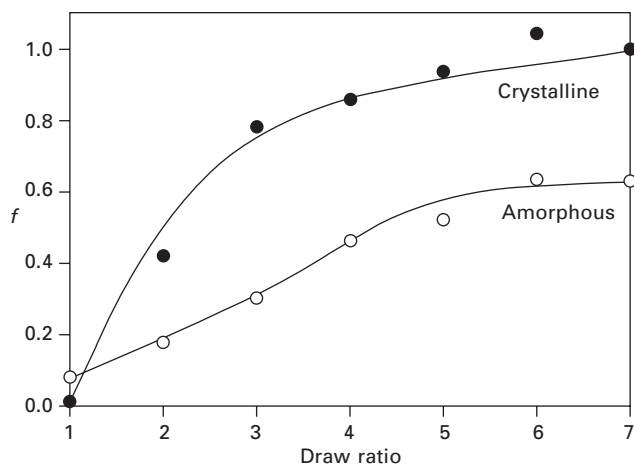
Infrared spectroscopy has been used extensively to investigate the structure development of PA films and relatively few studies have been made on PA fibers.^{49,50} Band assignments for PA66 and PA6 were reported by a number of different groups.⁵¹⁻⁵³ Quintanilla attributed the bands at 936 and 1144 cm^{-1} to the *trans* and *gauche* conformations of methylene segments in PA66.⁵³ Using these bands, *trans* and *gauche* conformations of methylene segments in PA66 were quantified. Having found much ambiguity in the infrared band assignments for PA66, Vasanthan and Salem revisited some of these band assignments in their recent work.⁴⁴ It was demonstrated that earlier assignments of the bands at 1144 and 1180 cm^{-1} to the noncrystalline phase of PA66 were found to be incorrect, whereas the bands at 924 and 1136 cm^{-1} were assigned to the noncrystalline phase. Bands at 936 and 1200 cm^{-1} were also confirmed as crystalline bands whilst the 924 cm^{-1} band was confirmed as an amorphous band. Normalized absorbance of bands at 1200, 936 and 924 cm^{-1} were plotted against fiber density and the extinction of the crystalline and amorphous sensitive bands corresponded to the reported amorphous and crystalline density values. Determination of PA66 crystallinity has been carried out by using an infrared method.⁴⁴ The values from this study are shown in Table 7.1 along with crystallinity obtained by DSC and density measurement; all three methods showed a reasonable agreement with each other.⁴⁴

The 936 cm^{-1} crystalline band has been used to determine the crystalline orientation of PA66 fibers as a function of spinning speed and molecular

Table 7.1 Crystallinity values obtained from three different methods (T_p and T_r are Preset and Reset temperatures)

T_p	T_r	% Crystallinity		
		Density	IR	DSC
25	25	30.9	31.2	40.1
	40	30.7	29.8	43.6
	80	30.9	30.7	40.4
	120	30.2	27.6	40.5
	160	32.6	30.6	40.3
	200	38.4	32.1	42.6
	240	48.3	42.3	43.6
150	25	34.8	35.2	44.0
	40	35.0	34.4	
	80	34.8	38.6	
	120	35.1	35.1	
	160	35.3	33.2	
	200	38.3	38.1	
	240	49.0	41.5	
200	25	45.4	42.1	
	40	45.9	42.3	
	80	46.1	43.2	
	120	46.1	45.1	
	160	46.9	48.6	
	200	46.4	43.7	
	240	48.7	43.7	

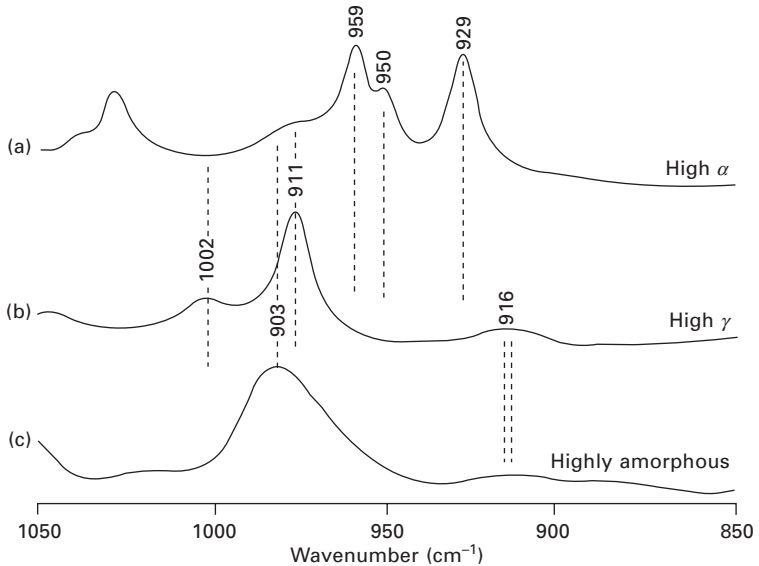
weight and as a function of draw ratio.^{46,54} The transition moment angle of the 936 cm^{-1} vibration has been determined using X-ray and polarized ATR-FTIR spectroscopy for high viscosity and low viscosity PA66 as 39° and 41° .⁵⁴ The crystalline orientation values obtained by IR and amorphous orientation obtained by combination of IR and birefringence as a function of spinning speed were compared. Crystalline orientation obtained by IR was in agreement with crystalline orientation obtained by X-ray diffraction. A sharp increase in crystalline orientation was observed at lower spinning speed and a practically insignificant increase in amorphous orientation was observed at lower spinning speed. Polarized IR spectroscopy in the transmission mode was used to measure the transition moment angle of the vibrations at 936 cm^{-1} , and was found to be 48° .⁵⁵ Crystalline orientation was determined from the band at 936 cm^{-1} , and the increase in orientation with increasing draw ratio was observed (Fig. 7.9). Amorphous orientation obtained using a combination of birefringence and crystalline orientation obtained by polarized IR is also shown in Fig. 7.9. It was found that the amorphous orientation develops more slowly than the crystalline orientation, which is typical behavior for flexible chain polymers.



7.9 Crystalline and amorphous orientation of PA66 fibers versus draw ratio, reprinted from ref. 46.

In PA6, the bands at 930 and 960 cm^{-1} have been attributed to α crystalline phase, the bands at 919 and 973 cm^{-1} have been assigned to γ crystalline phase and the 983 cm^{-1} band has been attributed to the amorphous phase.^{47,56} Unpolarized spectra taken for drawn fibers having α , γ and amorphous phases are shown in Fig. 7.10. Depending upon the thermal and mechanical treatment, the fractions of the α , γ and amorphous phases can change dramatically. The bands at 930 and 973 cm^{-1} have been used to measure the crystalline orientation of α and γ crystalline phases, respectively. Since the direction of the transition moment is not known for the amorphous phase, only the dichroic ratio of the 983 cm^{-1} band was reported.⁵⁶ Other problems with the band at 983 cm^{-1} are its low intensity and the fact that it is highly submerged by strong overlapping bands, so that reliable curve fitting is often impossible. A band at 1124 cm^{-1} associated with C–C skeletal vibrations was recently used to determine the amorphous orientation of PA6. Figure 7.11 shows the α crystalline orientation obtained by infrared spectroscopy and X-ray diffraction along with amorphous orientation obtained using the IR band at 1124 cm^{-1} and amorphous orientation obtained by combination of IR spectroscopy and birefringence. It was shown that the amorphous orientation stays constant at lower draw ratios, and increases at higher draw ratios.⁴⁷

Bower used Raman spectroscopy to determine molecular orientation.⁵⁷ He showed that for samples with uniaxial symmetry it is necessary to measure five independent components of the scattered radiation. Unlike infrared dichroism and birefringence, Raman spectroscopy can yield the fourth moment of the orientation distribution in addition to the second moment. However, Raman spectroscopy has not been used extensively to investigate oriented PA fibers, and only a few papers exist in the literature.^{57–59} One of

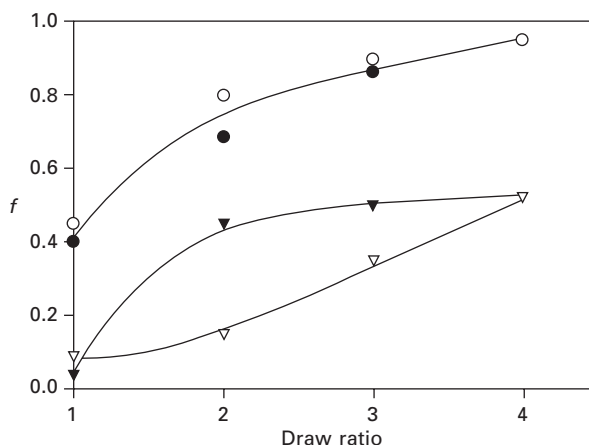


7.10 Unpolarized IR spectra in the region from 1050 to 850 cm^{-1} of PA6: (a) high α content; (b) high γ content; (c) highly amorphous; adapted from ref. 56.

the major experimental problems is polarization scrambling that arises from multiple reflections and refractions of the incident and scattered radiation near the surface of the sample, and it is necessary to employ special sampling techniques to reduce this effect.^{57,58} The anisotropic scattering properties of oriented PA6 fibers have been studied by polarized Raman spectroscopy and a complete assignment of Raman bands for PA6 has been made.⁵⁹

7.3.3 NMR spectroscopy

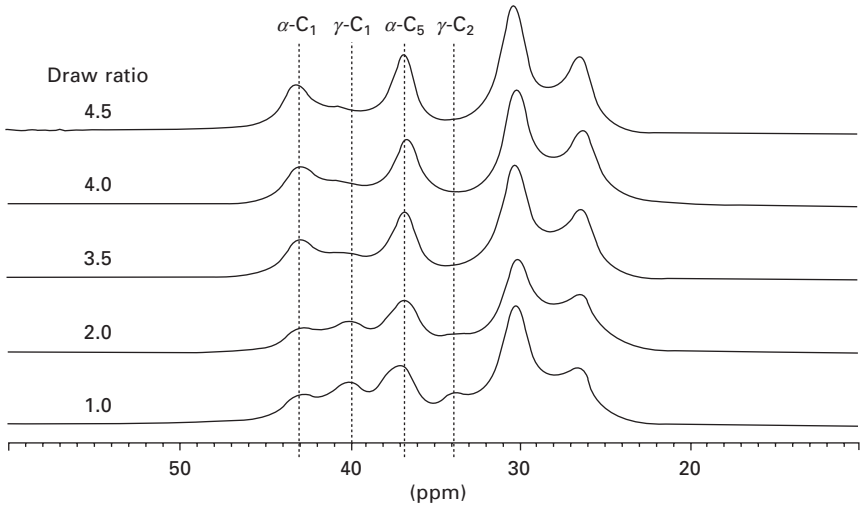
Nuclear magnetic resonance (NMR) spectroscopy is another form of absorption spectroscopy that can be applied to investigate PA fibers. In strong magnetic fields at excitation frequencies in the radio frequency region, materials can absorb electromagnetic radiation at frequencies governed by the characteristics of the atomic nuclei and their chemical or structural environment. This effect is restricted to nuclei with nuclear spin not equal to zero. Since the nuclear spin differs from zero only if the number of protons and/or neutrons are odd, nuclei having an equal number of protons and neutrons (e.g., ^{12}C and ^{14}N) cannot be measured and nuclei with spin $\frac{1}{2}$ are favored (e.g. ^{13}C , ^1H , ^{15}N and ^{19}F). Nuclei with higher spin possess a quadrupole moment, which leads to unfavorable line broadening. The NMR spectra of spin $\frac{1}{2}$ nuclei are commonly used to study polymer structure.⁶⁰



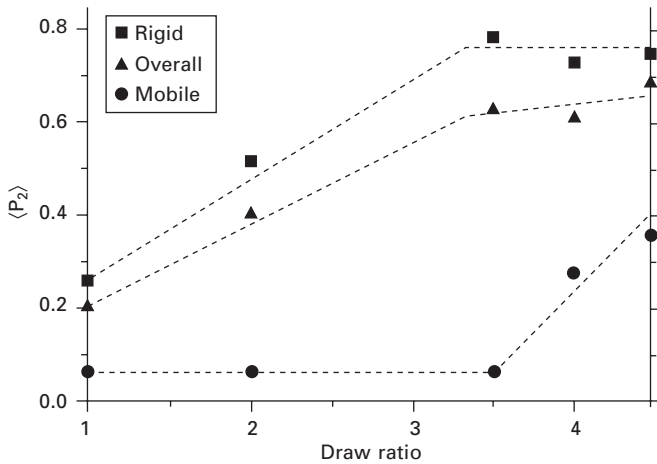
7.11 Comparison of α crystalline and amorphous orientation obtained by X-ray and FTIR methods: α crystalline orientation from FTIR (○), α crystalline orientation from WAXD (●), amorphous orientation from FTIR (▽) and amorphous orientation from WAXD and birefringence (▼), reprinted from ref. 47.

It is relatively straightforward to obtain high resolution NMR spectra from fibers dissolved in solution because of rapid local motion of polymer chains. PA fibers should be characterized in the solid state NMR and a number of different methods and pulse sequences were developed. ‘Magic angle’ spinning and cross-polarization from protons must be applied to remove line broadening due to chemical-shift anisotropy and signal enhancement, respectively. The introduction of two-dimensional NMR has greatly enhanced the power and versatility of the NMR technique.⁶¹

A few solid state NMR spectra of PA fibers are reported. Solid state ^{13}C and ^{15}N NMR spectra of the α , γ and amorphous phases of PA6 have been obtained.^{62,63} The observed chemical shift differences were discussed in terms of hydrogen bonding and chain packing. It was shown that hydrogen bonding interaction is stronger in the γ phase than in the α phase. The effect of drawing on structure and orientation has been studied by Schreiber *et al.*⁶⁴ and solid state ^{13}C NMR spectra of PA6 fibers drawn to different draw ratios are shown in Fig. 7.12. It appears that undrawn PA6 fiber shows chemical shifts associated with an α crystalline phase and a γ crystalline phase which is completely converted to an α crystalline phase at high draw ratio. From this investigation, orientations of the rigid (crystalline and rigid amorphous) and mobile phase (amorphous) was determined, the results of which are shown in Fig. 7.13. It is clear from Fig. 7.13 that the orientation of the rigid phase increases rapidly up to a draw ratio of 3.5, and levels off at higher draw ratios, whilst the mobile amorphous phase stayed disordered at low draw



7.12 Methylene resonances (CH_2) of ^{13}C CPMAS spectra of drawn PA6 fibers, adapted from ref. 64.



7.13 Effect of draw ratio on the orientation parameter $\langle P_2 \rangle$ of PA6 fibers by solid state NMR spectroscopy, adapted from ref. 64.

ratios and increased rapidly at higher draw ratios. Two-dimensional solid state NMR spectroscopy has been used to investigate the average molecular orientation of hot-drawn PA6 fibers at draw ratios in the range 1 to 5.5 at 175°C . Average orientation here included the ordered crystalline and less ordered amorphous phase.⁶⁵

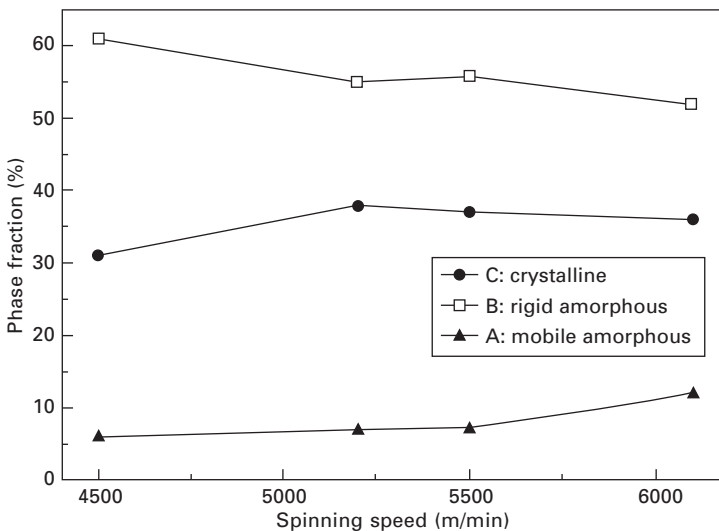
Spin-lattice relaxation times using a rotating frame ($T_{1\rho}$) measurement

were reported for PA6 fibers spun at different spinning speeds. Three different relaxation times were identified and attributed to crystalline, rigid amorphous and amorphous phases. Correlation times determined for each phase provided information about the mobility of each phase at various spinning speeds. The fraction of each phase for PA6 fibers spun at different speeds was determined from correlation times and the results are shown in Fig. 7.14.^{66,67}

7.4 Influence of microstructure on properties

7.4.1 Heat setting

PA fibers undergo various heat-setting processes during spinning, drawing, texturing, and fabric finishing and dyeing. Knowledge of the relation between thermal history, processing conditions and microstructure changes of these fibers is very important in order to control mechanical properties and dimensional stability. Annealing is usually applied to modify the microstructure and impart permanent set to semicrystalline polymers. Structural changes during heat setting of PA66 and PA6 fibers were investigated in detail.^{56,68–70} It was concluded that heat setting of PA fibers increases the crystallinity, crystallite size and crystal perfection. It has recently been shown that polymers of lower crystallinity, such as oriented PET and PA66 fibers, can show strongly time-dependent stress-relaxation behavior.^{71–73} Moreover, there are some intriguing indications that simple time–temperature

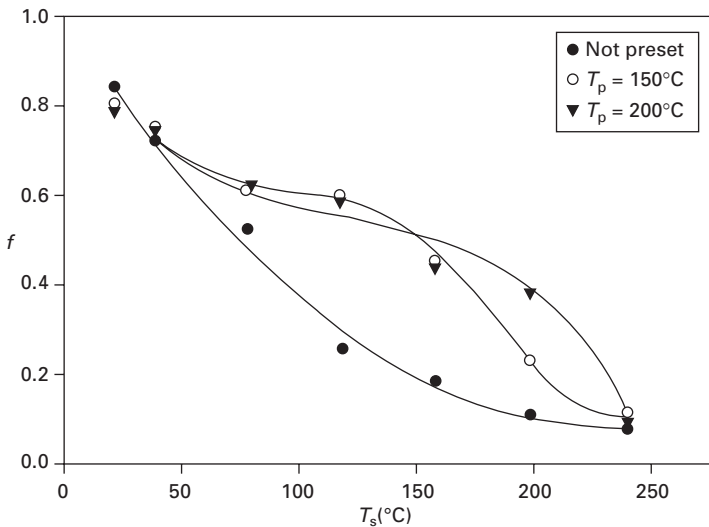


7.14 Phase fraction of the individual phases of PA6 fibers as a function of spinning speed, reprinted from ref. 67.

superposition may be applicable to these polymers despite their crystallinity and the development of additional crystallinity during the stress relaxation process. Heat setting of PA66 fibers was investigated by measuring fractional 'twist' recovery f with temperature and time. The decay in fractional 'twist' recovery f with heat setting temperature T_s for a partially oriented PA66 yarn is shown in Fig. 7.15, in which the heat setting time t_s at each heat-setting temperature is 2 minutes. For an as-received yarn f decreases monotonically with increasing T_s , whereas yarns that were pretreated at 150°C and 200°C for 30 minutes show a distinct plateau followed by a higher temperature setting process. It was shown that fractional recovery (f) depends on heat setting temperatures, and time and crystallinity provide partial crosslinking that delays the onset of the flow regime and increases the time constant of relaxation at a given temperature.⁷⁴ Heat setting of PA fibers is complicated by polymorphic transition and moisture sorption, and a detailed study is in progress in our laboratory.

7.4.2 Mechanical properties

The mechanical properties of PA66 and PA6 fibers depend on crystallinity and orientation. Heat setting of PA66 and PA6 fibers at fixed length increases crystallinity, crystallite size and crystalline perfection.⁷⁵ The initial modulus of the fibers was determined from the slope of the stress–strain curve at small strains and these data for PA66 and PA6 fibers showed no significant



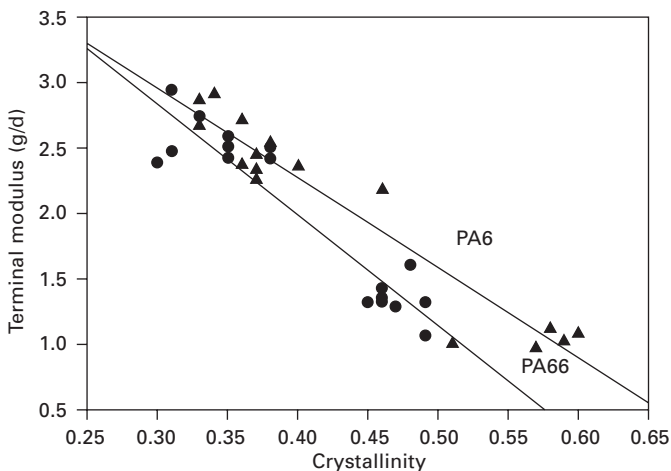
7.15 Fractional recovery versus heat-setting temperature of PA66 fibers after various presetting treatments.

changes with various presetting and heat setting conditions. Significant effects on the terminal modulus, breaking load and elongation at break with presetting were, however, observed.⁷⁴ It has also been shown that tensile properties such as elongation at break and modulus correlate reasonably well with birefringence. For example, mechanical properties of high speed spun PA6 fibers show an increase in initial modulus, tenacity and yield strength up to 5000 m/min and a decrease above 5000 m/min.

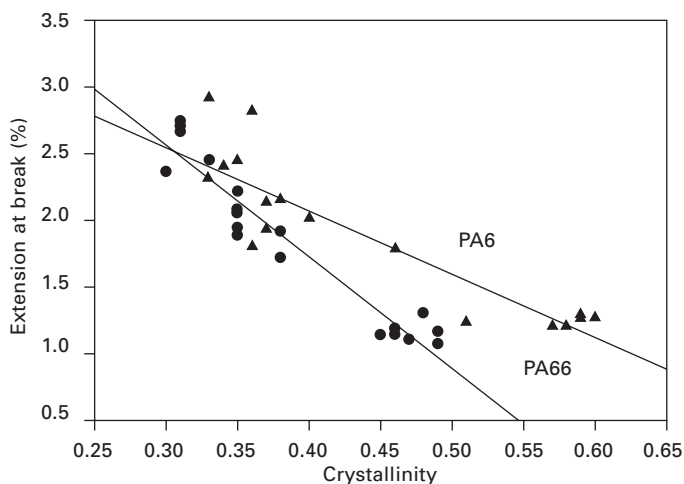
The terminal modulus of PA66 and PA 6 fibers has been shown to depend on heat setting temperatures, T_s . It has also been shown that terminal modulus depends on presetting temperatures, T_p . Terminal modulus of as-received and preset (at 150°C) PA 66 and PA 6 yarns have approximately the same value up to the heat setting temperature, T_s , of 160°C. The terminal modulus is dramatically reduced for PA6 and PA66 fibers preset at 200°C. Average extension at break (%) as a function of presetting and heat setting temperatures showed a decrease with increasing presetting as well as heat setting temperatures. A very good correlation between crystallinity and terminal modulus and extension at break has been established (Figs 7.16 and 7.17).⁷⁴

7.4.3 Dyeing behavior

The rate of dye diffusion in PA fibers is highly dependent on the microstructural state of the polymer. For example, small changes in crystallinity, amorphous orientation and crystal chain folding appear to produce very large changes in the dye diffusion coefficient. The sensitivity of the dye diffusion coefficient to small structural changes has always presented problems in commercial



7.16 Terminal modulus versus crystalline fraction for PA66 (●) and PA6 (▲) fibers.



7.17 Extension at break versus crystalline fraction for PA66 (●) and PA6 (▲) fibers

practice, because minor fluctuations in fiber processing condition such as spinning, drawing, texturing or heat setting can lead to significant changes in dyeing properties, and consequently to non-uniform dyeing of the end product. In PA fiber, dye uptake has been shown to decrease with increasing dry heat setting temperature. It was believed that small molecules diffuse into the amorphous matrix of a fiber through voids due to segmental mobility. The rate of dye diffusion in partially oriented yarns is highly dependent on the microstructural state of the polymer that influences the segmental mobility.^{76,77}

Dye uptake and diffusion of disperse and acid dyes in PA66 and PA6 fibers have been recently studied.^{76,77} Dye uptake has been shown to decrease with increasing heat setting temperature and this was attributed to an increase in crystallinity. The diffusion coefficient of acid and dispersed dye in PA66 fibers showed a decrease with increasing heat setting temperature. On the other hand the diffusion coefficient of acid dye in PA6 fibers decreased as the heat setting temperature increased, reaching a minimum and then increasing very sharply at high temperatures. Dye uptake was approximately the same for all draw ratios, though diffusion coefficient decreased with increasing draw ratios. A sharp decrease in diffusion coefficient with increasing draw ratio of the PA66 and PA6 yarn was correlated with an increasing amorphous orientation.

7.5 Conclusions

It has been shown that PA fibers can be spun by number of different techniques.

However, melt spinning is the most common method. Microstructural properties of these PA fibers can be manipulated after processing, by either heat setting or drawing. Knowledge of the relation between thermal history, processing conditions and microstructural changes of these fibers is very important in order to control their mechanical properties and dimensional stability for various end uses. This can only be accomplished by measuring structural parameters of density, birefringence, crystalline and amorphous orientation by infrared spectroscopy and solid state NMR spectroscopy. These methods have been discussed in this chapter.

7.6 Future trends

It is well known that the highest elastic moduli reported for synthetic polymers are much smaller than their theoretical values. Ultra-drawn high molecular weight polyethylene and Kevlar are the only fibers that showed moduli close to theoretical values. Moduli observed for PAs are one-twentieth of the theoretical values. Of particular interest is obtaining high-modulus fibers from PAs either by modifying the processing methods or by incorporating nanoparticles in the polymer matrix. These high-modulus fibers will be highly beneficial for applications that need high-strength fibers. Attempts have been made to some extent to prepare high-strength PA fibers by temporarily eliminating hydrogen bonds during processing by complexing with additives. Recently we reported a method to prepare PA66 fibers using Lewis acid. Several new and innovative methods to produce high strength PA fibers are presently being investigated. Another approach will be preparing PA fibers from various PA hybrids obtained from montmorillonite and carbon nanotubes. Development of nano-engineered fibers would provide exceptional strength and transport properties; however, this would require reasonable understanding of the many process and structure properties of fibers derived from PA hybrids. Research is likely to continue in this field for many years to come.

7.7 References

1. Ahroni S M, *n-Nylons: Their Synthesis, Structure, and Properties*, Wiley, New York, 1997.
2. Kohan M I, ed., *Nylon Plastic Handbook*, Hanser, New York, 1995.
3. Odian G, *Principles of Polymerization*, Wiley-Interscience, New York, 1991.
4. Allcock H R, Lampe F W, Mark J E, *Contemporary Polymer Chemistry*, 3rd edn, Prentice Hall, Upper Saddle River, NJ, 2003.
5. Murthy N S, 'Hydrogen bonding, mobility, and structural transition in aliphatic polyamides', *J. Polym. Sci., Polym. Phys. Ed.*, 2006, **44**, 1763–1782.
6. Kotek R, Jung D, Tonelli A E, Vasanthan N, 'Novel methods for obtaining high modulus aliphatic polyamide fibers', *J. Macromol Sci.*, 2005, **45**, 201–230.
7. Vasanthan N, Kotek R, Jung D W, Shin I D, Salem D R and Tonelli A E, 'Lewis

- acid-base complexation of polyamide 66 to control hydrogen bonding, extensibility, and crystallinity', *Polymer*, 2004, **45**, 4077–4085.
8. Quistwater J M R, Dunell B A, 'Dynamic mechanical properties of nylon-66 and the plasticizing effect of water vapor on nylon', *J. Polym. Sci.*, 1958, **28**, 309–318.
 9. Postema A R, Smith P, 'Ultra-drawing of polyamides – the hydrogen-bond barrier', *Polym. Commun.*, 1990, **31**, 444–447.
 10. Zachariades A E, Porter R S, 'Reversible plasticization of nylon-6 and nylon-11 with anhydrous ammonia and their deformation by solid-state coextrusion', *J. Appl. Polym. Sci.*, 1979, **24**, 1371–1382.
 11. Chuah H H, Porter R S, 'A new drawing technique for nylon-6 by reversible plasticization with iodine', *Polymer*, 1986, **27**, 241–246.
 12. Kanamoto T, Zachariades A E, Porter R S, 'The effect of anhydrous ammonia on the crystalline-state deformation of nylon-6 and nylon-6,6', *J. Polym. Sci., Polym. Phys. Ed.*, 1982, **20**, 1485–1496.
 13. Chuah H H, Porter R S, 'Solid-state co-extrusion of nylon-6 gel', *Polymer*, 1986, **27**, 1022–1029.
 14. Kalb B, Pennings A J, 'Maximum strength and drawing mechanism of hot drawn high molecular weight polyethylene', *J. Mater. Sci.*, 1980, **15**, 2584–2590.
 15. Ciferri A, Ward I M, *Ultra-High Modulus Polymers*, Applied Science, London, 1977.
 16. Zachariades A E, Kanamoto T, 'New model for the high modulus and strength performance of ultradrawn polyethylenes', *J. Appl. Polym. Sci.*, 1988, **35**, 1265–1281.
 17. Suzuki A, Endo A, 'Preparation of high modulus nylon 46 fibres by high-temperature zone-drawing', *Polymer*, 1997, **38**, 3085–3089.
 18. Pennings A J, Smook J, Boer J, Gogolewski S, Hutten P F, 'Process of preparation and properties of ultrahigh strength polyethylene fibers', *Pure Appl. Chem.*, 1983, **55**, 777–798.
 19. Smith P, Lemstra P J, 'Ultra-high strength polyethylene filaments by solution spinning-drawing', *J. Mater. Sci.*, 1980, **15**, 505–514.
 20. Brandrup J, Immergut E H, eds, *Polymer Handbook*, 3rd edn, Wiley, New York, 1989, pp. vi, 311.
 21. Dasgupta S, Hammond W B, Goddard III W A, 'Crystal structures and properties of nylon polymers from theory', *J. Am. Chem. Soc.*, 1996, **118**, 12291–12301.
 22. Ziabicki A, Kedzierska Z, 'Orientation phenomena in fiber formation from polymer melts. II. Effects of structure on orientation. Condensation polymers', *J. Appl. Polym. Sci.*, 1962, **6**, 111–118.
 23. Ziabicki A, Kedzierska Z J, 'Orientation phenomena in fiber formation from polymer melts. I. Preliminary investigations on polycapromide', *J. Appl. Polym. Sci.*, 1959, **2**, 14–23.
 24. Bankar V G, Spriuell J E, White J L, 'Melt spinning of nylon 6: structure development and mechanical properties of as-spun filaments', *J. Appl. Polym. Sci.*, 1977, **21**, 2341–2358.
 25. Danford M D, Spriuell J E, White J L, 'Structure development in the melt spinning of nylon 66 fibers and comparison to nylon 6', *J. Appl. Polym. Sci.*, 1978, **22**, 3351.
 26. Gogolewski S, Pennings A J, 'High-modulus fibers of nylon-6 prepared by a dry-spinning method', *Polymer*, 1985, **26**, 1394–1400.
 27. Smook J, Vos G J H., Doppert H L, 'A semiempiric model for establishing the

- drawability of solution-spun linear polyamide and other flexible chain polymers', *J. Appl. Polym. Sci.*, 1990, **41**, 105–116.
28. Kwon Y D, Kavesh S, Prevorsek D C, 'High tenacity and modulus polyacrylonitrile fiber and method', European Patent Appl. 0,144,793, 19 June 1985.
 29. Kwon Y D, Kavesh S, Prevorsek D C, 'Method of preparing high strength and modulus polyvinyl alcohol fibers', US Patent 4,440,711, 3 April 1984.
 30. Hancock T A, Spruiell J E, White J L, 'Wet spinning of aliphatic and aromatic polyamides', *J. Appl. Polym. Sci.*, 1977, **21**, 1227–1247.
 31. Kalb B, Pennings A J, 'Maximum strength and drawing mechanism of hot drawn high molecular-weight polyethylene', *J. Mater. Sci.*, 1980, **15**, 2584–2590.
 32. Cho J W, Lee G W, Chun B C, 'Mechanical properties of nylon 6 fibers gel-spun from benzyl alcohol solution', *J. Appl. Polym. Sci.*, 1996, **62**, 771–778.
 33. Matsuo M, Sato R, Yanagida N, Shimazu Y, 'Deformation mechanism of nylon 6 gel and melt films estimated in terms of orientation distribution function of crystallites', *Polymer*, 1992, **33**, 1640–1648.
 34. Kunugi T, Suzuki A, Hashimoto M, 'Preparation of high-modulus and high-strength nylon-6 fiber by the zone-annealing method', *Polymer*, 1982, **23**, 1193–1198.
 35. Kunugi T, Suzuki A, Hashimoto M, 'Mechanical properties and superstructure of high-modulus and high-strength nylon 6-fibre prepared by the zone-annealing method', *Polymer*, 1982, **23**, 1199–1023.
 36. Kunugi T, Ikuta T, Hashimoto M, 'Preparation of ultra-high-strength nylon-6 fiber by a multistep zone-annealing method', *Polymer*, 1982, **23**, 1983–1987.
 37. Kunugi T, Chida K, Suzuki A, 'Preparation of high-modulus nylon6 fibers by vibrating hot drawing and zone annealing', *J. Appl. Polym. Sci.*, 1998, **67**, 1993–2000.
 38. Kanamoto T, Zachariades A E, Porter R S, 'The effect of anhydrous ammonia on the crystalline-state deformation of nylon-6 and nylon-6,6', *J. Polym. Sci., Polym. Phys. Ed.*, 1982, **20**, 1485–1496.
 39. Richardson A, Ward I M, 'Production and properties of fibers spun from nylon6/lithium chloride mixtures', *J. Polym. Sci., Polym. Phys. Ed.*, 1981, **19**, 1549–1565.
 40. Vasanthan N, Kotek R, Jung D W, Shin I D, Salem D R, Tonelli A E, 'Lewis acid-base complexation of polyamide 66 to control hydrogen bonding, extensibility, and crystallinity', *Polymer*, 2004, **45**, 4077–4085.
 41. Li Y, Huang Z M, Lu Y D, 'Electrospinning of nylon 6, 66, 1010', *Eur. Polym. J.*, 2006, **42**, 1696–1704.
 42. Zussman E, Burman M, Yarin A L, Khalfin R, Cohen Y, 'Tensile deformation of electrospun nylon 6,6 nanofibers', *J. Polym. Sci., Polym. Phys. Ed.*, 2006, **44**, 1482–1489.
 43. Stephens J, Chase D B, Rabolt J F, 'Effect of electrospinning process on polymer crystallization chain conformation in nylon 6 and nylon 12', *Macromolecules*, 2004, **37**, 877–881.
 44. Vasanthan N, Salem D R, 'Infrared spectroscopic characterization of oriented polyamide 66: band assignment and crystallinity measurement', *J. Polym. Sci., Polym. Phys. Ed.*, 2000, **38**, 516–524.
 45. Vasanthan N, Salem D R, 'FTIR spectroscopic characterization of structural changes in polyamide 6 fibers during annealing and drawing', *J. Polym. Sci., Polym. Phys. Ed.*, 2001, **39**, 536–547.
 46. Vasanthan N, Ruetsch S B, Salem D R, 'Structure development of polyamide 66 fibers by X-ray diffraction and FTIR spectroscopy', *J. Polym. Sci., Polym. Phys. Ed.*, 2002, **40**, 1940–1948.

47. Vasanthan N, 'Orientation and structure development in polyamide 6 fibers upon drawing', *J. Polym. Sci., Polym. Phys. Ed.*, 2003, **41**, 2870–2877.
48. Salem D R, Vasanthan N, 'Spectroscopic methods: infrared, Raman and nuclear magnetic resonance', in Salem D. R. (ed.), *Structure Formation in Polymeric Fibers*, Hanser, Munich, 2001.
49. Sandeman I, Keller A, 'Crystallinity studies of polyamides by infrared, specific volume and X-ray methods', *J. Polym. Sci.*, 1958, **41**, 101–135.
50. Arimoto H, 'Alpha–gamma transition of nylon 6', *J. Polym. Sci., Part A*, 1964, **2**, 2283–2295.
51. Rotter J, Ishida H, 'FTIR separation of nylon 6 chain conformations: clarification of the mesomorphous and gamma-crystalline phases', *J. Polym. Sci., Polym. Phys. Ed.*, 1992, **30**, 489–495.
52. Arimoto H, Ishibashi M, Hirai M, Chatani M, 'Crystal structure of gamma-form of nylon 6', *J. Polym. Sci., Part A*, 1965, **3**, 317–326.
53. Quintanilla L, Pastor J M, 'Structural analysis of polyamide-6,6 reinforced with glass fiber by the use of fourier transform infra-red spectroscopy with photoacoustic detection and differential scanning calorimetry', *Polymer*, 1994, **35**, 5241–5246.
54. Samanta S R, Lanier W W, Miller R E, Gibson J R M E, 'Fiber structure study by polarized infrared attenuated total reflection spectroscopy: orientation development of nylon 66 at various spinning speeds', *J. Appl. Spec.*, 1990, **44**, 1137–1142.
55. Vasanthan N, Salem D R, 'Structure characterization of heat set and drawn polyamide 66 fibers by FTIR spectroscopy', *Material Innovations*, 2001, **4**, 155–160.
56. Murthy N S, Bray R G, Correale S T, Moore R A F, 'Drawing and annealing of nylon-6 fibers: studies of crystal growth, orientation of amorphous and crystalline domains and their influence on properties', *Polymer*, 1995, **36**, 3863–3873.
57. Bower D I, 'Investigation of molecular orientation distributions by polarized Raman scattering and polarized fluorescence', *J. Polym. Sci., Polym. Phys. Ed.*, 1972, **10**, 2135–2153.
58. Hirschfeld H, Chase D B, 'FT-Raman spectroscopy: development and justification', *J. Appl. Spec.*, 1986, **40**, 133–137.
59. Song K, Rabolt J F, 'Polarized Raman measurements of uniaxially oriented poly(ϵ -caprolactam)', *Macromolecules*, 2001, **34**, 1650–1654.
60. Tonelli A E, *NMR Spectroscopy and Polymer Microstructure: The Conformational Connection*, Wiley, New York, 1989.
61. Schmidt-Rohr K, Spiess H W, *Multidimensional Solid State NMR and Polymers*, Academic Press, London, 1994.
62. Murthy N S, Hatfield G R, Glans J H, 'X-ray-diffraction and nuclear-magnetic-resonance studies of nylon-6/I₂/KI complexes and their transformation into the gamma-crystalline phase', *Macromolecules*, 1990, **23**, 1342–1346.
63. Weeding T L, Veeman W S, Angad Guar H, Huysmans W G B, 'Structural investigation of polyamide-6 and polyamide-6 composites using carbon-13 cross polarization/magic angle spinning NMR', *Macromolecules*, 1988, **21**, 2028–2032.
64. Schreiber R, Veeman W S, Gabielse W, Arnauts J, 'NMR investigations of orientational and structural changes in polyamide-6 yarns by drawing', *Macromolecules*, 1999, **32**, 4647–4657.
65. Tzou D L, Spiess H W, Curran S, 'Solid State C13 NMR characterization of molecular orientation of hot drawn nylon 6', *J. Polym. Sci., Polym. Phys Ed.*, 1994, **32**, 1521–1529.
66. Kwak S-Y, Kim J H, Lee J-C, 'Correlation between local mobility and mechanical

- properties of high speed melt-spun nylon-6 fibers', *J. Polym. Sci., Polym. Phys. Ed.*, 2001, **39**, 993–1000.
67. Kwak S-Y, Kim J H, Kim S-Y, Jeong H G, Kwon I H, 'Microstructural investigation of high speed melt-spun nylon-6 fibers produced with variable spinning speeds', *J. Polym. Sci., Polym. Phys. Ed.*, 2000, **38**, 1285–1293.
 68. Elad J, Schultz J M, 'Microstructural rearrangement during heat treatment of drawn nylon 66 fiber', *J. Polym. Sci., Polym. Phys. Ed.*, 1984, **22**, 781–792.
 69. Salem D R, Moore R A F, Weigmann H D, 'Macromolecular order in spin oriented nylon 6 (polycapraamide) fibers', *J. Polym. Sci., Polym. Phys. Ed.*, 1987, **25**, 567–589.
 70. Gupta V B, 'Heat setting', *J. Appl. Polym. Sci.*, 2002, **83**, 586–609.
 71. Buckley C P, Salem D R, 'High temperature viscoelasticity and heat setting of poly(ethylene terephthalate)', *Polymer*, 1987, **28**, 69.
 72. Buckley C P, Salem D R, 'Heat setting of oriented poly(ethylene terephthalate): Effects of deformation mode, strain level, and heating medium', *J. Appl. Polym. Sci.*, 1990, **41**, 1707–1721.
 73. Hearle J W S, Wilding M A, Auyeung C, Ihmayed R A, 'Note on the heat setting of nylon 66', *J. Text. Inst.*, 1990, **81**, 214–217.
 74. Vasanthan N, 'Effect of heat setting temperatures on tensile mechanical properties of polyamide fibers', *Text. Res. J.*, 2004, **74**, 545–550.
 75. Murthy N S, Minor H, Latif R A, 'Effect of annealing on the structure and morphology of nylon 6 fibers', *J. Macromol. Sci., Physics*, 1987, **B26**, 425–444.
 76. Vasanthan N, Huang X X, 'Effect of polymer microstructure on dye diffusion in polyamide 66 fibers', *J. Appl. Polym. Sci.*, 2003, **89**, 3803–3807.
 77. Vasanthan N, 'Effect of the microstructure on the dye diffusion and mechanical properties of polyamide-6 fibers', *J. Polym. Sci., Polym. Phys. Ed.*, 2007, **45**, 349–357.

Yarn imaging and advances in measuring yarn characteristics

R. FANGUEIRO and F. SOUTINHO, University of Minho, Portugal

Abstract: This chapter discusses two integrated fields, the imaging techniques applied to yarn structures, and the latest advances in measuring yarn characteristics. The chapter first reviews the use of digital image processing in yarns, considering its importance, applications and recent advances. The chapter then discusses new developments in measuring yarn characteristics and online systems for measuring yarn quality.

Key words: yarn imaging, digital image processing, special measurements, online systems.

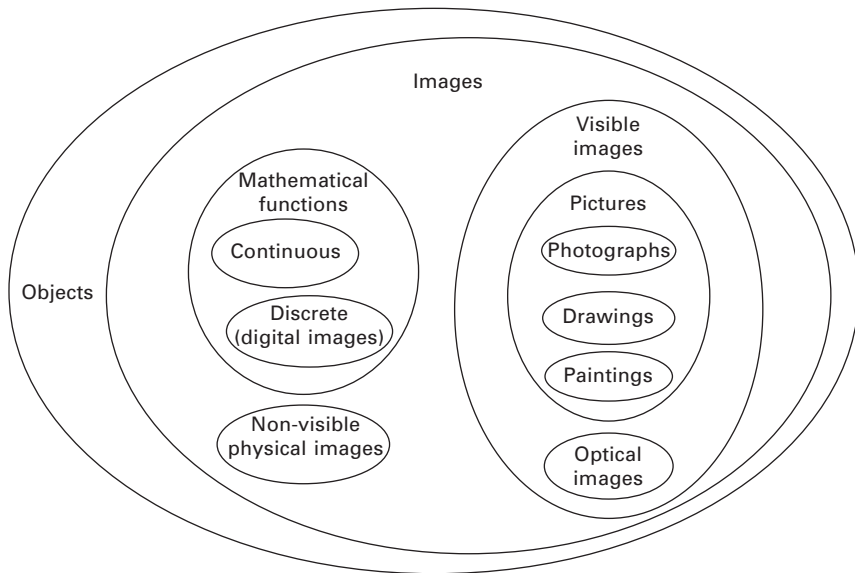
8.1 Introduction

Image processing and analysis can be defined as the act of examining images for the purpose of identifying objects and judging their significance. [1] Image analysis studies remotely sensed data, using logical processes to detect, identify, classify, measure and evaluate the significance of physical objects, their patterns and spatial relationships.

8.1.1 The concept of image

An image contains descriptive information about the object it represents. Images occur in various forms, some visible and others not, some abstract and others physical, some suitable for computer analysis and others not. It is thus important to be aware of the different types of images. [2]

Images can be classified into several types, based on their form or their method of generation. [2] It is instructive to employ a set theory approach. If a set of objects is considered, and images form a subset thereof, there is a correspondence between each image in the subset and the object represented. Within the set of images itself, there is a very important subset containing all the visible images – those which can be seen and perceived by the eye. Within this set again, there are several subsets representing the various methods of generating the image. These include photographs, drawings and paintings. Another subset contains optical images, that is, those formed with lenses, gratings and holograms. Figure 8.1 represents this schematically.



8.1 Image classification.

8.1.2 Importance of image processing in industrial processes

Image processing techniques are based on using analogue or digital optoelectronic devices and systems that allow an image with specific information distribution to be placed at the input or output of the system. [3] In the past, many tasks in manufacturing, such as inspection and assembly, were performed by human operators. Systematic assembly and inspection operations performed in an appropriate sequence or implemented in parallel lend themselves to image-controlled automation.

The necessary functions for imaging equipment include: [4]

- Exploiting and imposing environmental constraints
- Capturing an image
- Analysing the image
- Recognizing certain objects within it
- Initiating subsequent actions in order to complete the task at hand.

Remotely sensed data are analysed using various image processing techniques and methods, including analogue image processing and digital image processing. [1]

Visual/analogue processing techniques are applied to hard-copy data such as photographs or printouts, and interpret particular elements of the image. Whether analogue or digital, the image processing technique includes image

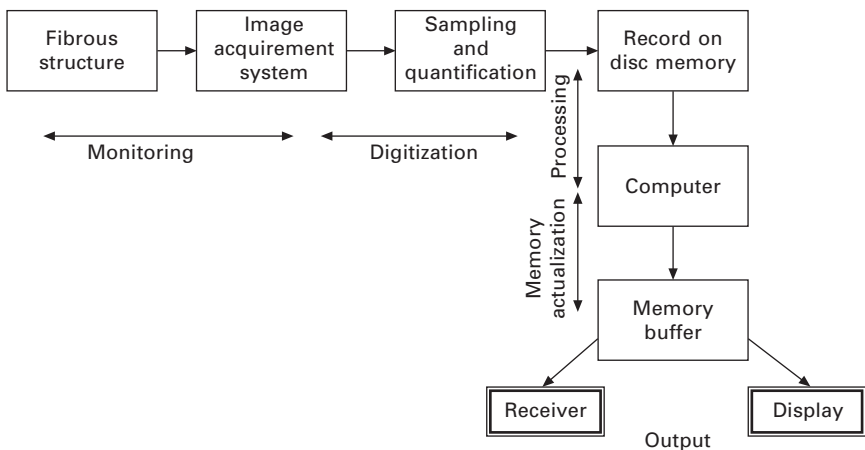
recognition and computer graphics. Image analysis is connected with image detection and processing, projection, transmission and storage, as well as image recognition and generation.

Important applications of image processing include industrial machine vision applications (automated visual inspection, process control, parts identification, robotic guidance and control), space exploration, astronomy, diagnostic medical imaging (medical image processing, medical image reconstruction) and scientific analysis. [4] Nowadays, image processing techniques are developing rapidly due to advances in informatics (information science and technology) and microprocessing technology.

8.1.3 Digital image processing

Digital image processing comprises a collection of techniques for manipulating digital images using computers [2] and has been applied to almost every type of imagery, with different degrees of success. Digital image techniques have been used in textiles for years [5], mainly for examining and analysing the structural parameters of yarns.

At its most basic level, digital image processing requires a computer to process images and two pieces of special equipment, an image digitizer and an image display device. In their standard form, images are not directly amenable to computer analysis. Since computers work with numerical (rather than pictorial) data, an image must be converted to numerical form before it can be processed by a computer. Figure 8.2 shows a proposed system for image processing. The digital image produced by the digitizer goes into temporary storage on a suitable device. In response to instructions from



8.2 System for image processing [3].

the operator, the computer executes image-processing programs on images called up from a library. During execution, the input image is read into the computer line by line.

Digital analysis can be used for identifying and measuring the geometrical dimensions of textile objects with very small dimensions; in particular, it enables the structure of the objects investigated to be analysed. [6]

8.2 Image processing techniques in fibrous material structures

8.2.1 Introduction to image processing techniques in fibrous materials structures

Computer vision is becoming more affordable both as a research tool and in process quality control. It has the advantage of providing more extensive characterization of the test product, at high speeds and resolutions, as well as being non-contact. [7] Electronic images contain more visual information than the human eye can discern. After a textile product is imaged, procedures may be used to yield more detailed structural conformation and to calculate different parameters. [8]

Image processing techniques have been applied to pilling evaluation, fabric texture and defect recognition, drape analysis, morphological measurements of fibre, and grading yarn appearance. [9] Digital image analysis also permits a more detailed study of the basic structural parameters of linear textile products, such as thickness, hairiness and number of twists. [6] In addition, this technique enables the above characteristics and others, such as twist parameter and linear density coefficient, to be estimated.

Image processing techniques can be used to image longitudinal and transverse cross-sections of fibres, fibre diameters, and linear textile products, which allows possible yarn faults and their causes to be determined. The images obtained can help to create two-dimensional (2D) and three-dimensional (3D) textile products. Digital image processing of textile product images is mainly concerned with processing 2D images.

Imaging techniques can be used to obtain detailed information about fibrous structures in the laboratory as well as in the production environment. Such evaluation has positive implications for measuring textile quality during production. [8]

8.2.2 Basic concepts used for digital image processing in fibrous material structures

Digital analysis of 2D images is based on processing the image acquired using a computer. The image is described by a 2D matrix of real or imaginary

numbers represented by a definite number of bytes. [3] Digital image processing includes: [3]

- Image acquisition and modelling
- Improving image quality and highlighting distinguishing features
- Reinstating the desired image features
- Compressing image data.

Image modelling is based on digitizing the real image. This process consists of sampling and quantifying the image. The digital image is defined by spatial image and grey-level resolution. The smallest element of the digital image is called a pixel. The number of pixels and the number of levels of brightness may be unlimited. [3]

Improving image quality and highlighting distinguishing features are the most commonly used techniques in image processing. The process of improving image quality does not increase the essential information represented by the image data, but increases the dynamic range of selected features of the acquired object, which facilitates their detection. [3]

Reinstating desired image features is connected with eliminating and minimizing any image features which lower its quality. Acquiring images by optical, optoelectronic or electronic methods involves the unavoidable degradation of some image features during the detection process. Aberrations, internal noise in the image sensor, blurring caused by camera defocusing, as well as turbulence and air pollution in the surrounding atmosphere, may affect quality. [3]

Image data compression is based on minimizing the number of bytes needed to represent the image. The compression effect is achieved by transforming the given digital image to a different number table in such a manner that the preliminary information is packed into a smaller number of samples. [3]

The main problem with analysing the structural parameters of textiles is the quality of the samples. [10] Numerous computer methods for identifying the structural parameters of fibrous structures can be found. However, they can only be applied to high-quality samples of products with relatively simple structures and low density. They are useless for samples damaged or partially destroyed due to deformation, burning or milling, as archaeological textiles often are. Another problem is that some fabric parameters, such as yarn crimp, cannot be determined using traditional methods due to unclear fabric cross-section and brittleness of the yarn and fibres.

8.3 Yarn characterization

8.3.1 State of the art

The correct and accurate evaluation of yarns is of major importance to the textile industry, as final fabric quality depends directly on yarn quality. Several

companies have developed equipment for testing yarns. The Tester 5 from Uster and the Multitester from Zweigle are notable for their contributions to the development of quantitative yarn characterization. However, these machines are expensive, require a considerable amount of space for installation and present limited resolution and precision for evaluating certain yarn parameters. As a result, some yarn producers do not have their own yarn testing facilities and instead subcontract to dedicated testing laboratories. [11]

Yarn can be analysed for different characteristics using image analysis, such as blend characteristics, thickness, diameter, hairiness, number of twists, geometrical dimensions and irregularity.

Numerous researchers have introduced different illumination and image processing techniques for yarn characterization. [12] For example, scanning electron microscopy (SEM) can be used to examine the physical characteristics of the fibres in a yarn. SEM allows specimens to be examined without coating and drying, and also permits structural changes in textile materials to be observed under different conditions, such as wetting and heating. [8]

Cybulska and colleagues [6, 10, 13] proposed a method for estimating yarn structure using digital image analysis. The yarn's basic structural parameters, such as thickness, hairiness and twist, are assessed by applying image processing techniques expanded by numerical methods. Numerical structural characteristics are obtained at every point of the yarn length, as well as acceptable average values and dispersion measures for the yarn's structural parameters. The first stage of analysis is to reconstruct an image of the sample itself, which involves multiplied application of the appropriate filtering and non-linear image transformations to obtain an image that recovers the texture of the fabric. It is necessary to take into account changes in the sample, such as shrinkage and other deformations due to ageing in hazardous environments. Two different methods for yarn modelling are presented. The first consists of forming the yarn from previously created 3D models of fibres by wrapping, twisting or nodding them. The method allows some predetermined features to be set, such as yarn unevenness or hairiness for staple yarns. The second method consists of giving the linear element texture with properties determined by the yarn's structural properties. The presence of fibres is reflected by concavities and convexities on the cylindrical yarn surface. The method can be used to simplify the first method or as an alternative way to form the virtual yarn.

Kopias *et al.* [14] used image digitization to evaluate pneumatically spliced polyurethane and textured yarns. For image digitization, they applied a method based on a scanner connected to a computer equipped with software programs designed for automatic object recognition. Abnormalities in the automatic image recognition process were eliminated manually.

Computer vision techniques have been used for yarn characterization research for more than 20 years. Several studies have been reported using

computer vision to measure one or more characteristics simultaneously. The commercial testers Uster Tester 4SX and Lawson Hemphill YPT were the first equipped with testing modules with CCD sensors. Computer vision probably provides the widest range of possibilities for hairiness assessment, enabling both simulation of current indices and development of new ones. [12]

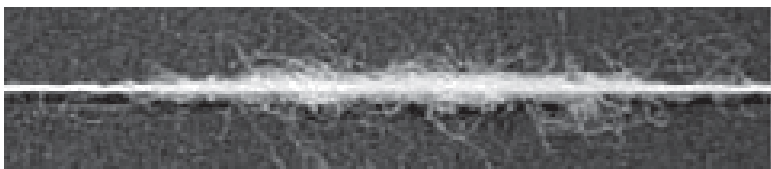
8.3.2 Measuring yarn irregularity

The production of a yarn is not completely controllable if the amount of fibre in the processes is variable. Moreover, fibres are not regular in shape and geometry, and can be blended with foreign elements. The principal causes of yarn irregularity may be summarized as: [15]

- Variations in fibre characteristics
- Random arrangements of fibres
- Non-random arrangement of fibres caused by faulty production
- Irregular twisting
- Existence of foreign elements in the fibre.

The regularity of a yarn fundamentally depends on the fibres and their arrangement within the yarn. [15] The main sources of yarn irregularity are random fibre arrangement and fibre-length effects, drafting waves, twist variation and foreign elements. [16] Figure 8.3 shows a yarn with thick and thin points. Two methods are commonly used in the textile industry for measuring yarn irregularity, one employing optical sensors to measure irregularity in diameter and the other using capacitive sensors to measure variation in mass. Charge-couple device (CCD) sensors are likely to replace conventional optical sensors owing to their much higher resolution capabilities and versatility. [12]

In capacitive measurement, the irregularity of the yarn is detected from variations in electric capacitance generated as the yarn specimen moves through the gap of a fixed air condenser. In photoelectric measurement, the irregularity is measured from fluctuations in light intensity or shadow on the sensor caused by a light beam passing across the yarn cross-section. Table 8.1 compares optical and capacitive methods.



8.3 Thick and thin points in the yarn.

Table 8.1 Comparison between optical and capacitive methods

Method	Advantages	Disadvantages
Optical	<ul style="list-style-type: none"> • Sees like eye • Suitable for hairiness determination • More sensitive for diameter variations • The fibre material does not affect measurement due to conductivity 	<ul style="list-style-type: none"> • Discrete sampling causing lower resolution • Irregular shape of yarn cross-section • Inhomogeneous radiant intensity • Sensitive to vibrations during measuring
Capacitive	<ul style="list-style-type: none"> • Continues sampling 	<ul style="list-style-type: none"> • Sensitive to both temperature and humidity • Not suitable for hairiness calculation • Sensitive to fibre material

Source: Ref. 16.

One of the early methods used to measure diameter irregularity was to compare the amount of light measured by a photocell before and after insertion of a yarn, the difference being proportional to the diameter. The photocell readings were calibrated using wires with known diameters. This technique was, however, affected by surface hairs, resulting in a significant and inconsistent rise in diameter measurements. [12] Another common method was direct manual measurement of yarn diameter, using magnified images obtained from a microscope or by projecting the shadow on a screen through magnifying lenses. However, this method was not favoured due to its tedious nature.

Another approach to determining diameter irregularity is optical filtering. Rodrigues *et al.* [17] explain that it is possible to separate the hairs from the core yarn using a special filtering mask with coherent dark-field imaging. Chu and Tsai [18] introduced an area compensation method to overcome inhomogeneous light intensity, one of the main restrictions in traditional optical methods that use photoelectric sensors.

It is evident that the light and illumination arrangement play an important role in acquiring and pre-processing yarn images. According to the literature, illumination methods for yarn imaging can be categorized in three main groups: back-lit (e.g., Zweigle G565), front-lit (e.g., Cybulska [13]), and dark field (e.g., Uster Tester Hairiness Attachment). Back-lit illumination is the most common method, especially for measuring diameter. [12]

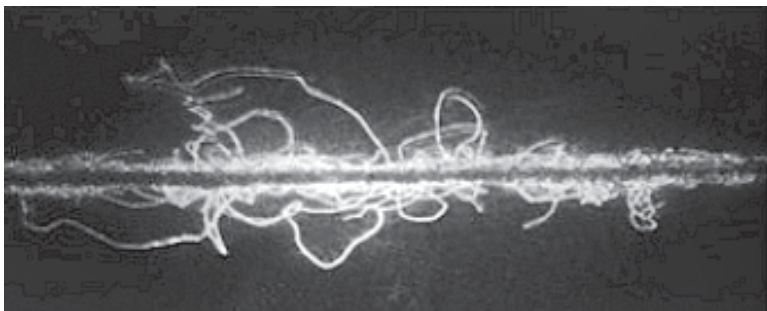
The main problem in image processing for yarn irregularity is defining the boundaries between the core and the surrounding hairs. For back-lit and front-lit images, the most common approach is to set a certain threshold value and identify the longest interval of yarn pixels as the core. However, the diameter measured will be strongly affected by this threshold level. In

addition, when using high resolutions, assuming that the longer duration signals represent the core can sometimes cause hairs lying along the scan line to be identified as the core. At high resolutions, there is also typically no significant change in the intensity of the CCD signal between highly dense surface fibres and the core. This increases the core diameter measurement if a single threshold is applied. Cybulska [13] presented a technique to define core boundaries for front-lit yarn images. The method initially found the core edges from the connected intervals of foreground pixels having the greatest length by scanning each line in the image perpendicular to the core axis. These initial boundaries were then corrected according to some predefined curves along which points generating the edge of the yarn core are assumed to be randomly distributed.

8.3.3 Measuring yarn hairiness

Hairiness is the result of fibres escaping from the strand. It is generally desirable to reduce yarn hairiness as much as possible since it causes significant problems in both yarn production and in subsequent textile operations. Such problems include higher friction during spinning, greater fly fibres, and increased yarn breaking during weaving. Yarn production costs need to be minimized while maintaining yarn hairiness and yarn strength within required limits. [19]

Measuring yarn hairiness (Fig. 8.4) is traditionally based on microscopic, weighing and photoelectric methods. [20] Image processing methods are still under development, but to classify hairiness accurately, they require a well-defined algorithm to distinguish the hairs from the main core, a camera with a high level of optical magnification and a computer-based system with high computational resources to process results within an acceptable time. These characteristics severely increase the cost. [20]



8.4 Hairiness in the yarn.

8.3.4 Yarn System Quality (YSQ)

Yarn System Quality (YSQ) is presented as an innovative, low-cost, portable and high-precision yarn evaluation tester for quality control of yarn characteristics under laboratory conditions. [11, 20] It has a modular format, which can integrate yarn hairiness, mass, regularity and diameter measurements simultaneously, and enables the determination of some yarn production characteristics.

Quantifying yarn hairiness and diameter variation (with a sampling resolution length of 1 mm) is carried out using photodiodes. Diameter characterization, based on samples 0.5 mm wide, uses a linear photodiode array. Measurement of mass variation, based on samples of 1 mm, employs a parallel plate capacitive sensor. In YSQ measurement parameters based on optical sensors, a coherent signal processing technique with Fourier analysis is used to obtain linear and consistent output signal variations, and the measurement systems are automatically calibrated. YSQ introduces new statistical yarn parameters and new signal processing approaches for periodic error analysis, and establishes a reliable method of yarn characterization, as, depending on the resolution used, it is possible to obtain parameters by direct measurement. [20] YSQ is thus a system that reduces equipment costs and offers superior product quality and high production efficiency.

In comparison with available commercial systems, YSQ presents several new characteristics. These include the simultaneous use of coherent optical signal processing for characterizing yarn hairiness and diameter; auto-calibration procedures for determining yarn hairiness reference and diameter; direct detection of nep irregularities via integration and measurement of yarn mass variation based on 1 mm capacitive sensors; determining new parameters in yarn analysis allowing highly precise yarn characterization; use of three signal processing techniques; enabling accurate characterization of periodic errors; automatic determination of yarn production characteristics; modular integration of yarn mass measurement, hairiness measurement, diameter variation measurement and precise diameter determination; high portability due to its smaller size; and suitability for yarn quality control use in the laboratory or industry environment. [11, 20]

8.3.5 Computer vision for textured yarn interlacements

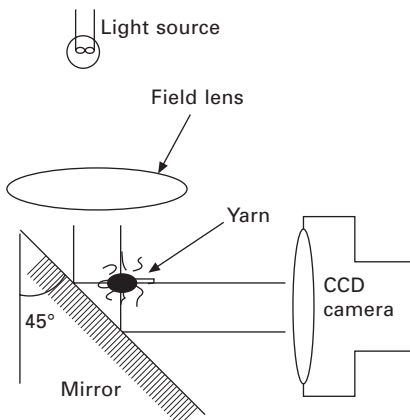
False-twist textured yarns lack inter-filament cohesion, and consequently a number of difficulties are observed during unwinding and fabric-forming processes. One modern technique for imparting cohesion in false-twist textured yarns is air-intermingling (interlacing). Air-intermingling uses a nozzle to create a very turbulent, high-speed airflow. This creates regular but intermittently entangled nodes in the open structure of the textured yarn, commonly known in the industry as 'nips'.

The frequency and regularity of nips and their stability under applied loads are important criteria in assessing the performance of mingling nozzles and the quality of the intermingled yarns. A system has been developed that automatically detects nips in yarns with or without applied tension, which can otherwise be seen by the naked eye in the absence of tension. [7]

The system is divided into two main parts, the yarn transport section and the yarn imaging/analysis section. [7] For each part, a separate PC is used, but the two are connected. The imaging PC controls all operations, and sends instructions to the transport control PC, which can operate in a stand-alone fashion if necessary. The yarn is imaged using a 1024 pixel line scan CCD camera that scans up to 10 kHz. For a yarn travelling at 10 m/s the scan-to-scan resolution is 1 mm. Two orthogonal views of the yarn in the same cross-sectional plane are used to characterize the yarn. A mirror inclined at 45° to the viewing plane achieves this, as shown in Fig. 8.5. This technique has been shown to provide more accurate evenness data for staple fibre yarns.

8.3.6 Image processing to control nanofibre production

Nanotechnology is an emergent technology that is developing quickly and is gaining greater importance in many fields. Nanotechnology can be defined as the science and technology related to understanding and controlling matter at the nanoscale, mainly oriented towards the research and development of materials, devices and systems with novel properties and functions due to their dimensions or components. Nanomaterials are generally characterized as materials with dimensions of 100 nm or less. Electrospinning is a process that creates polymer nanofibres with diameters in the range of nanometres to a few microns. [12] The fibre diameter, structure and physical characteristics



8.5 System to control textured yarn interlace [7].

of nanofibres can be effectively tailored by controlling various parameters that affect the electrospinning process. [21]

Although electrospinning is based on quite simple principles, a lot of work has been done to understand how various parameters influence the process and the characteristics of the resulting nanofibres. Research into electrospinning under different conditions has used SEM to examine different aspects, including fibre diameter, porous fibre surface, arrangement of the fibres, etc. [21]

Classical methods of analysis, such as water retention, deliver quantitative information about pore structure, and inverse volume exclusion chromatography provides information about pore size distribution, but neither provides any information on their spatial distribution. [22] Real-time observations of the electrospinning process have been made, using high-speed, high-magnification imaging techniques. Yarns electrospun from polyethylene oxide have been analysed using wide-angle X-ray diffraction (WAXD), optical microscopy, and environmental scanning electron microscopy (ESEM). [23] The internal morphology of the main artificial fibres can be visualized by applying fluorescence and transmission electron microscopy to fibre cross-sections. A more detailed examination of the internal pore structure of fibres can be made by combining information about pore accessibility (from fluorescence microscopy) and the visualized pore structure. [24]

8.3.7 Commercially available yarn characterization testers

The following yarn characterization testers are used by yarn manufacturers to evaluate the different properties of yarns.

Multitester[®] from Zweigle

Zweigle's Multitester[®] consists of three individual modules: ZT 5, OASYS[®] and G 567. The MT-Multitester can be customized as an individual stand-alone module or in sets of two or three. This system presents three different sensors to give an all-round picture of sliver, roving and yarn evenness and hairiness.

The G 567 Yarn Hairiness Tester measures hairiness using a newly developed optical measuring head with a laser light source, which has an extremely long working life at constant light output. The G 567 covers nine fibre length zones, from 1 mm to 15 mm, in one pass, producing objective, reproducible data. It is controlled by a PC that also analyses the test results. Any desired number of measurements can be made on a bobbin. The G 567 becomes a fully automated tester by adding a bobbin changer with 24-bobbin capacity. The G 567 operates independently. [25]

The ZT 5 module is an evenness tester with capacitive sensors. For measuring yarns, either measuring channel of the capacitive yarn sensor may be used, depending on the yarn count. For users intending only to test yarns, the sensor on the left, intended for rovings and slivers, may be omitted. [25]

The OASYS[®] module is an optical system for visually assessing yarns in woven and knitted fabrics. The system operates on the principle of absolute optical measurement using infrared light. [26] The structure of a yarn is subject to variations of a periodic or random character. The measuring system compares the yarn diameter with the constant reference mean and records variations in length and diameter. The reference mean is established in the first 100 m of testing. This system uses an infrared light sensor operating with a precision of 1/100 mm over a measuring field length of 2 mm and at a sampling interval also of 2 mm. The speed of measurement may be selected on a graduated scale between 100 and 400 m/min. The sensor is unaffected by ageing of the light source, extraneous light, contamination, temperature or humidity. It is also unaffected by yarn characteristics such as colour, conductivity and lustre. Defects are classified in respect of their length and their variation in diameter. The system provides the coefficient of variation of the diameter values, CV(%), a CV(L) curve, a histogram that shows diameter distribution, and a spectrogram that shows wavelengths of the periodic defects in the yarn. [26] The essential function of the OASYS[®] system lies in its ability to simulate yarn irregularities on boards and woven and knitted fabrics using previously measured yarn data.

Uster Tester 5

The Uster Tester 5 is an offline yarn testing device that has six sensor options and provides a detailed yarn profile in less than 60 seconds. The Uster Tester 5-S800, the most recent design, measures the most important quality parameters, such as evenness and yarn imperfections, with high precision at 800 m/min testing speed. This system uses capacitive and optical sensors, and can determine the evenness, number of thin places, thick places and neps, periodic mass variations, variance–length curve, hairiness, remaining dust and other contaminating particles in yarns, diameter, diameter variation, roundness, density, number of foreign fibres, and count. [27]

The Uster Tester 5 apparatus is characterized by: [27]

- OH Sensor: hairiness – a perceptive indication of touch and wear
- OM Sensor: diameter and shape – advanced prediction of appearance
- OI Sensor: accurate measurement of dust and other contaminants
- FM Sensor: classification of foreign fibres
- KBS: advanced identification of machine defects.

Keisokki KET-80 and Laserspot

The Keisokki KET-80 and Laserspot [16] are two types of evenness tester based on capacitive and optical measurement principles, respectively. Like the Uster Tester, KET-80 provides a U% and a CV(%), a CV(L) curve, and a spectrogram. It also provides a deviation rate, DR%, which is defined as the percentage of the summed-up length of all partial irregularities exceeding the preset cross-sectional level to the test length. In practice, however, the yarn signal is primarily processed by the moving average method for a certain reference length. As a result, long-term irregularities are likely to be detected. The Laserspot evenness and hairiness instrument uses laser light and is based on the Fresnel diffraction principle. With this principle, the yarn core is separated from hairs, allowing yarn diameter and hairiness to be measured at the same time.

Flying Laser Spot Scanning System

The Flying Laser Spot Scanning System [16] consists of three parts: the sensor head, the specimen feeding device, and the data analysis system. When an object is placed in the scanning area, the flying spot generates a synchronization pulse that triggers the sampling. The width between the edge of the first and last light segments determines the diameter of the yarn. Depending on the spot size and specimen feeding speed, the measurement values may vary, therefore it is important to calibrate the system for the feeding speed and the spot size.

8.4 Special advances in measuring yarn characteristics

8.4.1 Introduction to special advances in measuring yarn characteristics

Growing international competition, increasing cost pressure, customer demand for high and consistent product quality, the variety of products and the need to quickly satisfy customer demand make modern and efficient quality control systems extremely important. [26] Quality control should be applied to every process in the textile production line and not just to the finished fabric. The goal is early determination and elimination of faults. One important part of quality control is textile inspection. Fast, continuous quality inspection and the increasing number of fibre materials and applications require modern, efficient test and analytical methods.

Quality inspection can be separated into two different fields: [26]

- Offline inspection, which is used to check the properties of the finished product (e.g. bobbin) in testing laboratories

- Online inspection, which is used to monitor process parameters (e.g. yarn tension, yarn speed) on the production line.

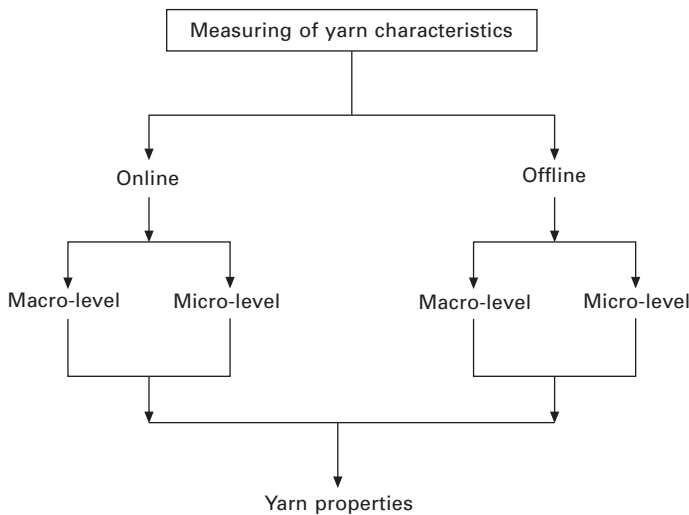
Quality control is related to measuring yarn characteristics, and both methods of quality inspection can involve analysing the yarn at the macro- and micro-level. [26]

Special techniques for measuring yarn characteristics have been developed in recent years and applied to analysing yarn structures. Physical characteristics are checked at the macro-level and molecular properties at the micro-level. Figure 8.6 shows the different quality inspection methods for artificial fibres.

The methods currently used to measure yarn characteristics include a multiplicity of offline measurement systems which test physical properties as well as molecular structures and morphologies. Online methods are only used for determining physical properties, although using online determinations to obtain information on the molecular structure and morphology would be beneficial. Table 8.2 presents different techniques used to measure the main yarn characteristics at macro- and micro-levels offline. [26]

8.4.2 Yarn quality in the spinning process

Yarn production is the first procedure in textile formation. As yarn is the basis for all subsequent procedures, the following yarn properties must be optimized fibre fineness, fibre staple length, yarn strength, elongation, purity and rigidity. [28] During yarn production, yarn characteristics must be quality controlled at the following levels: [28]



8.6 Fields of quality inspection methods for man-made fibres.

Table 8.2 Macro-and micro-level tests

Macro-level (offline)	Micro-level (offline)
Yarn count	Differential scanning calorimetry (DSC)
Fibre diameter	Scanning electron microscopy (SEM)
Yarn evenness	Birefringence measurement
Stress-strain behaviour	Infrared spectroscopy (IR spectroscopy)
Mechanical crimp	Wide angle X-ray scattering (WAXS)
Shrinkage behaviour	Small angle X-ray scattering (SAXS)
Interlacing of textured and flat filaments	Near-infrared (NIR spectroscopy)
	Nuclear magnetic resonance (NMR spectroscopy)

Source: Ref. 26.

- Opening, cleaning and blending of raw materials: uniform opening, more detailed opening gradually, continuous formation of new levels during cleaning, appropriate feeding of the material, correct placing of the material for blending
- Carding: removing neps and very short fibres, making fibres parallel
- Combing: uniformity of the sliver produced, condition of combs, neps, static electricity, weight of incoming or outgoing sliver
- Drafting: cylinder diameter, draft, pressure on the rollers
- Sliver formation: sliver uniformity, draft, twist
- Spinning: draft, twist, sliver quality and weight, adjustments, yarn uniformity, yarn strength
- Package preparation: breaks, machine speed, knots
- Twisting and steaming of the yarn: breaks, twists, single yarn defects, time.

The majority of fabric defects are caused by defects in the yarns. Table 8.3 presents the potential causes of different defects. Yarn defects may be defined as yarn irregularities that can lead to difficulties in subsequent production stages, or to defects in the fabric. These faults can be divided into three main classes: thick points, thin points and neps. [29]

Developing electronic imaging capable of predicting the visual quality of woven or knitted fabrics is expected to enhance the quality of yarn and fabric development processes in the textile industry.

8.5 Online systems for measuring yarn quality

8.5.1 State of the art concerning online systems for measuring yarn quality

Introducing image analysis techniques in the textile industry could enhance quality through the efficient use of metrology and control. There is a body of research on the online quality control of textile substrates. [15]

Table 8.3 Potential causes for different types of defects

Defect	Potential causes
Spinning defects	Yarn piecing at the ring spinning machine; piecing character – aleatory; Lint in yarn Arraying of fibres flattened and paralleled, adjacent of wound round the yarn Thickening Foreign additions
Yarn including foreign particles	Waste deposition on parts of the spinning machines Improper carding Strand incorrect drafting on ring spinning machine
Corkscrews	Non-correlation of torsion coefficient with yarn application (for high torsion coefficient) Presence in the yarn of thin areas accumulates high torsions
Greasy yarns	Excessive oiling of spinning machine parts Yarn handling with dirty hands (binding)
Wrinkles	Too small division in the drafting assembly Eccentrically disposed arms and cylinders at drafters Improper parameters of humidity and temperature in the working shed
Pilled yarn	Usage of blends with fibres having high differences between their characteristics (length density, length) Worn out parts of spinning machines, producing accentuated yarn frictions Non-correlation of divisions with mean length of processed fibres Microclimate parameters below normal limits
Yarns with adjacent foreign particles	Improper cleaning of fibrous stock during unpacking, opening and blending operations Insufficient cleaning of operating parts (especially of card rollers covering)
Yarn imperfections	Usage of inferior quality raw materials, with a high impurity content Improper technological processing Eccentric up and down cylinders in the drafting assembly Insufficient pressure at upper cylinder level
Neps	Improper carding presence of a large number of neps in the card web Improper combing Improper technological parameters for spinning preparation operations Improper quality of semi-products (carded silver, drafted silver, top, roving)
Double yarns	Simultaneous feeding of two slivers at the ring spinning machine Improper yarn piecing

Source: Ref. 28.

Online methods are only used for determining physical properties. It would be beneficial if online determination could be used to obtain information on molecular structure and morphology, because physical properties could then be derived from these parameters [26]. Being able to use a measurement system for more than one yarn property would lead to cost reduction in quality control. Computers, microprocessors and online measurement and monitoring of different parameters in the preparatory and spinning processes have become common features of modern spinning machines. Greater emphasis on diversification and manufacturing of yarns for export means that online measurement of evenness and yarn faults is now essential, but it requires expensive instruments and software. [29]

According to Suh *et al.* [30], no commercial system exists for predicting or visualizing fabric qualities directly from yarn diameter or mass measurements taken online. The systems currently available (such as CYROS[®], Uster[®] EXPERT[®] and OASYS[®]), visualize yarn and fabric qualities through various types of images created directly from yarn profiles captured from measurement systems. However, these systems are not completely satisfactory due to the way the yarn data are converted to fabric images and because the images often have to be judged visually in the absence of a quantitative measure. Nor do any of the existing systems ‘map’ or ‘fingerprint’ the quality of a woven or knitted fabric for an entire roll or at any specific location within a roll. Therefore, there are no methods for judging and ranking the visual or physical qualities of fabric rolls produced by a given machine at different time points or from different yarns, or from more than one machine. Another unsolved technical issue is defining and measuring the ‘most ideal yarn signals’, whether optical, capacitive, or ‘fused’ opto-capacitive, that best depict the true fabric image. The optical and capacitive methods currently being used are known to be grossly inadequate due to distortion of actual yarn images within a fabric.

Suh *et al.* [30] present a system for electronically imaging the quality attributes (weight, uniformity of appearance, physical properties, etc.) of woven and knitted fabrics directly from an online yarn mass/diameter measurement system without having to go through the actual fabrication processes. They have examined and expanded mathematical theories and the corresponding algorithms for image simulation, data reduction and data mapping onto the structural geometry of woven and knitted fabrics, at both micro- and macro-scales. According to Suh *et al.* two different yarn profile measurement systems have been developed [16, 30]:

- *Data fusion*: This system comprises measuring, combining and analysing data from multiple sensors. Although data fusion has been implemented in many engineering systems, it has not been widely used in textiles due to the non-linear interaction of multiple inputs to multiple outputs.

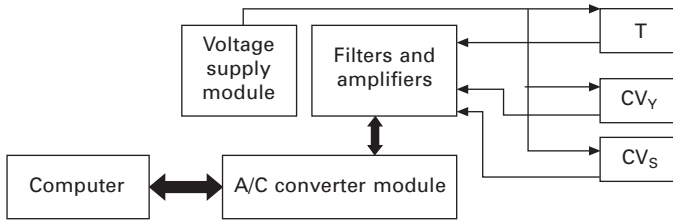
Additionally, different sensors have different sampling rates, precision, accuracy, bandwidth, etc., which makes combining measurements difficult. A line-scan camera and a mass sensor capture yarn data in real time. For each millimetre of yarn, the counter generates a pulse, triggering the camera and the mass sensor. The data from the camera and mass sensor are collected and stored in an array. The size of the array is cross-checked with the location information provided by the counter. A new hardware system that enables input tension and speed to be controlled while simultaneously measuring output tension, yarn diameter (every 1 mm) and capacitance (every 8 mm) has been developed.

- *Multiple yarn diameter measurement:* This is a new system for measuring yarn diameters at more than one angle to obtain a better average for the diameter and compute the overall ‘eccentricity index’ of the yarn along the axis. First, assuming the yarn is circular, the yarn is held between the camera and the light source and rotated clockwise in 12 steps each of 30 degrees for a full rotation. At each step, a picture of the yarn diameter is taken to examine the yarn profile. The data are analysed by a Matlab program to produce a cross-sectional image of the yarn. Software has been developed that communicates with the hardware to collect data and store them in a file for further analysis.

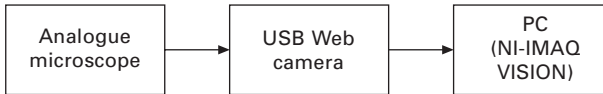
Lotka and Jackowski [31] present an online system for analysing the quality parameters of yarns formed in rotor spinning, which is carried out by means of a computer measuring system and pays particular attention to yarn tension. Yarn tension is a phenomenon inseparably connected with spinning, and is also of fundamental importance in rotor yarn formation. The problem of dynamic yarn tension fluctuations is of paramount importance, because they may cause a decrease in yarn quality parameters, such as irregularity of linear density, elongation and tenacity, and therefore an increase in the number of faults.

The system allows continual recording of linear density of the yarn, linear density of the sliver and yarn tension. The basic elements of this system are a computer and three measuring heads connected to the computer by means of a measuring interface. The T-measuring head (based on a tensometric gauge) measures yarn tension, and two Uster electro-capacity measuring heads determine irregularities in linear density. Figure 8.7 presents a block schematic of the computer measuring system. The measuring interface consists of an analogue-to-digital converter module, filters, amplifiers, and a voltage supply module. The system is flexible and adaptable to any PC. The software permits the spinning process to be controlled, and visualizes the parameters measured, as well as conducting data capture, processing and retrieving.

YSQ (see also Section 8.3.4) represents a low-cost system for determining



8.7 Block schema of the computer measuring system. T: yarn tension measuring head; CV_Y: yarn linear density measuring head; CV_S: sliver linear density measuring head; A/C: analogue-to-digital converter [32].



8.8 YSQ system schematic [20].

yarn production characteristics. The system includes a USB web camera associated with a microscope and using monochromatic illumination. The image processing technique was developed using IMAQ Vision software from National Instruments. The custom application analyses an image source and determines the desired yarn production characteristics, namely, the fibre twist orientation, the twist step and twist orientation in folded yarns, and the number of cables (folded or spun yarn). The system was validated by comparing the results with electron microscope images. [20] It is illustrated in Fig. 8.8.

8.5.2 Commercially available devices for measuring yarn quality

Uster solutions

Uster Sliverguard[®]

The Uster Sliverguard[®] is an automatic, modular online system for quality control in sliver production. The system monitors measurement fluctuations, unevenness and periodic faults on the production line directly. As soon as the defined limits are exceeded, an alarm or a machine stop is triggered. This modular online monitoring and auto-levelling system is used in spinning preparation for short staple spinning mills. It is sold as a retrofit sliver monitoring solution for drawframes, combers and cards, and also as an OEM product for monitoring and auto-levelling. The system permits continuous monitoring of all major visible sliver quality parameters: linear mass (A%),

evenness (CV%, CVL%), periodic faults in spectrogram form, and short thick-places (>1.5 cm length). [27]

The conventional offline method of sliver quality monitoring involves checking count and unevenness values, and visually checking the spectrogram only two to three times per shift. This creates problems because only a very short sliver production is supervised (less than 0.02%), the moment a machine fault produces poor sliver quality is not known, thick places in the sliver cannot be captured and, in the case of auto-levelling drawframes, performance is not continuously supervised. [27] The Uster Sliverguard[®] system can be introduced on drawframe, card and camber machines as a retrofit solution.

Uster Quantum 2[®]

The Uster Quantum 2[®] is considered as a yarn clearer, and is integrated with intelligent advanced sensing technology such as Computer Aided Yarn (CAY) clearing. This system monitors online quality options in a package comprising Uster Quantum Expert[®], Uster CAY, true hairiness measurement, vegetable filter, splice classification and Classimat. [27] The system separates critical quality outlier bobbins and quantifies them for the entire production on a continuous basis. Some product highlights include: [27]

- Combination of capacitive basic clearing with foreign fibre clearing
- Advanced clearing limit optimization using CAY (Computer Aided Yarn) clearing
- Detection of foreign fibres at low intensity
- Vegetable filter, to filter out vegetable matter that disappears after bleaching
- Total testing – quality monitoring of the complete production on the same basis as the Uster Tester and Uster Classimat Quantum
- Splice classification per position with CAY
- Detection of white and coloured polypropylene.

Uster Ring Expert

Uster Ring Expert is used for online quality and production monitoring and monitors machine settings, production data and quality data simultaneously. The system monitors each individual spinning position. The information supplied is used for process optimization. It is designed to monitor individual spindles for reliable measurement of end breaks and traveller speed. End break frequency, slipping spindles, production, efficiency and stoppages are systematically monitored. [27]

Barco solutions

BarcoProfile is a system with applications in online yarn quality control on air-jet and friction spinning machines, on winders for technical yarns and also on air-jet texturing machines and in spinning blow-room preparation and ring spinning.

Application in rotor spinning machines

BarcoProfile, also known as Schlafhorst's Corolab, is an optical yarn measurement system used on rotor spinning machines. The system measures the yarn diameter for every millimetre of yarn. It can also perform all the above-mentioned open-end (OE) yarn clearer functions, together with detection of foreign fibre material, and allows OE yarn spinners to deliver contamination-free yarn to their customers. [32]

The BarcoProfile optical yarn clearer is available for all kinds of OE spinning machines. Apart from the yarn clearer functions, BarcoProfile also substitutes for time-consuming laboratory-based spot checks, because of its built-in 100% online and real-time quality assurance functions. [32] The sensor measures the shadow cast by the yarn on the photoreceiver. State-of-the-art opto-electronics ensure supreme stability in even the most adverse environments. This allows an absolute measurement and leads to a detector capable of detecting even the faintest gradual diameter changes. Based on the measured diameter values, software algorithms reconstruct and analyse the yarn profile. Positions are stopped based on user-selectable criteria.

Application in air-jet texturing

BarcoProfile is also used as a quality monitoring system for air-jet texturing. Using conventional opto-electronics, the receiver signals are converted into an absolute and accurate diameter value, which serves as the basis for several types of analysis. [32] The standard measuring accuracy is 0.01 mm, with an optional increase to 0.005 mm. This allows the detection of even the faintest changes in textured yarn diameter. The processed information, together with the most important production data, is sent to a central unit where it is stored in a local database. Via a WindowsCE[®]-based software interface, the users of the BarcoProfile system get online and real-time information on both textured yarn quality and production.

BarcoProfile halts production when something is wrong, and reports on the quality being produced, which positions are approaching off-quality tolerances, and where the exceptions are. [32] The most important analyses performed by the BarcoProfile system are the online calculation of CV%, the thick and thin yarn count channel (for this channel, BarcoProfile makes use

of the direct correlation between yarn count and measured yarn diameter) and the detection and classification of thick and thin defects. [32]

8.6 Future trends

Image processing techniques are applied to yarn structure to measure some structural and morphological characteristics like irregularity, hairiness, number of twists and yarn appearance. Moreover, image processing is used in special on-line systems to measure yarn quality during the spinning process. In the last few years the rapid evolution in the equipment used for image capturing and analysis has provided an important input for the development of the digital image processing, especially for scientific analysis situations.

One of the most important trends that will lead the development of image processing techniques in the near future is the analysis of yarns containing fibres with special structures, like different cross-sections, and functionalities, mainly provided by the incorporation of certain agents during their production steps. The arrangement of these types of fibres in the yarns and their influence on the yarn parameters will result in new achievements in image analysis. Furthermore, techniques for analysing yarns based in micro and, mainly, nanofibers and their on-line quality control are an important future trend.

Yarn structure is being customized according to the needs of each particular application, mostly for technical purposes. This trend seems to be one of the most important issues to be faced by image analysis.

Besides, it is expected that the advances in informatics and image acquisition and modelling, in general, will contribute positively in this particular area of yarn analysis technique. These advances, combined with image quality and image compression improvements, will be particularly relevant in yarn production environments.

8.7 Sources of further information and advice

The objective of this chapter has been to present, in an integrated and concise form, the imaging techniques applied to yarn structures, and the latest advances in measuring yarn characteristics. For further information the reader should consult more specialized literature, like those suggested below:

- *Image Processing and Analysis*, Vol. 2, Y.J. Zhang (1999)
- *Introduction to Image Processing and Analysis*, John C. Russ and J. Christian Russ, CRC Press (2008)
- *Adaptive Image Processing: A Computational Intelligence Perspective*, K.H. Yap, L. Guan, S.W. Perry and H.S. Wong, 2nd edn, CRC Press (2009)
- *Image Engineering: Processing, Analysis, and Understanding*, Y.J. Zhang, Cengage (2005)

- *Image Processing and Pattern Recognition: Fundamentals and Techniques*, F.Y. Shih, Wiley (2009)
- *Mathematics of Digital Images*, S. Hoggar, Cambridge University Press (2006)
- GIS Tutorials: <http://www.gisdevelopment.net/tutorials/tuman005.htm>
- USTER Company: <http://www.uster.com/UI/default.aspx>
- Image processing: http://en.wikipedia.org/wiki/Image_processing

8.8 References

1. GIS Development. The Geospatial Resource Portal; Tutorial: Image Processing and Analysis. Available from <http://www.gisdevelopment.net/tutorials/tuman005.htm> (accessed 20 November 2008).
2. Castleman, K.R. (1996), *Digital Image Processing*, Prentice Hall, Upper Saddle River, NJ, pp. 3–5.
3. Drobinia, R. and Machnio, M.S. (2006), 'Application of the image analysis technique for textile identification', *Autex Research Journal*, 6(1), 40–47.
4. Awock, G.W. and Thomas, R. (1996), *Applied Image Processing*, McGraw-Hill, New York.
5. Song, G., Huang, G. and Ding, X. (2006), 'Study on automatic stitch length measuring system with digital image processing technique', *Journal of the Textile Institute*, 99(5), 415–420.
6. Cybulska, M. (1997), 'Analysis of warp destruction in the process of weaving using the system for assessment of the yarn structure', *Fibres & Textiles in Eastern Europe*, 5(4), 68–72.
7. Millman, M.P. Acar, M. and Jackson, M.R. (2001), 'Computer vision for textured yarn interlace (nip) measurements at high speeds', *International Journal of Mechatronics*, 11, 1025–1038.
8. Zhang, T. (2003), Improvement of Kenaf yarn for apparel applications, Master Thesis, Graduate Faculty of Louisiana State University, Baton Rouge, LA.
9. Xu, B.G., Murrells, C.M. and Tao, X.M. (2008), 'Automatic measurement and recognition of yarn snarls by digital image and signal processing methods', *Textile Research Journal*, 78(5), 439–456.
10. Cybulska, M., Florczak, T. and Maik, J. (2005), 'Archaeological textiles – Analysis, identification and reconstruction', 5th World Textile Conference, Autex 2005, 27–29 June 2005, Portorož, Slovenia.
11. Carvalho, V. and Soares, F. (2008), 'Automatic yarn characterization system,' IEEE Sensors 2008 Conference, Italy.
12. Ozkaya, Y.A., Acar, M. and Jackson, M.R. (2005), 'Digital image processing and illumination techniques for yarn characterization', Loughborough University Mechanical Engineering Department Mechatronics Research Group, *Journal of Electronic Imaging*, 14(2).
13. Cybulska, M. (1999), 'Assessing yarn structure with image analysis methods', *Textile Research Journal*, 69, 369–373.
14. Kopias, K., Mielicka, F. and Stempien, Z. (1998), 'An attempt to estimate spliced yarn using computer image analysis', IMTEX 98 International Scientific Conference, Technical University of Łódź, Poland.

15. Castellini, C., Francini, F., Longebardi, G., Tribilli, B. and Sansoni, P. (1996), 'On-line textile quality control using optical Fourier transforms', *Optics and Lasers in Engineering*, 24, 19–32.
16. Gunay, M. (2005), Characterization and quantification of woven fabric irregularities using 2-D anisotropy measures, Dissertation submitted for the degree of doctor, fibre and polymer science, North Carolina State University, Raleigh, NC.
17. Rodrigues, F.C. Silva, M. S. and Morgado, C. (1983), 'The configuration of a textile yarn in the frequency space: A method of measurement of hairiness', *Journal of the Textile Institute*, 74(4), 161–169.
18. Chu, W.C. and Tsai, I. (1996), 'A new photoelectric device for the measurement of yarn diameter and yarn evenness. Part I: Improvement of the variance of radiant intensity using the area compensation method', *Journal of the Textile Institute*, 87(3), 484–495.
19. Barella, A. and Manich, A.M. (1997), 'Yarn hairiness update', *Textile Progress*, 26(4), 1–27.
20. Carvalho, V.H. (2008), Automatic yarn characterization system, PhD Thesis, University of Minho, Portugal.
21. Piroi, C., Harpa, R., Cristian, I. and Radu, C. (2007), 'Electrospinning of polymer nanofibres – Recent developments', CORTEP Conference, Technical University, Iași, Romania.
22. Abu Rous, M., Ingolic, E. and Schuster, K.C. (2005), 'Visualization of the nano-structure of lyocell and other cellulose for a basic understanding of their functional and wellness properties', 5th International Istanbul Textile Conference, *Recent Advances and Innovations in Textile and Clothing*, Istanbul, May.
23. Deitzel, J.M., Kleinmeyer, J.D., Hirvonen, J.K. and Beck Tan, N.C. (2001), 'Controlled deposition of electrospun poly(ethylene oxide) fibers', *Polymer*, 42(19), 8163–8170.
24. Abu Rous, M., Ingolic, E. and Schuster, K.C. (2005), 'Revelation of the pore structure of lyocell and other cellulose applying fluorescence and electron microscopy', 5th World Textile Conference, Autex 2005, 27–29 June 2005, Portorož, Slovenia.
25. Zweigle Textilprüfmaschinen, available from <http://www.Zweigle.com> (accessed 18 November 2008).
26. Blascu, V., Grigoriu, A. and Vrinceanu, N. (2007), 'Some aspects concerning quality control for manmade fibres', CORTEP Conference, Technical University, Iași, Romania.
27. Uster Technologies, Textile Quality Controlling, available from <http://www.Uster.com> (accessed 18 November 2008).
28. Zampetakakis, A., Katsaros, G., Visileanu, E., Vulpe, G. and Niculescu M. (2005), 'Quality and defect analysis for yarns, knitted, woven fabrics and clothing products', 5th World Textile Conference, Autex 2005, 27–29 June 2005, Portorož, Slovenia.
29. Chatterjee, S.M., Bhattacharyya, S. and Majumdar, A. (2004), 'On-line measurement of yarn faults through interfacing with computer', *The Institution of Engineers (India) Journal*, Vol. 84, February.
30. Suh, M.W., Jasper, W. and Cherkassky, A. (2003), '3-D electronic imaging of fabric qualities by on-line yarn data', NTC Project, National Textile Center Annual Report, North Carolina State University, Raleigh, NC.
31. Lotka, M. and Jackowski, T. (2003), 'Yarn tension in the process of rotor spinning', *Autex Research Journal*, 3(1), 23–27.
32. BMS Monitoring System, available from <http://www.visionbms.com> (accessed 2 December 2008).

The structure of polyolefin fibres

R R MATHER, Heriot-Watt University, UK

Abstract: The structure of polyolefin fibres is considered at various levels, with particular reference to polypropylene and polyethylene fibres. At the macromolecular level, the architecture of the polymer chains is discussed: chemical structure, molar mass and molar mass distribution. On a larger scale, the arrangements of these chains within the fibre are also discussed. In addition, fibre profile is considered: fibre size and cross-sectional shape, hollow fibres, bicomponent fibres, fibre blends, and crimp. The final sections include influences of processing conditions on polyolefin fibre structure, gas plasma treatments of polyolefin fibres and auxetic polyolefin fibres.

Key words: polypropylene, polyethylene, crystal morphology, fibre profile.

9.1 Introduction

Polyolefin fibres consist essentially of saturated aliphatic hydrocarbon macromolecules. In *Textile Terms and Definitions*, a polyolefin fibre is defined as a manufactured fibre in which the fibre-forming substance is any long-chain synthetic polymer composed of at least 85% by mass of ethene, propene or other olefin units.¹ By far the most prominent polyolefin fibre commercially is polypropylene (PP). However, polyethylene (PE) fibres also enjoy commercial usage. Many of these fibres are produced by gel spinning,² which is the subject of a separate chapter in this book, and there is commercial interest too in PE fibres produced by solid-state extrusion.³ The chemical structures of PP and PE are given in Table 9.1.

This chapter is, therefore, largely confined to PP and PE fibres. Other polyolefin fibres have been produced, notably from poly(4-methyl-1-pentene), poly(1-butene) and poly(3-methyl-1-butene). Poly(1-butene) has found some use in film and pipe applications and poly(4-methyl-1-pentene) in medical equipment and microwave oven trays,⁴ but the commercial interest in processing fibres from these higher molar mass polyolefins is marginal. The chemical structures of these polyolefins are also given in Table 9.1. In addition, some fibres are produced from copolymeric polyolefins, such as ethene-propene, ethene-octene and even ethene-propene-butene copolymers. Fibres containing mixtures of different polyolefins are also produced commercially, such as bicomponent multifilaments where each filament contains a PP core and a PE sheath. When the fibres are heated, the PE sheath can melt and so bond the multifilaments into resilient monofilament yarns. PP/PE bicomponent fibres are widely used for producing non-woven fabrics, whereby fibres are

Table 9.1 Structures of some polyolefins

Polymer	Repeat unit
Polyethylene	$-(\text{CH}_2-\text{CH}_2)-$
Polypropylene	$-(\text{CH}_2-\text{CH})-$ CH_3
Poly(4-methyl-1-pentene)	$-(\text{CH}_2-\text{CH})-$ CH_2 CH / \ $\text{CH}_3 \ \text{CH}_3$
Poly(1-butene)	$-(\text{CH}_2-\text{CH})-$ CH_2 CH_3
Poly(3-methyl-1-butene)	$-(\text{CH}_2-\text{CH})-$ CH / \ $\text{CH}_3 \ \text{CH}_3$

bonded by the air-through-type thermal bonding process. Still other types of polyolefin fibre consist of different grades of the same polyolefin. Such fibres can, for example, be readily crimped, as discussed in Section 9.6.5. Fibres from blends of PP with other polymers, such as polyamide and polyester, are also available.

It can be seen then that, as a result of the wide variety of compositions that can occur among polyolefin fibres, together with the versatility available in their processing conditions, a considerable range of fibre structures can be produced. In this chapter, the structure of polyolefin fibres is considered at various levels. At the macromolecular level, the architecture of the constituent polymer chains is important: chemical structure, molar mass and molar mass distribution (polydispersity). On a larger scale, the arrangements of these macromolecular chains within the fibre are also significant. Finally, the appearance of the fibre must be considered: fibre cross-section, fibre size, hollow fibres, and crimp. In the following sections, these aspects of polyolefin fibre structure are treated in turn.

9.2 Structures and configurations of polyolefin chains

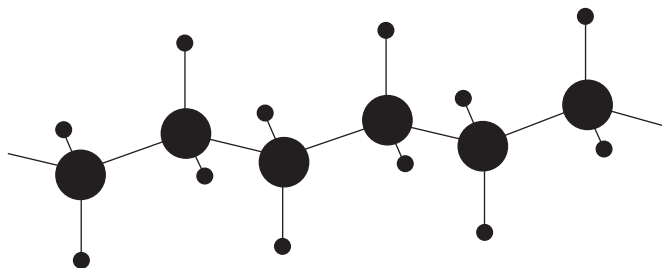
With the exception of PE, polyolefins are in practice polymers of α -olefins of general formula, $\text{CH}_2=\text{CHX}$, where X represents an alkyl group. Thus, every other carbon atom along the main chain is asymmetric. The size and

complexity of X largely govern the configuration of the polymer chain. Indeed, the nature of X indirectly governs the crystalline properties of the polymer and the changes undergone by the crystals during elongational strain, such as occurs in fibre formation.

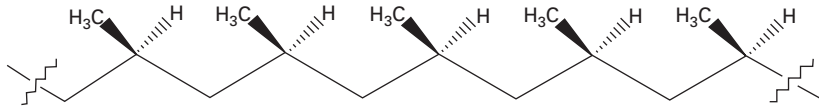
The various forms of commercial PE also in practice possess some asymmetric carbon atoms. These asymmetric carbon atoms arise from chain branching of the polymer, notably in low density polyethylene (LDPE) and in linear low density polyethylene (LLDPE). PE fibres are, however, very largely produced by melt extrusion of high density polyethylene (HDPE) or gel spinning of ultra-high molecular weight polyethylene (UHMWPE), and in both cases, the incidence of chain branching is low.

PE chains, which contain no asymmetric carbon atoms, tend to adopt a zig-zag conformation, as illustrated in Fig. 9.1. The polymer chains of PP and other α -olefin polymers can adopt a variety of configurations. As an example, the three different stereoisomeric forms which PP chains may assume are shown schematically in Fig. 9.2 in fully extended planar projections. In planar projections of isotactic PP chains, all the methyl side groups are situated uniformly on the same side of each chain. In practice, the chains normally adopt a three-dimensional helical configuration (Fig. 9.3). This highly regular structure favours the formation of PP fibres with superior mechanical properties: the use of isotactic grades of PP is, therefore, commercially very important. In syndiotactic PP chains, the methyl groups alternate in a regular fashion between the two sides of each chain. Syndiotactic PP chains can also adopt a helical configuration. In atactic PP chains, the methyl groups are arranged randomly on the two sides of the chain.

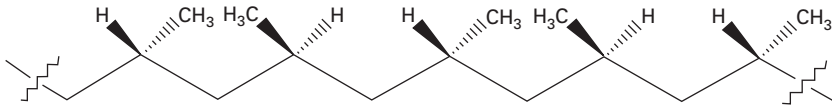
An important characteristic of a polymer is its dispersity, a term defined as the ratio of the weight-average molar mass, M_w , to the number-average molar mass, M_n . The higher the dispersity, the greater is the distribution of chain lengths in the polymer. Many polyolefins are produced using Ziegler–Natta catalysts,^{5,6} and their dispersities are generally high, a feature which renders melt processing more demanding and tends to reduce the mechanical performance of the fibres produced from them. The dispersities of HDPE



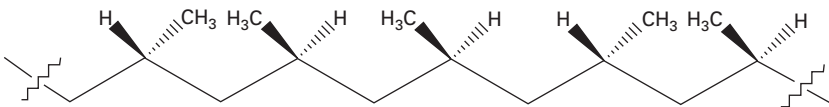
9.1 Schematic illustration of a PE chain.



Isotactic – methyl groups same side



Syndiotactic – methyl groups alternate



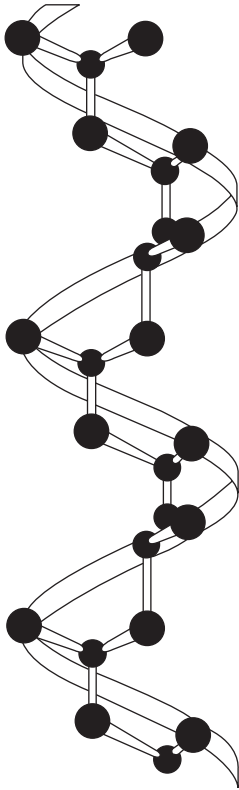
Atactic – methyl groups randomly arranged

9.2 Stereoisomeric structures of polypropylene (reprinted from *Synthetic Fibres: Nylon, Polyester, Acrylic, Polyolefin*, ed. J.E. McIntyre, Woodhead Publishing, Cambridge, 2005).

grades produced using Ziegler–Natta catalysts normally range between 5 and 20. M_w can be as high as 1 000 000 g mol⁻¹ but fibres can be produced from grades of such high molar mass only by gel spinning.^{2,7} For HPDE grades which can be melt-spun, the highest value of M_w is about 200 000 g mol⁻¹.⁷

The dispersities of PP grades normally range between 4 and 8. Thermal cracking of these grades gives rise to a reduction in molar mass and a lower range of dispersities, 3–6, due primarily to the elimination of the high molar mass ‘tail’ in the molar mass distribution. These modified PP grades, often called controlled-rheology (CR) grades, are especially suitable for fibre formation. For most fibre applications, M_w is in the range 200 000–350 000 g mol⁻¹. However, for the production of monofilaments, M_w may be as high as 600 000 g mol⁻¹, and for the production of meltblown nonwovens, as low as 150 000 g mol⁻¹. The melt flow index, MFI, of PP fibres generally lies between 10 and 40, but for PP monofilaments the MFI is normally 1–11, and for meltblown nonwovens it is in the range 100–1500.

More recently, fibres consisting of isotactic PP produced using metallocene catalysts have been attracting increasing interest. Metallocene catalysts are more specific and more active than Ziegler–Natta catalysts and can be designed in such a way that only chains of isotactic PP are produced. By



9.3 Helical configuration of an isotactic PP polymer chain (reprinted from *Synthetic Fibres: Nylon, Polyester, Acrylic, Polyolefin*, ed. J.E. McIntyre, Woodhead Publishing, Cambridge, 2005).

contrast, isotactic grades of PP made using Ziegler–Natta catalysts contain small proportions of atactic PP, typically up to 5%. Moreover, metallocene grades of PP possess a narrower molar mass distribution, of dispersity *ca.* 2.5. However, due to small local irregularities in the polymer chains, where individual propene monomers have been inserted in a reverse manner, the melting points of commercial metallocene grades of PP are often about 15°C lower than PP grades produced using conventional Ziegler–Natta catalysts.⁸ Metallocene catalysts are also applied to the formation of speciality polyolefin elastomers, which can be used for the production of highly elastic spun-bond, and even meltblown non-woven fabrics.

9.3 Arrangements of polyolefin chains

As with other polymer fibres, there are in polyolefin fibres various degrees of organisation both within and between the constituent polymer chains. These

degrees of organisation range from crystalline regions, where segments of the polymer chains are arranged into well-defined lattice structures, through to amorphous regions, consisting of assemblies of random interpenetrating polymer chains.

Various concepts have been put forward for considering the different extents of organisation which the polymer chains may adopt within a fibre. Several decades ago, Hearle listed 10 structural forms that can be considered to occur in linear polymers,⁹ most of which, he suggested, are relevant to fibre structure. He also pointed out that 'the structure of man-made fibres is likely to be a mess', certainly in the case of commercial fibres.⁹ A very full review of the complexities of models for the organisation of polymer fibre chains, especially in polyamide and polyester fibres, has also much more recently been written by Hearle.¹⁰ Even with polyolefin fibres, where complications from any polar interactions hardly arise, the arrangements of these chains will still be complex.

Nevertheless, the range of degrees of organisation that the polymer chains in commercial polyolefins can adopt needs to be taken on board, and in this respect the concept of a spectrum of order/disorder, described by Tomka *et al.*, would appear to be particularly useful.¹¹ At one extreme of the spectrum is the truly amorphous structure, and at the other end is the ideal crystalline structure. Among the many structures in between these two extremes is one that may have particular relevance to PP fibre technology. In this structure, regular polymer chain conformations are envisaged, in which the chains are parallel but displaced along their axes, but the chains' lateral packing remains irregular. This degree of ordering may be of the type primarily responsible for paracrystallinity in PP fibres, and indeed paracrystallinity has also been observed in PE.¹²

In addition to the concept of the order/disorder spectrum, there are a number of other important factors. The locations within each fibre of the regions comprising the various levels of order and disorder should be taken into account. So too should the degree of orientation of the polyolefin chains in the direction of the fibre axis and the degree of orientation of the bonds and segments constituting the chains. The resolution of all these aspects experimentally is an ambitious task, although the advent of advanced microscopy techniques, such as scanning probe microscopy and environmental scanning electron microscopy, may well assist progress. Molecular and microstructural modelling techniques may be useful too.¹¹

Because of all these factors, the concept of degree of crystallinity when applied to polyolefin fibres must be treated with caution. A variety of techniques is available for determining degree of crystallinity, such as X-ray diffraction, fibre density, heats of fusion and Raman spectroscopy,^{6,13,14} but the different techniques can give rise to different values.

9.4 Crystalline structures

9.4.1 Polyethylene

PE usually adopts an orthorhombic crystal cell structure. The cell dimensions are $a = 0.741$ nm, $b = 0.494$ nm and $c = 0.255$ nm. Because there are no alkyl groups projecting at regular intervals from the backbones of the PE chains, they can approach one another much more closely than is the case with other polyolefin chains. As a result, there is close packing of the PE chains, which all lie in a planar zig-zag fashion in the direction of the c -axis. The a and b dimensions, therefore, characterise the side-by-side packing of the PE chains.¹⁵

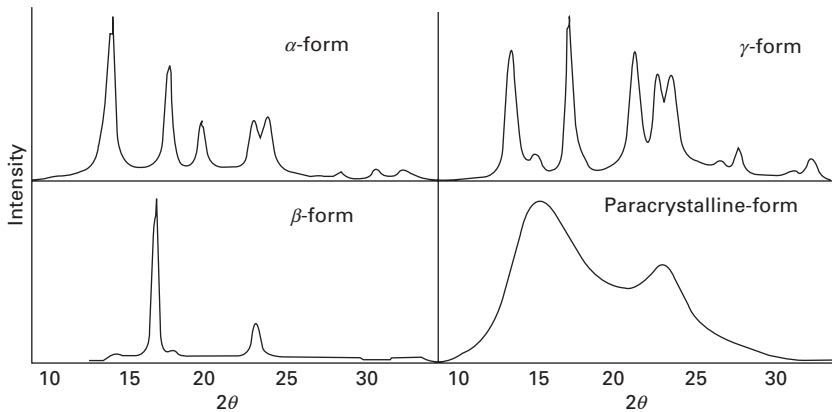
Another crystal form, the pseudo-monoclinic, is formed during stretching of HDPE at low temperatures, such as may occur in some types of PE fibre processing. For example, gel-spun UHMWPE fibres contain mostly orthorhombic domains, but some monoclinic domains are also present.² The cell parameters of the pseudo-monoclinic form are $a = 0.405$ nm, $b = 0.485$ nm, $c = 0.254$ nm, $\alpha = \beta = 90^\circ$ and $\gamma = 105^\circ$. Above 50°C , this crystal form tends to revert to the orthorhombic form. A third crystal form of PE, triclinic, has also been identified: $a = 0.4285$ nm, $b = 0.480$ nm, $c = 0.254$ nm, $\alpha = 90^\circ$, $\beta = 110^\circ$ and $\gamma = 108^\circ$.

9.4.2 Polypropylene

For PP, three distinct crystalline forms have been identified: α -monoclinic, β -trigonal and γ -orthorhombic. A common feature of all three forms is the helical conformation of the constituent PP chains. The forms display narrow, sharp peaks in wide-angle X-ray scattering (WAXS) patterns (Fig. 9.4). However, they also display some features which are highly unusual in polymer crystallography. An excellent review of the structure and morphology has been written by Lotz *et al.*¹⁶

The α -form is the most stable and also the most important in the context of PP fibres. Its monoclinic lattice has unit cell dimensions $a = 0.665$ nm, $b = 0.2096$ nm, $c = 0.650$ nm, $\alpha = \gamma = 90^\circ$ and $\beta = 99.3^\circ$. The PP chains lie in the direction of the c -axis. The structure contains both left-handed and right-handed helical PP chains, and any given helix for the most part lies next to helices of the opposite chirality.¹⁷

Crystals of the β -form can be obtained with the use of special nucleating agents. Initially, it was considered that the β -cell structure was hexagonal,¹⁸ but it is now recognised that the cell structure is trigonal: $a = b = 0.1101$ nm and $c = 0.650$ nm.^{19,20} An unexpected feature of the β -structure is that it is frustrated:^{16,21} the structure does not follow the normal crystallographic convention of structural equivalency. Frustrated structures are usually associated with the crystal lattices of magnetic systems.



9.4 WAXS patterns of α , β , γ and paracrystalline polypropylene (reprinted from *Synthetic Fibres: Nylon, Polyester, Acrylic, Polyolefin*, ed. J.E. McIntyre, Woodhead Publishing, Cambridge, 2005).

The orthorhombic γ -form can be obtained by crystallisation of PP at high pressure or of PP with a small proportion of comonomer at low pressure. The γ -form may also be observed in WAXS patterns of isotactic PP with shorter chain lengths. It is hence of interest too in connection with metallocene PP, in which there are shorter isotactic chain lengths on account of occasional regio-irregularities in the chains.⁸ Although the γ -form had originally been considered to consist of triclinic cells, it was revealed by Brückner and Meille²² that the triclinic cell is a subcell of a much larger orthorhombic cell: $a = 0.854$ nm, $b = 0.993$ nm and $c = 4.241$ nm. A strange feature of the γ -form structure is that it consists of a series of bilayers of antichiral PP chains in a crossed pattern. The chains are tilted at 80° or 100° to one another.¹⁶

A paracrystalline, or 'smectic', form has also been identified, whose WAXS peaks are broad and more poorly defined, and only of moderate intensity (Fig. 9.4). The PP chains within the paracrystalline structure also adopt a helical conformation.²³ A liquid crystalline model for the paracrystalline structure is becoming increasingly accepted, proposing a 'liquid-like' lateral packing of parallel PP helical chains, together with a high degree of registry in the direction of the chains.²⁴ This model correlates with one of the structures in the order/disorder spectrum discussed in Section 9.3.

9.4.3 Other polyolefins

The crystal cell structures of the other polyolefins in Table 9.1 are of interest, in comparison to those of PE and PP. Poly(1-butene) exhibits extensive crystal polymorphism: the crystal forms include I (hexagonal), II (tetragonal), III

(orthorhombic) and I' (hexagonal). Form I is thermodynamically the most stable, but form II is the form produced on rapid cooling from the melt. Form II then transforms to form I, a process which takes several days at ambient temperatures. Forms III and I' can be obtained by crystallisation from suitable solvents and are transformed to form I on heating. These crystal changes have severely restricted the commercial potential of poly(1-butene).

Poly(3-methyl-1-butene) possesses two crystalline forms: monoclinic and pseudo-orthorhombic. Poly(4-methyl-1-pentene) possesses tetragonal crystals.

9.5 Crystal morphology

The crystallinity in freestanding PE and PP arises from the presence of crystallites, generally of dimension less than 100 nm. The crystallites are made up of thin lamellae, and the direction of the polymer chains lies across the thickness of each lamella. Thus, the chains within each crystallite are folded many times in order that it can accommodate them. The lamellae, in turn, are arranged into spherulitic structures, whose diameter can be as high as a few millimetres. Each spherulite grows in a radial manner from a nucleus. The arrangement of the polymer chains will be denser and more regular within the spherulites than in the regions between them, so that clearly defined boundaries are observable.

It is noteworthy that isotactic α -PP crystals exhibit branching of lamellae, a feature which appears to be unique in polymer crystallography.¹⁶ Extensive evidence has now been assembled that this lamellar branching is an intrinsic property of isotactic α -PP. Each daughter lamella branches away from its mother lamella at an angle of *ca.* 80°. In PP fibre extrusion, for example, an additional component whose chain axis is approximately at right angles to the fibre direction may sometimes develop.¹⁶

When under elongational strain, as in fibre formation, the spherulitic morphology generally gives way progressively to a fibrillar morphology, although recently the coexistence of undeformed spherulites adjacent to fibrils has been observed.²⁵ Two distinct models have been proposed for this transformation. One approach consists of the rupture of lamellae and their subsequent reorganisation; the other invokes crystal melting and subsequent reorganisation.

The first approach has been put forward by Samuels, dealing mostly with PP fibres²⁶ and by Peterlin, based mainly on studies of PE.²⁷ Under elongational strain, the spherulites stretch out into ellipsoids. This deformation process is maintained until the lamellae within the spherulites can no longer accommodate the stress imposed on them, and the folded polymer chains within the lamellae slip, twist and even unfold.²⁷ Spherulitic deformation eventually results in the formation of small fibrils,²⁸ ranging from tens of

nanometres to microns.^{29,30} In addition, those polymer chains originally present in the less dense regions outside the spherulites become much more stretched along the fibre axis and hence closely aligned to one another. Strain-induced crystallisation can then occur, with the formation of new crystalline domains. Greater deformation causes the fibrils to slide past one another, and the tie molecules, which link the fibrils, are also stretched. Eventually, the deformation stress is too great for the fibre to support, and the sample breaks.

The other model was originally proposed by Flory and Yoon.³¹ They suggested that localised melting may occur due to the stress applied to the spherulites, and this melting is then followed by recrystallisation. Although the model of Flory and Yoon has generally found less favour since it was first proposed, much more recent work by Li and Cheung on the deformation of β -PP provides some support for this model.³²

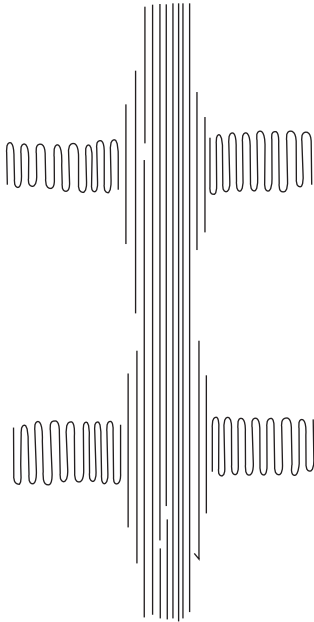
It is interesting to note that in the formation of PP fibrils, the appearance of 'shish-kebab' structures has been reported,^{29,30} in which a central core consisting of extended PP chains (shish) is surrounded by sections with folded chain crystals (kebab). Shish-kebab PE structures have also been reported.³ Shish-kebabs are formed by a two-stage crystallisation process.^{33,34} The first stage, shish formation, comprises the nucleation and formation of fibrils aligned parallel to the direction of strain. In the second stage, kebab formation, there is epitaxial overgrowth of lamellae in the fibrils, with the latter acting as nuclei. Figure 9.5 shows a schematic illustration of a shish-kebab structure.

9.6 Fibre profile

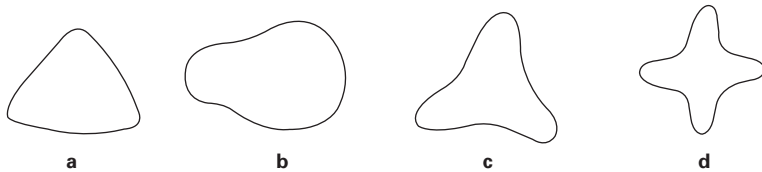
9.6.1 Fibre cross-section

Most polyolefin fibres are extruded as filaments with circular cross-sections. However, these filaments possess a waxy handle, which is perhaps not surprising when it is recalled that polyolefins are polymeric hydrocarbons. This waxy handle can be reduced, or even virtually eliminated in fibres with suitable non-circular cross-sections, and indeed a variety of fibres are produced with cross-sections such as triangular, multilobal and cross-shaped, as illustrated schematically in Fig. 9.6.

Not only does cross-sectional shape influence fibre handle, but it also affects fibre bulk, insulation ability, resilience and lustre. Thus, fibres with more exotic cross-sectional shapes often pack more loosely than those with circular cross-sections: hence, fibre bulk is correspondingly increased, and better insulation is provided. In addition, fibres with non-circular cross-sections will tend to bend more readily in some directions than in others, and give rise to improved resilience. The scattering of light from the surfaces of fibres with more complex cross-sections is less uniform, and the appearance



9.5 Schematic representation of 'shish-kebab' morphology.



9.6 Examples of non-circular filament cross-sections: **a** triangular, **b** bilobal, **c** trilobal, **d** cross-shaped.

of these fibres is consequently softened. Moreover, the extent of soiling, if moderate, is much better concealed in fibres of complex cross-section, although soiling becomes more apparent when the channels become filled with soil particles.

Melt spinning of non-circular polyolefin fibres requires special spinneret profiles for extrusion. There are three principal considerations in designing spinneret holes for producing profiled filaments: die-swell, melt viscosity of the polyolefin and the surface tension of the extruded molten filaments.³⁵ Die-swell is especially significant in polyolefin fibre extrusion: the dilation on egress from the spinneret hole can be as high as two to three times. Moreover, die-swell from non-circular spinneret holes is uneven. For example, there is more die-swell from the longer sides of a rectangular spinneret hole than from the shorter sides, whilst at the corners there is virtually no die-swell at all.³⁶

Surface tension tends to promote more rounded configurations in extruded melt filaments. However, the surface tensions of polyolefin melts are low, a factor that renders the formation of more complex cross-sections more readily achievable than for many other types of melt spun fibre. Indeed, depending on the grade of polyolefin used and the processing conditions applied, fibre cross-sections of varying degrees of sharpness can be produced. Factors promoting sharper profiles are throughput, lower melt flow index and spinning temperature, coupled with rapid cooling of the molten filaments and low draw-down ratio.³⁵ However, the drawability of the as-spun fibres thus produced is also lower, and so drawing conditions have to be correspondingly adjusted.

9.6.2 Hollow fibres

Not only have polyolefin fibres with exotic cross-sections attracted commercial interest, so too have hollow polyolefin fibres. These fibres are well suited to applications where heat insulation and enhanced bulk are important, as in sleeping bags, pillows and mattresses. Hollow fibres appear too to be less prone to soiling and pilling, and they possess a subdued lustre. They can also incorporate a variety of chemicals: hence they can be used as filters for removing unwanted substances or as agents for the controlled release of specific chemical compounds, such as antimicrobial products. Fibres with two or more holes are sometimes preferred, as they are less prone to flatten under pressure. As an example, one commercially available PP fibre product, Asota[®] AFC, whose fibre cross-sections are characterised by three circular holes, arranged equidistantly from one another, is used to minimise shrinkage cracks in concrete as it hardens and to reduce fire damage in it.³⁷

Hollow PP fibres with very narrow pores in their walls are used in mechanical lungs. A mechanical lung is essentially a gas exchanger, which supplies oxygen to the blood and removes carbon dioxide from it. Both gases pass freely through the pores in the walls of the hollow fibre, but the passage of blood through them is impeded by the narrow cross-section (< 50 nm) and the hydrophobicity of PP.

Although hollow fibres can be processed by indirect extrusion techniques, based on the 'islands-in-the-sea' concept,³⁸ they are often processed by direct spinning techniques, using spinneret holes of suitable designs. Indeed, like non-circular polyolefin fibres, polyolefin hollow fibres are well suited to production by direct spinning techniques.

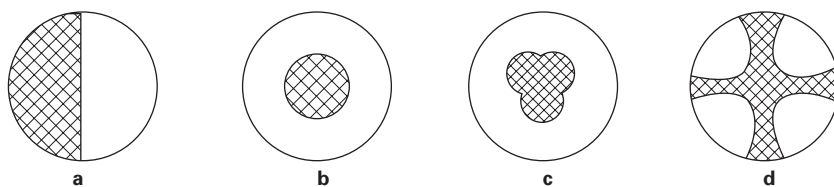
9.6.3 Bicomponent fibres

Bicomponent fibres consist of two polymers arranged in clearly defined phase morphologies. Examples are side-by-side and sheath-core structures,

but much more complex structures have also been formed, as illustrated in Fig. 9.7. In the case of polyolefin fibres, the two components would comprise a polyolefin and another chemically distinct polymer. The second polymer could be a different polyolefin: for example, fibres consisting of a PP core and a PE sheath are used in the production of spun-bonded nonwoven fabrics using a thermal bonding process. Moreover, two different grades of the same type of polyolefin could also strictly be considered to form bicomponent fibres, provided the two grades exist in clearly different bulk phases within each fibre. However, bicomponent fibres are usually considered to consist of polymers of different chemical composition. The term conjugate fibres tends to be given to fibres where there are structural differences between components of the same chemical composition.

Bicomponent fibres can possess a number of advantages over fibres consisting of just one component. In polyolefin bicomponent fibres, the second component may improve aspects of mechanical performance, such as the provision of reduced creep and reduced thermal shrinkage at elevated temperatures. Since polyolefin fibres cannot be dyed, unless a suitable additive has been blended with the polyolefin prior to extrusion, the second polymer may enable successful dyeing. Bicomponent polyolefin fibres are also produced for the purpose of imparting crimp. In the previous section, it was mentioned that hollow fibres can be produced from 'islands-in-the-sea' fibres. These represent further examples of bicomponent fibres, from which the island component can be dissolved to render the resulting fibre hollow. The dissolved component needs to diffuse through the walls of the sea component. Alternatively, if polyolefin island fibres of narrow cross-section are present, removal of the sea component gives rise to polyolefin microfibrils.

Of particular importance in the behaviour of bicomponent fibres is the nature of the interface between the two polymer phases. In order to avoid splitting of the fibre into the two separate polymer phases, the adhesion between them across the interface must be strong enough to withstand further processing of the fibre, its subsequent fabrication into product, and the wear and tear to which the product may be subjected. However, because



9.7 Cross-sectional structures of some bicomponent fibres: **a** side-by-side, **b** simple sheath-core, **c** more complex sheath-core, **d** cross-shaped 'core'.

of the hydrocarbon nature of polyolefins, their affinity for other types of common fibre-forming polymer, such as polyamide and polyester, is low. Thus, where imparting crimp is sought through differences in shrinkage, the internal stresses that result at the interface may well be sufficient to cause splitting. This problem is more acute where the extent of the interface is small, as in simple side-by-side bicomponent structures, illustrated in Fig. 9.7a. Insufficient cohesion is even likely to occur between two different types of polyolefin, e.g. PE and PP. It has been observed too between two different grades of PP, where different phases exist within the fibre because of the widely differing molar masses of the grades.³⁵ (Although such fibres would be considered to be conjugate fibres rather than bicomponent fibres, it may be argued nevertheless that the widely different average polymer chain lengths in the two phases render them chemically distinct anyway!)

To overcome this problem, a variety of approaches are available. The underlying strategies involve modifying the chemistry of the interface and increasing the area of the interface. A fibre structure in which one component protrudes into the other, or even one where both components protrude into each other, markedly increases the area of the interface and hence correspondingly increases the extent of adhesion across it. Chemical modification of the interface may be achieved through the use of a compatibilising agent, a polymer whose structure contains segments similar to those in each component. Compatibilising agents act in essentially the same manner that surfactants (such as detergents) act to emulsify oils in water.

For some types of process, however, splitting of the components may be advantageous. Thus, where polyolefin microfibrils are to be produced from 'segmented pie' morphologies involving two components, splitting is required for the removal of the unwanted component. In this respect, the low interfacial adhesion between the two component polymers renders polyolefins attractive for the formation of microfibrils.

9.6.4 Fibres from polyolefin blends

Fibres based on polyolefin blends, containing a smaller proportion of a second component, often display matrix-fibril morphologies, as illustrated in Fig. 9.8. Such fibres are also called 'biconstituent fibres'. Whereas the production of bicomponent fibres requires specialised extrusion equipment, blended fibres can be produced by conventional single-screw equipment. Over the past two decades, there has been interest in reinforcing PP fibres with fibrils of thermotropic liquid crystalline polymers (TLCPs).³⁹ Whilst the initial modulus of PP fibres is commonly 6 GPa or less, that of TLCPs is generally as high as 50–60 GPa, and some TLCPs possess moduli >100 GPa. The structures that give rise to such high moduli in TLCPs are discussed in Chapter 14. Although TLCPs are far more expensive than PP, there is



9.8 Schematic representation of a matrix–fibril morphology.

considerable attraction in the potential for marked improvements in PP fibre mechanical performance from the addition of only a small proportion of TLCP. Furthermore, TLCPs exhibit surprisingly low viscosities when in the liquid crystalline state, a property that would facilitate PP fibre extrusion.

To be effective as a reinforcing agent, the TLCP should exist as fibrils aligned along the fibre axis. One of the main factors governing the morphology of the TLCP constituent is the proportion of TLCP. Thus, in one report,⁴⁰ it was noted that at very low concentrations (2.5%), a TLCP that was an aromatic copolyester of 6-hydroxy-2-naphthoic acid and *p*-benzoic acid exists primarily as small particles in the as-spun fibre. At concentrations of 5–10% the TLCP was present as long fibrils oriented along the fibre axis. However, at 15%, the TLCP formed a network structure, rendering the fibre brittle. Other important factors influencing TLCP fibre morphology are the conditions of extrusion and the properties of the PP/TLCP interfaces.

One difficulty, however, arises from the high melt temperatures of many TLCPs (even as high as 280°C or more), so that the PP matrix tends to be degraded during extrusion. A further complication may arise when the as-spun fibres are drawn, for the TLCP fibres can tend to fragment. One approach to overcoming this latter difficulty is the use of a polymeric compatibilising agent, which is itself liquid crystalline at the drawing temperatures used.⁴¹ The compatibilising agent acts as a lubricant at the PP/TLCP interfaces during drawing but promotes interfacial adhesion in the final drawn fibre. It has been suggested too that, where fibril fragmentation is not detected in the drawn fibres, the improvement in fibre modulus arises not just from the TLCP fibrils but also from increases in PP crystallinity and PP chain orientation.⁴²

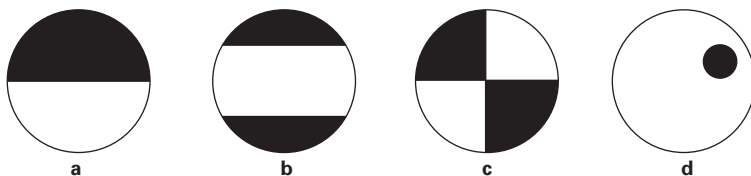
9.6.5 Crimp

The introduction of crimp into polyolefin fibres can be achieved by thermomechanical means – as with many other melt spun fibres. Straight filaments are mechanically deformed into a crimped structure, which is then heat set. The thermal relaxation of the stresses produced from mechanical deformation allows a permanent crimp. On a commercial scale, the stress relaxation process must occur sufficiently quickly not to slow down production. However, in the case of PP fibres, for example, stress relaxation is usually too slow. In addition, crimp in the two most important polyolefins, PE and PP, may not in practice be permanent, because their glass transition temperatures are below ambient temperatures.

An alternative approach is to produce polyolefin fibres that possess crimp as an integral part of their structure. These fibres consist of two phases, which have different lengths. The difference in length is usually achieved as a result of different shrinkage during processing. Such fibres may be bicomponent fibres, as discussed in Section 9.6.3, but equally self-crimping may be achieved in conjugate fibres, where the emphasis is on differences in polyolefin structure rather than in chemical composition.

The extent of curvature in the crimped fibre is proportional to the magnitude of the difference in shrinkage between the two components during relaxation. The component with the greater shrinkage is on the inside of the helical coil that is formed. The extent of shrinkage of each component depends on its structural morphology, the influence of any additives in the component, the degree of fibre extension during spinning and drawing, and the conditions of fibre relaxation. For good crimp in PP fibres, the two components should differ in length by 10–20% after shrinkage.³⁵ The maximum curvature of crimp that can generally be obtained in practice is 4–5 times the filament cross-section.

The nature of the distributions between the two polyolefin components in a conjugate fibre greatly influences its potential for crimping. The greatest crimp can be achieved in conjugate fibres with only one interface, with the maximum potential for crimp through the centre of the fibre cross-section.³⁵ Thus, in Fig. 9.9, a conjugate fibre of cross-sectional character **a** is likely to achieve greater crimp than one of character **b**. Furthermore, crimp is unlikely



9.9 Schematic representations of distributions in conjugate fibres.

to be achieved in the more complex segmented structure illustrated in **c**. In addition, greater crimp is likely to result where the interface is straight; thus, fibres of character **a** will achieve greater crimp than those with character **d**.

It has already been noted that crimp arises from structural asymmetry across the filament cross-section: there are variations in overall polymer chain orientation, the extents of different organisation which these chains may adopt (as discussed in Section 9.3) and the nature of the constituent crystallites. A key factor too is the degree of row nucleated (or strain induced) crystallinity⁴³ induced on cooling of the filament after leaving the spinneret. Indeed, the presence of row nucleated crystallinity in at least one component of the conjugate fibre is a necessary condition for self-crimping.³⁵

Self-crimp can be produced by a number of means, and details of these processes are amply discussed elsewhere.³⁵ Many require the extrusion of two polyolefin melt streams side by side. The streams may differ in the grade of polymer (different molar masses or different molar mass distributions), or spinning temperature. They may alternatively differ in the type of additive present in the polymer, such as plasticiser to alter the rheology, or nucleating agent to affect the crystallisation characteristics on subsequent cooling of the filaments. However, such approaches require more complex extrusion equipment. One ingenious approach that has been tried with the use of a conventional single extruder is to spin filaments with a bilobal cross-section (notably a figure-of-eight cross-section, as depicted in Fig 9.6b).³⁵ The smaller lobe of the filament will cool more quickly than the larger lobe. Crimping results on relaxation of the filament, with the smaller lobe on the inside of the coil. In another approach, the Autocrimp[®] process, the polyolefin melt is forced through the spinneret such that stress differences are built into opposing sides of the freshly extruded filaments.⁴⁴

A widely adopted approach is the differential cooling of the individual filaments during draw-down, achieved by asymmetrical quenching from a flow of air directed at rightangles to the filaments. Increasing the velocity of the air flow tends to increase the crimp obtained.⁴⁵ The part of the filament directly exposed to the airflow solidifies more quickly than the part on the opposite side of the filament, where there is some protection from the airflow. Thus, the exposed side becomes more difficult to attenuate, with the result that it acquires greater row nucleated crystallinity and smaller crystallite size. In consequence, the filament becomes crimped, and indeed the crimp is often further enhanced on cold drawing. It has also been observed that for a given filament cross-section, there is an optimum fibre density for maximum crimp in an as-spun filament.⁴⁵

As with a bicomponent fibre, the difference in the potential for shrinkage between the two components in a conjugate fibre may induce splitting. Means of overcoming this difficulty include increasing the area of the interface

separating the two components and applying a third component that adheres well to both polymers. Both these approaches resemble those adopted to avoid splitting in bicomponent fibres (Section 9.6.3). For conjugate fibres, a third approach is also available. An asymmetric sheath-core structure, as illustrated in Fig 9.9d, often serves to prevent splitting, although the degree of crimp in the fibre will be appreciably reduced.³⁵

9.6.6 Thick cross-sections and thin cross-sections

Introduction

The majority of polyolefin fibres produced are in the form of multifilaments, either as continuous filaments or staple. Nevertheless, there is a well-established market in thicker polyolefin fibres and, increasingly, in polyolefin microfibrils and even nanofibrils. The market for monofilaments (count > 100 dtex) was the first commercial market to be penetrated by PP fibres, in view of the high tenacity that could be produced at relatively low cost. Microfibrils are used extensively in nonwoven technologies; but nanofibrils of still smaller cross-section are commanding rapidly increasing interest, again primarily for nonwoven applications.

Monofilaments

Monofilaments can be produced by broadly the same methods as those used for the production of multifilaments. However, monofilaments produced in this way tend to curl,³⁵ and this tendency renders them unsuitable for many applications. Processing at low speeds and extrusion into water overcomes curling.

Some studies on the morphologies of PP monofilaments have been published. It has been reported, for example, that the diameter of a PP monofilament varies markedly with draw-down ratio after extrusion, but is less dependent on the subsequent draw ratio applied (drawing was conducted at 90°C).⁴⁶ In another study, crystal morphology was investigated in both as-spun and drawn monofilaments.³⁰ With increasing draw-down, progressive deformation from spherulitic to fibrillar morphology was noted at the filament surface, with some shish-kebab morphology also being observed. At very low draw-down, the centres of the spherulites at the filament surface were raised rather than depressed, and it was tentatively suggested that these spherulites contained β -PP crystals instead of the expected α -form. Increasing draw-down also produced a progressive change in the filament bulk from α -form crystallinity to paracrystallinity. The nature of the fibrillar structures in the drawn filaments depended on the drawing conditions. Filaments drawn at elevated temperatures contained α -PP crystals. However, wide-angle X-ray scattering indicated that a cold-

drawn filament appeared to exhibit a form of paracrystallinity, though different from that shown in Fig. 9.4d.

Thin cross-sections

Microfibres (count < 1 dtex) and increasingly nanofibres (count < 0.3 dtex) are assuming steadily increasing importance in polyolefin fibre technology. Microfibres can be produced directly by melt extrusion, although extrusion rate has to be reduced and extensive draw-down is required. Filaments consisting of microfibres produced in this way may suffer from extensive variation in thickness as a result of variability in cross-section of the constituent microfibres. An alternative method for producing microfibres is by the 'islands-in-the-sea' approach, in which the 'sea' is dissolved to leave behind the microfibres. Melt-blowing also produces microfibres, and indeed fibres of fineness as low as 0.01–0.2 dtex are often produced; such fibres can thus be considered as nanofibres. Nanofibrillation may also perhaps become an established technique for producing polyolefin nanofibres.

Polyolefin nanofibres can be produced by electrospinning, a technique discussed at length in Chapter 17. Techniques have been reported, for example, for electrospinning polyolefin nanofibres from solution and from the melt. Thus, poly(1-butene) and poly(4-methyl-1-pentene) have recently been successfully spun from mixed solvent systems at room temperature.^{47,48} In the case of poly(4-methyl-1-pentene), the fibre morphology was found to be strongly influenced by the nature of the solvent system, whilst with poly(1-butene) different crystalline structures resulted depending on the processing conditions used. In PP fibres produced by melt electrospinning,⁴⁹ it was observed that those with the highest molar mass possessed the largest cross-sections. Fibres of low molar mass could possess cross-sections as small as 1 μm , or even slightly lower. In addition, fibre cross-section decreased with increasing strength of the applied electric field.

9.7 Processing–structure relationships

9.7.1 Introduction

In application, the structure of polyolefin fibres (at all levels!) determines their physical, thermal and mechanical properties and is a major influence on the technological performance of the fabrics produced from them. In turn, structure in a synthetic fibre is governed by the grade of polymer from which it has been processed (and the additives present in the polymer) and the processing conditions applied to produce this structure. As has been discussed in some of the previous sections, the cross-sectional profile is controlled by the profiles of the spinneret holes. The size of the cross-section is largely

governed by the extent of draw-down during the extrusion process and the elongation achieved during subsequent drawing. Other dimensional factors, such as crimp frequency, result from finishing processes such as texturing, or from the presence of two (or more) components in the fibre.

Ideally, the most desirable structure for a synthetic fibre is one of invariant cross-section in which the polymer chains are extended and aligned in perfect orientation along the fibre axis. For polyolefin fibres probably the nearest to this ideal chain alignment has been achieved through the gel spinning of UHMWPE, discussed in Chapter 12 of this book. After melt spinning, however, the polyolefin chains are extensively folded. Indeed, it is far from clear that the alignment of polyolefin chains can be improved in fibres derived from melt-spinning and subsequent drawing, because of the chain entanglements occurring in the melt, which are then retained in the solid fibres.

For discussion of the relationships between processing and structure in polyolefin fibres, the processing stages may be conveniently considered as follows: processing of the melt, solidification of the melt and draw-down of the filaments formed, and finally the subsequent drawing process.

9.7.2 The polyolefin melt

Detailed discussions of the passage of a polyolefin through a melt extruder have been provided elsewhere.^{35,50} What is of concern here is the nature of the melt as it leaves the spinneret holes. Just prior to the egress of the melt from a narrow spinneret hole, the melt undergoes shear flow, but on egress, there is a rapid change to elongational flow, for the melt is no longer constrained by the walls of the spinneret hole. As the melt then starts to cool, there is an increase in its viscosity. The release of elastic energy, as the melt emerges from the spinneret hole, gives rise to extensive die-swell, which has a profound effect on spinning speed.

Distortions of the extruded polyolefin fibre can sometimes result at this stage of the melt extrusion process. One type of distortion is melt fracture, which refers to the distortion of the surface of the extruded melt. It arises from oscillations in the output of polymer through the spinneret hole. Extruded PP melts are particularly susceptible to this phenomenon. The fluctuations give rise to variations in cross-section along the length of the extruded filament, often in the form of helical indentations. Severe melt fracture renders filament extrusion impossible. Factors that intensify melt fracture include higher flow rates through the spinneret hole, a decrease in the ratio of hole length to hole diameter, reduced temperature of the melt and increased molar mass.³⁵ Molar mass distribution has also been shown to exert a pronounced effect on susceptibility to melt fracture in PP melts.⁵¹

Some fibres emerge exhibiting a sharkskin, which has the form of ridges running approximately at rightangles to the fibre axis. The cross-section of

the fibre remains, however, virtually uniform; the defects are confined to the fibre surface. As the melt leaves a spinneret hole, so the surface of the filament undergoes an extensional acceleration. The surface stress thus generated is larger, the higher the viscosity of the melt. Moreover, filaments with high modulus will also tend to give high surface stress. For this reason, polyolefin grades of higher molar mass are more prone to sharkskin, and furthermore narrow molar mass distribution also appears to promote it.³⁵ Other processing conditions that promote sharkskin are low extrusion temperatures and high extrusion velocities.

Another source of instability in the filament melt emerging from the spinneret is draw resonance. This term refers to periodic fluctuations in diameter in the filament melt. Whereas melt fracture appears to commence at a particular value of throughput rate, draw resonance will occur only when the filament is being stretched.⁵² Draw resonance begins, therefore, at a critical draw-down ratio. Both PP and HDPE are prone to draw resonance, but it appears to be less of a problem with LDPE. The intensity of draw resonance is influenced by the molar mass distribution of the polyolefin and also by the shear deformation of the melt in the spinneret holes. The presence of additives, such as pigments and stabilisers, can also promote draw resonance. Moreover, additives that exist in solid particulate form during fibre extrusion may cause knots (short irregular sections) in as-spun fibres.

9.7.3 Solidification of the filament melt and filament draw-down

Crystallinity

After the polymer melt has emerged in the form of filaments from the spinneret holes, it rapidly cools. At the same time, the extruded filaments are attenuated due to the extensional force applied to them during draw-down. On solidification, the rate of crystallisation of polyolefins is innately high, yet it is beneficial if an extensive crystalline structure is formed only after the subsequent drawing stage (discussed in Section 9.7.4), to allow a high draw ratio to be achieved. With PP fibres, this apparent paradox can be resolved by choosing extrusion conditions that produce paracrystalline as-spun fibres.^{53–55} Paracrystalline PP fibres can be readily obtained by rapid cooling of the melt into a water bath,^{56,57} whereas quenching by air often produces PP fibres in the α -monoclinic state. However, under carefully controlled conditions, paracrystalline fibres can also be obtained by air quenching.^{53,58} As-spun PE fibres are formed with a well defined orthorhombic crystalline structure, irrespective of spinning conditions.⁵⁷ Poly(1-butene) fibres are formed with a well defined hexagonal structure in air, but rapid quenching gives instead a tetragonal structure, which then ages to the more stable hexagonal form.⁵⁷ As-spun poly(4-methyl-1-pentene) fibres possess a well defined tetragonal structure.⁵⁷

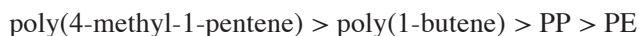
The extent of crystallinity in as-spun fibres depends both on the grade of polymer extruded and the extrusion processing conditions.^{53, 58} The magnitude of the spinline stress has been noted as particularly important in this respect.^{53,59,60} It has been observed that an increase in spinline stress increases the overall crystallinity of the as-spun fibres produced. In turn, spinline stress can be increased by raising cooling rate and winding speed and by lowering metering pump speed and spinning temperature. In contrast to this observation, however, work on the extrusion of PP monofilament has revealed that crystallinity can decrease with increase in winding speed.³⁰ The effects of filament speed on crystallinity are discussed in detail in Chapter 5.

Spinning temperature also plays a part. Lower spinning temperatures favour the onset of crystallisation but reduce the mobility of the polyolefin chains. The degree of crystallinity increases with increasing molar mass as well. Molar mass distribution is another important factor: a greater proportion of longer chains in PP fibres, for example, promotes the formation of α -monoclinic crystals and raises the degree of crystallinity.

It is noteworthy too that the presence of pigment particles can affect the crystalline structures of synthetic fibres.⁶¹ Thus, as-spun PP fibres coloured with a phthalocyanine pigment have been observed to be in the α -monoclinic form, even when extruded under conditions where the uncoloured fibres are in a paracrystalline state. As-spun PP fibres coloured with a quinacridone pigment can contain both α - and β -forms, though on heating of the fibres, the β -form transforms to the α -form.

Orientation

The overall orientation of the polyolefin chains in as-spun fibres is largely determined by the degree of stretching during draw-down (the draw-down ratio). Kitao *et al.* reported that, at lower draw-down ratios, the chain orientation in as-spun polyolefin fibres increases with increasing draw-down ratio.⁶² At draw-down ratios between 8 and 80, however, they reported no further increase in chain orientation in PE and PP fibres, although there is an increase in poly(1-butene) fibres. They also concluded that crystalline regions contribute more to overall orientation than non-crystalline regions. Moreover, in addition to the orientation of crystals along the fibre axis, orientation at rightangles to the fibre axis may occur at draw-down ratios of <50 . These conclusions have been largely confirmed by Choi and White,⁵⁷ who have also reported that crystal orientation is correlated better with spinline stress than with draw-down ratio. They report that at a given spinline stress, the ranking of the crystal orientation is:



9.7.4 Fibre drawing

The structures of drawn polyolefin fibres are markedly influenced by the structures of the precursor as-spun fibres and by the drawing conditions employed,^{54,55} notably draw ratio and draw temperature.

Polyolefin fibres can deform in a draw stage either inhomogeneously, where there is a marked necking effect, or homogeneously, without any necking. In PP fibres, neck formation is favoured by lower temperatures, increased draw speeds, higher orientation of the polymer chains and the presence of monoclinic crystals in the as-spun fibre.³⁵ Drawing of fibres with larger cross-sections is also more likely to involve necking.

Neck formation arises from variation in the distribution of stress along a filament, as a result of tensile deformation during drawing. Such stress variation may arise from small variations in cross-sectional area or from other inhomogeneities along the length of the filament. Once a neck has formed, however, it is essential that the thin portion maintains a constant cross-section, through strain hardening. Strain hardening will occur if there is increased orientation of the polyolefin molecules in the direction of the fibre axis. In this respect, the angle of the neck is likely to be important. If there is a sharp neck angle, leading to a more pronounced necking effect, there will be a higher degree of overall chain orientation. However, the draw process may also become unstable.

Draw ratio has a considerable influence on the character of the drawn fibres, and several empirical relations have been proposed to relate draw ratio to overall chain orientation.^{63,64} Draw temperature is also an important factor, because temperature influences the mobility of the structural units during deformation. Drawing at ambient temperatures, for example, converts as-spun PP fibres with α -monoclinic crystalline structures into more oriented, yet less ordered structures with reduced crystallite size, increased lattice strains and defects that are similar to the paracrystalline form.⁶⁵ Subsequent annealing, however, transforms this disordered structure into a highly ordered α -monoclinic structure, with a high overall chain orientation.

Drawing at low temperature can induce the formation of microvoids, which elongate in the direction of the fibre axis as a result of the tensile force applied.⁶⁶ The formation of these microvoids occurs in the interspherulitic regions.⁶⁷ The number of microvoids can, however, be considerably reduced by annealing. Drawing at more elevated temperatures can be considered to be similar to a combination of cold drawing followed by annealing.⁶⁵ Fibres with highly ordered and highly oriented structures are formed. In contrast to cold drawing, there is no formation of necks and a steady reduction in filament cross-section is observed. The structural changes occurring during drawing at higher temperatures include healing of crystal defects, a reduction in the number of tie molecules, relaxation of the non-crystalline material

in each fibre and increased mobility of the polymer chains throughout the fibre.²⁷

The development of flaws and defects during the drawing of polyolefins, particularly to high draw ratio, has been the subject of extensive investigation. In the drawing of paracrystalline PP fibres at 60°C, for example, the development of longitudinal defects, often several μm long, has been demonstrated.⁶⁶ Moreover, at higher draw ratios (≥ 7), the drawn fibres were observed to contain transverse bands of defects, which alternate with homogeneous sections along the length of each fibre. As the draw ratio increases, the defect bands increase in length and proportion until they occupy very nearly all of the fibre. The defects were identified as regions of reduced density.

A similar distinct longitudinal morphology was observed in some highly drawn polyethylenes.^{68,69} A regular morphology of alternating transverse bands and rows of etched pockets was observed, termed Pisa structure by the authors on account of their resemblance to the façade of the Leaning Tower. In addition, transverse sections of the highly drawn fibres revealed large voids and some featureless patches. This morphology was termed mesa structure by the authors, in view of its resemblance to features of the North American desert.

9.8 Plasma treatments and auxetic fibres

9.8.1 Plasma treatments

One of the most exciting developments currently occurring in textile technology is the application of gas plasmas,⁷⁰ and in this respect, polyolefin fibres are no exception. Although gas plasma treatments were first applied some decades ago, it is only much more recently that they have been developed on a commercial scale. Gas plasmas are energetic sources of radiation and chemical species that have a complexity of interactions both with one another and with the substrate being treated. The plasma atmosphere consists of a mixture of ions, free radicals, electrons and UV radiation. Through the application of gas plasmas, polyolefin fibre surface topography – and also surface chemistry – may be altered, whilst the fibre bulk remains unaffected.

Plasma treatments may be given at atmospheric pressure or at very low pressure. A variety of different gases may be applied, and mixtures of gases have also been used. Depending on the type of gas and the conditions under which the plasma is generated, different effects may be experienced by a polyolefin fibre. Thus, plasma treatment with a noble gas, such as helium or argon, may alter the detailed topography of the surface, to generate roughness on a micro or even nano scale, and also increased surface porosity. Plasma treatment may, moreover, alter the chemical nature of the surface through the introduction of various functional groups to the polyolefin chains at

the fibre surface. Gases such as oxygen, nitrogen and ammonia may give this effect. In addition, suitable chemical modification of the fibre surface allows the grafting of polymer chains to provide still further modification. Alternatively, plasma treatment may cause deposition on the fibre surface of a thin polymeric coating with a crosslinked structure. Thus, fluorocarbons can bring about plasma polymerisation and render the polyolefin fibre surfaces highly resistant to oils, as well as aqueous media. More detailed accounts of the effects of plasma treatments on polyolefin fibre surfaces can be found in companion volumes.^{50,70}

9.8.2 Auxetic fibres

Auxetic materials possess negative Poisson's ratios, ν : in contrast to most materials, they become thicker when stretched, with an increase in void volume. A wide variety of auxetic materials have been produced over the past 20 years or so, and these materials include auxetic PP fibres.

It has been shown that auxetic fibres can be produced by melt spinning, but with some modifications. In particular, a lower processing temperature seems to be required throughout the extrusion equipment. For example, it has been reported that a temperature as low as 159°C can achieve the extrusion of auxetic PP fibres, for which $\nu = -0.60 \pm 0.05$.⁷¹ Characterisation by scanning electron microscopy revealed that the PP fibres possessed a modified version of the typical auxetic polymeric microstructure of nodules interconnected by fibrils. More recently, a method has been reported for producing auxetic PP fibres with tailored values of ν .⁷²

9.9 Conclusion

This chapter has very largely centred on PP fibres and, to a lesser extent, on PE fibres too. The emphasis on these two types of fibre reflects their commercial dominance in relation to other polyolefin fibres. Polyolefin fibre structure has been discussed from a molecular level to a visible level, and the features of fibre processing that give rise to particular fibre structures have also been considered. Although polyolefin fibres have been known for many decades, the variety of structures that they adopt continues to multiply. The advent of polyolefin nanofibres represents an especially exciting field of study. So too do the structural features of auxetic fibres and the scope for altering the chemistry and topography of polyolefin fibre surfaces. The influence of the incorporation of nanoparticles, such as clays and carbon nanotubes, on polyolefin fibre structure will become increasingly important in a commercial context.

A significant challenge is the direct production of polyolefin fibres actually during olefin polymerisation. It has, however, already been reported that PE

nanofibres are formed during ethene polymerisation in a mesoporous silica using a titanium based metallocene catalyst.⁷³ It is intriguing too that the crystals of these PE nanofibres consist of extended polymer chains rather than the folded chains that are normally encountered.

9.10 Sources of further information

Reference 35 includes detailed accounts of many structural aspects of PP fibres, and a few of these aspects are also discussed in reference 51. Reference 50 includes discussion of polyolefin fibres structures generally. All three references highlight, in addition, fibre processing and fibre properties. Polyolefin fibres are also featured extensively in *Structure Formation in Polymeric Fibers*, edited by D.R. Salem, Hanser, Munich, 2000.

9.11 References

1. McIntyre J.E. and Daniels P.N., *Textile Terms and Definitions*, 10th edn, The Textile Institute, Manchester, 1995.
2. Van Dingenen J.L.J., 'Gel-spun high-performance fibres', in *High-performance Fibres*, editor Hearle J.W.S., Woodhead Publishing, Cambridge, 2001, pp. 62–92.
3. Weedon G., 'Solid-state extrusion high-molecular weight polyethylene fibres', in *High-performance Fibres*, editor Hearle J.W.S., Woodhead Publishing, Cambridge, 2001, pp. 132–155.
4. Buchanan D.R., 'Olefin fibres', in *Kirk-Othmer Encyclopedia of Chemical Technology*, Vol. 16, 3rd edn, John Wiley & Sons, New York, 1981, pp. 357–385.
5. Albizzati E., Giannini U., Collina G., Noristi L. and Resconi L., 'Catalysts and polymerizations', in *Polypropylene Handbook*, editor Moore E.P., Hanser, Munich, Vienna and New York, 1996, pp. 11–111.
6. Cowie J.M.G. and Arrighi, V., *Polymers: Chemistry and Physics of Modern Applications*, 3rd edn, CRC Press, Boca Raton, FL, 2008.
7. Ward I.M. and Cansfield D.L.M., 'High-performance fibres', in *Advances in Fibre Science*, editor Mukhopadhyay S.K., The Textile Institute, Manchester, 1992, pp. 1–24.
8. Schmenk B., Miez-Meyer R., Steffens M., Wulforth B. and Gleixner G., 'Polypropylene fiber table', *Chem Fibers Int*, 2000, **50**, 233–253.
9. Hearle J.W.S., 'The structural mechanics of fibers', *J Polym Sci, Part C*, 1967, **20**, 215–251.
10. Hearle J.W.S., 'Fiber formation and the science of complexity', in *Structure Formation in Polymeric Fibers*, editor Salem D.R., Hanser, Munich, 2000, pp. 521–552.
11. Tomka J.G., Johnson D.J. and Karacan I., 'Molecular and microstructural modelling of fibres', in *Advances in Fibre Science*, editor Mukhopadhyay S.K., The Textile Institute, Manchester, 1992, pp. 181–206.
12. Hoseman R., 'Molecular and supramolecular paracrystalline structure of linear synthetic polymers', *J Polym Sci, Part C*, 1967, **20**, 1–17.
13. Morton W.E. and Hearle J.W.S., *Physical Properties of Textile Fibres*, 3rd edn, The Textile Institute, Manchester, 1993.

14. Nielsen A.S., Batchelder D.N. and Pyrz R., 'Estimation of crystallinity of isotactic polypropylene using Raman spectroscopy', *Polymer*, 2002, **43**, 2671–2676.
15. Bunn C.W., 'The crystal structure of long-chain normal paraffin hydrocarbons. The "shape" of the $>CH_2$ group', *Trans Faraday Soc*, 1939, **35**, 482–491.
16. Lotz B., Wittman J.C. and Lovinger A.J., 'Structure and morphology of poly(propylenes): a molecular analysis', *Polymer*, 1996, **37**, 4979–4992.
17. Cheng S.Z.D., Janimak J.J. and Rodriguez J., 'Crystalline structures of polypropylene homo- and copolymers', in *Polypropylene Structure Blends and Composites. Vol 1 Structure and Morphology*, editor Karger-Kocsis J., Chapman & Hall, London, 1995, pp. 31–55.
18. Turner-Jones A. and Cobbold A.J., 'The β -crystalline form of isotactic polypropylene', *J Polym Sci, Part B*, 1968, **6**, 539–546.
19. Meille S.V., Ferro D.R., Brückner S., Lovinger A.J. and Padden F.J., 'Structure of β -isotactic polypropylene: a long-standing structural puzzle', *Macromolecules*, 1994, **27**, 2615–2622.
20. Lotz B., Kopp S. and Dorset D., 'Original crystal structure of polymers with tertiary helices', *C R Acad Sci Ser IIB*, 1994, **319**, 187–192.
21. Dorset D.L., McCourt M.P., Kopp S., Schumacher M., Okihara T. and Lotz B., 'Isotactic polypropylene, β -phase: a study in frustration', *Polymer*, 1998, **39**, 6331–6337.
22. Brückner S. and Meille S.V., 'Non-parallel chains in crystalline γ -isotactic polypropylene', *Nature*, 1989, **340**, 455–457.
23. Miller, R.L., 'Existence of near-range order in isotactic polypropylenes', *Polymer*, 1960, **1**, 135–143.
24. Cohen Y. and Saraf R.F., 'A direct correlation function for mesomorphic polymers and its application to the "smectic" phase of isotactic polypropylene', *Polymer*, 2001, **42**, 5865–5870.
25. Warren J.M., Mather R.R., Neville A. and Robson D., 'Gas plasma treatments of polypropylene tape', *J Mater Sci*, 2005, **40**, 5373–5379.
26. Samuels R.J., 'Spherulite structure, deformation morphology, and mechanical properties of isotactic polypropylene fibers', *J Polym Sci, Part C*, 1967, **20**, 253–284.
27. Peterlin A., 'Molecular model of drawing polyethylene and polypropylene', *J Mater Sci*, 1971, **6**, 490–508.
28. Samuels R.J., *Structural Polymer Properties, the Identification, Interpretation and Application of Crystalline Polymer Structure*, John Wiley & Sons, New York, 1974.
29. Hautojarvi J. and Leijala A., 'A morphological study of melt-spun polypropylene filaments by atomic force microscopy', *J Appl Polym Sci*, 1999, **74**, 1242–1249.
30. Risnes O.K., Mather R.R. and Neville A., 'Probing the morphology of polypropylene fibres by scanning probe microscopy', *Polymer*, 2003, **44**, 89–100.
31. Flory P.J. and Yoon D.Y., 'Molecular morphology in semicrystalline polymers', *Nature*, 1978, **272**, 226–229.
32. Li J.X., Cheung W.L. and Chan C.M., 'On deformation mechanisms of [β]-polypropylene 2. Changes of lamellar structure caused by tensile load', *Polymer*, 1999, **40**, 2089–2102.
33. Hosier I.L., Bassett D.C. and Moneva I.T., 'On the morphology of polyethylene crystallised from a sheared melt', *Polymer*, 1995, **36**, 4197–4202.
34. Schulz J.M., Hsaio B.S. and Samon J.M., 'Structural development during the early stages of polymer melt spinning by in-situ X-ray techniques', *Polymer*, 2000, **41**, 8887–8895.

35. Ahmed M., *Polypropylene Fibers – Science and Technology*, Elsevier, Amsterdam, Oxford and New York, 1982.
36. Han C.D., 'Rheology of shaped fiber formation', *J Appl Polym Sci*, 1971, **15**, 1091–1097.
37. Swicofil product information: <http://www.swicofil.com/asota.html>
38. Hongu T. and Phillips G.O., *New Fibers*, 2nd edn, Woodhead Publishing, Cambridge, 1997, p. 215.
39. Krishnaswamy R.K. and Baird D.G., 'Fibers from polymer blends and copolymers', in *Structure Formation in Polymeric Fibers*, editor Salem D.R., Hanser, Munich, 2000, pp. 397–424.
40. Qin Y., Brydon D.L., Mather R.R. and Wardman R.H., 'Fibres from polypropylene and liquid crystal polymer (LCP) blends: 1. Effect of LCP concentration', *Polymer*, 1993, **34**, 1196–1201.
41. Miller M.M., Cowie, J.M.G., Brydon D.L. and Mather, R.R., 'Fibres from polypropylene and liquid crystal polymer blends using compatibilizing agents: 3. Assessment of graft side chain liquid crystalline compatibilizers based upon acrylic acid – functionalised polypropylene', *Polymer*, 1997, **38**, 1565–1568.
42. Sukananta P. and Bualek-Limcharoen S., 'In situ modulus enhancement of polypropylene monofilament through blending with a liquid-crystalline copolyester', *J Appl Polym Sci*, 2003, **90**, 1337–1346.
43. Spruiell J.E., 'Structure formation during melt spinning', in *Structure Formation in Polymeric Fibers*, editor Salem D.R., Hanser, Munich, 2000, pp. 5–93.
44. Anon., 'Extrusion process for polypropylene yarns with built-in 3D helical crimp', *Chem Fibers Int*, 1996, **46**, 110.
45. Matsuo T., 'Polypropylene fibers crimped by asymmetrical quenching', *J Text Machinery Soc of Japan*, 1977, **23**, 29–34.
46. Lim J.Y. and Kim S.Y., 'High-modulus, high-strength, thick polypropylene monofilament production: response surface analysis approach', *J Polym Sci, Part B*, 2003, **41**, 1175–1182.
47. Lee K.-H., Givens S.R., Chase D.B. and Rabolt J.F., 'Electrostatic polymer processing of isotactic poly(4-methyl-1-pentene) fibrous membrane', *Polymer*, 2006, **47**, 8013–8018.
48. Lee K.-H., Snively C.M., Givens S.R., Chase D.B. and Rabolt J.F., 'Time-dependent transformation of an electrospun poly(1-butene) fibrous membrane', *Macromolecules*, 2007, **40**, 2590–2599.
49. Lyons J., Li C. and Ko F., 'Melt-electrospinning, part 1: processing parameters and geometric properties', *Polymer*, 2004, **45**, 7597–7603.
50. Mather R.R., 'Polyolefin fibres', in *Synthetic Fibres: Nylon, Polyester, Acrylic, Polyolefin*, editor McIntyre J.E., Woodhead Publishing, Cambridge, 2005, pp. 235–292.
51. Sen K., 'Polypropylene fibres', in *Manufactured Fibre Technology*, editors Gupta V.B. and Kothari V.K., Chapman & Hall, London, 1997, pp. 457–459.
52. Han C.D., Lamonte R.R. and Shah Y.T., 'Studies on melt spinning. III. Flow instabilities in melt spinning: melt fracture and draw resonance', *J Appl Polym Sci*, 1972, **16**, 3307–3323.
53. Wang I.-C., Dobb M.G. and Tomka J.G., 'Polypropylene fibres: an industrially feasible pathway to high tenacity', *J Text Inst*, 1995, **86**, 383–392.
54. Wang I.-C., Dobb M.G. and Tomka J.G., 'Polypropylene fibres: exploration of conditions resulting in high tenacity', *J Text Inst Part 1*, 1996, **87**, 1–12.

55. Sheehan W.C. and Cole T.B., 'Production of super-tenacity polypropylene filaments', *J Appl Polym Sci*, 1964, **8**, 2359–2388.
56. Piccardo S., Saiu M., Brucato V. and Titomanlio G., 'Crystallisation of polymer melts under fast cooling. II. High purity iPP', *J Appl Polym Sci*, 1992, **46**, 625–634.
57. Choi C.-H. and White J.L., 'Comparative study of structure development in melt spinning polyolefin fibers', *Int Polym Processing*, 1998, **13**, 78–87.
58. Yang R.D., Mather R.R. and Fotheringham A.F., 'Relationship between structure and spinning processing of as-spun PP fibres', *Int Polym Processing*, 1999, **14**, 60–68.
59. Spruiell J.E. and White J.L., 'Structure development during polymer processing. Melt spinning of polyethylene and polypropylene', *Polym Eng Sci*, 1975, **15**, 660–667.
60. Nadella H.P., Henson H.M., Spruiell J.E. and White J.L., 'Melt spinning of isotactic polypropylene: structure development and relationship to mechanical properties', *J Appl Polym Sci*, 1977, **21**, 3003–3022.
61. Broda J. and Wlochowicz A., 'Influence of pigments on supermolecular structure of polypropylene fibres', *Eur Polym J*, 200, **36**, 1283–1297.
62. Kitao T., Ohya S., Firukawa J. and Yamashita S., 'Orientation of polymer molecules during melt spinning. II. Orientation of crystals in as-spun polyolefin fibers', *J Polym Sci, Polym Phys*, 1973, **11**, 1091–1109.
63. Sheehan W.C. and Wellman R.E., 'Relationship between molecular orientation and draw ratio of polypropylene monofilaments', *J Appl Polym Sci*, 1965, **9**, 3597–3603.
64. de Vries H., 'The relationship between birefringence and draw ratio of man-made fibers', *J Polym Sci*, 1959, **34**, 761–778.
65. Nadella H.P., Spruiell J.E. and White J.L., 'Drawing and annealing of polypropylene fibers: structural changes and mechanical properties', *J Appl Polym Sci*, 1978, **22**, 3121–3133.
66. El Maaty M.A.I., Bassett D.C., Olley R.H., Dobb M.G., Tomka J.G. and Wang I.-C., 'On the formation of defects in drawn polypropylene fibres', *Polymer*, 1996, **37**, 213–218.
67. Samuels R.J., 'Quantitative characterization of deformation in polypropylene fibers', *J. Polym Sci, A-2*, 1968, **6**, 2021–2041.
68. Amornsakchai T., Olley R.H., Bassett D.C., Al-Hussein M.O.M., Unwin A.P. and Ward I.M., 'On the influence of initial morphology on the internal structure of highly drawn polyethylene', *Polymer*, 2000, **41**, 8291–8298.
69. Amornsakchai T., Bassett D.C., Olley R.H., Unwin A.P. and Ward I.M., 'Remnant morphologies in highly-drawn polyethylene after annealing', *Polymer*, 2001, **42**, 4117–4126.
70. Shishoo R. (ed.), *Plasma Technologies for Textiles*, Woodhead Publishing, Cambridge, 2007.
71. Alderson K.L., Alderson A., Smart G., Simkins V.R. and Davies P.J., 'Auxetic polypropylene fibres. Part 1. Manufacture and characterisation', *Plastics, Rubbers, Composites*, 2002, **31**, 344–349.
72. Alderson K.L., Alderson A., Davies P.J., Smart G., Ravirala N. and Simkins V.R., 'The effect of processing parameters on the mechanical properties of auxetic polymeric fibres', *J Mater Sci*, 2007, **42**, 7991–8000.
73. Tajima K. and Aida T., 'Controlled polymerisations with constrained geometries', *Chem Commun*, 2000, 2399–2412.

The structure of acrylic, polyvinylalcohol and polyvinylchloride fibers

H C KIM, Chonbuk National University, South Korea

Abstracts: This chapter discusses acrylic, modacrylic, polyvinylalcohol (PVA) and polyvinylchloride (PVC) fibers which are prepared by the addition polymerization method. The chapter first reviews the history of the development of the fibers and describes the chemical structures of the polymers. The chapter then describes the detailed spinning methods to manufacture the fibers, and finally discusses the properties of the fibers.

Key words: acrylic fiber, modacrylic fiber, polyvinylalcohol (PVA) fiber, polyvinylchloride (PVC) fiber.

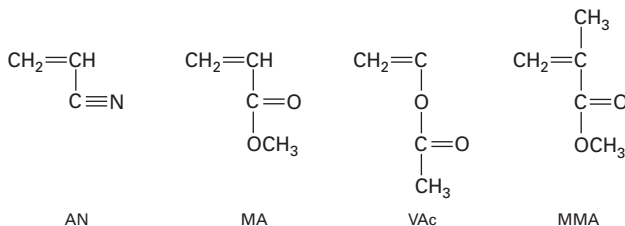
10.1 Acrylic and modacrylic fibers

10.1.1 Chemical structure

Polyacrylonitrile is synthesized through the polymerization of an acrylonitrile monomer. The polymer is difficult to process because it decomposes before reaching its melting point and is insoluble in general solvents. Acrylic fibers are mainly obtained by solution spinning, which requires another comonomer to enhance the solubility in the solvent.

Acrylic fibers are defined as a fiber containing more than 85% of acrylonitrile (AN). Other comonomers used in the copolymerization are methylacrylate (MA), vinylacetate (VAc), methylmethacrylate (MMA), etc.¹ Figure 10.1 shows the chemical structures of acrylonitrile and these comonomers.

Control of the copolymer composition is difficult because the solubility, resonance characteristics and dipole moment of the comonomers are significantly different from that of acrylonitrile. Combinations of acrylonitrile–



10.1 Chemical structures of acrylonitrile and the comonomers used in acrylic fibers.

methylacrylate are widely used because they have similar polymerization factors.

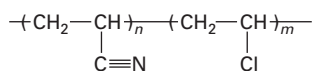
Modacrylic fibers are defined as a fiber containing less than 85% but more than 35% acrylonitrile. Modacrylic fibers generally contain substantial levels of halogen-containing comonomers such as vinyl chloride, and the fiber is intended to have flame retardant properties.² Vinyon, Dynel and Kanekalon contain 60% of acrylonitrile (n) and 40% of vinyl chloride (m), as shown in Fig. 10.2.

There are three types of comonomers used in acrylic and modacrylic fibers: neutral comonomers, ionic comonomers and halogen-containing comonomers. Neutral comonomers, such as MA, VAc and MMA, are copolymerized to increase the solubility in a spinning solution and improve the diffusivity of the dye in fiber molecules. Ionic comonomers, such as sodium styrene sulfonate and sodium methallyl sulfonate, are used to impart cationic dyeing sites. Acrylic fibers generally obtain their dyeing sites from sulfonate and sulfate initiator fragments at the polymer chain ends. The molecular weight of the polymer needs to be sufficiently high to exhibit reasonable dope viscosity, but low enough to provide many dyeing sites. When dyeability is not achieved, high molecular weight sulfonate monomers are copolymerized to provide additional cationic dyeing sites. Halogen-containing comonomers, usually vinyl chloride, vinylidene chloride and vinyl bromide, confer flame retardant properties to the fiber. Acrylic fibers do not include these copolymers but almost all modacrylic fibers include a high level of halogen-containing comonomers to impart flame retardant properties.

Acrylic fibers were first produced by duPont under the trade name of Orlon in 1944.³ Other acrylic fibers developed shortly after include Acrilan (Monsanto), Dolan (Hoechst) and Dalon (Bayer). Modacrylic fibers were first introduced by Union Carbide under the trade name of Vinyon N. Other modacrylic fibers include Dynel (Union Carbide), Vernel (Eastman), Teklan (Courtaulds) and Kanekalon (Kaneka).

10.1.2 Preparation

All commercial acrylic fibers are prepared using wet or dry spinning methods. Melt spinning cannot be applied because the acrylic polymers degrade upon heating. Polymers are dissolved in the appropriate solvent to form a spinning dope. In the wet spinning process, the spinning dope is extruded into a coagulation bath containing the non-solvent and then washed, stretched,



10.2 Chemical structure of typical modacrylic fiber.

annealed and subjected to additional processing.⁴ In the dry spinning process, the spinning dope is extruded into the air heated above the boiling point of the solvent. The solidified fiber is then washed free of solvent and processed like wet-spun fibers.

There are strong dipolar bonds between the nitrile groups of an acrylic polymer. The solvents for acrylic polymers should contain functional groups that react with nitrile groups and break the strong dipolar bonds, thereby allowing dissolution to occur.⁵ *N,N'*-dimethylformamide (DMF) is a good solvent for this purpose. Dimethylacetamide (DMAc) and dimethylsulfoxide (DMSO) are also used. A concentrated aqueous solution of inorganic salts such as NaSCN and ZnCl₂ can also dissolve the acrylic polymer. DMF is the most important solvent because it is used in both wet and dry spinnings. All the other solvents are used in wet spinning with DMAc being the second major solvent. Aqueous solutions of NaSCN and HNO₃ are the most commonly used inorganic solvents for wet spinning. The proportions of DMF, DMAc, NaSCN and HNO₃ consumed in the commercial production of acrylic fibers are 24%, 24%, 20% and 10%. Table 10.1 shows the typical polymer concentrations of various solvents.

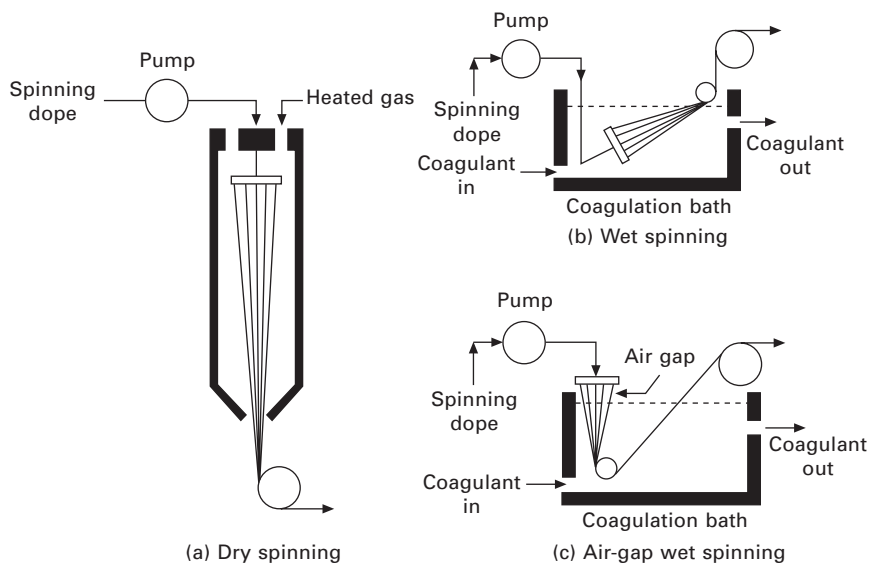
There are three methods in solution spinning to produce acrylic fiber: dry spinning, wet spinning and air-gap wet spinning.^{6,7} Figure 10.3 shows schematic diagrams of these methods.

In dry spinning, DMF is used mainly as a solvent on account of its low boiling point and low cost.⁸ The air temperature is heated to 200°C in order to evaporate the DMF. However, DMF is not completely removed and 5–25% of the DMF remains in the undrawn fiber. The quantity of solvent remaining is dependent on the air temperature, column length and take-up speed. The remaining DMF helps orientate the molecular chains in the following drawing process. The rate of solvent evaporation in the fiber increases with increasing air temperature but the orientation of the molecular chain decreases.

In the wet spinning method, the spinning dope is extruded through a spinneret containing 20 000–100 000 holes with diameters of 0.05–0.25 mm. The spinneret is immersed in the coagulation bath and the fibers are solidified as they are removed from the spinneret through the substitution of solvent and non-solvent in the fiber. The solidification speed is affected by the

Table 10.1 Typical polymer concentrations

Solvents	Concentration
DMF (dry spun)	25–32%
DMF, DMAc, DMSO (wet spun)	20–28%
NaSCN, 45–55% in water (wet spun)	10–15%
ZnCl ₂ , 55–65% in water (wet spun)	8–12%
HNO ₃ , 65–75% in water (wet spun)	8–12%



10.3 Schematic diagrams of the spinning methods.

concentration of the spinning dope, the ratio of solvent/non-solvent and the temperature of the coagulation bath. The rate of solidification increases with increasing concentration of the spinning dope and amount of non-solvent in the coagulation bath. The temperature of the spinning dope and coagulation bath is generally 25–125°C and 0–50°C, respectively.

Air-gap wet spinning is a modification of wet spinning and the spinneret is placed approximately 1 cm above the coagulation bath.⁹ Since the spinneret is not immersed in the coagulation bath, the temperature of the spinning dope can be controlled independently regardless of the coagulation bath temperature. Molecular chains in the fiber can be highly oriented because coagulation does not occur immediately after extrusion and there is no resistance in the coagulation bath. Therefore, the high take-up speed and high tenacity fiber can be obtained by air-gap wet spinning.

The fibers obtained from either a wet spinning coagulation bath or a dry spinning column have low strength and high elongation. Such undrawn fibers should be drawn in order to have reasonable mechanical properties. Drawing causes the polymer chains to become oriented along the fiber axis, resulting in a high modulus and strength. The fibers are easily stretched in water or steam that is held close to 100°C because the glass transition temperature of the wet acrylic fiber is 75°C.

10.1.3 Properties

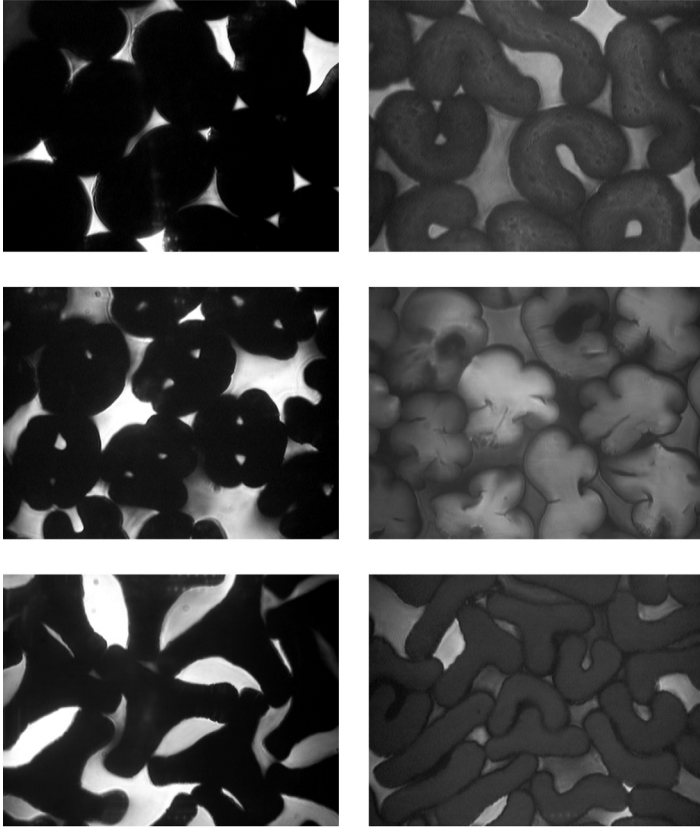
In wet spinning, the structure of the freshly coagulated fiber is determined by the conditions in the coagulation bath.¹⁰⁻¹³ The density of the coagulate fiber is 0.4–0.5 g/cm³, which is much smaller than the 1.17 g/cm³ of the original polymer. This indicates that the fiber is extremely porous. The fiber structure is a result of counter-diffusion of the solvent and non-solvent as well as phase separation of the acrylic polymer. A cross-section of the coagulated fiber shows tear-shaped voids known as macro-voids, which begin near the outer edge of the fiber and extended to the center. The void size is determined by the rate of diffusion and phase separation. It increases with increasing rate of diffusion and phase separation. The number and size of the voids have a major influence on the fiber properties, such as the tensile strength and abrasion strength.

The voids are stretched during the drawing process, and are finally eliminated in the collapsing process. In the collapsing process, the fibers are passed through heated zones and/or hot rollers, and the water is driven from the internal fibrillar network and eliminated. Acrylic fibers generally have a strength of 2–4 g/d and an elongation of 30–60%.

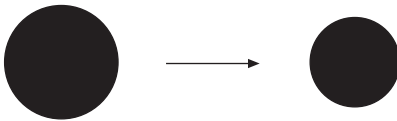
The cross-section of the wet spun acrylic fiber is quite different. Each manufacturer uses a different spinning process, which gives rise to a characteristic cross-section. The cross-section of the fiber might be determined by changing the coagulation bath conditions such as the solvent/non-solvent ratio and temperature. Figure 10.4 shows various cross-sections of acrylic fibers.

When a round-shaped cross-section spinneret is used, the cross-section of the fiber will be either round or dumbbell in shape.¹⁴ The dumbbell-shaped fiber is obtained when a weak skin is formed through coagulation and the volume is reduced by solvent diffusion from the center of the fiber. A round fiber is obtained either by increasing the coagulation rate to build up a thick skin for maintaining a round shape during solvent diffusion, or by decreasing the coagulation rate to build up a thin skin for uniform solvent diffusion. The other modified shapes such as the star-shape, C-shape and H-shape are produced with shaped spinnerets and coagulation conditions to maintain the desired cross-sections.

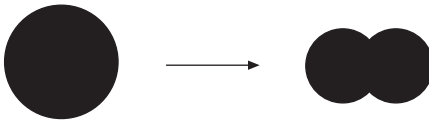
In dry spinning, the solvent is removed by heat and the outer parts solidify faster than the inner parts, resulting in a skin/core structure. As the solvents are diffused further from the core, the skin reduces inward to give either a circular or a dumbbell-shaped cross-section. Figure 10.5 shows the mechanism for the formation of the cross-section during solidification. A circular cross-section is formed when the rate of evaporation is equal to or smaller than the rate of diffusion. However, the skin collapses to a dumbbell shape when the rate of evaporation is greater than the rate of diffusion.



10.4 Cross-sectional shapes of the acrylic fibers.



(a) Evaporation rate \approx diffusion rate



(b) Evaporation rate $>$ diffusion rate

10.5 Changes in the cross-sections during evaporation in dry spinning.

Acrylic fibers are mainly produced as staple fibers. The production quantity of acrylic filaments is low because there are no good methods for adding texture to an acrylic filament. The fiber should be heated to the melting point of the polymer to allow successful texturing but the acrylic polymer does not melt.

Table 10.2 summarizes the physical properties of some acrylic fibers.¹⁵ The fibers are chosen to represent different processes, end uses and deniers. The tenacity ranges are 2.2–3.6 g/d and the elongation ranges are 33–64%. As the denier increases, the tenacity decreases and elongation increases, which suggests that the molecular orientation decreases with increasing fiber thickness. The boiling water shrinkage of acrylic fiber is quite low.

The tensile properties of acrylic staple fiber were compared with those of other staple fibers and are listed in Table 10.3.¹⁶ Compared with nylon and polyester fibers, acrylic fiber has a lower elongation and lower work of rupture, which suggests that the mechanical properties of acrylic fibers are inferior to those of nylon or polyester. However, the work of rupture of an

Table 10.2 Physical properties of the acrylic fibers

Fiber	Acrilan B-16	Orlon 42	Euroacril	Courtelle	Dow type 500	Acrilan B-96	Zefran 253A
Producer	Monsanto	du Pont	ANIC	Courtaulds	Dow	Monsanto	Dow
End use	Textile	Textile	Textile	Textile	Industrial	Carpet	Carpet
Denier	1.2	3.4	3.1	4.5	6.0	15.0	15.0
Tenacity (g/d)	3.6	3.0	2.7	2.5	3.5	2.2	2.3
Elongation (%)	42	33	35	64	33	56	62
Initial modulus (g/d)	44	45	41	37		21	20
Boiling water shrinkage (%)	1.0	0.7	0.7	1.2	1.0	1.0	1.0

Table 10.3 Comparison of the mechanical properties of acrylic fiber with the other fibers

Fiber	Tenacity (g/d)	Elongation (%)	Work of rupture (g/d)	Initial modulus (g/d)
Acrylic	3.05	25	0.53	70
Nylon 66	4.18	43	1.14	11.3
Polyester	4.31	37	1.34	99
Cotton	5.09	6.5	0.17	82.5
Wool	1.24	42.5	0.35	26

acrylic fiber is higher than that of wool, which is significant because acrylic fibers have replaced wool in many markets.

Polyacrylonitrile fiber is recognized as the most important and promising precursor for the manufacture of carbon fibers. The advantages are a high degree of molecular orientation, a higher melting point and a greater yield of the carbon fiber. Acrylic fibers form a thermally stable, highly oriented molecular structure when subjected to a low-temperature heat treatment, which is not significantly disrupted during the carbonization treatment at higher temperatures, giving rise to a carbon fiber with good mechanical properties.

10.2 Polyvinylalcohol fiber

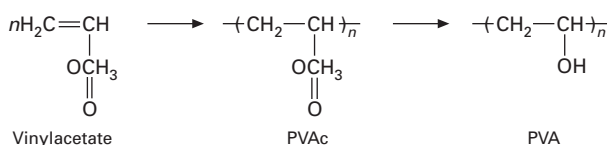
10.2.1 Chemical structure

Polyvinylalcohol (PVA) is believed to be obtained by the polymerization of a vinylalcohol monomer. However, vinylalcohol is unstable and cannot be isolated at high concentrations. Instead of the polymerization of a vinylalcohol monomer, PVA is alternatively prepared by the hydrolysis of polyvinylacetate (PVAc), as shown in Fig. 10.6.

Vinyl acetate is produced either by the vapor phase reaction of acetylene and acetic acid or by a reaction of ethylene, acetic acid and oxygen. The polymerization of vinyl acetate to produce PVAc proceeds through a free-radical mechanism.

The hydrolysis of PVAc to obtain PVA was first reported by Herman and Haehnel in 1924.¹⁷ Later Herman *et al.*¹⁸ produced PVA fiber using a solution spinning method and reported that the water resistance of the fiber can be improved using various physical and chemical treatments. Using their techniques, commercial PVA fiber was produced under the name of Synthofil, but production was soon stopped on account of the product's insufficient water resistance.

In 1939, Sakurada *et al.* at Kyoto University¹⁹ and Yazawa *et al.* at Kanekafugi Spinning Co., Ltd²⁰ developed a boiling water-insoluble PVA fiber through heat treatment and formalization. They produced PVA fiber using a wet spinning method. The fibers were not attacked by boiling water after a formalization reaction followed by heat treatment. Soon after World



10.6 Process to synthesize polyvinylalcohol.

War II, Kurashiki Rayon Co., Ltd (now Kuraray Co., Ltd) began producing commercial PVA fiber. The PVA fiber was called ‘vynylon’ in Japan and ‘vinal’ in the USA.

10.2.2 Preparation

PVA fiber is manufactured by solution spinning. Since PVA is difficult to melt by heat, melt spinning cannot be applied to obtain PVA fiber. Wet spinning, dry spinning or air-gap wet spinning, where an air gap is placed between spinneret and coagulation bath, can be used.

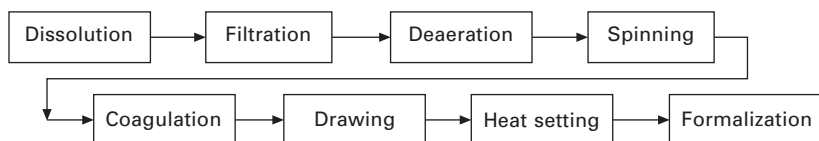
Wet spinning

PVA fibers are mainly manufactured by dissolving PVA in hot water to make a spinning solution and by coagulating it in a sodium sulfate bath.²¹ Figure 10.7 shows the typical wet spinning process for manufacturing PVA fibers.

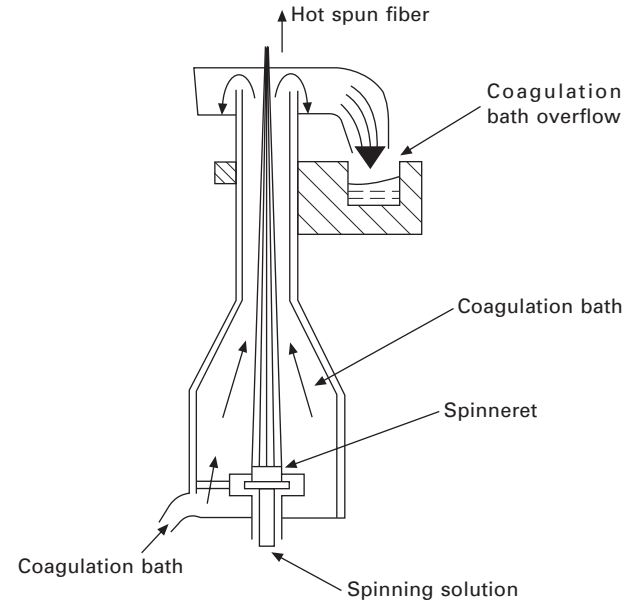
For the industrial production of PVA fibers, a 1500–2000 degree of polymerization is mostly used as the raw materials. PVA is mixed with water and heated to 100°C with steam. The mixture is maintained at this temperature for several hours while it is stirred until the PVA is dissolved completely. The concentration of PVA in the solution for commercial production is usually approximately 10–20%.

An aqueous PVA solution is filtered, deaerated, and transferred to a spinning machine. The vertical spinning machine shown in Fig. 10.8 is effective for PVA spinning because coagulated fibers tend to float in the bath due to their lower density of PVA fiber compared with that of a sodium sulfate solution bath. Moreover, the coagulation speed of PVA is much slower and vertical spinning machine has the advantage of extending the dip length.

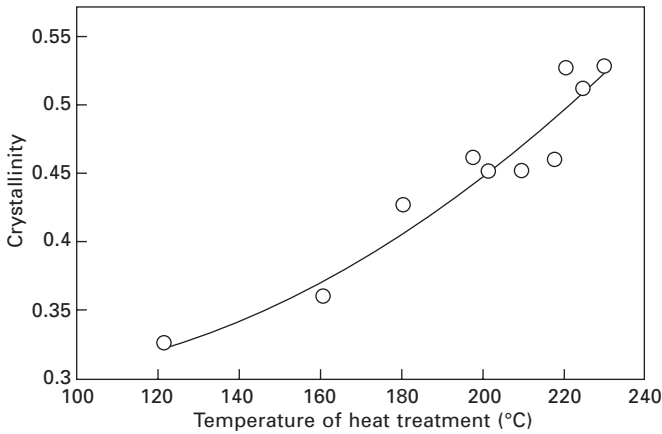
Many chemicals have been tested as coagulants with the most effective being sodium sulfate.²¹ The solubility of sodium sulfate in water reaches its maximum between 40°C and 50°C. Hence, the temperature of the coagulation bath is usually maintained in this range. After the fiber is spun in the coagulation bath, it is washed and dried. The dried fiber is hot-drawn to increase its tenacity, and heat-set to increase its hot water resistance. Both the hot-drawing and heat-set processes are carried out at temperatures between 210°C and 240°C.



10.7 Flow diagram to obtain PVA fiber by wet spinning.



10.8 Diagram of vertical spinning machine.



10.9 The change in crystallinity as a function of the heat treatment temperature.

Heat-setting is a process used to improve the hot-water resistance. In the heat-setting process, the crystallinity of a PVA fiber increases as a result of the removal of water and the formation of a new hydrogen bond between the molecules. As shown in Fig. 10.9, the crystallinity increases with increasing heat-set temperature.²²

Heat-set fibers are resistant to hot water at 90°C but this is not sufficient in some applications. When better hot-water resistance is required, formalization

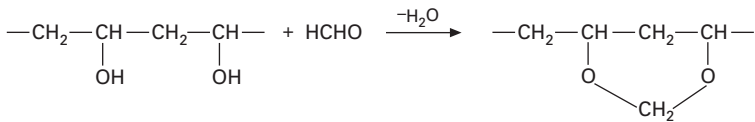
is carried out to impart intermolecular cross-linking between the two hydroxyl groups, as shown in Fig. 10.10.

In the formalization process, the PVA fiber is immersed in a bath containing an aqueous solution of formalin, sulfuric acid and sodium sulfate. The fiber becomes resistant to boiling water when 30–40% formalization is achieved.

The cross-sections have a dumbbell shape with a double layer structure with an apparently porous inner portion, as shown in Fig. 10.11. The circular cross-section becomes crushed as the water is removed. Moreover, dehydration and coagulation of the skin layer occurs rapidly whilst that of the core layer is delayed. Therefore, a dumbbell shape skin/core structure is formed.

Another wet spinning method is to coagulate an aqueous PVA solution in an alkaline bath such as sodium hydroxide. Sodium hydroxide quickly penetrates and reduces the rate of dehydration, which results in the coagulated filament forming a gel-like structure. The filament can be drawn at a higher draw ratio, and the fibers prepared using this method are characterized by the high tenacity, low elongation and circular cross-section. However, since spun fibers tend to stick together, the number of spinneret holes cannot exceed 1000. Therefore, this spinning method is not applied commercially.

The above problem is solved using the cross-linking wet spinning method with boric acid.^{23,24} In the cross-linking spinning method, a small amount



10.10 Chemical reaction for the formalization of PVA fibers.



10.11 Dumbbell shape skin/core structure of PVA fiber.

of boric acid is added to the aqueous PVA solution, and the spinning dope is extruded in the alkaline coagulation bath. NMR reveals the formation of borate ion-aided cross-linking based on the mono-diol complex in the spinning dope, as shown in Fig. 10.12. Cross-linking is formed through an ionic bond between the PVA-bound borated ion and the PVA-chelated sodium ion.²⁵

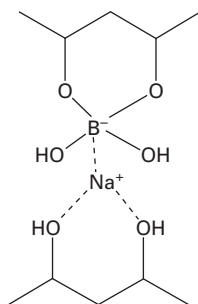
After a PVA-bound borated ion is formed in the spinning dope, it is spun in the alkaline coagulation bath. The alkali quickly penetrates the PVA fiber immediately after spinning, and cross-linking is formed between the oriented molecular chains. As a result, a gel is formed and the entanglements of the PVA chains are minimized. This allows the fiber to be drawn at a higher draw ratio. However, cross-linking between the PVA chains increases the difficulty in drawing the fiber. Hence, the cross-links should be broken before drawing using an acid bath treatment. The tenacity of the fiber can be increased to 20 g/d using this method.

Dry spinning

In the dry spinning process, a PVA fiber is obtained by spinning a concentrated aqueous solution of PVA from a spinneret into air.²⁶ The concentration is usually 40–45% for low-draft spinning where the draft ratio is approximately 1, and 20–40% for high draft spinning where the draft ratio is from 1 to several tens.

The solution is solid at room temperature, which means that the spinning process is similar to melt spinning. Mixtures of PVA powder and water are converted to granules and then subjected to spinning. The granules are melted in an extruder, and the solution is filtered, deaerated and transferred to a spinneret. The spun fibers are solidified by hot air and the solidified fibers are fed immediately to a drying machine. The fibers are completely dried and taken up by a winder.

The take-up speed of dry spinning is 300–600 m/min, which is higher than that of wet spinning, where the take-up speed is approximately 50



10.12 Borated ion-aided cross-linking.

m/min. Nitivy Co. in Japan produces PVA filaments at 9.5 tons/day under the brand name of 'Solvron' using a dry spinning method. Solvron is soluble in water at temperatures between 20°C and 100°C.

Air-gap wet spinning

One of the main characteristics of PVA fibers is their high tenacity. A tenacity of 10–13g/d can be obtained using the conventional wet spinning method. However, various methods have been investigated to obtain high tenacity fibers up to 30g/d, which is similar to the tenacity of aramid fiber.

Air-gap wet spinning is a useful technique for producing high tenacity fibers via gel spinning.²⁷ In air-gap wet spinning, PVA is dissolved in dimethylsulfoxide (DMSO) at a concentration of 13–17%, and spun in a methanol coagulation bath.²⁸ There is a 10–20 mm air gap between the spinneret and the coagulation bath, and the air gap acts as an adiabatic layer. The potential lateral interaction between PVA chains through the hydroxyl group leads to quicker gelation. As the PVA solution (e.g. 140°C) is cooled by immersion in methanol at a sufficiently low temperature, such as –20°C, the PVA chains can quickly undergo mobility reduction, resulting in the formation of small crystals. These crystals act as physical cross-links in the PVA gel, and the fiber may have a low entanglement density, which can result in the formation of a highly drawable PVA fiber.

In order to obtain high tenacity fiber, the as-spun fibers are drawn at a draw ratio as high as possible at temperatures above 175°C. The hot-drawn filament is characterized by its high tenacity and low elongation. When the fiber is drawn at higher temperatures, it has superior hot-water resistance without formalization.

Recently, Kuraray developed a low cost process known as the K-II process. One of the disadvantages of air-gap wet spinning is the sticking of fibers in the air. After the fibers are spun they do not immediately coagulate in air, which means that the fibers have a tendency to stick together. Therefore, the pitch of the spinneret hole should be greater in order to avoid sticking, which increases the production cost due to the lower number of holes in the spinneret.

In the K-II process, PVA is dissolved in DMSO and spun in a methanol coagulation bath where the spinneret is immersed. Since the spun fibers coagulate quickly, there is less tendency to stick together and the pitch of the nozzle hole can be closer. As a result, production cost decreases. The main technique of the K-II process is the complete insulation of the spinneret. Insulation of the spinneret is very important because a high-temperature spinning dope is spun in a low-temperature coagulation bath to form a gel.

10.2.3 Properties

PVA fibers are divided into two categories: water-soluble and water-insoluble fibers. Water-insoluble fibers are mainly used in textiles, and are produced by heat treatment and formalization. Approximately 80% of PVA fibers are a staple fiber and approximately 20% are filament fibers. Since PVA fibers have excellent physical and chemical properties, such as strength, modulus, heat resistance and adhesive strength, 90% of PVA fibers are highly adaptable for industrial uses. In recent years, apparel applications have constituted only a small percentage of PVA fiber total consumption.

Commercial PVA fibers have a wide range of strength and elongation. The strength of high tenacity PVA fiber is up to 17 g/de, and an even a higher tenacity of 30 g/de, which corresponds to the tenacity of aramid fiber, has recently been reported.²⁷ High tenacity PVA fiber has a lower elongation at break than high tenacity fibers made from polyester or nylon. PVA fibers are used as ropes, sewing thread and fishing nets on account of their high tenacity and low elongation.

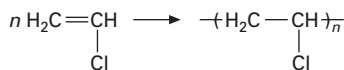
Good adhesion to rubber, abrasion resistance and heat stability, as well as low heat shrinkage and resistance to chemicals, are generally required for applications in the rubber industry. Since PVA fibers contain hydroxyl groups in the chemical structure, latex is easily attached to form a rubber compound. Hence, PVA fibers have excellent characteristics for such requirements, and are largely used in the rubber industry as rubber hoses, conveyer belts and tire cords.²⁹

PVA cut fibers are also used as reinforcing fibers in FRC (fiber reinforced cement). Asbestos fibers were used as fibers for FRC in the past but are strongly prohibited by law in many countries nowadays due to health problems. Applications in the field of FRC require strong adhesion force with cement and high chemical resistance to alkali. PVA fibers meet such requirements and are considered to be a suitable replacement for asbestos fibers.³⁰

10.3 Polyvinylchloride fiber

10.3.1 Chemical structure

Polyvinylchloride (PVC) fiber is made from PVC polymer. PVC is polymerized by radical polymerization using a vinyl chloride monomer, as shown in Fig. 10.13.



10.13 Polymerization of polyvinylchloride.

PVC polymer was first synthesized by Regnault in 1938.³¹ The main usage of PVC is not as a fiber. It is mainly used as an engineering plastic and is one of four major plastic materials. PVC fibers were produced commercially in the 1930s using a melt spinning method. However, the process was unacceptable due to the problems caused by the high melt viscosity and thermal degradation during melt spinning.³² A wet spinning method was also attempted using solvents such as cyclohexanone, tetrahydrofuran or dimethylformamide, but these were commercially unsuccessful.

Progress in making PVC fibers by a dry spinning method was brought about using common solvents.³³ In Germany, an acetone-soluble polymer was obtained by the chlorination of PVC, and Pe-Ce fiber was produced in 1934. In the United States, a vinyl chloride and acetate copolymer was synthesized, and Vinyon was produced using an acetone solvent in 1935.

The PVC fibers currently on the market are Rhovyl and Teviron. Rhovyl was first produced in France in 1949 using a dry spinning method in a mixture solvent of acetone–carbon disulfide. In 1956, Teijin, a Japanese company, found that an acetone–benzene binary mixture dissolves PVC at elevated temperatures and produced Teviron using a dry spinning method.

Currently, PVC fibers are also used as wig fibers on account of their flame retardant property due to the presence of chlorine in the chemical structure. Fibers of the thickness of human hair are not generally obtained using a solution spinning method because the solvent is difficult to remove when the fiber is thick. However, fibers of this thickness are obtained using a melt spinning method. Toyokalon and Kanekalon AD-70 are manufactured in Japan, and Falang is manufactured by Uno & Company in Korea to produce wig fibers using a melt spinning method.

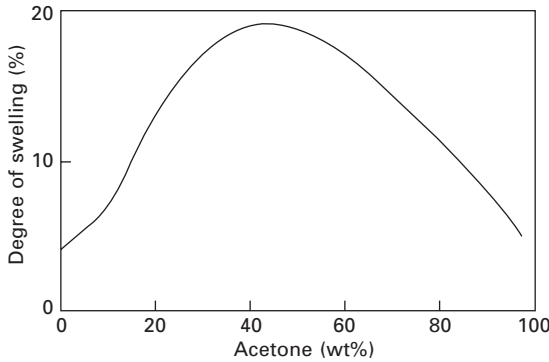
10.3.2 Preparation

Dry spinning

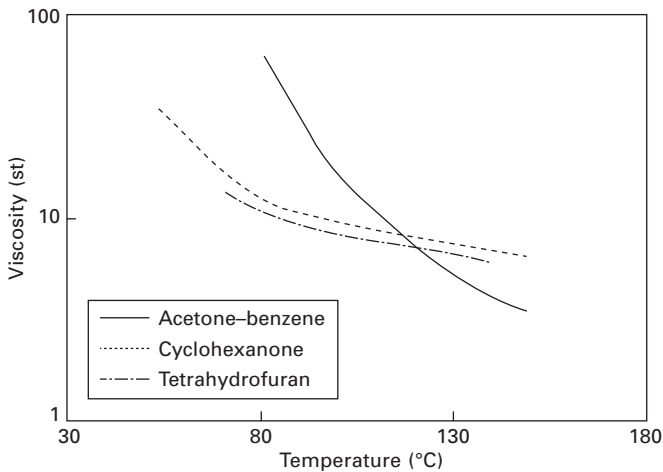
Most PVC fibers are produced using a dry spinning method, with Teviron and Rhovyl being the most representative fibers. PVC polymer is dissolved in a solvent, and the spinning dope is deaerated and filtered. The spinning dope is fed into the spinneret through a gear pump and spun out to a hot atmosphere. The undrawn fiber is obtained by evaporating the solvent, then drawn to increase the strength, and heat-set to reduce the level of thermal shrinkage.

Teviron is spun from an acetone–benzene mixture solvent. When PVC is treated with an acetone–benzene solvent at room temperature it does not dissolve but swells. The degree of swelling depends on the ratio of acetone and benzene.³⁴ Figure 10.14 shows the effect of the mixture ratio on the degree of swelling. As shown in the figure, the maximum degree of swelling is obtained at a ratio of 40% acetone and 60% benzene.

If the temperature is increased, swollen PVC is dissolved and the viscosity



10.14 Effect of the acetone content in a binary mixture of acetone-benzene on the degree of swelling.



10.15 Changes in viscosity in the three different solvents as a function of temperature.

of the solution decreases. Figure 10.15 shows the temperature dependence of a PVC solution in three different solvents. As the temperature increases, the viscosity of the PVC solution decreases rapidly regardless of the solvent used.

In the case of Rhovyl, the fiber was spun from a mixed acetone-carbon dioxide solvent.³⁵ After dissolution, the polymer solution is spun into a hot air chamber. The temperature of the heating zone of the spinning chamber is 120°C. The solvent is evaporated by heating, and the undrawn fiber is taken up at a winding speed of 170 m/min. It is then drawn in boiling water to align the molecules and give the fibers their mechanical properties. After drawing, the fibers have a shrinkage potential of 25% to 55% at 98°C. In order to reduce the level of thermal shrinkage, boiling water and steam

treatments are applied to the drawn fiber. Thermovyl, Fibravyl and Isovyll fibers are classified according to the degree of thermal shrinkage.³⁶

Melt spinning

PVC fibers are used as wig fiber on account of the flame retardant property of a vinyl containing polymer, and such a thick fiber is produced by melt spinning. The main difficulties with melt spinning are the thermal degradation and low fluidity of the PVC melt. The degradation temperature of PVC is about 210°C, slightly higher than the melt processing temperature (170–180°C); hence, PVC tends to decompose easily during a melt process. Moreover, since the viscosity of the molten polymer is quite high, it is difficult to manufacture a fiber through a small diameter spinneret. Therefore, the selection of an excellent heat stabilizer and lubricant is quite important for the successful melt spinning of a PVC fiber.³⁷

Cadmium/zinc³⁸ or organo-tin³⁹ heat stabilizers are widely used to produce PVC fiber. Recently, Calcium/zinc stabilizers have been used as a substitute for the previous stabilizers because cadmium is toxic and an organo-tin stabilizer is too expensive. A lubricant is also necessary to enhance the fluidity of a molten polymer in the spinneret. Montan wax, stearic acid and hydrocarbon wax are useful lubricants. The addition of a processing aid is helpful for preventing ‘fish eyes’ in the drawn fiber.

PVC fiber is produced by melt spinning using the following method. PVC powder and various additives are mixed together in a super mixer and dry blended. The dry blend is fed into an extruder and the extrudate is pelletized using a hot cutting method. The pellet is fed into a melt spinning machine and the fibers are produced while passing through a spinneret. The fiber is wound up using a take-up device, and the undrawn fiber is obtained. The undrawn fiber is then drawn using a drawing machine to enhance the mechanical properties and the drawn fiber is heat-set to decrease the level of thermal shrinkage.

10.3.3 Properties

The PVC fiber has several characteristics that distinguish it from other fibers. As mentioned earlier, PVC fiber is an outstanding flame retardant fiber because of its chlorine-containing chemical structure. It is also used as a material for health energy-saving because of its excellent heat retention, moisture permeability and negative electrostatic properties.

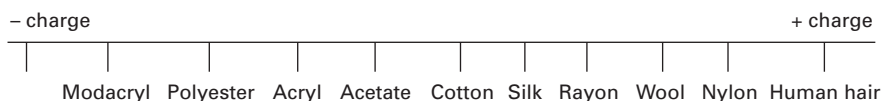
When PVC fiber is exposed to fire, it burns slightly and most of it scorches. However, it extinguishes itself as soon as it is removed from the fire. The limiting oxygen index (LOI) is a highly revealing index of the fire retardant qualities of fibers, and Table 10.4 shows the LOI of various fibers.⁴⁰

PVC fibers do not produce any incandescent droplets that can be dangerous when they come in contact with the skin. Therefore, PVC fiber avoids multiplication of heat sources and flame spreading. PVC fibers are an almost non-hygroscopic fiber, and are readily affected by static electricity. Figure 10.16 shows a triboelectric series of various fibers, in which PVC fiber is negatively charged when rubbed with other fibers.

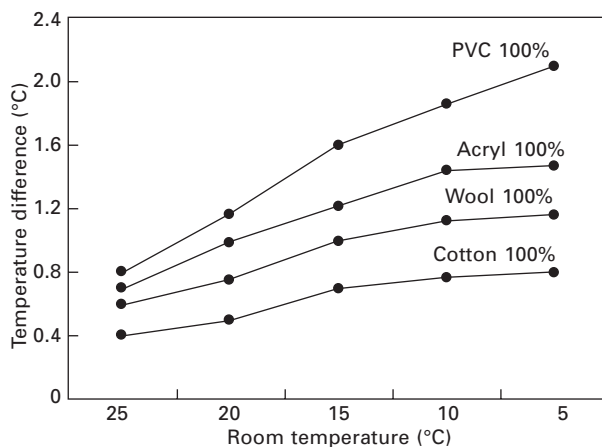
The high electrical insulation of PVC fibers gives them exceptional triboelectrical properties, which make them feel very comfortable when worn as clothing. The negative electrical charge due to textile rubbing against the skin is kept on the surface of the fiber. In contact with skin, the static electricity causes slight vaso-dilatation, which gives the sensation of warmth. Figure 10.17 shows the heat-retaining quality of PVC fibers. PVC is undoubtedly

Table 10.4 LOI of various fibers

Fiber	LOI (%)	Ignition point (°C)
PVC	36	503
Aramid	29–33	471
Modacryl	26–28	315
Wool	25	500
Polyester	21	416
Nylon	21	420
Polypropylene	19	400



10.16 Triboelectric series of various fibers.



10.17 Comparison of the heat-retaining capacity.

superior to wool.⁴¹ Therefore, PVC fiber is the most suitable fiber for use in textiles requiring good heat-retention qualities, such as underwear, blankets and winter wear.

10.4 References

1. Lewin M and Pearce E M, *Handbook of Fiber Science and Technology: Vol. IV, Fiber Chemistry*, New York and Basel, Marcel Dekker, 1983, Chapter 3.
2. Shriver L C and Fremon G H, US Patent 2,420,330, 1947.
3. Latham R C and Houtz R C, US Patent 2,404,714, 1944.
4. Masson J C, *Acrylic Fiber Technology and Applications*, New York, Basel, Hong Kong, Marcel Dekker, 1995, Chapter 4.
5. Mark H F, Atlas S M and Cernia E, *Man-Made Fibers, Science and Technology, Vol. 3*, New York, London, Sydney, Interscience Publishers, 1968, 136–243.
6. Bajaj P and Kumari M S, 'Developments in acrylic fibers: an overview', *Man-Made Textiles in India*, 1987, 211–223.
7. Bajaj P and Kumari M S, 'Modification of acrylic fibers: an overview', *JMS-Rev., Macromol. Chem. Phys.*, 1987, **C27**(2), 181–217.
8. Masson J C, *Acrylic Fiber Technology and Applications*, New York, Basel, Hong Kong, Marcel Dekker, 1995, Chapter 5.
9. East G, McIntyre J and Patel G, *J. Text. Inst.*, 1984, **75**, 196.
10. Baojun Q, Ding P and Zhenqiou W, *Adv. Polym. Technol.*, 1986, **6**, 509.
11. Rende A, *J. Appl. Polym. Sci.*, 1972, **16**, 585.
12. Vaidya A and Gupta D, *Textile Res. J.*, 1989, **59**, 601.
13. Kawanishi K, Komatsu M and Inoue T, *Polymer*, 1987, **28**, 980.
14. Craig J P, Knudsen J P and Holland V F, *Text. Res. J.*, 1962, **32**, 435.
15. Hobson P H and McPeters A L, *Kirk-Othmer Encyclopedia of Science and Technology, Vol 1*, 3rd end, New York, Wiley-Interscience, 1978, 234.
16. Ford J E, *Fiber Data Summaries*, Manchester, Shirley Institute, 1966, 283.
17. Herman W and Haehnel W O, German Patent 450,286, 1924.
18. Herman W and Haehnel W O, German Patent 685,048, 1939.
19. Sakurada I, Lee S and Kawakami H, Japanese Patent 147,958, 1939.
20. Yazawa M, Meguro S, Yazima M and Ozawa T, Japanese Patent 153,812, 1939.
21. Sakurada I, *Polyvinyl Alcohol Fibers*, New York and Basel, Marcel Dekker, 1985, 163–185.
22. Sakurada I and Nukushina Y, *Kobunshi Kagaku*, 1960, **17**, 13.
23. Ashikaga T and Kosaka T, US Patent 3,660,556, 1969.
24. Fujiwara H, Shibayama M, Chen J H and Nomura S, *J. Appl. Polym. Sci.*, 1989, **37**, 1403.
25. Shibayama M, Sato M, Kimura Y, Fujiwara H and Nomura S, *Polymer*, 1988, **29**, 336.
26. Sakurada I, *Polyvinyl Alcohol Fibers*, New York and Basel, Marcel Dekker, 1985, 249–267.
27. Cha W I, Hyon S H and Ikada Y, *J. Polym. Sci., Part B, Polym. Phys.*, 1994, **32**, 297.
28. Fukunishi Y, Akiyama A, Sato T, Sano H and Ohmory A, US Patent 5,238,995, 1993.
29. Nakamura H, *Sen-i Kikai Gakkaishi (Sen-i Kogaku)*, 1972, **25**, 801.

30. Sakuragi I, *Sen-i Gakkaishi*, 2000, **56**, 232.
31. Regnault V, *Ann. Chim. Physique*, 1938, **69**, 51.
32. Rein H and Davidshoefer F, *Chemische Textilfasern Filme und Folien*, ed. R. Pummerer, Stuttgart, Ferdinand Enke Verlag, 1952, 583.
33. Lewin M and Pearce E M, *Handbook of Fiber Science and Technology: Volume IV, Fiber Chemistry*, New York and Basel, Marcel Dekker, 1985, 569.
34. Doty P, *J. Polym. Sci.*, 1946, **1**, 90.
35. Rhone-Poulenc, French Patent 969,363.
36. Moncrieff R W, *Man-Made Fibers*, 6th edn, London and Tonbridge, The Whitefriars Press, 1975, 523.
37. Gächer R R and Müller H, *Plastic Additives*, 2nd edn, Munich, Vienna, New York, Hanser Publishers, 1987, 193.
38. Shinye K, Jenko K and Ryusou S, Japanese Patent 2001-98414, 2001.
39. Isamuchi K, Kou Y, Ikro N and Ichisei Y, Japanese Patent 9-56624, 1997.
40. Rhovyl Sales Group, *Rhovyl Fibres, FT-1*, 2001.
41. Tevion Sales Group, *Technical Information on Teijin 'Tevion' Polyvinylchloride Fiber*, 2004.

The processing, structure and properties of elastomeric fibers

J U OTAIGBE S and A MADBOULY, The University of Southern Mississippi, USA

Abstract: This chapter surveys the recent progress in the science and technology of elastomeric fibers in a number of applications in the textile and allied industry. The chemical structure, fiber formation and the relationship between structure and properties of a few representative examples of technologically important elastomeric fibers such as polyurethane, styrene block copolymers, polyolefin, and elastomeric polymer alloys are described to illustrate the benefits of the science and technology of elastomeric fibers that may provide a basis for future progress in this important technological field.

Key words: elastomeric fibers, Spandex[®], polymer alloy fibers, electrospinning, nanofiber, copolymer fibers, mechanical properties, elastic recovery and extensibility, processing, polyurethanes, textiles and sportswear.

11.1 Introduction

Only a few of the plethora of commercial natural and synthetic polymers can be made into useful fibers. This is because a polymer must meet certain requirements before it can be successfully and efficiently converted into a fibrous product. Some of these important requirements are: (i) the polymer must have long, linear, and flexible chains; (ii) the side groups of the polymer chains should be polar and small in size; (iii) the polymers should be dissolvable in a common organic solvent or meltable for extrusion; and (iv) the polymer chains should be capable of being oriented or crystallized under elongational and shear flow conditions during the extrusion process.

Elastomeric fibers are typically synthetic fibers containing at least 85 wt% of a segmented polyurethane (Oertel, 1994; Rubin, 1990). In general the fibers are characterized by high elastic recovery (up to 99% recovery) and high extensibility (up to 500%), to an extent that depends on their exact chemical composition and fabrication method used to produce them. Unlike rubber fibers that are produced as monofilaments, these relatively thin elastomeric fibers are used in modern style and high comfort clothing. Elastomeric fibers were first produced commercially in 1930 by DuPont Company and marketed under the tradename of Spandex[®] (or Elastane[®]). Current producers of elastomeric fibers include RadicGroup (RadicSpandexTM), Dow Plastics Co. (Pellathane[®]), Hysoung Company (Creora[®]), and DuPont Company

(Lycra[®] Spandex). The special properties of elastomeric fibers include superior oxidation resistance, excellent resistance to dry-cleaning solvents, good dyeability, excellent retention of properties after exposure to ultraviolet light, excellent resistance to body oils, and excellent toughness that avoids the need for fiber protection during knitting. In a number of elastic textile applications, these characteristics of modern elastomeric fibers make them the materials of choice in elastic textile applications, replacing rubber fibers and creating new markets such as active sportswear, medical textile, and comfort stretch garments. As will be described later in this chapter, it is worthy to note that the characteristic properties of elastomeric fibers can be tailored to specific applications by varying the chemical composition, the polymerization and fiber production method used.

Recent advancements in production techniques have spurred new and successful uses in manufacturing textile products for a number of functional application areas. As already mentioned elastomeric fibers can be elongated for more than 100% regardless of any crimp, and when stretched and released, retract quickly and forcibly to substantially their original length. The fibers are either composed of homopolymers, such as polybutadiene and polyisoprene, or made by copolymerizing two or more monomers, using either block or graft polymerization techniques. Typically, one of the monomers forms the hard or crystalline segment that functions as a thermally stable component which softens and flows under shear, as opposed to the chemical crosslinks between polymeric chains in a conventional, thermosetting rubber. The other monomer forms the soft or amorphous segment that contributes the rubbery characteristic. The fiber properties can be controlled by varying the ratio of the monomers and the lengths of the hard and soft segments. Block copolymerization techniques are used to create long-chain molecules that have various sequences or block copolymers of hard and soft segments while graft polymerization methods involve grafting one polymer chain to another as branches. The grafting techniques just mentioned offer more possibilities to varying the resulting copolymer composition and properties because both the backbone monomer and the grafted branches can be made to be rubbery, glassy (i.e., hard), or some relative composition of both.

There are four traditional thermoplastic elastomer types that can be used to produce elastomeric fibers, i.e., polyurethanes, polyester copolymers, styrene copolymers, and the olefinics. Mechanical properties of fibers produced from the first two types are generally better than those of the last two. Recent thermoplastic elastomers used in fiber manufacture may be divided into two classes of high-performance materials, namely thermoplastic polyamide (nylon) elastomers and elastomeric alloys. The latter consists of polymer alloys of an olefinic resin and rubber while the polyamide thermoplastic elastomers are low-density, high-elongation materials with good solvent and abrasion resistance. Although elastomeric alloys are based on olefins,

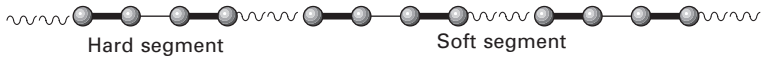
their proprietary manufacturing methods give them better properties than conventional thermoplastic olefins.

To illustrate the science and technology of elastomeric fibers that may provide a basis for future progress in this important technological field, the chemical structure, fiber formation and the relationship between structure and properties of a few representative examples of elastomeric fibers such as polyurethane, styrene block copolymers, polyolefin, and elastomeric polymer alloys are described in the following sections of this chapter. Because of space limitations, a number of published papers and monographs in this field have been omitted but the interested reader might find them in the references of the cited bibliography.

11.2 Polyurethane fibers

As already mentioned, polyurethane fiber (Spandex[®] or Elastane[®]) is a synthetic fiber known for its exceptional elasticity (or stretchability). Spandex[®] is stronger, lighter, and more versatile and durable than rubber. In fact, Spandex[®] fibers can be stretched to almost 500% of their length. The Spandex[®] fiber technology was invented in 1959, and when first introduced it revolutionized many areas of the clothing industry and found a number of important replacement applications for rubbers previously used in many applications. Spandex[®] is the preferred trade name in North America, while Elastane[®] is most often used elsewhere. Two well-known trademarks for Spandex[®] or Elastane[®] are Invista's brand names Lycra[®] and Elasthan[®]. Spandex[®] fiber is round in cross-section, thus offering extra elasticity and good elongation. The material has superior resistance to degradation caused by sunlight, perspiration and chlorine, making it ideal for various kinds of active wear and swimwear.

The special elastic property and wide industrial application of Spandex[®] fibers is a direct result of the material's polyurethane (PU) chemical structure that is a multiblock copolymer comprising alternating soft polyester or polyether and hard polyurethane–urea segments. These two segments undergo microphase separation into hard and soft phases, respectively, below and above their glass transition temperatures. This microphase separation is responsible for the excellent elastomeric properties of PU. By varying the structure, the molecular weight of the segments, and the ratio of the soft to the hard segments, a broad range of physical properties can be obtained. The materials can be hard and brittle, soft and tacky, or anywhere in between. Figure 11.1 depicts schematically the structure of PU elastomer as multiblock hard segments (urethane) and soft segments (polyester or polyether diol). The TEM shows how these two segments can phase-separate into nanoscale morphology. The very small dark particles in the micrograph are the hard segments and the bright matrix is the soft segments (Madbouly *et al.*, 2007).

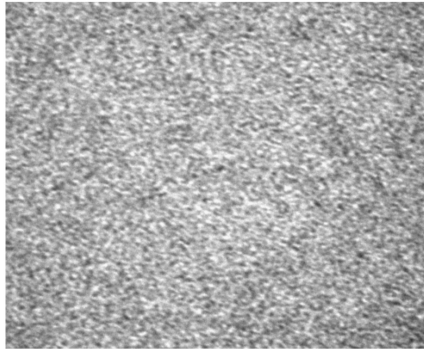


~~~~~ = Long chain diol (high molecular weight)

———— = Diisocyanate

——— = Short chain diol (low molecular weight)

● = Urethane group



100 nm

**11.1** Schematic diagram of the hard and soft segments of PU structure. The TEM shows microphase separation morphology for the hard segments (dark particles) and polyester soft segments (bright matrix). Adapted from Madbouly *et al.*, 2007.

Various types of diisocyanates can be used to synthesize PU (Madbouly and Otaigbe, 2009). The diisocyanates can be either aromatic or aliphatic with different chemical reactivities. The aromatic diisocyanates are more reactive than aliphatic ones, which can only be used if their reactivities match the specific polymer reaction and special properties desired in the final product. For example, polyurethane fibers made from aliphatic isocyanates are stable to light (Oertel, 1994; Szycher *et al.*, 1983; Schollenberger and Stewart, 1972; Brauman *et al.*, 1981), while fibers made from an aromatic isocyanate will undergo photo-degradation (Schollenberger *et al.*, 1958; Adams and Anderson, 1950; Hepburn, 1992).

The soft segments used in polyurethane elastomers are typically dihydroxy terminated long chain macroglycols with low molecular weight ( $M_w = 500\text{--}5000\text{ g/mol}$ ) such as polyethers, polyesters, polydienes and polyolefins. Polyester-based urethanes have relatively good material properties but are susceptible to hydrolytic cleavage of the ester linkage, while polyether-

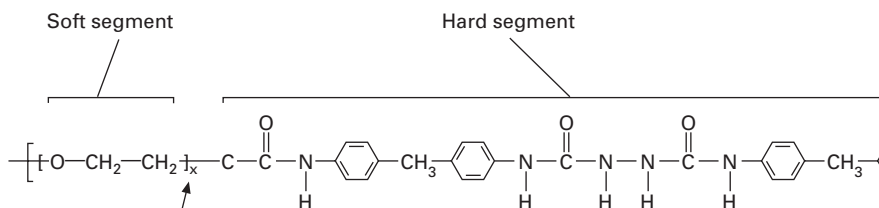
based urethanes have relatively high resistance to hydrolytic chain scission. Caprolactones offer a good compromise between the polyether and polyester types. Polyethylene oxide (PEO)-based urethanes exhibit poor water resistance due to the hydrophilic nature of the ethylene oxide. Polypropylene oxide (PPO) has also been widely used because of its low cost and reasonable hydrolytic stability (Frisch and Dieter, 1975). Abrasion resistance of the urethanes is outstanding among elastomers, low-temperature flexibility is good, oil resistance is excellent up to approximately 82°C, and load-bearing capability ranks with the best of the elastomers. Additives can be used to improve dimensional stability (or heat resistance), reduce friction, or increase flame retardancy and fungus resistance (or weatherability).

The low molecular weight diol and diamine chain extenders play a very important role in polyurethanes properties and applications. Without a chain extender, a polyurethane formed by directly reacting diisocyanate and polyol generally has very poor physical properties and often does not exhibit microphase separation. Thus, the introduction of a chain extender can increase the hard segment length to permit hard-segment segregation, resulting in excellent mechanical properties such as an increase in the modulus and an increase in the hard-segment glass transition temperature ( $T_g$ ) of the polymer fiber. Polyurethane chain extenders can be categorized into two classes: aromatic diol and diamine, and the corresponding aliphatic diol and diamine. In general, polyurethanes that are chain-extended with an aliphatic diol or diamine produce softer materials than do their aromatic chain-extended counterparts (Dieterich *et al.*, 1993). The chemical structure of Spandex<sup>®</sup> is very complicated because it has both urea and urethane linkages in the backbone of the main chain, as depicted in Structure 11.1.

## 11.3 Production of polyurethane fibers

### 11.3.1 Solution dry spinning method

Spandex<sup>®</sup> fibers are traditionally produced using four different methods, namely: (i) melt extrusion, (ii) reaction spinning, (iii) solution dry spinning, and (iv) solution wet spinning. The first step of these four methods involves

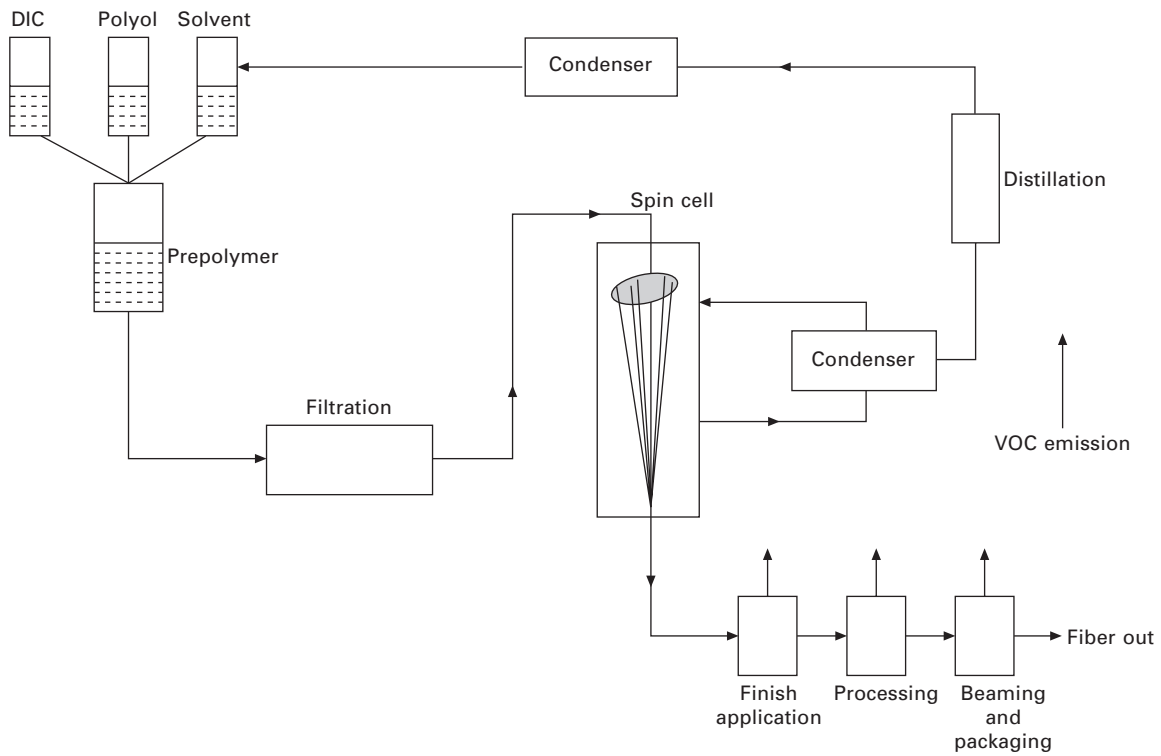


Structure 11.1 Chemical structure of spandex<sup>®</sup>.

the chemical reaction of the monomers to produce a prepolymer. The resulting prepolymer undergoes further reaction in various ways, and is subsequently drawn out to produce a long fiber. Solution dry spinning is used to produce the main industrial products of Spandex<sup>®</sup> (i.e. up to 90% of the world's Spandex<sup>®</sup> fibers are dry-spun from solution). Figure 11.2 shows a schematic diagram for the solution dry spinning method. In this method the production of the prepolymer is done initially by mixing polyol with a diisocyanate (DIC) monomer. The reactants are mixed in a reaction vessel and under the right conditions they react to form a prepolymer. Because the ratio of the component materials produces fibers with varying characteristics, it is strictly controlled. A typical ratio of polyol to diisocyanate may be 1:2. The prepolymer is further reacted with an equal amount of diamine to increase the molecular weight in a chain extension step as already mentioned. The resulting solution is diluted with a solvent to produce the spinning solution. The solvent (e.g. THF) helps to make the solution thinner and more easily handled so that it can then be pumped into the fiber production cell. The spinning solution is pumped into a cylindrical spinning cell where it is cured and subsequently converted into fibers. In this cell, the polymer solution is forced through a metal plate with small holes called a spinneret. This production step causes the solution to be aligned into strands of liquid polymer. As the strands pass through the cell, they are heated in the presence of nitrogen and solvent gas, making the liquid polymer to chemically react and form solid strands. Specific amount of the solid strands are bundled together as the fibers exit the cell to produce the desired thickness. A compressed air device is normally used to twist the fibers together. Each fiber of Spandex<sup>®</sup> is made up of many small individual fibers that adhere to one another due to the natural stickiness of their surfaces. The fibers are then treated with a finishing agent such as magnesium stearate or another polymer such as poly(dimethyl siloxane). These finishing materials prevent the fibers from sticking together, an important and desirable requirement in textile manufacture. After this treatment, the fibers are passed through a series of rollers onto a spool or bobbin.

### 11.3.2 Electrospinning method

The polyurethane (PU) fibers can also be produced via the electrospinning process (Predicini and Farris, 2003). This method has been known since 1934. In this method fiber properties depend on electric field uniformity, polymer viscosity, electric field strength and distance between the nozzle and collector. The idea of the electrospinning process is based on an external electric field applied to charged polymer fluids or melts. This external electric field leads to electric charges on the polymer surface that overcome the surface tension, and consequently a jet is produced. This electrical force can also lead to a very thin jet as it travels. In the case of polymer fluid, the common organic

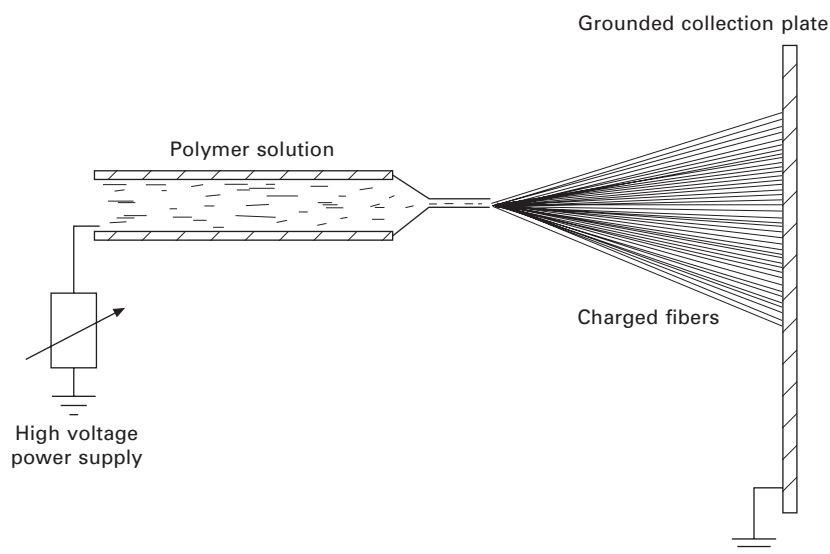


11.2 Schematic diagram of solution dry spinning process.



solvent is evaporated extremely fast (millisecond timescale) to produce electrically charged nanofibers. The technique is valid only for charged polymer solutions or melts with sufficient molecular entanglements. In the electrospinning process, a charged droplet of solution suspended at the end of a capillary deforms into a conical shape, or Taylor cone, when subjected to a Coulombic force (Taylor, 1969). The Taylor cone is formed due to a balancing of the repulsive nature of the charge distribution on the droplet's surface and the surface tension of the liquid (Reneker *et al.*, 2000). As the charge is increased above a critical voltage, a stable jet is discharged from the tip of the Taylor cone. A jet of low molecular weight fluid breaks up into small droplets, a phenomenon termed electrospraying, while a polymer solution with sufficient chain overlap and entanglements does not break up but undergoes the so-called bending instability that causes a whiplike motion between the capillary tip and the grounded target (Hohman *et al.*, 2001). The instabilities of the electrically forced jet in the electrospinning technique have been studied (Shin *et al.*, 2001). One theoretical model for interpreting the relationship between bending instability, electric field, and solution flow rate has been reported (Shin *et al.*, 2001). It is this bending instability that accounts for the high degree of single fiber drawing, resulting in submicrometer-sized fibers.

Figure 11.3 shows a schematic diagram of the electrospinning process. The resulting electrospun nonwoven fiber mats have a high specific surface area,

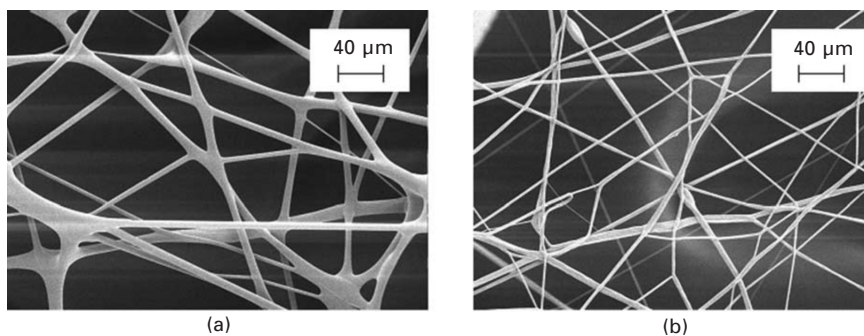


11.3 Schematic diagram of electrospinning process. Adapted from Hao and Zhang, 2007.

high porosity, and small pore size. This process normally produces fiber with diameters of nanometers to submicrometers. Fibers with ranges of diameters less than 1000 nm are very difficult to obtain from other conventional fiber production techniques. The nanofibers obtained by the electrospinning process can be used for many applications such as filtration devices, membranes, optics, vascular grafts, protective clothing, molecular templates, and tissue scaffolds (Bhattacharai *et al.*, 2004; Kim *et al.*; 2004; Ma *et al.*, 2005).

The morphology of PU fibers strongly depends on the chemical structure, the molecular weight and the percentage of hard and soft segments. Linear and branched PU will produce different fiber morphologies. For example, linear PU ( $M_w = 42\,000$  g/mol and  $M_w/M_n = 1.56$ ) based on poly(tetramethylene oxide) polyester (soft segment) with 2000 g/mol and 35 wt% hard segment produces fibers with average diameters of  $5.5 \pm 1.8$   $\mu\text{m}$  (Figure 11.4a). In contrast, a highly branched PU fiber ( $M_w = 91\,900$  g/mol and  $M_w/M_n = 5.78$ ) based on poly(tetramethylene oxide) polyester (soft segment) with 2000 g/mol and 30 wt% hard segment produces fibers with average diameters of  $4.0 \pm 1.5$   $\mu\text{m}$  as shown in Figure 11.4b. The two types of PU fibers shown in Fig. 11.4 were obtained using the electrospinning method at 20 kV, 10 ml/h volumetric flow rate, and 20 cm from the syringe needle to the collecting target (McKee *et al.*, 2005). Although there is a significant change in the morphology of the two samples, both of them can be used to obtain nonwoven fiber mat of approximately  $10 \times 10$   $\text{cm}^2$  without any bead defects (McKee *et al.*, 2005).

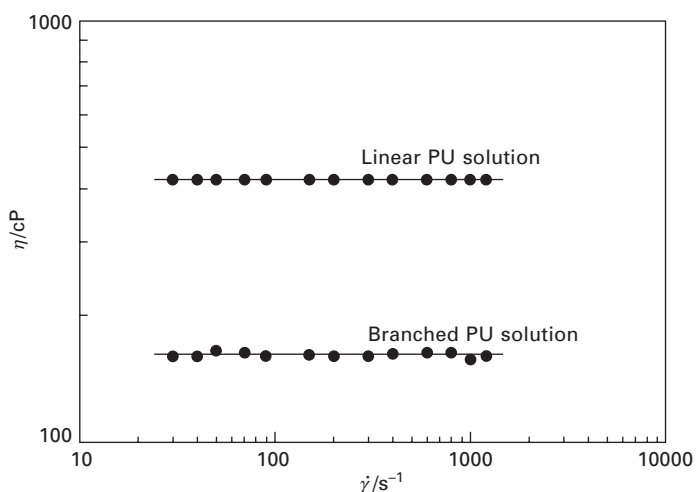
The rheological behavior of the linear and branched PU fiber solutions in THF (10 wt% PU) is considerably different. Although the viscosities of the solutions of the two different fibers show Newtonian behavior over the entire range of shear flow, the zero-shear viscosity of the linear PU ( $M_w = 42\,000$  g/mol) solution is more than twice that of the branched one ( $M_w =$



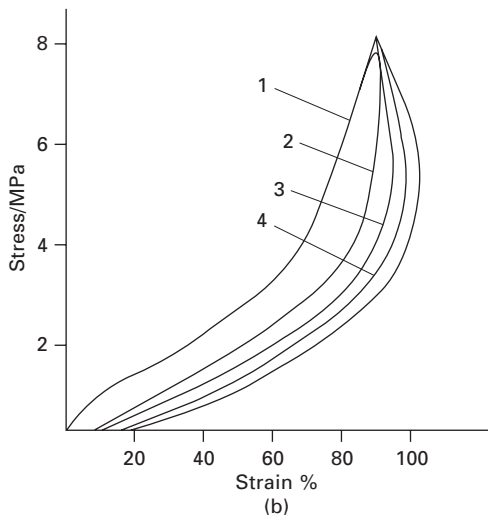
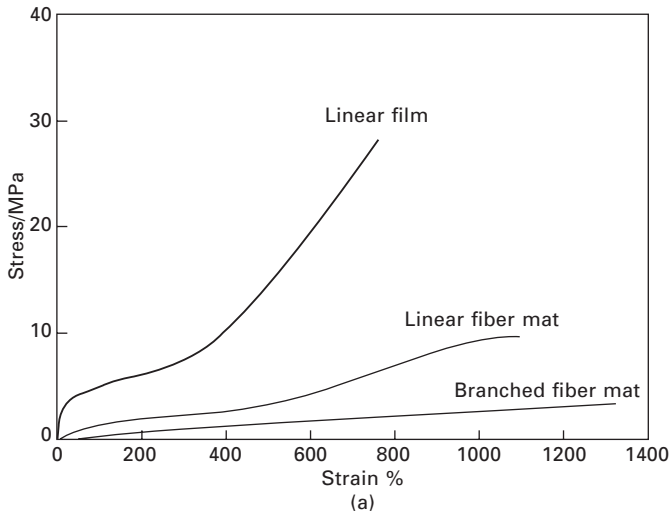
11.4 FESEM (field emission scanning electron microscopy) images of electrospun (a) linear poly(urethane urea) and (b) highly branched poly(urethane urea) fibers described in the text. Adapted from McKee *et al.*, 2005.

91 900 g/mol) (i.e. 420 and 160 cP, respectively) as clearly shown in Fig. 11.5. The lower value of zero-shear viscosity of the branched PU fiber solution is attributed to the fact that the branched polymer chain has small hydrodynamic volume compared to that of the linear PU fiber solution (McKee *et al.*, 2005).

The tensile stress–strain properties of the two fibers just described are compared with that of linear PU films in Fig. 11.11a. The measurements were made according to ASTM D 3368 using an Instron<sup>®</sup> tensile tester operating at a crosshead displacement rate of 15 mm/min (McKee *et al.*, 2005). Clearly, Fig. 11.6 show that different mechanical properties can be obtained for the three different samples (i.e., the branched PU fibers shows the highest degree of elongation at break compared to that of the linear PU fibers and film). The branched PU fibers can be elongated up to 1300% strain at break, while the linear fiber and film reached 970% and 830% strain at break, respectively. The high value of elongation of the electrospun fibers is related to the increased tear resistance of the fiber mats compared to that of the neat PU film. The interconnected network of the electrospun fibers hinders tear propagation, resulting in higher elongation prior to break (McKee *et al.*, 2005). It is also clear that the microporous character of the electrospun fibers is a direct reason for the very low Young's modulus of the electrospun fibers (i.e., 1 and 4 MPa for branched and linear PU fibers, respectively) compared to that of the linear PU film (17 MPa).



11.5 Shear rate dependence of viscosity for linear polyurethane and highly branched polyurethane solutions. Modified from McKee *et al.*, 2005.

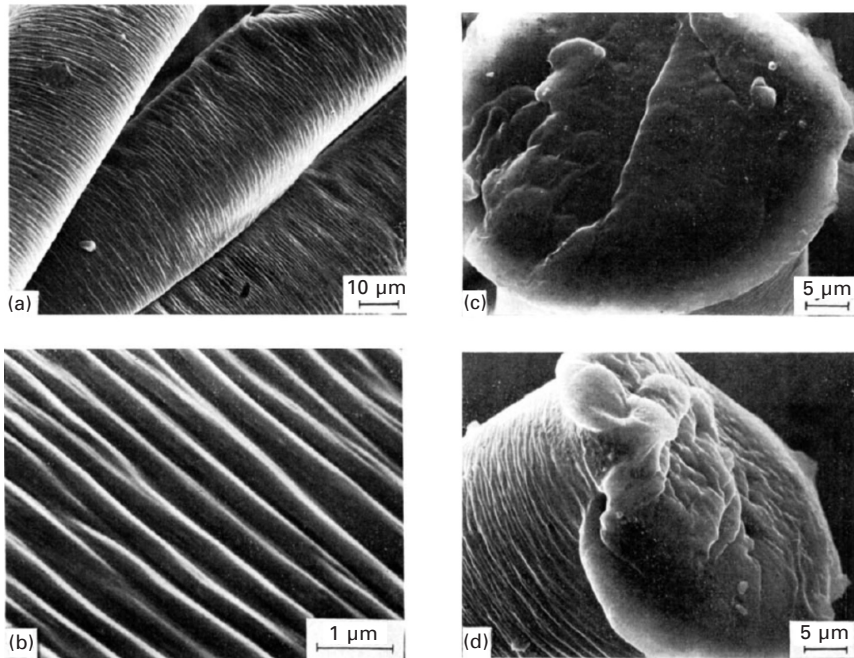


11.6 (a) Stress–strain curves for linear, highly branched polyurethane fibers and linear polyurethane film. Modified from McKee *et al.*, 2005. (b) The hysteresis behavior for PU elastomeric yarn. Modified from Blazhaitis *et al.*, 1970.

The hysteresis or extension and recovery characterization of polyurethane elastomeric yarn was investigated by Blazhaitis *et al.* (1970) as shown in Fig. 11.6b. The hysteresis loop of the fifth cycle (curves 3 and 4) shows that the losses are very small. The performance loss of high-elastic yarn in the recovery after extension are considerable in the first 3–4 cycles, after which the loss becomes stable and less marked.

## 11.4 Polyester copolymer fibers

The poly(ether ester) (PEE) fiber is one of the most important materials that can be used for a number of potential applications. Poly(ether ester) is multiblock (or segmented-block) copolymers of the (AB) type comprising semicrystalline polyester (hard) segments and noncrystalline polyether (soft) segments. Their excellent characteristics as thermoplastic elastomers as well as their morphology are well studied, particularly in the case of PEE based on poly(butylene terephthalate) (PBT) and poly(tetramethylene oxide). Fiber formation from the melt of a copolymer based on PBT and PEG 1000 was studied by Gogeva *et al.* (1990). The characteristics of the starting polymer, the processing conditions and the properties of the final fibers were considered (Gogeva *et al.*, 1990). The surface of the fiber was investigated by SEM as shown in Fig. 11.7. The processing of this fiber from the melt was carried out at a spun rate of 800 m/min and stretching of approximately 3.64 times at a rate of 1195 m/min at 80°C. Clearly, a regular structure with a period of about 390 nm is observed perpendicular to the fiber axis (Figs 11.7a and



11.7 TEM micrographs of the surface of a poly(ether ester) fiber (66 wt% PBT): (a) and (b) as-stretched (spun at 800 m/min and stretched 3.64 times at a rate of 1195 m/min and 80°C); (c) and (d) fracture surface as obtained from the tenacity measurements. Adapted from Gogeva *et al.*, 1990.

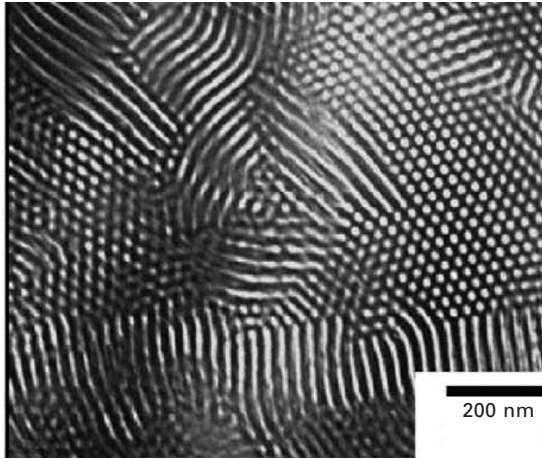
11.7b). The fracture surface of the fiber (Figs 11.7c and 11.7d) confirms the elastic nature of the copolymer.

## 11.5 Styrene copolymers elastomeric fibers

The styrenics are the lowest-priced thermoplastic elastomers. They are block copolymers produced with hard polystyrene segments interconnected with soft segments of a matrix such as polybutadiene, polyisoprene, ethylene-propylene, or ethylene-butylene. These elastomers are commercially available from Shell (Kraton<sup>®</sup>) in several molding and extrusion grades ranging in hardness from 28 to 95 Shore A. The tensile strength of these materials is lower, the elongation is higher than that of styrene-butadiene-rubber (SBR) or natural rubber, and the weather resistance is about the same. The weather resistance characteristics can be improved by the addition of resins such as polypropylene or ethylene-vinyl acetate. The styrenic elastoplastics resist water, alcohols, and dilute alkalis and acids. They are soluble in, or are swelled by, strong acids, chlorinated solvents, esters, and ketones. They also have excellent low-temperature flexibility down to  $-85^{\circ}\text{C}$  ( $-120^{\circ}\text{F}$ ).

### 11.5.1 Styrene-butadiene-styrene (SBS) triblock copolymer fiber

SBS triblock copolymer is a typical microphase-separated thermoplastic elastomer. When the polystyrene concentration is relatively low, the domains are spherical; with increasing concentration, the domains become cylindrical and then lamellar (or plate-like). Such well-developed morphology requires careful sample preparation. In general, the morphology is irregular and its degree of complexity depends on the thermal and mechanical history of the preparation, as well as the interactions between each block (Helfand and Wasserman, 1976). Thermodynamic theories reported by Leibler (1980) and Matsen and Schick (1994) explain miscibility of block copolymers and the resultant morphologies. The rubbery butadiene chains interconnect glass polystyrene domains which act as reinforcing fillers or physical crosslinks. A typical TEM of SBS film morphology is shown in Fig. 11.8 (Yang *et al.*, 2006). Note that solution casting from toluene was used to obtain the SBS film depicted in Fig. 11.8. The polybutadiene (PB) domains can be selectively stained by  $\text{OsO}_4$  vapor; the bright and dark regions in the TEM micrograph represent the PS and PB domains, respectively. Cylindrical SBS morphology can be clearly seen in Fig. 11.8. This morphology can be easily modified not only by varying the concentration of the blocks but also by controlling the processing conditions such as type of solvents used for casting films, method of extrusion, annealing temperatures, and blending with suitable homopolymers (Gohil, 1986). A difference in the interaction between blocks



11.8 TEM photograph for SBS triblock copolymer. Modified from Yang *et al.*, 2006.

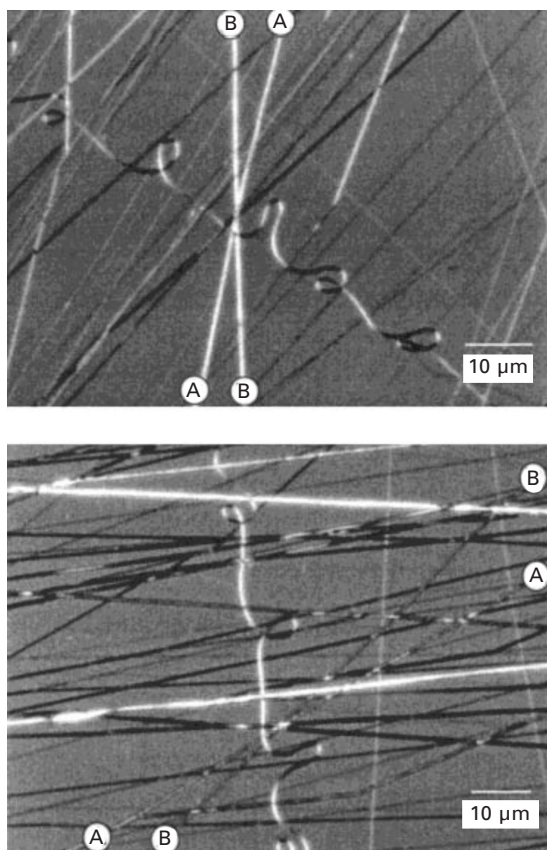
of a polymer ultimately affects its morphology. This is evident from the morphological changes in block copolymer films prepared from solvents having different solvent powers (Gohil, 1986).

Fong and Reneker (1999) produced SBS electrospun fiber (Kraton D1101, 31 wt% PS with  $M_w$  and  $M_w/M_n$  151 000 g/mol and 1.12, respectively) from a mixture of 75 wt% tetrahydrofuran and 25 wt% dimethylformamide with 14 wt% polymer concentration. Tetrahydrofuran is a good solvent for both polystyrene and polybutadiene blocks, and the addition of 25% dimethylformamide improves the stability of the electrospinning jet. The electrospinning apparatus used by Fong and Reneker had a high-voltage power supply (160  $\mu$ A at 30 kV). They applied positive high voltage through a copper wire to the SBS solution inside a glass pipette and placed a grounded copper sheet 30 cm below the tip of the glass pipette. Several glass microscope slides covered by films of evaporated graphite were placed on the copper sheet. The pipette was tilted a few degrees from the horizontal so that surface tension maintained a small droplet of the solution at the tip without dripping. As the electrical potential was gradually increased to 24 kV, a jet was created. The jet, formed by electrical forces, followed a complicated stretching and looping trajectory as it dried and solidified. The resulting electrically charged nanofibers were collected on films of graphite for electron microscopy, or on a rotating drum covered with aluminum foil to produce a nonwoven elastomeric fabric. The mass flow rate of the polymer solution, carried by the jet, was around 50 mg/min (Fong and Reneker, 1999).

Typically, diameters of SBS electrospun nanofibers are about 100 nm. The aligned SBS nanofibers can be elongated to more than three times

their original lengths without breaking. Figure 11.9 shows SBS nanofibers as the sample was observed between crossed polarizers, and then rotated. In the upper picture, fibers A–A and B–B are bright. Turning the sample clockwise by about  $45^\circ$  causes these nanofibers to become dark, as shown in the bottom picture. The bright and dark segments in the looped nanofiber move along the loops and remain approximately parallel to each other as the sample is rotated. These observations show that the electrospun nanofibers are birefringent. Both the elongational flow (Mackley and Keller, 1975; Perkins *et al.*, 1997) and the rubberlike strain of the molecular network may contribute to the birefringence of Fig. 11.9.

In addition to the smooth nanofibers, very thin nanofibers with small beads are sometimes obtained in practice. Beads form, while the jet is still fluid, if the force that tends to extend the nanofiber is reduced, for example by the



11.9 The birefringence of electrospun SBS fibers. Adapted from Fong and Reneker, 1999.

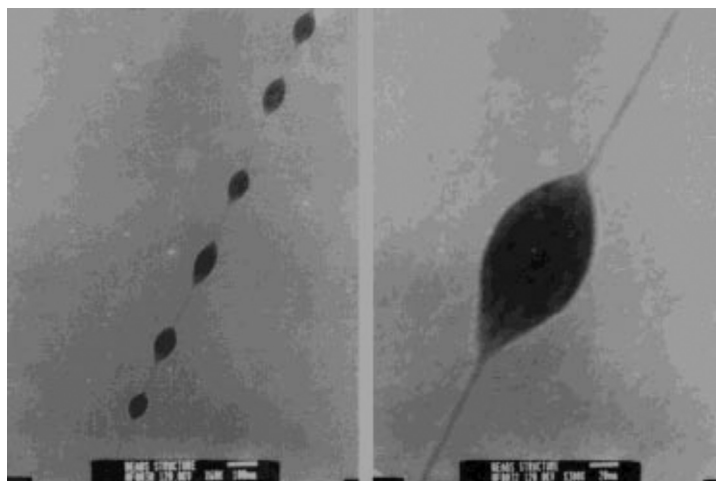


neutralization of the excess charge on the fibers with ions created in air by a corona discharge. Surface tension in the small fiber creates a pressure that forces the solution into the beads (Fong and Reneker, 1999; Yarin, 1993). An electron micrograph of an example of a beaded fiber reported by Fong and Reneker is shown in Fig. 11.10. This figure shows beads with diameters of about 60 nm that were elongated in the direction of the fiber axis. The distance between the beads is around 100 nm.

## 11.6 Polyolefin elastomeric fibers

The market for polyolefins manufactured with metallocene technology is growing exponentially as they are increasingly meeting commercial expectations. The continued success of the polyolefins is due to producers positioning themselves for success through consolidation and the introduction of new products. Metallocene-catalyzed polymers represent a significant advance in polymer synthesis and production. Unlike other catalyzed polymers, the structure and molecular weight of metallocene-catalyzed polymers are relatively easy to control. These characteristics enable production of precisely structured polymers in large, regulated amounts. Global demand for metallocene-based polyolefins was several billion pounds in 2000, according to a new study by Houston-based Chemical Market Resources Inc. (CMR). North America and Europe accounts for 47% (or 1075 million pounds) and 25% (or 579 million pounds) of that demand, respectively.

Thermoplastic olefin (TPO) elastomers are available in several grades,

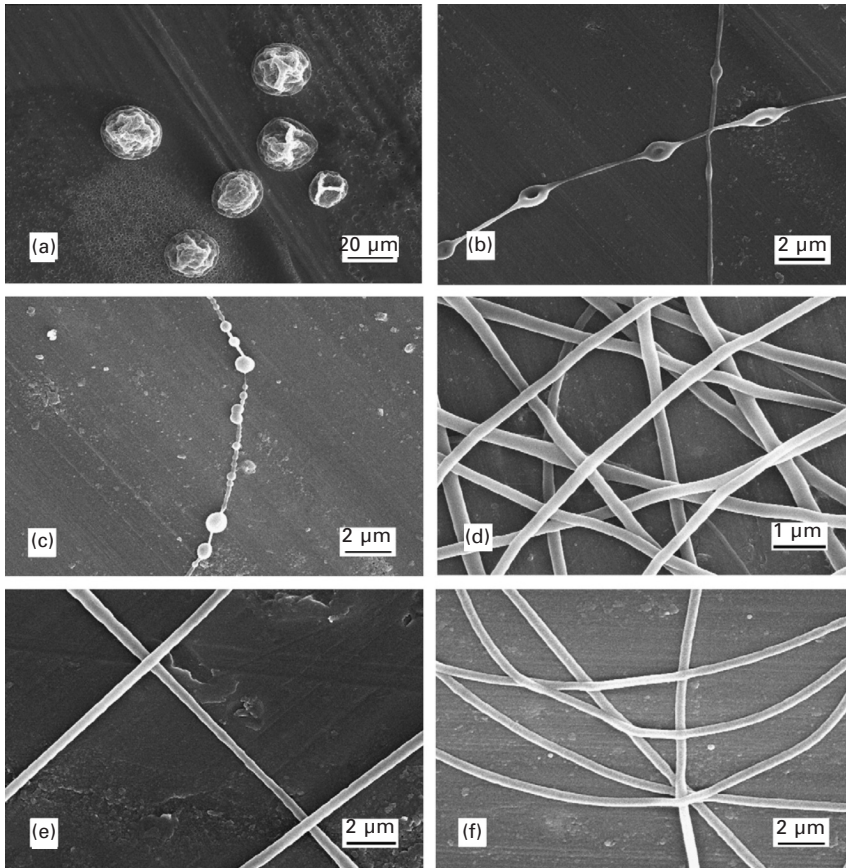


11.10 Beaded nanofiber of SBS copolymer, stained with osmium tetroxide. Adapted from Fong and Reneker, 1999.

having room-temperature hardnesses ranging from 60 Shore A to 60 Shore D. These polyolefin-based materials have the lowest specific gravities of all thermoplastic elastomers. They are uncured or have low levels of crosslinking. Material cost is mid-range among the elastoplastics. These elastomers remain flexible down to  $-50^{\circ}\text{C}$  and are not brittle at approximately  $-70^{\circ}\text{C}$ . They are autoclaveable and can be used at service temperatures as high as  $135^{\circ}\text{C}$  in air. The TPOs have good resistance to some acids, most bases, and many organic materials such as butyl alcohol, ethyl acetate, formaldehyde, and nitrobenzene. They are attacked by chlorinated hydrocarbon solvents.

### 11.6.1 Polybutadiene elastomeric fibers

Polybutadiene was one of the first types of synthetic elastomer, or rubber, to be invented. It is good for uses that require exposure to low temperatures. Tire threads are often made of polybutadiene copolymers. Belts, hoses, gaskets and other automobile parts are made from polybutadiene because it can withstand cold temperatures better than other elastomers. Syndiotactic 1,2-polybutadiene (*s*-PB) elastomeric fibers produced using an electrospinning technique from dichloromethane solutions ( $\text{CH}_2\text{Cl}_2$ ) have been recently reported (Hao and Zhang, 2007). Dichloromethane is the best common solvent which can be used to produce nanofibers of *s*-PB via the electrospinning technique. The other solvents have very poor fiber-forming ability. The effects of processing variables (including applied voltage, tip to target distance, and feed rate of the solution to the capillary tip) and solution properties (solvent, viscosity, concentration, conductivity, surface tension, etc.) on electrospun fiber morphology have been extensively investigated in the literature for a variety of polymeric systems (Reneker and Chun, 1996; Megelski *et al.*, 2002; Lee *et al.*, 2002). It has been shown for a number of polymer/solvent systems that increasing the solution concentration or viscosity decreases the number of bead defects and increases the overall fiber diameter of the electrospun fibers (Zong *et al.*, 2002a). Moreover, researchers have electrospun polymer solutions with varying concentrations and viscosities to yield fibers with various structures and textures (Zong *et al.*, 2002b; Jun *et al.*, 2003). Figure 11.11 depicts the SEM morphologies of *s*-PB nano-elastomeric fibers obtained from electrospinning of different concentrations of *s*-PB in  $\text{CH}_2\text{Cl}_2$  (Hao and Zhang, 2007). Clearly, the figure shows that the concentration of *s*-PB in  $\text{CH}_2\text{Cl}_2$  can significantly affect the morphology and fiber formation. When the concentration of *s*-PB is  $\leq 3$  wt% no good fibers can be produced. For 1 wt% *s*-PB, half spheres with porous structure about 15 nm in diameter can be clearly seen in Fig. 11.11a. Morphologies like fiber-beads have been observed for 2 and 3 wt% *s*-PB samples. Typical *s*-PB elastomeric fibers can be seen for  $\geq 4$  wt% *s*-PB in Figs 11.11d–f.



11.11 Electroprocessed structures from: (a) 1 wt%, (b) 2 wt%, (c) 3 wt%, (d) 4 wt%, (e) 5 wt%, and (f) 6 wt% s-PB in dichloromethane. Adapted from Hao and Zhang, 2007.

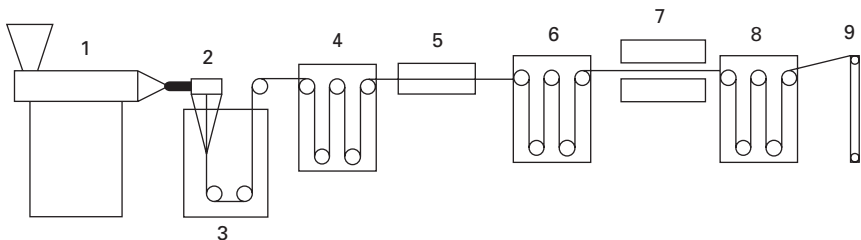
## 11.7 Elastomeric polymer alloy fibers

This class of thermoplastic elastomers consists of mixtures of two or more polymers that have received a proprietary treatment to give them properties significantly superior to those of simple blends of the same constituents. The two types of commercial elastomeric alloys are melt-processible rubbers (MPRs) and thermoplastic vulcanizates (TPVs). MPRs have a single phase while TPVs have two phases. Thermoplastic vulcanizates are essentially a fine dispersion of highly vulcanized rubber in a continuous phase of a polyolefin. Critical to the properties of a TPV are the degree of vulcanization of the rubber and the quality of its dispersion. The crosslinking and fine dispersion of the rubber phase give a TPV with high tensile strength (7.58–26.89 MPa), high elongation (375–600%), resistance to compression and tension set, oil

resistance, and resistance to flex fatigue. TPVs have excellent resistance to attack by polar fluids, fair-to-good resistance to hydrocarbon fluids, and a maximum service temperature of 135°C (275°F). Elastomeric alloys are available in the 55A to 50D hardness range and with ultimate tensile strengths ranging from 5.5 to 27.5 MPa. The specific gravity of MPRs and TPVs respectively ranges from 1.2 to 1.3 and from 0.9 to 1.0. Commercial applications of elastomeric alloys include automotive protective boots, hose covering, electrical insulation, seals, gaskets, medical tubing and syringe plungers, architectural glazing seals, and roofing sheet. Fibers from these materials are described in the following two sections.

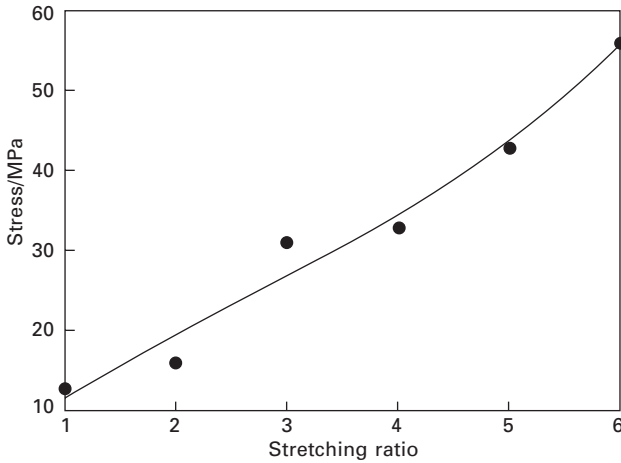
### 11.7.1 Olefinic/EPDM alloy fiber alloy

Commercial olefin-based thermoplastic elastomers obtained by dynamic vulcanization with EPDM rubber (density 0.94 g/cm<sup>3</sup>, hardness 40D) has been used to produce monofilaments through the traditional melt spinning extrusion technique (Spiridonov *et al.*, 2005). The elementary steps for producing elastomeric fibers from this material are depicted in Fig. 11.12 with the following descriptions: (1) an extruder with a constant value of compression ratio is used to melt the elastomeric belts; (2) one or more spinning gear pumps receive the molten polymer and send it through the spinning pack to homogenize the product; (3) quenching of the extruded filaments into a cooling water tank; (4) stretching the fibers through the rollers sets; (5) immersing the fibers in a hot water bath; (6) stretching the fibers again; (7) relaxation of the fibers; (8) stretching again; and (9) winding of the fibers through the winding machine. Extrusion dies of 10 and 16 mm in diameter are typically used for this process. The stretching ratio is set from 2:1 to 7:1. The fibers with a stretching ratio 1:1 are obtained without a stretching step right after the cooling tank. The monofilament diameters obtained from this process typically range from 2 to 5 mm.

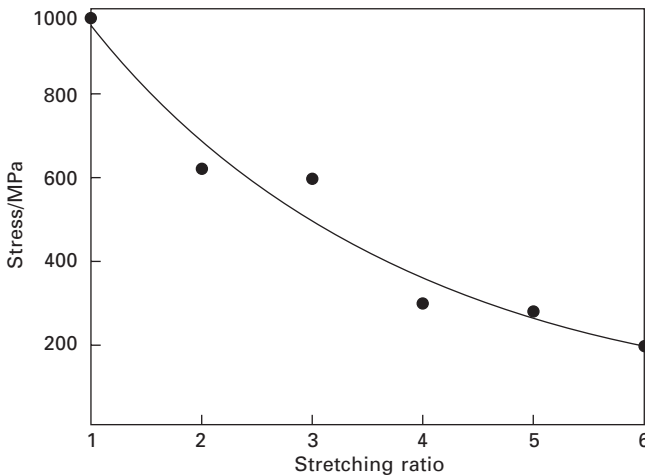


11.12 Melt spinning extrusion process: 1 extruder, 2 spinneret, 3 cooling water tank, 4 first stretching zone, 5 hot water bath, 6 second stretching zone, 7 relaxation zone (heater), 8 third stretching zone, 9 winding device. Modified from Spiridonov *et al.*, 2005.

Figure 11.13 illustrates the stretching ratio dependence of stress at break for olefinic/EPDM elastomeric fiber alloy. Obviously, the stress increases exponentially with increasing value of stretching ratio. However, the percent elongation decreases strongly with increasing stretching ratio as shown in Fig. 11.14. This behavior is related to the orientation of the polymeric chains of the fiber parallel to the stretching force (Roff and Scott, 1971; Fried, 1995). When the fibers are stretched the polymeric chains are oriented partially and

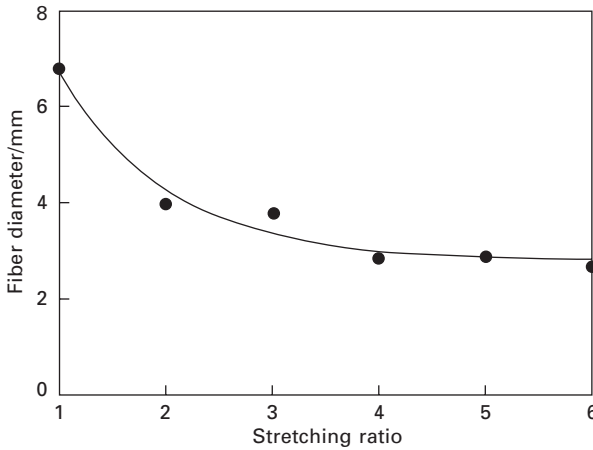


11.13 Stretching ratio dependence of tensile stress of olefinic/EPDM elastomeric fiber alloy. Modified from Spiridonov *et al.*, 2005.

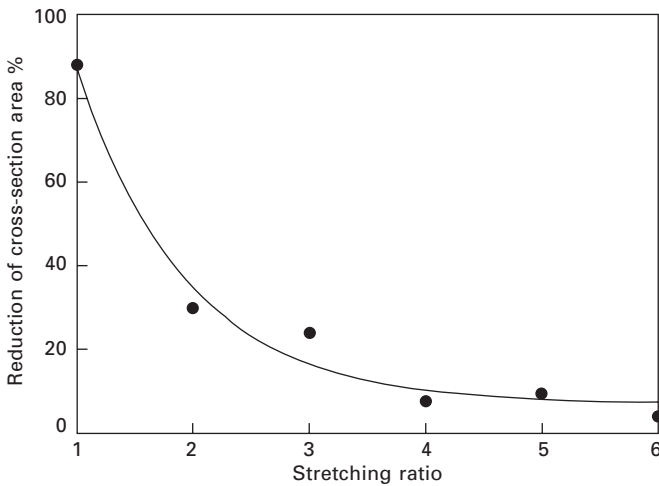


11.14 Stretching ratio dependence of percent elongation of olefinic/EPDM elastomeric fiber alloy. Modified from Spiridonov *et al.*, 2005.

consequently the fibers maintain their elastic behavior. The stretching ratio of these fibers can reach up to 7:1, after which the fiber starts to break. At a stretching ratio value of 6:1 a so-called ‘rough and peel’ surface structure of the fiber is observed. The diameters and cross-sectional area of the monofilaments are also changed significantly with increasing stretching ratio, i.e. the fiber diameters and the cross-sectional area decrease strongly with increasing stretching ratio as shown in Figs 11.15 and 11.16, respectively.



11.15 Stretching ratio dependence of fiber diameter of olefinic/EPDM elastomeric fiber alloy. Modified from Spiridonov *et al.*, 2005.

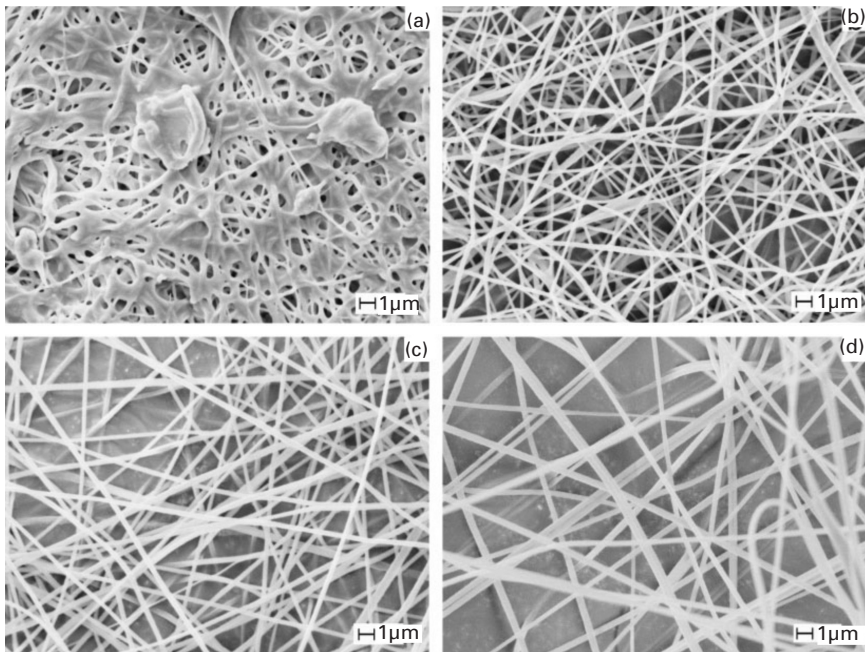


11.16 Stretching ratio dependence of percent reduction of the cross-section area of olefinic/EPDM elastomeric fiber alloy. Modified from Spiridonov *et al.*, 2005.

## 11.7.2 PU/PAN alloy fibers

Another example of thermoplastic polymer alloys that can be used to produce nanofibers is a mixture of crosslinkable elastomeric polyester urethane (PEU) with a thermoplastic polyacrylonitrile (PAN) (Fang *et al.*, 2007). Either crosslinking a polymer phase or interlocking both polymers to form a so-called ‘interpenetrating network’ has been an established strategy to compatibilize an immiscible polymer blend (Brown, 2002). In addition, a slightly crosslinked elastomer has been found to be more effective in toughening a thermoplastic material than its noncrosslinked counterpart (Lee, 1993).

Electrospinning of PEU/PAN polymer blend without any crosslinking reaction has also been used to produce fibrous structures (Fang *et al.*, 2007). When the overall concentration of PEU/PAN blend was kept at the same value in dimethylformamide (9 wt%), the ratio between the PEU and the PAN was found to influence the fiber morphology. As illustrated in Fig. 11.17, three different PEU/PAN ratios (PEU/PAN = 2:1, 1:1, 1:2 w/w) resulted in different fiber morphology. When the PEU/PAN ratio is 2:1, the



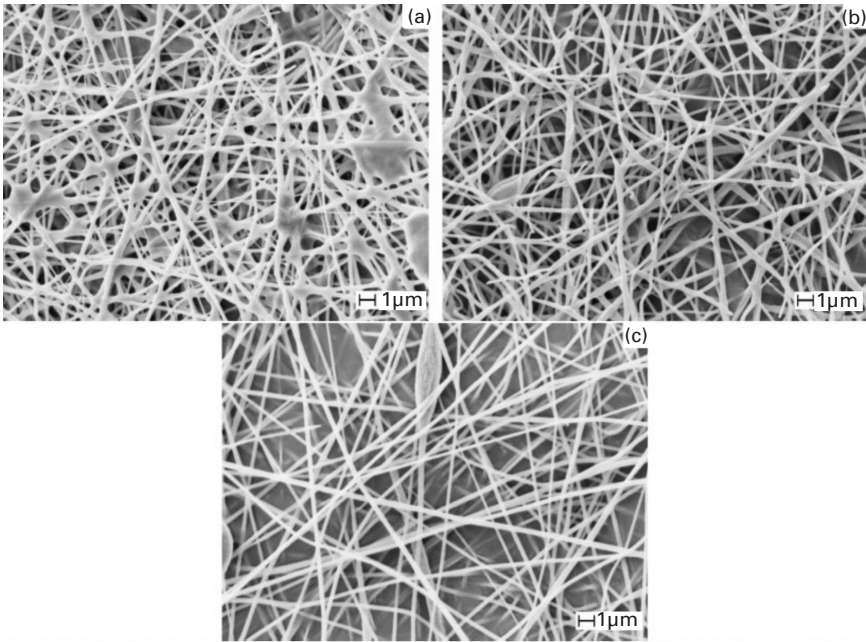
11.17 SEM images of noncrosslinked nanofibers: (a) PEU 6 wt% and PAN 3 wt% (PEU/PAN ratio w/w 2:1); (b) PEU 4.5 wt% and PAN 4.5 wt% (PEU/PAN ratio w/w 1:1); (c) PEU 3 wt% and PAN 6 wt% (PEU/PAN ratio w/w 1:2); and (d) PEU 0% and PAN 9 wt%. Adapted from Fang *et al.*, 2007.

PEU concentration is 6 wt%. Electrospinning of such a polymer solution resulted in a fibrous product, though the fibers tended to stick together to form an interconnected web structure (Fang *et al.*, 2007). This suggests that the addition of PAN to the PEU solution has facilitated the formation of nanofibers in electrospinning. When the PEU concentration is reduced to 4.5 wt% (PEU/PAN ratio = 1:1), individual fibers containing a small amount of fiber beads are produced. Further reduction of the PEU concentration to 3 wt% (PEU/PAN ratio = 1:2) leads to nonsticky and uniform fibers (Fang *et al.*, 2007). The fiber diameter from the different PEU/PAN ratios is in the range of 200–300 nm. By comparison, the pure PAN nanofibers electrospun with the same overall concentration have fiber diameters in the range of 354–664 nm (Fig. 11.17d). The PEU/PAN ratio also influences the fiber diameter by slightly decreasing it with an increase in the PEU component, even if the same overall polymer concentration is used. The change in the fiber diameter can be attributed to the effect of the PEU/PAN ratio on the solution properties.

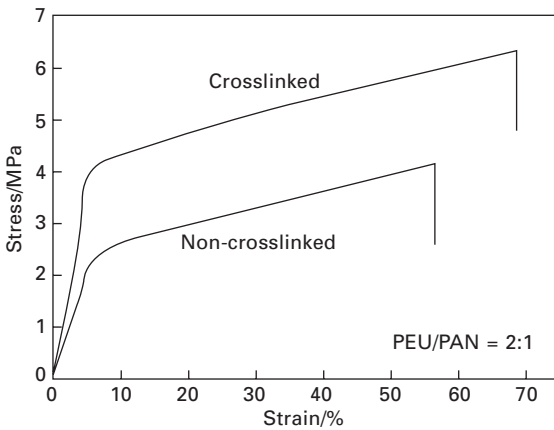
The crosslinked PEU/PAN fibers just described were prepared by Fang *et al.* (2007) by adding a crosslinker (Imprafix VP LS 2323, Bayer Mat. Sci., Germany) and catalyst (Imprafix TH LSG, Bayer Mat. Sci., Germany) (2.5 wt% each based on the weight of PEU) to the PEU/PAN solutions prior to electrospinning. As soon as the crosslinker and catalyst are added to the PEU/PAN solutions, the PEU chains start to crosslink (Fang *et al.*, 2007). The presence of the crosslinker and catalyst has a little effect on the fiber morphology. As shown in Fig. 11.18, the crosslinked PEU/PAN fibers have similar fiber morphology to the noncrosslinked fibers, except that the crosslinked fibers from the PEU/PAN (2:1) solution are less interconnected than the noncrosslinked fiber mat. The presence of the crosslinker leads to a fiber diameter increase when the solution contains a higher composition of PEU (i.e., PEU/PAN = 2:1 and 1:1). In contrast the fiber diameter is observed to decrease slightly when the PEU composition is low (i.e., PEU/PAN = 1:2) (Fang *et al.*, 2007).

The tensile stress–strain curves for the noncrosslinked and the crosslinked electrospun fiber mats with PEU/PAN = 2:1 ratio are shown in Fig. 11.19. With the same PEU/PAN ratio, the tensile strength of the crosslinked fiber mats is more than 50% greater than that of the noncrosslinked fiber mats, and the crosslinked fiber mats have a higher elongation at break than the noncrosslinked ones (Fang *et al.*, 2007). The crosslinking reaction leads to a 79% increase in the tensile strength and a 29% increase in the elongation at break for this composition ratio (PEU/PAN ratio = 2:1). These results indicate that the crosslinking reaction enhances the interaction between PEU and PAN chains.





11.18 SEM images of crosslinked PEU/PAN fibers: (a) PEU/PAN = 2:1; (b) PEU/PAN = 1:1; (c) PEU/PAN = 1:2. Adapted from Fang *et al.*, 2007.



11.19 Stress–strain curves for noncrosslinked and crosslinked electrospun fiber mats with PEU/PAN = 2:1 ratio. Modified from Fang *et al.*, 2007.

## 11.8 Conclusions and future trends

This chapter surveys the current science and technology of elastomeric fibers with enhanced benefits in a number of applications in the textile and allied industries. In general, the quality of elastomeric fibers has shown significant improvements since they were first developed. Strict quality control tests, according to industry standards, on the starting materials and final products are essential to ensure production of a consistent end product with prescribed properties. Future advances in polymer (fiber) science and engineering will help continue their improvement. For example, researchers have found that by changing the starting raw materials and the fiber production method in a clever way they can develop fibers which have even better properties such as stretching and weathering characteristics. Other characteristics of elastomer fibers can be improved by using various fillers and polymer additives. Because of the desirable characteristics of elastomeric fibers, it is likely that increased research and development attention will be focused in the future on these complex but important industrial materials. For example, it is likely that advanced textile fabrics will be produced which incorporate the versatile Spandex<sup>®</sup> fibers with conventional fibers such as in the commercially available polyamide/Spandex fiber blends described above. Industry efforts to improve cost-to-performance ratio of elastomeric fibers and products made from them may spur discovery of new manufacturing processes that will focus on producing fibers faster and more efficiently.

## 11.9 Acknowledgements

Professor Otaigbe thanks the US National Science Foundation for its financial support through contract grants CBET 0752150 and 0317646; and he is indebted to a number of collaborators in industry with whom he had the privilege to work on projects cited in this chapter.

## 11.10 References

- Adams R, Anderson J L (1950), 'Quinone imines. II. *p*-Quinone diacyl- and diaroylimines', *J Am Chem Soc*, 72, 5154–5157.
- Bhattarai S R, Bhattarai N, Yi H K, Hwang P H, Cha D I, Kim H Y (2004), 'Novel biodegradable electrospun membrane: scaffold for tissue engineering', *Biomaterials*, 25, 2595.
- Blazhaitis G I, Kaplanas V I, Pashkyavichus V V (1970), 'Finishing technology and range of fabrics from polyurethane elastomeric yarns', translated from *Khimicheskie Volokna*, 2, 65–67.
- Brauman S K, Mayorga G D, Heller J (1981), 'Light stability and discoloration of segmented polyether urethanes', *Annals Biom Eng*, 9 (1), 45–58.
- Brown S B (2002), in *Polymer Blends Handbook*, ed. L. A. Utracki, Kluwer Academic, Dordrecht, The Netherlands.

- Dieterich D, Schmelzer H, Oertel G (1993), *Polyurethane Handbook*, 2nd edn, Hanser Publishers, Munich.
- Fang J, Lin T, Tian W, Sharma A, Wang X (2007), 'Toughened electrospun nanofibers from crosslinked elastomer-thermoplastic blends', *J Appl Polym Sci*, 105, 2321-2326.
- Fong H, Reneker D H (1999), 'Elastomeric nanofibers of styrene-butadiene-styrene triblock copolymer', *J Polym Sci, Part B: Polym Phys*, 37, 3488-3493.
- Fong H, Chun I, Reneker D H (1999), 'Beaded nanofibers formed during electrospinning', *Polymer*, 40, 4585-4592.
- Fried J R (1995), *Polymer Science and Technology*, Prentice Hall, Englewood Cliffs, NJ.
- Frisch K C, Dieter J A (1975), 'Overview of urethane elastomers', *Polym-Plast Tech Eng*, 4 (1), 1-21.
- Gogeva T, Fakirov S, Mishinev J, Sarkisova L (1990), 'Poly(ether ester) fibers', *Acta Polymerica*, 41(1), 31-36.
- Gohil R M (1986), 'Electron microscopic studies of SBS block copolymers. I. A method to study the temperature dependence of phase separation', *Coll Polym Sci*, 264, 847-853.
- Hao X, Zhang X (2007), 'Syndiotactic 1,2-polybutadiene fibers produced by electrospinning', *Mater Lett*, 61, 1319-1322.
- Helfand E, Wasserman Z R (1976), 'Block copolymer theory. 4. Narrow interphase approximation', *Macromolecules*, 9, 879-888.
- Hepburn C (1992), *Polyurethane Elastomers*, 2nd edn, Elsevier Applied Science, New York.
- Hohman M M, Shin M, Rutledge G, Brenner M P (2001), 'Electrospinning and electrically forced jets. I. Stability theory', *Phys Fluids*, 13, 2201.
- Jun Z, Hou H, Schaper A, Wendorff J H, Greiner A (2003), 'Poly-L-lactide nanofibers by electrospinning: influence of solution viscosity and electrical conductivity on fiber diameter and fiber morphology', *e-Polymers*, 2003.
- Kim K, Luu Y K, Chang C, Fang D, Hsiao B S, Chu B, Hadjiargyrou M (2004), 'Incorporation and controlled release of a hydrophilic antibiotic using poly(lactide-co-glycolide)-based electrospun nanofibrous scaffolds', *J Controlled Release*, 98, 47-56.
- Lee K H, Kim H Y, La Y M, Lee D R, Sung N H (2002), 'Influence of a mixing solvent with tetrahydrofuran and *N,N*-dimethyl formamide on electrospun poly(vinyl chloride) nonwoven mats', *J Polym Sci, Part B: Polym Phys*, 40, 2259-2268.
- Lee W H (1993), in *Polymer Blends and Alloys*, ed. M.J. Folkes and P.S. Hope, Blackie Academic & Professional, London.
- Leibler L (1980), 'Theory of microphase separation in block copolymers', *Macromolecules*, 13, 1602-1617.
- Ma Z, Kotaki M, Ramakrishna S (2005), 'Electrospun cellulose nanofiber as affinity membrane', *J Memb Sci*, 256, 115-123.
- Mackley M R, Keller A (1975), 'Flow-induced polymer chain extension and its relation to fibrous crystallization', *Phil Trans Roy Soc London, Ser A: Math, Phys Eng Sci*, 278, 29-66.
- Madbouly S A, Otaigbe J U (2009), 'Recent advances in synthesis characterization and rheological properties of polyurethanes and POSS/polyurethane nanocomposites dispersions and films', *Prog Polym Sci*, 2009 (in press).
- Madbouly S A, Otaigbe J U, Nanda A K, Wicks D A (2007), 'Rheological behavior of POSS/polyurethane-urea nanocomposite films prepared by homogeneous solution polymerization in aqueous dispersions', *Macromolecules*, 40, 4982-4991.

- Matsen M W, Schick M (1994), 'Lamellar phase of a symmetric triblock copolymer', *Macromolecules*, 27, 187–192.
- McKee M G, Park T, Unal S, Yilgor I, Long T E (2005), 'Electrospinning of linear and highly branched segmented poly(urethaneurea)', *Polymer*, 46, 2011–2015.
- Megelski S, Stephens J S, Chase D B, Rabolt J F (2002), 'Micro- and nanostructure surface morphology on electrospun polymer fibers', *Macromolecules*, 35, 8456–8466.
- Oertel G (1994), *Polyurethane Handbook*, 2nd edn, Hanser Publishers, New York.
- Perkins T T, Smith D E, Chu S (1997), 'Single polymer dynamics in an elongational flow', *Science*, 276, 2016–2021.
- Predicini A, Farris R J (2003), 'Mechanical behavior of electrospun polyurethane', *Polymer*, 44, 6857–6862.
- Reneker D H, Chun I (1996), 'Nanometer diameter fibers of polymer, produced by electrospinning', *Nanotechnology*, 7, 216–223.
- Reneker D H, Yarin A L, Fong H, Kooimbhongse S (2000), 'Bending instability of electrically charged liquid jets of polymer solutions in electrospinning', *J Appl Phys*, 87, 4531.
- Roff W J, Scott J R (1971), *Film Plastics and Rubbers: a Handbook of Common Polymers*, Butterworths, London.
- Rubin 11, editor (1990), *Handbook of Plastics Materials and Technology*: Wiley, New York.
- Schollenberger C S, Stewart F D (1972), 'Thermoplastic urethane structure and ultraviolet stability', *J Elastoplastics*, 4, 294–331.
- Schollenberger C S, Scott H, Moore G R (1958), 'Polyurethan VC, a virtually cross-linked elastomer', *Rubber World*, 137, 549–555.
- Shin Y M, Hohman M M, Brenner M P, Rutledge G C (2001), 'Experimental characterization of electrospinning: the electrically forced jet and instabilities', *Polymer*, 42, 9955.
- Spiridonov P, Lambrinos E, Peng Z (2005), 'Extrusion of monofilaments of thermoplastic elastomers', *Synthetic Metals*, 152, 61–64.
- Szycher M, Poirier V L, Dempsey D J (1983), 'Development of an aliphatic biomedical-grade polyurethane elastomer', *J Elast Plast*, 15 (2), 81–95.
- Taylor G I (1969), *Proc Roy Soc London, Ser A*, 313, 453.
- Yang H, Sa U, Kang M, Ryu H S, Ryu C Y, Cho K (2006), 'Near-surface morphology effect on tack behavior of poly(styrene-*b*-butadiene-*b*-styrene) triblock copolymer/rosin films', *Polymer*, 47, 3889–3895.
- Yarin A L (1993), *Free Liquid Jets and Films: Hydrodynamics and Rheology*, Longman, Harlow, and Wiley, New York.
- Zong X, Kim K, Fang D, Ran S, Hsiao B S, Chu B (2002a), 'Structure and process relationship of electrospun bioabsorbable nanofiber membranes', *Polymer*, 43, 4403–4412.
- Zong X Fang D, Kim K, Ran S, Hsiao B S, Chu B, Brathwaite C, Li S, Chen E (2002b), 'Nonwoven nanofiber membranes of poly(lactide) and poly(glycolide-co-lactide) via electrospinning and application for anti-adhesions', *Polymer Preprints (ACS)*, 43, 659–660.

## Production and properties of high-modulus and high-strength polyethylene fibres

I M WARD, University of Leeds, UK and P J LEMSTRA, Technical University Eindhoven, The Netherlands

**Abstract:** The production and properties of high-modulus and high-strength polyethylene fibres are described. Low molecular weight (LMW-PE) fibres are produced by melt spinning of fibres with controlled morphology, followed by hot drawing to a high draw ratio. Ultra high molecular weight (UHMW-PE) fibres of high stiffness and strength are produced by solution(gel)-spinning followed by drawing to high draw ratios. Solvent-free processing routes and solid/melt routes for UHMW-PE fibres are also described. Commercial applications for both LMW-PE and UHMW-PE fibres are discussed.

**Key words:** high-modulus, high-strength, polyethylene fibres, melt spinning, solution(gel)-spinning.

### 12.1 Introduction

In the period from 1966 to 1970, there was increasing interest in the possibility of producing oriented polymers with high tensile stiffness ( $>40$  GPa) and strength ( $>1$  GPa). Two routes were envisaged to achieve this: synthesis of normal polymers with very rigid units in the polymer chain, and novel processing to give fully extended molecular chains from flexible polymers. These two routes have both been successful, the first most notably by synthesis of the aramids (Kevlar and Twaron) and the second by highly drawn polyethylene (Certran, Dyneema and Spectra).

Although it was well known in the fibre industry that stiffness and strength related to the molecular alignment achieved in tensile drawing, the draw ratios for commercial fibres such as polyester (Terylene and Dacron) and nylon were comparatively low ( $\sim 4-6$ ) and the properties fell far short of theoretical estimates. For polyethylene, for example, Treloar<sup>1</sup> had given estimates of at least 200 GPa for the Young's modulus, which compared with values of a few GPa measured for drawn films.

## 12.2 Melt spun high-modulus polyethylene fibres

### 12.2.1 Tensile drawing

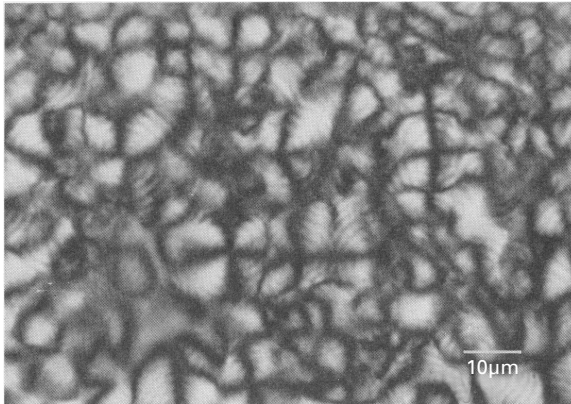
The development of high-modulus polyethylene fibres can be said to have been initiated by some interesting results obtained by Andrews and Ward<sup>2</sup> on the tensile drawing behaviour of a range of polyethylenes with different molecular weight distributions, collected as a result of GPC studies of degraded polyethylenes for morphological studies. Because only a few grams of these samples were available, a small-scale fibre spinning facility was constructed and small quantities of the spun fibres were stretched in an Instron tensile testing machine. In spite of considerable scatter in the results, two very important conclusions were reached. First, the draw ratio was sensitive to the weight average molecular weight  $\bar{M}_w$  in that higher  $\bar{M}_w$  polymers showed lower draw ratios. Secondly, there was a very good correlation between the Young's modulus of the drawn fibres and the draw ratio, irrespective of the molecular weight and molecular weight distribution of the samples. Very encouragingly the Young's modulus increased from 4 to 20 GPa as the draw ratio increased from 7 to 13.

These initial studies suggested that it would be worthwhile to undertake a detailed study of the tensile drawing behaviour of polyethylene with a view to obtaining higher-modulus materials, with the suggestion that this required a significantly higher draw ratio. The strategy adopted was to obtain a range of polyethylene homopolymers with different molecular weight characteristics, varying both  $\bar{M}_w$  and  $\bar{M}_n$ , and carefully controlling the initial morphology and maintaining identical tensile drawing conditions (temperature and strain rate) for all the samples in the first instance. A convenient procedure was to produce thin sheets by compression moulding with a mould temperature of 160°C and adopting controlled cooling conditions which varied from rapid quenching directly into water at ambient temperature to slow cooling at about 8°/min to 110°C followed by quenching into water. This latter treatment was selected to permit the crystallization to occur at low supercooling. It was appreciated that low supercooling might be advantageous for three reasons:

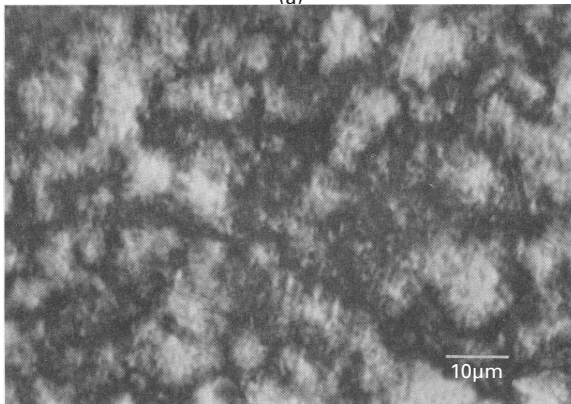
1. Fatou and Mandelkern's<sup>3</sup> studies of the crystallization rates of different molecular weight polyethylenes showed that differences of rate were only observed at low degrees of supercooling. For high supercooling the crystallization rates were very rapid for all species so that no distinction could be observed.
2. Previous studies on polyethylene by Way and Atkinson<sup>4</sup> suggested that the segregation of low molecular weight species could be important, and might act as a plasticizer in the subsequent drawing process. In much later research Barham and Keller<sup>5</sup> confirmed this result by removing low

molecular weight material from polyethylenes prior to tensile drawing. The issue here is that at low degrees of supercooling the polymer is at a temperature above the melting point of the low molecular weight species so that segregation occurs irrespective of the rates of crystallization.

3. By crystallizing at low supercooling, the overall rate of crystallization is slow, and this leads to a different morphology, which can be clearly seen in optical micrographs. Whereas rapidly quenched materials show the characteristic banded spherulitic structure (Fig. 12.1a) the slow cooled polymer shows regions of homogeneous orientation (Fig. 12.1b). Later studies of this morphology by SAXS, Raman spectroscopy and nitric acid etching followed by GPC confirmed the regular lamellar texture of these slow cooled materials.<sup>6</sup>



(a)



(b)

12.1 Optical micrographs (crossed polarizers) of thin sections (20 μm) obtained from (a) quenched and (b) slow cooled sheets of linear polyethylene of low molecular weight (Reproduced with kind permission of John Wiley & Sons Inc.)

In the initial study by Andrews and Ward, the tensile drawing was undertaken in an Instron tensile testing machine where the polymer draws through a neck, as in the case of poly(ethylene terephthalate) and nylon, where the initial cross-section is reduced to the final cross-section by deformation in the neck only, so that there is a 'natural draw ratio' which defines the limiting extensibility of the material. Capaccio and Ward recognized two key issues regarding tensile drawing:

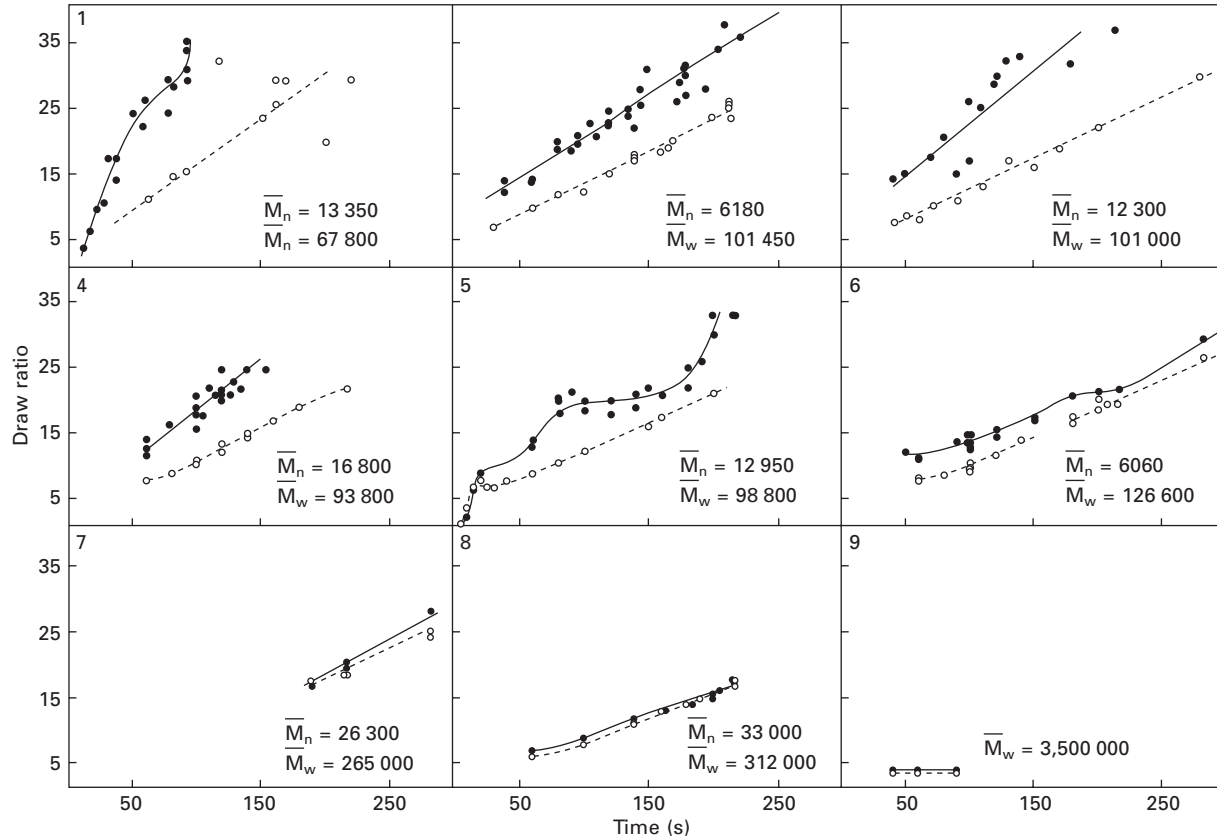
1. In general there is continuous drawing of material beyond the neck if the overall sample continues to be stretched, i.e. the draw ratio varies along the sample from unity in the extreme of the undrawn cross-section to a maximum value in the central section of the drawn material. The maximum draw ratio therefore increases with time until eventually failure occurs.
2. It is important to undertake the tensile drawing at above ambient temperature if the highest draw ratio is to be achieved for a given polymer in terms of both molecular weight and morphology.

With all these ideas in mind Ward and his colleagues<sup>7-14</sup> undertook a series of experiments on the tensile drawing of polyethylene with a wide range of molecular weights. Ideally for each grade of polymer the draw temperature should be chosen to give adequate molecular mobility without the onset of 'flow drawing' where deformation occurs without any significant alignment of molecules in the polymer. It is essential that the molecular chains can slide through the crystals, i.e., there is a direct link with the  $\alpha$ -relaxation process, and later studies by Wilding and Ward<sup>15</sup> showed that this process played a key role in yield and creep behaviour.

A key set of results was obtained by adopting a standard procedure for tensile drawing of a range of polyethylene homopolymers. Sheets were prepared by compression moulding at 160°C followed by either direct quenching into cold water or slow cooling to 120°C followed by quenching into cold water. Dumbbell samples with 2 cm gauge length were then drawn in air at 75°C in an Instron tensile testing machine at a cross-head speed of 10 cm/min, the drawing continuing until failure occurred. As described above, the draw ratio varied along the length of the extended sample with a region in the centre where it reached a maximum constant value. Specimens were cut from this region for measurement of Young's modulus by a dead-loading creep experiment. This was determined by the secant modulus calculated from the 10 s isochronal stress strain curve at a strain of  $10^{-3}$ .

The key results are shown in two figures. Figure 12.2 shows the draw ratio ( $\lambda$ ) as a function of time of draw. Two features are especially noticeable. First, for low molecular weight samples spectacularly high draw ratios were observed, and the time of draw for these to be achieved differed markedly for the two different initial thermal treatments. These results confirm the



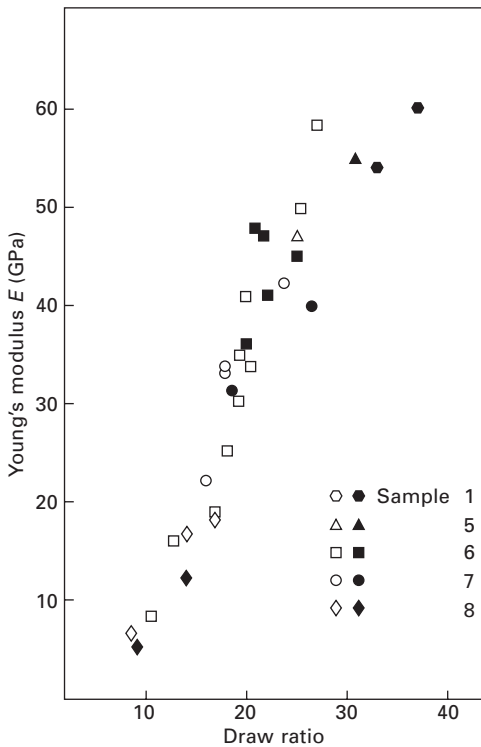


12.2 Draw ratio ( $\lambda$ ) vs. time of draw for linear polyethylene quenched (open circles) and slow cooled (solid circles) (Reproduced with kind permission of John Wiley & Sons Inc.)

ideas presented above reporting the importance of molecular weight and morphology on the deformation behaviour. Secondly, there is an overall effect of molecular weight with the high draw ratios limited to the lower molecular weight samples. These results had to be reviewed in the light of the choice of a comparatively low draw temperature, and will be discussed later.

Figure 12.3 shows the Young's modulus as a function of draw ratio, and these results clearly confirm and extend the results of Andrews and Ward, showing that to a very good approximation the modulus relates only to the draw ratio, irrespective of the molecular weight and initial morphology of the sample (although, of course, these affect the extent of draw). This conclusion was novel at the time, but is now commonplace and well accepted.

The easiest drawing was shown by the slow-cooled low molecular weight material and is attributed to the easier unfolding of a more regular lamellar texture (similar to the comparatively easy draw of polymer single crystals reflected by Porter and co-workers<sup>16</sup>), the reduction in tie molecules between

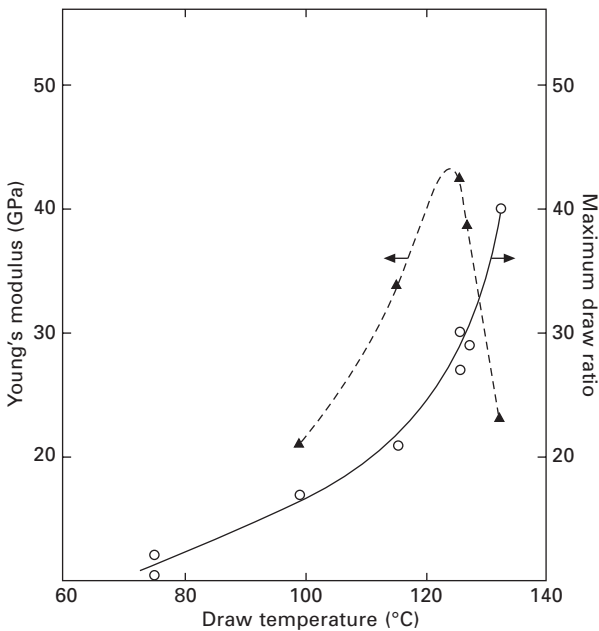


12.3 Room-temperature 10 s Young's modulus at low strains ( $10^{-3}$ ) as a function of draw ratio for a number of quenched (open symbols) and slow-cooled (solid symbols) samples (Reproduced with kind permission of John Wiley & Sons Inc.)

lamellae due to the slower crystallization at low degrees of supercooling, and the segregation of low molecular weight material (seen by the appearance of a narrow line component in the NMR spectrum<sup>17</sup>). This segregation of low molecular weight material also leads to easier draw for the lower  $\bar{M}_n$  materials as shown in Fig. 12.1.

The results presented in Fig. 12.2 are for a drawing at 75°C at a comparatively slow strain rate (10 cm/min on 2 cm samples  $\int 0.6 \text{ s}^{-1}$ ) and bring out very clearly differences due to molecular weight. Further research showed that by increasing the draw temperature higher molecular weight samples could be drawn to high draw ratios<sup>14</sup>. For example, a sample with  $\bar{M}_w = 8 \times 10^5$  can be drawn to draw ratio 40. However, as shown in Fig. 12.4, above 120°C flow drawing occurs where there is a reduction in cross-section but the molecular network is not being extended effectively to produce strain-hardening and increased modulus.

At this stage of the researches it was concluded that the drawing process for high-modulus polyethylene related to the deformation of a molecular network, as had been concluded for polyethylene terephthalate.<sup>18</sup> The importance of physical entanglements was emphasized by the limitation that



12.4 Plots of maximum draw ratio attainable (○) vs. draw temperature for high molecular weight ( $M_w = 8 \times 10^5$ ) linear polyethylene. The values of the corresponding room-temperature moduli (▲) for the different draw ratios are also shown (Reproduced with kind permission of John Wiley & Sons Inc.)

very high molecular weight polymers could not be drawn to high draw ratio. The importance of morphology was seen to be important for low molecular weight polymers so that the initial structures can be unravelled easily.

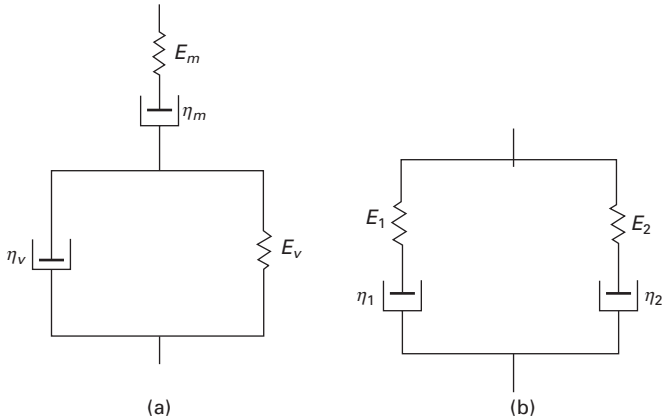
The Leeds research on high draw polyethylene was the subject of a patent portfolio which was held by BTG and the technology was licensed first to SNIA (Italy) and then to Hoechst Celanese (USA) with whom the Leeds group collaborated (in addition to some preliminary development work with ICI Fibres). The fibres were marketed under the trade names Tenfor (SNIA) and Certran (Hoechst-Celanese) until Hoechst decided to focus on pharmaceuticals. The guidelines for the practical processing in the two stage melt spinning and hot drawing process can be summarized as follows:

1. The spun yarn morphology should follow the understanding described above for compression moulded sheets. This involves identifying a polyethylene homopolymer with the correct molecular weight distribution and placing a heated shroud immediately below the spinneret to ensure that the initial crystallization occurs at a low degree of supercooling. A low spun yarn orientation is also essential.
2. Hot drawing is carried out in several stages to ensure adequate heat transfer and enable successive drawing to take place at increasingly higher temperatures.

### 12.2.2 Tensile creep behaviour

The tensile drawing research was consolidated and extended by subsequent research on the tensile creep and recovery behaviour. It was very soon appreciated that although very high moduli were being obtained, the drawn materials showed very significant creep, even at ambient temperatures, so that there were major limitations with regard to permanent load-bearing applications. In a series of investigations Wilding and Ward<sup>19-22</sup> explored the effect of molecular weight, copolymer content and crosslinking on the creep and recovery of drawn polyethylenes. An initial key observation was that higher draw ratio materials showed reduced creep, and this was a general rule for all compositions. The interpretation of the data was in terms of spring and dashpot models and these were successful in providing adequate descriptions of both creep and recovery and later stress relaxation as well as giving a basis for some degree of physical understanding. In the first instance the model shown in Fig. 12.5a describes the distinction seen between recoverable creep for short-time loading and unloading (the Voigt element) and non-recoverable creep (the Maxwell element) for longer-time loading.

An important observation was that whereas the comparatively short-time behaviour was linearly dependent on the stress (the Voigt element), the long-



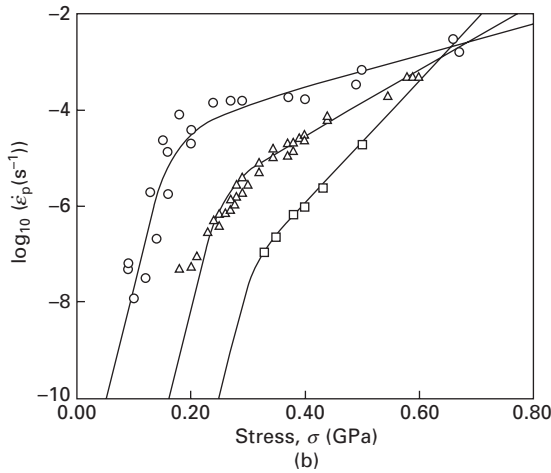
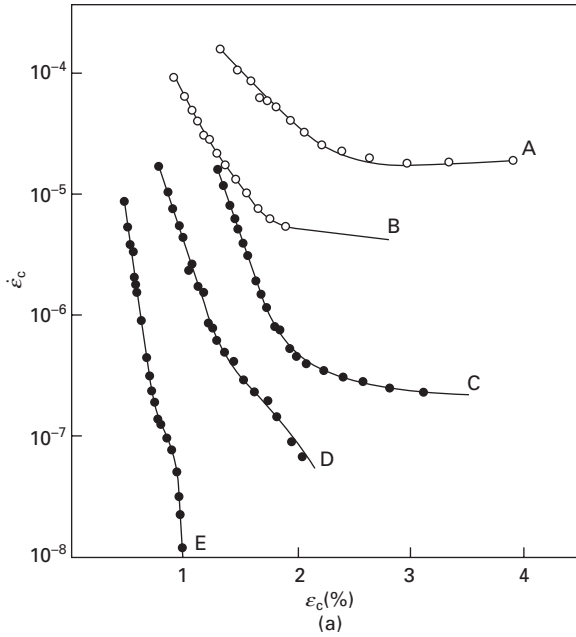
12.5 Mechanical models for creep and recovery (Reproduced with kind permission of Elsevier Limited)

time permanent creep was not linearly dependent on the stress and could be modelled by the Eyring equation for thermally activated processes, where the creep rate  $\dot{\epsilon}_p$  is given by

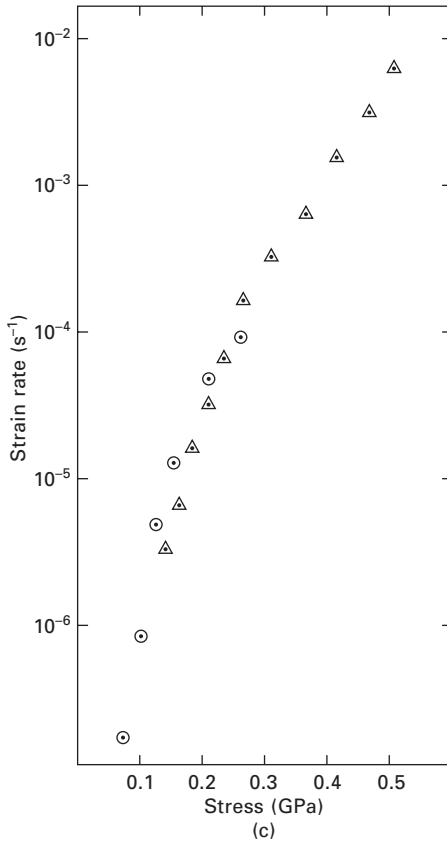
$$\dot{\epsilon}_p = \dot{\epsilon}_0 \left( \exp - \frac{\Delta H}{kT} \right) \left( \sinh \frac{\sigma v}{kT} \right) \tag{12.1}$$

for a stress  $\sigma$ , where  $\Delta H$  and  $v$  are the activation energy and the activation volume respectively.

Wilding and Ward followed the methodology proposed by Sherby and Dorn<sup>23</sup> of plotting creep rate (rather than creep strain) as a function of time or strain. For different stress levels this gives a series of curves such as shown in Fig. 12.6a, where for high stress the creep rate reaches a constant value, which was termed the plateau creep rate, but for low stress the creep rate falls steadily and within the measurement time no plateau strain rate is observed. It proved instructive to plot the plateau strain rates as a function of applied stress as shown in Fig. 12.6b. Such plots can be used for two major purposes. First, the plateau creep rates fall very rapidly for decreasing stress so that it is possible to define an applied stress level as a ‘critical stress’, below which permanent deformation can be regarded as negligible. This has been used for engineering applications such as geotextiles. Secondly, these plots provide clear discrimination between different samples. For example, as shown in Fig. 12.6(b) copolymers show better creep behaviour than homopolymers. This observation led to the examination as to whether there was a definitive link between the creep behaviour and tensile drawing, and it was shown that the yield stress observed in a constant strain rate test was equivalent to the creep rate in a constant applied stress experiment. This is shown schematically in Figure 12.6(c). Creep and yield are found to be best



12.6 (a)  $\dot{\epsilon}_c$  as a function of  $\epsilon_c$  for low molecular weight (C, D, E) and high molecular weight (A, B) samples of oriented linear polyethylene; the lines are visual fits. Stress level: A, 0.2; B, 0.15; C, 0.2; D, 0.15; E, 0.1 GPa (Reproduced with kind permission of Elsevier Limited). (b) Log plateau strain rate versus stress for linear polyethylene ( $\circ$ ) and copolymers ( $\triangle$ ,  $\square$ ) (Reproduced with kind permission of John Wiley & Sons Inc.). (c) Yield stress in constant strain rate test ( $\triangle$ ) compared with plateau strain rate for different applied stress for oriented polyethylene ( $\odot$ ) (Reproduced with kind permission of Elsevier Limited)



12.6 Cont'd

described by the two-process model of Figure 12.5(b), where the plateau creep rates relate to the deformation of two thermally activated processes acting in parallel, exactly as proposed previously for yield behaviour by Bauwens and others.<sup>24,25</sup>

Detailed modelling showed that the two activated processes in Fig. 12.5(b) represented by  $\eta_1$  and  $\eta_2$  are very different in that the dashpot  $\eta_1$  has a larger activation volume and a smaller pre-exponential factor  $\dot{\epsilon}_0$  than the corresponding quantities for the dashpot  $\eta_2$ .

Detailed measurements for these high-modulus polyethylene materials, carried out over a range of stresses and temperatures, showed that the activation volume for the low activation value process  $\eta_2$  was in the range of  $100 \text{ \AA}^3$  and the activation energy of the order of 30 kcal/mol. The result suggested that this key process involves slip in the crystalline regions and has kinship with the  $\alpha$ -relaxation process observed in dynamic mechanical measurements. Any physical interpretation of the larger activation value process

( $\eta_1$  is of the order of  $500 \text{ \AA}^3$ ) is much more tentative but it is interesting to speculate that this relates to the molecular network acting in parallel with the crystalline material in the structure. The idea is attractive because it has been shown that this process makes a much greater relative contribution in the creep behaviour for samples of higher molecular weights, for crosslinked samples and for copolymers where the crystal slip process can be inhibited by the presence of branch points. As might be expected, these differences can also be identified in the tensile drawing behaviour.<sup>26</sup>

It was shown that major improvements in the creep behaviour could be obtained by use of electron or  $\gamma$ -irradiation to give a significant degree of crosslinking. Woods, Busfield and Ward<sup>27</sup> showed that this was best achieved by irradiation in an atmosphere of acetylene. The crosslinking mechanisms were analysed in detail in a series of studies by Jones, Salmon, Ward and coworkers.<sup>28-32</sup> It was shown by electron spin resonance and ultraviolet spectroscopy measurements that irradiation in acetylene gave rise to the formation of diene, triene and tetraene groups. It was proposed that polymer bridges, mostly involving the diene groups, form crosslinks between radical pairs.<sup>29</sup> Computer modelling of amorphous polyethylene chains showed that this proposal of diene bridges is consistent with predicted radical pair distances of about  $5.6 \text{ \AA}$  between adjacent polyethylene chains.

### 12.2.3 Fibre strength

Whereas for considerations of achieving high-modulus PE fibres it has been appropriate to discuss the two processing routes for the melt-spun and gel-spun fibres separately, it is more instructive with regard to fibre tensile strength to consider both together.

It is well known for polymeric fibres that fibre strength can be related to molecular weight, and that for both polymeric and inorganic fibres, such as glass fibre, strength can also relate to fibre diameter. A key fundamental issue is therefore how to distinguish between limitations in strength due to intrinsic factors such as molecular weight and molecular orientation (more generally morphology) and extrinsic factors such as flaws or fibre diameter.

It is convenient to discuss the effects of molecular weight, including results for both melt-spun and gel-spun fibres. Following the seminal research of Flory,<sup>33</sup> it is accepted that fibre tensile strength relates to the number average molecular weight  $\overline{M}_n$  where the strength  $\sigma$  is given by

$$\sigma = A - \frac{B}{\overline{M}_n} \quad 12.2$$

Flory showed that this relationship implies that the tensile strength of a blend of different molecular weight fractions relates to the weight average summation of the strengths of the individual components.



An important practical result is that the gel-spun fibres show very much greater tensile strengths than the melt-spun fibres, with tensile strengths reaching as great as 8 GPa, compared with maximum values in the range 1–2 GPa for melt-spun fibres. Smith, Lemstra and Pijpers<sup>34</sup> made a key comparison between melt-spun and drawn fibres, gel-spun and drawn fibres, solid state extruded materials and surface growth fibres. To obtain equivalence between the different processing methods, in each case the ratio of tensile strength to modulus was determined. Although there could be some cases such as solid-state extruded materials where the strength was limited by flaws, it was important that no significant differences were seen between melt-spun and gel-spun fibres when both routes were used for polymer of identical molecular weight. These researches together with other researches by Smith and Lemstra<sup>35</sup> suggested strong molecular weight effects, but with some reservations regarding  $\overline{M}_n$  or  $\overline{M}_w$  as the key variable. In another study, for melt-spun and drawn fibres Wu and Black<sup>36</sup> concluded very firmly that tensile strength related to  $\overline{M}_n$  with no positive effects attributable to  $\overline{M}_w$  or polydispersity.

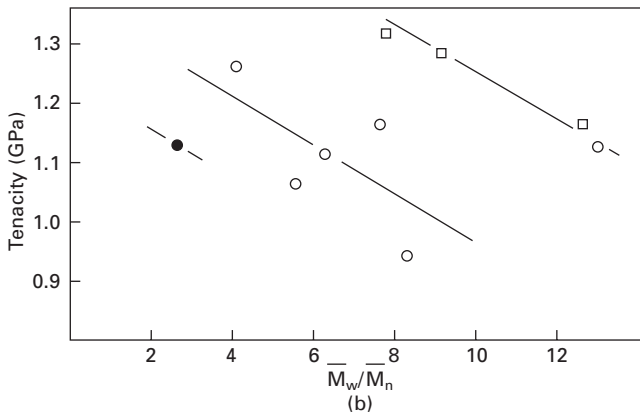
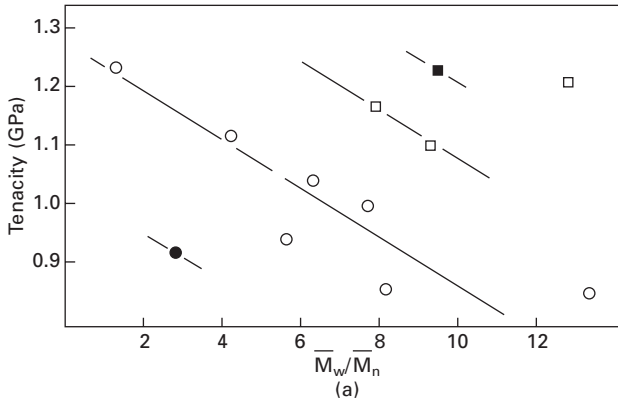
Somewhat later studies by Ward and co-workers addressed these issues of molecular weight dependence for melt-spun and drawn fibres.<sup>37,38</sup> The tensile strength was measured at  $-55^\circ\text{C}$  to ensure that in all cases brittle fracture occurred with no element of ductility. Fibres were produced at fixed modulus by drawing to fixed draw ratio to ensure that similar structures were obtained. Measurements for draw ratios 15 and 20 are shown in Figs 12.7(a) and 12.7(b) to illustrate the dependence of tensile strength on the polydispersity  $\overline{M}_w/\overline{M}_n$  for different values of  $\overline{M}_w$ . It can be seen that the Flory equation (12.2) above is confirmed to a good approximation. Next, by extrapolating the data in Figs 12.7(a) and 12.7(b) to  $\overline{M}_w/\overline{M}_n = 1$ , the theoretical strength of monodisperse samples can be predicted, and this gave the relationship

$$\sigma = KM^{0.25} \quad 12.3$$

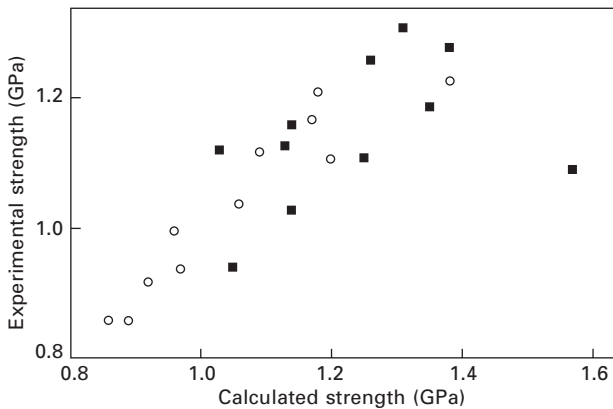
where  $K = 68$  MPa for draw ratio 15 and 78 MPa for draw ratio 20.

Furthermore, it was then possible to follow Flory's procedure of assuming that a blend of different molecular weight fractions can be assumed to be predicted by the weight average summation. Hallam *et al.*<sup>38</sup> therefore used the molecular weight distribution obtained by GPC to predict the tensile strength for their melt-spun and drawn samples. The comparison between these predictions and experimental results is shown in Fig. 12.8. It can be seen that there is a reasonable correlation, which confirms the Flory equation and also a theoretical model for the tensile strength of binary mixtures of high and low molecular weight polyethylene proposed by Termonia, Greene and Smith.<sup>39</sup>

So far it has been accepted that it is possible to relate fibre strength to intrinsic factors, on the assumption of comparing samples of similar



12.7 The dependence of  $-55^{\circ}\text{C}$  tensile strength on molecular weight ratio ( $\bar{M}_w/\bar{M}_n$ ), for a draw ratio ( $\lambda$ ) of (a) 15 and (b) 20. The symbols indicate different  $\bar{M}_w$  values: (●) 60 000, (○) 100 000, (□) 222 000, (■) 330 000. (a) draw ratio  $\lambda = 15$  (b)  $\lambda = 20$  (Reproduced with kind permission of Springer Science and Business Media)

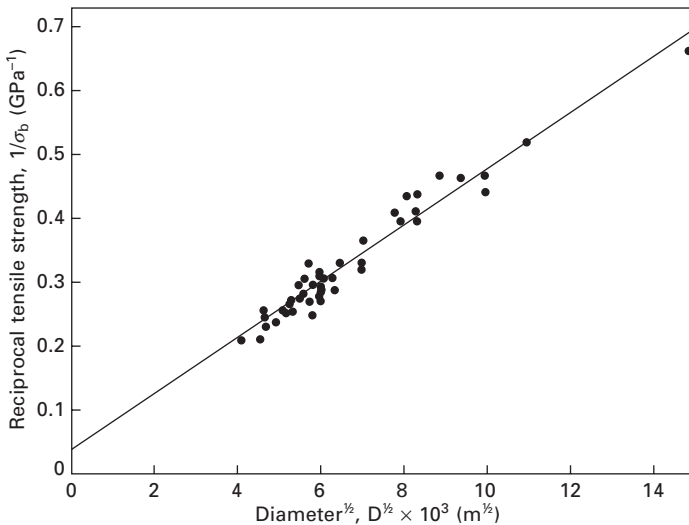


12.8 Comparison of experimental and calculated tensile strength values: (○)  $\lambda = 15$ , (■)  $\lambda = 20$ . (Reproduced with kind permission of Springer Science and Business Media)

processing in terms of draw ratio, hence the relevance of comparisons for samples of identical modulus. Next, we consider the possible relevance of extrinsic factors, notably fibre diameter and flaws.

Ward and coworkers<sup>40</sup> explored the use of Weibull analysis to determine whether the strength of melt-spun and drawn fibres is determined by flaws, and whether these are surface or volume flaws. For low draw ratio fibres, Weibull plots of failure probability versus strength show a high Weibull modulus, corresponding to a narrow distribution of strengths, which is consistent with failure being determined by the intrinsic factors of molecular weight and draw ratio. On the other hand, high-modulus melt-spun and drawn fibres, especially for low molecular weight samples, showed a lower value of the Weibull modulus in good agreement with that obtained from plots of  $\ln(\text{tensile strength})$  versus  $\ln(\text{diameter})$  corresponding to a volume distribution of flaws. Results for high molecular weight melt-spun and drawn fibres were not so clear and hinted at the effects of surface flaws rather than volume flaws. In one respect the results for these melt spun-fibres agreed with those for the gel-spun fibres in confirming significant effects of fibre diameter. The SNIA fibre process relied on low-diameter drawn filaments to give adequate strengths, although these were still only in the range of 1.5 GPa.

Results presented by Smook *et al.*<sup>41</sup> suggested that as the fibre diameter in gel-spun and drawn samples is reduced from 120  $\mu\text{m}$  to 20  $\mu\text{m}$  the tensile strength is increased from 2 GPa to 4.5 GPa. Assuming the classic Griffith



12.9 Linear strength–diameter relationship observed for fully oriented UHMW PE filaments (Reproduced with kind permission of Springer Science and Business Media).

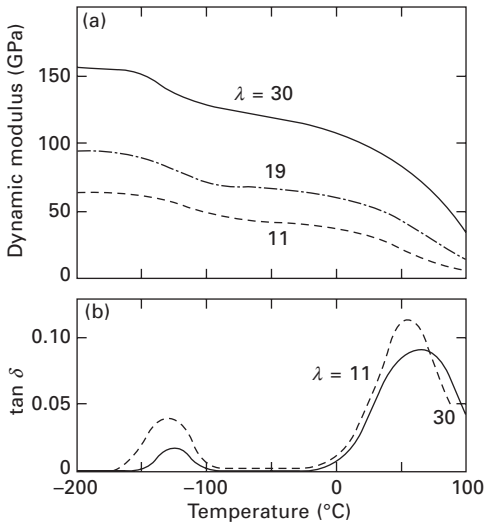
relationship  $\sigma \propto 1/d^{1/2}$  this corresponded remarkably well with the data of Smook *et al.* as shown in Fig. 12.9. It can be seen that extrapolation to zero diameter gives a strength value of 26 GPa which was suggested to be close to the theoretical estimate of 25 GPa based on the C–C bond strength.

Although the suggestion that the tensile strength of gel-spun fibre is diameter-dependent agrees with the Weibull analysis of Amornsakchai *et al.*<sup>40</sup> on commercial gel-spun fibres, it is in conflict with the result of Bastiaansen.<sup>42</sup> Bastiaansen compared the tensile strength of different diameter gel-spun fibres at constant modulus, having established that for his samples the relationship between tensile strength and modulus is the same for all samples, irrespective of diameter. Smook *et al.*,<sup>41</sup> on the other hand, compared fibres of different diameter in which the modulus increased as the diameter decreased. The fibres of Smook *et al.*, similar to those used by Bastiaansen, had a similar modulus–tensile strength relationship to that shown by Smith *et al.*<sup>34</sup> This suggests that the increased strength of the lower diameter gel-spun fibres can be attributed to their higher modulus and need not be due to their lower diameter.

It can be concluded that mechanism of failure of gel-spun fibres may not follow the flaw-induced mechanism of melt-spun fibres. This is an area worthy of further study.

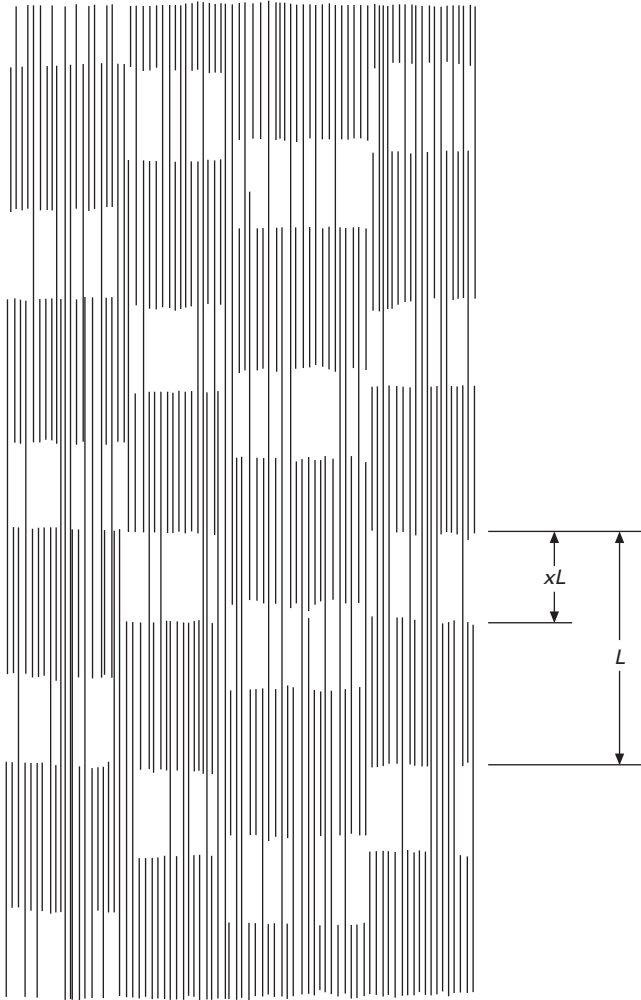
#### 12.2.4 Dynamic mechanical behaviour and structure of melt-spun and drawn fibres

Understanding of the structure of high-modulus melt-spun and drawn fibres rests on a combination of structural data based primarily on wide-angle and small-angle X-ray diffraction and electron microscopy, and dynamic mechanical measurements. The mechanical measurements show very considerable temperature dependence (Fig. 12.10) with two clear relaxation processes, the  $\alpha$ -relaxation *ca.* 105°C attributed to crystal slip (discussed above as the principal mechanism for yield and high temperature creep) and the  $\gamma$ -relaxation conventionally associated with local internal rotations of the polymer chain. At –200°C, the storage modulus is 160 GPa, approaching the value of 240 GPa predicted (and determined experimentally by X-ray measurements) for the extended chain modulus of polyethylene. The first model proposed by Barham and Arridge<sup>43</sup> to explain the very high modulus of these materials proposed that the fibres were akin to a fibre-reinforced composite with long needle-like crystals in a lower modulus matrix. This model gave a good representation of the increasing modulus with increasing draw ratio in terms of increasing the aspect ratio of the crystals, which were assumed to deform affinely. However, later research by Gibson, Davies and Ward,<sup>44</sup> confirmed by more recent work by Sadler and Barham,<sup>45</sup> led to an alternative model which is more consistent with both structural and mechanical data.



12.10 (a) Dynamic modulus and (b)  $\tan \delta$  plotted against temperature for drawn LPE at indicated draw ratio ( $\lambda$ ) (Reproduced with kind permission of *Phil. Trans R. Soc. A*).

Although the two-point SAXS pattern is still observed in these highly drawn fibres even at the highest draw ratios, the average crystal length (the longitudinal crystal thickness) determined from the integral breadth of the WAXS 002 reflection and from dark field electron microscopy increases from  $\sim 200 \text{ \AA}$  to  $500\text{--}600 \text{ \AA}$  with increasing draw ratio.<sup>46</sup> The long period, determined from the SAXS pattern, remains approximately constant at  $150\text{--}250 \text{ \AA}$  depending on draw temperature. This result is consistent with a structure where the alternating blocks of crystalline and amorphous material, which are the essence of the Takayanagi and Peterlin models for the structure of oriented crystalline polymers, become linked by crystalline bridges as shown schematically in Fig. 12.11. This model forms the basis for a simple Takayanagi model where the proportion of crystalline bridges which gives continuity to the structure can be determined quantitatively from a combination of WAXS and SAXS measurements on the assumption that the formation of the bridges is a random process analogous to condensation polymerization and defined by a parameter  $p$  which describes the probability of a crystalline sequence traversing the intercrystalline region to link two adjacent lamellae. This model can also be considered to generate a structure akin to a fibre composite where the crystalline bridge sequences act as the reinforcing fibres, but it has a different genesis from the Barham and Arridge model in that drawing increases the proportion of the reinforcing fibres, not just their aspect ratio.



12.11 A schematic representation of the structure of the crystalline phase of highly oriented linear polyethylene (Reproduced with kind permission of Elsevier Limited)

### 12.2.5 Thermal properties

The thermal properties of the high-modulus melt-spun PE fibres provide further insight into their structure and the underpinning studies of their production. Capaccio and Ward<sup>47</sup> showed that the irreversible shrinkage and the shrinkage forces observed at temperatures up to and including the melting point are consistent with the stretching of a molecular network. On heating above the melting point complete contraction was observed. This continuity of structure through the drawing process is confirmed by neutron

scattering results of Sadler and Barham<sup>45</sup> and by electron microscopy studies of Bassett and coworkers<sup>48</sup> on the Leeds-produced materials.

The thermal expansion behaviour of the compression-moulded and hot-drawn samples is remarkable in showing very high negative thermal coefficients of expansion. Orchard *et al.*<sup>49</sup> proposed that these arise because of the effects of frozen-in material stresses due to the highly stretched molecular network which will wish to retract at temperatures where there is sufficient internal mobility. A simple model was able to correlate the negative thermal expansion to the shrinkage stresses measured by Capaccio and Ward.

Finally, with regard to thermal properties, the large superheating effects shown by the high draw ratio fibre and films are worthy of mention, and were studied in some detail by Clements *et al.*<sup>50,51</sup> These are attributed to the conformational constraints on the amorphous regions and can lead to melting temperatures as high as 145°C.

### 12.2.6 Commercialisation of melt-spun high-modulus PE fibres

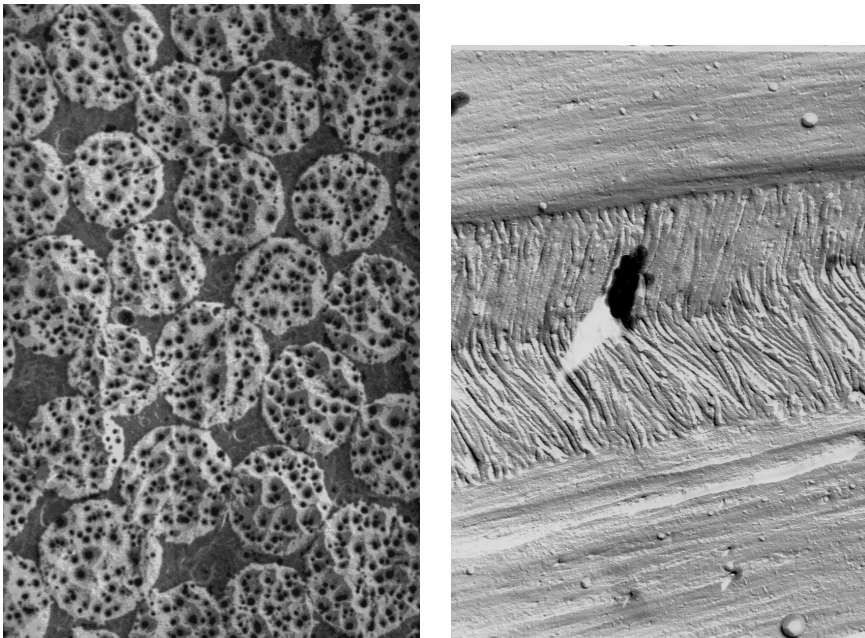
The commercialisation of the melt-spun route for PE fibres was started by SNIA Fibres, Italy, after some initial involvement of ICI Fibres, Harrogate, UK. In the early 1990s the SNIA production plant was transported to Charlotte, North Carolina, and the fibres were subsequently marketed by Hoechst-Celanese under the trade name Certran (renamed from the SNIA Tenfor). The tensile properties were 40 GPa for modulus and 1.4 GPa for tensile strength and the primary applications included safety belts, ropes, dental floss, fishing nets, sail cloth, sewing thread and protective clothing.<sup>52</sup>

In an attempt to expand the market for the Certran fibres, the Leeds University group explored their potential for composite materials, initially by considering the production of fibre/resin composites. It was found necessary to develop plasma treatment of the fibres preferably in an oxygen atmosphere, to improve the fibre–resin adhesion. This led to a series of researches by Ladizesky, Ward and coworkers,<sup>53–58</sup> showing that the plasma treatment led to general oxidation and crosslinking of the fibre surfaces in addition to extensive surface pitting which provided mechanical keying. Plasma treatment has also been applied to self-spun fibres by other workers, including Hild and Schwartz<sup>59</sup> and Li and Netravali.<sup>60</sup>

Ladizesky and Ward<sup>61,62</sup> found that epoxy and polyester resin composites incorporating the Certran fibres showed high values of stiffness and strength, together with excellent performance in Charpy impact tests. Hybrid composites with glass or carbon fibres were also produced, and these showed some very good combinations of mechanical properties, including damage tolerance and in the case of glass fibres adequate compressive strengths.<sup>63</sup>

These studies of polyethylene fibre composites led to a new development which has proved to be of both scientific interest and capable of commercial exploitation. It was recognized that for some applications such as ballistics and radome covers, it would be valuable to have very high fibre concentrations, in the latter case 100% if possible. The Leeds group showed that it was possible to produce 100% PE composites by a simple hot compaction process. An array of fibres or tapes perhaps layers of fabric, is heated to a temperature in the range of 137–140°C, which is just below the peak melting point of the PE fibres. This produces a thin skin of melted polymer on the surface of the fibres or tapes which on cooling recrystallizes epitaxially to form the matrix of a self-reinforced fibre composite<sup>64,65</sup> (Fig. 12.12).

With financial support from Hoechst-Celanese a small spin-off commercial company, Vantage Polymers Ltd, was set up with the first author as Managing Director. A continuous process for making hot compacted sheets was devised, incorporating a double-belt press, and conditions were established for postforming these sheets into a range of products from protective clothing to loudspeaker cones. The commercial activities have focused on hot compacted polypropylene, and full-scale commercial operations commenced within BP Amoco (now Propex Fabrics GmbH), at Gronau, Germany, in 2000, where there is a good fit with the production of woven polypropylene for geotextiles and carpet backing. Hoechst-Celanese is no longer manufacturing



12.12 Morphology of hot compacted PE fibre sheet (Reproduced with kind permission of Springer Science and Business Media)



Table 12.1 A comparison of typical properties of compacted PET, PE and PP sheets

|                                             | ASTM standard text | PET  | Polypropylene | PE   |
|---------------------------------------------|--------------------|------|---------------|------|
| Density (kg/m <sup>3</sup> )                |                    | 1400 | 910           | 970  |
| Tensile modulus (GPa)                       | D638M              | 5.82 | 5.06          | 28   |
| Tensile strength (MPa)                      | D638M              | 130  | 182           | 370  |
| Heat deflection temperature (1820 kPa) (°C) | D648               | 108  | 102           | 132  |
| Thermal expansion (x 10 <sup>-6</sup> /°C)  | D696               | 26.4 | 41            | -1.5 |
| Notched Izod strength (20°C) (J/m)          | D256               | 2020 | 4760          | 1340 |

the Certran fibres, having decided to focus its commercial activities on pharmaceuticals.

It is, however, of some interest to conclude this section with a table (Table 12.1) comparing key properties of hot compacted sheets from PE, PP and PET. Although PP shows the most outstanding impact performance, PE has a very good balance of properties, and hot compacted PE sheets are a contender for some commercial applications such as ballistics, radome covers and medical imaging screens. Extensive reviews of the hot compaction research have been presented elsewhere.<sup>66,67</sup>

## 12.3 Fibres based on ultra-high-molecular weight polyethylene

### 12.3.1 Solution(gel)-spinning

As discussed in the previous sections, the production of high-modulus polyethylene fibres via melt-spinning followed by subsequent and optimized drawing in the solid state, as pioneered by Ward *et al.*, has a 'natural' limit with respect to the molecular weight, notably the weight-average molar mass  $M_w$ . The limiting factors are:

- *Melt-viscosity.* The viscosity of polymer melts increases strongly with increasing molar mass, in general the so-called zero-shear viscosity scaling with  $M_w^{3,4}$ , and processing high molar mass polyethylenes via the melt becomes increasingly difficult with increasing  $M_w$ . In fact, polyethylenes with  $M_w > 10^6$  g/mol, the so-called UHMW-PE grades (ultra-high molecular weight polyethylenes), are considered to be intractable like other high molar mass polymers, e.g. PTFE. Processing of UHMW-PE is performed by compression-moulding and subsequent machining into parts or via (slow) ram-extrusion processes into simple profiles.
- *Limited drawability in the solid state.* It was shown convincingly by Ward *et al.*, as discussed earlier in this chapter, that the drawability of melt-crystallized polyethylenes decreases with increasing molar mass

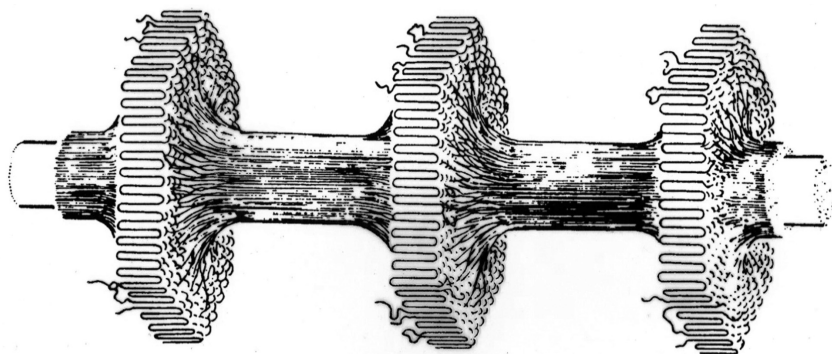
towards a limiting natural draw ratio of approximately 5 for UHMW-PE grades. The limited draw ratio, accompanied by marked strain hardening upon draw, makes UHMW-PE the most wear resistant polymer used in demanding applications such as artificial hip-joints, i.e. UHMW-PE is highly resistant to draw and, consequently, molecules cannot be aligned in parallel or chain-extended as a result of tensile draw.

The processing limitations of intractable polymers, possessing either too high a molar mass, limited thermal stability or too high a melting temperature, can be overcome in practice by using solvents, i.e. solution-spinning rather than melt-spinning, and is common practice in the production of fibres of poly(vinyl alcohol), poly(acrylonitrile) and the aromatic polyamides Kevlar<sup>®</sup> and Twaron<sup>®</sup>, to name a few examples. There were some early reports in the 1960s by Zwick (see Zwick *et al.*<sup>68</sup>) on solution-spinning of UHMW-PE, but the intention at that time was shaping of UHMW-PE into fibres and tapes; no attempt was made to pursue chain-extension which, in retrospect, is quite remarkable, since the fact that an extended PE chain possesses an *E* modulus close to 200 GPa had been known since Treloar's seminal paper of 1960.<sup>1</sup>

In fact, the development of oriented PE fibres via solution routes took quite a tortuous path until finally, at the end of the 1970s, the so-called solution(gel)-spinning route for producing high-strength and high-modulus PE fibres possessing tenacity of 3–4 GPa and *E* modulus > 100 GPa was discovered at DSM (see below).

The first observation of chain-extension of long polyethylene chains in solutions was made by Mitsuhashi using a simple Couette apparatus in the early 1960s. He reported the formation of fibrous 'string-like' polyethylene structures upon stirring linear polyethylene in xylene. His findings remained largely unnoticed because the results were published in a local Japanese journal.<sup>69</sup>

In the 1960s, Pennings, van der Mark and Kiel<sup>70</sup> performed experiments to fractionate polyethylenes at the DSM central laboratories in Geleen, the Netherlands, starting from UHMW-PE in dilute solutions. They observed structures similar to those reported by Mitsuhashi but with much more detail and they coined the term 'shish-kebab' morphologies (see Fig. 12.13) characterized by a core of (partly) extended chain molecules on which lamellar crystals precipitate (nucleate). In numerous parallel studies by Peterlin<sup>71</sup> and Keller and Odell,<sup>72</sup> substantiated theoretically by Frank<sup>73</sup> and de Gennes,<sup>74</sup> the development of shish-kebab structures in stirred dilute solutions of UHMW-PE was understood. In an elongational flow field, e.g. in vortices in the Couette apparatus, the individual chains will stretch out fully beyond a critical strain rate  $\dot{\epsilon}_{cr}$  and this critical strain rate  $\dot{\epsilon}_{cr}$  depends on the molar mass, scaling with  $M^{-1.5}$ . Consequently, longer chains are more readily extensible. In the case of stirring dilute supercooled solutions of UHMW-PE,



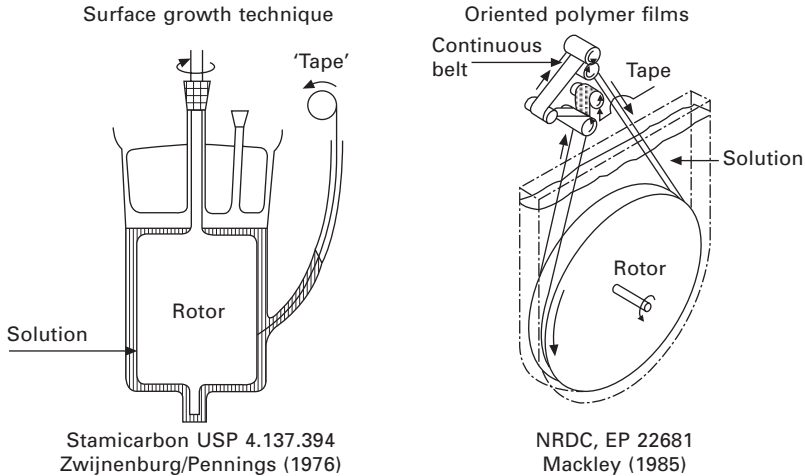
12.13 Structure of 'shish-kebab', courtesy Dr Mary Hill, Bristol University.

the high(er) molar mass tail will be extended and crystallize in supercooled solutions, whereas the lower mass fraction will use the extended-chain core as an (epitaxial) nucleus to form the so-called lamellar overgrowth. The observation of shish-kebab structures has been an important step towards understanding chain-extension in processing supercooled polymers, and also in melt-processing of polyethylenes. However, the presence of lamellar overgrowth is prohibitive for obtaining high-modulus fibres/tapes since only a fraction (the 'shish') of the polymer is (more or less) extended. The maximum  $E$  modulus reported for consolidated 'shish-kebab' structures into films was in the order of 25 GPa.

Pennings continued his work on UHMW-PE at the University of Groningen in the early 1970s and his PhD student Arie Zwijnenburg made a remarkable discovery.<sup>75</sup> In a Couette-type apparatus (see Fig. 12.14) a dilute supercooled solution of UHMW-PE in xylene was stirred slowly and from the surface of the inner rotor a fibrous, tape-like PE structure could be drawn continuously by immersing a seed fibre to the surface of the inner rotor (polyethylene or even cotton or nylon) and subsequently slow pulling. These withdrawn fibrous PE structures possessed an  $E$  modulus > 100 GPa and a tenacity of 3 GPa! This so-called surface growth technique had many disadvantages with respect to homogeneity of the withdrawn PE 'fibre' and the very slow take-up speed (with a lot of breakage) but it proved that UHMW-PE structures could be made experimentally, possessing superior mechanical properties.

The mechanism of the surface-growth technique was not well understood at that time but the explanation came later after the discovery of the solution(gel)-spinning process of UHMW-PE at DSM laboratories in Geleen in 1979: see Fig. 12.14.

Attempts have been made to scale up the surface-growth technique by constructing larger rollers and multiple take-up points from the surface, but these attempts did not materialize into a real process, mainly due to the



12.14 The surface growth technique of Zwijnenburg/Pennings and the rotor technique developed by Mackley.

very slow take-up speeds of the PE filaments in the order of centimetres per minute. Mackley<sup>76</sup> adopted the surface-growth technique for making tapes using a continuous belt (see Fig. 12.14) around the rotor surface. In this way, tapes could be produced possessing an  $E$  modulus of approximately 60 GPa at take-up/roll-off speeds of several metres per minute but this technique also never materialized into an industrial process.

At the end of the 1970s, Smith and Lemstra conducted some solution-spinning experiments at DSM Central Laboratories using UHMW-PE and a simple piston to pump a dilute solution of UHMW-PE, typically 1% w.w. in decalin, through an orifice of diameter approximately 1 mm. The extruded filament was quenched into a water bath and a gel-like filament was obtained, comprising only 1% of UHMW-PE polymer in 99% of solvent! Upon storage of the as-spun/extruded gel-like filaments syneresis occurred as a result of (further) crystallization, a well-known phenomenon in polymer gels. Stretching these gel-like filaments at elevated temperatures, but below the dissolution temperature, resulted in UHMW-PE fibres with properties similar to those found by Zwijnenburg and Pennings using the surface-growth technique, typically with  $E$  modulus > 100 GPa and a tenacity of 3 GPa or more. It was recognized immediately that the major advantage over the surface-growth technique was the possibility of a continuous solution-spinning operation, but the fact that the gel-like filaments were highly stretchable, with draw ratios typically above 50, did not come as a surprise, since it was shown at the same time by the Bristol group of Keller and coworkers that polymer gels were ideal precursors to obtain highly oriented structures by subsequent drawing of gels, albeit that UHMW-PE was not studied.<sup>77</sup> The large amount of solvent was considered to act as a plasticizer during draw.

The remarkable observation was, however, that *even after complete removal* of solvent from the as-spun/extruded gel-filaments, e.g. by extracting the solvent or just by simple evaporation of the solvent decalin, the as-spun/dried UHMW-PE filaments were still ultra-drawable. In conclusion, the solvent does not play a significant role in the drawing process but it does generate a precursor which is highly drawable. Apparently, the constraints which limit the drawability of melt-crystallized UHMW-PE in the solid state, as observed by Ward and coworkers, can be removed by spinning or casting from dilute solutions.

In subsequent studies,<sup>78</sup> the influence of the initial polymer concentration in solution on the drawability of the as-spun/extruded filaments was studied systematically and it was found that the maximum attainable drawability,  $\lambda_{\max}$ , scales with the square root of the inverse of the initial polymer concentration  $\varphi$  as:

$$\lambda_{\max} \sim \varphi^{-0.5} \quad 12.4$$

From these experimental observations it was concluded that the constraints which limit the drawability of UHMW-PE in the solid state are the trapped entanglements which act as semi-permanent crosslinks upon draw. Upon dissolution, the number of entanglements is reduced roughly proportionally to the degree of dilution, i.e. the so-called molar mass between entanglements,  $M_e$ , scales with  $\langle M_e \rangle_{\text{sol.}} \sim \langle M_e \rangle / \varphi$ .

The value of  $\langle M_e \rangle$  in the case of polyethylenes is typically 1200 g/mol as derived from the plateau modulus. In a semi-dilute solution, e.g. 1% w/v, the  $\langle M_e \rangle$  value is increased by a factor of approximately 100.

The maximum draw ratio of an individual random coil chain is given by:

$$\lambda_{\max} \sim L_{\text{ext}} / \sqrt{\langle R^2 \rangle} \quad 12.5$$

In equation 12.5,  $L_{\text{ext}}$  is the length of the fully extended chain and  $\sqrt{\langle R^2 \rangle}$  the end-to-end distance of the random coil, in fact the root-mean-square distance. Since  $L_{\text{ext}}$  scales with  $M$  and  $\sqrt{\langle R^2 \rangle}$  with  $\sqrt{M}$ , the maximum draw ratio scales with  $\sqrt{M}$ .

In the case of an entangled system where entanglements act as physical crosslinks,  $\lambda_{\max}$  scales with  $\sqrt{M_e}$  in analogy with crosslinked rubbers, and consequently:

$$\lambda_{\max} \sim \sqrt{M_e} / \varphi \quad 12.6$$

This simple model of trapped entanglements governing the ultimate drawability is a simplified model but explains many observations very well, such as:

- The dependence of the maximum draw ratio on the initial polymer concentration in solution

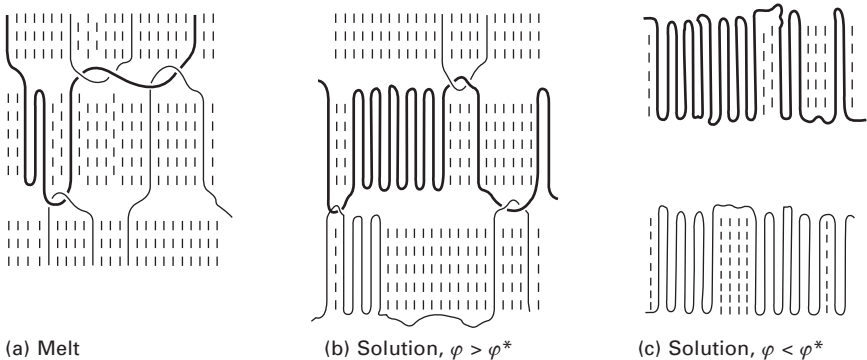
- During slow crystallization from solutions and also melts, as shown by Ward and coworkers, the drawability in the solid state is enhanced. This observation demonstrates convincingly that it is not the morphology/crystallinity that is important for the deformation behaviour in the solid state but trapped entanglements, since during slow crystallization the polymer chains are reeled in on the crystal surface, i.e. crystallization is a disentangling process.

A simple model for the role of trapped entanglements is given in Fig. 12.15, showing the difference in the trapped entanglement density upon crystallization from respectively (a) the polymer melt, (b) semi-dilute solutions and (c) infinitely dilute solutions.

In this simplified model, one could conclude that in the case of dilute solutions, no entanglements are trapped and there is, consequently, no coherence between the individual single crystals, and one would expect no drawability. This is, in fact, contradictory to classical experimental observations made by Statton<sup>79</sup> that sedimented single-crystal mats can also be drawn rather easily into oriented structures. Apparently, there are connections between the individual single crystals which can transfer the applied load during drawing. This will be explained below in Section 12.3.3.

Nowadays, solution(gel)-spinning of UHMW-PE is optimized and commercialized, initially by DSM and its licensees Toyobo (Japan) and Allied (now Honeywell) in the USA. The term solution(gel)-spinning is, in fact, wrong, suggesting that gels are extruded rather than true solutions in the thermodynamic sense. The gel-like filaments are formed after extruding the solutions, upon cooling the as-spun filaments in air or in a quench bath.

Crystallized from:



12.15 Simple entanglement model explaining the difference in entanglement-density upon crystallization from (a) the melt, (b) semi-dilute solutions and (c) dilute solutions, below the overlap concentration  $\varphi^*$ .

Needless to say, extruding dilute solutions of UHMW-PE, in the order of 1% w/v, is commercially not very attractive, in fact the whole process becomes a solvent recovery plant rather than a fibre-producing operation. On a laboratory scale, making homogeneous solutions of UHMW-PE is a tedious process, due to extensive Weissenberg effects. On an industrial scale, twin-screw co-rotating extruders are very efficient machines to make homogeneous semi-dilute solutions of UHMW-PE and the relationship between drawability vs. initial polymer concentration is still valid. In commercial operations the aim is to have a high throughput of polymer, with UHMW-PE concentrations typically of 10% or more, and to compensate for loss of drawability with increasing concentration, multi-stage drawing is performed to obtain ultimate chain alignment in the fibre up to the maximum drawing temperature of 155°C. Above this ultimate drawing temperature, PE transforms from an orthorhombic crystal structure into the hexagonal phase. In the hexagonal phase, the chains can rotate (rotator phase) and cannot sustain, as an ensemble, any load.<sup>80</sup>

It is beyond the scope of this chapter to discuss details of the technology and, moreover, most of the details are not in the public domain or are hidden in the patent literature, but recent publications demonstrate that there is a renewed interest in the formation of shish-kebab structures during spinning semi-dilute solutions of UHMW-PE in order to maximize fibre properties, e.g. the recent work of Toyobo R&D members Murase<sup>81</sup> and Ohta in cooperation with others from the University of Kyoto.<sup>82</sup> It has to be noted that in this case the formation of shish kebabs is studied during shear/extension in semi-dilute solutions and not in dilute solutions as originally pioneered by Pennings (see above). In the case of semi-dilute solutions, shear-induced phase separation occurs according to the model proposed by Murase *et al.*<sup>83</sup> and the phase-separated micro-domains will form the 'shish'. Upon controlling the shish-kebab formation the Toyobo company claims to make PE fibres with tenacities > 6 GPa.

DSM and its licensee Toyobo at the time of writing are by far the biggest producers of high-performance PE fibres based on UHMW-PE, sold under the trade name Dyneema<sup>®</sup>, but Chinese competitors are coming up, e.g. Ningbo Dacheng. The total production volume of high-performance PE fibres is approximately 10 000 tonnes per year but is expanding rapidly in areas such as ropes and in ballistics (helmets, bullet-proof vests). The production volume is relatively small compared with that of other high-performance fibres such as the aramids and carbon fibres, but the profit margins are substantial, especially in niche applications such as fishing lines and medical sutures.

PE fibres never made it in engineering composites due to their highly anisotropic properties and pronounced creep. In fact, creep and the drawing process to make PE fibres are rather similar, albeit at a different time-temperature scale. In the process of ultra-drawing UHMW-PE into extended-

chain structures, the drawing temperature is close to (but always below) the melting temperature which has its maximum at 155°C. In this way, the original folded-chain crystals are transformed finally into chain-extended structures. During creep tests, the temperature is usually lower and the applied load is adjusted to prevent premature breakage but chain slippage occurs similar to the final stage of ultra-drawing. There is no lock-in mechanism in oriented PE fibres despite many attempts to permanently crosslink the PE fibres afterwards or to use copolymers to provide internal barriers for extensive chain slippage. In this respect, UHMW-PE solution(gel)-spun fibres differ from melt-spun PE fibres as discussed earlier in this chapter, the differences probably being related to the high degree of crystallinity and less amorphous parts in the fibre to induce crosslinks, e.g. by using acetylene as used by Ward and coworkers (see above). Consequently, crosslinking of PE fibres, after drawing, proved to be not successful whereas the use of copolymers, e.g. by incorporating a small amount of propylene units in the UHMW-PE chains, has the effect of lowering creep but also makes ultra-drawing more difficult.<sup>84</sup> As a rule of thumb one can state 'easy draw = easy creep'. Despite the problems with creep, UHMW-PE fibres are used as mooring ropes and notably to anchor deep-sea oil rigs, replacing steel wires. The density of PE is lower than that of water, whereas the heavy steel wires can break under their own weight!

In ballistics, UHMW-PE fibres are superior in view of their high strength, high  $E$  modulus and low density (close to but below 1000 kg/m<sup>3</sup>), resulting in a high specific impact energy at a low strain-to-break (*ca.* 4%). The first large-scale use of synthetic fibres in armour protection was of woven nylon 6,6 (also called artificial silk) used in combination with steel plates to produce the 'flak jackets' during World War II. Nylons also possess a high impact energy, approximately the integral of the stress-strain curve, but due to the low  $E$  modulus and the large strain-to-break, the so-called 'trauma' (the maximum deformation without perforation that is seen on the rear side of the protective material) is too large. In this respect, the claim that spider silk is superior in toughness (impact) might well be true, but due to its low  $E$  modulus, similar to nylon fibres, the trauma is also prohibitive for any protective application. The aromatic polyamides possess, due to their high  $E$  modulus, a much better ballistic performance compared with the aliphatic polyamides and the *natural polyamide*, viz. spider silk, but the specific impact (performance by weight) is lower than for PE fibres in view of the rather high density of the aromatic polyamides, *ca.* 1400 kg/m<sup>3</sup>.

The open and patent literature is rather confusing with respect to proper understanding and modelling of ballistic performance. The state-of-the-art is the use of unidirectional (UD) cross-ply laminates. In this laminate, straight fibres are laid in a 0°/90° fibre arrangement and an adhesive resin is used as the matrix (glue). In a UD laminate the energy distribution along the



fibres is fast and efficient because the fibres are completely straight without cross-over points as in woven textiles. Whether PE tapes rather than fibres could perform better in ballistics, in view of their better packing density, has not yet been demonstrated convincingly. In this respect it has to be noted that not only does energy dissipation on impact occur along the fibres, but delamination of the fibre/matrix interfaces can also contribute significantly, as demonstrated by nature in the design of shells.

### 12.3.2 Solvent-free processing routes for UHMW-PE

The main disadvantage of the solution(gel)-spinning route is the use of a large amount of solvent in processing UHMW-PE, typically >90% of solvent which is needed to obtain:

- spinnability (low viscosity to make fine-denier yarns), and
- the required disentangled state for high drawability.

Taking for granted that entanglements play a dominant role in ultra-drawing, the ultimate question is: 'can disentangled UHMW-PE (precursors) be generated directly in the reactor, i.e. during polymerization?' UHMW-PE is usually made in a polymerization reactor at relatively low temperatures (to obtain a high molar mass) using supported Ziegler–Natta catalyst systems.

The structure and morphology of so-called virgin, i.e. as-polymerized or nascent, crystallizable polymers has been a topic since the 1960s. Upon polymerization in dilute and supercooled solutions, which is the case in the synthesis of high molar mass polyethylenes (relatively low polymerization temperatures), the growing polymer chain will tend to crystallize since it experiences a 'cold environment', and depending on the number of active sites on the surface of the catalyst and the local reaction temperature (which is not necessarily the same as the overall temperature in the reactor), the individual chain might crystallize before encountering neighbouring chains. Hence the ideal situation could be reached, of obtaining completely disentangled UHMW-PE reactor powders.

In a series of papers, Chanzy *et al.*<sup>85,86</sup> describe how nascent UHMW-PE powder consists partly of extended-chain crystals, based on a morphology study (electron microscopy) and because of the high melting temperature, in the order of 140–142°C. It was demonstrated by Smith *et al.*<sup>87</sup> that UHMW-PE powders obtained by polymerizing ethylene at low temperature and consolidated into films *below* the melting temperature could be ultra-drawn into high-modulus tapes with  $E$  modulus > 100 GPa, and these films are ultra-drawable. This proves the concept that solvent-free routes to produce oriented PE structures directly from UHMW-PE reactor powders are feasible in principle.

The exceptionally high melting temperature of UHMW-PE reactor powders, in the order of 142–144°C, to be compared with 135°C for melt-crystallized and solution-crystallized (UHMW) polyethylenes, was used as evidence that during low temperature polymerizations the growing chains at the catalyst surface crystallize as extended-chain crystals. In fact, these high melting temperatures are close to the so-called equilibrium melting temperature  $T_m^0$  of polyethylene which is reported to be 145.5°C (or even lower, 141.5°C, depending on whom to believe) and has its parallel in similar high melting points observed by Wunderlich *et al.*<sup>88</sup> for chain-extended PE crystals obtained by high-pressure crystallization. Next to the observation of a high melting point, the nascent UHMW-PE reactor powders do not show any long-range order in SAXS investigations.

In conclusion, the combination of a high melting temperature and absence of long-range order substantiate the assertion that the PE chains in nascent (virgin) UHMW-PE reactor powders are (partly) chain-extended.

In later studies, Tervoort-Engelen and Lemstra<sup>89</sup> studied in more detail the morphology of UHMW-PE reactor powders by electron-microscopy and DSC. The conclusion was that UHMW-PE reactor powders consist of highly meta-stable folded-chain crystals that are randomly present (which explains why no SAXS long-range order can be detected) and that the high melting point is not related to the original morphology but is the result of extensive reorganization processes during heating (in a dynamic calorimeter). The rationale is that the growing chains on the supported catalyst (Ziegler–Natta) will form their own crystal, i.e. mono-molecular crystals, and consequently not only the fold-length is in the order of 10 nm but also the lateral dimensions are limited in size, giving rise to highly meta-stable crystals which are prone to reorganize (thicken) during heating.

The melting point  $T_m$  of folded-chain (lamellar) crystals is given by the well-known Gibbs–Thomson equations:

$$T_m = T_m^0 [1 - 2\sigma_e/(c\rho\Delta H) - 2\sigma/(a\rho\Delta H) - 2\sigma/(b\rho\Delta H)] \quad 12.7$$

In equation 12.7,  $T_m$  is the observed melting point,  $T_m^0$  is the equilibrium melting point,  $\sigma_e$  is the surface energy of the fold plane,  $\sigma$  is the lateral surface free energy, and  $\rho$  is the density. The thickness of the crystal (fold-length) is expressed by  $c$ , and  $a$  and  $b$  are the lateral sizes. Usually  $a$  and  $b \gg c$ , and consequently the last two terms in the parentheses can be ignored. However, in the case of ‘monomolecular crystals’,  $a$  and  $b$  are in the order of the fold length  $c$  and give further rise to the meta-stability of the crystals.

The alternative view on reorganization of metastable UHMW-PE crystals leading to a high (end) melting temperature could not be confirmed by any microscopy experiment. The lamellar thickness of crystals in annealed UHMW-PE powders never surpassed a value of 30 nm as shown by Kurelec *et al.*<sup>90</sup> upon annealing UHMW-PE reactor powders for hours close to the

melting temperature. Extended-chain PE structures have never been observed in as-received or annealed UHMW-PE powders. Microscopy studies (ESEM) revealing fibrillar structures in UHMW-PE reactor powders are misleading in this respect, because these fibrillar structures could well be the result of handling the powders after polymerization (e.g. drying in fluid beds) or the result of chain stretching during the growth of the individual reactor granule (replication mechanism).

The problems related to morphologies induced by factors others than pure competition between chain growth from the catalyst surface vs. crystallization can be overcome by using homogeneous (post)-metallocene type catalysts, e.g. a living catalyst. In this case a dissolved catalyst molecule initiates the growth of the polymer chain in solution. Also homogeneous catalysts in solution produce UHMW-PE powders possessing high melting temperatures, in the order of 142–145°C, and upon consolidation into films, obtained by compression-moulding below the melting temperature, ultra-drawing resulted in tapes with *E* modulus values up to 140 GPa.

In a detailed study, combining solid-state NMR, X-rays (WAXS and SAXS) and (D)DSC, Rastogi and coworkers<sup>91</sup> showed convincingly that the high melting temperature of nascent UHMW-PE is the result of delayed (slow) melting. Annealing at 135°C, the melting point for melt-crystallized and solution-crystallized UHMW-PE for prolonged times resulted in progressive and, at the end, complete melting of UHMW-PE reactor powders.

The ‘mystery’ connected to the high melting temperature of UHMW-PE reactor powders seems to be solved by now and is explained by the arrangement, i.e. the topology, of the long UHMW-PE molecule within the folded-chain crystals. In the case of melt-crystallized UHMW-PE, the topology of the chains in the crystal is not too far away from the conformation in the melt, i.e. random coils. The crystallization process results in folded-chain crystals containing loose loops and non-adjacent re-entry as had been shown already by Fischer<sup>92</sup> in 1979. Fischer showed that in melt-crystallized high molecular weight polyethylenes, the chain conformation can be considered to be close to a random coil, based on neutron-scattering experiments.

In the case of nascent UHMW-PE crystals, the loops are tight and adjacent re-entry prevails as shown by solid-state NMR experiments. Melting upon annealing occurs by cooperative detachment of chain stems from the crystal (lateral) surfaces, which is a time-dependent (and time-consuming) process. Upon fast heating, the melting temperature of nascent UHMW-PE crystals is higher compared with melt-crystallized analogues, due to a larger gain in entropy  $\Delta S$  ( $T_m = \Delta H/\Delta S$ ).

In recent decades, numerous attempts have been made to utilize the concept of nascent (virgin) UHMW-PE reactor powders for the production of high-modulus films and tapes, notably by Porter, Kanamoto and coworkers.<sup>93</sup> The outstanding issue is no longer the structure and morphology of nascent

(virgin) UHMW-PE reactor powders, which is understood by now, but how to obtain the optimum UHMW-PE reactor powders for consolidation into films and subsequent ultra-drawing. In this respect it is interesting to note that the first report on making high-modulus tapes based on nascent UHMW-PE was a classical commercial UHMW-PE grade: Hercules Hifax 1900. Apparently this classical UHMW-PE grade already possessed the favourable characteristics needed for solid-state ultra-drawability.

Nowadays, a multitude of techniques are available to optimize the catalysis and chemistry towards the optimum structure/morphology of nascent UHMW-PE reactor powders. A direct approach is to use modern homogeneous (post) metallocene catalysts, e.g. Mitsui-FI catalyst, to produce UHMW-PE at low temperatures. These catalysts are to some extent 'living' and the molar mass distribution is rather narrow compared with the classical Ziegler–Natta type catalysts that are used in industry. The main disadvantages are the expense of these living homogeneous catalyst systems (1 mole of catalyst produces 1 mole of PE, albeit that, using hydrogen, multiple chains can be made by one catalyst molecule) and notably the occurrence of reactor fouling. The growing PE chains in the supercooled solutions will crystallize but the process of crystallization involves at first a nucleation step. Homogeneous nucleation is rare in polymer systems and, consequently, the long PE chains nucleate on 'hot' surfaces such as the stirrer and reactor walls, the intrinsic disadvantage of a polymerization process initiated by a homogeneous catalyst. Reactor fouling can be overcome by selecting solvents which promote homogeneous nucleation but this leaves another problem, the bulk-density of the generated UHMW-PE reactor powders.

Ideally one produces disentangled UHMW-PE reactor powders on a supported catalyst to generate powder particles which can be handled in an industrial operation (free flowing, high bulk density, etc.). Homogeneous catalyst can be impregnated into a porous support but the danger is that the active chains are in too close proximity and, hence, the growing chains become entangled before crystallization.

At the time of writing, companies operating in the field of UHMW-PE, e.g. Mitsui, Ticona and DSM, are optimizing catalyst systems and polymerization procedures to generate the optimum precursors for solid-state processing into high-modulus products (tapes, films). Not much literature is yet available, neither in the open nor in the patent literature. Kanamoto and coworkers<sup>94</sup> also showed that even with an active Ziegler–Natta heterogeneous catalyst, UHMW-PE reactor powders could be made showing favourable drawing characteristics, albeit that the ethylene (monomer) pressure had to be reduced during polymerization, indicating that the polymerization rate has to be slow to prevent premature entangling.

In conclusion, solid-state processing of UHMW-PE reactor powders with an optimum structure/morphology to enhance subsequent drawability into

chain-extended high-modulus structures could well be an option in the (near) future as an alternative route for the solution(gel)-spinning process. However, there are intrinsic disadvantages such as handling polymer powder particles (flow, uniform distribution, etc.) and solid-state processing below  $T_m$  using expensive devices such as a belt-press to consolidate the reactor powders into coherent films. Last but not least, tapes are produced which possess a similar  $E$  modulus compared with PE fibres based on UHMW-PE. Whether tapes based on UHMW-PE perform better in ballistics has still to be seen. The strength is lower but the packing density of tapes in UD-laminates is favourable compared with fibres (see Fig. 12.16).

### 12.3.3 On the borderline between solid and melt

In the previous two sections, the emphasis was on how to get disentangled UHMW-PE structures as precursors for subsequent ultra-drawing. Using a solvent (solution-spinning) is a straightforward method and solid-state processing, using optimum polymerization conditions, is a more sophisticated approach.

The next question to be addressed is ‘what happens if (completely) disentangled UHMW-PE is heated into the melt?’ Is it possible to generate an initially disentangled UHMW-PE melt possessing a lower viscosity (due to lack of entanglements) which is favourable for both processing and subsequent drawing?

This question was already being addressed at the start of the solution(gel)-spinning process in the early 1980s and expectations were running high, since it was expected that disentangled long chains need a relatively long time to become (completely) entangled again. The reptation concept of de Gennes, i.e. that chains follow their own contour length with a characteristic reptation or disengagement time scaling with  $M^3$ , substantiates a novel approach to processing UHMW-PE starting from disentangled UHMW-PE. Based on available self-diffusion coefficients measured with neutron-scattering on deuterated PE samples, one can calculate that for very high molar mass PE, the time it takes for re-entangling can be from a few minutes up to several hours.

All attempts in the 1980s and 1990s to utilize disentangled UHMW-PE precursors for melt-processing failed.<sup>95</sup> In fact, based on extensive rheological experiments, measuring the characteristic rheological values ( $G'$ ,  $G''$ ) upon



12.16 Packing density in UD laminates, tapes vs. fibres.

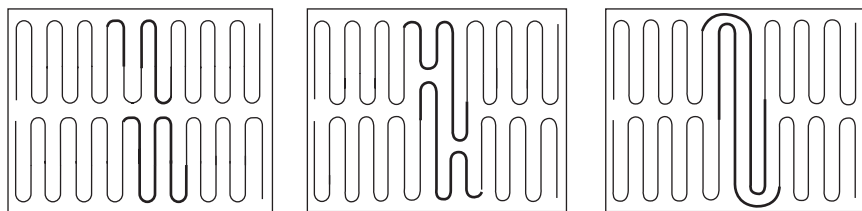
heating of solution-cast or nascent UHMW-PE powders into the melt, no memory effect was observed at all. Heating melt-crystallized, solution-cast or compacted UHMW-PE powders (films) from the solid state into the melt showed that several very different samples all possess the same (high) melt-viscosity and the modulus in the melt ( $G'$ ) was *ca.* 2 MPa, giving a value for  $\langle M_e \rangle$  of *ca.* 1200 g/mol. Upon cooling from the melt, i.e. recrystallization, the favourable drawing characteristics are lost!

Apparently, our notion of chain entanglements (interhooked chains) needs some revision. It is clear that any absence of a memory effect, reflecting the original disentangled state, can disappear in a very short timescale, at least in the time which is needed to thermally equilibrate the sample in the rheometer, suggesting that complete entangling has occurred. It has to be taken into account that during melting, especially melting of nascent crystals (low entropy), there is an entropy gain on melting, in fact the (adjacent) long-chain molecules change from a compact conformation into a random coil conformation. This process is very fast and has been referred to as chain-explosion in the literature, based on neutron-scattering experiments by Barham and Sadler<sup>96</sup> and explained theoretically by de Gennes.<sup>97</sup> Nevertheless, a fast interpenetration of individual chains does not necessarily imply full entangling. In the meantime various 'romantic' models have been proposed for chain entanglements.<sup>98</sup>

In order to dwell upon future possibilities with respect to processing UHMW-PE on the 'borderline between solid and melt', one has to focus on the fate of an individual molecule rather than on an ensemble of chains. The chain dynamics of individual chains can be probed to some extent, combining various techniques such as solid-state NMR, neutron-scattering, laser-Raman spectroscopy and microscopy.

#### *Chain mobility below the melting temperature*

It has been shown by Rastogi *et al.*<sup>99</sup> that stacked lamellar crystals, obtained by careful sedimentation from dilute solutions, can double their thickness upon annealing below the melting temperature. This intriguing phenomenon



12.17 Sliding diffusion resulting in lamellar doubling.

is explained by sliding diffusion of molecular stems penetrating surrounding crystals: see Fig. 12.17.

The important observation is that these 'doubled lamellar crystals' still possess ultra-drawability, which is understandable in view of a simple entanglement model since in the process of doubling no additional entanglements are created as a result of sliding diffusion (see Fig. 12.17). The phenomenon of lamellar doubling might well explain the classical experiments of Statton on the drawing of single-crystal mats (see above). Sliding diffusion, i.e. interpenetration of molecular stems, provides cohesion between the individual lamellar crystals, enabling the stress to be transmitted upon draw.

### *Chain mobility upon slow melting*

Upon heating above the melting point and subsequent recrystallization, the drawability is lost as discussed above (chain explosion), but it was shown recently by Lippits<sup>100</sup> that upon (very) slow and controlled heating of UHMW-PE reactor powder, the *G* modulus of the resulting melt remained at a much lower level than upon fast heating. Rastogi *et al.*<sup>101</sup> attributed this low(er) melt-viscosity to a so-called 'heterogeneous' melt in which the molecules are partly entangled, from both ends, and partly remain disentangled, the central part of the molecule being related to slow melting from the lateral surface of mono-molecular crystals. Upon cooling, i.e. recrystallization, the drawability in the solid state remained substantially higher than upon crystallization.

In theory, a novel route could be envisaged based on the following steps:

1. Polymerizing disentangled UHMW-PE, nascent powder.
2. Slowly heating into the 'non-equilibrium' melt and shaping into a fibre or tape in the molten state.
3. Optimized drawing (multi-stage) into high-modulus structures (chain-extension) in the semi-solid state.

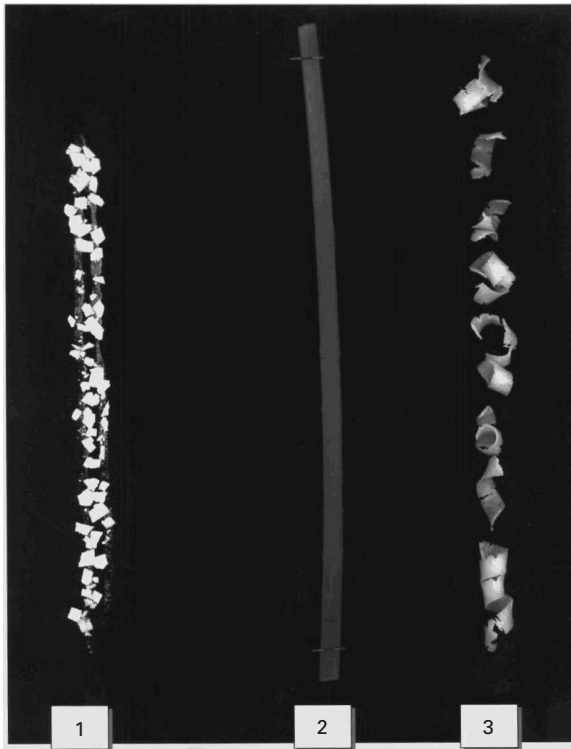
This proposed route, however, is of academic interest for the moment, since the controlled slow heating (0.25°C/min) and melting step has to be controlled precisely to avoid overheating and premature 'chain explosion' and subsequent loss of drawability upon recrystallization.

Nevertheless, the experiments attempting to follow the dynamics of individual chains upon annealing below the melting temperature and/or on passing slowly through the melting regime provide a stimulus to addressing the individual chain during processing and drawing rather than an ensemble of many chains. Up to now, the basic concept was to disentangle an ensemble of chains via dissolution or to prevent premature entangling by controlled

low temperature polymerization, i.e. the disentangled nascent UHMW-PE powder. In subsequent processing steps, drawing and/or compacting/drawing, care is taken to prevent re-entangling.

Focusing on an individual chain, in particular very long chains such as we are dealing with in the case of UHMW-PE, the first question is ‘why can UHMW-PE crystallize so fast?’ The current answer is that upon crystallization the reeling-in of an individual chain can be relatively fast. Reeling-in of long chains on the crystal surface implies reeling out from the entangled melt at relatively high speed. Another way of reeling out long PE chains is in contact with a (metal) surface as encountered during extrusion. One of the authors (PJJ) observed already some 20 years ago that UHMW-PE powder can be extruded into seemingly homogeneous strands in a narrow temperature region, i.e. 150–155°C: see Fig. 12.18. Increasing the extrusion temperature resulted in extensive melt-fracture.

At the time of this observation, the explanation for this peculiar phenomenon was that in the narrow temperature window, around 150°C, UHMW-PE entered into the semi-solid hexagonal phase, but that could not be proved



12.18 Extrusion of UHMW PE (1) below the melting point, (2) between 145 and 155°C and (3) above 155°C.



experimentally. It is more likely that on the interface between UHMW-PE and the metal surface of the extruder barrel, individual chains are reeled out, providing an orientation layer facilitating flow. Time will show whether addressing long-chain molecules individually, e.g. extruding UHMW-PE powders in a specific temperature window followed by multi-stage drawing, will result in the ultimate solvent-free processing route for UHMW-PE fibres and tapes.

## 12.4 References

1. Treloar L R G (1960), Calculations of elastic moduli of polymer crystals: I. Polyethylene and nylon 66, *Polymer*, **1**, 95–103.
2. Andrews J M and Ward I M (1970), The cold drawing of high density polyethylene, *J. Mater. Sci.*, **5**, 411–417.
3. Fatou J G and Mandelkern L (1965), Effect of molecular weight on fusion of polyethylene, *J. Phys. Chem.*, **69**, No. 2, 417–428.
4. Way J L, Atkinson J R and Nutting J (1974), The effect of spherulite size on the fracture morphology of polypropylene, *J. Mater. Sci.*, **9**, 293–299.
5. Barham P J and Keller A (1976), A study on the achievement of high-modulus polyethylene fibres by drawing, *J. Mater. Sci.*, **11**, 27–35.
6. Capaccio G, Wilding M A, Longman G W and Ward I M (1978), Morphology of bulk-crystallized linear polyethylene: Study by small-angle X-ray scattering, Raman spectroscopy and gel-permeation chromatography, *J. Macromol. Sci. Phys.*, **B15**, 381–407.
7. Capaccio G and Ward I M (1973), Properties of ultra-high modulus linear polyethylenes, *Nature Phys. Sci.*, **243**, 130, 143.
8. Capaccio G and Ward I M (1974), Preparation of ultra-high modulus linear polyethylenes; effect of molecular weight and molecular weight distribution on drawing behaviour and mechanical properties, *Polymer*, **15**, 233–238.
9. Capaccio G and Ward I M (1975), Ultra-high-modulus linear polyethylene through controlled molecular weight and drawing, *Polym. Eng. Sci.*, **15**, 219–224.
10. Capaccio G and Ward I M (1975), Effect of molecular weight on the morphology and drawing behaviour of melt crystallized linear polyethylene, *Polymer*, **16**, 239–243.
11. Capaccio G, Crompton T A and Ward I M (1976), The drawing behaviour of linear polyethylene. I. Rate of drawing as a function of polymer molecular weight and initial thermal treatment, *J. Polym. Sci., Polym. Phys. Ed.*, **14**, 1641–1658.
12. Capaccio G, Chapman T J and Ward I M (1975), Preparation of ultra-high modulus linear polyethylenes: effect of initial crystallisation conditions, *Polymer*, **16**, 469.
13. Capaccio G, Crompton T A and Ward I M (1976), Ultra-high modulus polyethylene by high temperature drawing, *Polymer*, **17**, 644–645.
14. Capaccio G, Crompton T A and Ward I M (1980), Drawing behaviour of linear polyethylene. II. Effect of draw temperature and molecular weight on draw ratio and modulus, *Pol. Sci. Pol. Phys. Edn*, **18**, 301–309.
15. Wilding M A and Ward I M (1984), Creep behaviour of ultra high modulus polyethylene: Influence of draw ratio and polymer composition, *J. Polym. Sci., Polym. Phys. Ed.*, **22**, 561–575.

16. Kanamoto T, Tsuruta A, Tanaka K, Takeda M and Porter R S (1983), On ultra-high tensile modulus by drawing single crystal mats of high molecular weight polyethylene, *Polym. J.*, **15**, 327–329.
17. Smith J B, Manuel A J and Ward I M (1975), Broadline NMR studies of ultra-high modulus polyethylenes, *Polymer*, **16**, 57–65.
18. Allison S W, Pinnock P R and Ward I M (1966), The cold drawing of polyethylene terephthalate, *Polymer*, **7**, 66–69.
19. Wilding M A and Ward I M (1978), Tensile creep and recovery in ultra-high modulus linear polyethylenes, *Polymer*, **19**, 969–976.
20. Wilding M A and Ward I M (1981), Creep and recovery of ultra high modulus polyethylene, *Polymer*, **22**, 870–876.
21. Wilding M A and Ward I M (1981), Routes to improved creep behaviour in drawn linear polyethylene, *Plast. Rub. Proc. Appl.*, **1**, 167–172.
22. Wilding M A and Ward I M (1984), Creep behaviour of ultra high modulus polyethylene: Influence of draw ratio and polymer composition, *J. Polym. Sci., Polym. Phys. Ed.*, **22**, 561–575.
23. Sherby O D and Dorn J E (1958), Anelastic creep of polymethyl methacrylate, *J. Mech. Phys. Solids*, **6**, 145–162.
24. Bauwens-Crowet C and Bauwens J C (1983), Effect of thermal history on the tensile yield stress of polycarbonate in the  $\beta$  transition range, *Polymer*, **24**, 921–924.
25. Roetling J A (1965), Yield stress behaviour of polymethylmethacrylate, *Polymer*, **6**, 311–317.
26. Capaccio G, Crompton T A and Ward I M (1984), The drawing behaviour of polyethylene copolymers, *J. Polym. Sci., Polym. Phys. Ed.*, **22**, 475–484.
27. Woods D W, Busfield W K and Ward I M (1987), Improved mechanical behaviour in ultra-high modulus polyethylenes by controlled cross-linking, *Plast. Rub. Proc. Appl.*, **5**, 157–164.
28. Jones R A, Salmon G A and Ward I M (1993), Radiation induced crosslinking of polyethylene in the presence of acetylene: a gel fraction, UV-visible, and ESR spectroscopy study, *J. Polym. Sci., Part B, Polym. Phys.*, **31**, 807–819.
29. Jones R A, Salmon G A and Ward I M (1994), An infra-red spectroscopic study of changes in unsaturation resulting from irradiation of isotropic and uniaxially oriented polyethylene films in the presence of acetylene, *J. Polym. Sci., Part B: Polym. Phys.*, **32**, 469–479.
30. Jones R A, Taylor D J R, Stepto R F T and Ward I M (1996), Computer modeling of the formation of radical pairs in amorphous high density polyethylene (HDPE), *J. Polym. Sci., Part B: Polym. Phys.*, **34**, 901–908.
31. Jones R A, Ward I M, Taylor D J R and Stepto R F T (1996), Reactions of amorphous PE radical-pairs in vacuo and in acetylene: a comparison of gel fraction data with Flory–Stockmayer and atomistic modelling analyses, *Polymer* **37**, 3643–3657.
32. Jones R A, Groves D J and Ward I M (1997), An investigation into the relationship between ‘gel-effective’ and total numbers of crosslinks in irradiated LLDPE, *Polym. In.*, **44**, 300–310.
33. Flory P J (1945), Tensile strength in relation to molecular weight of high polymers, *J. Amer. Chem. Soc.*, **67**, 2048–2050.
34. Smith P, Lemstra P J and Pijpers P L (1982), Tensile strength of highly oriented polyethylene. II. Effect of molecular weight distribution, *J. Polym. Sci., Polym. Phys. Ed.*, **20**, 2229–2241.

35. Smith P and Lemstra P J (1981), Tensile strength of highly oriented polyethylene, *J. Polym. Sci., Polym. Phys. Ed.*, **19**, 1007–1009.
36. Wu W and Black W B (1979), High strength polyethylene, *Polym. Eng. Sci.*, **19**, 1163–1169.
37. Hallam M A, Cansfield D L M, Pollard G and Ward I M (1986), A study of the effect of molecular weight on the tensile strength of ultra-high modulus polyethylenes, *J. Mater. Sci.*, **21**, 4199–4205.
38. Hallam M A, Pollard G and Ward I M (1987), Relationship between tensile strength and molecular weight of highly drawn polyethylenes, *J. Mater. Sci. Lett.*, **6**, 975–976.
39. Termonia Y, Greene W R and Smith P (1986), Tensile strength of oriented filaments of binary mixtures of high and low molecular weight polyethylenes, *Polym. Commun.*, **27**, 295–298.
40. Amornsakchai T, Cansfield D L M, Jawad S A, Pollard G and Ward I M (1993), The relation between filament diameter and fracture strength for ultra-high-modulus polyethylene fibres, *J. Mater. Sci.*, **28**, 1689–1698.
41. Smook J, Hamersma W and Pennings A J (1984), The fracture process of ultra-high strength polyethylene fibres, *J. Mater. Sci.*, **19**, 1359–1373.
42. Bastiaansen C W M (1992), Tensile strength of solution-spun, ultra-drawn ultra high modulus weight polyethylene fibres, 1. Influence of fibre diameter, *Polymer* **33**, 1653–1655.
43. Barham P J and Arridge R G C (1977), A fiber composite model of highly oriented polyethylene, *J. Polym. Sci., Polym. Phys. Ed.*, **15**, 1177.
44. Gibson A G, Davies G R and Ward I M (1978), Dynamic mechanical behaviour and longitudinal crystal thickness measurements on ultra-high modulus linear polyethylene: a quantitative model for the elastic modulus, *Polymer*, **19**, 683–694.
45. Sadler D M and Barham P J (1970), Structure of drawn fibres: 3. Neutron scattering studies of polyethylene fibres drawn beyond the neck, *Polymer* **31**, 46–50.
46. Clements J, Jakeways R and Ward I M (1978), Lattice modulus and crystallite thickness measurements in ultra-high modulus linear polyethylene, *Polymer*, **19**, 639–644.
47. Capaccio G and Ward I M (1982), Shrinkage, shrinkage force and the structure of ultra high modulus polyethylenes, *Colloid Polym. Sci.*, **260**, 46–55.
48. Amornsakchai T, Olley R H, Bassett D C, Al-Hussein, M O M, Unwin A P and Ward I M (2000), On the influence of initial morphology on the internal structure of highly drawn polyethylene, *Polymer*, **41**, 8291–8298.
49. Orchard G A J, Davies G R and Ward I M (1984), The thermal expansion behaviour of highly oriented polyethylene, *Polymer*, **25**, 1203–1219.
50. Clements J, Capaccio G and Ward I M (1979), Melting behaviour of ultra high modulus linear polyethylene, *J. Polym. Sci.: Polym. Phys. Ed.*, **7**, 693–703.
51. Clements J and Ward I M (1982), Superheating effects on the melting of ultra-high modulus linear polyethylene, *Polymer*, **23**, 935–936.
52. Farrow G (1996), Processing, *Properties and Applications of the High Performance Melt Spun Polyethylene Fibres*, ACS Meeting, New Orleans, March.
53. Ladizesky N H and Ward I M (1983), A study of the adhesion of drawn polyethylene fibre/polymeric resin systems, *J. Mater. Sci.*, **18**, 533–544.
54. Ladizesky N H and Ward I M (1989), The adhesion behaviour of high modulus polyethylene fibres following plasma and chemical treatment, *J. Mater. Sci.*, **24**, 3763–3773.

55. Nardin M and Ward I M (1987), Influence of surface treatment on adhesion of polyethylene fibres, *Mater. Sci. Technol.*, **3**, 814–826.
56. Tissington B, Pollard G and Ward I M (1991), A study of the influence of fibre/resin adhesion on the mechanical behaviour of ultra-high-modulus polyethylene fibre composites, *J. Mater. Sci.*, **26**, 82–92.
57. Woods D W and Ward I M (1993), Study of the oxygen treatment of high modulus polyethylene fibres, *Surface and Interface Analysis*, **20**, 385–392.
58. Ladizesky N H and Ward I M (1995), A review of plasma treatment and the clinical application of polyethylene fibres to reinforcement of acrylic resins, *J. Mater. Sci., Mater. Med.*, **6**, 497–504.
59. Hild D N and Schwartz P (1992), Plasma-treated ultra-high strength polyethylene fibers. Part II. Increased adhesion to poly(methyl methacrylate) *J. Adhesion Sci. Technol.*, **6**, 897–917.
60. Li Z F and Netravali A N (1992), Surface modification of UHSPE fibers through allylamine plasma deposition. II. Effect on fiber and fiber/epoxy interface, *J. Appl. Polym. Sci.*, **44**, 333–346.
61. Ladizesky N H and Ward I M (1986), Ultra high modulus polyethylene fibre composites: I – The preparation and properties of conventional epoxy resin composites, *Comp. Sci. Technol.*, **26**, 129–164.
62. Ladizesky N H, Sitepu M and Ward I M (1986), Ultra high modulus polyethylene fibre composites: II – Effect of resin composition on properties, *Comp. Sci. Technol.*, **26**, 169–183.
63. Ladizesky N H and Ward I M (1986), Ultra high modulus polyethylene fibre composites: III – An exploratory study of hybrid composites, *Comp. Sci. Technol.*, **26**, 199–224.
64. Hine P J, Ward I M, Olley R H and Bassett D C (1993), The hot compaction of high modulus melt spun polyethylene fibres, *J. Mater. Sci.*, **28**, 316–324.
65. Olley R H, Bassett D C, Hine P J and Ward I M (1993), Morphology of compacted polyethylene fibres, *J. Mater. Sci.*, **28**, 1107–1112.
66. Ward I M and Hine P J (2004), The science and technology of hot compaction, *Feature Article, Polymer*, **45**, 1413–1427.
67. Hine P J and Ward I M (2005), High stiffness and high impact strength polymer composites by hot compaction of oriented fibers and tapes, Chapter 16 of *Mechanical Properties of Polymers Based on Nanostructure and Morphology*, edited by Michler G H and Balta-Calleja F J, Taylor and Francis, London.
68. Zwick M (1965), Patent application NL 6501248.
69. Mitsuhashi S (1963), *Bull. Text. Res. Inst.*, **66**, 1.
70. Pennings A J, van der Mark J M A and Kiel A M (1965), Fractionation of polymers by crystallization from solution, III. On the morphology of fibrillar polyethylene crystals grown in solution, *Kolloid-Z. u. Z. Polymere*, **205**, 160–162.
71. Peterlin A J (1966), *Pure Appl. Chem.*, **12**, 563–568.
72. Keller A and Odell J A (1985), *Colloid Polym. Sci.*, **263**, 181–201.
73. Frank F C (1970), *Proc. Roy. Soc. London ser. A*, **319**, 127–136.
74. De Gennes P G (1974), *J. Chem. Phys.*, **60**, 15–18.
75. Zwijnenburg A (1978), PhD thesis, University of Groningen, The Netherlands.
76. Mackley M (1985), European Patent 22687.
77. Lemstra P J, Cudby M and Keller A (1978), Gelation crystallization of poly(vinyl chloride), *J. Polym. Sci., Polym. Phys. Ed.*, **16**, 1507–1514.
78. Smith P, Lemstra P J and Booij H C (1981), Ultradrawing of high-molecular-weight

- polyethylene cast from solution. 2: Influence of initial polymer concentration, *J. Polym. Sci.: Polym. Phys. Ed.*, **19**, 877–888.
79. Statton W O (1967), Coherence and deformation of lamellar crystals after annealing, *J. Appl. Phys.*, **38**, 4149–4153.
  80. Lemstra P J, van Aerle N A M J and Bastiaansen C W M (1987), Chain-extended polyethylene, *Polym. J.*, **19**, 85–97.
  81. Murase H (2005) Flow-induced phase separation and crystallization in semidilute solutions of ultrahigh molecular weight polyethylene, PhD thesis, Kyoto University, Japan.
  82. Murase H, Kume T, Hashimoto T and Ohta Y (2005), Time evolution of structures under shear-induced phase separation and crystallization in semidilute solution of ultrahigh molecular weight polyethylene, *Macromolecules*, **38**, No. 21, 8719–8728.
  83. Murase H, Kume T, Hashimoto T and Ohta Y (2005), Shear-induced structures in semidilute solution of ultrahigh molecular weight polyethylene at temperature close to equilibrium dissolution temperature, *Macromolecules*, **38**, No. 15, 6656–6665.
  84. Bastiaansen C W M (1992), PhD thesis, Eindhoven University of Technology, The Netherlands.
  85. Chanzy H D, Revol J F, Marchessault R H and Lamande A (1973), Nascent structures during the polymerization of ethylene, *Kolloid-Z. u. Z. Polymere*, **251**, 563–576.
  86. Chanzy H D and Marchessault R H (1974), Nascent structures during the polymerization of ethylene, *Colloid Polym. Sci.*, **252**, 8–14.
  87. Rotzinger B P, Chanzy H D and Smith P (1989), High strength/high modulus polyethylene; synthesis and processing of ultra-high molecular weight powders, *Polymer*, **30**, 1814–1819.
  88. Prime R B, Wunderlich B and Melillo L (1969) Thermal analysis and electron microscopy of the melting process in polyethylene, *J. Polym. Sci. A-2*, **7/12**, 2091–2097.
  89. Tervoort-Engelen Y M T and Lemstra P J (1991), Morphology of nascent ultra-high molecular weight polyethylene, chain-extended vs. chain-folded crystals, *Polym. Commun.*, **32/11**, 343–345.
  90. Kurelec L, Rastogi S, Meier R and Lemstra P J (2000), On the borderline between solid and melt, phase transformations in nascent ultra-high molecular weight polyethylene reactor powder at elevated pressure as revealed by *in-situ* Raman spectroscopy, *Macromolecules*, **33**, 5593–5601.
  91. Lippits D R, Rastogi S and Höhne G W H (2006), Melting kinetics in polymers, *Phys. Rev. Lett.*, **96**, 218303: 1–4.
  92. Stamm M, Fischer E W and Dettenmaier M (1979), Chain conformation in the crystalline state by means of neutron scattering methods, *Faraday Discussions of the Chemical Society*, 263–278.
  93. Porter R S and Kanamoto T (2004), *Polym. Eng. Sci.*, **34**, 266–268.
  94. Samo H, Iwanami Y, Matsuura K, Yokoyama S and Kanamoto T (2001), Ultradrawing of ultrahigh molecular weight polyethylene reactor powders prepared by highly active catalyst system, *Polymer*, **42**, 5859–5864.
  95. Bastiaansen C W M (1992), Oriented structures based on flexible polymers, PhD thesis, Eindhoven University of Technology, The Netherlands.
  96. Barham P and Sadler D (1991), A neutron scattering study of the melting process of polyethylene crystals, *Polymer*, **32**, 939–944.

97. De Gennes P G (1995), Explosion à la fusion, *C.R. Acad. Sci. Paris II*, **321**, 363–365.
98. Yamazaki S, Fangming G, Watanabe K, Okada K, Toda A and Hikosaka M (2006), Two- step formation of entanglement from disentangled polymer detected by using nucleation rate, *Polymer*, **47**, 6422–6428.
99. Rastogi S, Spoelstra A B, Goossens J G P and Lemstra P J (1997), Chain mobility in polymer systems: on the borderline between solid and melt. 1. Lamellar doubling during annealing of polyethylene, *Macromolecules*, **30**, 7880–7889.
100. Lippits D (2006), PhD thesis, Eindhoven University of Technology, The Netherland.
101. Rastogi S, Lippits D R, Peters C W M, Graf R, Yao Y and Spiess H W (2005), Heterogeneity in polymer melts from melting of polymer crystals, *Nature Materials*, **4**, No. 8, 635–641.

## Structure and properties of aramid fibres

---

S VAN DER ZWAAG, Technical University Delft,  
The Netherlands

**Abstract:** This chapter describes the concepts behind poly(*p*-phenylene terephthalamide) aramid fibres and the technological translations of the concept into commercially attractive high performance fibres. The fibres are characterised by a unique microstructure determined by the chemistry of the polymer and the properties of the spindope as well as the spinning and further processing conditions. The correlation between the nature of the molecule as well as the microstructure and some principal mechanical properties are explained.

**Key words:** aramid fibres, fibre spinning, microstructure, modulus, strength.

### 13.1 Introduction

When designing high-modulus, high-strength polymeric fibres the challenge is relatively straightforward: the molecules should be as slender as possible without bulky side groups, the molecules should have a sufficiently high number of intermolecular interactions per single monomer unit, and the molecules should be aligned to a high degree of perfection along the fibre axis, preferably without chain entanglements or other local distortions. To reach this aim basically two routes are available: either starting with long flexible molecules and designing a spinning process in which the unavoidable entanglements and other regions of molecular disorder are removed by a carefully controlled drawing process (see Chapter 12: UHMW PE fibres), or starting with shorter 'rigid rod' molecules and making use of their natural high packing density and high degree of local molecular orientation characteristic of liquid crystalline solutions (this chapter, Chapters 14, 16 and Chapter 5 of *Handbook of Textile Fibre Structure, Volume II*). Depending on the nature and strength of the intermolecular bonds, sufficient molecular mobility to macroscopically orient the molecules in the desired direction may be obtained by raising the temperature or by using a solvent in which to dissolve the molecules.

The poly(*p*-phenylene terephthalamide) PpPTA aramid fibres to be described in more detail in this chapter are based on an aromatic, rigid rod molecule with the ability to form two lateral hydrogen bonds per monomer unit. They are an excellent example of the latter approach to designing high-modulus, high-strength polymeric fibres. Due to the aromatic amide structure and the high degree of lateral bonding, not only a high strength but also a good chemical resistance and an excellent thermal stability can be expected. In

this chapter, some details of the actual aramid fibre production process are described, while linking each process step to the intended microstructure and linking the microstructure realised to the final (mechanical) properties.

### 13.2 Chemistry of aramid fibres

The poly(*p*-phenylene terephthalamide) PpPTA molecule is synthesised from two readily available monomers, 1,4-phenylenediamine (PPD) and terephthaloyl dichloride (TDC), using a complex solvent consisting of NMP (*N*-methyl pyrrolidone) and  $\text{CaCl}_2$ . The development of this polymerisation process and some of its less attractive alternatives have been described in [Vol89]. The polymerisation is shown schematically in Fig. 13.1.

Since the polymer is synthesised via a polycondensation route, the degree of polymerisation is relatively low and special attention should be taken to ensure a sufficient degree of polymerisation. For industrially produced PpPTA the number-averaged molecular weight is just below 20 000, corresponding to a degree of polymerisation of around 80 and a chain length of 110 nm. Polydispersity of the molecule varies between 2 and 3 depending on the stirring rate during polymerisation, the temperature and the purity of the starting materials. For PpPTA in concentrated sulphuric acid the intrinsic viscosity  $\eta$  correlates with the weight average molecular weight  $M_w$ , as [Sch 76]

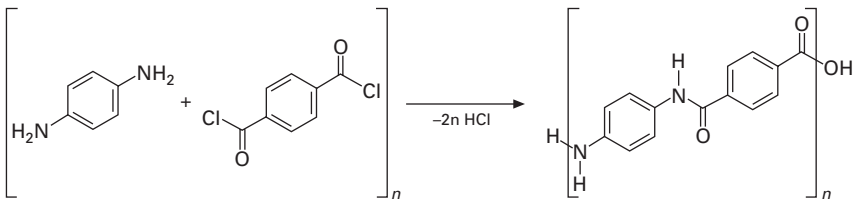
$$\eta = 7.9 \times 10^{-5} M_w^{1.06} \quad (\text{for } M_w > 12000)$$

$$\eta = 2.8 \times 10^{-7} M_w^{1.70} \quad (\text{for } M_w < 12000)$$

For good fibre properties the inherent viscosity should exceed a value of 4 dL/g. After polymerisation the polymer is washed, dried and crushed leading to a fine yellow granular material.

### 13.3 Relationship between spinning conditions and resulting microstructure

Given the rigid rod nature of the polymer and the strong intermolecular bonds between the molecules, the polymer has a very high melting point,



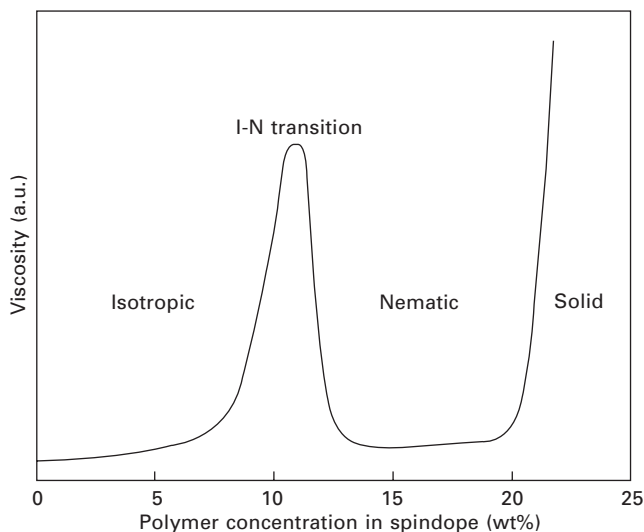
13.1 Schematic diagram of the polymerisation of PpPTA from its monomers TDC and PPD.



even beyond its decomposition temperature. This clearly prohibits thermally induced molecular mobility as the route to aligning the molecules along a fibre and therefore excludes melt spinning processes for the production of aramid fibres. Hence solvent-based spinning is the natural route for making aramid fibres.

The number of solvents available to dissolve PpPTA to significant levels is limited, with sulphuric acid at concentrations  $>99.5\%$  being the most widely used because of its low price and high maximum solubility for PpPTA. The viscosity plot of the PpPTA–H<sub>2</sub>SO<sub>4</sub> mixtures as a function of the polymer concentration shows two domains (Fig. 13.2).

There is a low concentration region of up to 10% where the viscosity increases more or less linearly with polymer concentration. It is followed by a second region between 13 and 20 wt% in which the viscosity is relatively low and more or less constant. In the first concentration regime the solution is in an isotropic state, i.e. the aramid molecules have no molecular orientation correlation, while in the second concentration regime the solution is in a liquid crystalline nematic state, i.e. the aramid molecules have a high local axial orientation correlation but no positional correlation. At a concentration of about 20 wt% and a temperature of 80°C the solution has reached its maximum solubility while being in a more or less stable liquid state. At higher temperatures the spindope is unstable and polymer degradation occurs rapidly. To minimise the amount of sulphuric acid handling, the polymer concentration in the spindope is kept as high as possible while staying clear of the solubility limit, as undissolved particles have a very detrimental effect

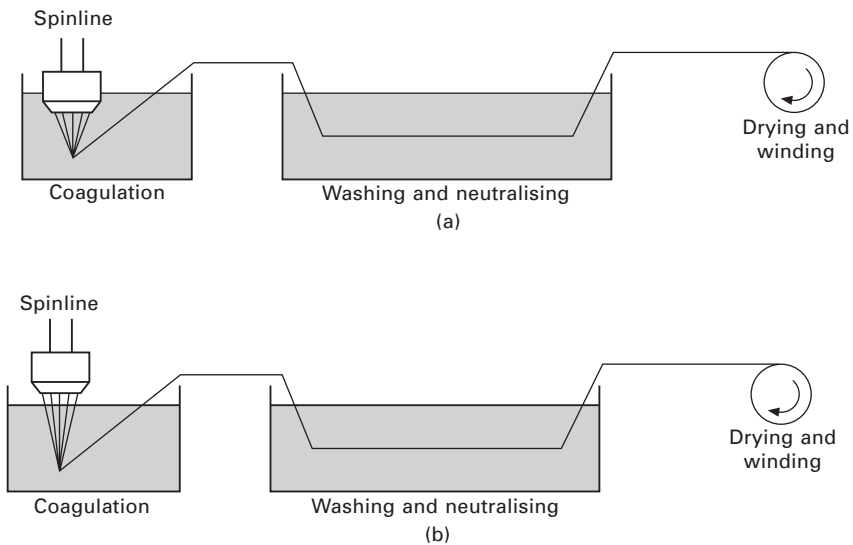


13.2 Viscosity of PpPTA–sulphuric acid solutions versus polymer concentration (schematic).

on both the spinline stability and the final fibre properties. Of course, the use of such an aggressive solvent puts severe demands on the material selection for all principal spinline units, such as storage tanks, tubing, extruders, metering pumps, filters, spinnerets and washing units, but also on all metallic structures and products in the vicinity of the spinning line.

Having defined the desired spindope composition, the remainder of the spinning process itself can now be designed. To produce thin filaments it is necessary to extrude the spindope via a spinneret into a large number of parallel jets (typically of the order of 1000) which are then brought into contact with a coagulation bath which removes the solvent from the spindope, leaving behind a filament with a low residual acid concentration ready for washing, neutralisation, drying and additional processing. Two fibre spinning processes for spinning solvent based polymeric systems exist: the classical wet spinning process (Fig. 13.3a) as used very successfully in cellulose fibre spinning, and the dry-wet spinning process (Fig. 13.3b).

For aramid fibre spinning only the dry-wet spinning process is employed. In this process the thermal conditions for optimal spindope flow and spindope coagulation can be easily decoupled. For good flow behaviour the spindope should be at a modest temperature of about 80°C while for good coagulation conditions a bath temperature of less than 10°C is required. In addition, the ability to stretch the extruded spindope in the air gap can be used to increase the average molecular orientation beyond the flow alignment induced in the spinneret channel [Pic92]. There is an interesting transition in deformation



13.3 Wet spinning processes: (a) classical wet spinning, (b) dry-wet spinning process.

behaviour for the spindope in its passage through the spinneret channel and the air gap. While the deformation in the spinneret channel is primarily of a shear nature, the deformation in the air gap is of a purely extensional nature.

The key fibre formation process occurs in the coagulation bath where the highly aligned and tensioned sulphuric acid jet of spindope is brought into contact with a non-solvent. The precise state of the spindope, be it liquid or solidified, when entering the coagulation bath is not known, just as the precise nature of the steps taking place during the coagulation process are barely understood. Work by Gardner *et al.* [Gar83] and others [Xu84, Iov82] has shown that for the polymer concentrations used in the spindope the nematic liquid crystalline solution forms ordered solvate crystals at lower temperatures. The solvate crystals are made up of hydrogen-bonded sheets consisting of polymer chains alternating with sulphuric acid molecules. As pointed out by Northolt [Nor 90] the XRD data for these polymer solvate crystals show surprisingly sharp reflections even sharper than that of the oriented nematic solution, suggesting that the solvate crystals are rather large and free of defects. It is not clear whether the short residence time in the air gap, of the order of only 100  $\mu\text{s}$ , is sufficient to form these crystals even for the highly aligned and tensioned condition prevailing. Nevertheless, the observation might be interpreted as the spindope striving towards a high degree of molecular perfection prior to coagulation.

During the coagulation the sulphuric acid is removed from the polymer solvate crystals and the PpPTA crystal structure is formed. It should be stressed that during this process 80 wt% of the spindope is removed, leading to large lateral mass fluxes and accompanying lateral shrinkage of the filaments. This lateral shrinkage of the filament due to the removal of the sulphuric acid is the principal reason why good quality aramid filament can only be spun up to a diameter of about 13  $\mu\text{m}$ . For filaments with a larger diameter most often a hollow core is formed, which is detrimental for strength. The hollow core will also trap sulphuric acid residues which are even more detrimental for the filament stability and filament lifetime under stress. The preferred orientation of the hydrogen bonds in the PpPTA crystal with respect to the polymer solvate—coagulant interface depends on the nature of the coagulant [Har79a, Har79b, Zwa09]. The aramid filament gathers significant strength during the early stages of the coagulation process, which makes fibre handling relatively easy and allows spinning at higher speeds even when the hydrostatic interaction between the quasi-stationary coagulation bath and the moving filaments leads to non-insignificant stress levels.

At the next step in the spinning process the remaining sulphuric acid within and between the filaments is removed by a succession of washing steps and a final neutralisation step. During this stage of the process probably

no further major microstructure development takes place and the principal processes are probably the removal of sulphuric acid from regions with an increased sulphuric acid level due to statistical fluctuations in the local packing density. It may not be excluded that the micro or sub-micro voids observed in aramid filaments are related to such trapped regions of sulphuric acid.

The final stage of the spinning process is an on-line drying stage to remove the absorbed and adhering water. During this drying process a light or modest tension is applied but no significant stretching takes place, highlighting again that the crucial fibre microstructure formation takes place during the coagulation stage. Before winding the fibre bundles on a bobbin, a spin finish is applied to give the yarn the proper handling characteristics as well as other characteristics deemed desirable for the final application [Lan07]. The final product is a bundle of smooth filaments of a circular cross-section and a characteristic semi-shining yellow colour, which is caused by conjugation through the amide bond [Yan91].

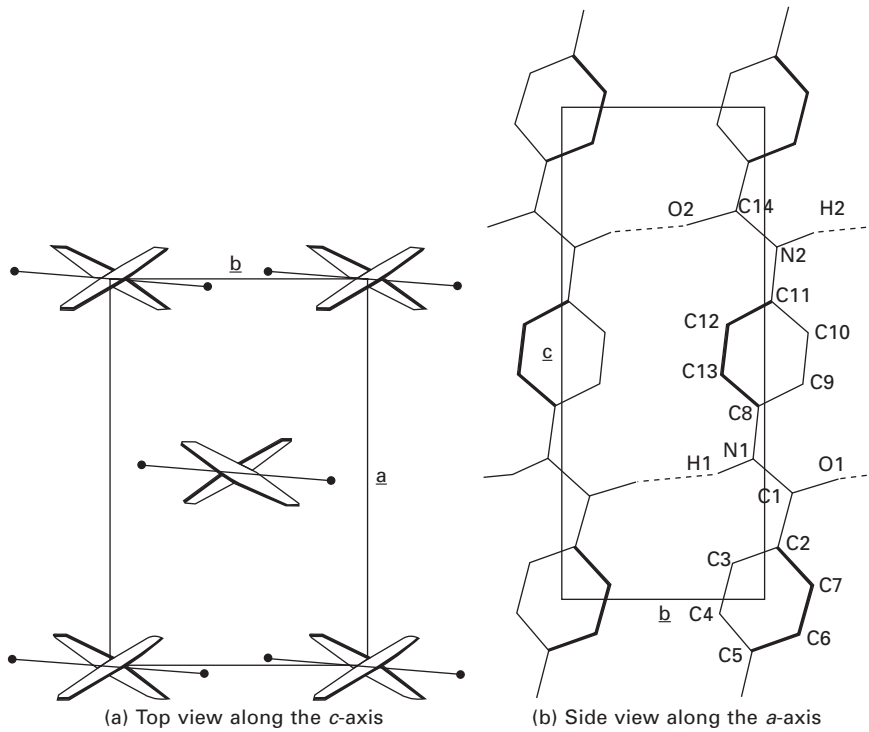
As is to be expected, the PpPTA fibres show a high degree of paracrystallinity with no signs of an amorphous phase. The crystal structure of PpPTA spun from high polymer concentrations was found to be monoclinic with pseudo-orthorhombic symmetry and two chains per unit cell [Nor73] as shown in Fig. 13.4.

Along the direction of the *c*-axis the atoms are bonded by covalent bonds; along the *b*-axis the molecules are bonded by hydrogen bonds (two hydrogen bonds over the length of a unit cell) while along the *a*-axis the van der Waals interactions are responsible for the strong lateral interaction, which is important for the final mechanical properties. The differences in bond type lead to large anisotropies in some of the physical properties, such as optical refractive index, elastic modulus, and thermal expansion coefficient [Iye03].

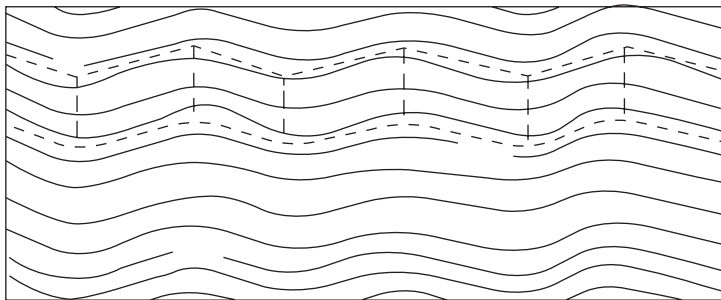
Such a difference in axial and lateral physical properties is typical for oriented polymers but the aramid fibres are remarkable for their difference in the bond strength in the radial and tangential directions. The development of the M5 fibre based on the related PIPD molecule was led by the notion that a higher lateral homogeneity at the crystal level would be advantageous for a number of properties, in particular the compressive properties [Lam98].

Surprisingly, PpPTA spun from isotropic spinning solutions yields a slightly different crystal structure [Har79a, Har79b] with the hydrogen-bonded plane through the centre of the unit cell. This difference could not be related to known differences in the structure of the solvate crystals.

Based on TEM, XRD and SEM microstructural studies, the aramid fibre seems to be composed of a parallel array of fibrils of about 60 nm diameter [Nor80]. Each fibril consists of a series of crystallites arranged end-to-end, and polymer molecules can form part of more than one crystallite (see Fig. 13.5).



13.4 PpPTA crystal structure.



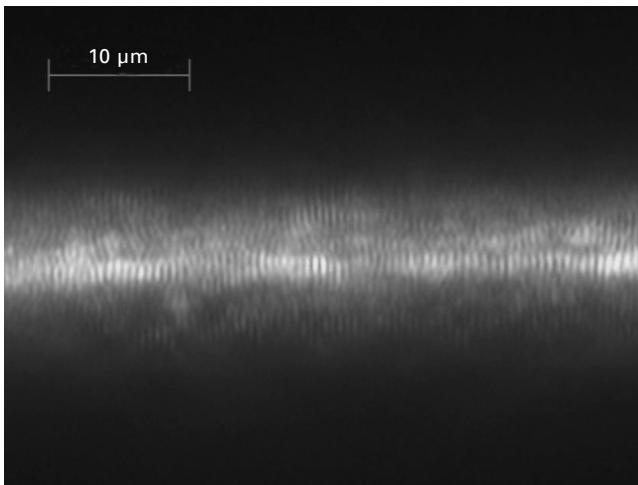
13.5 Schematic diagram of the proposed microfibrillar structure.

This model reflects the local misorientation angle distribution of the molecular axis along the filament length determined by XRD. Later modifications refined the original featureless model and added a distinct fibril diameter and a skin–core fibril size difference [Mor83] or oriented tie-molecules linking neighbouring fibrils [Pan83].

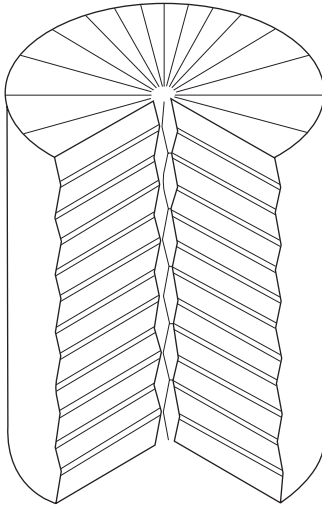
TEM and optical examination in transmission using crossed polarisers also revealed that the axial orientation angle does not vary randomly within the misorientation distribution function as assumed in the structure model illustrated in Fig. 13.5, but shows a well-defined periodicity resulting in a so-called pleated sheet structure [Dob77]. There is good evidence that the pleated sheet consists of parallel oriented crystals which are oriented such that the *b*-axis, i.e. the axis parallel to the intermolecular hydrogen bonds, is perpendicular to the fibre surface. The angle between the two planar surfaces of the pleated sheet structure is about  $170^\circ$ , i.e. each pleat has a misorientation angle of about  $5\text{--}7^\circ$  to the filament axis, and this misorientation angle also applies to the crystallites forming the pleated sheet. The pleat spacing is surprisingly constant and is always of the order of 250–400 nm. A typical high magnification optical image of an aramid fibre between crossed polarisers is shown in Fig. 13.6, where the dark lines perpendicular to the filament axis mark the positions at which the average molecular orientation is fully aligned with the filament axis.

Although the schematic diagram for the pleated sheet structure as proposed by Dobb (Fig. 13.7) has been widely accepted, it is not quite consistent with the fact that for good quality aramid fibres generally no disruption of the pleated sheet structure in the core of the filament is observed, which necessarily would follow from geometrical arguments based on the proposed model.

The precise physical origin of the pleated sheet has not been established unambiguously since the pleated sheet periodicity is not easy to vary by changing the spinning conditions. Horio *et al.* [Hor85] observed a significant



13.6 Optical micrograph of an aramid filament between crossed polarisers (aligned parallel and perpendicular to the filament axis).



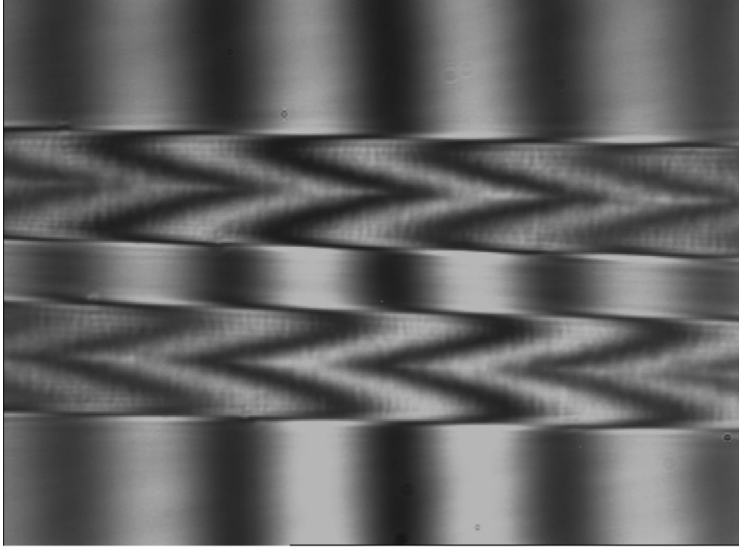
13.7 Schematic diagram for the pleated sheet structure as proposed by Dobb [Dob77].

increase in the pleated sheet length when raising the sulphuric acid concentration to 60% in the coagulation bath. They suggested that the pleated sheet is the result of a recoil process of the extruded spindope entering the static surface of the coagulation bath and that the periodicity of the pleated sheet depends on the coagulation rate. However, other experiments linking the pleated sheet spacing and the stress state in the top of the coagulation bath did not confirm this hypothesis.

Finally, it should be pointed out that a similar pleated sheet morphology has recently been observed in electrospun fibres of quasi-linear platinum compounds [Fon06], but this observation sheds no further light on the origin of the pleated sheet structure.

The radial texture of the crystallites in aramids can be measured using TEM diffraction experiments on thin-fibre cross-sections but can also be determined from retardation profiles through the diameter of a whole filament using optical interference microscopy [War83]. By varying the refractive index of the immersion oil and studying the changes in the retardation profile, the lateral and tangential refractive indices can be measured relatively easily. In Fig. 13.8 the optical retardation pattern in a regular aramid fibre is shown.

The degree of radial texture depends on the solubility parameter of the coagulation medium and can be tuned from an isotropic (i.e. no lateral texture) to a well-developed radial texture when spinning in water ( $\Delta n_{\text{lat}} = 0.045$ ). It should be pointed out that for a given spindope this change in lateral texture does not lead to a change in tensile strength provided filaments without obvious spinning defects in the microstructure are obtained. Earlier



13.8 Optical retardation profile for light polarised perpendicular to the filament axis using an interference contrast microscope.

claims in the original DuPont patents based on a comparison of fibres spun from spindopes with different polymer concentrations incorrectly claimed that such a relation between lateral texture and tensile strength exists.

The resulting aramid fibre is a very smooth yellow fibre with a high relative density and hence a low internal porosity, which adds to its chemical stability. The PpPTA fibre microstructure retains its characteristics upon heating, either with or without an imposed tensile stress, but as is to be expected the crystal perfection, dimensions and orientation increase upon thermal loading. This compaction of the microstructure and removal of imperfections in the local molecular packing lead to changes in the physical parameters such as modulus, refractive indices, density and CTE as well as moisture content. A detailed report on the changes in structure and properties as a function of the post-treatment conditions has been presented by Rao *et al.* [Rao01]. In their paper they also presented hydrostatic compression at elevated temperatures as an alternative method to improve the molecular order in as-spun fibres.

### 13.4 Relationship between microstructure and resulting properties

The first quantitative model to link the mechanical properties of aramid fibres to their physical microstructure is that of Northolt [Nor80], in which the aramid fibre structure is regarded as an end-to-end arrangement of



crystallites oriented at a small angle  $\phi$  with respect to the filament axis, as indicated in Fig. 13.5.

Upon straining the arrangement two principal deformation mechanisms take place: the crystals are stretched along their principal axis, leading to an elongational extension, and the crystals are sheared to reduce the misalignment with the loading direction, leading to a shearing deformation. The coupled interaction of both deformation modes leads to the following equations for the elastic compliance,  $S$ , of the aramid fibre, and the elastic strain,  $\varepsilon$ , as a function of the imposed stress, which both resemble their counterparts for the elastic loading of unidirectional composites:

$$S = 1/E = 1/e_c + \langle \sin^2 \phi \rangle / 2g \quad 13.1$$

$$\varepsilon = \sigma/e_c + 0.5 \langle \sin^2 \phi \rangle [1 - \exp(-\sigma/g)] \quad 13.2$$

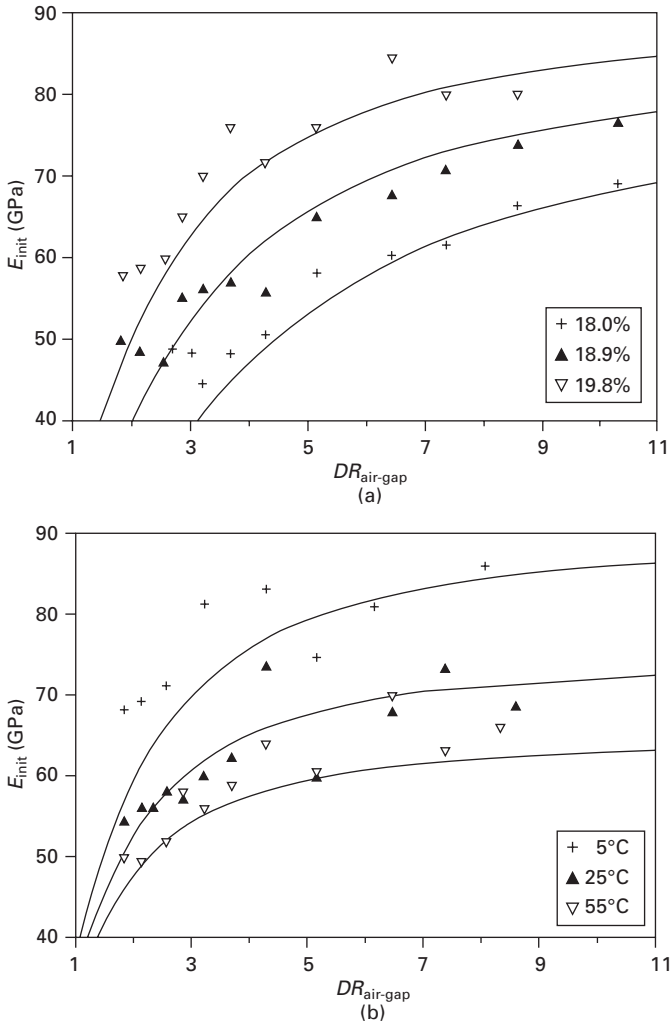
where  $S$  is the elastic compliance,  $E$  is Young's modulus,  $e_c$  is the chain modulus (200–230 GPa),  $\langle \sin^2 \phi \rangle$  is the average molecular misorientation and  $g$  is the average shear modulus of the crystallite for a shear deformation parallel to the  $c$ -axis of the crystallite (2.0 GPa). It should be pointed out that the above equation holds both for fibres with different initial degrees of molecular orientation but also for the development of the modulus as a function of the imposed loading stress. As follows from equations 13.1 and 13.2, the stress–strain curve of an aramid filament is intrinsically concave. (The initially straight section of the stress–strain curve up to a strain of typically 0.5% is due to more intermolecular interaction at a more mesoscopic level not accounted for in the Northolt model.) This reorientation of the crystallites upon fibre straining can be determined easily using ultrasonic modulus measurements [Nor80, Nor89].

From these equations it is clear that the ratio between the elongation due to the chain extension and that due to the shearing extension depends on the initial modulus of the fibre. This is confirmed by Raman spectroscopy measurements on a range of aramid fibres which showed a much higher shift in the  $1610 \text{ cm}^{-1}$  resonance band per unit of strain for high modulus fibres than for low modulus fibres [Zwa87], in quantitative agreement with the model prediction.

Equation 13.1 also indicates that the elastic modulus of aramid fibres is intrinsically limited by that of the chain modulus and therefore will always remain below a value of 200–230 GPa. It also shows that the actual modulus of aramid fibres is set by controlling the average molecular misorientation angle  $\phi$ . The molecular order in the filament is likely to reflect the average molecular order in the lyotropic aramid–sulphuric acid spindope, which is temperature and polymer concentration dependent, as well as the stretching of that spindope in the air gap. The relation between spinning conditions and final modulus in the absence of further straining of the fibre in the spinline

has been studied quantitatively by Picken *et al.* [Pic92] and was found to agree well with the theoretical predictions (see Fig. 13.9).

Finally, these equations also indicate that the modulus of aramid fibres can also be lowered by chemical modification of the aramid molecule such that the average shear modulus  $g$  is reduced. This would, however, require a change in the chemical composition of the molecule and/or the use of co-polymers. No such studies have been reported in the literature, but a related study on aramid fibres made from PPTA-DAB copolymers (4,4'-benzalinedylene-



13.9 Fibre modulus versus draw ratio for (a) various spindope concentration conditions and (b) various coagulation bath conditions. After Picken van der Zwaag and Northolt [Pic92].

terephthalamide) and PPTA-NDC (naphthalene-dicarboxylic acid), in which the periodicity of the hydrogen bond network was intentionally disturbed, showed no significant effect [Bos95], on either modulus, static strength or lifetime. In contrast, in the case of PAN- and pitch-based carbon fibres the crucial  $d(002)$  lattice spacing can be varied by suitable processing, leading to significant changes in the shear modulus of these materials [Bal96] and to significant changes in the elastic modulus (for a given orientation) and compression strength values [Kum93].

As applies to all high-performance fibres, the strength of PpPTA fibres depends on a multitude of parameters: those which determine the maximum achievable level and those that reduce the level realised in practice. Typical parameters determining the maximum strength level are the inherent viscosity of the polymer [Wey80] and the polymer concentration in homogeneous lyotropic spindopes [Kwo65]. Typical parameters reducing the maximum achievable strength are wide molecular weight distributions for the polymer, inhomogeneous spindopes, incorrect temperature settings along the spinline, unstable flow in the spinneret and resonance phenomena in the air gap, unfavourable physico-mechanical coagulation conditions leading to fibre inhomogeneities of all sorts, filament damage during washing and drying and many others. Given the multitude of parameters in determining the strength of aramid fibres, formulating accurate and complete physical models for the strength of aramid (and other high performance polymer) fibres is not possible. Furthermore, models aimed at predicting the 'ideal' aramid fibre strength should be tested against fibres free of structural and technological defects and produced under optimised conditions only.

The early theoretical and non-quantitative models for the strength of aramid fibres were based on the microfibrillar structure supposed to form the basis of the aramid fibres. The fibrils are connected by taut tie-molecules and failure was assumed to take place when enough tie-molecules or chains in the vicinity of segregated chain ends had fractured [Pen90, Ter85]. Several non-quantitative modifications of their models have been proposed, later including slightly more refined microstructure descriptions, but leaving the core of the concepts intact. A major drawback of these simple models is that they do not take into account any effect of non-affine deformation of the material up to the point of fracture. Furthermore, the early models implicitly predict a brittle fracture morphology, i.e. a fracture surface perpendicular to the fibre axis, while good quality aramid fibres tested in simple tension invariably show a high degree of splitting parallel to the filament axis. This observation led Baltussen and Northolt to the formulation of fracture strength models in which the microstructural changes during the deformation preceding fracture not only were taken into account, but were used to formulate a physical model for the fibre failure [Bal 04, Nor02, Bal01, Bal99, Nor85]. As pointed out earlier, straining of the fibre involves both elastic stretching

of the molecules in the chain direction as well as shear rotation of the crystallites. This shearing of the crystallites leads to a gradual build-up of intercrystallite shear stresses parallel to the filament axis. The rate of build-up clearly depends on the initial fibre modulus.

The Northolt *et al.* fibre strength model [Nor05] is based on the assumption that fibre fracture,  $\sigma_b$ , occurs when the local shear strength,  $\tau_b$ , is exceeded:

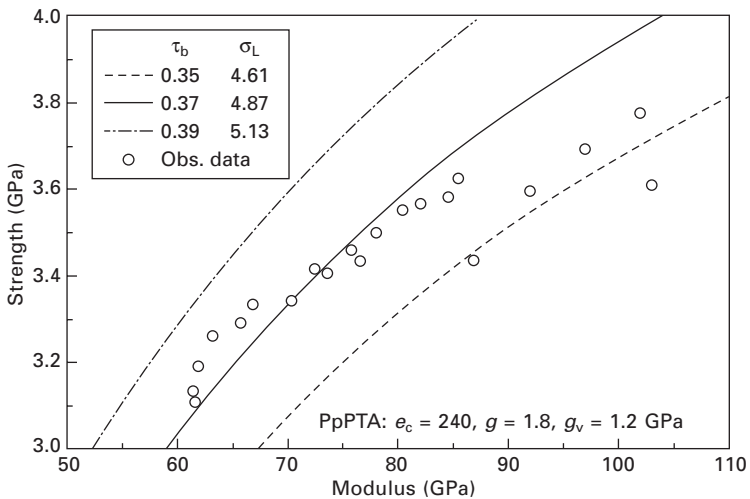
$$\tau_b = -\sigma_b \sin \phi_b \cos \phi_b \tag{13.3}$$

where  $\phi_b$  is the misorientation angle at the moment of fracture. It can be shown that the failure condition is reached when the following equality holds:

$$2g(\Phi - \phi_b) = \sigma_b \sin \phi_b \cos \phi_b \tag{13.4}$$

where  $\Phi$  is the initial misorientation angle and  $\phi_b$  the final misorientation angle. This equation was derived under the simplifying assumption of a single shear modulus  $g$  and a single misorientation angle  $\phi$ . However, Northolt *et al.* also presented a refinement of the model by taking into account the misorientation angle distribution and postulating a critical percentage of all intercrystallite shear bonds to be overloaded before fibre fracture does occur. Their model led to an interesting and quite realistic prediction of the relation between the fibre strength and the fibre modulus, shown in Fig. 13.10.

Of course, the above physical model for the tensile and creep strength applies only to an idealised fibre without any (multi-scale) microstructure and more



13.10 Aramid fibre strength versus fibre modulus, for various fractions of intercrystallite interfaces overloaded in shear. After Northolt and Baltussen [Nor02].

importantly without any defective polymer material (low molecular weight residue, degraded polymer) or fibre defects (porosity, foreign inclusions, local distortions due to fluctuations in coagulation conditions, defibrillation due to handling, etc.) or deformation-induced defects. To build a more realistic fibre strength model applicable under engineering conditions, a statistical fracture mechanics-based strength model taking into account the presence of pre-existing rather than deformation-induced defects is a good alternative.

The statistical description of strength of brittle materials was introduced by Weibull [Wei51] and is an extension of the Griffith model for brittle fracture. The model is based on the concept that any fibre loaded in tension will fail at the location of its most serious defect, i.e. the defect resulting in the lowest fracture strength. Furthermore, it is assumed that the defects are uniformly distributed along the fibre length. The cumulative failure probability function,  $P$ , which represents the fraction of filaments that failed at or below a stress  $\sigma$  is then given by

$$P(\sigma) = 1 - \exp[-L_0 (\sigma/\sigma_0)^m] \quad 13.5$$

where  $L_0$  is the test length of the fibre,  $\sigma_0$  a normalisation scalar and  $m$  the so-called Weibull modulus, which for aramid fibres is typically of the order of 10. It is readily demonstrated that for a test length  $L$  the average strength of filaments  $\langle\sigma\rangle$  is given by

$$\langle\sigma\rangle = \sigma_0 L^{-1/m} \Gamma(1 + 1/m) \quad 13.6$$

where  $\Gamma$  is the gamma function. The Weibull model and the concept of the effective length have been used to explain the significant length dependence of the strength of filaments, bundles, the weak length dependence of the strength of weakly twisted yarns and the length-independent strength of optimally twisted yarns and impregnated UD prepreps [Zwa89].

The Weibull modulus of aramid fibres is typically of the order of 10–15, which is a relatively high value with respect to very brittle fibres such as carbon ( $m = 3-7$ ) [Nai08] and  $\text{Al}_2\text{O}_3$  [Ber03] but relatively low with respect to more ductile materials such as HMPE fibres ( $m = 10-30$ ) [Amo93]. In general, the Weibull modulus decreases with increasing brittleness of the material. For a given class of fibres, the magnitude of the Weibull parameter is a good indication of the overall process control in the spinning line, while the magnitude of the scalar  $\sigma_0$  is more an indication of the quality of the polymer and the coagulation conditions.

Of course, the filament microstructure determines not only the principal mechanical properties such as stiffness and tensile strength, but also other mechanical properties such as fatigue strength, compression strength, wear resistance and thermal resistance. For all these latter properties the relationships between microstructure and properties are less clear, probably because they are the result of interacting phenomena at various length scales and involve

the sample geometry and pre-treatment and the precise testing conditions as well. Furthermore, such information is generally kept confidential by the fibre producers and the information cannot easily be extracted from laboratory experiments under non-production conditions. However, a better and more quantitative understanding between the microstructural parameters of the aramid fibres and these industrially relevant properties would be highly desirable, not only for aramid fibres but for all high performance polymeric fibres.

### 13.5 Future trends

After an initially slow start during the 1970s the production of PPTA aramid has grown consistently over many years since the 1990s with typical growth figures of about 10–15% per year to a current estimated production volume worldwide of about 50 000 tonnes per year. Growth figures are reported to be limited by the current production capacity of the two principal producers holding the important original patent rights, DuPont and Teijin (having bought the aramid business from Akzo in 2000). Given the fact that the original patents are about to expire, several new producers in Russia, Korea and China have announced their intention to start the production of aramid fibres, too, and some companies have even shown fibres of surprisingly good quality. So it is expected that the aramid business will grow even more strongly to meet the demands from a very wide range of industries. Current demands are for protective applications (protection against heat, sharp objects and ballistic objects), rubber applications (tyres, hoses, conveyor belts, etc.), ropes and cables (for load-bearing cables but also as load-bearing shields around optical communication cables and as reinforcement in thermoplastic pipes for critical application in the oil production industry) and fibrous applications (such as technical paper and seals for the chemical industry). All applications make use of the excellent thermal, mechanical and chemical resistance of the material, not only at room temperature but also at moderately high temperatures.

It is to be expected that the major new developments in aramid technology will centre around chemical modifications of the PPTA molecule (either as copolymer or as mixtures) to reach new performance levels or at the spinning technology to produce the current range of aramid base products (yarns, chopped fibres, pulp, fabrics) more efficiently and hence at lower cost.

### 13.6 Acknowledgements

The author acknowledges stimulating interactions with many former colleagues at Akzo Nobel when investigating the structure and properties of aramid fibres. Special thanks are due to Maurits Northolt, Frans Schenkels, Henk

Maatman, Ary Weeda, Frits Elkink, Stephen Picken, Bärbel Schaffers-Korff and the late Herman Weyland.

### 13.7 References

- [Amo93] T. Amornsakchai, D.L.M. Cransfield, S.A. Jawad and I.M. Ward. The relation between filament diameter and fracture strength for UHM polyethylene fibres. *J. Mater. Sci.* 28 (1993) 1689–1698
- [Bal96] J.J.M. Baltussen. PhD thesis, Technical University of Delft, the Netherlands, 1996
- [Bal99] J.J.M. Baltussen and M.G. Northolt. The stress and sonic modulus versus strain curve of polymer fibres with yield. *Polymer* 40 (1999) 6113–6124
- [Bal01] J.J.M. Baltussen and M.G. Northolt. The viscoelastic extension of polymer fibres: creep behaviour. *Polymer* 42 (2001) 3835–3846
- [Bal04] J.J.M. Baltussen and M.G. Northolt. The Eyring reduced time model for viscoelastic and yield deformation of polymer fibres. *Polymer* 45 (2004) 1717–1728
- [Ber03] M.H. Berger and D. Jeulin. Statistical analysis of the failure stresses of ceramic fibres: Dependence of the Weibull parameters on the gauge length, diameter variation and fluctuation of defect density. *J. Mater. Sci.* 38 (2003) 2913–2923
- [Bos95] M. Bosman, S. van der Zwaag and F.A.M. Schenkels. The effect of local distortions in the intramolecular hydrogen bond network on the lifetime of aramid yarns. *J. Mater. Sci. Lett.* 14 (1995) 1440–1443
- [Dob77] M.G. Dobb, D.J. Johnson and D.J. Saville. Supramolecular structure of a high modulus polyaromatic fibre. *J. Polym. Sci., Polym. Phys. Ed.* 12 (1977) 2201–2010
- [Fon06] M. Fontana, W. Caseri and P. Smith. Polymeric quasi one-dimensional platinum compounds. *Platinum Met. Rev.* 50 (2006) 112–118
- [Gar83] K.H. Gardner, R.R. Matheson P. Avakian, Y.T. Chia and T.D. Gierke. A partial phase diagram and crystal solvates for the poly(*p*-phenylene terephthalamide) – sulphuric acid system. *Abstr. ACS Meeting* 186 (1983) nr macr-14, 37–42
- [Har79a] K. Haraguchi, T. Kajiyama and M. Takayanagi. Uniplanar orientation of poly(*p*-phenylene terephthalamide) crystals in thin films and its effect on mechanical properties. *J. Appl. Polym. Sci.* 23 (1979) 903–914
- [Har79b] K. Haraguchi, T. Kajiyama and M. Takayanagi. Effect of coagulation conditions on the crystal modification of poly(*p*-phenylene terephthalamide). *J. Appl. Polym. Sci.* 23 (1979) 915–924
- [Hor85] M. Horio, S. Ishikawa and K. Oda. Fine structures of fibres and films made from lyotropic liquid crystals of polymers. *J. Appl. Polym. Sci.* 41 (1985) 269–292
- [Iov82] M.M. Iovleva and S.P. Papkov. Polymer crystalline solvates. *Polymer Science USSR* 24 (1982) 236–239
- [Iye03] R.V. Iyer, K. Sooraynarayana, T.N. Guru Row and K. Vijayan. Low temperature crystallographic data on Kevlar 49 fibres. *J. Mater. Sci.* 38 (2003) 133–139
- [Kum93] S. Kumar, D.F. Anderson and A.S. Crasto. Carbon fibre compressive strength and its dependence on structure and morphology. *J. Mater. Sci.* 28 (1993) 423–433
- [Kwo65] S.L. Kwolek. US Patent 3,819,587, 1965
- [Lam98] M. Lammers, E.A. Klop, M.G. Northolt and D.J. Sikkema. Mechanical properties and structural transitions in the new rigid-rod polymer fibre PIPD ('M5') during the manufacturing process. *Polymer* 39 (1998) 5999–6005

- [Lan07] P.J. de Lange, P.G. Akker, E. Maeder, S.L. Gao and R.J. Young. Controlled interfacial adhesion of Twaron<sup>®</sup> aramid-fibres in composites by the finish formulation. *Compos. Sci. Tech.* 67 (2007) 2027–2035
- [Mor83] R.J. Morgan, C.O. Pruneda and W.J. Steele. The relationship between the physical structure and microscopic deformation and failure processes of poly(*p*-phenylene terephthalamid) fibres. *J. Polym. Sci., Polym. Phys. Ed.* 21 (1983) 1757–1767
- [Nai08] K. Naito, Y. Tanaka, J.M. Yang and Y. Kagawa. Tensile properties of ultrahigh strength PAN-based, ultrahigh modulus pitch-based and high ductility pitch-based carbon fibers. *Carbon* 46 (2008) 189–195
- [Nor73] M.G. Northolt and J.J. van Aartsen. Crystal and molecular structure of poly(*p*-phenylene terephthalamide). *J. Polym. Sci. Lett.* 11 (1973) 333–337
- [Nor80] M.G. Northolt. Tensile deformation of fibres: an experimental and theoretical analysis. *Polymer* 21 (1980) 1199–1208
- [Nor85] M.G. Northolt and R. van der Hout. Elastic extension of an oriented crystalline fibre. *Polymer* 26 (1985) 310–316
- [Nor89] M.G. Northolt, J.H. Kampschreur and S. van der Zwaag. Chain stretching and crystal rotation during stretching of PPTA fibres. In *Integr. Fund Polym Sci and Techn.* 3 (1989) 157–165. Editors P.J. Lemstra and L.A. Kleintjes. Elsevier. London
- [Nor90] M.G. Northolt and D. Sikkema. Lyotropic main chain liquid crystal polymers. *Adv. Polym. Sci.* 98 (1990) 115–177
- [Nor02] M.G. Northolt and J.J.M. Baltussen. The tensile and compressive deformation of polymer and carbon fibers. *J. Appl. Polym. Sci.* 83 (2002) 508–538
- [Nor05] M.G. Northolt, P. den Decker, S.J. Picken, J.J.M. Baltussen and R. Schlatmann. The tensile strength of polymer fibres. *Adv. Polym. Sci.* 178 (2005) 1–108
- [Pan83] M. Panar, P. Avakian, R.C. Blume and H.H. Yang. Morphology of poly(*p*-phenylene terephthalamide) fibres. *J. Polym. Sci., Polym. Phys. Ed.* 21 (1983) 1955–1969
- [Pen90] J.P. Penning, H. van der Werf, M. Roukema and A.J. Pennings. On the theoretical strength of gelspun hotdrawn UHMW polyethylene fibres. *Polym. Bull.* 23 (1990) 347–357
- [Pic92] S.J. Picken, S. van der Zwaag and M.G. Northolt. Molecular and macroscopic orientational order in aramid solutions: a model to explain the influences of some spinning parameters on the modulus of aramid yarns. *Polymer* 33 (1992) 2998–3006
- [Rao01] Y. Rao, A.J. Waddon and R.J. Farris. The evolution of structure and properties in poly(*p*-phenylene terephthalamide) fibres. *Polymer* 42 (2001) 5925–5935
- [Sch76] J.R. Schaefgen, V. Folidi, F.M. Logillo, V.H. Good, L.W. Gulrich and F.L. Kilian. Viscosity–molecular weight relationships in rigid-chain aromatic polyamides. *Polym. Prep.* 17 (1976) 69–75
- [Ter85] Y. Termonia, P. Meakin and P. Smith. Theoretical study of the influence of the molecular weight on the maximum tensile strength of polymer fibres. *Macromolecules* 18 (1985) 2246–2252
- [Vol89] L. Vollbracht. In *Comprehensive Polymer Science, Volume 5*. Editor G. Allen. Pergamon, Oxford, 1989
- [War83] S.B. Warner. On the radial structure of Kevlar. *Macromolecules* 16 (1983) 1546–1548
- [Wei51] W. Weibull. A statistical distribution function of wide applicability. *J. Appl. Mech.* 18 (1951) 293–305
- [Wey80] H.G. Weyland. The effect of anisotropy in wet spinning of poly(*p*-phenylene terephthalamide). *Polym. Bull.* 3 (1980) 331–335
- [Xu84] D.F. Xu, K. Okuyama, F. Kumamaru and M. Takayanagi. Morphological and



- structural studies on large spherulites of poly(*p*-phenylene terephthalamide). *Polym. J.* 16 (1984) 31–40
- [Yan91] H.H. Yang. *Kevlar Aramid Fibers*. John Wiley & Sons, New York, 1991
- [Zwa87] S. van der Zwaag, M.G. Northolt, R.J. Young, I.M. Robinson, C. Galiotis and D.N. Batchelder. Chain stretching in aramid fibres. *Polym. Commun.* 28 (1987) 276–279
- [Zwa89] S. van der Zwaag. The concept of filament strength and the Weibull modulus. *J. Testing and Evaluation* 17 (1989) 292–298
- [Zwa09] S. van der Zwaag *et al.* On the relation between coagulation conditions and the lateral texture in PPTA filaments. To be submitted

# The structure and properties of high-modulus, high-tenacity Vectran™ fibres

Y YAMAMOTO and J NAKAGAWA,  
Kuraray Co. Limited, Japan

**Abstract:** High-strength polyarylate fibre is manufactured from rigid polymers with a molten liquid-crystalline property by the melt spinning method, unlike other high-strength fibres. Its commercialization was attempted in the 1980s but only our company's product Vectran™ is manufactured and marketed today on a commercial basis. This chapter describes the previous research into thermotropic liquid crystal and its fibre formation, and especially the fibre characteristics of Vectran™ as the representative polyarylate fibre and some examples that use those characteristics.

**Key words:** thermotropic liquid crystal polymer, Vectran™, polyarylate fibre, melt spinning, solid-phase polymerization, high strength, high modulus, very low equilibrium moisture regain, high cut resistance.

## 14.1 Introduction

There are two types of polymeric crystal: concentration transition liquid crystal (henceforth known as lyotropic liquid crystal) and temperature transition liquid crystal (henceforth known as thermotropic liquid crystal). Lyotropic liquid crystal products available on the market include an aramid fibre, Kevlar™, derived from the research by Kwolek *et al.* of DuPont, and Twaron™, which has the same molecular structure, from Akzo (currently, Teijin). Recently, a PBO fibre, Zylon™, has been produced on a commercial basis by Toyobo, based on the technology of Dow Chemical. Pioneering research into thermotropic liquid crystal polymer was also implemented by others, including Economy<sup>1</sup> of Carborundum, Jackson<sup>2</sup> of Eastman Kodak, and Calundann<sup>3</sup> of Celanese Chemicals. The thermotropic liquid crystal polymers in Table 14.1<sup>4</sup> are already on the market, but as for the fibre there is only Vectran™, which was created by Kuraray based on the technology of Celanese. Generally, a liquid crystal polymer means thermotropic liquid crystal, but here we will also describe the application of polymeric liquid crystal to fibres, including a little about lyotropic liquid crystal, together with their usage.

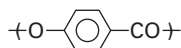
Table 14.1 Commercial thermotropic liquid crystal polymer resins

| Type                                    | Chemical structure (presumption) | Supplier (trade name)                                                                          |
|-----------------------------------------|----------------------------------|------------------------------------------------------------------------------------------------|
| Flexible group introduction type        |                                  | Unitika (Rodrun)<br>Mitsubishi Engineering Plastics Corporation (Novaccurate)                  |
| Aromatic ring substitution type         |                                  | DuPont (HX)<br>Granmont (Granlar)                                                              |
| Rod-like molecule copolymerization type |                                  | Solvay Advanced Polymers (Xydar)<br>Nippon Oil (Xydar)<br>Sumitomo Chemical (Sumika Super LCP) |
|                                         |                                  | Ticona (Vectra)<br>Polyplastics (Vectra)<br>Ueno Fine Chemicals Industry (Ueno LCP)            |

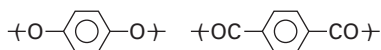
## 14.2 Thermotropic liquid crystal and its fibre formation

Generally, the basic structure of a wholly aromatic polyester is typically:

- a self-condensation polyester of *p*-hydroxy-benzoic acid (HBA), melting point 610°C:



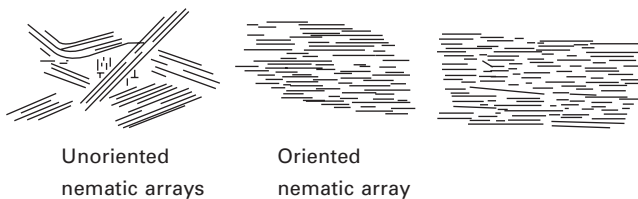
- a copolyester consisting of terephthalic acid (TA) and hydroquinone (HQ), melting point 600°C:



For these polymers, the melting points are higher than their decomposition points (400–450°C),<sup>5</sup> because their molecules are too rigid, and the process of forming in the liquid crystal state is difficult. Consequently, a method is used to lower the melting point to no more than the decomposition point by sacrificing a little of the rigidity and crystallinity of the polymer. This is done by:

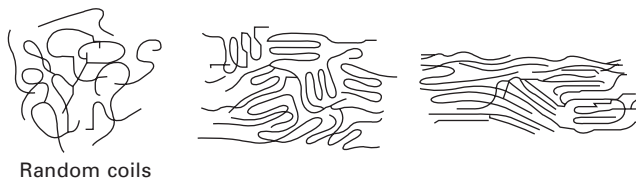
1. The introduction of a flexible alkyl group into the main chain
2. The copolymerization of rigid molecules
3. The introduction of a substitution group to the aromatic ring of the main chain.

Many thermotropic liquid crystal polymers have been developed as engineering plastics by these methods. To obtain fibres from thermotropic liquid crystal polymers, a pellet-form polymer is dried and, after melting with an extruder, is formed into fibres by ordinary melt-spinning. High molecular orientation takes place while it passes through the nozzle, and the structure is maintained until the fibre is solidified by cooling, with a sufficiently long relaxation time. The molecules are already orientated in the as-spun fibre and so drawing is virtually unnecessary. The fibre has considerable tenacity and initial modulus in this state, and a thermal treatment is implemented to further improve its performance. The purpose of the thermal treatment is to increase the tenacity and initial modulus and improve heat resistance. Generally, the thermal treatment of thermotropic liquid crystal fibres is performed under reduced pressure and the by-products generated are eliminated in an inert gas or air. As described later, the molecular weight is increased by a solid-phase polymerization reaction caused by the thermal treatment. Figure 14.1 shows



[Polymer] → [as-spun fibre] → [heat-treated fibre]

(a) Fibre formation of thermotropic crystal polymer



[Polymer] → [as-spun fibre] → [drawn fibre]

(b) Fibre formation of flexible polymer

14.1 Schematic diagram of fibre formation.

a schematic diagram of fibre formation for a thermotropic liquid crystal polymer in comparison with a flexural polymer. Although many studies have been made of fibre formation in a molten liquid crystal polymer, currently the only one being manufactured and marketed industrially is Vectran™.

#### 14.2.1 Fibre of the flexible group introduction type

The copolyester that contains 40 mol% of polyethylene terephthalate (PET) has been copolymerized with HBA (henceforth shown as PET/HBA = 40/60), forming an industrially interesting polymer costwise, but one that is not suitable for producing fibre, as described in the reports by Acierno *et al.*<sup>6</sup> and Jackson *et al.*<sup>7</sup> PET/HBA = 40/60 is a random copolymer,<sup>8</sup> but it is thought that when the ratio is 20/80, block-like parts of HBA are created.<sup>9</sup> It has also been reported that the strength can be increased to 3.11 GPa<sup>10</sup> by removing the foreign particles generated from block polymerization of HBA, allowing it to be formed into fibre. Jackson *et al.* have reported that a copolyester of CPA – HQ/HBA = 20/80 – has been formed into fibres using a polymer of carboxybenzene propionic acid (CPA) and HQ instead of PET, and that a tenacity of 17.8 cN/dtex and a modulus of elasticity 850 cN/dtex were obtained.<sup>5</sup>

#### 14.2.2 Fibre of rod-like molecule copolymerization type

Vectran™ is obtained from a polymer of HBA and hydroxynaphthoic acid (HNA). The X-ray analysis of Blackwell made it clear that the polymer used is a random copolymer.<sup>11</sup> According to Yoon, it has been reported that the polymer of HBA/HNA: 73/27 was spun and, when a thermal treatment was applied for 30 minutes at a temperature of 270°C, the tenacity increased to 24.8 cN/dtex, and finally reached about 26.3 cN/dtex.<sup>12</sup> In the HBA/HNA system, the tenacity markedly increases, but the modulus of elasticity only increases by a small margin with a thermal treatment. It is worth noting that for the fibre obtained from a copolymerization of biphenol (BP) and TA with reduced HNA, HBA/HNA/BP/TA = 60/5/17.5/17.5, using a thermal treatment between 300°C and 310°C improved not only the tenacity but also the modulus of elasticity, from 560 cN/dtex to 980 cN/dtex.<sup>13</sup> Fibre formation of the HBA/TA/BP liquid crystal polymer was also studied by Economy *et al.*<sup>14</sup> It is interesting that there are two types of copolymer: one where thermal treatment increases the tenacity but hardly increases the initial modulus, and another where thermal treatment increases both the tenacity and the initial modulus. One example of the former is the copolymer of HBA/HNA, and the copolymer of HBA/HNA/BP/TA is an example of the latter.

### 14.2.3 Fibre of aromatic ring substitution type

The melting point of a homopolymer of phenylhydroquinone (PhHQ) and TA is 341°C, making melt spinning possible. Jackson *et al.* formed the polymer into fibres, and, by thermal treatment at 340°C for one hour, obtained a fibre with tenacity 28.2 cN/dtex and initial modulus 803 cN/dtex.<sup>5</sup> When a copolymerization system is employed, the melting point is lowered further and it becomes possible to form fibre from the high molecular weight polymer. According to Zimmerman, draw resonance often takes place in polymer fibre forming when the crystal melting heat  $\Delta_c H$  is below 10 J/g, but when supercooled spinning is performed at a temperature between the melting point and the solidification point, smooth fibre forming is possible, avoiding draw resonance.<sup>15</sup> By this method, a polymer with the composition of PhHQ–TA/BP–TA/HBA = 80/10/10 ( $\eta_{inh}$ : 9.3 dl/g, melting point: 288°C) can be formed into fibres at 324°C, and a tenacity of 17.7 cN/dtex is obtained without thermal treatment.

Table 14.2 shows the solid state properties of the reported thermotropic liquid crystal fibres.<sup>16</sup> Of these, there are few that achieve industrial-level production.

## 14.3 Thermotropic liquid crystal fibre (polyarylate fibre)

Currently, the only industrially manufactured fibre is the wholly aromatic polyester (polyarylate) fibre Vectran™, which consists of the copolymer system of HBA and HNA. Kuraray began investigating the industrial manufacture of fibre from thermotropic liquid crystal polymers in 1985 after receiving the necessary technology from Celanese Co., which was already developing ways of fibre forming. In 1990, Kuraray constructed a 400 metric tonnes/year plant in the Saijo Factory and began the manufacturing operation, and by the end of 2007 the production capacity was 1000 metric tonnes/year. While aramid fibres are expanding the size of the market, the company is continuing the development of thermotropic liquid crystal fibre in the fields of dope-dyed yarns and fine yarns (200 dtex or less), utilizing its low hygroscopicity, low temperature characteristic, low creep property and wear resistance, which are the characteristics of wholly aromatic polyester, and taking advantage of melt-spinning for the production process. Since 2002, high-modulus-type Vectran™ UM has been added to the product line-up, and the company has been penetrating the field of tension members of optical fibres. The following describes fibre forming for polyarylate, in particular for Vectran™, the characteristics of its fibre structure and its usage.<sup>17</sup>

Table 14.2 Composition of liquid crystal polymers and fibre properties

| Type* | Polymers<br>Composition <sup>†</sup> | Ratio (mol%)   | $\eta_{inh}$ | As-spun fibre<br>Tenacity<br>(cN/dtex) | Initial modulus<br>(cN/dtex) | Heat-treated fibre<br>Tenacity<br>(cN/dtex) | Initial modulus<br>(cN/dtex) |
|-------|--------------------------------------|----------------|--------------|----------------------------------------|------------------------------|---------------------------------------------|------------------------------|
| A     | PET/HBA                              | 40/60          | –            | 2.9                                    | 173                          | –                                           | –                            |
|       | PET/HBA                              | 40/60          | –            | 8.9                                    | –                            | 22.2                                        | –                            |
|       | CPA-HQ/HBA                           | 20/80          | –            | 6.1                                    | 415                          | 17.9                                        | 847                          |
| B     | HBA/HNA                              | 75/25          | 5.7          | 10.7                                   | 477                          | 17.7                                        | 485                          |
|       | HBA/HNA                              | 73/27          | –            | –                                      | –                            | 26.3                                        | –                            |
|       | HBA/HNA/TA/BP                        | 60/5/17.5/17.5 | 6.5          | 7.0                                    | 560                          | 24.5                                        | 980                          |
| C     | PhHQ-TA                              | 100            | 3.0          | 3.0                                    | 350                          | 28.2                                        | 803                          |
|       | PhHQ-TA/HBA                          | 83.8/16.2      | 2.4          | 5.4                                    | 353                          | 30.7                                        | 428                          |
|       | PhHQ-TA/BP-TA/HBA                    | 80/10/10       | 9.3          | 17.7                                   | –                            | –                                           | –                            |
|       | CIHQ-TA/CIHQ-NA                      | 70/30          | 2.6          | 5.4                                    | 483                          | 26.8                                        | 465                          |

\*A: Flexible group introduction type

B: Rod-like molecule copolymerization type

C: Aromatic ring substitution type

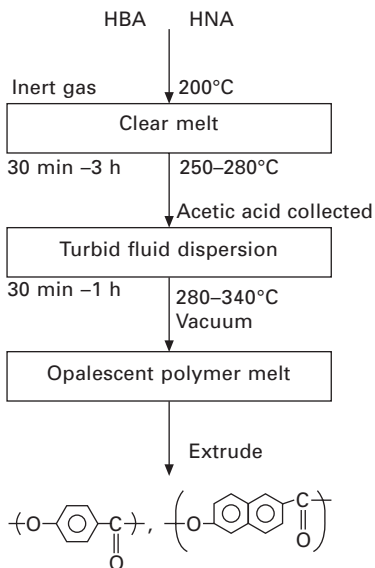
<sup>†</sup>NA: 2,6-naphthalenedicarboxylic acid, PhHQ: phenylhydroquinone.

### 14.3.1 Polymerization of the raw material

The raw material is a copolymer of HBA and HNA, and the ratio of copolymerization of HNA is 25–30% (Vectra™ made by Polyplastic Co., Ltd). The general polymerization method of the polymer is as follows. First, the monomers are acetylated, and then the prepolymers are made by condensation polymerization using a catalyst such as potassium acetate. The temperature is further elevated and full polymerization is conducted under reduced pressure. Figure 14.2 illustrates the main features of the reaction.<sup>18</sup> For the high modulus type, it is necessary to increase the number of linear components in the molecules, and so multi-component system polymers, in which HNA is reduced and BP–TA components are added, are adopted.

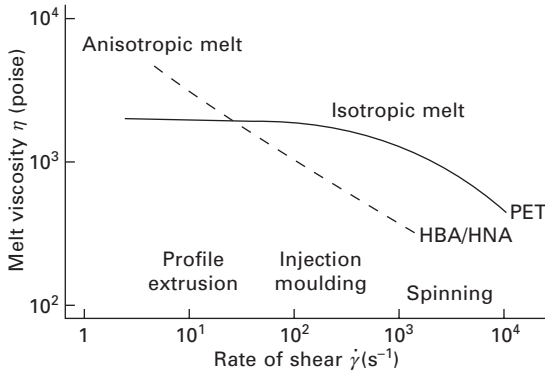
### 14.3.2 Melt spinning and molecular orientation

Hydrolysis and thermal decomposition, which take place in melting, make the polymer deteriorate and markedly lower its spinnability due to the gas generated. To reduce the lowering of  $\eta_{\text{inh}}$  that takes place during spinning, it is necessary to reduce the moisture content of the pellet and use a device to lower the melting point as far as possible. Ordinarily, the polymer can be dried to make the moisture content no more than 50 ppm. Figure 14.3 shows the relationship between the shearing speed and the melt viscosity. Generally, for flexible polymers such as PET, the viscosity change is small in the low shear region, but for the molten liquid crystal polymer (HBA/

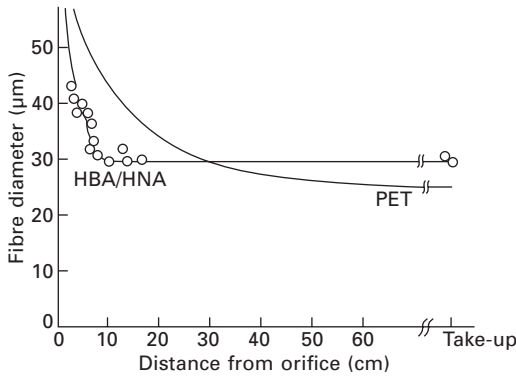


14.2 Polymerization process of copolymer HBA/HNA.





14.3 Relationship between shear rate and viscosity.



14.4 Attenuation behaviour of extruded streams.

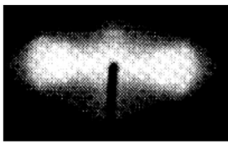
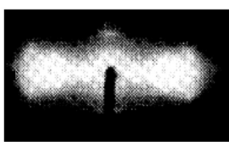
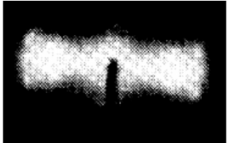
HNA) the change is linear, the non-Newtonian property is strong, and the effect of temperature change is large. There is no drawing process in the fibre forming of molten liquid crystal polymers, unlike flexible polymers, and so the fineness of the as-spun fibre is the same as the fineness of the final product. Therefore, in order to obtain a greater fineness, it is necessary to make the nozzle diameter smaller or the fibre-forming draught larger. In a thermotropic liquid crystal polymer, a high degree of molecular orientation takes place while passing through the nozzle from the low shear region; therefore, it is difficult to make the fibre-forming draught larger. Thus, in order to obtain a fine fibre, the nozzle diameter has to be smaller, and therefore the shear speed increases. When the shear speed increases, the melt viscosity lowers, which is preferable for fibre forming a high  $\eta_{inh}$  polymer.

Figure 14.4 shows examples of the attenuation behaviour of extruded streams. PET, which is a flexible polymer, attenuates rapidly down to a diameter of 30 cm from the orifice and then only gradually until it is taken

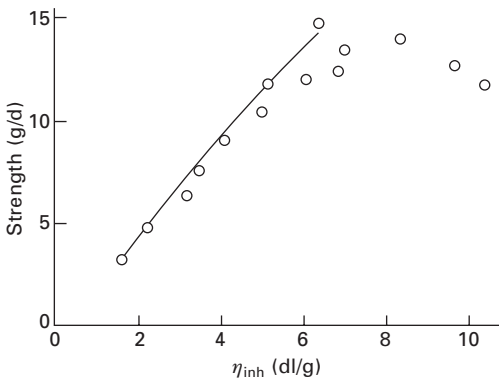
up. On the other hand, HBA/HNA attenuates rapidly just below the orifice, and the attenuation is nearly complete at a distance of 10 cm from the orifice. Figure 14.5 shows the relationship between the X-ray photograph and degree of orientation of the crystal ( $F_c$ ) for the released fibre discharged from the nozzle (draught  $D_f = 1$ ), the as-spun fibre ( $D_f = 25$ ), and the heat-treated fibre. It can be seen that there is a high degree of orientation only with the nozzle shear ( $10^4\text{--}10^5\text{ s}^{-1}$ ), and that crystallization is increased by the heat treatment but the orientation is hardly changed.

### 14.3.3 Performance of the as-spun fibre and the effect of heat treatment

Figure 14.6 shows the results<sup>3</sup> by Calundann *et al.* on the relationship between the inherent viscosity ( $\eta_{inh}$ ) and the tenacity of as-spun fibre. When  $\eta_{inh}$  is about 7 dl/g, the maximum tenacity of 13.2 cN/dtex is reached. When  $\eta_{inh}$  is further elevated, the melt viscosity gets higher and normal fibre forming

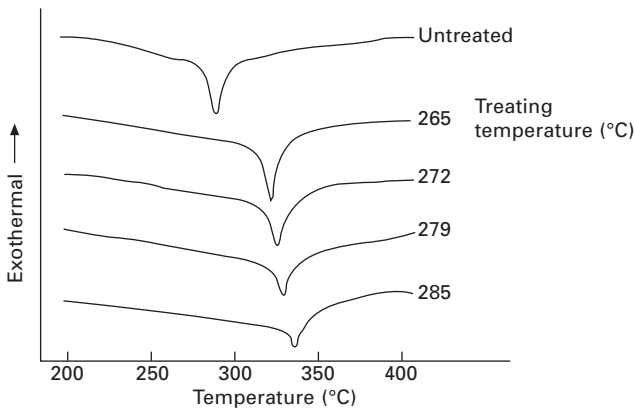
| Sample                | Released fibre                                                                    | As-spun fibre                                                                     | Heat-treated fibre                                                                 |
|-----------------------|-----------------------------------------------------------------------------------|-----------------------------------------------------------------------------------|------------------------------------------------------------------------------------|
| X-ray photograph      |  |  |  |
| Fibre-forming draught | 1                                                                                 | 25                                                                                | 25                                                                                 |
| Degree of orientation | 86                                                                                | 88                                                                                | 88                                                                                 |

14.5 Relationship between the X-ray photograph and degree of orientation of the crystal.



14.6 Relationship between  $\eta_{inh}$  and strength of as-spun fibre.

cannot be implemented; on the contrary, the tenacity is lowered. To further improve the as-spun fibre, heat treatment is implemented at a temperature no greater than the melting point. Figure 14.7 shows the DSC curve of the fibre obtained by changing the thermal treatment temperature. As the temperature gets higher, the endothermic peak of melting moves to the side of higher temperature and the peak area gets smaller. The heat-treated fibre with the peak exceeding 300°C cannot be molten under normal pressure and, when the temperature is further elevated, the fibre decomposes, keeping the fibrous form. The heat treatment time and the tenacity reached fluctuate, largely depending on the manufacturing conditions of the polymer and the heat treatment method. According to Yoon *et al.*, it has been reported that a 24.8 cN/dtex tenacity was finally obtained when the polymer of HBA/HNA = 73/27 was spun and then a heat treatment was applied at 270°C.<sup>12</sup> Our results showed that the maximum tenacity of 30.0 cN/dtex was obtained when the final temperature was set at 285°C and the heat treatment was carried out for about 20 hours. Table 14.3 shows the changes in the structural factors



14.7 DSC curves of heat-treated fibre.

Table 14.3 Change of structure factors and molecular weight upon heat treatment

|                                                  | As-spun fibre | Heat treated fibre |
|--------------------------------------------------|---------------|--------------------|
| $\alpha$ -transition temperature $T_\alpha$ (°C) | 88            | 97                 |
| $\tan \delta$ (max.)                             | 0.104         | 0.105              |
| Sonic velocity (km/s)                            | 8.64          | 8.65               |
| Crystal orientation (°C)                         | 88            | 88                 |
| Specific weight                                  | 1.40          | 1.41               |
| X-ray crystallinity (%)                          | 45            | 46                 |
| Molecular weight $M_n/10^4$                      | 1.63          | 4.89               |
| $M_w/10^4$                                       | 3.84          | 14.5               |
| $M_z/10^4$                                       | 6.88          | 27.5               |

caused by heat treatment. The primary dispersion temperature  $T_{\alpha}$  becomes elevated, but the degree of orientation hardly changes, and the degree of crystallization, obtained from the specific gravity and X-ray photograph, increases by only a small margin. On the other hand, the value of the average molecular weight increases roughly threefold.<sup>16</sup> With regards to the structural change by heat treatment, Takahashi *et al.* point out that the alignment of HBA and HNA in the molecular chain does not change but the *a*-axis and *b*-axis are changed, and there is the possibility of aggregation of sequences with increased HBA,<sup>19</sup> and Krigbaum *et al.* point out that the HNA is blocked by the melt interchange.<sup>20</sup>

#### 14.4 High initial modulus type

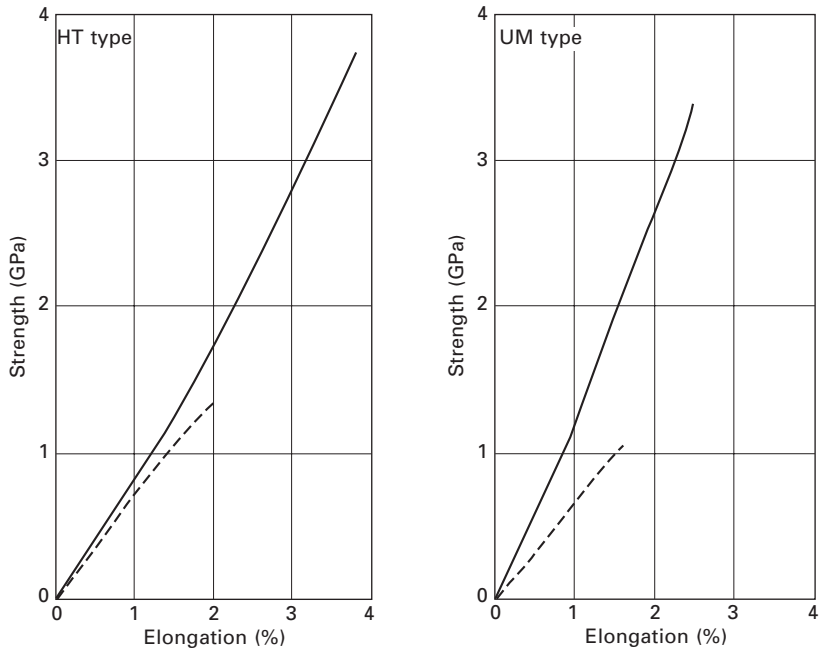
For liquid crystal fibre, it is difficult to apply a tension treatment under a temperature as high as that used in the case of lyotropic liquid crystal fibre, because the melting point is low. It is difficult to greatly improve the initial modulus even if a tension treatment (or micro-drawing) is applied at a temperature no higher than the melting point. In order to obtain a high modulus, it is necessary to increase the linear components in the molecular structure. These types of polymers have a melting point as high as 330–350°C and so the spinning temperature can be higher. To achieve good fibre forming, it is necessary to increase the drying and shorten the detention time as much as possible to avoid thermal decomposition. In the case of a high initial modulus-type (UM) polymer, the tenacity of the as-spun fibre and the modulus are nearly the same as those of a regular type (HT), but when heat treatment is applied, both the tenacity and initial modulus are improved. Figure 14.8 compares the tenacity elongation curves of HT and UM before and after heat treatment.

#### 14.5 Properties of polyarylate fibre

Table 14.4 shows the general fibre properties<sup>21</sup> of Vectran™ in comparison with those of para-aramid fibre (PPTA). Vectran™ and PPTA have nearly the same tensile characteristics and possess 2–3 times the tenacity and 4–5 times the initial modulus of PET. The tensile properties of high-tenacity fibres are generally affected by the ambient temperature but those of Vectran™, for example at –70°C. are the same as its properties at room temperature, indicating its possible use at extremely low temperatures. Vectran™ has very low equilibrium moisture absorbency, and this is its most important characteristic when compared with PPTA. Figure 14.9 shows the creep behaviour of Vectran™. It can be noted from the figure that its elongation change with time is extremely low or, in other words, its dimensional stability is high. In addition, Vectran™ exhibits a superior performance for

Table 14.4 Comparison of fibre properties between Vectran™ and para-aramid (PPTA)

| Property                                  |                                                                       | Vectran™ |      | Para-aramid (PPTA) |                      |
|-------------------------------------------|-----------------------------------------------------------------------|----------|------|--------------------|----------------------|
|                                           |                                                                       | HT       | UM   | Regular            | High initial modulus |
| Density (g/cm <sup>3</sup> )              |                                                                       | 1.41     | 1.40 | 1.44               | 1.44                 |
| Decomposition temperature (°C)            |                                                                       | >450     | >450 | >500               | >500                 |
| Limiting oxygen index (LOI) (%)           |                                                                       | 28       | 30   | 30                 | 30                   |
| Equilibrium moisture regain               | 20°C, 65% RH (%)                                                      | 0.05     | 0.07 | 4.2                | 4.1                  |
|                                           | 20°C, 90% RH (%)                                                      | 0.1      | 0.1  | 5.5                | 5.5                  |
| Tensile property                          | Tenacity at 20°C (cN/dtex)                                            | 24.2     | 21.5 | 20.3               | 20.8                 |
|                                           | Tenacity at -70 °C (cN/dtex)                                          | 29.1     | 25.2 | 18.1               | 17.5                 |
|                                           | Elongation at 20°C (%)                                                | 4.0      | 2.8  | 3.6                | 2.4                  |
|                                           | Initial modulus at 20°C (cN/dtex)                                     | 530      | 740  | 490                | 781                  |
| Rate of shrinkage                         | Dry 180°C, 30 min (%)                                                 | 0.15     | 0.04 | 0.10               | 0.04                 |
|                                           | Wet 100°C, 30 min (%)                                                 | 0.15     | 0.01 | 0.15               | 0.04                 |
| Strength retention after thermal exposure | Dry 250°C, 300 h (%)                                                  | 85       | 81   | 48                 | 56                   |
|                                           | Wet 120 °C, 300 h (%)                                                 | 77       | 71   | 86                 | 79                   |
| Chemical resistance                       | H <sub>2</sub> SO <sub>4</sub> 10%, 70°C, 100 h (%)                   | 93       | –    | 19                 | –                    |
|                                           | NaOH 10%, 20°C, 10 000 h (%)                                          | 97       | –    | 68                 | –                    |
|                                           | C <sub>6</sub> H <sub>6</sub> CH <sub>3</sub> , 100%, 20°C, 100 h (%) | 98       | –    | 99                 | –                    |



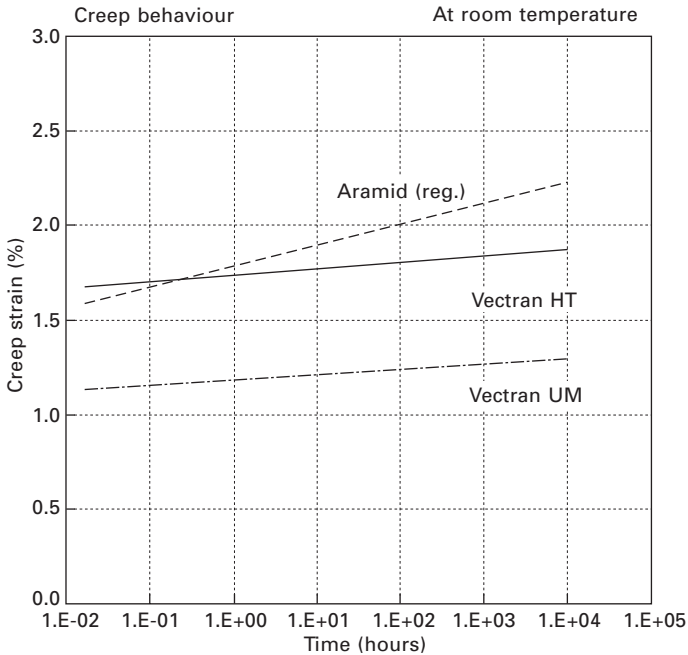
14.8 Comparison of extensional behaviour between Vectran™ HT fibre and UM fibre.

wear resistance and resistance to cutting when compared with other super-fibres. Vectran™ has superior acid resistance to PPTA, but although its alkali resistance is better than that of the PET fibre, it decreases in weight as a result of peeling off by hydrolysis. This tendency is strong, especially at high temperatures, and so precautions are taken for its use. It is thought that deterioration takes place in ammonia and an acidic gas atmosphere. Its solvent resistance is as good as that of PPTA.

## 14.6 Examples using the characteristics of Vectran™

### 14.6.1 Sheet and film-related materials

Mainly as a result of its high strength, high modulus, very low equilibrium moisture absorbency, good low-temperature mechanical properties and high cut resistance, Vectran™ has been used for sheet material in airships, reinforcing foundation cloth for high-pressure hoses and pipes, and foundation cloth for various other items including competition yacht sails.



14.9 Comparison of creep property between Vectran™ and para-aramid (PPTA).

*Foundation cloth of airbags used for the landing of NASA’s Mars explorers*

In July 1997, a NASA explorer, ‘Mars Pathfinder’, landed on Mars, followed by ‘Spirit’ and ‘Opportunity’ in January 2004. Airbags using Vectran™ foundation cloth were used for all those spaceships. The temperature on the surface of Mars is thought to range from –50 to –100°C and this foundation cloth was used because its low-temperature and cut-resistance properties had been evaluated as excellent.

*Sheet material for an airship floating in the stratosphere*

In the ‘Stratospheric Platform Plan’ implemented by the Japan Aerospace Exploration Agency (JAXA) (in which an unmanned airship was floated in the stratosphere, which is 20 km above the surface of Earth, for use in communications, broadcasting and the observation of Earth), Vectran™ cloth was used as the foundation cloth for the sheet materials of the airship in order to reduce its weight and increase its strength, enabling it to fly at an altitude of 16.4 km. This sheet material had a structure in which both surfaces

of the Vectran™ cloth and EVOH film were laminated with polyurethane film. The weight of this sheet material was 114 g/m<sup>2</sup> while its strength was about 2.9 kN/cm or more. This sheet material also had excellent gas barrier properties, preventing the leakage of helium gas, and excellent weatherability, preventing the deformation of the airship hull in the stratosphere where the temperature was about -56°C and the atmospheric pressure only 5% of that at ground level.

#### 14.6.2 Cords, tension members and net-related items

Mainly because of its high strength, high modulus, very low equilibrium moisture absorbency, high abrasion resistance and low creep property, Vectran™ is used for the cords of blinds and wire screens, cords as substitutes for wires (supporting cords for tennis and volleyball nets and course ropes for indoor pools), earphone cables, tension members for optical fibre cables, and various nets used for baseball.

##### *Fishing lines*

Vectran™ is used for fishing lines in lure fishing and boat fishing. It has been well accepted for the following reasons: it is water-resistant, it can resist the abrasion that occurs between the fishing line and the guides of the fishing rod, it has the high specific gravity required for the fishing line to sink smoothly into water, low elongation, high modulus and low creep properties required for accurately detecting fish biting, good water draining properties, and also the appropriate degree of high rigidity needed for fishing line usage.

##### *Spun-dyed cords as substitutes for wires*

The ends of metal wires used for volleyball and tennis nets and the course ropes of swimming pools can cause safety problems. Cords made from Vectran™ have been popularly accepted because they have no such safety problem, are lighter, neither sag nor extend during use (due to their high modulus and low creep properties), do not rust, and additionally can be dyed with colours such as black and blue in the manufacturing stage of the filament yarn.

#### 14.6.3 Safety and protection-related items

Mainly as a result of its high strength and high cut, heat and abrasion resistance, Vectran™ is used for manufacturing protective clothes and materials including gloves, aprons and protective nets for dangerous animals. This material can be safely used for applications where heat resistance is



required and combustion is likely to occur, because it will not generate gases containing cyanogen compounds, which are generated when aramid fibre burns. Gloves used for meat processing need to be sterilized after use, and as gloves made of Vectran™ have excellent resistance to sodium hypochlorite, they can be used repeatedly.

## 14.7 Conclusion

Owing to the unique characteristics of organic high-tenacity fibres, it is thought that their use will increase in safety and protection-related areas, energy-saving areas (because of the potential contribution to weight reduction), and areas of extreme environmental conditions, in addition to conventional application areas. Their usage will also become more sophisticated. As a result, the authors hope that various unique materials will be produced from this high-tenacity polyarylate fibre through the diversification of raw materials used for it and the addition of various functions using additives, which will lead to the manufacture of products with new functions and characteristics.

## 14.8 References

1. Carborundum, US Patent 3,637,595, 1972.
2. Jackson Jr W J and Kuhfuss H F, *J. Polym. Sci., Chem. Ed.*, **14**, 2043, 1976.
3. Calundann G W and Jaffe M, 'Anisotropic polymers, their synthesis and properties', *Proceedings of the Robert A. Welch Conference on Chemical Research, XXVI. Synthetic Polymers*, 1982.
4. Inoue M, *Plastics Age*, **140**, May 1990.
5. Jackson Jr WJ, *Brit. Polym. J.*, **12**, 154, 1980.
6. Acierno D, La Mantia F P and Polizzotti G, *Macromolecules*, **15**, 1456, 1982.
7. Jackson Jr WJ, Japanese Patent (examined), 56-18016, 1981.
8. Mitchell G R and Windle A H, *Polymer*, **23**, 1269, 1982.
9. Zachariades A, Economy J and Logan J A, *J. Appl. Polym. Sci.*, **27**, 2009, 1982.
10. Unitika, Japanese Patent (laid open), 88-264914, 1988.
11. Gutierrez G A, Chivers R A, Blackwell J, Stamatoff J B and Yoon H, *Polymer*, **24**, 937, 1983.
12. Yoon H N, *Colloid & Polym. Sci.*, **268**, 230, 1990.
13. Hoechst-Celanese, US Patent 4,473,682, 1984.
14. Carborundum and Dart Industries, Japanese Patent (examined), 82-24407, 1982.
15. Zimmerman J, *J. Appl. Polym. Sci.*, **39**, 2067, 1990.
16. Nakagawa J, *Sen-i Gakkaishi*, **47**, P-589, 1991.
17. Nakagawa J, in *Advanced Fiber Spinning Technology*, ed. T. Nakajima, Woodhead Publishing, Cambridge, 1994, Chapter 7 (160–171).
18. Tai-Shung Chung, *Polym. Eng. Sci.*, **26** (7), 901, 1986.
19. Xiao C F and Takahashi T, *Sen-i Gakkaishi*, **46**, 49, 1990.
20. Yang D K and Krigbaum W R, *J. Polym. Sci., Part B, Polym. Phys.*, **27**, 1837, 1989.
21. Yamamoto Y, *Jpn. Res. Ass. Text.*, **47**, 34, 2006.

## The structure of high-modulus, high-tenacity (poly-*p*-phenylenebenzobisoxazole) fibres

---

T KITAGAWA, Toyobo Co., Ltd, Japan

**Abstract:** PBO fibre is made of rigid-rod molecules and has the extended-chain structure. The detail has been revealed with X-ray diffraction, small-angle X-ray scattering, electron microscopy and vibrational spectroscopy. Stress distribution in the structure of the fibre under tension is measured. The structural difference between the three PBO fibres made with different preparations is also discussed.

**Key words:** extended-chain structure, wide-angle X-ray diffraction, small-angle X-ray scattering, electron microscopy, Raman scattering, crystalline modulus, Raman shift factor.

### 15.1 Introduction

The advent of PPTA (poly-*p*-phenyleneterephthalamide) fibre in the 1970s was a big surprise to the people who worked with the physical properties of synthetic fibres, because PPTA is made from a so-called extended-chain structure (Dobb *et al.* 1977) and has high mechanical properties. These characteristics result from the structure of the polymer, which has a straight molecular backbone parallel to the fibre axis and a dense-packed crystal structure. The fibre morphology is controlled using a dry-jet, wet-spinning method. The molecule is so rigid that it spontaneously aligns in the same direction in solution to form a liquid crystal.

PBO (poly-*p*-phenylenebenzobisoxazole) is one of the polybenzazoles containing an aromatic heterocyclic ring. The success of PPTA provided an incentive to find a new material. The molecule was first developed by US Air Force researchers in a project which was searching for new ladder polymers, whose heat resistance and mechanical properties are better than those of PPTA fibres. Initially, PBZT (poly-*p*-phenylenebenzobisthiazole) was thought to be more promising than PBO, but later it was decided that PBO had more advantageous mechanical properties and the main research direction was changed. Dow Chemical received a patent licence from the Stanford Research Institute for commercial production and developed a new synthesis method for the monomer and polymerization stage. During this period, the economic potential of PBO in synthesis and polymerization improved. In 1991, Dow Chemical decided to work with Toyobo and their joint research bore fruit in 1994 with the development

of a new spinning technology, which led to the production of the current PBO fibre.

## 15.2 Synthesis and polymerization

The polymerization of PBO takes place in polyphosphoric acid from 4,6-diamino-1,3-benzenediol dihydrochloride with terephthalic acid. A method to prepare 4,6-diamino-1,3-benzenediol dihydrochloride using 1,2,3-trichlorobenzene as a starting material has been invented. The successive stages of nitration, hydroxylation, hydrogenation and reduction produce a final monomer with high purity. During polymerization, the phosphoric acid content adjustment method enables the polymer to reach a high molecular weight.

## 15.3 Molecular design and theoretical modulus

One of the main reasons for the interest in developing high-modulus, high-strength fibres is to calculate the theoretical (ultimate) modulus and compare the value with the actual value of the crystalline modulus. Lattice dynamics is one of the most promising methods because the suitability of the molecular parameters used in the calculation can be checked and modified by vibrational spectroscopic measurements. Tashiro and Kobayashi (1996) revealed how to trace the deformation process of macromolecules under stress using lattice mechanics. A method for predicting the modulus values by solving quantum-mechanics equations is also available.

Adams *et al.* (1989) and Tashiro and Kobayashi (1996), Tashiro *et al.* 1995 calculated the crystalline modulus (theoretical limit) for PBZT and PBO using a semi-empirical molecular orbital calculation and lattice dynamics, respectively. The results are listed in Table 15.1. It can be seen from the theoretical calculations that PBO displays a higher modulus than PBZT. Because the PBO molecule has a slightly straighter molecule shape, it is proved to have a higher modulus than PBZT by mechanical theory. Therefore, PBO was chosen as the target material to develop.

## 15.4 Fibre structure

### 15.4.1 Previous works

Krause *et al.* (1988) reported the crystallite size, microfibril texture and molecular orientation of PBO using X-ray diffraction and electron microscope methods. The fibre is made of highly oriented molecular chains but its crystallite size is small compared with that of PPTA. Shimamura *et al.* (1983) were the first to observe the molecular chain alignment and defects included in

Table 15.1 Calculated modulus values for PBO and PBZT fibres

| Modulus (GPa) |      | Method | Reference         |                                |
|---------------|------|--------|-------------------|--------------------------------|
| PBO           | PBZT |        |                   |                                |
| 670           | 528  | MNDO   | Quantum mechanics | Wierschke <i>et al.</i> (1992) |
| 690           | 620  | AM1    | Quantum mechanics | Wierschke <i>et al.</i> (1992) |
| 460           | 405  |        | Lattice mechanics | Tashiro and Kobayashi (1991)   |

the PBO crystal using high-resolution electron microscopy (HREM). Martin and Thomas (1989) also examined the PBO molecular orientation and a translational disorder of chains along the fibre axis by HREM and electron diffraction (ED). Information about the crystal structure is also important for understanding the morphological characteristics and the relation between the structure and mechanical properties of PBO. Fratini *et al.* (1989) proposed a crystal structure model by use of an X-ray study. Tashiro *et al.* (1998) proposed another type of crystal structure model from X-ray diffraction and computer simulation methods. Takahashi (1999) also proposed a model of a PBO crystal by neutron diffraction. The relationship between the process and microfibril structure formation was investigated by Bai and Price (1992) and Kumar *et al.* (1994) using small-angle X-ray scattering (SAXS). Raman spectra also provide unique information on the molecular deformation caused by tensile force. Young *et al.* (1990) applied this method to a stressed PBO fibre and estimated the Raman band shift with stress.

One of the most important problems to be solved for PBO fibre is to find a way to explain the difference between the crystalline modulus and the fibre modulus. As mentioned above, the crystalline modulus is about 460 GPa, while actual fibres show only 180–360 GPa. It is important to clarify the reason for this large gap between the values for the crystalline (theoretical) modulus and the actual modulus achieved as a fibre.

PBO fibre consists of fully extended chains. Most of the so-called super (high-modulus and high-strength) fibres also consist of highly oriented chains and show a modulus closer to the crystalline (theoretical) modulus. However, PBO fibre achieves only 60% of its potential, even the HM (heat-treated high-modulus type) fibre, in spite of its fully extended chain structure. In general, the tensile modulus of super fibres is said to be controlled by the degree of molecular orientation. It has already been found that HM fibre has a highly oriented molecular structure, the orientation of which exceeds that of PPTA. But it has also been confirmed by SAXS that HM fibre possesses a periodic density fluctuation along the fibre axis. The presence of this periodicity is one of the structural characteristics of heat-treated PBO fibre produced by water coagulation and has not been found in high-modulus type PPTA. This periodic density fluctuation may be one reason why the fibre modulus is lower than the theoretical value. The translational disorder

of chains in a PBO crystal is another factor to be taken into consideration. In a PBO crystal, the interactions between neighbouring chains are weak because the molecular chains are connected only by van der Waals forces and electrostatic forces. This weak intermolecular interaction might induce a slippage of neighbouring chains by applying a tension along the fibre and reducing the fibre modulus. Therefore, a structural investigation of the PBO chains under deformation is important in order to understand the mechanism for modulus improvement.

#### 15.4.2 Structural study of PBO AS, HM and HM+ fibres

##### *Current PBO fibres*

There are two commercially available PBO fibres (AS and HM) and one experimental fibre (HM+) (Table 15.2). The AS fibre is spun from polyphosphoric acid solution (dope) using a dry-jet wet-spinning method. The solution is extruded from the spinneret, guided through an air gap and coagulated in a water bath, followed by a washing and drying process. After being extruded from the spinneret, the solution is extended in the air gap, and the fibre structure is formed after coagulation. The high molecular orientation of the structure is achieved during this process. The HM fibre is produced from the AS fibre by heat treatment. To increase the fibre modulus further, extruded dope filaments are coagulated in the non-aqueous liquid, followed by washing, drying and heat-treatment processes, when the solution concentration and composition are the same as for the commercial fibres. The experimental fibre made in this way (called HM+) displays a higher modulus with slightly lower strength than the HM fibre.

##### *Wide-angle X-ray diffraction*

An analysis using X-ray diffraction was used to obtain information about molecular orientation and crystal size. Some sharp diffraction spots on the equator and streak-like layer lines were observed in the fibre diagram. Off-axis spots were not observed clearly. Some authors link these streak-like

*Table 15.2* Mechanical properties of PBO fibres

| Fibre | Strength (GPa) | Modulus (GPa) |
|-------|----------------|---------------|
| AS    | 5.8            | 180           |
| HM    | 5.8            | 270           |
| HM+   | 4.7            | 350           |

layer lines on fibre diagrams to a spatial disorder of the crystal along the fibre axis. Shimamura *et al.* (1983) proposed a model to explain this type of translational disorder in PBZT fibre and called it axial shift. The shape of the spots on the equator was very sharp in the azimuthal direction. This indicates that the alignment of molecules in the PBO fibre is highly parallel to the fibre direction. Unit cell parameters of PBO are tabulated in Table 15.3.

X-ray diffraction intensity profiles, measured using symmetry transmission, are shown in Fig. 15.1. The apparent crystal size is obtained by estimating the broadening of the diffraction peak using Scherer's equation. After heat treatment, the diffraction spots became sharp and intensified, indicating that the apparent crystallite size became larger. It is interesting to note that the HM+ fibre shows the narrowest peak profiles among the three fibres, implying that the fibre has the biggest crystallite size. The results are shown in Table 15.4.

#### *Molecular orientation and fibre modulus*

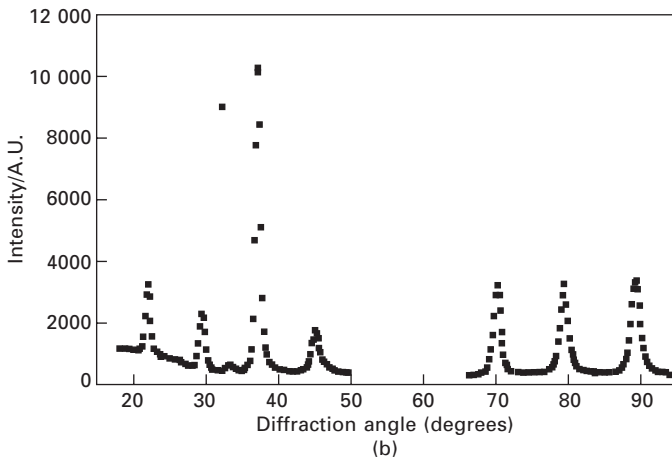
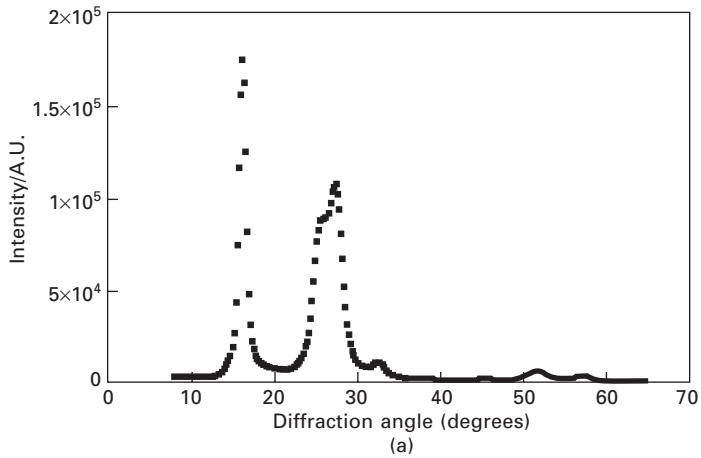
In general, it is thought that the Young's modulus of fibres made of rigid-rod polymers depends greatly on the crystal orientation. Northolt (1980) proposed a mechanical model of crystal orientation. According to this model, the fibre is regarded as being built up of a parallel array of identical fibrils which are subjected to a uniform stress along the fibre axis. A crystallite in the fibrils is composed of rigid-rod polymer chains running linearly and at an angle with the fibre axis. The effects of the molecular stretch and the orientation change of the molecules were considered in this model. The inverse of the fibre modulus (compliance) can be expressed as a linear function of crystal orientation as follows:

$$1/E = 1/E_c^{\text{true}} + \langle \sin^2 \Phi \rangle / 2G$$

where  $E$  is the Young's modulus of the fibre,  $E_c^{\text{true}}$  is the crystalline modulus,  $G$  is the shear modulus due to the change of the molecular orientation (the rotation of the crystallites) and  $\Phi$  is the angle between the chain axis and the fibre axis. This equation is valid when  $\Phi$  is close to zero. It can be seen

Table 15.3 Unit cell parameters of PBO fibres

| Crystal system | Space group                      | Unit cell |        |        |                    | Reference                    |
|----------------|----------------------------------|-----------|--------|--------|--------------------|------------------------------|
|                |                                  | a (nm)    | b (nm) | c (nm) | $\gamma$ (degrees) |                              |
| Monoclinic     |                                  | 1.1201    | 0.354  | 1.205  | 101.3              | Fratini <i>et al.</i> (1989) |
| Monoclinic     | P11a-C <sub>s</sub> <sup>2</sup> | 1.115     | 0.360  | 1.214  | 100.0              | Tashiro <i>et al.</i> (2001) |
| Monoclinic     |                                  | 0.5651    | 0.357  | 0.603  | 101.4              | Takahashi (1999)             |



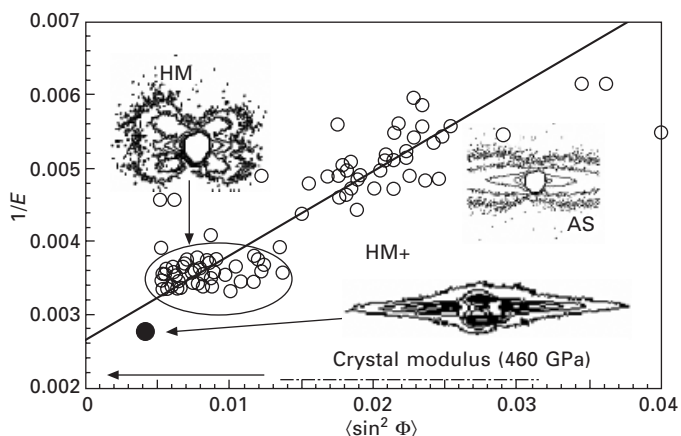
15.1 Wide-angle X-ray scattering profiles for the HM+ fibre: (a) equatorial; (b) meridional.

Table 15.4 Crystallite size for PBO fibres

| Fibre | X-ray<br>Apparent crystallite size (nm) |       |       | ED<br>Crystallite size (nm) |                     |
|-------|-----------------------------------------|-------|-------|-----------------------------|---------------------|
|       | (200)                                   | (010) | (003) | (200)                       | (010) + $\bar{2}10$ |
| AS    | 5.5                                     | 2.7   | 9.6   | 3.9                         | 3.5                 |
| HM    | 11                                      | 4.2   | 16.0  | 6.9                         | 5.3                 |
| HM+   | 11                                      | 4.6   | 16.2  |                             |                     |

that the intercept of the measured compliance plotted against orientation  $\langle \sin^2\Phi \rangle$  is consistent with the PPTA crystalline modulus.

The inverse of the Young's modulus for PBO fibres prepared under different processing conditions is plotted against  $\langle \sin^2\Phi \rangle$  in Fig. 15.2. Here,



15.2 The inverse of PBO Young's modulus against  $\langle \sin^2 \Phi \rangle$ . ○: Coagulated through water; ●: coagulated through non-aqueous solution.

the orientation  $\langle \sin^2 \Phi \rangle$  is calculated from the intensity distribution of (200) in the azimuthal direction. The crystalline modulus and the shear modulus can be estimated to be 370 GPa and 4 GPa, respectively, from the intercept and the slope of the straight line fitted to the plotted points.

Nishino *et al.* (1995), Lenhert and Adams (1989), Davies *et al.* (2001, 2003, 2004, 2005a,b) and the author himself (2000a,b, 2001, 2002a,b) measured the crystal strain of PBO HM fibre under tension by X-ray diffraction. They concluded that the measured crystalline modulus was 460–480 GPa, which was far higher than that predicted on the basis of Northolt's model. This means that the Young's modulus of PBO fibre cannot reach the measured crystalline modulus even if all the molecules in the fibre are aligned completely parallel to the fibre direction. PBO fibre contains a disordered region, which would prevent the fibre modulus achieving the crystalline modulus even if the molecules were perfectly aligned.

### Fine structure

Fibre structure formation through phase separation should occur during the coagulation process. Cohen and Thomas (1985, 1998a,b) and David and Edwin (1991) have studied the structure formation of PBZT fibre and film. It is said that filaments (solution) extruded from a spinneret transform into a swollen microfibrillar network when the nematic rigid-rod solution touches a coagulant. Passing through the coagulation process, the network loses its open spaces and forms a dense fibrillar structure. Existing open spaces are thought to become microvoids.



SAXS patterns of HM and HM+ fibre are inset in the Northolt plot in Fig. 15.2. In the AS fibre, the pattern becomes a streak-like scattering and appears on the equator, which would result from microvoids elongated in the fibre direction. During the heat treatment process, this streak disappears and a four-point pattern similar to the shape of a butterfly appears, indicating the existence of density fluctuations along the fibre axis. Bai and Price (1992), Bai (1998) and Kumar *et al.* (1994), and Hunsaker *et al.* (1992) reported the same four-point patterns in their heat-treated PBO fibres.

Because PBO is spun through the process of phase separation, the fibre includes microvoids. In order to estimate the diameter sizes of microvoids in PBO fibre, Guinier's method is applied to AS fibre. The logarithm of the intensity after background correction is plotted against the square of the scattering vector. The data exhibit linearity and the slope allows us to obtain the average diameter of the microvoids, about 2.4 nm.

The four-point pattern proves the existence of density fluctuation along the fibre axis. There is an equation that is able to simulate a SAXS pattern pertaining to the fibril structure model. The comparison between actual and predicted patterns based on the above equation implies that inclined periodicity like a parallelogram (having 25 nm as the long period, 20 nm as the width of the fibril and 60° as the oblique angle) exists in the fibre.

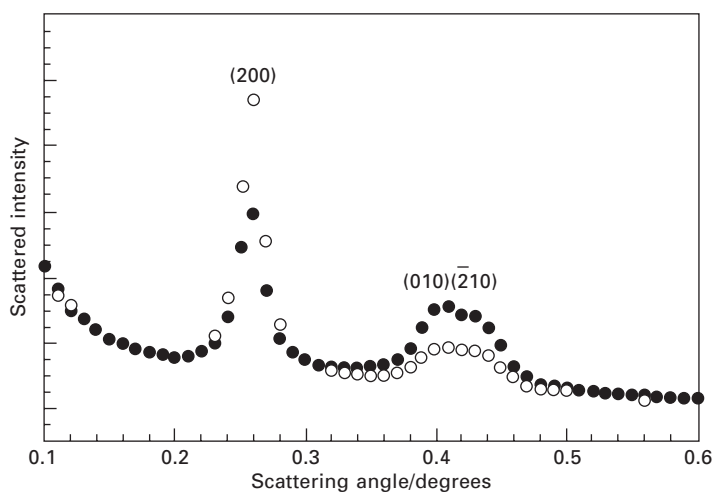
It should be noted that HM+ is also made through heat treatment but does not have the four-point pattern that is characteristic of HM (heat-treated PBO fibre with water coagulation). This means that a more homogeneous structure is realized along the fibre axis in the HM+ fibre. It is also noted that the SAXS pattern shows the same strong equatorial streak as the AS fibre but the size of the microvoids is definitely larger (~6 nm), as seen from the analysis by Guinier's method. The source of this streak is unclear; however, improving the crystallite size in the fibril of the HM+ fibre would produce a larger boundary than the AS fibre and give such a SAXS streak.

### *Electron microscopy*

Electron microscope studies were performed to analyse the structure of PBO fibres more clearly. The electron diffraction (ED) patterns from longitudinal ultra-thin sections of PBO fibres allow us to estimate crystal size and orientation in the fibril. Because ED patterns of HM fibre have many spots, HM fibre is believed to have a higher crystallinity than AS fibre. It should also be noted that the intensity of (200) reflection is abnormally stronger than those of (010) and ( $\bar{2}$ 10) reflections. This tendency is not the same in WAXS. As already shown in previous sections, the *c*-axis of PBO crystal is highly oriented to the fibre direction. However, the way in which the *a*- and *b*- axes are aligned on the transverse cross-section of the fibre is still unknown. If the two axes are oriented to the radial direction, this preferential alignment affects ED

patterns. If the  $a$ -axis is preferentially oriented to the radial direction, the (200) reflection should be more intense than the (010) and ( $\bar{2}10$ ) reflections. To prove this, an ultra-thin section was tilted and inspected at the sample stage in TEM, then ED patterns were observed to determine the preferential direction of the crystal axis more clearly. The section contained the centre of the original fibre and the rotation axis was parallel to the fibre axis. The incident electron beam was exposed from the direction of the rotation axis. After the section was tilted  $30^\circ$  from the horizontal line, the diffracted intensity of the (200) plane decreased, but the intensities of the (010) and ( $\bar{2}10$ ) increased (Fig. 15.3). This means that the direction of the  $a$ -axis of the crystal is mostly perpendicular to the direction of incident electron beam unless it is tilted. It can be concluded that the  $a$ -axis is oriented along the radial direction of the fibre.

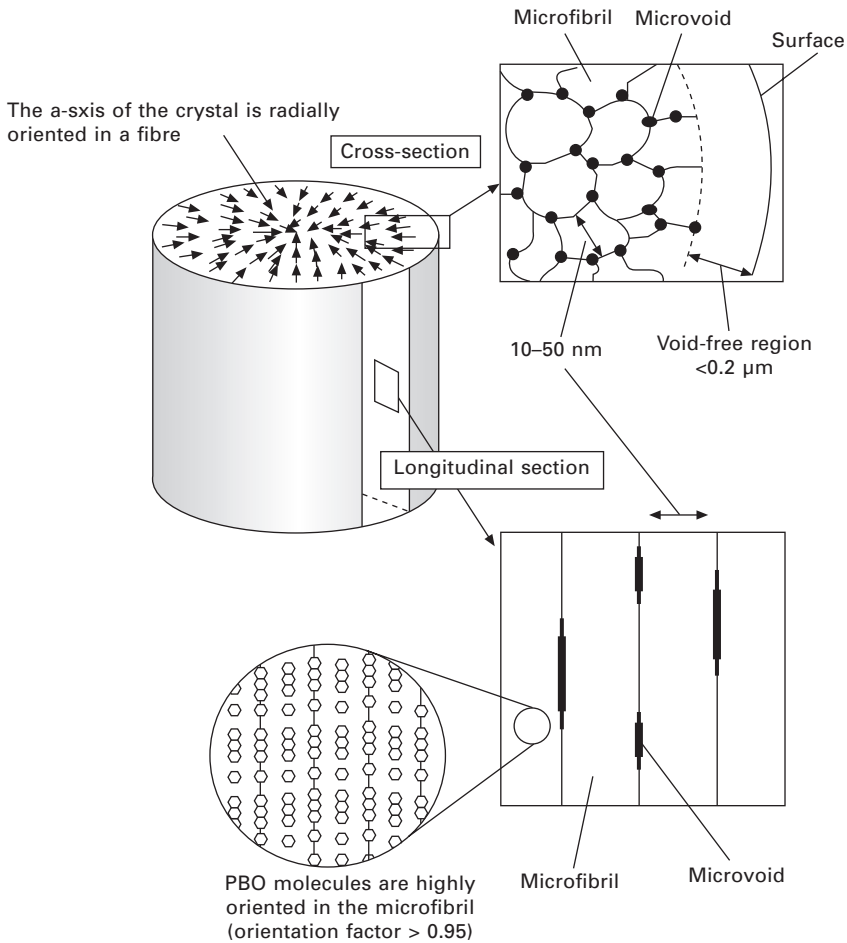
The lattice image (high-resolution electron micrograph) is a powerful tool to clarify local molecular alignment in the fibre, as many researchers have already applied this method to high performance fibres. Excellent alignment of (200) lattice fringes, which represent the alignment of PBO molecules, can be observed even in AS fibre and the local orientations of PBO crystals are improved by heat treatment. Heat treatment also improves the crystal size. It should be noted that the length of the coherency of the crystal continues for over 40 nm, which is longer than the crystal size measured by DF image and WAXS. Adams *et al.* (1989) also observed a similar long-range coherency in their lattice image of PBO and mentioned that molecules existed throughout the crystal region. Therefore, it is believed that PBO fibres are also composed of many extended chains.



15.3 Electron diffraction from an ultrathin section of PBO. ○: Tilt angle 0; ● tilt angle  $30^\circ$ .

### 15.4.3 Fibre structure model for PBO fibre

To summarize the above-mentioned observations, a fibre model of AS fibre is proposed as shown in Fig. 15.4. The structure is formed from microfibrils (initially 10–50 nm in diameter) and contains many capillary-like microvoids, which exist between the microfibrils before drying. These microvoids will be connected to each other through cracks or openings between the microfibrils. There is a void-free region on the actual surface of the fibre. The microfibril is made of extended PBO molecules, highly oriented to the fibre axis. The Hermann's orientation function measured by WAXS is estimated to be over 0.95. A preferential orientation exists and the *a*-axis of the PBO crystal is aligned radially in the cross-section of the fibre. In the case of HM fibre, the Hermann's orientation function value becomes 0.99 or higher.



15.4 Fibre structure model for PBO.

## 15.5 PBO fibre structure under deformation

The HM+ fibre, which has the highest modulus value among the three current PBO fibres, does not show a four-point pattern, suggesting that it has a more homogeneous structure than HM fibre along the fibre axis. Even for HM+ fibre the modulus reaches only 80% of the theoretical limit. It is necessary to clarify the reason for this large gap between the crystalline and fibre modulus. One method is to observe the change in the fibre structure under tension. Fibre in general contains a so-called amorphous region, which may deform more than the region made completely of crystal. X-ray diffraction and Raman scattering have been used for this.

### 15.5.1 Crystalline modulus

To measure the crystalline modulus of the three PBO fibres, the intensity of X-ray diffraction from each stressed fibre was measured with a conventional X-ray diffractometer combined with some in-house stress apparatus. To put stress on the sample fibre along the fibre axis, it was fixed to the stress apparatus, then the apparatus was mounted on a wide-angle X-ray goniometer to collect scattering intensities from the meridian of the fibre. To measure the diffraction angle of the (00*m*) layer lines (*m* is an integer) with great precision, palladium powder was spread on the sample fibre and the diffraction spots of the PBO fibre were measured together with those of the palladium in the same diffraction-angle range of an imaging plate, because the spots from the palladium were used for reference. It was seen that the position of the highest peak moved towards a lower angle and that the breadth of the diffraction profile became wider as the applied stress was increased. By analysing the Bragg spacings of the meridional reflection (the highest peak position) as a function of applied stress, the tensile deformation of the polymer chain was calculated using the following equation:

$$\varepsilon_c = -\cot\theta\Delta(2\theta)/2$$

where  $2\theta$  is the diffraction angle of the *m*th meridional layer line and  $\Delta(2\theta)$  the difference of the diffraction angle between a stress and no-stress situation.

The apparent crystalline modulus for the HM+ fibre was estimated as  $460 \pm 20$  GPa from the slope of the straight line in the figure, which was almost the same as that of HM (460 GPa), but different from that of AS (430 GPa). Published values (Nishino *et al.* 1995 and Lenhert and Adams 1989) of the crystalline modulus and theoretical modulus also give values in the same range (460–480 GPa). It is interesting to note that the apparent crystalline modulus of PBO does not depend to a great extent on the fibre modulus of HM and HM+ fibres. The value obtained for HM and HM+ fibres may be the limit and supports the idea that 460 GPa is the real crystalline modulus.

### 15.5.2 Hosemann's analysis with stress

Hosemann (1967) proposed a theory to analyse such dependence. This theory takes into consideration not only the crystallite size but also the degree of ordering in the crystalline lattice to explain the observed broadening of the X-ray diffraction profile. In this case, the integral breadth  $\delta\beta$  (the total area of the profile divided by the maximum peak height) is explained as follows:

$$\delta\beta = \delta\beta_0 + (\pi gm)^2/c$$

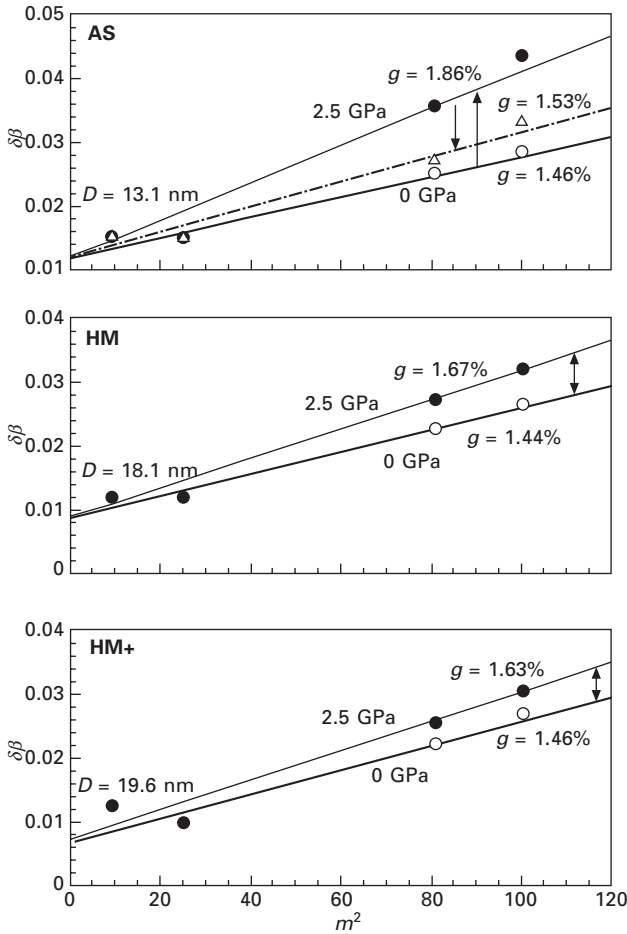
where  $\delta\beta_0$  is the integral breadth determined only by the real crystallite size along the fibre axis,  $g$  the ordering parameter of the crystalline lattice,  $m$  the index of meridional diffraction and  $c$  the Bragg spacing of the (001) plane. Hosemann's plot at 0 GPa and 2.5 GPa of stress is shown in Fig. 15.5. The real crystallite size  $D$  is evaluated from the equation  $D = 1/\delta\beta_0$  and is indicated in the same figure together with  $g$ . The ordering parameter  $g$  depends strongly on the applied stress while the crystallite size stays constant. It is also interesting that the AS fibre shows a relatively large hysteresis with stress; the thick line in the figure after relaxation of stress deviates from the original line at zero stress. As mentioned previously, molecular orientation also changes with stress. The HM and HM+ fibres do not show any permanent structural change with stress; their reactions are confirmed to be reversible.

It can be seen that there is no fibre modulus dependence of  $g$  at zero stress while the  $g$  values under stress (2.5 GPa) are decreased in the order of AS (180 GPa) > HM (280 GPa) > HM+ (360 GPa). The morphology of the PBO fibre is different for AS, HM and HM+. It should be noted that HM+ in particular has a more homogeneous structure along the fibre axis, as revealed by SAXS. This may be the reason why there is less change in the crystalline ordering under deformation in the HM+ fibre.

### 15.5.3 Application of vibrational spectroscopy to analyse fibre structure

#### *Change of vibrational frequencies with stress*

In the previous section, the importance of the concentration of structural defects in PBO fibre is explained. As described previously, no SAXS four-point pattern was found, which should be taken into account in understanding the effects of the concentration of structural defects and inhomogeneity (density fluctuation) along the fibre axis. The interaction between the neighbouring chains in the PBO fibre is due to van der Waals forces and electrostatic forces. The interaction strength is so weak that a micro slippage occurs easily between them. Stress distribution exists in the molecules under tension. Termonia *et al.* (1985, 1986, 1987) and Smith *et al.* (1989) proposed a lattice model to



15.5 Stress dependence of Hosemann's plot for the three PBO fibres.   
 ○: 0.0 GPa; ●: 2.5 GPa; △: 0.0 GPa after relaxation.

predict the effects of a break in the molecule bonds on the stress–strain curves of ultra-high molecular weight polyethylene (UHMW-PE) and PPTA fibres. The question of to what extent the chain ends contribute to the modulus reduction and the stress distribution due to the existence of the chain end is still unresolved. Other types of defect structure, such as the amorphous region and conformational irregularity, may also play a part.

This stress distribution is a reflection of structural incompleteness in the fibre structure. The source of this stress distribution may be related to structural defects such as chain ends, molecular misorientation and inhomogeneity along the fibre axis. It is known that Raman spectroscopy can evaluate such stress distribution by measuring the band shift caused by tensile stress. The shift rate (the frequency shift of the Raman band by 1 GPa tensile stress)

is expressed as a function of the geometry of the molecules of which the fibre is composed and the force constants of the bonds connecting the atoms in each molecule. The rate value also varies with the fibre's structural inhomogeneity.

Compared with general polymers, the Raman intensity from PBO fibre was appreciably high due to the Raman resonance effect coming from the electronically conjugated structure of the skeletal chain. It could be seen that most of the Raman bands shifted towards a lower frequency as a result of the application of tensile stress and the width of these bands became wider. Vibrational frequencies were found to become lower almost linearly with an increase of applied stress. The frequency shift was reversible with the bands returning to their original positions with decreasing tensile stress for the HM and HM+ fibres. The rate of frequency shift differed from band to band and was determined by the balance between harmonic and unharmonic force constants and the vibrational mode of these bands.

The band shift was found to depend on the preparation history of the samples or the fibre modulus as shown in Table 15.5. It is interesting to note that the rate of Raman shift decreases for most of Raman bands as the fibre modulus becomes higher. This dependence is related to the morphology of the fibre sample, especially to the orderliness of the fibre structure; morphological change affects the stress distribution that results in a change in the behaviour of stress-induced Raman shift. In order to develop this discussion it is necessary to first establish the intrinsic shift factors of the observed crystalline state. For this purpose, we carried out an extrapolation of the observed shift factors to the point of the crystalline modulus, as indicated in Table 15.5. These extrapolated shift factor values were compared with the theoretical calculation.

The band broadening is also related to stress distribution in the fibre. The Raman band profile was found to become broader as the applied tensile stress was increased. Most of the bands broadened with increasing stress, but a few peaks kept the same FWHMs (full width at half-height maximum). This implies that the stress distribution in the fibre becomes broader with increasing stress. It is also found that the bands that produce less broadening show smaller shift factors. This increasing rate of the FWHM may act as a measure for expressing how the broadening of the stress distribution is increased with increasing stress. Table 15.5 shows this parameter against the fibre modulus and assignments for the vibration mode are given in Table 15.6. It is also extrapolated to the limit of the crystalline modulus (460 GPa). If the broadening parameter only represents the increasing rate of stress distribution inside the fibre, an extrapolation to the crystalline modulus value should give a null value of FWHM for all the bands, but in actual fact, some bands fall to zero FWHM and some still have a non-zero FWHM. One reason for this might stem from the use of the observed crystalline modulus

Table 15.5 Raman shift and broadening factors

| Frequency<br>(cm <sup>-1</sup> ) | Shift factor<br>(cm <sup>-1</sup> /GPa) |       |       |              |            | Broadening factor<br>(cm <sup>-1</sup> /GPa) |       |       |              |
|----------------------------------|-----------------------------------------|-------|-------|--------------|------------|----------------------------------------------|-------|-------|--------------|
|                                  | AS                                      | HM    | HM+   | Extrapolated | Calculated | AS                                           | HM    | HM+   | Extrapolated |
| 1619                             | -2.93                                   | -3.20 | -3.57 | -3.8         | -4.03      | 2.36                                         | 1.96  | 1.87  | 1.44         |
| 1586                             | -                                       | -     | -     | -            | -3.90      | -                                            | -     | -     | -            |
| 1557                             | -2.49                                   | -3.05 | -3.12 | -3.6         | -4.43      | 0.00                                         | 0.00  | 0.00  | 0.00         |
| 1542                             | -3.40                                   | -3.67 | -4.00 | -4.4         | -4.42      | 4.17                                         | 3.27  | 2.67  | 1.50         |
| 1488                             | -3.45                                   | -4.00 | -4.41 | -4.9         | -3.04      | -                                            | -     | -     | -            |
| 1336                             | -                                       | -     | -     | -            | -0.93      | -                                            | -     | -     | -            |
| 1307                             | -1.38                                   | -1.56 | -1.66 | -1.9         | -1.35      | 0.27                                         | 0.00  | 0.00  | 0.00         |
| 1279                             | -3.17                                   | -3.50 | -3.67 | -3.8         | -2.42      | 4.45                                         | 2.67  | 2.43  | 0.60         |
| 1176                             | -0.47                                   | -0.43 | -0.27 | -0.39        | -0.94      | 0.00                                         | 0.00  | 0.00  | 0.00         |
| 1168                             | -0.45                                   | -0.39 | -0.43 | -0.43        | -0.96      | -0.41                                        | -0.34 | -0.34 | -0.36        |
| 930                              | -0.8                                    | -0.84 | -0.82 | -0.82        | -0.40      | 0.69                                         | 0.48  | 0.46  | 0.55         |
| 822                              | 0.00                                    | 0.00  | -     | 0.00         | -0.40      | -                                            | -     | -     | -            |
| 795                              | -                                       | -     | -     | -            | 0.15       | -                                            | -     | -     | -            |
| 755                              | 0.00                                    | 0.47  | -     | 0.25         | -0.29      | -                                            | -     | -     | -            |
| 728                              | -0.6                                    | -0.77 | -     | -0.70        | -0.36      | -                                            | -     | -     | -            |
| 487                              | -1.12                                   | -1.3  | -1.41 | -1.5         | -0.62      | -                                            | -     | -     | -            |
| 215                              | -                                       | -     | -     | -            | -0.41      | -                                            | -     | -     | -            |



Table 15.6

| Measured IR               |                               |          |                           |          |                                |                  |                                                  |
|---------------------------|-------------------------------|----------|---------------------------|----------|--------------------------------|------------------|--------------------------------------------------|
| $l^*$ (cm <sup>-1</sup> ) | $\perp^*$ (cm <sup>-1</sup> ) | <b>I</b> | Raman (cm <sup>-1</sup> ) | <b>I</b> | Calculated (cm <sup>-1</sup> ) | Symmetry species | Approximate description of normal mode vibration |
|                           | 3099                          | m        |                           |          | 3052                           | A <sub>1</sub>   | C-H stretch                                      |
|                           |                               |          |                           |          | 3052                           | B <sub>2</sub>   | C-H stretch                                      |
|                           | 3068                          | m        |                           |          | 3051                           | A <sub>1</sub>   | C-H stretch                                      |
|                           |                               |          |                           |          | 3050                           | B <sub>2</sub>   | C-H stretch                                      |
|                           | 3036                          | m        |                           |          | 3050                           | B <sub>2</sub>   | C-H stretch                                      |
|                           |                               |          |                           |          | 1738                           | A <sub>1</sub>   | PB ring stretch                                  |
| 1630                      |                               | s        |                           |          | 1657                           | B <sub>2</sub>   | P ring stretch                                   |
|                           | 1619                          | s        | 1619                      | vs       | 1609                           | A <sub>1</sub>   | PB ring stretch + C-C' stretch                   |
| 1581                      |                               | s        | 1586                      | vw       | 1649                           | B <sub>2</sub>   | P ring stretch + C-C' stretch                    |
|                           | 1557                          | s        | 1557                      | s        | 1575                           | A <sub>1</sub>   | P ring stretch + B ring def + C-C'               |
|                           | 1540                          | sh       | 1542                      | s        | 1553                           | A <sub>1</sub>   | P ring stretch + B ring def                      |
|                           | 1497                          | s        |                           |          | 1518                           | A <sub>1</sub>   | C-O + C-C' + O ring def                          |
| 1495                      |                               | s        |                           |          |                                |                  |                                                  |
|                           | 1488                          | sh       | 1488                      | vw       | 1502                           | A <sub>1</sub>   | P ring stretch + C-C' stretch                    |
| 1460                      |                               | w        |                           |          | 1481                           | B <sub>2</sub>   | O ring stretch + P ring def                      |
|                           | 1430                          | w        |                           |          | 1490                           | A <sub>1</sub>   | BO ring stretch                                  |
|                           | 1414                          | s        | 1418                      | vw       | 1412                           | B <sub>2</sub>   | PO ring stretch                                  |
|                           | 1392                          | w        |                           |          | 1452                           | A <sub>1</sub>   | O ring def                                       |
| 1390                      |                               | w        |                           |          |                                |                  |                                                  |
| 1366                      |                               | s        |                           |          | 1368                           | B <sub>2</sub>   | C-N                                              |
|                           | 1330                          | w        | 1336                      | vw       | 1338                           | A <sub>1</sub>   | BO ring stretch                                  |
| 1310                      |                               | w        | 1307                      | m        | 1306                           | A <sub>1</sub>   | P ring def                                       |
|                           | 1308                          | w        |                           |          |                                |                  |                                                  |
| 1292                      |                               | w        |                           |          |                                |                  |                                                  |
| 1285                      |                               | w        |                           |          |                                |                  |                                                  |
|                           | 1275                          | w        | 1279                      | s        | 1284                           | A <sub>1</sub>   | P ring def                                       |

|      |      |    |      |    |      |                |                        |
|------|------|----|------|----|------|----------------|------------------------|
| 1237 |      | vw |      |    | 1203 | B <sub>2</sub> | BO ring def            |
|      | 1209 | w  | 1208 | vw |      |                |                        |
|      | 1176 | vw | 1176 | m  | 1126 | A <sub>1</sub> | PBO ring def           |
|      |      |    | 1168 | m  | 1116 | A <sub>1</sub> | PBO ring def           |
| 1156 |      | sh |      |    |      |                |                        |
| 1147 |      | m  |      |    | 1176 | B <sub>2</sub> | PB ring def            |
| 1118 |      | m  |      |    |      |                |                        |
|      | 1116 | m  |      |    | 1091 | A <sub>1</sub> | PO ring def            |
| 1110 |      | m  |      |    | 1157 | B <sub>2</sub> | BO ring def            |
| 1059 |      | m  |      |    | 1065 | B <sub>2</sub> | BO ring def            |
|      | 1055 | m  |      |    |      |                |                        |
|      | 1041 | sh |      |    |      |                |                        |
| 1010 |      | w  |      |    | 1018 | B <sub>2</sub> | B ring def             |
|      |      |    |      |    | 980  | B <sub>1</sub> | B C-H o.p.             |
|      |      |    |      |    | 976  | B <sub>1</sub> | P C-H o.p.             |
|      |      |    |      |    | 974  | B <sub>1</sub> | B C-H o.p.             |
|      | 927  | m  | 930  | s  | 974  | B <sub>1</sub> | P C-H o.p.             |
|      |      |    |      |    | 959  | A <sub>2</sub> | P C-H o.p.             |
|      |      |    |      |    | 956  | A <sub>2</sub> | P C-H o.p.             |
| 919  |      | m  |      |    | 1003 | B <sub>2</sub> | C-O                    |
| 871  |      | m  |      |    | 888  | B <sub>2</sub> | B ring def             |
|      | 852  | m  |      |    | 858  | A <sub>1</sub> | O ring def             |
|      | 832  | vw |      |    |      |                |                        |
| 830  |      | vw |      |    | 839  | B <sub>2</sub> | BO ring def            |
|      | 820  | w  | 822  | vw | 784  | A <sub>1</sub> | BO ring def            |
|      | 806  | sh | 795  | vw | 741  | A <sub>1</sub> | O ring def             |
| 758  |      | vw | 755  | vw | 810  | B <sub>2</sub> | BO ring def            |
|      |      |    | 728  | vw | 718  | B <sub>2</sub> | O ring def             |
| 708  |      | w  |      |    |      |                |                        |
|      | 706  | w  |      |    | 614  | B <sub>2</sub> | P ring def             |
|      |      |    |      |    | 549  | B <sub>2</sub> | B ring def             |
|      |      |    |      |    | 542  | A <sub>2</sub> | C-C' torsional mortion |

Table 15.6 Cont'd

| Measured IR             |                        |   | Raman<br>(cm <sup>-1</sup> ) | I   | Calculated<br>(cm <sup>-1</sup> ) | Symmetry<br>species | Approximate description of normal mode vibration |
|-------------------------|------------------------|---|------------------------------|-----|-----------------------------------|---------------------|--------------------------------------------------|
| //* (cm <sup>-1</sup> ) | ⊥* (cm <sup>-1</sup> ) | I |                              |     |                                   |                     |                                                  |
|                         |                        |   | 487                          | vw  | 524                               | B <sub>1</sub>      | C-C' torsional mortion                           |
|                         |                        |   |                              |     | 492                               | A <sub>1</sub>      | B bring def                                      |
|                         |                        |   |                              |     | 466                               | A <sub>1</sub>      | BO ring def                                      |
|                         |                        |   |                              |     | 429                               | B <sub>2</sub>      | C-C' anti-symmetric stretch                      |
|                         |                        |   |                              |     | 408                               | A <sub>2</sub>      | P torsional mortion                              |
|                         |                        |   |                              |     | 381                               | B <sub>2</sub>      | C-C' bend                                        |
|                         |                        |   |                              |     | 372                               | A <sub>2</sub>      | P torsional mortion                              |
|                         |                        |   |                              |     | 345                               | A <sub>2</sub>      | B torsional mortion                              |
|                         |                        |   |                              |     | 312                               | A <sub>2</sub>      | B torsional mortion                              |
|                         |                        |   |                              |     | 296                               | B <sub>1</sub>      | O torsional mortion                              |
|                         |                        |   |                              |     | 258                               | B <sub>1</sub>      | BO torsional mortion                             |
|                         |                        |   |                              |     | 249                               | B <sub>1</sub>      | C-C' torsional mortion                           |
|                         |                        |   |                              |     | 211                               | A <sub>2</sub>      | C-C' torsional mortion + P o.p.                  |
|                         |                        |   |                              |     | 208                               | B <sub>1</sub>      | C-C' torsional mortion                           |
|                         |                        |   | 215                          | vww | 197                               | A <sub>1</sub>      | C-C' bend                                        |
|                         |                        |   |                              |     | 165                               | B <sub>1</sub>      | B torsional mortion                              |
|                         |                        |   |                              |     | 152                               | A <sub>2</sub>      | C-C' torsional mortion                           |
|                         |                        |   |                              |     | 124                               | B <sub>1</sub>      | B torsional mortion                              |
|                         |                        |   |                              |     | 112                               | B <sub>2</sub>      | C-C' bend                                        |
|                         |                        |   |                              |     | 61                                | A <sub>2</sub>      | O torsional mortion                              |
|                         |                        |   |                              |     | 52                                | B <sub>1</sub>      | B torsional mortion                              |

\*The direction of the transition dipoles //: parallel to the fiber axis; ⊥ perpendicular, to the fiber axis.

I: absorption of IR bands or intensity of the Raman bands.

v: very; s: strong; m: medium; w: weak; sh: shoulder.

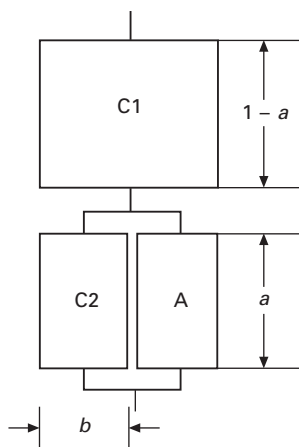
P: phenylene; B: benzene; O: oxazole; def: deformation; o.p.: out-of-plane.

in this extrapolation: even the crystalline modulus itself shows a morphology dependence. In addition, the Raman bands should have their own intrinsic widths originating from the limited lifespan of thermal vibrations.

The Raman shift factor is a function of molecular geometry and harmonic and anharmonic force constants. An internal coordinate showing higher efficiency for stretching a polymer chain shows a higher frequency shift of the corresponding vibrational band. In addition, if the anharmonicity is larger for this vibrational mode, the shift factor becomes even larger. For example, the band at  $1619\text{ cm}^{-1}$  was assigned to the stretching mode of the phenylene and benzothiazole rings coupled with the stretching mode of the CC bond connecting these two rings. This band was shifted at the observed and calculated rates of  $-3.80\text{ cm}^{-1}/\text{GPa}$  and  $-4.04\text{ cm}^{-1}/\text{GPa}$ , respectively. This relatively large shift factor is thought to come from the high efficiency of these stretching modes for the chain deformation as well as the high anharmonicity of the electronically conjugated ring structure. On the other hand, the band at  $930\text{ cm}^{-1}$  was assigned to the CH out-of-plane deformation mode of the phenylene ring and had a shift factor of  $-0.82\text{ cm}^{-1}/\text{GPa}$  (the calculated value  $-0.39\text{ cm}^{-1}/\text{GPa}$ ). This relatively small shift factor is considered to relate to the origin of this band. The CH out-of-plane mode does not contribute very much to the effective stretching of the skeletal chain.

#### *Raman shift factor and morphology of fibres*

In order to understand the morphological effect on the Raman shift factor, a mechanical series-parallel model was introduced (Fig. 15.6). The Raman shift factor decreased with an increment of the bulk modulus, logically explained



15.6 A mechanical series-parallel model. C1 and C2 stand for crystalline part and A for amorphous part.

by the assumption of a concentration of stress by the crystalline tie chains. This interpretation assumed that the amorphous part did not contribute to the Raman bands tabulated in the analysis, because those observed bands came mainly from the crystalline region. In the case of PBO, on the other hand, the Raman band shift factor was smaller for the sample with a lower fibre modulus. PBO fibre is made of rigid-rod chains, therefore it is assumed that the chains in the amorphous part may take the extended form, which contributes about as much to the Raman scattering as the crystalline part does. Parallel packing of the rigid chain segments seems difficult in the amorphous region and so these chain segments do not contribute to the X-ray scattering from the crystal lattice.

According to the mechanical series–parallel model shown in Fig. 15.6, the apparent crystalline modulus ( $E_c^{\text{app}}$ ) and the bulk fibre modulus ( $E_{\text{bulk}}$ ) are given as follows:

$$E_c^{\text{app}} = \frac{E_c^{\text{true}} x}{1 - a + ab/[b + (1 - b)E_a/E_c^{\text{true}}]}$$

$$E_{\text{bulk}} = \frac{1}{(1 - a)/E_c^{\text{true}} + a/[b E_c^{\text{true}} + (1 - b)E_a]}$$

where  $E_c^{\text{true}}$  is the true Young's modulus of the crystalline part,  $E_a$  is the Young's modulus of the amorphous part, and the degree of crystallinity is given by  $x = 1 - a + ab$ . The parameters  $a$  and  $b$  are defined in Fig. 15.6. The average frequency  $\langle \nu \rangle$  is expressed as follows:

$$\langle \nu \rangle = \nu_0 + \alpha_C q \sigma_{\text{bulk}}$$

where

$$q = \frac{b E_c^{\text{true}} + (1 - b)E_a - a(1 - b) E_a(1 - \alpha_A/\alpha_C)}{b E_c^{\text{true}} + (1 - b)E_a}$$

where  $\sigma_{\text{bulk}}$  is the bulk stress,  $\alpha_C$  is the Raman shift factor for the crystalline part and  $\alpha_A$  is the factor for the amorphous part. The parameters  $a$ ,  $b$ ,  $E_c^{\text{true}}$ ,  $E_a$ ,  $\alpha_C$  and  $\alpha_A$  were adjusted so that the observed values of  $E_{\text{bulk}}$ ,  $E_c^{\text{app}}$  and  $\langle \nu \rangle$  could be reproduced as reasonably as possible. Values of the parameters so obtained are tabulated in Table 15.7. The  $E_c^{\text{app}}$ ,  $E_{\text{bulk}}$  and  $\alpha$  ( $= \alpha_C q$ : apparent Raman shift factor) calculated for the models are listed in Table 15.8. The parameter  $b$  is almost zero for all the samples, indicating an application of the mechanical series model to PBO fibres. The parameter  $\alpha_A$ , a shift factor of the amorphous band, is almost zero, too. The measured apparent crystalline modulus differs, being slightly lower in AS (430 GPa) than in HM and HM+, but the results based on the simulation show the same value (460 GPa). Therefore the Raman band of the amorphous region is considered to contribute to the intensity of the crystalline band at the original frequency position. By increasing the quality of the PBO fibre from AS to HM and

Table 15.7 Obtained suitable parameters for the series model

| $E_c^{\text{true}}$<br>(GPa) | $E_a$<br>(GPa) | $\alpha_c$<br>( $\text{cm}^{-1}/\text{GPa}$ ) | $\alpha_A$<br>( $\text{cm}^{-1}/\text{GPa}$ ) |
|------------------------------|----------------|-----------------------------------------------|-----------------------------------------------|
| 460                          | 70             | -3.80                                         | 0.0                                           |

Table 15.8 Comparison between measured and calculated shift factors  $\alpha$ 

|                                                     | AS    | HM    | HM+   |
|-----------------------------------------------------|-------|-------|-------|
| $E_{\text{bulk}}$ (GPa)                             | 187   | 258   | 352   |
| $a$                                                 | 0.26  | 0.14  | 0.055 |
| $b$                                                 | 0.0   | 0.0   | 0.0   |
| $\alpha$ : measured ( $\text{cm}^{-1}/\text{GPa}$ ) | -2.93 | -3.20 | -3.57 |
| calculated ( $\text{cm}^{-1}/\text{GPa}$ )          | -2.80 | -3.27 | -3.59 |

HM+, the contribution of the C phase is increased more reasonably, consistent with the observations from X-ray diffraction and the electron microscope. Because the amorphous region is assumed to contribute to the Raman bands but not to the X-ray scattering profile, the Raman shift factor is changed depending on the relative content of C and A parts but the crystalline modulus is essentially the same for the three types of fibres. They are also consistent with the observations.

## 15.6 Future trends

### 15.6.1 Crystallographic analysis for PBO

Professor Tashiro has dedicated himself to elucidating the structure and properties of PBO crystal. Several research groups have proposed a crystal model based on X-ray and electron diffraction data. However, their models can only reproduce the observed equatorial intensities. There is less agreement about the layer line. Professor Tashiro has developed a new system to analyse the structure of polymer crystals using a specific combination of X-ray diffraction, electron diffraction, vibrational spectroscopy and computer simulations. Moreover, he is designing a new type of three-dimensional PBO molecule with a conventional polymer crystal lattice. It is predicted that the molecule will have a high Young's modulus of 700–1800 GPa, the maximum value of which is significantly higher than that of diamond crystal (1050 GPa).

### 15.6.2 In-situ study to analyse fibre structure formation during spinning

During spinning, the oriented structure of the PBO polymer solution is transformed into a crystallite phase in an air gap, followed by coagulation. To

analyse this structural evolution, (Ran *et al.*, 2002a,b) Professors Benjamin Chu and Benjamin S. Hsiao have combined wide-angle X-ray diffraction and small-angle X-ray scattering with a synchrotron radiation source. This has revealed that the best model to describe the intermediate structure before coagulation is a biaxial nematic phase based on a plank-shaped structural unit with a PBO-polyphosphoric acid complex. After coagulation, the (010) reflection was found to be formed ahead of the (200) reflection, which revealed that the first stage of coagulation was the formation of PBO molecular stacks.

### 15.6.3 Structural study of a single PBO fibre with synchrotron radiation

Synchrotron radiation was also introduced by Dr Davies, Dr Riekkel and Professor Young to obtain single-fibre diffraction patterns of PBO. The crystal modulus was calculated as 430–470 GPa. The fibre showed an increase in the degree of orientation in both the skin and core parts of the fibre under deformation. Under high levels of deformation, a lattice difference existed between crystallite orientation in the AS fibre skin and core. A micro-focused synchrotron beam was also used to investigate radial fibrillar texturing in PBO through a variation in equatorial reflection intensity across the fibre. It was found that the *a*-unit axis was oriented radially about the fibre axis. These findings support the fibre model shown in Fig. 15.4.

## 15.7 Conclusions and comments

Morphological features were inspected by X-ray diffraction and electron microscope methods, in which a new ultra-high modulus HM+ fibre was prepared using non-aqueous coagulation with conventional heat treatment under tension. It was found that the molecular orientation of the fibre as well as its structural inhomogeneity along the fibre axis was the factor that controlled the fibre modulus. Compliance was treated as a function of crystallite orientation. The predicted modulus based on Northolt's equation was 370 GPa, which was less than the crystal modulus (460 GPa). The four-point pattern changed when the fibre was made with a different coagulant. The existence of a preferential orientation for the *a*-axis of PBO crystal was proved.

In order to discover the deformation mechanism of the fibre, X-ray diffraction patterns from the fibre under tensile stress were investigated and analysed. Based on Hosemann's paracrystal theory, the ordering parameter for lattice distortion was also evaluated. This ordering parameter was found to decrease with an increase in the fibre modulus. Lattice distortion was thought to relate to the distribution of stress along the molecular chain and

therefore to the structural inhomogeneity or the structural defects in the fibre. The HM+ fibre was considered to contain a very low concentration of defects and a low degree of structural inhomogeneity, giving the highest Young's modulus among the three types of fibre.

Raman spectroscopy was applied to clarify the relationship between the stress distribution in the fibre structure and the morphology. The Raman shift factor of the  $1619\text{ cm}^{-1}$  band corresponding to phenylene ring vibration was investigated. It was discovered that the shift factor strongly depended on the fibre modulus. It was also found that band-profile broadening occurred and its degree became higher as the fibre modulus decreased, indicating that stress distribution was induced in the fibre structure, and the rate also depended on inhomogeneity in the fibre structure.

Normal-mode calculation under quasi-harmonic approximation was performed and the Raman shift factor for PBO was also predicted. The measured values agreed with the theoretically predicted values. Fibre modulus dependencies of the band shift and peak-profile broadening were examined with a mechanical series-parallel model. The model explained them fairly well but some further study is still needed to understand the stress distribution under strong tensile stress.

It is well known that mechanical properties strongly depend on the fibre structure. From the analytical point of view, the high modulus nature of PBO fibre is considered to stem from its molecular geometry, strong chemical bonds (large force constants) and extended fibre structure along the fibre axis. The relationship between mechanical properties and fibre structure could be quantitatively interpreted quite well using a mechanical series-parallel model. This study has given us many useful indications needed for the development of new polymer materials with excellent mechanical properties. The author believes it will be possible to make new polymers in the near future, the mechanical properties of which will greatly exceed those of PBO fibre.

## 15.8 References and further reading

- Adams W W, Kumar S, Martin D C, Shimamura K (1989), 'Lattice imaging of poly(*p*-phenylene benzobisoxazole) fibre', *Polymer Communications* **30** 285–287.
- Bai S J (1998), 'Axial X-ray scattering on high-performance polymeric fibres', *Journal of Polymer Science, Part B: Polymer Physics* **32** 2575–2583.
- Bai S J, Price G E (1992), 'Small-angle X-ray scattering on fibres of heteroaromatic polymers', *Polymer* **33** 2136–2142.
- Cohen Y, Thomas E L (1985), 'Structure formation during spinning of poly(*p*-phenylenebenzobisthiazole) fibre', *Polymer Engineering and Science* **25** 1093–1096.
- Cohen Y, Thomas E L (1988a), 'Microfibrillar network of a rigid rod polymer. 1. Visualization by electron microscopy', *Macromolecules* **21** 433–435.
- Cohen Y, Thomas E L (1988b), 'Microfibrillar network of a rigid rod polymer. 2. Small-angle X-ray scattering', *Macromolecules* **21** 436–441.



- David C M, Edwin L T (1991), 'Ultrastructure of poly(*p*-phenylenebenzobisoxazole) fibres', *Macromolecules* **24** 2450–2560.
- Davies R J, Montes-Moran M A, Riekel C, Young R J (2001), 'Single fibre deformation studies of poly(*p*-phenylene benzobisoxazole) fibres. Part 1. Determination of crystal modulus', *Journal of Materials Science* **36** 3079–3087.
- Davies R J, Montes-Moran M A, Riekel C, Young R J (2003), 'Single fibre deformation studies of poly(*p*-phenylene benzobisoxazole) fibres. Part 2. Variation of crystal strain and crystallite orientation across the fibre', *Journal of Materials Science* **38** 2105–2115.
- Davies R J, Eichhorn S J, Riekel C, Young R J (2004), 'Crystal lattice deformation in single poly(*p*-phenylene benzobisoxazole) fibres', *Polymer* **45** 7693–7704.
- Davies R J, Burghammer M, Riekel C (2005a), 'Modeling structural disorder within single poly(*p*-phenylenebenzobisoxazole) fibres using a submicrometer synchrotron beam', *Macromolecules* **38** 3364–3370.
- Davies R J, Eichhorn S J, Riekel C, Young R J (2005b), 'Crystallographic texturing in single poly(*p*-phenylene benzobisoxazole) fibres investigated using synchrotron radiation', *Polymer* **46** 1935–1942.
- Dobb M G, Johnson D J, Saville B P (1977), 'Direct observation of structure in high-modulus aromatic fibres', *Journal of Polymer Science: Polymer Symposia* **58** 237–251.
- Fratini A V, Lenhart P G, Resch T J, Adams W W (1989), 'Molecular packing and crystalline order in polybenzobisoxazole and polybenzobisthiazole fibres', *Materials Research Society Symposium Proceedings* **134** 431.
- Hosemann R (1967) 'Combined Analysis of Small-Angle Scattering of Reflections (000) and (hkl)' in '*Small-Angle X-ray Scattering*' edited by Brumberger H, published by Gordon and Breach, Science Publishers, 169–196.
- Hunsaker M E, Price G E, Bai S J (1992), 'Processing, structure and mechanics of fibres of heteroaromatic oxazole polymers', *Polymer* **33** 2128–2135.
- Kitagawa T, Yabuki K (2000a), 'An investigation into the relationship between internal stress distribution and a change of poly-*p*-phenylenebenzobisoxazole (PBO) fibre structure', *Journal of Polymer Science, Part B: Polymer Physics* **38** 2901.
- Kitagawa T, Yabuki K (2000b), 'A relationship between the stress distribution and the peak profile broadening of meridional X-ray diffraction from poly-*p*-phenylenebenzobisoxazole (PBO) fibre', *Journal of Polymer Science, Part B: Polymer Physics* **38** 2937.
- Kitagawa T, Murase H, Yabuki K (1998), 'Structural study on poly-*p*-phenylenebenzobisoxazole (PBO) fibre', *Journal of Polymer Science, Part B: Polymer Physics* **36** 39.
- Kitagawa T, Ishitobi M, Yabuki K (2000), 'An analysis of deformation process on poly-*p*-phenylenebenzobisoxazole (PBO) fibre and a structural study of the new high-modulus type PBO HM+ fibre', *Journal of Polymer Science, Part B: Polymer Physics* **38** 1605.
- Kitagawa T, Yabuki K, Young R J (2001), 'An investigation into the relationship between processing, structure and properties for high-modulus PBO fibres. Part 1. Raman band shift and broadening with tension and compression', *Polymer* **42** 2101.
- Kitagawa T, Tashiro K, Yabuki K (2002a), 'Stress distribution in poly-*p*-phenylenebenzobisoxazole fibre as viewed from vibrational spectroscopic measurement under tension. 1. Stress-induced frequency shifts of Raman bands of molecular deformation mechanism', *Journal of Polymer Science, Part B: Polymer Physics* **40** 1269–1280.
- Kitagawa T, Tashiro K, Yabuki K (2002b), 'Stress distribution in poly-*p*-phenylenebenzobisoxazole fibre as viewed from vibrational spectroscopic measurement

- under tension. 2. Analysis of inhomogeneous stress distribution in PBO fibre', *Journal of Polymer Science, Part B: Polymer Physics* **40** 1281–1287.
- Krause S J, Haddock T B, Vezie D L, Lenhart P G, Hwang W-F, Price G E, Helminiak T E, O'Brien J F, Adams W W (1988), 'Morphology and properties of rigid-rod poly(*p*-phenylene benzobisoxazole) (PBO) and stiff-chain poly(2,5(6)-benzoxazole) (ABPBO) fibres', *Polymer* **29** 1354–1364.
- Kumar S, Warner S, Grubb D T, Adams W W (1994), 'On the small-angle X-ray scattering of rigid-rod polymer fibres', *Polymer* **35** 5408–5412.
- Lenhart P G, Adams W W (1989), 'X-ray diffraction studies of the axial tensile modulus of rigid-rod polymer fibres', *Materials Research Society Symposium Proceedings* **134** 329.
- Martin D C, Thomas E L (1989), 'Morphology of rigid-rod polymer fibres: an overview', *Materials Research Society Symposium Proceedings*, **134** 415.
- Nishino T, Matsui R, Nakamae K, Gotoh Y, Nagura M (1995), 'Elastic modulus of the crystalline regions of poly(*p*-phenylene benzobisthiazole) and poly(*p*-phenylene benzobisoxazole) and its temperature dependence', *Seni Gakkai Preprints* **G-149**.
- Northolt M G (1980), 'Tensile deformation of poly(*p*-phenylene terephthalamide) fibres, an experimental and theoretical analysis', *Polymer* **21** 1199–1204.
- Ran S, Burger C, Fang D, Zong X, Cruz S, Chu B, Hsiao B S, Bubeck R A, Yabuki K, Teramoto Y, Martin D C, Johnson M A, Cunniff P M (2002a), 'In-situ synchrotron WAXD/SAXS studies of structural development during PBO/PPA solution spinning', *Macromolecules* **35** 433–439.
- Ran S, Burger C, Fang D, Zong X, Chu B, Hsiao B S, Ohta Y, Yabuki K, Cunniff P M (2002b), 'A synchrotron WAXD study on the early stages of coagulation during PBO fibre spinning', *Macromolecules* **35** 9851–9853.
- Shimamura K, Minter R, Thomas E L (1983), 'Lattice imaging of high modulus poly(*p*-phenylene benzobisthiazole) fibres', *Journal of Materials Science Letters* **2** 54.
- Smith P, Termonia Y (1989), 'Effect of chain-end segregation on the theoretical tensile strength of polyethylene and Kevlar<sup>®</sup>', *Polymer Communications* **30** 66–68.
- Takahashi Y (1999), 'Neutron structure analysis and structural disorder of poly(*p*-phenylene benzobisoxazole)', *Macromolecules* **32** 4010–1014.
- Tashiro K, Kobayashi M (1991), 'Theoretical Young's moduli of poly(*p*-phenylenebenzobisthiazole) and poly(*p*-phenylenebenzobisoxazole)', *Macromolecules* **24** 3706–3708.
- Tashiro K and Kobayashi M (1996), 'Molecular theoretical study of the intimate relationships between structure and mechanical properties of polymer crystals', *Polymer* **37** 1775–1786.
- Tashiro K, Kobayashi M, Yabuki K (1995), 'Theoretical prediction of three-dimensionally conjugated novel polymers with excellent mechanical and electric properties: stiffer than diamond', *Synthetic Metals* **71** 2101–2102.
- Tashiro K, Yoshino J, Kitagawa T, Murase H, Yabuki K (1998), 'Crystal structure and packing disorder of poly(*p*-phenylenebenzobisoxazole): Structural analysis by an organized combination of X-ray imaging plate system and computer simulation technique', *Macromolecules* **31** 5430–5440.
- Tashiro K, Hama H, Yoshino J, Abe Y, Kitagawa T, Yabuki K (2001), 'Confirmation of the crystal structure of poly(*p*-phenylene benzobisoxazole) by the X-ray structure analysis of model compounds and the energy calculation', *Journal of Polymer Science, Part B: Polymer Physics* **39** 1296–1311.
- Termonia Y, Smith P (1986), 'Theoretical study of the ultimate mechanical properties of poly(*p*-phenylene-terephthalamide) fibres', *Polymer* **27** 1845–1849.

- Termonia Y, Smith P (1987), 'Influence of weak-link chain defects on the theoretical strength of perfectly ordered and oriented polyethylene', *Polymer Communications* **28** 60–61.
- Termonia Y, Meakin P, Smith P (1985), 'Theoretical study of the influence of the molecular weight on the maximum tensile strength of polymer fibres', *Macromolecules* **18** 2246–2252.
- Wierschke S G, Shoemaker J R, Haaland P D, Pachter R, Adams W W (1992), 'Electronic structure and properties of strained polymers: 2. Rigid-rod PBI, PBO and PBZT', *Polymer* **33** 3357–3368.
- Young R J, Day R J, Zakikhani M (1990), 'The structure and deformation behaviour of poly(*p*-phenylene benzobisoxazole) fibres', *Journal of Materials Science* **25** 127–136.

## The structure of high-modulus, high-tenacity PIPD 'M5' fibre

J W S HEARLE, University of Manchester, UK

**Abstract:** Current high-modulus, high-tenacity fibres have poor transverse properties. Sikkema proposed a way of improving these by multi-directional hydrogen bonding in poly[2,6-diimidazo[4,5-b:4',5']pyridinylene-(2,5-dihydroxy)phenylene], PIPD. The polymer was synthesised and spun into M5 fibres. The crystal structure has been determined. More recently an alternative explanation of the improved transverse properties has been presented. The commercial future of M5 fibres is uncertain.

**Key words:** PIPD polymer, PIPD synthesis, PIPD crystal structure, fibre transverse properties, M5 fibre.

### 16.1 The problem of lateral weakness

HM-HT fibres have high axial strength due to their molecular alignment. In polymers such as PBO, there are only weak van der Waals bonds in the transverse direction between their linear molecules. In the para-aramids, such as *Kevlar*, there are stronger hydrogen bonds between –CO.NH– groups, but these are only in one plane, with weak bonding in the perpendicular direction. The consequence of the lack of transverse bonding is poor resistance to shear between molecules, which allows for easy yield in axial compression. Kink bands form as the molecules buckle at a nanometre scale. Repeated cycling leads to axial compression fatigue failure. A potential for advance was recognised, if this defect could be removed by achieving stronger transverse bonding.

### 16.2 Chemistry of PIPD

Sikkema (2001) describes his ambition 'to create polymers as *rigid-rod like* as PBO, with *strong intermolecular hydrogen bonds*.' The synthesis of poly[2,6-diimidazo[4,5-b:4',5']pyridinylene-(2,5-dihydroxy)phenylene], PIPD, provided the solution. The polymer has been converted on a pilot scale<sup>1</sup> to the M5 fibre by conventional air gap wet-spinning of a solution in methane sulphonic acid of PIPD with a molecular weight of 60 000 to 150 000. Lammers *et al.* (1999) describe structural transitions during the

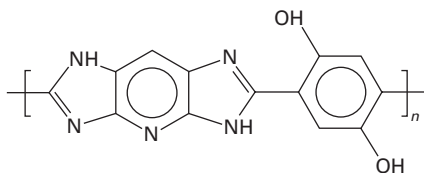
<sup>1</sup>The commercial future of M5 fibre is uncertain.

manufacture of PIPD fibres. They report that the tensile modulus increases from 195 GPa in as-spun fibre to 320 GPa in fibre that has been heat treated at 400°C. Extrapolation to zero angle of orientation gives values of 320 and 500 GPa respectively. The corresponding values of shear modulus are 3.8 and 7.4 GPa.

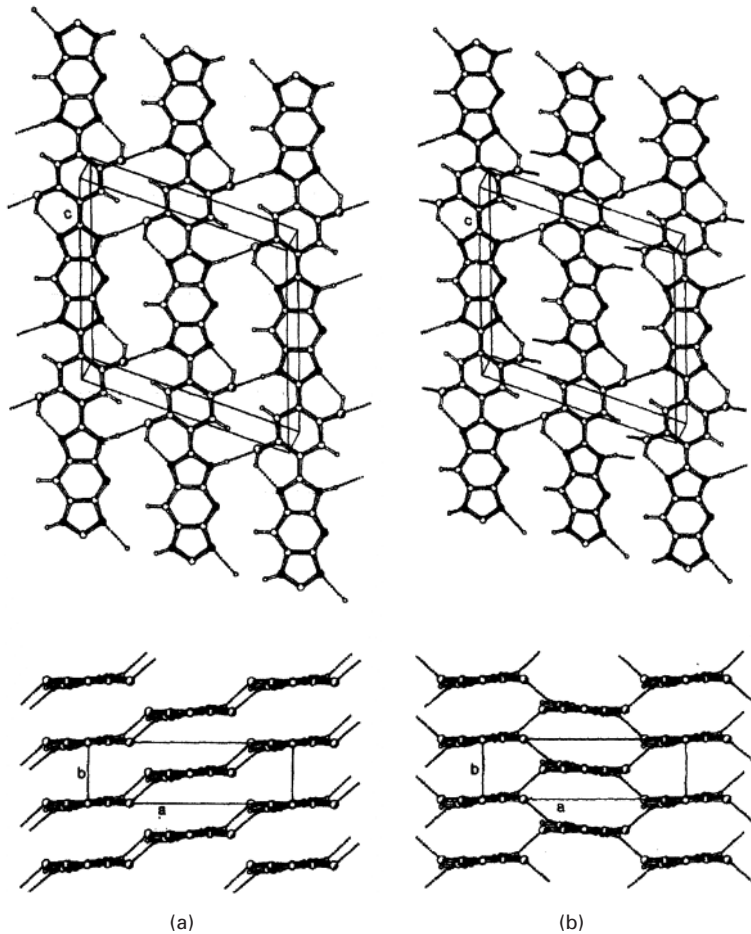
The chemical formula of PIPD is shown in Fig. 16.1. The basic form has the same [5-6-5] rings alternating with benzene [6] rings as are found in PBO and the related polymers from the USAF research. The important differences are the two hydroxyl [-OH] groups appended to the benzene rings and the replacement of the oxygen [>O] of PBO by imidazole [>NH] groups in the five-membered rings. Hydrogen bonding occurs between the -OH and >NH groups. Klop and Lammers (1999) report that the >C.H and >N groups on the central ring may interchange irregularly, so that any crystal lattice would be imperfect, though, because of the similarity in size, this does not affect the X-ray diffraction pattern. There are now two explanations of the way in which the hydrogen bonding leads to a higher shear modulus and greater resistance to axial slip between molecules, which in turn leads to a compressive strength that is at least four times that of PBO fibres.

### 16.3 Crystal structure

The crystal structure of PIPD was investigated by Klop and Lammers (1999) and led to the first explanation. They found that the X-ray diffraction pattern of M5 fibre, which had been heat-treated at 500°C, was satisfied by both a triclinic and a monoclinic lattice, Fig. 16.2. In the triclinic form, the hydrogen bonding links the PIPD molecules into two-dimensional sheets, with interactions between the sheets. In the monoclinic form the hydrogen bonding is bidirectional, so that the structure is three-dimensional, with covalent bonds along the chains and hydrogen bonds between the chains. In order to distinguish between the forms, the transverse spacings were determined by X-ray diffraction at temperatures from 50 to 500°C. With the triclinic form, a difference in thermal expansion in the two transverse directions, due to the difference in bonding, was expected to lead to a differential change in spacing. In the diffraction data there was no splitting of the 3.34 Å spacing, which showed that the thermal expansion was the same in both directions



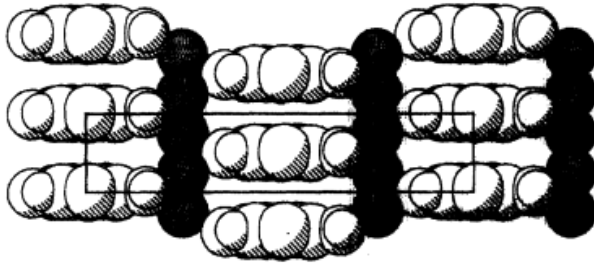
16.1 Formula of PIPD.



16.2 Possible crystal lattices of PIPD: (a) triclinic; (b) monoclinic.

and the monoclinic, in which bonding is similar in both directions, was therefore taken to be the correct structure. The calculated density of the crystal is  $1.77 \text{ g/cm}^3$ .

The as-spun fibre shows a different diffraction pattern due to the presence of absorbed moisture. Klop and Lammers (1999) describe the structure as ‘a two-dimensionally ordered hydrate [in which] the polymer chains are packed regularly in lateral directions, but ... lack longitudinal register’. The section through the structure in Fig. 16.3 illustrates how the 200 spacing increases from  $5.98 \text{ \AA}$  for heat-treated to  $8.38 \text{ \AA}$  for as-spun. The 110 spacing is hardly changed at  $3.33 \pm 0.01 \text{ \AA}$ . The hydrate  $\text{PIP.D.4H}_2\text{O}$  contains 21.4% by weight of water and has a density of  $1.60 \text{ g/cm}^3$ . A progressive change in X-ray scattering was found on heating in dry nitrogen from 20 to  $450^\circ\text{C}$ .



16.3 Lattice with water molecules between PIPD molecules in as-spun fibre.

The moisture regain of M5 fibres in ambient conditions is quoted as 2%. Measurements of the X-ray diffraction of PIPD fibres at the European Synchrotron Radiation Facility by Montes-Morán *et al.* (2002) indicated a  $6.22 \text{ \AA}$  200 spacing, which is slightly but significantly greater than  $5.98 \text{ \AA}$  for the heat-treated fibre. This indicates that the crystal structure is less perfect. The main purpose of this investigation was to determine crystal moduli of three rigid-rod polymers from changes in the crystal lattice during extension. The tensile modulus of PIPD was found to be 450 GPa, which is slightly higher than that of PBO and substantially greater than that of the sulphur analogue, PBT.

## 16.4 Modulus calculations

Hageman *et al.* (1999) report *ab initio* calculations to estimate the chain modulus and electronic and optical properties of both the monoclinic and triclinic PIPD crystals. Takahashi (2002, 2003) made neutron and X-ray diffraction studies and came up with some differences in the crystal structure, particularly in relation to the hydrogen bonding.

The alternative explanation of the high shear modulus was proposed by Hageman *et al.* (2005), who used VASP (Vienna *ab initio* simulation package) to investigate the crystal structure and shear of PIPD crystals based on nearest and next-nearest neighbour bonding. They found that the triclinic structure had a lower energy than the monoclinic and that the shear modulus of the triclinic at 7.7 GPa was higher than for the monoclinic at 5.2 GPa. They indicate compressive strengths of 0.7 GPa for the monoclinic and 2.1 GPa for the triclinic. Nevertheless, they stress the importance of the hydrogen bonding in giving much higher shear moduli and compressive strength than in PBO. In the triclinic structure, hydrogen bonding, which is concentrated in the sheets, resists shear in their plane. The high shear resistance between sheets is attributed to a strong interaction between the rings, which would presumably also prevent the higher thermal expansion suggested by Klop

and Lammers (1999). This is reminiscent of the role of interaction between benzene rings in polyethylene terephthalate. In view of these results, Hageman *et al.* (2005) favour the triclinic structure. They attribute the lower shear resistance between sheets in the monoclinic structure to the hydrogen bonds forcing the rings into less favourable positions, thus reducing the overall interaction. In PBO, they postulate a high shear resistance between sheets due to ring interaction, but assume that shear would be easy within sheets due to the absence of hydrogen bonding.

## 16.5 Coarse structure and conclusion

There is no published information on the larger-scale structure of M5 fibres, except that there is a high degree of orientation in the direction of the fibre axis. It can be assumed that the structure is broadly similar to the structure of other HM-HT linear polymer fibres. The molecules will be packed in crystalline order in fibrillar or quasi-fibrillar units, which show some disorder in their packing together. Water molecules will be absorbed at discontinuities between the fibrils.

The achievement of improved transverse properties in M5 fibre is an important indicator of the influence of details of chemical and physical structure on mechanical properties of high-modulus, high-tenacity polymer fibres. However, the commercial future of M5 fibres is uncertain, possibly due to problems of long-term instability in warm, moist conditions, as was found with PBO fibres.

## 16.6 References

- Hageman J C L, van der Horst J W and de Groot R A (1999), An *ab initio* study of the structural and physical properties of a novel rigid-rod polymer PIPS, *Polymer*, **40**, 1313–1323.
- Hageman J C L, de Wijs G A, de Groot R A and Klop E A (2005), The role of the hydrogen bonding for the shear modulus of PIPD, *Polymer*, **46**, 9144–9154.
- Klop E A and Lammers M (1999), XRD study of the new rigid-rod polymer fibre PIPD, *Polymer*, **39**, 5987–5988.
- Lammers M, Klop E A, Northolt M G and Sikkema D J (1999), *Polymer*, **39**, 5999–6005.
- Montes-Morán M A, Davies R J, Riekel C and Young R J (2002), Deformation studies of single rigid-rod based fibres. Part I. Determination of crystal modulus, *Polymer*, **43**, 5219–5226.
- Sikkema D J (2001), PIPD or 'M5' rigid-rod polymer fibre, in *High-performance Fibres*, Hearle J W S, editor, Woodhead Publishing, Cambridge, UK, 108–115.
- Takahashi Y (2002), Neutron structure analysis of poly(pyridobisimidazole) (PIP), *Macromolecules*, **35**, 3942–3945.
- Takahashi Y (2003), Crystal structure of poly(pyridobisimidazole) (PIP), *Macromolecules*, **36**, 8652–8655.



## Electrospinning and its influence on the structure of polymeric nanofibers

---

K GARG, S A SELL and G L BOWLIN, Virginia Commonwealth University, USA

**Abstract:** Electrospinning is a process of creating solid continuous fibers of material with diameter in the micro- to nanometer range by using electric fields. Electrospinning has attracted increased attention in the past few years in a broad range of biomedical and industrial applications due to the ease of forming fibers with a wide range of properties. This chapter discusses the basic electrospinning technique and the factors that influence the process and the resulting nanofibers. Information on the creation of various types of nanofibers (such as hollow, helical, porous, flat, aligned, non-woven and conductive) has also been provided. The section on fiber structure describes some of the unique features of electrospun fibers. The chapter ends with a description of the impact of structure on the properties of fibers (such as mechanical, thermal, transport and surface).

**Key words:** electrospinning, nanofibers, Taylor cone, non-woven fabrics.

### 17.1 Introduction

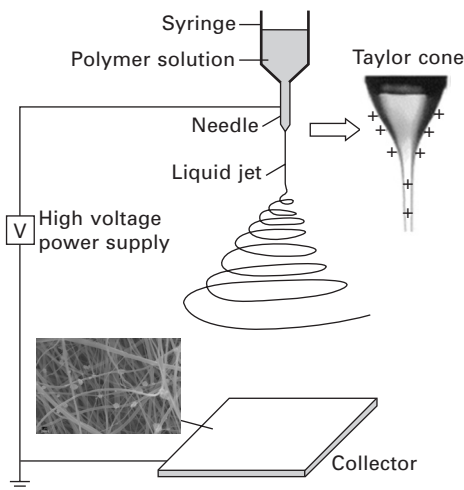
Polymeric nanofibers can be created in a variety of ways such as drawing, template synthesis, self-assembly, phase separation and electrospinning (Ramakrishna *et al.*, 2005). Electrospinning is a process of creating solid continuous fibers of material with diameter in the micro-to nanometer range by using electric fields. Compared to mechanical drawing, electrospinning produces fibers of thinner diameters via a contactless procedure (Li and Xia, 2004a). It is less complex than self-assembly and can be used for a wide range of materials, unlike phase separation. Electrospinning has attracted increased attention in the past few years in a broad range of biomedical and industrial applications due to the ease of forming fibers with a wide range of properties. Some of the major advantages of electrospun fibers are the high surface to volume ratio, adjustable porosity and flexibility to spin into a variety of shapes and sizes.

This chapter discusses the basic electrospinning technique and the factors that influence the process and the resulting nanofibers. In addition, some of the instability issues (such as bending and branching) and parameters that cause bead defects in fibers have been elucidated. Some innovations in the field of electrospinning that lead to the various types and properties of the electrospun fibers have also been covered. This is followed by information

on the creation of various types of nanofibers such as hollow, helical, porous, flat, aligned, non-woven and conductive. Another topic on composites has been included which discusses carbon nanotubes, encapsulated structures and polymer blends. The section on fiber structure describes some of the unique features of electrospun fibers. The chapter ends with a description of the impact of structure on the properties of fibers (such as mechanical, thermal, transport and surface).

### 17.1.1 Description

The most basic electrospinning setup consists of three major components: a high voltage power supply, a syringe with a blunt-tip needle and a metal collecting screen (Fig. 17.1). The syringe holds the polymer solution (or melt). With the use of a syringe pump, the solution can be fed at a constant and controllable rate. One electrode is connected to the needle holding the spinning solution and the other is attached to the collecting screen (usually a grounded conductor). When high voltage (typically in the range of 0–30 kV) is applied to the needle holding the polymer solution, a charge is induced on the surface of the liquid drop. As a result the drop comes under the action of two types of electrostatic forces: mutual electrostatic repulsion between the surface charges, and the coulombic force applied by the external electric field. As a consequence of these electrostatic interactions, the liquid drop elongates into a conical object known as the Taylor cone. Once the intensity of the electric field attains a certain critical value, the electrostatic



**17.1** Basic setup of the electrospinning process. Reprinted with permission from Li and Xia (2004a). Copyright Wiley-VCH Verlag GmbH & Co. KGaA, Weinheim, Germany.

forces overcome the surface tension of the polymer solution and force the ejection of the liquid jet from the tip of the Taylor cone. Before reaching the collector screen the liquid jet elongates and solvent evaporates, leading to the formation of a randomly oriented, non-woven mat of thin polymeric fibers on the collector (Li and Xia, 2004a; Huang *et al.*, 2003).

### *Important parameters*

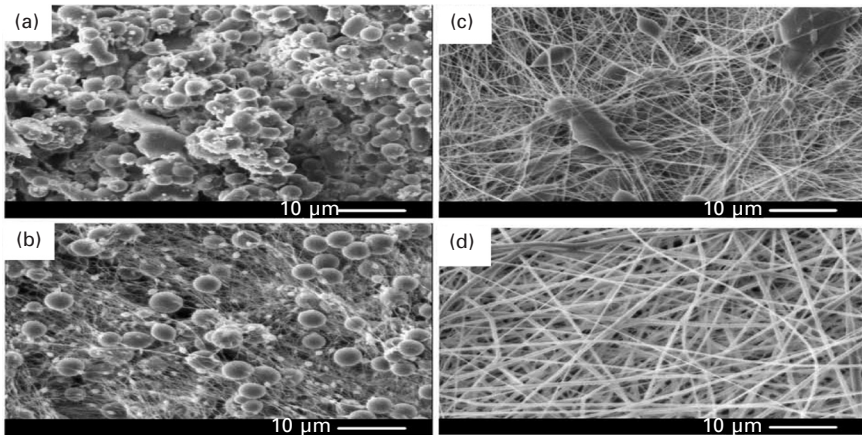
The morphology and properties of the electrospun fibers can be manipulated by a number of process variables. These parameters have been classified into three broad categories: solution properties, controlled variables and ambient parameters. Solution properties include the concentration, polymer molecular weight, conductivity, surface tension, dipole moment and dielectric constant. Controlled variables include the feeding rate, voltage, air-gap distance, collector composition and geometry. The ambient parameters include the temperature, humidity and air velocity. Some of these main factors are discussed below (Doshi and Reneker, 1995).

#### Concentration

Solution viscosity is one of the major variables to control the fiber size and morphology when spinning polymeric fibers. Defects in the form of full bead structure and the presence of junctions and bundles are seen at low polymer concentrations. This indicates that the fibers were still wet when reaching the collector, a characteristic of electro spraying rather than spinning. With increase in polymer concentration, a uniform fiber structure with few beads and junctions is formed. Too concentrated polymer solutions are difficult to electrospin as the droplet dries out at the tip before the jet can be initiated. Figure 17.2 shows scanning electron microscopy (SEM) images of poly(D,L-lactide) (PDLA) electrospun from dimethyl formamide and the corresponding viscosities. Additionally, the diameter of the fibers increases with increasing solution concentration (Zong *et al.*, 2002; Pham *et al.*, 2006).

#### Field strength

The shape of the liquid drop at the needle tip is greatly affected by the field strength. At low voltages, the jet initiates from the Taylor cone of the droplet suspended at the tip. This produces a bead free structure. With increase in voltage, the volume of the drop at the tip becomes smaller and the Taylor cone oscillates and recedes. The jet originates from the liquid surface within the tip and results in the formation of beaded fibers. As the voltage is increased further, jet initiation occurs at some point inside the needle, the droplet at the tip disappears and many beads are seen (Fig. 17.3). The shape of the



17.2 Concentration effect on microstructures of electrospun PDLA nanofibers at constant processing conditions and variable concentrations of (A) 20 wt%, (B) 25 wt%, (C) 30 wt% and (D) 35 wt%. Reprinted from Zong *et al.* (2002) with permission from Elsevier.

beads gradually changes from spindle-like to spherical-like with increase in voltage (Pham *et al.*, 2006; Zong *et al.*, 2002).

### Flow rate

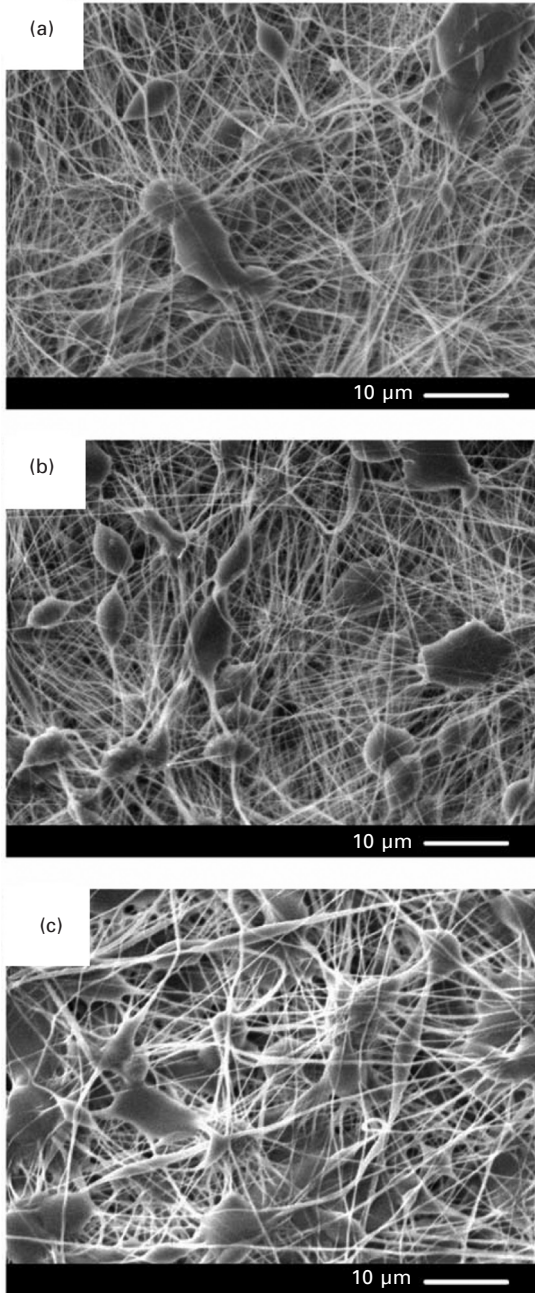
Studies have shown that low feeding rates result in fibers with smaller diameters and spindle-like beads. On the other hand, a higher feeding rate results in larger droplets at the tip of the needle which get carried away with a faster velocity. Therefore, the electrospun fibers do not get a chance to dry before reaching the collector. This results in larger beads and junctions (Pham *et al.*, 2006; Zong *et al.*, 2002).

### 17.1.2 Instabilities

The path of the electrically charged polymer jet is indefinite and the jet is subjected to a number of electrically driven instabilities. Some of these are described in this section: branching, formation of physical beads and bending instability.

#### *Branching*

Changes in shape and charge per unit area of the jet may result from its elongation and the evaporation of the solvent. This shifts the balance between the surface tension and electrical forces and the jet becomes unstable. In



17.3 Electric field effect on microstructures of the electrospun PDLA membranes at (A) 20 kV, (B) 25 kV and (C) 30 kV (all other processing conditions constant). Reprinted from Zong *et al.* (2002) with permission from Elsevier.

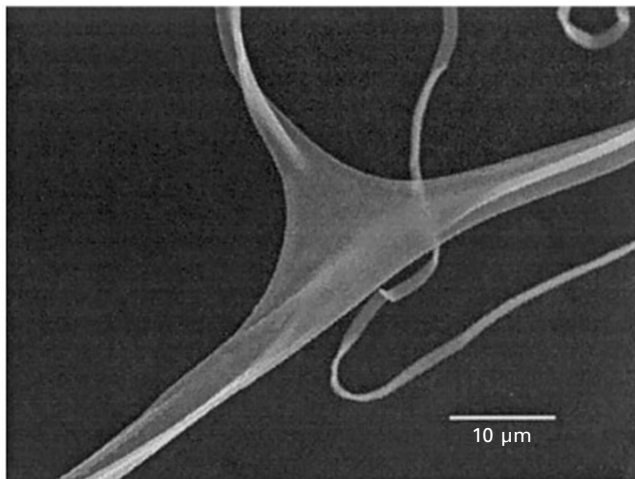
order to reduce its local charge per unit surface area, the unstable jet ejects a smaller jet from the surface of the primary jet (Koombhongse *et al.*, 2001). An example is shown in Fig. 17.4. The formation of branches in jets and fibers occurs in more concentrated and viscous solutions and also at unusually high electric fields (Reneker and Yarin, 2008).

### *Bending instability*

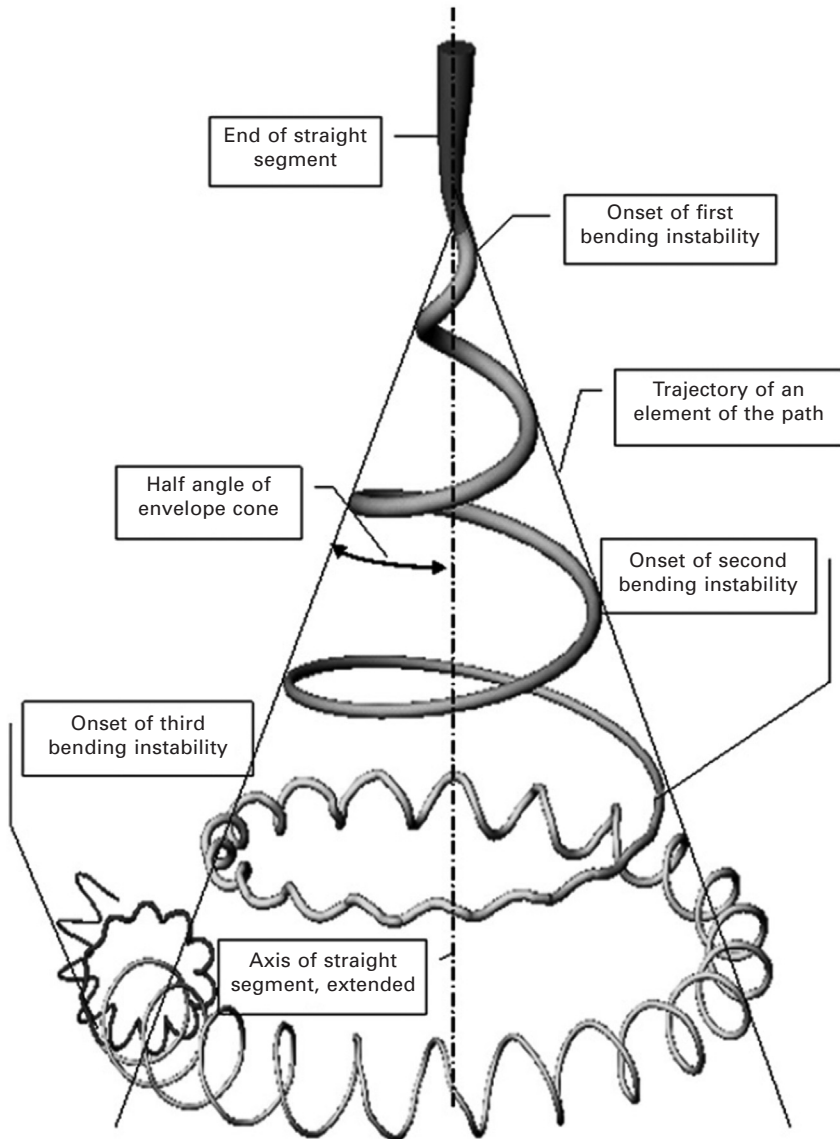
When the polymer jet becomes very long and thin, the time required for excess charge to redistribute itself along the full length of the jet becomes longer. The location of the excess charge then tends to change with the elongation. The repulsive Coulomb forces between the charges carried with the jet elongate the jet in the direction of its axis until the jet solidifies. This leads to an implausibly high velocity at the thin leading end of the straight jet. As a result, the jet bends and develops a series of lateral excursions that grow into spiraling loops (Fig. 17.5). Each of these loops grows larger in diameter as the jet grows longer and thinner (Reneker and Yarin, 2008; Reneker *et al.*, 2000).

### *Bead defects in fibers*

A number of spinning parameters influence the formation of beads in the resulting fibrous mat. With increase in the applied voltage, jet velocity is increased and the solution is removed from the tip more quickly. When the



17.4 SEM image of branched fibers from 10% poly(ether imide) in 1,1,1,3,3,3-hexafluoro-2-propanol (Koombhongse *et al.*, 2001) (Reprinted with permission from John Wiley & Sons Inc.)



17.5 Diagram showing onset and development of bending instabilities (Reneker and Fong, 2005) (Reprinted with permission, copyright 2006 American Chemical Society).

volume of the droplet on the tip becomes smaller, the Taylor cone shape oscillates and becomes asymmetrical. This leads to the formation of beads. The effect of solution concentration on bead formation has also been reported (Fig. 17.2). Highly viscous solutions have been shown to produce more

uniform fibers with fewer beads. The shape of the beads also changed from spherical to spindle-like when the polymer concentration was changed from low to high levels (Zong *et al.*, 2002). It has also been found that by reducing the surface tension of a polymer solution, fibers could be obtained without beads. The addition of ethanol lowered the surface tension of poly(ethylene oxide) (PEO) and poly(vinyl alcohol) (PVA) aqueous solutions (Pham *et al.*, 2006). The addition of salts leads to a higher charge density on the surface of the ejected polymer jet, which results in more electric charges carried by the electrospinning jet. With increase in the charges carried by the jet, higher elongation forces are imposed to the jet under the electric field. The overall tension in the fibers depends on the self-repulsion of the excess charges on the jet. Therefore, as the charge density increases, the beads become smaller and more spindle-like (Fig. 17.3). It was also found that with lower solution feeding rates, smaller fibers with spindle-like beads were formed (Zong *et al.*, 2002).

### 17.1.3 Electrospinning process variations

Several innovative electrospinning processing techniques to enhance the function and properties of electrospun fibers are described in this section. Desirable physical and biological properties of electrospun nanofibrous scaffolds can be obtained by using these schemes.

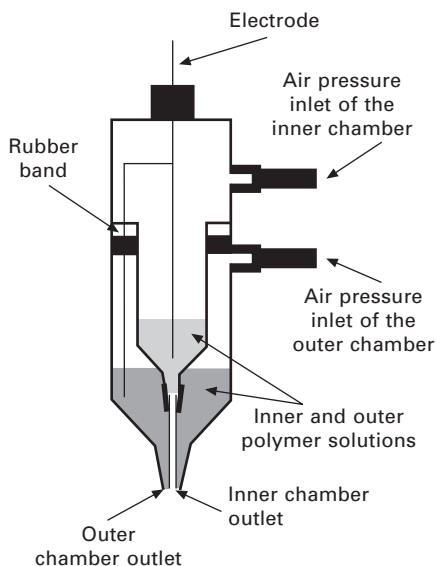
#### *Core shell spinning*

The electrospinning of a concentric jet solution was first reported by Sun *et al.* (2003). In this process two polymer solutions can be co-electrospun without direct mixing. The experimental setup is shown in Fig. 17.6. A core-shell structure with polycaprolactone (PCL) as the shell and gelatin as the core was fabricated by Zhang *et al.* (2004). A method to coaxially spin polyurethane (PU) (shell)/nylon-6 (core) nanofibers was developed by Han *et al.* (2007). It was found that the core-shell nanofibers exhibited properties between those of the individual materials. They also demonstrated that it is feasible to attach core-shell compound nanofibers to a textile substrate. This technique can be used for encapsulating, protecting and delivering various compounds. It can also be used for functionalizing the surface without affecting the core.

#### *Blowing assisted electrospinning*

This technology has been used for aqueous hyaluronic acid (HA), which could not be electrospun using conventional electrospinning due to its very high solution viscosity and high surface tension at fairly low solution concentrations



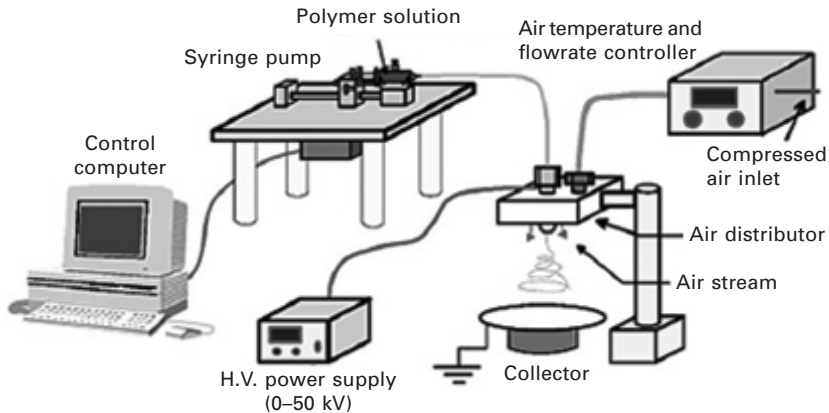


17.6 Experimental setup for co-electrospinning to produce core-shell nanofibers (Sun *et al.*, 2003). Reproduced with permission, copyright Wiley-VCH Verlag GmbH & Co. KGaA, Weinheim, Germany.

(Um *et al.*, 2004). In this process air flows parallel to the straight portion of the jet concentrically surrounding the polymer jet (Ramakrishna *et al.*, 2005). The experimental setup is shown in Fig. 17.7. It was found by Um *et al.* (2004) that the combination of air blowing force and the applied voltage is capable of overcoming the high viscosity as well as the high surface tension of the polymer solution. The elevated temperature of the blowing air can further reduce the solution viscosity of the HA solution. The air can also aid in faster solvent evaporation. The fiber diameter can be customized by controlling the flow rate and temperature of the blown air.

#### *Multilayer and mixed electrospinning*

Multilayer and mixed electrospinning was demonstrated by Kidoaki *et al.* (2005) to fabricate scaffolds containing different polymers. The fibrous mesh can consist of layers sequentially collected on the same target collector. Such a three-layered scaffold composed of segmented PU, styrenated gelatin and type I collagen can be used as an artificial blood vessel scaffold (Kidoaki *et al.*, 2005). In mixing electrospinning, two or more different polymer solutions can be electrospun from two or more different polymer syringes under different processing conditions.



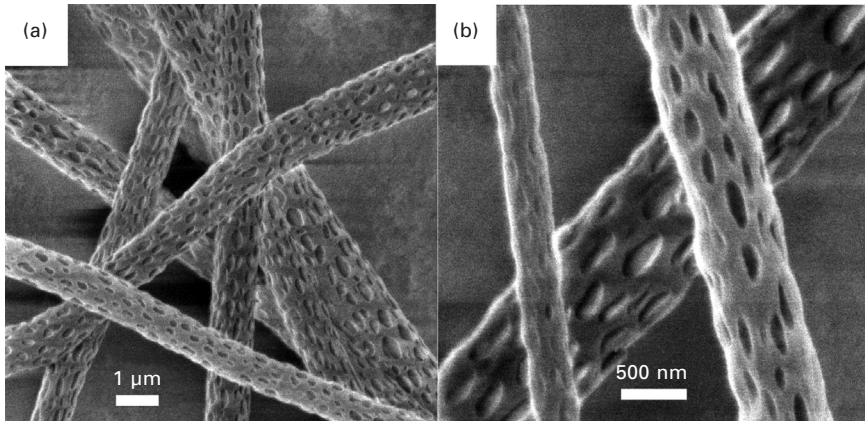
17.7 Experimental setup of forced air assisted electrospinning device (Um *et al.*, 2004) (Reprinted with permission, copyright 2004 American Chemical Society).

## 17.2 Types of fibers produced by electrospinning

Variation in the morphology of the electrospun fibers can be obtained by changing the parameters of electrospinning. A wide range of shapes can be created and properties can be controlled to suit various applications.

### 17.2.1 Porous nanofibers

It is possible to vary the size of the structure from a few tens of nanometers to 10 microns based on the type of polymers, solvents and the electrospinning conditions. Porous structures have a larger surface area and are beneficial to many applications like catalysis, filtration, absorption, fuel cells, solar cells, batteries and tissue engineering. Megelski *et al.* (2002) reported changes in the shape and size of nanopores in the electrospinning of polystyrene (PS). They found that with increase in concentration the pore size increases and the pore shape becomes more rounded. Additionally, the pore size distribution was not affected by changing the voltage, but increases with increasing flow rate. They also investigated electrospun fibers of polymers such as poly(methyl methacrylate) (PMMA) and polycarbonate (PC). They reported that solvent vapor pressure and atmospheric humidity had a strong influence on the pore formation. It was postulated that a highly volatile solvent will undergo rapid evaporation and result in surface cooling of the electrospinning jet. This may induce phase separation and moisture condensation, promoting the formation of porous structures. An example of porous nanostructure of poly(L-lactide) (PLLA) spun in dichloromethane is shown in Fig. 17.8. The size and the density of pores are also increased by increasing the humidity



17.8 SEM images of porous fibers obtained via electrospinning of a solution of PLLA in dichloromethane. (Bognitzki *et al.*, 2001). Reproduced with permission, copyright Wiley-VCH Verlag GmbH & Co. KGaA, Weinheim, Germany.

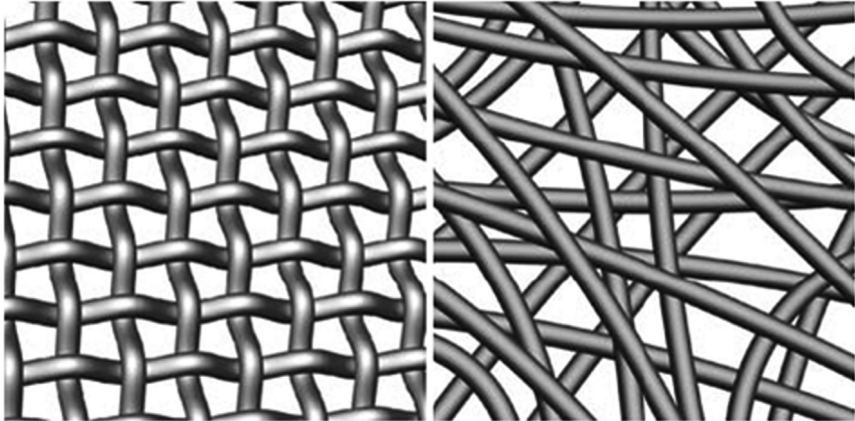
levels. Increasing humidity results in circular pores on the fibers (Megelski *et al.*, 2002).

### 17.2.2 Non-woven nanofibers

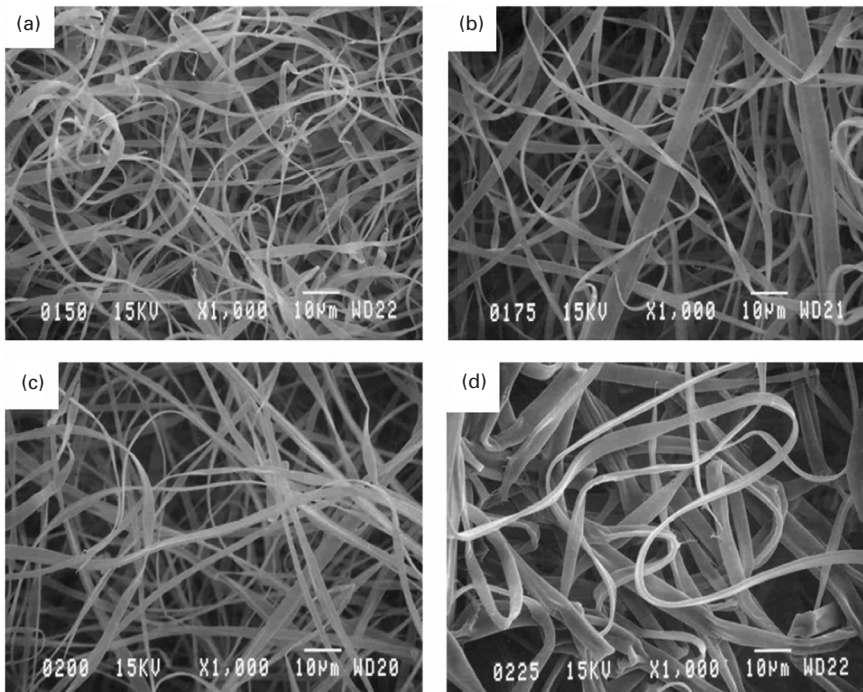
The velocity of the polymer jet during electrospinning is very high near the collector, and the resulting nanofiber is typically deposited in a random manner without proper orientation (Liang *et al.*, 2007). Most nanofibers obtained by electrospinning are in non-woven form and can be used for a small number of applications such as filtration, tissue scaffolds, implant coating film and wound dressing. The non-woven mat of electrospun fibers is highly porous, has a large interconnected void volume and possesses high surface to volume ratio. The woven fabrics compartmentalize the pore volume more regularly (Fig. 17.9) whereas the entangled fibrous mat has a pseudo-bicontinuous structure (Burger *et al.*, 2006).

### 17.2.3 Flattened or ribbon-like nanofibers

Flattened nanofibers are created with high molecular weight polymers and high polymer concentration. Solvent evaporation reduces with higher solution viscosity and wet fibers that reach the fiber collector are flattened by the impact. The impact of solution concentration can be seen in Fig. 17.10. The flat ribbon shape can be attributed to the collapse of an outer skin formed on the surface of the jet. Ribbons have been observed in the electrospinning of Nylon-6 clay composites, polycarbonates, PVA (Burger *et al.*, 2006), elastin (Boland *et al.*, 2004) and hemoglobin (Barnes *et al.*, 2006).



17.9 Artistic representation of woven (left) and non-woven (right) fabrics (Burger *et al.*, 2006). Reprinted, with permission, from the *Annual Review of Materials Research*, Volume 36 © 2006, by Annual Reviews, www.annualreviews.org.



17.10 SEM images of electrospun hemoglobin in 2,2,2-trifluoroethanol at the following concentrations: (A) 150 mg/mL, (B) 175 mg/mL, (C) 200 mg/mL, and (D) 225 mg/mL (1000× magnification, scale bar is 10 µm) (Barnes *et al.*, 2006) (Reprinted with permission, courtesy of INDA, Association of the Norwegian Fabric Industry).

### 17.2.4 Hollow fibers

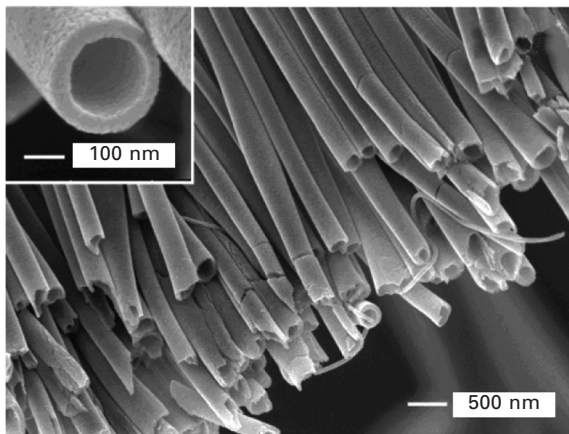
To attain hollow fibers, the template/mandrel should be degradable or extractable without destroying the coating layer. Such structures with hollow interiors are used in a wide range of application such as nanofluidics and hydrogen storage (Li and Xia, 2004a). Also, by employing a direct coaxial spinning method (Fig. 17.11), hollow nanofibers can be made.

### 17.2.5 Helical fibers

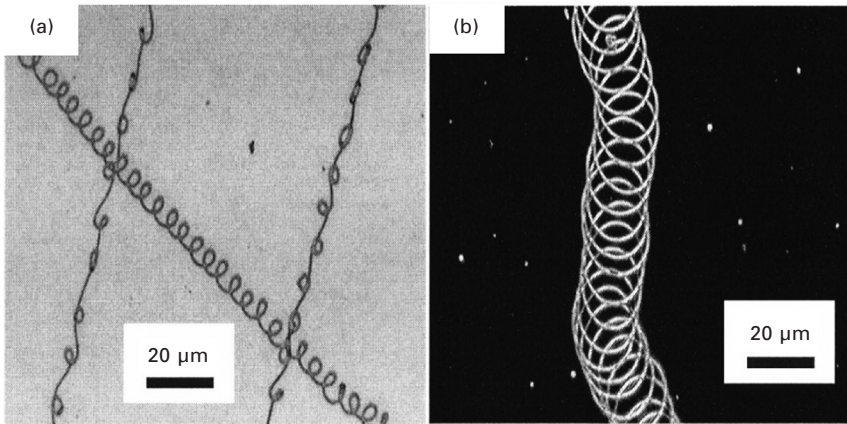
Helical fibers can be used in microelectromechanical system devices, advanced optical components and drug delivery systems. Helical fibers made of a mixture of PEO and poly(aniline sulfonic acid) (PASA) have been reported (Kessick and Tepper, 2004). The creation of helical loops can be attributed to the electrochemical property of the conductive PASA polymer (Fig. 17.12). It is suggested that there was equilibrium between the electrostatic repulsive force and the viscoelastic restoring force in the electrospun polymer jet. When a fiber is collected at the metal surface, the charges from PASA regions are transferred to the fiber surface. This force imbalance resulted in fiber structural rearrangement to restore the force equilibrium.

### 17.2.6 Aligned fibers

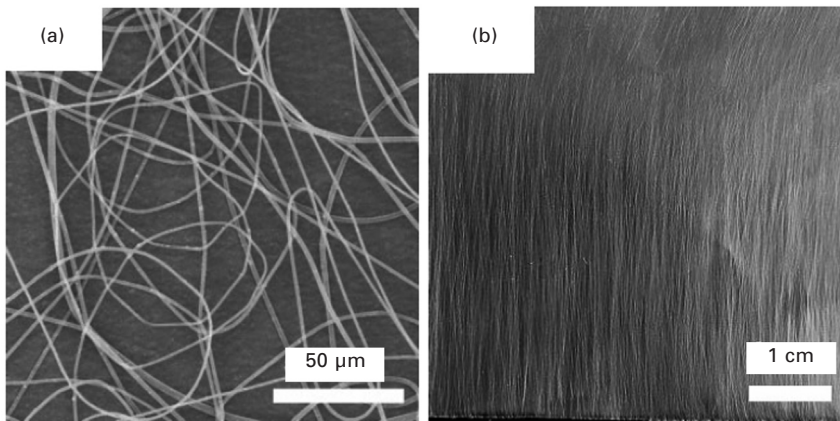
Oriented nanofiber webs show mechanically anisotropic tensile properties and higher hydrophilicity compared to randomly collected fibrous mats (Kim, 2008). A comparison is shown in Fig. 17.13. Collectors with various



17.11 Hollow fibers fabricated by direct coaxial electrospinning (Li and Xia, 2004b) (Reprinted with permission, copyright 2004 American Chemical Society).



17.12 Fibers produced from (a) 6 wt% PEO and 0.75 wt% PASA in water, (b) 8.5% PEO and 0.75% PASA in water. Reproduced with permission from Kessick and Tepper (2004), copyright 2004, American Institute of Physics.



17.13 Randomly oriented electrospun mat (a) and a highly aligned fibrous mat (b). Reproduced with permission from Yang *et al.* (2007). Copyright Wiley-VCH Verlag GmbH & Co. KGaA, Weinheim, Germany.

geometries have been used to produce aligned fibers. A rotating cylindrical drum collector allows for greater alignment compared to a stationary target. This method has been extensively used in our lab to produce aligned electrospun fibrous mats of polymers such as poly(glycolic acid) (PGA) (Boland *et al.*, 2001), type I collagen fibers (Matthews *et al.*, 2002), polydioxanone (PDO) (Boland *et al.*, 2005), fibrinogen (McManus *et al.*, 2006) and PDO–elastin blends (Sell *et al.*, 2006). However, the degree of alignment is not very good

as a substantial number of misaligned fibers are collected. To improve the alignment of fibers, a sharp pin with a negative potential can be introduced in the rotating mandrel. The pin in the mandrel is placed directly below the tip of the needle. The results showed that PMMA was better aligned than fibers collected on just a rotating mandrel (Sundaray *et al.*, 2004). To control the path of the spinning polymer jet, the electric field can be modified using auxiliary electrodes made of parallel conducting strips. These auxiliary electrodes can be given a negative voltage to concentrate the electric field along the orientation of the parallel strips (Bornat, 1987). Two parallel electrodes can also be placed below the needle with a gap in between them to better align the electrospun fibers. The results show that the fibers tend to align themselves across the gap between the electrodes. Mutual electrostatic repulsion further enhances the parallel and relatively uniform distribution of the fibers (Li *et al.*, 2003).

### 17.2.7 Conductive fibers

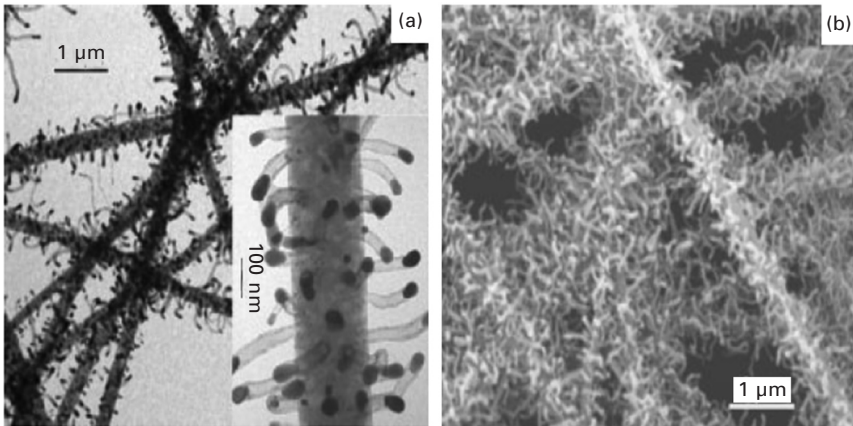
Polyaniline (PA) has been electrospun from a sulphuric acid solution. The polymer jet was collected in water to coagulate the PA and wash out the sulphuric acid. Scanning tunneling microscopy and resistivity measurements made on the tufts of fibers proved PA to be an electrical conductor. The electrical conductivity of PA also became evident when the collected nanofibers extended in the direction of the applied electric field rather than forming a typical non-woven mat (Reneker and Yarin, 2008).

### 17.2.8 Composite nanofibers

Fibers with different compositions can be electrospun using various techniques to produce a wide range of structures with desired properties. Such composites can be used for specific applications. Some examples are discussed below.

#### *Carbon nanotubes*

Carbon nanofibers have been made by converting electrospun polyacrylonitrile (PAN) to carbon by thermal carbonization treatment. The PAN solution contained iron-bearing molecules which decomposed during the carbonization treatment and formed iron-rich particles on the surface of the carbon nanofiber. These particles then catalyzed the growth of many multiwall carbon nanotubes that formed branches attached to the carbon nanofiber (Fig. 17.14). The interstices between the multiwall nanotubes provide channels for flow of various molecules like water, hydrogen and oxygen and can be used for the construction of fuel cell electrodes. Such composites have been shown to possess enhanced electrical conductivity, tensile strength, thermal



17.14 Transmission (a) and scanning (b) micrographs of carbon nanotubes on nanofibers produced by electrospinning of PAN, carbonization of PAN and catalytic growth of carbon nanotubes. Reproduced with permission from Hou and Reneker (2004). Copyright Wiley-VCH Verlag GmbH & Co. KGaA, Weinheim, Germany.

deformation temperature, thermal and dimensional stability (Reneker and Yarin, 2008).

### *Encapsulated structures*

Many biological molecules, chemicals and other particulate materials have been dissolved in polymer solution and electrospun. Green fluorescent labeled albumin molecule has been electrospun from a solution of poly(ethylene oxazoline) in water. The protein molecules were found to be uniformly dispersed inside the nanofibers. Encapsulated trypsin was found to remain active for eight weeks at room temperature after the surrounding nanofibers redissolved. It has also been found that if a particle larger than the diameter of the nanofibers flows into the polymer jet, the jet temporarily expands to encase the particle and then shrinks back to its nanoscale dimension (Reneker and Yarin, 2008).

### *Polymer blends*

A blend of synthetic and natural polymers was created for use as a bioresorbable vascular graft by Sell *et al.* (2006). PDO and elastin solutions were blended in different ratios to mimic the structure and properties of the native artery. Elastin was incorporated for bioactivity and PDO was used to enhance the mechanical properties of the electrospun fibrous mat. Boland *et al.* (2004) demonstrated the electrospinning of a blend of collagen



and elastin for use as vascular tissue engineered constructs. Zhang *et al.* (2005) created gelatin and PCL electrospun blends that exhibited enhanced mechanical properties and better wettability than that obtained from PCL or gelatin alone. A mixture of heparin and poly(ethylene glycol) (PEG) was electrospun for potential use as a wound dressing; the presence of PEG slowed down the release of heparin and permitted better biological outcomes (Casper *et al.*, 2005).

## 17.3 Fiber structure

Nanofibers produced by electrospinning exhibit a range of unique features and properties that are not seen in one-dimensional structures produced by other techniques. Some of the remarkable properties are described in this section.

### 17.3.1 Fiber diameter

An ideal target for electrospinning is to have consistent and controllable fiber diameters. The fiber diameter primarily depends upon the spinning parameters, most important being the solution concentration. Higher viscosity results in a larger fiber diameter (Huang *et al.*, 2003). Demir *et al.* (2002) reported a power law relationship stating that fiber diameter was proportional to the cube of the polymer concentration. Another parameter affecting the fiber diameter is the applied electrical voltage. In general it has been found that a higher applied voltage results in the ejection of more fluid in a jet, leading to larger fiber diameters. However, when spinning silk-like polymers and bisphenol-A polysulphone, fiber diameter has been shown to decrease with increasing applied voltage (Pham *et al.*, 2006). Huang *et al.* (2006) have reported very small diameter ( $\sim 1.6$  nm) nylon fibers with only one or three molecules in the cross-section. Molecular weight does not have a noticeable effect on the fiber diameter. Higher solution conductivity results in a smaller fiber diameter. Zong *et al.* (2002) found that salts with smaller ionic radii produced smaller diameter fibers and vice versa. They suggested that higher charge density led to higher mobility of ions with smaller radii. Higher mobility resulted in increased elongation forces exerted on the polymer jet, creating a smaller fiber (Zong *et al.*, 2002). Lower flow rates produced fibers with smaller diameters. Increase in temperature led to decrease in solution viscosity, producing smaller diameter fibers (Pham *et al.*, 2006).

### 17.3.2 Complex pore structure

In electrospun nanofibers, two types of pores can be identified: pores on or within each fiber, and pores between the fibers on a nanofibrous membrane.

Compared to the conventional techniques of fiber fabrication (e.g. extrusion), electrospun fibers are much thinner in diameter and have high surface to volume ratio. Due to the entanglement of fibers, a high density of pores can be formed. When compared to mesoporous materials (e.g. molecular sieves), the specific surface area of the electrospun fibers is lower, but the pores are relatively large and fully interconnected to form a three-dimensional network (Li and Xia, 2004a). The knowledge of pore size and porosity is crucial in determining the membrane's performance. Pore size determines the type of substance or species that can permeate through, whereas porosity is a measure of the flow across the membrane. SEM can be used to determine the pore size of the electrospun membranes, but not the porosity. Furthermore, only the pore sizes on the top surface can be measured, while pores beneath the surface cannot be analyzed. Sell *et al.* (2008) described a method to determine the hydraulic permeability of an electrospun nanofibrous structure to accurately determine its pore size and fiber diameter.

### 17.3.3 Molecular alignment

A high degree of molecular alignment results from the very large effective spin draw ratio exerted by the electrostatic fiber stretching process. It has been found through electron diffraction analysis that polymer chains in electrospun poly(ferrocenyldimethylsilane) were extended and aligned along the fiber axis. Structures of electrospun PEO were investigated by optical and atomic force microscopy and it was concluded that the fibers possessed a surface layer of highly ordered polymer chains (Li and Xia, 2004a).

### 17.3.4 Surface structure

Nanofibers have been shown to become rougher with increase of the electrical potential (Huang *et al.*, 2003). Deitzel *et al.* (2001) suggested that by controlling the spinning current the bead defect density of the electrospun fibers can be controlled. The use of a metal collector results in the formation of smooth fibers (Pham *et al.*, 2006). Another parameter that influences surface structure is solution concentration. Low viscosity solutions produced beaded electrospun structures which are considerably rougher than completely fibrous structures (Acatay *et al.*, 2004).

### 17.3.5 Crystal orientation

Electrospinning significantly retards the crystallization process. This retardation can be attributed to the rapid solidification of the stretched chains at high elongation rates. Thus, the stretched chains do not have enough time for crystal formation. Although the polymer chains are non-crystalline in the

nanofibers, they are highly oriented (Zong *et al.*, 2002). As a result of defects in crystallization, the glass transition temperature and the crystallization peak temperature also decrease (Huang *et al.*, 2003).

### 17.3.6 Gradient structures in fibers

A bimodal distribution of fiber diameters may result from high concentration solutions. A secondary population of smaller fibers is produced in addition to the primary population once the solution concentration exceeds a certain critical value (Deitzel *et al.*, 2001). This phenomenon was attributed to fiber splaying events. Electrospinning of PU fibers at 12.8 wt% yielded fibers with three different-sized diameters (Demir *et al.*, 2002). Dual-porosity scaffolds can be generated by electrospinning a suspension of salt and clay particles in the polymer solution, followed by salt leaching and gas foaming processes. The resulting scaffolds have nanosized pores at the fiber interstitial space and microsized pores formed by salt particles and gas bubbles (Liang *et al.*, 2007). Immiscible polymer solutions can also be electrospun to form a two-phase structure in the resulting fibrous mat.

## 17.4 Influence of structure on properties

The properties of nanofibers can be largely attributed to their physical and chemical structure. This section describes the effect of morphological features and internal structure on the properties of the electrospun nanostructures.

### 17.4.1 Mechanical properties

Nanofibers have better mechanical properties than microfibers of the same polymer (Huang *et al.*, 2003). Also, aligned nanofibers collected by a rotating drum are likely to have better tensile properties than specimens extracted in the transverse direction (Ramakrishna *et al.*, 2005). Due to the small diameter of the nanofibers, it is generally difficult to measure the mechanical properties of a single fiber. The measurements are usually taken for fibrous mats which mask the overall material specific properties. Also, cross-sectional area measurement is difficult due to the porosity of these materials. Therefore, the modulus measured for mats or yarns is not considered to be accurate (Wang *et al.*, 2004). Gu *et al.* (2005) reported the mechanical properties of a single electrospun PAN ultrafine fiber using a cantilever technique. They found that with higher applied voltage, higher Young's modulus is obtained. The high electric force acting on the jet ejects the polymer solution at high speed, which in turn leads to good orientation of the molecule chains within the electrospun fibers. Thus, higher modulus of the electrospun fibers is obtained (Gu *et al.*, 2005). It has also been documented that values for

modulus increase with increase in fiber diameter. Boland *et al.* (2005) reported that the modulus values for aligned fibrous PDO structures produced from 71–167 mg/ml concentration solutions were significantly higher than from the aligned 42–56 mg/ml PDO concentrations.

#### 17.4.2 Chemical composition

The chemical composition of an electrospun polymer is different from that of its bulk form. Duan *et al.* (2004) demonstrated this by performing functional group detection using Fourier Transform Infrared (FT-IR) spectroscopy. Casting films of PEO, chitosan and chitosan–PEO had different absorption bands from chitosan–PEO nanofibers. It was suggested that chitosan experienced phase separation in chitosan–PEO solution and that no chitosan element is found on the surface of nanofibers electrospun from chitosan–PEO solution (Duan *et al.*, 2004).

#### 17.4.3 Transport properties

An electrospun fibrous mat generally has high porosity but a very small pore size. As a result, they have higher convective resistance to air flow compared to microporous polytetrafluoroethylene (PTFE) membranes while the resistance to the transport of water vapor was much lower than that of polymer membrane and membrane laminates. Typically, materials with high rates of water vapor diffusion and low air permeability are promising candidates for protective clothing applications (Gibson *et al.*, 1999).

#### 17.4.4 Thermal properties

Electrospinning significantly lowers the glass transition temperature and the melting temperature of the material. This can be attributed to the very large surface area to volume ratio of the electrospun membranes (Zong *et al.*, 2002). Polymer with more free volume allows easier movement of molecular chain thus lowering the glass transition temperature (Ramakrishna *et al.*, 2005).

#### 17.4.5 Surface reflection and scattering

Small angle X-ray scattering (SAXS) techniques were used to investigate the structure and morphology of PLLA electrospun fibers. Since the electrospun fibers were randomly oriented in the membrane, the pattern represented scattering in all directions. The interpretation of SAXS can be complicated as it may contain several contributions including microfibrillar structure, surface reflection/scattering of nanofibers and void morphology (Zong *et al.*, 2002).

#### 17.4.6 Conductivity of nanofibers

Considering the fact that the rate of electrochemical reaction depends upon the surface area of the electrode, Norris *et al.* (2000) exploited the high surface area to volume ratio of the electrospun fibers to form conductive nanofibrous membranes. This was achieved by the blending of the conducting polymer, PA and PEO, in various blending ratios. Fibers having a desired conductivity were produced by controlling the ratio of PA to PEO in the blend (Norris *et al.*, 2000). Such conductive membranes can be used for making high performance batteries and other applications including electrostatic dissipation, corrosion protection, electromagnetic interference shielding, and photovoltaic devices (Huang *et al.*, 2003).

#### 17.4.7 Surface properties

Hydrophilic materials show a low water contact angle while hydrophobic materials show high water contact angle. Acatay *et al.* (2004) demonstrated that the fibrous architecture of electrospun materials imparts hydrophobic characteristics to the membrane due to its sub-micron scale roughness. Compared to polysulphone (PSU) films which had a contact angle around 70–90°, the PSU electrospun membranes exhibit higher contact angles of around 140°. The degree of hydrophobicity in electrospun fibers can be tuned by changing the spinning parameters (e.g. viscosity) and chemical modification techniques (Acatay *et al.*, 2004).

### 17.5 Future trends and conclusion

The past few years have witnessed explosive growth in the field of electrospinning. Electrospun nanofibrous scaffolds have displayed tremendous promise and potential for a broad range of applications such as tissue engineering, wound dressing, drug delivery, filtration, protective clothing and affinity membranes. In this chapter, several specific advantages of electrospun fabrics that make them superior to fabrics created by existing techniques have been discussed. However, there are many challenges that still need to be overcome. For instance, it is still difficult to electrospin fibers with diameters below 100 nm. More studies need to be conducted in order to have better control of the size and morphology of electrospun nanofibers. Due to the molecular weight and solubility limitations of conjugated organic polymers, it has not been possible to electrospin them. Also, a correlation between the processing parameters and the secondary structure of electrospun nanofibers remains to be established. Furthermore, all electrospinning techniques described so far lead to the formation of a two-dimensional structure. Processing technologies to make three-dimensional

constructs need to be improved. Research on electrospinning is expected to become even more interdisciplinary in the near future. Many desirable properties have been achieved by innovations in electrospinning (core-shell spinning, blowing-assisted spinning, multilayer spinning) and post-processing techniques. Fabrication of nanofibers from materials such as metals and ceramics has extended the capability of this technique to new applications. It is hoped that this chapter will provide useful information for future research and development in the rapidly evolving field of electrospinning.

## 17.6 Sources of further information and advice

Darrell H. Reneker, Alexander L. Yarin and Gregory C. Rutledge have vast experience in electrospinning processing technique and theoretical modeling of electrified jets. Gary L. Bowlin and Seeram Ramakrishna have published extensively on biomedical applications of electrospun scaffolds. These groups are the leaders in their field and will be the key sources of information as the ever-expanding field of electrospinning forges forward. Comprehensive books by some of these researchers have been included in the references (Ramakrishna *et al.*, 2005; Reneker and Fong, 2005).

## 17.7 References

- Acatay, K., Simsek, E., Ow-Yang, C. and Menciloglu, Y. Z. (2004) Tunable, superhydrophobically stable polymeric surfaces by electrospinning. *Angew Chem Int Ed Engl*, 43, 5210–5213.
- Barnes, C. P., Smith, M. J., Bowlin, G. L., Sell, S. A., Tang, T., Matthews, J. A., Simpson, D. G. and Nimitz, J. C. (2006) Feasibility of electrospinning the globular proteins hemoglobin and myoglobin. *J Engineered Fibers and Fabrics*, 1, 16–28.
- Bognitzki, M., Czado, W., Frese, T., Schaper, A., Hellwig, M., Steinhart, M., Greiner, A. and Wendoeff, J. H. (2001) Nanostructured fibers via electrospinning. *Advanced Materials*, 13, 70–72.
- Boland, E. D., Wnek, G. E., Simpson, D. G., Pawlowski, K. J. and Bowlin, G. L. (2001) Tailoring tissue engineering scaffolds using electrostatic processing techniques: a study of poly(glycolic acid). *J Macromol Sci*, 38, 1231–1243.
- Boland, E. D., Matthews, J. A., Pawlowski, K. J., Simpson, D. G., Wnek, G. E. and Bowlin, G. L. (2004) Electrospinning collagen and elastin: preliminary vascular tissue engineering. *Front Biosci*, 9, 1422–1432.
- Boland, E. D., Coleman, B. D., Barnes, C. P., Simpson, D. G., Wnek, G. E. and Bowlin, G. L. (2005) Electrospinning polydioxanone for biomedical applications. *Acta Biomater*, 1, 115–123.
- Bornat, A. (1987) Production of electrostatically spun products. US Patent no. 4,689,186.
- Burger, C., Hsiao, B. S. and Chu, B. (2006) Nanofibrous materials and their applications. *Ann Rev Mater Sci*, 36, 333–368.
- Casper, C. L., Yamaguchi, N., Kiick, K. L. and Rabolt, J. F. (2005) Functionalizing

- electrospun fibers with biologically relevant macromolecules. *Biomacromolecules*, 6, 1998–2007.
- Deitzel, J. M., Kleinmeyer, J., Harris, D. and Beck Tan, N. C. (2001) The effect of processing variables on the morphology of electrospun nanofibers and textiles. *Polymer*, 42, 261–272.
- Demir, M. M., Yilgor, I., Yilgor, E. and Erman, B. (2002) Electrospinning of polyurethane fibers. *Polymer*, 43, 3303–3309.
- Doshi, J. and Reneker, D. H. (1995) Electrospinning process and applications of electrospun fibers. *J. Electrostat*, 35, 151–160.
- Duan, B., Dong, C., Yuan, X. and Yao, K. (2004) Electrospinning of chitosan solutions in acetic acid with poly(ethylene oxide). *J Biomater Sci Polym Ed*, 15, 797–811.
- Gibson, P. W., Schreuder-Gibson, H. L. and Rivin, D. (1999) Electrospun fiber mats: transport properties. *AIChE J*, 45, 190–195.
- Gu, S. Y., Wu, Q. L., Ren, J. and Vancso, G. J. (2005) Mechanical properties of a single electrospun fiber and its structures. *Macromol Rapid Commun*, 26, 716–720.
- Han, X. J., Huang, Z., He, C. and Liu, L. (2007) Preparation and characterization of core-shell structured nanofibers by coaxial electrospinning. *High Performance Polymers*, 19, 147–159.
- Hou, H. and Reneker, D. H. (2004) Carbon nanotubes on carbon nanofibers: a novel structure based on electrospun polymer nanofibers. *Advanced Materials*, 16, 69–73.
- Huang, P. C., Chen, S., Lai, C., Reneker, D. H., Qiu, H. and Yr, Y. (2006) Electrospun polymer nanofibers with small diameter. *Nanotechnology*, 17, 1558–1563.
- Huang, Z. M., Zhang, Y. Z., Kotai, M. and Ramakrishna, S. (2003) A review on polymer nanofibers by electrospinning and their applications in nanocomposites. *Comp Sci Technol*, 63, 2223–2253. DOI: 10.1016/S0266-3538(03)00178-7.
- Kessick, R. and Tepper, G. (2004) Microscale polymeric helical structures produced by electrospinning. *Appl Phys Lett*, 84, 4807. DOI: 10.1063/1.1762704
- Kidoaki, S., Kwon, I. K. and Matsuda, T. (2005) Mesoscopic spatial designs of nano- and microfiber meshes for tissue-engineering matrix and scaffold based on newly devised multilayering and mixing electrospinning techniques. *Biomaterials*, 26, 37–46.
- Kim, G. H. (2008) Electrospun PCL nanofibers with anisotropic mechanical properties as a biomedical scaffold. *Biomed Mater*, 3, 25010. DOI:10.1088/1748-6041/3/2/025010
- Koombhongse, S., Liu, W. and Reneker, D. H. (2001) Flat polymer ribbons and other shapes by electrospinning. *J Polym Sci*, 39, 2598–2606.
- Li, D. and Xia, Y. (2004a) Electrospinning of nanofibers: reinventing the wheel? *Adv Mater*, 16, 1151–1170. DOI: 10.1002/adma.200400719
- Li, D. and Xia, Y. (2004b) Direct fabrication of composite and ceramic hollow nanofibers by electrospinning. *Nano Letters*, 4, 933–938.
- Li, D., Wang, Y. and Xia, Y. (2003) Electrospinning of polymeric and ceramic nanofibers as uniaxially aligned arrays. *Nano Lett*, 3, 1167–1171.
- Liang, D., Hsiao, B. S. and Chu, B. (2007) Functional electrospun nanofibrous scaffolds for biomedical applications. *Adv Drug Deliv Rev*, 59, 1392–1412. DOI: 10.1016/j.addr.2007.04.021.
- Matthews, J. A., Simpson, D. G., Wnek, G. E. and Bowlin, G. L. (2002) Electrospinning of collagen nanofibers. *Biomacromolecules*, 3, 232–238.
- McManus, M. C., Boland, E. D., Koo, H. P., Barnes, C. P., Pawlowski, K. J., Wnek, G. E., Simpson, D. G. and Bowlin, G. L. (2006) Mechanical properties of electrospun fibrinogen structures. *Acta Biomater*, 2, 19–28.
- Megelski, S., Stephens, J. S., Chase, D. B. and Rabolt, J. F. (2002) Micro- and

- nanostructured surface morphology on electrospun polymer fibers. *Macromolecules*, 35, 8456–8466.
- Norris, I. D., Shaker, M. M., Ko, F. K. and Macdiarmid, A. G. (2000) Electrostatic fabrication of ultrafine conducting fibers: polyaniline/polyethylene oxide blends. *Synthetic Metals*, 114, 109–114.
- Pham, Q. P., Sharma, U. and Mikos, A. G. (2006) Electrospinning of polymeric nanofibers for tissue engineering applications: a review. *Tissue Eng*, 12, 1197–1211.
- Ramakrishna, S., Fujihara, K., Teo, W. E., Lim, T. C. and Ma, Z. (2005) *An Introduction to Electrospinning and Nanofibers*, World Scientific Publishing Co., Singapore.
- Reneker, D. H. and Fong, H. (2005) *Polymeric Nanofibers*, ACS Symposium Series 918, American Chemical Society, Washington DC.
- Reneker, D. H. and Yarin, A. L. (2008) Electrospinning jets and polymer nanofibers. *Polymer*, 49, 2387–2425. DOI :10.1016/j.polymer.2008.02.002.
- Reneker, D. H., Yarin, A. L., Fong, H. and Koombhongse, S. (2000) Bending instability of electrically charged liquid jets of polymer solutions in electrospinning. *Journal of Applied Physics*, 87, 4531–4547.
- Sell, S. A., McClure, M. J., Barnes, C. P., Knapp, D. C., Walpoth, B. H., Simpson, D. G. and Bowlin, G. L. (2006) Electrospun polydioxanone–elastin blends: potential for bioresorbable vascular grafts. *Biomed Mater*, 1, 72–80.
- Sell, S., Barnes, C., Simpson, D. and Bowlin, G. (2008) Scaffold permeability as a means to determine fiber diameter and pore size of electrospun fibrinogen. *J Biomed Mater Res A*, 85, 115–126.
- Sun, Z., Zussman, E., Yarin, A. L., Wendorff J. H. and Greiner, A. (2003) Compound core–shell polymer nanofibers by co-electrospinning. *Adv Mater*, 15, 1929–1932.
- Sundaray, B., Subramanian, V., Natarajan, T. S., Xiang, R. Z., Chang, C. C. and Fann, W. S. (2004) Electrospinning of continuous aligned polymer fibers. *Appl Phys Lett*, 87, 1222–1224.
- Um, I. C., Fang, D., Hsiao, B. S., Okamoto, A. and Chu, B. (2004) Electro-spinning and electro-blowing of hyaluronic acid. *Biomacromolecules*, 5, 1428–1436.
- Wang, M., Jin, H. J., Kaplan, D. L. and Rutledge, G. C. (2004) Mechanical properties of electrospun silk fibers. *Macromolecules*, 37, 6856–6864.
- Yang, D., Lu, B., Zhao, Y. and Jiang, X. (2007) Fabrication of aligned fibrous arrays by magnetic electrospinning. *Advanced Materials*, 19, 3702–3706.
- Zhang, Y., Huang, Z. M., Xu, X., Lim, C. T. and Ramakrishna, S. (2004) Preparation of core–shell structured PCL-r-gelatin bi-component nanofibers by coaxial electrospinning. *Chem Mater*, 16, 3406–3409.
- Zhang, Y., Ouyang, H., Lim, C. T., Ramakrishna, S. and Huang, Z. M. (2005) Electrospinning of gelatin fibers and gelatin/PCL composite fibrous scaffolds. *J Biomed Mater Res B Appl Biomater*, 72, 156–165.
- Zong, X., Kim, K., Fang, D., Ran, S., Hsiao, B. S. and Chu, B. (2002) Structure and process relationship of electrospun bioabsorbable nanofiber membranes. *Polymer*, 43, 4403–4412.



## Melt spinning and other techniques for the production of nanofibres and microfibres

---

Y OHKOSHI, Shinshu University, Japan

**Abstract:** The production methods of ultrafine fibre or nanofibre can be roughly classified into three types: self-organization, random and filament. Direct spinning, conjugate spinning, polymer blend spinning and laser-heated flow drawing belong to the filament type. Conjugate spinning is divided into a sea-island type, a divided (exfoliation) type and a multilayer type by the conjugate form. Ultra-fine fibre of diameter 2–6  $\mu\text{m}$  is produced on an industrial scale by this method. For multilayer conjugate spinning, by compiling the polyester layer and nylon layer alternately, fibre having an optical interference colouring nature was developed. By heating with laser irradiation, running fibre can be heated far more rapidly and uniformly than by heating by heat transfer. High-draw-ratio stable flow drawing is realizable by laser irradiation heating of running fibre, and ultrafine fibre of diameter about 1  $\mu\text{m}$  was made by this technique. The fiber can be stably drawn to a large draw ratio with minimal thermal degradation by rapid and uniform laser-irradiated heating of polymer melt extruded from the spinning nozzle to a high-temperature, low-viscosity state and by extending the polymer melt sharply with electrostatic power. Nanofiber with 39 nm diameter and 0.54 GPa tensile strength can be formed by combining conjugated spinning and laser-heated flow drawing.

**Key words:** nanofibres, microfibres, conjugated melt spinning, laser drawing, flow drawing, polymer blend.

### 18.1 Introduction

The surface area of a fibre is proportional to the diameter, whereas the fineness of the fibre is proportional to the square of the diameter, and the flexural rigidity of the fibre is proportional to the fourth power of the diameter. Therefore, if the diameter of a single fibre is 1/10 under the condition of the same total fineness, a flexible ultrafine fibre bundle, which will have 10 times the surface area and 1/100 the flexural rigidity, should be obtained. In particular, a fibre that has a diameter less than 10  $\mu\text{m}$  shows typical characteristics caused by its big surface area and low flexural rigidity. Fibres that have a diameter less than 10  $\mu\text{m}$  and less than 100 nm are generally termed (ultra)fine fibres and nanofibres respectively, but the terminological definition is not exact.<sup>1,2</sup>

The production methods of ultrafine fibres and nanofibres can be roughly classified into three types: (1) self-organization, (2) random, and (3) filament.<sup>1</sup> Carbon nanofibre (CNT) is a typical example of (1) and gel is also a typical

self-organization nanofibre aggregate. A trial attempt to create nanofibre directly in the polymerization process has also been reported.<sup>3–8</sup> For example, polyethylene fibre of 30–50 nm diameter is obtained by nanochannel spinning using mesoporous material including a polymerization catalyst.<sup>8</sup> This type of nanofibre tends to have a short length and many branches, which cause problems in controlling the aggregate structure of the nanofibre. Therefore, for most of these nanofibres, even if the nanofibre itself originally had a high function, it is difficult to produce a product with high functionality.

Melt blowing, electrospinning (electrospray),<sup>2,9,10</sup> centrifugal spinning, flash spinning, etc., are all used in the type (2) fibre manufacturing process. Although a longer fibre will be obtained from this process compared with type (1), because of the web-like form of the product it is generally difficult to use it as a fibre bundle. Since the product obtained is restricted to a sheet-like form, mechanical fabrication techniques, such as weaving, knitting and braiding, are difficult to apply and so the use of the product is also limited to filters, etc. Moreover, since a continuous fibre bundle is not obtained, uniform drawing and annealing is difficult, which generally causes inferior physical properties such as low tensile strength and low heat resistance, except for flash-spun fibres.<sup>1</sup> For these, melt blowing is used as a method of obtaining an ultrafine fibre web, by blowing away polymer extruded from the spinning nozzle by a hot and supersonic air jet. Although the diameter of the fibre obtained is usually several microns, a fibre of diameter 1  $\mu\text{m}$  or less can also be obtained. Alternatively, flash spinning is a technique used to produce a nonwoven fabric of high-strength ultrafine fibres by blowing a hot and high-pressure polymer solution from a spinning nozzle at supersonic speed, so that it is extended and then solidifies quickly. High molecular oriented fibre with a diameter from a submicron to tens of microns is obtained by this technique.

Direct spinning, conjugate spinning, polymer blend spinning and laser-heated flow drawing are used for type (3) production.<sup>1,11</sup> Since a continuous fibre bundle with unidirectionally oriented fibres is obtained, it is excellent for processing into products of various forms, such as cloth. There is also the important fact that it is easy to obtain ultrafine fibre which has excellent heat and mechanical physical properties, such as tensile strength, tensile modulus and heat resistance, since redrawing after take-up is possible. Although simple direct spinning is the best method for reliability and productivity, the manufacture of a fibre thinner than 3  $\mu\text{m}$  is difficult using this process.<sup>12</sup> On the other hand, as shown below, ultrafine fibres are obtained by conjugate spinning, polymer-blend spinning and laser-heated flow drawing. Moreover, a still finer fibre can be manufactured by combining these techniques.

## 18.2 Conjugated melt spinning

Fibre with a predetermined component arrangement in its cross-section can be made by extruding two or more kinds of components, which combine in the back of a spinning nozzle and elongate before extrusion. This technique is called conjugate spinning. By separating the obtained fibre along the fibre axis, an ultrafine fibre can be produced. Conjugate spinning is divided into a sea-island type, a divided (exfoliation) type and a multilayer type by the conjugate form. Ultrafine fibre with a diameter of 2–6  $\mu\text{m}$  is produced on an industrial scale by this method.<sup>13</sup> In particular, by using the sea-island type of conjugate spinning, an ultrafine fibre with a diameter of the order of a submicron can be manufactured by ultra-multi-island conjugate spinning for which the island number exceeds 1000. Using multilayer conjugate spinning, by compiling alternate polyester and nylon layers, a fibre with an optical interference colour (Morphotex<sup>®</sup>) was developed.<sup>14–16</sup> The fibre has 60 or more layers whose thickness, below 100 nm, is accurately controlled.

## 18.3 Melt spinning of polymer blends

An ultrafine fibre with a diameter from a submicron to several microns is obtained by making fibre from a mixture of two or more kinds of polymers, and removing the sea component afterwards. Although it used to be said that the spinning was generally difficult and a nanofibre of 100 nm or less in diameter could not be produced by the technique, it has been used successfully in producing continuous nylon-6 nanofibre of average diameter 60 nm by strictly controlling the flowing behaviour within the nozzle and the thinning process of the thread. The nanofibre exhibits special features, such as a water-swelling characteristic and a high water-retention property that is three or more times that of normal nylon.<sup>13</sup>

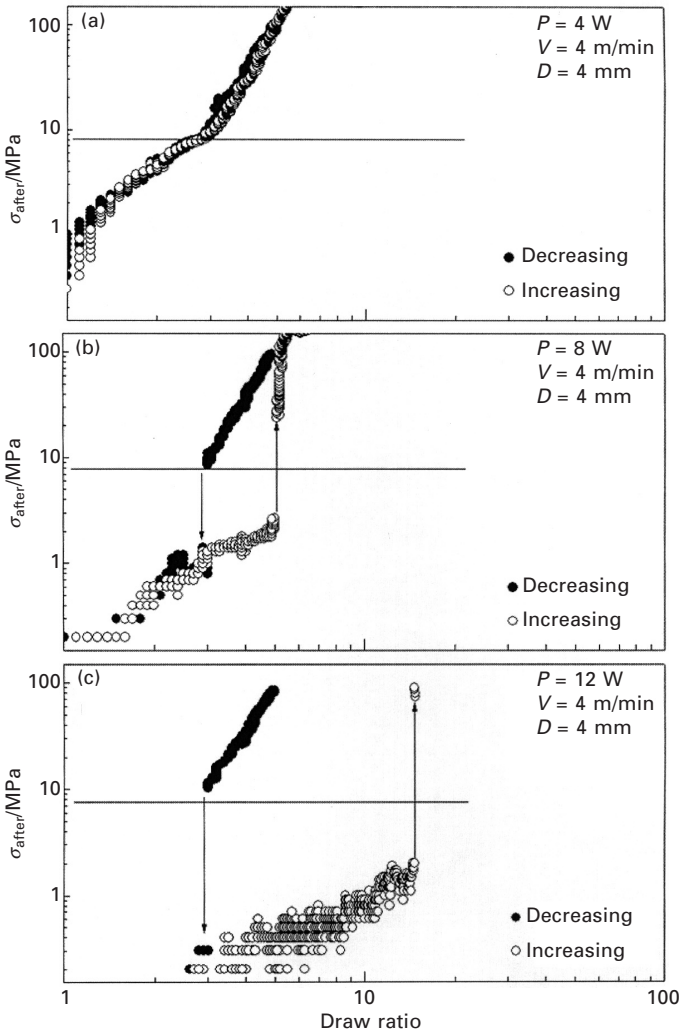
## 18.4 Laser-heated flow drawing

Generally, a molecule chain is oriented to the fibre axis by extending during the drawing process. For this reason, the maximum draw ratio is usually restricted to about 20, except in the case of ultra-drawing, used, for example, in the drawing of ultra-high molecular weight polyethylene for macromolecules with a small number of molecular entanglements, while the draw ratio of melt spinning can reach the thousands. However, if the fibre temperature is high enough and the drawing stress is small enough, the molecule chain cannot be oriented enough to cause orientation-induced crystallization, and then the fibre can be drawn with no structural limitation. This is called ‘flow drawing’. Even though there is no structural limitation, there is a restriction of drawing stability if the fibre is heated by ordinary heat transfer. Therefore,

the maximum flow draw ratio is limited to less than 10 in this case. The instability of flow drawing is caused by drawing in the heating region.<sup>17</sup> With ordinary heat transfer heating, it is impossible to avoid drawing in the fibre heating region because rapid and uniform heating is impossible by this method. However, using laser irradiation, running fibre can be heated far more rapidly and uniformly than by heat transfer. High-draw-ratio stable-flow drawing is actually made possible by the laser irradiation heating of running fibre,<sup>18, 19</sup> and ultrafine fibre with a diameter of about 1  $\mu\text{m}$  has been made by this technique.<sup>11, 20, 21</sup> Not only can this technique be used for manufacturing ultrafine fibre, but it can also be used for obtaining fibre from difficult thermo-processing materials, such as a polymer which has a particularly high melt viscosity or a polymer liable to thermo-degrade.

A catastrophic transition between a flow-drawing state and a neck-drawing state is shown in Fig. 18.1. Bordering on several MPa of drawing stress, discontinuous transition is observed between the neck-drawing state and the flow-drawing state. In the neck drawing state, the fibre deforms quickly in the short section as long as the fibre diameter and causes orientation-induced crystallization, while in the flow-drawing state the fibre deforms in the long section from several millimetres to hundreds of millimetres and does not cause orientation-induced crystallization. In the state of neck-drawing, the drawing point moves to the upper stream with the increase of energy irradiated to the fibre; therefore, since the temperature at the drawing point hardly changes, the drawing stress also depends very little on either the running speed or the laser power. On the other hand, in the state of flow-drawing, the fibre temperature rises monotonically with the increase in irradiated energy, and since elongational viscosity falls, the drawing stress also decreases with the irradiated energy. Therefore, the hysteresis between the neck-drawing state and the flow-drawing state increases with the increase in irradiated energy, and can be flow-drawn to the larger draw ratio. The drawing state observed by the measurements as shown in Fig. 18.1 is summarized in Fig. 18.2. Since the horizontal axis is proportional to the laser energy irradiated to the fibre, it almost corresponds to the fibre temperature for the flow-drawing state. This figure shows that the maximum flow draw ratio is increasing almost exponentially with the increase in the irradiated laser energy.

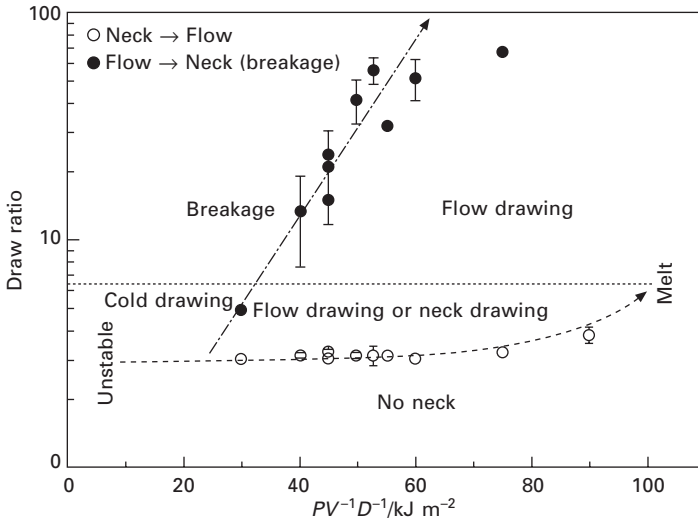
Although the flow drawing is stabilized by laser irradiation heating, it can be further stabilized by the application of a high voltage.<sup>23-25</sup> The fibre can be stably drawn to a large draw ratio with minimized thermal degradation by the rapid and uniform laser-irradiated heating of the polymer melt extruded from the spinning nozzle to a high-temperature and low-viscosity state, and by markedly extending the polymer melt with electrostatic power.



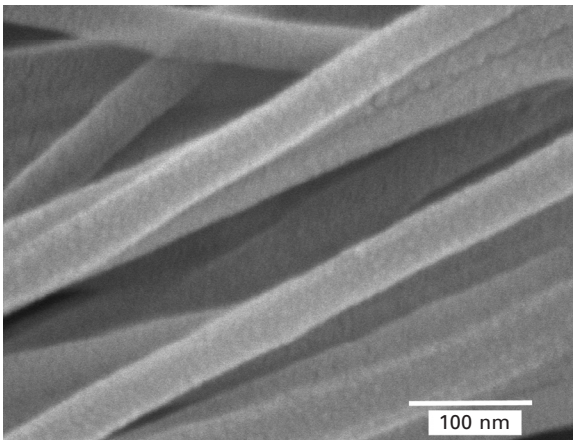
18.1 Drawing stress profiles measured for laser neck-drawing and laser flow-drawing.<sup>22</sup>  $P$ ,  $V$  and  $D$  are the laser power, the fibre feeding speed, and the diameter of the laser beam, respectively.

### 18.5 Nanofibres made by conjugated melt spinning and laser-heated flow drawing

Thinner fibres can be made by combining super-multi-island conjugate melt-spinning and laser-heated flow-drawing techniques. Figure 18.3 shows PET nanofibre made by conjugated melt spinning, flow drawing, and the extraction of the ‘sea’ component. The diameter of the obtained nanofibre, about 39 nm, corresponds to several times that of the diameter of microfibril. Moreover,



18.2 Drawing states obtained by the measurements as shown in Fig. 18.1.<sup>22</sup>



18.3 SEM image of PET nanofibres obtained by removing the 'sea' component of conjugated-spun and flow-drawn fibre.<sup>26</sup>

the conjugated spun and flow-drawn fibre has mechanical properties like those of polyester fibres used for commodities; i.e. 0.54 GPa tensile strength and 27% elongation at break.

### 18.6 Conclusion

Methods used to produce nanofibre or ultrafine fibres can be divided into two categories: self-organization together with chemical synthesis, and mechanical

drawing. The latter is further divided into filament-type techniques, by which continuous fibre bundles composed of unidirectionally oriented ultrafine fibres can be made, and random-type techniques, by which web-like product forms are mainly made. Nanofibres made by the filament-type production method have many merits, i.e. the product form has high flexibility and high mechanical and thermal properties. Some filament-type techniques are used to produce ultrafine fibres, i.e. conjugated melt spinning, melt spinning of polymer blend, laser-heated flow drawing, etc. A still finer fibre can be manufactured by combining not only these techniques but also melt blowing and electrospinning.

## 18.7 References

1. M. Okamoto, 'Saisin no boushi gijutsu', 205 (1992).
2. T. Ochi, *Sen-i to Kogyo*, **60**, P-266 (2004).
3. H. S. Yoon, *Nature*, **326**, 580 (1987).
4. W. S. Lyoo, B. C. Kim, W. S. Ha, *Polym. J.*, **30**, 424 (1998).
5. B. C. Kim, W. S. Lyoo, W. S. Ha, *Polym. J.*, **32**, 159 (2000).
6. K. Tajima, T. Aida, *Royal Soc., Chem. 2000: Chem. Commun.*, 2399 (2000).
7. K. Akagi, G. Piao, S. Kaneko, K. Sakamaki, H. Shirakawa, M. Kyotani, *Science*, **282**, 1683 (1998).
8. K. Kageyama, J. Tamazawa, T. Aida, *Science*, **285**, 2113 (1999).
9. Y. Yamagata, H. Matsumoto, *Kobunshi*, **52**, 829 (2003).
10. H. Takahashi, *Sen-i to Kogyo*, **60**, P-33 (2004).
11. A. Suzuki, *Kobunshi*, **52**, 833 (2003).
12. M. Yoshimura, *Kobunshi*, **47**, 416 (1998).
13. T. Ochi, *Sen-i to Kogyo*, **63**, P-423 (2007).
14. M. Yoshimura, K. Iohara, H. Tabata, S. Shimizu, *Sen-i to Kogyo*, **56**, P-348 (2000).
15. H. Tabata, M. Yoshimura, S. Shimizu, *Sen-i to Kogyo*, **57**, P-248 (2001).
16. M. Yoshimura, *Kobunshi*, **52**, 826 (2003).
17. K. Toriumi, A. Konda, *Sen-i Gakkaishi*, **40**, T-193 (1984).
18. Y. Ohkoshi, Japanese patent publication 2002-115117.
19. Y. Ohkoshi, J. Watanabe, W. Okumura, Y. Gotoh, M. Nagura, *Sen-i Gakkaishi*, **58**, 182 (2002).
20. A. Suzuki, N. Mochizuki, Japanese patent publication 2003-166115.
21. A. Suzuki, N. Mochizuki, *J. Appl. Polym. Sci.*, **88**, 3279 (2003).
22. Y. Ohkoshi, *Kinou-Zairyō*, **23**, 44 (2003).
23. N. Ogata, G. Lu, T. Iwata, S. Yamaguchi, K. Nakane, T. Ogihara, *J. Appl. Polym. Sci.*, **104**, 1368 (2007).
24. N. Ogata, S. Yamaguchi, N. Shimada, G. Lu, T. Iwata, K. Nakane, T. Ogihara, *J. Appl. Polym. Sci.*, **104**, 1640 (2007).
25. M. Takasaki, H. Fu, K. Nakata, Y. Ohkoshi, T. Hirai, *Sen-i Gakkaishi*, **64**, 29 (2008).
26. K. Nakata, K. Fujii, Y. Ohkoshi, Y. Gotoh, M. Nagura, M. Numata, M. Kamiyama, *Macromol. Rapid Commun.*, **28**, 792 (2007).

- 
- $\alpha^*$  law, 104
  - $\alpha$ -relaxation process, 362
  - acriflavin, 126
  - Acrilan, 306
  - acrolein, 201, 203
  - acrylic fibres, 126, 305–12
    - chemical structure, 305–6
    - acrylonitrile and comonomers
      - chemical structures, 305
    - comonomers types, 306
      - halogen-containing comonomers, 306
      - ionic comonomers, 306
      - neutral comonomers, 306
    - cross-sectional shapes, 310
    - definition, 305
    - formation mechanism during solidification, 310
    - mechanical properties, 311
    - physical properties, 311
    - preparation, 306–8
    - properties, 309, 311–12
    - solution spinning methods, 307–8
      - air-gap wet spinning, 308
      - dry spinning, 307
      - wet spinning, 307–8
    - spinning methods diagrams, 308
    - typical polymer concentrations, 307
  - air-gap wet spinning, 161, 308
  - Alcaligenes eutrophus*, 214
  - aliphatic polyesters, 188
    - chemistry, 209–13
    - degradation mechanism, 213
    - monomers, 210
    - sterilisation and packaging, 212–13
  - alum carmine stains, 124
  - ammonia, 300
  - amorphous region, 439
  - Amosite fibres, 139
  - Amphibole, 135
  - animal fibres, 138
  - antimony trioxide, 191
  - Antophyllite fibres, 139
  - aqueous hyaluronic acid, 467
  - Arabidopsis thaliana*, 214
  - aramid fibres, 208, 394–409, 416, 428
    - chemistry, 395
    - future trends, 409
    - polymerisation from its monomers
      - TDC and PPD, 395
    - relationship between microstructure and resulting properties, 403–9
      - fibre modulus vs draw ratio, 403–9, 405
      - fibre strength vs fibre modulus, 407
    - relationship between spinning conditions and resulting microstructure, 395–403
    - optical micrograph between crossed polarisers, 401
    - optical retardation pattern in regular aramid fibre, 403
    - pleated sheet structure as proposed by Dobb, 402
    - PpPTA crystal structure, 400
    - proposed microfibrillar structure, 400
    - viscosity of PpPTA–sulphuric acid solutions vs polymer concentration, 396
    - wet spinning processes, 397
  - argon, 299
  - AS fibres, 432–7



- as-spun fibre, 457
- asbestos, 139, 318
- Asota, 287
- astra blue, 123
- atomic force microscopy, 136, 137
- attenuated total reflectance spectroscopy, 25–6
- Autocrimp process, 292
- AVEBE amylose, 77
- Avrami equation, 165
- axial shift, 433
  
- Baeyer–Villiger oxidation, 211
- Barham and Arridge model, 368
- beam scattering, 54–63
  - Bragg's law as reflection of the X-ray beam on atomic layer planes, 58
  - centrosymmetric atomic scattering, 56
  - Fourier transforms in direct and reciprocal space, 58
  - orientation, 61–3
    - chain molecule diffusion pattern, 61
    - cylindrical coordinates of a helix, 62
    - threefold helix schematic representation, 64
  - scattering geometry, 54
  - space groups, 60
    - biological space groups, 60
  - temperature and disorder factor, 59
- bending instability, 332
- 4,4'-benzalinedylene-terephthalamide, 405–6
- benzothiazole ring, 447
- benzyl alcohol, 238
- berberine sulphate, 126, 128, 129
- Berek Compensator, 217
- Bessel function, 63
- Bio-PDO, 202
- Biopol, 214
- Boltzmann constant, 162
- Bragg spacing, 439, 440
- Bragg's law, 57, 66
  - X-ray beam reflection on atomic layer planes, 58
- Brassica napus*, 214
  
- bulk fibre modulus, 448
  
- <sup>13</sup>C-CP/MAS-NMR, 72–3
- calcium chloride, 124, 395
- calcofluor, 126, 127
- cantilever technique, 478
- caprolactone, 211, 329
- carbon fibres, 9
- carbon nanofibre, 484
- carbon nanotubes, 10, 300, 474–5
  - on nanofibres produced by electrospinning of PAN, 475
- carboxybenzene propionic acid, 416
- Carother's Law, 183
- cellulose, 123
- cellulose nanofibrils, 133
- cellulose nitrate, *see* nitrocellulose
- cellulose whiskers, 133, 137
- centrosymmetric atomic scattering function, 55
- Certran, 352, 359, 370, 372
- chain explosion, 385, 386
- chain extenders, 329
- chain modulus, 404
- Chardonnet process, 7
- Charpy impact test, 370
- Chemical Market Resources Inc., 340
- Chrysotile, 135, 139
- clays, 300
- coagulation process, 435
- cobalt catalyst, 201
- collapsing process, 309
- colloidal silver, 131
- Compton scattering, 89
- computer-aided procedure, 75
- computer simulations, 449
- confocal fluorescence microscopy, 127–9
- confocal reflection microscopy, 129–30
- conjugate fibres, 288
- conjugated melt spinning, 486, 488–9
  - multilayer type, 486
  - sea-island type, 486
- continuous polymerisation process, 192, 199, 203
- continuous polymerisation spin-draw route, 220
- controlled-rheology grades, 279
- conventional single-screw equipment, 289
- Corterra fibres, 224

- cotton, 5, 126, 374
- Couette apparatus, 373, 374
- Coulombic force, 332, 461
- Creora, 325
- Crocidolite fibres, 139
- Cross and Bevan reagent, 124
- crystalline modulus, 433, 435, 448
- crystalline polymers, 160–2
- crystallinity, 87–98
  - Hermans and Weidinger methods, 89–91
    - amorphous scattering vs integrated crystalline intensity, 90
  - powder X-ray diagram, 89
  - results and disorder factor D, 96–8
    - disorder parameter, 97
  - Ruland and Vonk, 91–6
    - Debye–Scherrer diffraction technique, 92
    - nomogram values of polypropylene, 93
- crystallisation, 166, 260
- crystallisation peak temperature, 478
- crystallite size, 98–106
  - Fourier method, 102–6
    - melt crystallised and annealed polyethylene, 105
    - non-uniform Fransen micelles, 107
  - gold vs nylon-6 x-ray diffraction profiles, 99
  - line width method, 100–2
  - Pearson VII functions, 100
- cuprammonium process, 7
  
- Dacron, 185, 352
- Dalon, 306
- data reduction, 64–70
  - random distribution, 67
  - single crystal rotation, 67
  - uniaxial fibre orientation in the normal beam technique, 67–70
  - cylindrical-shaped film detector in diffraction experiment, 69
  - diffraction experiment with a flat film as detector, 68
- Debye-Scherrer diffraction technique, 91
- decitex count, 217
- deformation process, 284
- Degussa process, 201
- Denapla, 265
  
- denier count, 217
- Dexon, 211
- dichroic ratio, 24
- differential interference contrast, 123
- differential scanning calorimetry, 195, 242, 381, 382
- diffraction, 48–52, 54
  - basic, 48–50
    - experimental setup, 49
    - packing arrangement and expected X-ray diffraction pattern, 50
  - optical transforms of chain molecules, 51–2, 54
  - projected continuous helix, 53
  - optical transforms of lattices, 50–1
    - idealised setup, 51
    - masks sequence and corresponding optical transforms, 52
    - optical transforms of circles of different sizes, 52
- diffraction spots, 46–7
- diffuse reflectance spectroscopy, 26
- diisocyanate monomer, 330
- dimethylacetamide, 307
- dimethylformamide, 338, 346, 462
- dimethylsulfoxide, 307, 317
- direct condensation, 258
- direct esterification method, 190
- dispersity, 278
- Dolan, 306
- Doufas' model, 172
- draw-bulking yarn, 219
- draw-down factor, 217
- draw ratio, 298
- draw textured-yarn, 219
- dry-jet-wet spinning, 161
- dry spinning, 161, 237, 307, 309
- Dyneema, 352
- Dynel, 306
  
- Elaspan, 327
- Elastane, 325, 327
- elastic compliance, 404
- elastic modulus, 399, 406
- elastic strain, 404
- elastin, 475
- elastomeric fibres
  - processing, structure, and properties, 325–49
  - conclusions and future trends, 349

- elastomeric polymer alloy fibres, 342–7
- polyester copolymer fibres, 336–7
- polyolefin elastomeric fibres, 340–1
- polyurethane fibres, 327–9
- production of polyurethane fibres, 329–35
- styrene copolymers elastomeric fibres, 337–40
- elastomeric polyester urethane, 346
- elastomeric polymer alloy fibres, 342–7
  - olefinic/EPDM alloy fibre alloy, 343–5
  - polyurethane/polyacrylonitrile alloy fibres, 346–7
- electromagnetic radiation, 24
- electron diffraction, 135, 139, 431, 436, 449, 477
- electron diffractogram, 71
- electron microscopy, 449, 450
  - fibre analysis, 130–5
    - scanning electron microscopy, 130–3
    - transmission electron microscopy, 133–5
- electron spin resonance, 363
- electrospinning, 239–40, 294
  - basic process setup, 461
  - composite nanofibres, 474–6
    - carbon nanotubes, 474–5
    - encapsulated structures, 475
    - polymer blends, 475–6
  - description, 461–3
- electrospun haemoglobin in 2,2,2-trifluoroethanol, 471
- electrospun PDLA
  - concentration effect on nanofibre microstructures, 463
  - electric field effect on membranes microstructures, 464
  - nanofibres from dimethyl formamide, 463
- experimental setup
  - core-shell nanofibres from co-electrospinning, 468
  - forced air assisted electrospinning device, 469
- fibre structure, 476–8
  - complex pore structure, 476–7
  - crystal orientation, 477–8
  - fibre diameter, 476
  - gradient structures in fibres, 478
  - molecular alignment, 477
  - surface structure, 477
- fibres produced from PEO and PASA, 473
- future trends and conclusion, 480–1
- hollow fibres fabricated by direct coaxial electrospinning, 472
- important parameters, 462–3
  - concentration, 462
  - field strength, 462–3
  - flow rate, 463
- influence of structure on properties, 478–80
  - chemical composition, 479
  - conductivity of nanofibres, 480
  - mechanical properties, 478–9
  - surface properties, 480
  - surface reflection and scattering, 479
  - thermal properties, 479
  - transport properties, 479
- influence on polymeric nanofibres structure, 460–81
- instabilities, 463, 465–7
  - bead defects in fibres, 465–7
  - bending instability, 465
  - branched fibres from poly(ether imide) in 1,1,1,3,3,3-hexafluoro-2-propanol, 465
  - branching, 463, 465
  - onset and development of bending instabilities, 466, 468
- porous fibres obtained via electrospinning of PLLA solution in dichloromethane, 470
- process variations, 467–8
  - blowing assisted electrospinning, 467–8
  - core shell spinning, 467
  - multilayer and mixed electrospinning, 468
- randomly oriented electrospun mat and highly aligned fibrous mat, 473
- types of fibres produced, 469–76
  - aligned fibres, 472–4

- conductive fibres, 474
- flattened or ribbon-like nanofibres, 470
- helical fibres, 472
- hollow fibres, 472
- non-woven nanofibres, 470
- porous nanofibres, 469–70
- woven and non-woven fabrics, 471
- electrospraying, 332
- electrostatic forces, 432, 440
- energy dispersive spectroscopy, 130
- energy dispersive X-ray analysis, 139
- environmental scanning electron microscopy, 132, 281, 382
- equilibrium melting temperature, 381
- Escherichia coli*, 202, 215
- ester interchange process, 190, 199
- European Synchrotron Radiation Facility, 458
- extended-chain structure, 429
- extended depth of field, 122
- Eyring equation, 360
- Falang, 319
- Federal Safety Specifications for Vehicles, 271
- Fibravyl, 321
- fibre reinforced cement, 318
- fibres
  - basic concept, 158–60
  - formation of shape and structure of fibres, 160
  - structural model and related characteristics of fibres, 158–60
  - behaviour analysis in fibre processing, 170–6
  - crystallisation kinetics in melt spinning process numerical analysis, 170–2
  - crystallisation on-line measurement, 172–3
  - orientation development on-line measurement, 173–6
  - relation between birefringence and stress/temperature, 174
  - changes in diameter and birefringence along spinning line
    - high molecular weight PET, 173
    - polypropylene, 175
  - conclusions and future trends, 176–7
  - development in synthetic production, 157–77
  - fundamental mechanism, 160–70
  - applied stress orientation on crystallisation rate, 168
  - crystallisation under non-isothermal conditions, 165–7
  - effect of flow on crystallisation, 168–70
  - limitation of theory based on assumption of isokinetic crystallisation, 170
  - molecular orientation, 162, 164–5
  - temperature-dependent behaviour of polymers, 167
  - types of crystalline polymers from fibre processing viewpoint, 160–2
- heat-retaining capacity comparison, 322
- hierarchical structure classification, 158–9
  - first-order structure, 158–9
  - second-order structure, 159
  - third-order structure, 159
- LOI of various fibres, 322
- microscopic analysis, 121–40
- nanofibres and microfibrils production classification, 484–5
- conjugated melt spinning, 486
- division, 489–90
- drawing states, 489
- drawing stress profiles, 488
- laser-heated flow drawing, 486–7
- melt spinning and other techniques, 484–90
- nanofibres made by conjugated melt spinning and laser-heated flow drawing, 488–9
- PET nanofibres, 489
- polymer blends melt spinning, 486
- stress-optical and stress-orientation coefficient of various polymers, 164
- structure and performance, 3–20
  - conclusion, 18–19
  - fibre structure development, 10–16
  - formation, 5–10
  - future trends, 19–20
  - traditional uses, 16–18

- structure formation behaviour in spinning and drawing processes, 163
- synthetic fibre categories, 215–22
  - continuous filament yarn, 215–20
  - staple fibre, 220–2
- triboelectric series of various fibres, 322
- see also* specific fibres
- fibrinogen, 473
- field emission SEM, 130, 137
- filament yarn melt-spinning, 215–20
  - F/Y melt spinner diagram, 216
  - filament yarn drawing, 217–19
  - filament yarn texturising, 219
  - industrial filament yarn, 220
- Flory equation, 364
- flow drawing, 486
- fluidised bed reactor, 195
- fluorescence microspectrophotometry, 126
- FMVSS 302 test, 271
- folded chain lamellae crystals, 159
- formalisation process, 315
- Fortisan, 7
- Fourier Transform Infrared spectroscopy, 135–6, 479
- Friedel–Crafts type catalysts, 189
- fringed micelle model, 159
  - micro-fibril, 159
- gel, 484
- gel permeation chromatography, 353, 354, 364
- gel spinning, 238, 276
- germanium dioxide, 191
- Gibbs–Thomson equations, 381
- glass fibre, 139, 363
- glass fibre reinforced plastics, 17
- glass transition temperature, 161, 260, 308, 327, 329, 478, 479
- glycerol/lactic acid, 124
- glycolic acid, 209
- godet, 216
- Griffith model, 366–7, 408
- guaiacyl lignin, 123–4
- Guinier's method, 436
- hagfish slime threads, 6
- HBA, *see p*-hydroxy-benzoic acid
- heat-setting, 313
- helium, 299
- hemicellulose, 123
- heparin, 476
- Hercules Hifax 1900, 383
- Hermann's orientation, 438
- hexafluoroisopropanol, 204, 211
- hexafluoroisopropanol solution, 240
- high density polyethylene, 278
- high-modulus, high-tenacity fibres, *see* HM-HT fibres
- HM fibres, 432–7
- HM+ fibres, 432–7
- HM-HT fibres, 4, 8–9
- HMLS yarn, 220
- Hosemann's paracrystal theory, 450
- hydroacetic acid, 209
- hydrogen bonds, 233
- hydrogen storage, 472
- hydroquinone, 414
- 6-hydroxy-2-naphthoic acid, 290
- hydroxynaphthoic acid, 416
- hysteresis, 220, 335
- Imprafix TH LSG, 347
- Imprafix VP LS 2323, 347
- infrared spectroscopy, 23–7
  - dynamic FTIR spectroscopic characterisation, 27
  - infrared absorption in polymeric materials, 23–4
  - local stress measurements, 26–7
  - polarisation and orientation analysis, 24–6
  - electric field vector orientation, 25
- inherent viscosity, 184
- inorganics, 9
- Instron tensile testing machine, 353, 355
- integral breadth, 440
- interference microscopy, 125
- interlocked shish-kebab structure, 159
- interpenetrating network, 346
- intrinsic viscosity, 184, 197
- iodine green stains, 124
- ion exclusion resins, 202
- irradiation, 212–13
- islands-in-the-sea concept, 214, 287, 288, 294
- ISO 14855, 268
- ISO 15985, 268
- isokinetic conditions, 170

- isotactic polypropylene, 233  
 Isovyl, 321
- Japanese Flame-retardant Fibre Products Association, 271  
 JIS K 7201, 270
- K-II process, 317  
 Kanekalon, 306  
 Kanekalon AD-70, 319  
 Kenaf/PLA board, 273  
 keratin-associated proteins, 5–6  
 Kevlar, 8, 233, 352, 373, 413, 455  
*Klebsiella pneumoniae*, 202  
 Kraton, 337  
 Kraton D1101, 338
- L-lactide, 213  
 lactic acid, 270  
 lactone, 182  
 lamellar overgrowth, 374  
 laser-heated flow drawing, 486–7, 488–9  
 laser irradiation, 487  
 laser-Raman spectroscopy, 385  
 layered paracrystalline model, 159  
 lead citrate, 133  
 Legendre polynomials, 32, 108  
 lignin, 123  
 Limit of Oxygen Index, 262, 270, 321  
 linear low density polyethylene, 278  
 liquid CO<sub>2</sub>, 130  
 liquid nitrogen, 130  
 longitudinal acoustic mode Raman spectroscopy, 26  
 Lorentz factor, 65–6  
 low density polyethylene, 278  
 Lycra, 327  
 Lycra Spandex, 326  
 Lyocell, 7  
 Lyon silk industry, 217  
 lyotropic aramid–sulphuric acid spindope, 404  
 lyotropic liquid crystal, 413  
   composition and fibre properties, 418
- M5 fibre, *see* PIPD fibre  
 macro-voids, 309  
 magnesium stearate, 330  
 Mark–Houwink equation, 184–5, 198, 200, 204
- Maule reagent, 123  
 Maule staining, 124  
 Maule test, 139  
 Maxon, 212  
 Maxwell element, 359  
 McLafferty rearrangement, 192, 203  
 mechanical theory, 430  
 melt flow index, 279  
 melt-processible rubbers, 342  
 melt spinning, 161, 235–7  
   and associated fibre processing, 215–22  
   filament yarn melt-spinning, 215–20  
   introduction, 215  
   spin finishes, 222  
   staple fibre, 220, 222  
 melting temperature, 479  
 meridional diffraction, 440  
 metallocene catalysts, 162, 279  
 micelles, 12–16  
   continuous structure, 14  
   fringed structure, 13  
   model, 13  
   modified fringed structure, 15  
   range of molecular order, 14  
   uniformed structure, 16  
 Michelson interferometer, 138  
 micro-drawing, 423  
 microfibrils, 484–90  
 microscopy  
   fibre analysis, 121–40  
     electron microscopy, 130–5  
     future trends, 140  
     identification of natural and artificial fibres, 138–9  
     infrared techniques, 135–6  
     optical microscopy, 121–30  
     scanning probe microscopy, 136–7  
     X-ray tomography and other techniques, 137–8  
 nylon mesh in selecting optimum accelerating voltage, 132  
 thermomechanical pulp fibres stained with berberine sulphate, 129  
 wood fibre  
   cell wall layers and individual cellulose microfibrils, 132  
   thermomechanical pulp fibres and fibre-cement board, 131

- microvoids, 298–9, 435
- Mirande's reagent, 124
- Mitsui-FI catalyst, 383
- modacrylic fibres
  - chemical structure, 305–6
    - typical modacrylic fibre chemical structure, 306
  - comonomers used
    - halogen-containing comonomers, 306
    - ionic comonomers, 306
    - neutral comonomers, 306
  - cross-section formation mechanism during solidification, 310
  - definition, 306
  - preparation, 306–8
  - properties, 309, 311–12
  - spinning methods diagrams, 308
  - three methods in solution spinning, 307–8
    - air-gap wet spinning, 308
    - dry spinning, 307
    - wet spinning, 307–8
  - typical polymer concentrations, 307
- molecular weight, 184–5
- Monacryl, 212
- monofil, 211
- monomers, 181, 210
- monomolecular crystals, 381
- Montan wax, 321
- Morphotex, 486
- mutual electrostatic repulsion, 461
  
- N*-methyl pyrrolidone, 395
- nanofibres, 10, 134, 484
  - production by melt spinning and other techniques, 484–90
- nanofibrillation, 294
- nanofluidics, 472
- naphthalene-dicarboxylic acid, 406
- natural fibres, 5–6
- NatureWorks, 188, 213, 258
- necking effect, 298
- nematic liquid crystalline solution, 398
- neutron diffraction, 431
- neutron scattering, 369–70, 385
- nitric acid etching, 354
- nitrocellulose, 6
- nitrogen, 300
- N,N'*-dimethylformamide, 307
  
- Northolt equation, 450
- Northolt model, 404, 435
- nuclear magnetic resonance spectroscopy, 34–9
  - classical magnetic moment in a static magnetic field, 36
  - Zeeman splitting of nuclear energy levels, 37
- nylon, 326, 352, 355, 374
- nylon 6, 467
- nylon 66, 8
- nylon fibres, 125, 126
  
- OLED technology, 224
- olefinic/EPDM alloy fibre alloy, 343–5
  - melt spinning extrusion process, 343
  - stretching ratio dependence
    - fibre diameter, 345
    - percent elongation, 344
    - percent reduction of cross-section area, 345
    - tensile stress, 344
- optical coherence tomography, 138
- optical interference microscopy, 402
- optical microscopy, 11
  - fibre analysis, 121–30
    - brightfield imaging of stained fibres, 123
    - confocal fluorescence microscopy, 127–9
    - confocal reflection microscopy, 129–30
    - histochemical staining of fibres, 123–5
    - interference microscopy, 125
    - optical techniques for unstained fibres, 121–3
    - polarised light microscopy of plant fibre, 125
    - widefield fluorescence microscopy, 125–7
- optical refractive index, 399
- orientation, 106–12, 114, 160
  - basics, 106–10
    - geometry for a fibre x-ray diffraction, 107
  - experimental determination, 111–12, 114
  - Bragg angle function, 112

- coefficients as a function draw ratio for 2 reflections, 115
- coefficients from fitted Pearson VII curves, 114
- normalised x-ray intensity distribution, 113
- order parameter, 113
- polar angle function, 111
- Orlon, 306
- oxygen, 300
- p*-benzoic acid, 290
- p*-hydroxy-benzoic acid, 414, 416
- palladium powder, 439
- PALM, 140
- para-aramid fibre, 423
- partial crystalline fibres
  - X-ray analysis of structure, 46–116
    - crystallinity and disorder, 87–98
    - data reduction, 64–70
    - diffraction, 48–52, 54
    - preferred orientation, 106–12, 114
    - reflection profile, crystallite size and disorder, 98–106
    - structure determination, 70–7, 79–81, 83, 85, 86–7
    - theoretical considerations, 54–63
- partially oriented yarn, *see* POY
- PASA, *see* poly(aniline sulfonic acid)
- PATAg procedure, 133
- PBO, *see* poly-*p*-phenylenebenzobisoxazole fibres
- PBT, *see* poly(butylene terephthalate)
- PBZT, *see* poly-*p*-phenylenebenzobisthiazole fibres
- PDS filament for sutures, 212
- Pe-Ce fibre, 319
- Pellathane, 325
- Pentex, 187, 206, 207, 208, 209
- PEO, 472
- Perlon-U, 186
- Peterlin model, 368
- phase contrast, 123
- phenylene, 447
- 1,4-phenylenediamine, 395
- phenylhydroquinone, 417
- phosgene, 183, 212
- phthalocyanine pigment, 297
- 4Pi, 140
- piezoelectric devices, 136
- PIPD fibre, 399, 455–9
  - chemistry, 455–6
  - coarse structure and conclusion, 459
  - crystal structure, 456–8
  - formula, 456
  - modulus calculations, 458–9
  - possible crystal lattices, 457
  - problem of lateral weakness, 455
  - spacing increase in heated as-spun fibre, 458
- plant fibres
  - confocal fluorescence and reflection microscopy, 128
  - division
    - bast fibres, 138–9
    - hardwood fibres, 138–9
    - monocotyledon fibres, 138–9
    - softwood fibres, 138–9
  - light microscopy, 122
- plateau creep rate, 360
- platinum catalyst, 201
- pleated sheet structure, 401
- PLLA, 479
- Poisson's ratios, 300
- polarised ATR-FTIR spectroscopy, 243
- polarised light microscopy, 130
- poly(1-butene) fibres, 283–4, 294, 296, 297
- poly[2,6-diimidazo[4,5-b:4',5']]pyridinylene-(2,5-dihydroxy)phenylene] fibre, *see* PIPD fibre
- poly(3-methyl-1-butene), 284
- poly(4-methyl-1-pentene), 284, 294, 296
- poly-*p*-phenylenebenzobisoxazole fibres, 429–51, 455, 458, 459
  - calculated modulus for PBO and PBZT fibres, 431
  - comparison between measured and calculated normal mode vibration, 444–6
  - comparison between measured and calculated shift factors, 449
  - crystallite size, 434
  - deformation of fibre structure, 439–49
  - crystalline modulus, 439
  - Hosemann's analysis with stress, 440



- electron diffraction from ultrathin section of PBO, 437
- fibre structure, 430–8
  - model, 438
  - previous works, 430–2
- future trends, 449–50
  - crystallographic analysis, 449
  - in-situ study of fibre structure formation during spinning, 449–50
  - structural study of single PBO fibre with synchrotron radiation, 450
- inverse of PBO Young's modulus, 435
- mechanical properties, 432
- mechanical series-parallel model, 447
- molecular design and theoretical modulus, 430
- obtained suitable parameters for series model, 449
- Raman shift and broadening factors, 443
- stress dependence of Hosemann's plot for three PBO fibres, 441
- structural study of PBO AS, HM and HM+ fibres, 432–7
  - current PBO fibres, 432
  - electron microscopy, 436–7
  - fine structure, 435–6
  - molecular orientation and fibre modulus, 433–5
  - wide-angle X-ray diffraction, 432–3
- synthesis and polymerisation, 430
- unit cell parameters, 433
- vibrational spectroscopy application to analyse fibre structure, 440–2
  - change of vibrational frequencies with stress, 440–2, 447
  - Raman shift factor and morphology of fibres, 447–9
- wide-angle X-ray scattering profiles for HM+ fibre, 434
- poly-*p*-phenylenebenzobisthiazole fibres, 429, 430, 431, 433, 435
- poly-*p*-phenyleneterephthalamide fibres, 429, 430, 431, 434, 441
- polyacrylonitrile, 237, 346, 474
- polyacrylonitrile fibres, 7–8, 312, 373
- polyamide 6 (PA6), *see* polyamide fibre
- polyamide 66 (PA66), *see* polyamide fibre
- polyamide fibre, 232–52, 289
  - $\alpha$  crystalline orientation and amorphous orientation, 246
  - characterisation, 240–8
    - density and birefringence, 240–1
    - IR spectroscopy, 242–5
    - NMR spectroscopy, 245–8
  - crystal structures of PA66 and PA6, 234
  - crystallinity values obtained from different methods, 243
  - electrospinning set-up, 239
  - extension at break vs crystalline fraction, 251
  - fibre formation, 233–40
    - dry spinning, 237
    - electrospinning, 239–40
    - gel spinning, 238
    - melt spinning, 235–7
    - spinning with plasticizers, 239
    - wet spinning, 237–8
    - zone drawing and zone annealing, 238
  - industrial-scale melt spinning apparatus, 235
  - microstructure influence on properties, 248–51
    - dyeing behaviour, 250–1
    - heat setting, 248–9
    - mechanical properties, 249–50
  - on-line birefringence vs distance of spinneret, 236
- PA6 fibres
  - draw ratio effect on orientation parameter, 247
  - methylene resonances of  $^{13}\text{C}$  CPMA spectra, 247
  - phase fraction as function of spinning speed, 248
  - unpolarised IR spectra, 245
- PA66 fibres
  - crystalline and amorphous orientation, 244
  - fractional recovery vs heat-setting temperature, 249
  - terminal modulus vs crystalline fraction, 250

- volume fraction
  - $\alpha$ ,  $\gamma$  and amorphous fraction as function of draw ratio for PA6 fibres, 242
  - crystallinity as function of draw ratio for PA66, 241
  - crystallinity as function of heat-setting temperature for PA66, 240
- wet spinning of fibres equipment, 237
- polyamide/Spandex fibres, 349
- polyaniline, 474
- poly(aniline sulfonic acid), 472
- polybutadiene, 337, 338
- polybutadiene elastomeric fibres, 341
  - electroprocessed structures, 342
- poly(butylene terephthalate), 186, 336, 458
  - chemistry, 198–200
  - crystal parameters, 200
  - manufacture, 199–200
  - Mark–Houwink parameters, 200
  - properties, 200
- polycaprolactam, 222
- polycaprolactone (PCL), 211–12, 222, 467
- polycarbonate (PC), 469
- polycondensation reaction, 181
- poly(dimethyl siloxane), 330
- polydioxanone, 212, 473, 475
- polydispersity, 277, 395
- poly(D,L-lactide) (PDLA)
  - nanofibres electrospun from dimethyl formamide, 463
- polyester, 8
- polyester copolymer fibres, 336–7
  - poly(ether ester) fibre surface, 336
- polyester fibres, 126, 181–225, 264, 289, 489
  - aliphatic polyesters chemistry, 209–13
    - degradation mechanism, 213
    - monomers, 210
    - polycaprolactone, 211–12
    - polydioxanone, 212
    - polyglycolide, 210–11
    - polylactide, 211
    - polytrimethylene carbonate, 212
    - sterilisation and packaging, 212–13
  - biodegradable polyester properties, 210
  - comparison of melting temperature and glass transition temperature, 206
  - disposable fibre chemistry, 213–15
  - effect of fibre structure on properties, 222–3
  - main types, 185–9
  - melt-spinning and associated fibre processing, 215–22
    - filament yarn melt-spinning, 215–20
    - introduction, 215
    - spin finishes, 222
    - staple fibre, 220, 222
  - monomers for biodegradable polyesters, 210
  - PBT chemistry, 198–200
  - PEN chemistry, 206–9
  - PET chemistry, 189–98
  - physical properties, 208
  - polymer viscosity and molecular weight, 184–5
  - production of 2,6-NDA by Mitsubishi Gas Chemical/Amoco process, 188
  - PTT or PPT chemistry, 200–5
  - world markets, future trends and thoughts for the future, 223–5
- polyester (polyarylate) fibre, *see* Vectran fibres
- polyester urethane (PEU)/polyacrylonitrile (PAN) alloy fibres
  - crosslinked PEU/PAN fibres, 348
  - stress-strain curves for noncrosslinked and crosslinked electrospun fibre mats, 348
- poly(ether ester), 336
- polyethylene, 81, 83, 85–7, 276
  - conformation and packing, 85
  - crystalline structure, 282
  - goniometer X-ray diagram, 84
  - structural parameters, 86
  - X-ray fibre diagrams, 83
- polyethylene fibre, 352–88, 485
  - comparison of experimental and calculated tensile strength values, 365

- comparison of typical properties of compacted PET, PE and PP sheets, 372
- creep and recovery mechanical models, 360
- creep rate plots, 361–2
- crystalline phase of highly oriented linear polyethylene, 369
- dependence of tensile strength on molecular weight ratio, 365
- draw ratio vs time of draw, 356
- dynamic modulus and  $\tan \delta$ , 368
- fibres based on UHMW-PE, 372–88
  - on the borderline between solid and melt, 384–8
  - solution (gel)-spinning, 372–80
  - solvent-free processing routes, 380–4
- hot compacted PE fibre sheet morphology, 371
- maximum draw ratio attainable vs draw temperature, 358
- melt spun high-modulus polyethylene fibres, 353–72
  - commercialisation, 370–2
  - dynamic mechanical behaviour and structure, 367–8
  - fibre strength, 363–7
  - tensile creep behaviour, 359–63
  - tensile drawing, 353–9
  - thermal properties, 369–70
- quenched and slow cooled sheets, 354
- Young's modulus as function of draw ratio, 357
- polyethylene fibres, 38–9
- poly(ethylene glycol), 476
- polyethylene naphthalate (PEN), 187
  - chemistry, 206–9
  - comparison of three unit cells, 207
  - melt polymerisation process, 206–7
  - melt-processing, 208–9
  - properties and morphology, 207
- poly(ethylene oxazoline), 475
- poly(ethylene oxide) (PEO), 329, 467
- polyethylene terephthalate nanofibre, 488
- polyethylene terephthalate (PET), 157, 185–6, 258, 355, 416, 459
  - birefringence and density plotted against take-up velocity, 169
  - chemistry, 189–98
  - CP, 193–5
  - DEG formation, 193
  - DSC trace for commercial PET polymer flake, 196
  - ethylbenzene and xylenes production from C<sub>8</sub> aromatic fraction, 190
  - Mark–Houwink coefficients, 198
  - morphology, 198
  - morphology showing various features, 219
  - oligomers, 197
  - physical parameter, 198
  - polymerisation from BHET monomer, 191
  - production of monomer BHET from TA and EG, 189
  - SPP, 195–7
  - typical continuous polymerisation unit, 194
- poly(ferrocenyldimethylsilane), 477
- poly(glycolic acid), 473
- polyglycolide, 210–11
- polyhexamethylene adipamide, *see* nylon 66
- poly(L-lactide) (PLLA), 469
- polylactic acid, 188
- polylactic acid fibres, 257–74
  - accelerated weathering test results, 272
  - aerobic composting test result, 267
  - anaerobic digestion test result, 268
  - antibacterial activity tested with *Staphylococcus aureus* ATCC 6538P inocula, 270
- applications, 272–4
  - clothing, 273–4
  - geotextiles, 272
  - home furnishings, 273
  - industrial fabrics, 272–3
  - wipes and nonwovens, 273
- biodegradation in compost at 60°C, 261
- change in tenacity and relative viscosity of PLA multifilaments, 267
- comparison of fibre/textile properties of PLA with those of PET, 264
- effects of melt-spinning take-up speed on crystallinity and thermal shrinkage, 266